Comets as natural laboratories:

Interpretations of the structure of the inner heliosphere

Yudish Ramanjooloo

University College London, Mullard Space Science Laboratory

Holmbury St. Mary, Dorking

RH5 6NT

Submitted for Ph.D. degree

Supervisor: Dr Geraint H. Jones

Prof Andrew J. Coates

Statement of Original Work

I, Yudish Ramanjooloo confirm that the work presented in this thesis is my own. Where information has been derived from other sources, I confirm that this has been indicated in the thesis.

The following publications resulted from the work performed in this thesis.

- IAUC 9261, Nov. 2013: Imaging of comet ISON, using 2.0m Liverpool telescope.
- A&G (2014) 55 (1): 1.32-1.35 doi:10.1093/astrogeo/atu038 (Available at http://www.bit.ly/yudish)
- Y. Ramanjooloo et al., Near-Sun Solar Wind Velocity Measurements from Multi-point Observations of Sun-grazing Comet C/2011 W3 (Lovejoy), (in preparation)
- G. H. Jones, Brandt J., Y. Ramanjooloo, Solar wind interaction with comet C/2004 Q2 (Machholz), (in preparation)

Abstract

Comets can be considered to be natural laboratories of the inner heliosphere, as their ion tails trace the solar wind flow. Much has been learnt about the heliosphere's structure from in situ solar wind spacecraft observations. Their coverage is however limited in time and space. This thesis proposes to address these constraints and ascertain the validity of analysing comets' ion tails as complementary sources of information on dynamical heliospheric phenomena and the underlying continuous solar wind.

Solar wind conditions influence comets' induced magnetotails, formed through the draping of the heliospheric magnetic field by the velocity shear in the mass-loaded solar wind. I present a novel imaging technique and software to exploit the vast catalogues of amateur and professional images of comet ion tails. My projection technique uses the comet's orbital plane to sample its ion tail as a proxy for determining radial solar wind velocities in each comet's vicinity. Making full use of many observing stations from astrophotography hobbyists to professional observatories and spacecraft, this approach is applied to several comets observed in recent years.

Complementary velocities, derived from folding ion rays and a velocity profile map built from consecutive images, are provided as an alternative means of quantifying the solar wind-cometary ionosphere interaction. I review the validity of these techniques by comparing near-Earth comets to solar wind models in the inner heliosphere and extrapolated measurements by ACE to a near-Earth comet's orbit. My radial velocities are mapped back to the solar wind source surface to identify sources of the quiescent solar wind and heliospheric current sheet crossings. Comets are found to be good indicators of solar wind structure, but the quality of results is strongly dependent on the observing geometry. Many ion tails also show a constant curvature, so far unexplained, which further complicates the interpretation of tails' orientations.

"There is one day every year, where we unknowingly pass the anniversary of the day the dinosaurs were wiped out by a comet." – u/dewinstainleigh (Reddit)

Table of Contents

List of Figures

List of Tables

1. Solar Wind

1.1. Introduction

The existence of the solar wind was not conjectured until the latter half of the past century. The first hints of the wind's existence came from observations of comets' ion tails (Hoffmeister 1943; Biermann 1957). Biermann argued that solar radiation pressure was not enough to explain the acceleration of plasma structures within comet tails. We now know that the solar wind not only dictates the orientation of cometary ion tails, but also directly influences their rapidly-changing morphologies.

The solar wind is, very generally, a bimodal stream of fully ionised, electrically neutral, fast plasma; its two states distinguished by their velocities, particle temperatures, density and composition, which vary with both time and space. A close correlation between the composition of the solar corona and the solar wind indicates that it is an extension of the hot solar corona that expands radially outwards into the solar system (Kivelson & Russell 1995). Due to the extreme temperature and energies in the outer corona, the solar wind's velocity reaches supersonic levels a few solar radii above the solar surface (Hundhausen 1972). This continuous outflow of collisionless solar plasma carries with it a remnant of the solar magnetic (**B**) field, known both as the interplanetary magnetic field (IMF) and the heliospheric magnetic field (HMF), that pervades interplanetary space (e.g. Kivelson & Russell 1995).

Variations in the solar wind's properties are large in the equatorial region compared to a more steady flow with small variations in the polar region (Schwenn 2001). Figure 1.1 is a polar plot of Ulysses/SWOOPS solar wind speeds during Ulysses's first near-polar orbit of the Sun, during solar activity minimum. The solar wind flows radially outwards from the Sun at supersonic and super-Alfvénic velocities, with velocities ranging from typically 450 km s^{-1} with large variations in the equatorial region, to around 750 km s^{-1} with a small scatter in the polar regions (Brandt & Snow 2000; McComas 2002). The Ulysses and the ACE (Advanced Composition Explorer) spacecraft, amongst others, have gathered an extensive wealth of data from which measurements of the solar wind speed, composition, magnetic field strength and direction have been made.

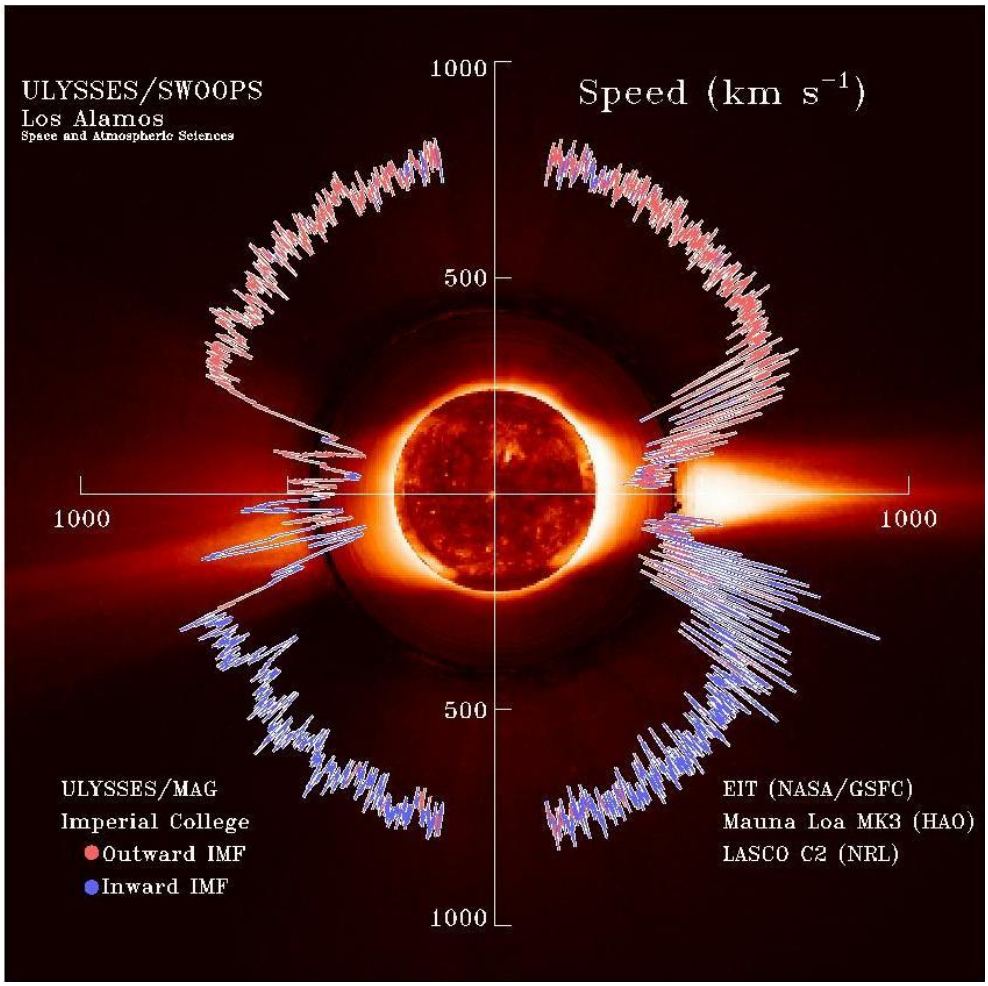

Figure 1.1: Diagram from Ulysses measurements of solar wind speed and magnetic polarity during solar minimum (McComas 2002).

The slow solar wind has been observed to originate above regions of closed magnetic field lines. During solar minimum, the high density, slow solar wind emanates from a 'belt of streamers' of about 20^{o} (Owens & Forsyth 2013) - 40^{o} (Schwenn 2001) width in latitude in the equatorial region, as seen in Figure 1.1. Coronal holes are regions with open magnetic fields, from which the homogeneously high speed, low density solar wind emerges. The latitudinal boundaries between the coronal holes and streamer belts are relatively narrow. The longitudinal boundaries are also sharp when close to the sun and become less well-separated with increasing heliocentric distance (r_H) (Schwenn 2001). Regions of opposite polarity are separated by the heliospheric current sheet (HCS). Figure 1.2 portrays an idealised scenario where the HCS structure hasn't been distorted by solar wind speed variations and large scale transient solar wind phenomena. Well beyond the scale of this figure, the heliopause, where the

solar wind and the interstellar medium meet, defines the heliospheric boundaries of the solar system (~100 AU from the Sun).

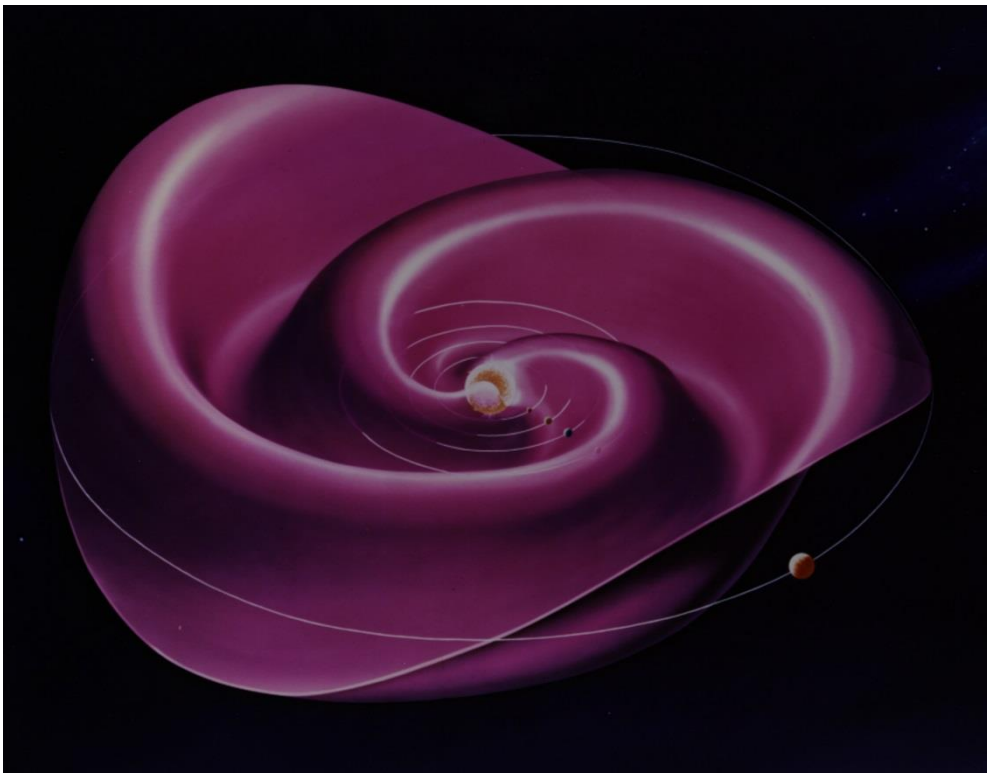

Figure 1.2: Image of three-dimensional structure of the heliospheric current sheet by W. Heil and J. M. Wilcox. The Sun rotates anti-clockwise with respect to other solar system bodies. Image courtesy of the Wilcox observatory webpage.

Ulysses's second orbit during solar maximum shows a much more complex and varied picture of the solar wind velocity compared to the well-ordered and uniform flow of the solar wind in two well defined regions during solar minimum (McComas 2002). The highest speed flows were generally limited to around 500 – 600 km s^{-1} during this period with only a few intervals, which lasted up to several days, reaching over 700 km s^{-1}. The solar cycle variation is evident from comparisons of Ulysses's velocity measurements against the sunspot numbers in Figure 1.3. At solar minimum, during the first orbit, the dark polar coronal holes dominate the corona at high latitudes, whilst during the second orbit, the bright streamers can be observed at all latitudes.

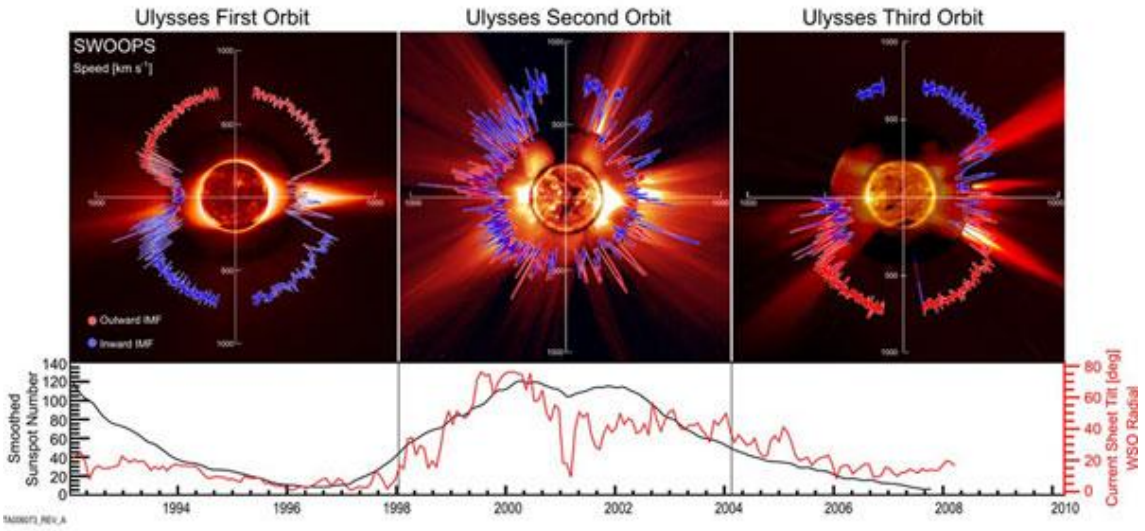

Figure 1.3: Solar wind latitudinal variations with solar cycle as measured by the SWOOPS instrument during Ulysses fast latitude scans. Bottom plot shows the sunspot numbers for the observing period, an indicator of solar cycle activity (McComas et al. 2008).

Typical solar wind parameters at 1 AU during solar minimum can be found in Table 1-1 and those of the solar ejecta and slow solar wind for solar maximum in Table 1-2 (both copied from Marsch (2006)).

Table 1-1: Fast (left) and slow (right) wind properties at 1 AU near solar activity minimum (Marsch 2006)

Characteristics	**Typical value or property**	**Typical value or property**
Wind speed (km s^{-1})	400 – 800	250 – 400
Proton density (cm^{-3})	3	10
Source region	Polar coronal holes	Top and sides of streamer belt
Signatures	Stationary for long times (weeks)	Sector boundaries embedded

Table 1-2: Properties of solar ejecta (left) and slow solar wind (right) at 1 AU near maximum (Marsch 2006)

Characteristics	**Typical value or property**	**Typical value or property**
Wind speed (km s^{-1})	400 – 2000	300 – 450
Proton density (cm^{-3})	10 and higher	10
Source region	Active regions, 30% related with erupting prominences	Streamers, sometimes active regions (ARs), small coronal holes
Signatures	Often as magnetic clouds; often associated with shocks	Shock waves often embedded

The solar wind can also be thought of as plasma flow tubes flowing radially outwards, dragging the frozen-in magnetic flux with them (e.g. Kivelson & Russell 1995) due to the near-infinitely electrically conductive plasma. These are often referred to as magnetic-flux tubes. As successive plasma parcels at the base of each flux tube move radially outward from a fixed location on the Sun, the source of the flux tube is also moving as the Sun rotates (Kivelson & Russell 1995). Streamlines connecting plasma parcels that share the same solar origin trace the Archimedean spiral configuration of the solar wind magnetic field as they expand radially into the heliosphere. Figure 1.4 illustrates the transition from non-radial expansion of the solar wind close to the Sun, to radial at the source surface and into the heliosphere. The source surface, ~ 2 to 2.5 $R_{\odot}$ from the Sun, is the hypothetical boundary at which the magnetic field and the plasma flow is assumed to become purely radial. Solar rotation combined with the anti-sunward flow of the plasma introduces an azimuthal component to the HMF and traces the Parker spiral. Its curvature is linked to the solar wind speed and the heliocentric distance. The angle between the magnetically linked flux tubes and the radial direction to the Sun is known as the Parker angle. Typically, it forms an angle of 45^{o} at the mean Earth orbit. Beyond the source surface, the solar wind is considered to be purely radial. Departures from radiality can occur within transient interplanetary solar wind phenomena such as co-rotating interaction regions and coronal mass ejections or when the solar wind encounters a magnetospheric obstruction within its flow. These interactions will cause a deflection of the bulk radial plasma outflow at the stream interface or at the CME's leading edge and introduce an azimuthal and/or meridional (north-south) component (Richardson et al. 1996; Jones et al. 2002; Owens & Cargill 2004).

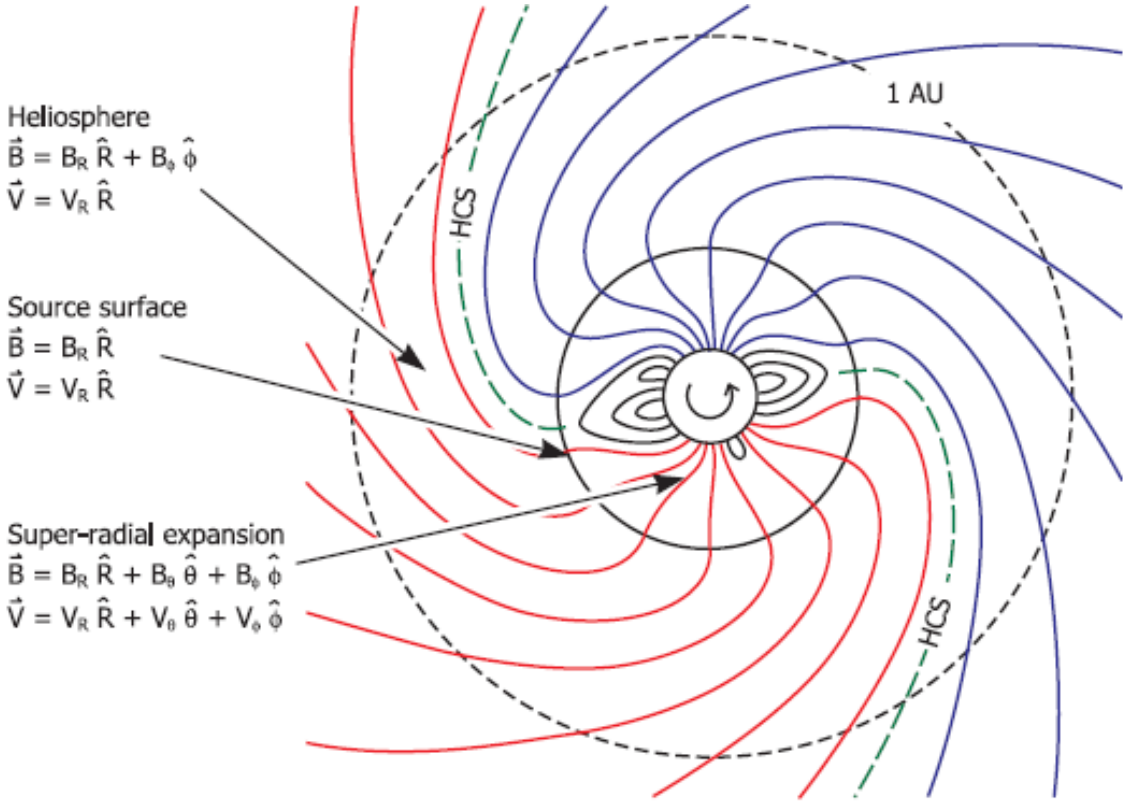

Figure 1.4: Extension of anti-parallel solar magnetic field from the Sun and into the heliosphere (Owens & Forsyth 2013). The HCS in green is typically formed above helmet streamers approximately at the centre of the streamer belt.

1.2. Coronal Holes

Coronal holes (CHs), found to lie above unipolar regions, are associated with rapidly expanding open magnetic fields and the acceleration of the high-speed solar wind (McComas 2002). At the minimum of the Sun's 11-year activity cycle, large coronal holes exist at the north and south heliographic poles and extend over a large fraction of the volume of the heliosphere. It could be argued that the 11-year cycle is but half of a full 22-year magnetic cycle for the sun to return to its initial magnetic state, i.e. for the dipole axis to switch from a North-South orientation to South-North and back to North-South to complete the 22 year cycle. Polar coronal holes are largest at solar minimum and often extend to lower latitudes during the declining phase of the solar cycle.

At solar maximum, McComas (2002) observed an initial shrinking of the large coronal polar holes. As the solar activity cycle progressed, the coronal holes disappeared as the corona

became increasingly complex. Multiple streamers were formed around the central streamer belt and extended to higher heliolatitudes and smaller coronal holes were observed at all heliolatitudes. Ulysses also observed strong, recurrent co-rotating interaction regions (CIRs) at the edges of the fast polar coronal holes (~10^o - 30^o heliolatitudes), formed from the interaction of these high speed solar wind streams and the slower solar wind regime from lower heliolatitudes (McComas 2002). Within this thesis, I refer to the transition from the slow to fast solar wind and vice versa as the transition region. This is not to be confused with the solar transition region, which is the layer of the solar atmosphere between the chromosphere and corona.

1.3. Co-Rotating Interaction Regions

The solar wind speed does not always remain uniform as it traverses the solar system. The velocity of solar wind can vary spatially and temporally throughout the interplanetary medium, due to its source region, and when it encounters obstacles in its path. Fast and slow solar wind can also interact turbulently with each other in space, with long-lived structures standing in the solar rotation frame being known as co-rotating interaction regions (e.g., Rouillard et al. 2008).

As the solar wind sweeps out across the solar system, it is inevitable that the plasma in the fast solar wind will catch up to and thus interact with the slower solar wind streams. The initial smooth interaction steepens into a forward shock as the solar wind becomes more supersonic, propagating westward and equatorward with respect to the ambient slower wind ahead of it, and a reverse shock, propagating eastward and poleward with respect to the faster solar wind ahead, as the heliocentric distance increases (Gosling & Pizzo 1999). The resulting shock waves can either accelerate or decelerate particles within the interacting plasma (Cravens 2004; Kivelson & Russell 1995; McComas 2002). The plasma between the two shocks becomes compressed and is deflected along the stream interface (Gosling et al. 1993), thus enhancing the plasma density and introducing non-radial components to the bulk plasma flow in this compression region. Fast solar wind plasma is deflected in the direction counter to solar wind rotation and slow solar wind along the solar rotation (Owens & Forsyth 2013). At the trailing end of the CIR, neighbouring fast and slow solar wind sources on the source surface

become increasingly spread out as the slow solar wind streams lag the fast solar flow. This results in a rarefaction region trailing the CIR, where the magnetic flux and plasma density are reduced (Owens & Forsyth 2013).

This type of interaction typically occurs at radial distances greater than 1 AU, where the density gradients at the intersection peak. In a rotating frame of reference, the co-rotating interaction regions would appear stationary. Although the interplanetary magnetic field lines are frozen into the solar wind plasma, there can be some contamination of material between the fast and slow solar wind populations, if a rotational discontinuity arises in the plasma flow. However, extensive mixing does not occur (Kivelson & Russell 1995), hence boundaries between the two regions are usually sharp at the leading edges (Forsyth & Marsch 1999). A tangential discontinuity at the stream interface, when it exists, allows demarcation between the slow and fast solar wind regimes (Schwenn 2001).

1.4. Coronal Mass Ejections

Coronal mass ejections (CMEs) are large-scale discrete and transient events. They are an important source of heliospheric variability in terms of plasma composition, velocity and magnetic field. These episodic eruptions from the Sun's corona inject large amounts of solar mass into the interplanetary medium at high velocities. Typically, the Sun loses 10^{14} – 10^{17} g of its mass per CME eruption (Vourlidas et al. 2002). Once they begin to interact with the interplanetary medium, they are known as interplanetary coronal mass ejections (ICMEs). If ICMEs are fast enough compared to their surroundings, they are preceded by a shock front, where particle acceleration can occur. Expanding as they propagate, ICMEs interact and disrupt the natural flow of the solar wind if they are travelling more quickly that the ambient plasma, sometimes producing chaotic magnetic enhancements and disturbances in the HMF structure in the sheath ahead of the ICME. The sheath refers to a region of compressed and deflected solar wind between the shock and the ICME's leading edge. Serious disruptions of the Earth's magnetosphere, including strong geomagnetic storms, have been associated with the eruptions of fast moving CMEs.

The frequency of CME occurrences varies with the solar cycle, ranging from an average of one CME every other day during solar minimum to several CMEs per day during solar maximum (St. Cyr et al. 2000). The mean linear speed of CMEs are derived from a first order fit to height-time measurements of the CME's leading edge in the LASCO C2 and C3 coronagraphs combined field of view of 2.1 to 32 $R_{\odot}$. Their mean speed is also directly influenced in the 11 year solar cycle spanning a range of 300 km s^{-1} at solar minimum to 500 km s^{-1} at maximum (Yashiro et al. 2004). Yashiro et al. (2004)'s statistical study further found a mean speed of 428 km s^{-1} for 'normal' CMEs and 957 km s^{-1} for halo CMEs. There isn't a definite upper limit for CME velocities; however, sporadic CME events with velocities exceeding 2000 km s^{-1} (Gopalswamy 2005; Tsurutani et al. 2006) and > 1800 km s^{-1} by ACE/SWEPAM (Skoug 2004) have been recorded. Yashiro et al. (2004) measured a CME width span of 20^{o} < width ≤ 120^{o} and recorded an increase from an average width of 47^{o} to 61^{o} as solar activity ramped up from minimum in 1996 to the early phase of solar maximum in 1999 before decreasing to 53^{o} in 2002 during the late phase of solar maximum. Most interestingly, Yashiro et al. (2004)'s study detected CMEs around the equatorial zone during solar minimum, in contrast to solar maximum, where CME eruptions occurred at all solar latitudes.

The model for the initiation of CMEs is not yet fully understood, however its origin is often associated with closed magnetic field regions such as active regions (Gopalswamy et al. 2009).

1.5. The Heliospheric Current Sheet

The heliospheric current sheet (HCS) is a natural component of the solar wind, separating magnetic field of opposite polarity embedded in the solar wind, as it radiates through the heliosphere. This warped separatrix, carried out by the solar wind, forms natural boundaries (also known as sector boundaries) in the interplanetary medium. Typically, there will be 2 to 4 sector boundaries in the ecliptic, with a ~ 27 day periodicity on Earth. This sector structure is the largest scale HMF structure. It is important to note that the HCS is a wavy sheet, often compared to a ballerina skirt, rotating with the Sun (e.g. Brandt & Snow 2000) and is tilted with respect to the ecliptic plane since the solar rotation and magnetic axes are not aligned.

The heliospheric current sheet is closest to the Sun's equatorial plane at solar minimum (Forsyth et al. 1997; Schwenn 2001). As solar activity increases, the HCS extends poleward as the solar cycle phase moves towards the solar maximum, when the heliospheric magnetic field reverses polarity (Forsyth et al. 1997). Brandt et al. (2000) concluded that the HCS can extend to latitudes of 45^{o} or higher from their observations of ion tail disconnection events. Using Ulysses data from high southern to high northern latitudes in 2000-2001, Jones et al. (2003) followed a gradual reversal in the orientation of the magnetic dipole field component during solar maximum, with the dipole axis crossing the solar equator during early 2000 – early 2001. This reversal was observed at heliolatitudes of > 80^{o}.

Structures and fluctuations in the HCS can be caused by "coronal mass ejections (CMEs), shears in the solar wind flow, solar wind eddies, waves or structure that results in multiple current sheets" (Brandt & Snow 2000). Forsyth et al. (1997) reported Ulysses's observations of a northward deflection of the HCS by 25^{o}.5 at solar minimum. This deflection was attributed to a long-lived active region.

Kinetic and MHD studies have hypothesised that velocity shears close to the HCS can lead to the formation of folds and ripples with increasing heliocentric distance (Merkin et al. 2011 and references therein). Extension of these folds into the heliosphere can lead to the hypothetical existence of a magnetic island of opposite polarity embedded within a unipolar magnetic field region. Merkin et al. (2011) showed that these simulations are resolution-sensitive and, with their MHD model, demonstrated the formation of an HCS fold by 1 AU and its subsequent disruption into a magnetic island by 1.5 AU due to mostly non-radial plasma motion.

1.6. Solar Wind Interaction with Solar System Objects

Planets (magnetised or unmagnetised), moons, asteroids and comets form natural obstacles in the solar wind flow. The magnetospheres, dynamo-generated or induced, of these bodies cause a deflection of the solar wind (Luhmann et al. 2004). These can be categorised into 4 groups (Kivelson & Russell 1995):

- Interaction with magnetised bodies, e.g. Earth, Jupiter and Saturn.
- Interaction with unmagnetised bodies with a dense atmosphere, e.g. Venus and Titan.
- Interaction with unmagnetised bodies with a weak atmosphere, e.g. comets.
- Interaction with unmagnetised bodies with no dense atmosphere and poor electrical conductivity, e.g. the Moon, asteroids and inactive cometary nuclei.

The intrinsic dynamo generated magnetic fields, for example at Earth, divert the solar wind plasma and HMF, around its magnetosphere. These interactions can result in large magnetic storms and create spectacular aurorae displays. Geomagnetic storms on Earth can be quite severe with the occasional CME being responsible for larger-scale disruptions.

The Moon is at the other extreme with no atmosphere, no large-scale magnetic field and is a poor electrical conductor. Prior to the early lunar missions, Earth's moon was predicted to have a classically induced magnetosphere (Luhmann et al. 2004). There is no bow shock formed and only extremely weak pick-up ion processes and thus the solar wind impacts the lunar surface directly and creates a wake behind it (Coates 2004). This particular solar wind interaction scenario will be elaborated upon in chapter 2 in the context of inactive cometary nuclei. In contrast to this model, a hypothetical atmosphereless molten metal body, which is highly electrically conductive, would have an induced magnetosphere due to a shielding current flow on its outer surface (Luhmann et al. 2004).

Cometary magnetosphere analogues: Mars, Venus and Titan

Mars, Venus and Titan all lack a global magnetic field, but possess an atmosphere and form a well-defined induced magnetosphere and magnetotail, the latter usually existing within Saturn's magnetosphere rather than in the solar wind. However, the Martian atmosphere is far thinner than that of Venus and Titan. Because of ionisation of their upper atmospheres, predominantly photoionisation, they possess ionospheres, and are thus subjected to solar wind interaction processes, where momentum and energy are imparted from the solar wind plasma to the collisionless outer ionospheric plasma (Bertucci et al. 2011).

Similarly to comets, these induced magnetospheres consist of a magnetic pile-up boundary, a region of magnetic enhancement from draped field lines, mass loading of the solar wind through the pick-up ion process, and deflection of the solar wind around the induced magnetosphere. Their magnetotails are induced on the nightside and share the characteristic of being defined by the upstream solar wind velocity and magnetic field orientation. A neutral current sheet separates the magnetotails' two lobes of opposite polarity.

Despite their similarities, each body contains unique characteristics which complicate our numerical simulations attempting to understand the numerous spacecraft observations available. At Mars, the boundary locations of its induced magnetosphere are influenced by the permanent localised crustal magnetic field enhancements (Bertucci et al. 2011; Luhmann et al. 2004). The Venusian magnetosphere is comparatively smaller than that of Mars, though the size of its magnetosheath is larger in terms of gyroradii than Mars (Bertucci et al. 2011). Its variable ionosphere is determined by variations in the incident EUV, which in turn is strongly dependent on the solar cycle, (Bertucci et al. 2011). Pioneer Venus Orbiter's primary mission's coincidence with solar maximum demonstrated that the ionospheric pressure balance currents in Venus's ionosphere were the dominant factor in balancing the magnetic pressure (Luhmann et al. 2004). Under conditions where the solar wind pressure is greater than Venus's outer ionospheric pressure, observations show that the solar wind magnetic field is not completely deflected and can penetrate into the ionosphere. Since the disappearance of the global dipole magnetic field of Mars 3.8 billion years ago, the solar wind has eroded most of the Martian atmosphere. This same process occurs at Venus when the solar wind diffuses through its ionosphere (Coates 2004).

The induced magnetosphere of Titan is the most complex of the three magnetic cavities presented here. Its orbit around Saturn of ~ 10 Saturnian radii, allows the moon to sometimes interact with the shocked solar wind (Cravens 2004). Titan lacks a permanent intrinsic magnetic field, which was confirmed by the Voyager and Cassini missions. Titan's ionosphere retains a long record of earlier background conditions that continue to influence its induced magnetosphere (Bertucci et al. 2011).

In chapter 2, I will focus only on the dynamical processes involved in the induced magnetospheres of comets due to the HMF, which are based on mass-loading.

1.7. The Comet-Solar Wind Paradigm

The comet-solar wind (comet-SW) paradigm [Figure 1.5], as described by Brandt & Snow (2000) from the Ulysses comet Watch (UCW) team of observers, shows a demarcation of the solar wind into two distinct regions under quiescent, non-solar maximum conditions:

- The equatorial region: The disturbed ion tails of comets 122P/de Vico in 1995 (Brandt et al. 1997), C/1992 B2 (Hyakutake) in 1996 (Snow et al. 2004) and C/1995 O1 (Hale-Bopp) in 1997 (Brandt & Snow 2000) reflected the variable nature of the slow solar wind outflow.

- The polar region: The ion tails of the comets listed above were observed to be relatively undisturbed. This suggested that the solar wind flow becomes less variable with increasing heliographic latitudes (Brandt & Snow 2000), matching expectations from Ulysses' first and third multi-latitudinal observations (McComas et al. 2008) .

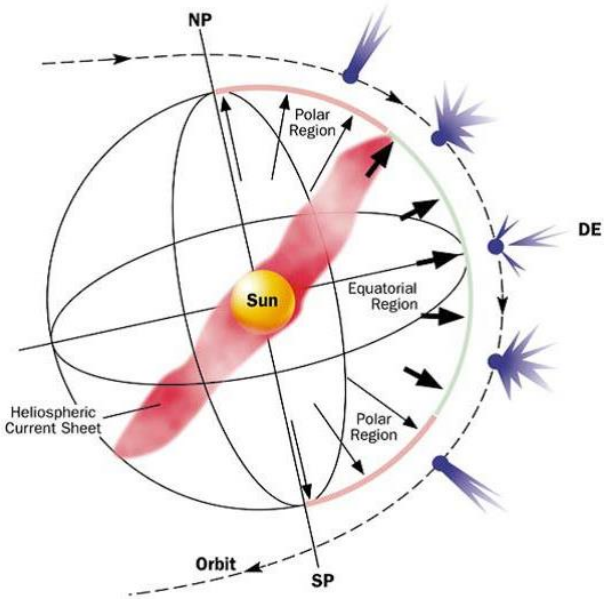

Figure 1.5: Cartoon illustrating the of comet-solar wind paradigm (Brandt & Snow 2000)

The two regions were separated by the maximum latitude of the heliospheric current sheet during solar minimum (Brandt & Snow 2000). The same model of the solar wind structure cannot be applied to observations near solar maximum [see second panel of Figure 1.3].

In Figure 1.5, the long and thin arrows show the relatively constant high-speed and low-density solar wind in the polar regions. The short and thick arrows represent the highly variable low-speed and high-density solar wind in equatorial region at solar minimum, which produces a disturbed ion tail. Visible disturbances such as knots and kinks increase in frequency when the comet is in an equatorial solar wind flow. Disconnection events (DEs), where the ion tail becomes detached from the comet head [Figure 1.6], occur only in the equatorial region, according to this paradigm, as a result of HCS crossings. The mechanisms leading to the DE are discussed in chapter 2. The above paradigm describing the solar wind structure makes use of the appearance of the comets' ion tail, the locations of the DE occurrence and the position angles of ion tails to infer the position of the HCS and the equatorial-polar region boundary. The comet observations I address in this thesis, and their interpretation, aim to help test and clarify several details of this paradigm.

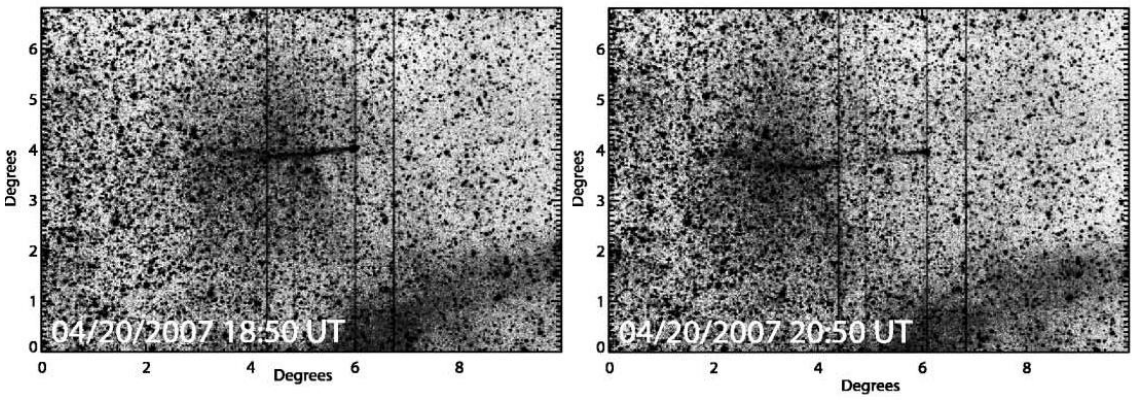

Figure 1.6: SECCHI HI-1 observations of the tail disconnection of comet Encke. These images were obtained from Vourlidas et al. (2007). The images are shown in reverse color and are histogram-equalized to emphasize faint structures. The faint cloud interacting with the comet is part of the ICME front, leading to the clear disconnection of the ion tail from the comet head.

"Light from the Sun travelled 93 million miles just to bounce off my thesis." – u/duerushedr (Reddit)

2. Comets

Comets have been the subject of wonder and study for centuries. Observations of famous comets, such as Halley's Comet, have been depicted and well recorded throughout history. Interstellar dust grains and gas, in the protoplanetary disk, condensed, underwent collisional coagulation rather than gravitational instability (Weidenschilling 1997) and gravitationally accreted to form icy planetesimals (Meech et al. 2004) approximately 4.6 billion years ago (Lamy et al. 2004).

These primitive bodies, consisting of frozen volatile ices, carbonaceous particles with complex hydrocarbons, and refractory grains, have survived virtually untouched since the conception of the solar system (Weissman et al. 2004; Weidenschilling 2004). Exceptions include surface alteration by ultraviolet (UV) radiation and cosmic rays, accretion and erosion by interstellar grains, heating from passing stars or nearby supernovae, collisional processing and sublimation processes during their passage in the solar system (Weissman et al. 2004 and references therein). Probing the structure of these small, primitive bodies whose origins lie beyond the frost line (> ~5 AU) in the solar system can shed light onto the dynamical and chemical evolution of the solar system from its protoplanetary disk to its current state. It is well established that they act as natural probes of the inner heliosphere as they loop around the Sun (Biermann 1957; Brandt 1968; Ip 1980; Ip 2004).

2.1. Introduction

Nomenclature

Naming conventions for comets have changed over time. The IAU's latest convention suggests naming newly discovered comets in the following format: 'C/ 2004 Q2'. This format has been adopted for all comets in this thesis.

- Comets are prefixed with the following (P/, C/ or D/) to indicate their nature.
  - P/ - Periodic comet
  - C/ - single apparition comet

  - D/ - Short-period comets that cannot be accurately predicted and are considered lost due to limited observations.

- The letter after the year denotes the half month in which the comet was observed, i.e. A and B refer to the first and second half of January respectively. The number indicates the order of discovery in that half month.

- Periodic comets follow a different rule and are named in the order in which their orbits were determined. For example, comet Halley bears the designation 1P/Halley, comet Encke is 2P/Encke and so on.

Tisserand Parameter

The Tisserand parameter is commonly used as a differentiator between different comet families as it remains approximately constant regardless of extreme changes in a comet's orbital elements when it is gravitationally perturbed by a planet (Marsden 2009).

$$T_J = \frac{a_J}{a} + 2\left[(1-e^2)\frac{a}{a_J}\right]^{1/2} cos(i)$$

The Tisserand equation presented here has been adopted from Coates & Jones (2009). *a*, *e* and *i* are the semimajor axis, eccentricity and inclination of the small body's orbit and a_J is the semimajor axis of Jupiter's orbit (assumed to be circular). It is a useful criterion for observational comparisons of two objects to determine whether they are different apparitions of the same object. T_J, Tisserand's parameter with respect to Jupiter as the perturbing body, is frequently used to distinguish asteroids ($T_J < 3$) from Jupiter-family comets ($2 < T_J < 3$). Most comets have $T_J < 3$, though Chiron-type and Encke-type comets have $T_J > 3$. Halley-type comets have $T_J < 2$.

Comet families

Comets can be classified into three main groups:

1. Short-period comets, for example the Jupiter-family comets, with an orbital period of less than 200 years. These mostly originate from a transneptunian reservoir of objects in low-inclination orbits, also known as the Kuiper belt, located ~ 30 – 50 Astronomical Units (AU) in the outer solar system or by planetary capture of long-period comets (Meech et al. 2004).
2. Long-period comets have a parabolic orbit with orbital periods of 200 years and greater. They originate from the outer Oort cloud, which is replenished by the inner Oort cloud (~ 10^5 AU from the Sun), and are considered to be dynamically new (Meech et al. 2004).
3. Until recently, the asteroid belt was an unlikely source for comets. Recent observations have shown multiple active rocks, now known as main belt comets (Hsieh & Jewitt 2006).
4. Sungrazing comets have their perihelion very close to the Sun, where they experience extreme thermal and tidal forces. Chapter 6 will address this remarkable group of comets in greater detail.

The orbital elements of the comets can slowly change over time with the gravitational perturbations of the Jovian planets (Meech et al. 2004), as well as much smaller effects such as sunward outgassing. Net outgassing acting upon the sunward side could also be a reason for the decreasing orbital periods of comets (Brandt & Chapman 2004).

2.2. Comet structure

An active comet consists of 5 main components: a nucleus, coma, ionosphere, magnetosphere and a neutral hydrogen cloud. With a solid nucleus at the centre and a luminous and spherical dust and gas envelope, also known as the coma, a comet also boasts two other easily recognisable features – the dust and ion tails extending across space. The brightness of the coma hinders our ability to directly image the nucleus from the Earth. From spacecraft missions, e.g. the Giotto encounter with comet Halley, we know that the nucleus is an icy conglomerate layered with a thick, dark dust crust. The recent Rosetta missions have shed further light onto the evolving morphology of a comet with decreasing heliocentric distance. The most relevant discoveries are addressed in section 2.7. Lastly, despite being one of the largest cometary

structures, the hydrogen cloud, extending from 10^6 – 10^7 km, is not a distinguishable feature with the naked eye. The neutral hydrogen coma is born out of charge exchange processes with the solar wind (see section 2.4.1), is extensive and undergoes a dynamical aberration due to comet motion (Fernandez & Jockers 1983).

Comets are chemically and morphologically complex (Reyniers et al. 2009). Spectroscopic observations of comets have shown an abundance of water molecules and ions. Emission lines from CN and C_2 molecules have also been discovered during the early formation of a coma. The composition of cometary nuclei will alter over time with each passage through the inner solar system, with more significant differences after multiple passes. Spectroscopic analysis of cometary comae and tails has revealed a surprising variety of refractory constituents, as well as, atoms, molecules and ions. Molecules detected include CO, CO_2, CH_4, CH_3OH, HCN, H_2CO, NH_3, N_2, CS and polycyclic aromatic hydrocarbons to name but a small fraction (Delsemme 1988; Altwegg et al. 1999; Cochran & Cochran 2002; Bockelée-Morvan et al. 2004).

2.3. Nucleus

Of the multiple techniques commonly used to estimate the nucleus size, only in situ measurements can provide an exact representation of the true size. Remote techniques commonly used to estimate the size are distant inactive observations, concurrent visual and thermal observations and coma modelling (Meech et al. 2004). Remote direct observations of cometary nuclei have been undertaken by Meech et al. (2004) with the Hubble Space Telescope and the Keck II telescope when the comets were inactive. Meech et al. (2004) recorded a radius size distribution range of 0.3 – 15.4 km for short-period comets and less than 4 to 56 km for long-period comets. The Giotto flyby of the nucleus indicated that 1P/Halley's nucleus measures 7.2 x 7.22 x 15.3 km with an albedo of 0.04 (Keller et al. 2004). Coupled with a mass estimate of 1 – 3 x 10^{14} kg (Rickman 1989), this yielded a nuclear density of 550 ± 250 kg m^{-3} (Keller et al. 2004). The nucleus of comet 19P/Borrelly was imaged by NASA's Deep Space 1 mission to be 8.0 x 3.15 km with an albedo of 0.029, although only half of 19P/Borrelly's illuminated hemisphere was observed.

Typical comets have a bulk density in the range of 500 to 1200 kg m^{-3}, with a “best” current value of 600 kg m^{-3} (Weissman et al. 2004). Recent Rosetta measurements have revealed comet 67P/Churyumov-Gerasimenko to be highly porous in the range of 70 - 80 %, confirming that cometary nuclei are likely to be highly porous (Sierks et al. 2015). More details on the Rosetta findings can be found at the end of this chapter. It bears noting that cometary nuclei are unmagnetised, as recently confirmed by ROMAP measurements on Philae (Auster et al. 2015), and hence, these km-sized obstructions in the solar wind do not produce a detectable effect, when inactive far from the Sun.

After assessing all of the evidence thus far, Weissman et al. (2004) concludes that the nucleus is likely a “collisionally processed rubble pile of smaller icy planetesimals”. The volatiles observed upon sublimation of the water-ice suggest that they are trapped as ‘impurities’ within the water ice. Depending on the location where it formed, the water ice can be in a crystalline phase (also known as a clathrate hydrate) or an amorphous phase, which match well with the rate of change of sublimation over a range of heliocentric distances (Meech et al. 2004; Brandt & Chapman 2004).

Beyond ~ 3AU from the Sun, solar insolation is insufficient for water ice sublimation, although Meech et al. (2004) reported that water ice sublimation was observed up to 5-6 AU from the Sun, based on their early photometric observations of comet 1P/Halley in 1984-1985 (Meech et al. 1986). When inactive, the comet behaves similarly to the lunar interaction with the solar wind. The HMF diffuses through the unmagnetised nucleus and forms an ion-void wake behind the nucleus, as long as the nucleus is comparable in size or larger than the solar wind ion gyroradius. The solar wind ions on the sunward side of the comet impact the surface layers, initiating sputtering processes (Coates & Jones 2009).

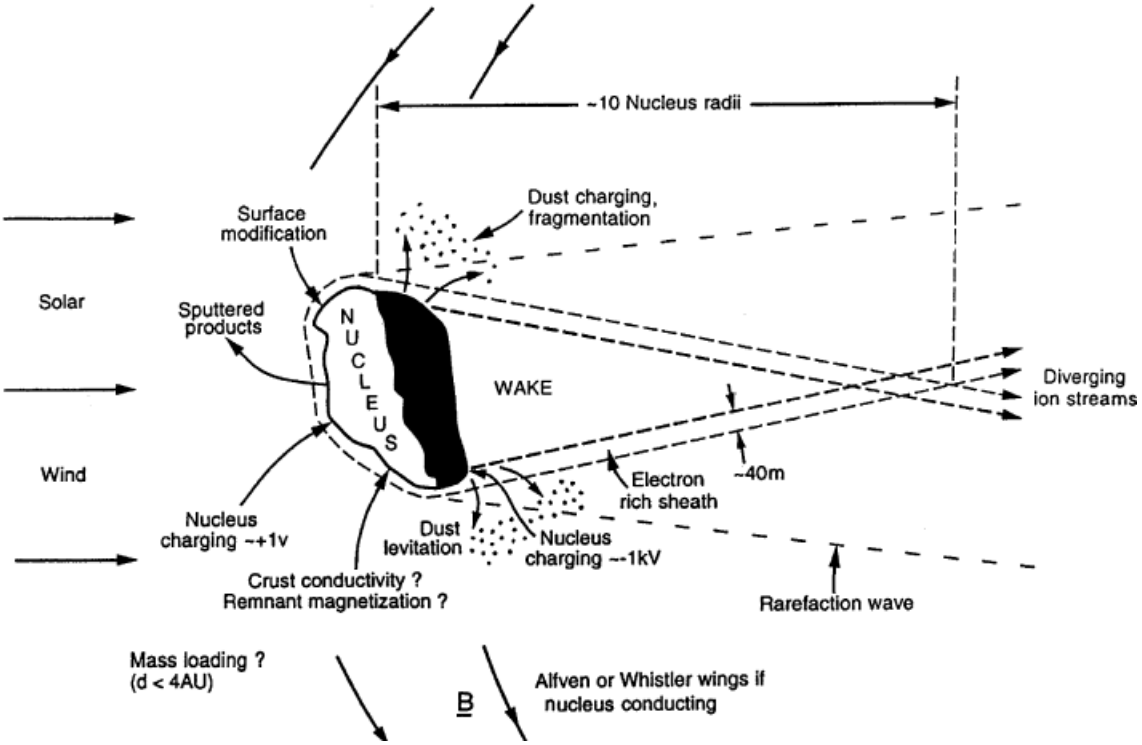

Figure 2.1: Solar wind interaction with an unmagnetised body (Coates 1997).

2.4. Coma

The coma, with sizes of the order of 10^6-10^7 km (Combi et al. 2004), is the brightest and most dominant feature of a comet. The brightness contrast with fainter features often overwhelms structures close to the nucleus. The recent flybys of comets only just revealed the diversity of the hidden shapes, sizes and appearances of cometary nuclei, which the luminous coma had previously rendered impossible to resolve using ground based methods.

The activity and thus the lifetime of the cometary nucleus is dependent on the comet's position in the solar system and its age. As a comet's orbit brings it closer to the Sun, the surface layers become sufficiently hot to trigger sublimation processes beneath the mantle. The frozen volatiles expand supersonically from the cometary surface (Reme 1991) with a bulk outflow velocity of ~1 km s^{-1} for water (Combi et al. 2004). Discrete gas vents as jets, as seen from the Giotto flyby of comet Halley, have been observed releasing neutral gas into the cometary atmosphere through gaps in the mantle. Dust grains are dragged along as the gas jets evolve off the comet's surface, creating an extensive atmosphere of neutral molecules and dust.

Cometary activity decreases as the comet moves away from the Sun. The pressure drop from reduced outgassing down to zero allows the dust to form a new crustal layer of surface cometary dust grains (Rickman & Huebner 1990). Subsequent inner solar systems passages would thus see a decrease in cometary activity through expenditure of volatiles and insulation of remaining inner volatiles.

The large size of the coma is due to the small mass, and hence low gravitational pull of the nucleus. Cometary activity is often defined by the water production rate (Bockelée-Morvan et al. 2004). In situ measured gas production rates at 4 comets have yielded a range of 10^{28}-10^{30} molecules/second (Coates & Jones 2009). The current outgassing rate of 67P/Churyumov-Gerasimeko is currently quite low, on the order of 10^{26} molecules per second and is expected to increase as the comet approaches its perihelion. Neutrals within the coma eventually become fully ionised during its encounter with the solar wind via a combination of the following ionisation processes: photodissociation of molecules via solar extreme ultraviolent (EUV) radiation; charge exchange with energetic solar wind protons; and electron impacts (Reme 1991). These create a cometary ionosphere of 10^3-10^4 km (Combi et al. 2004). Harris (1997) demonstrated that comet C/1996 B2 (Hyakutake)'s gas production could have included substantial contribution from dust grain sublimation rather than direct outgassing from the nucleus.

The equation below describes the relationship between the gas production rate Q, its ionisation time and the cometocentric distance. Variations in the gas production rate will influence the size and nature of the comet-solar wind interaction region (Coates 2004).

$$Q = \frac{Q_0}{R^2}\, e^{\left(\frac{-R}{v_e \tau}\right)}$$

Q (m^{-2} s^{-1}) is the comet's gas production rate, Q_0 (s^{-1}) is the original neutral gas species, v_e is the outflow velocity of the neutral coma gas, R is the distance from the nucleus and τ is the lifetime against ionisation timescale. Typically, a neutral atom outgassed from the nucleus will travel ~10^6 km before being ionised.

2.4.1. Ionisation Mechanisms

Cravens (1991a; 1991b) list the different processes that ionise sublimated cometary neutrals. The three main ionisation processes are discussed below:

Solar EUV radiation

This is the main ionising process as the solar EUV photons react with cometary neutrals via the following reactions:

$$h\nu + H_2O \rightarrow H_2O^+ + e \qquad (1)$$

$$h\nu + O \rightarrow O^+ + e \qquad (2)$$

Equation 1 dominates the reactions in the coma whilst equation 2 is the dominant process at large cometocentric distances down the tail, because at cometocentric distances larger than 10^5 km, most of the water molecules have been photodissociated by solar radiation forming a neutral coma of atomic hydrogen and atomic oxygen (Cravens 2004). The photoelectrons will have an energy of $E = h\nu - I$, where $h\nu$ is the energy of the photon and I is the ionisation potential of a given species (Cravens 1987).

Charge exchange with solar wind protons

Charge exchange of solar wind protons with heavy cometary neutrals (species M) is the second major contribution to ionisation within the coma (Cravens & Gombosi 2004). This process contributes to the contamination and mass-loading of the solar wind. The charge exchange process helps to regulate the dynamical heating and cooling of the plasma. Cravens (2002) proposed this mechanism as the source of cometary x-rays. This has been confirmed from X-ray spectroscopy of C/1999 S4 (LINEAR) by the Chandra telescope (Lisse et al. 2001).

$$H^+ + M \rightarrow H + M^+$$

Electron impact ionisation

Incident electrons can produce ions if their energy is higher than the ionisation potential of a neutral species (M) (Cravens et al. 1987).

$$e + M \rightarrow M^+ + e + e$$

2.5. Induced Magnetosphere

The newborn ions are picked up by the HMF via the Lorentz force and gyrate around the solar wind's frozen-in magnetic field lines. The ions are accelerated by the convection electric field of the solar wind and experience the force:

$$\overline{E}_{sw} = -\overline{v}_{sw} \times \overline{B}$$

$\overline{\mathrm{E}}_{\mathrm{SW}}$ is the solar wind electric field, $\overline{\mathrm{v}}_{\mathrm{SW}}$ is the solar wind velocity and $\overline{\mathrm{B}}$ is the HMF. The slow moving ions (~ 1 km s^{-1}) are essentially stationary with respect to the inbound solar wind ions (400 – 750 km s^{-1}). At the injection point, the pick-up ions' motion is best described as the summation of its gyrating cycloid trajectory about the HMF lines and its initial parallel motion along the field, adopting a helical Ring-Beam distribution (Coates & Jones 2009). Their gyration velocities are equal to v sin α, where α is the angle between the HMF and the radial plasma flow. This culminates in a mass-loading of the solar wind field lines, which become laden with heavy ions, such as water and oxygen. For conservation of momentum to hold true, the velocity of the HMF must decrease as the mass on the solar wind increase. The ion density variation within the coma thus dictates the interaction region. Most mass is added near the nucleus causing a velocity shear along the field line. This results in a draping of the HMF around the magnetotail structure, as seen in Figure 2.2 (Cravens & Gombosi 2004; Coates & Jones 2009), trapping plasma within, as first proposed by Alfvén (1957). The ion tail acts somewhat like a transparent wind sock. The motion of charged particles in a magnetic field induces a tail current sheet in the plane perpendicular to HMF orientation upstream. Unlike most planetary magnetospheric tails (e.g. Saturn and Earth), the current sheet orientation is highly variable, as is also seen at Venus and Titan.

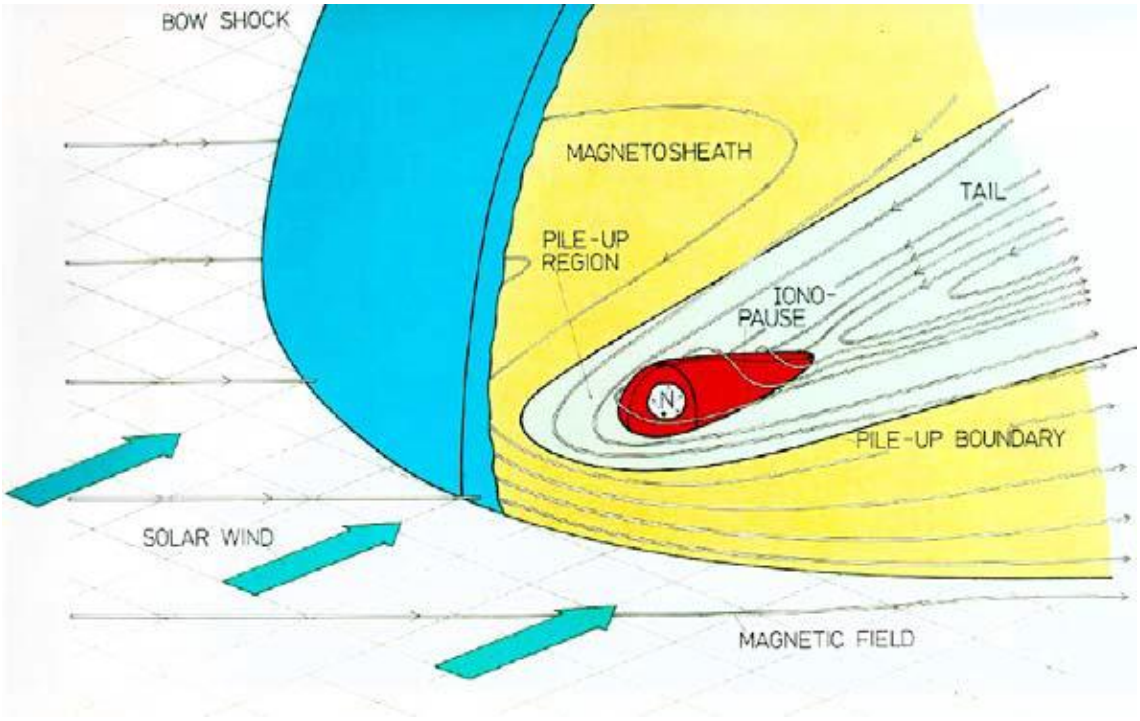

Figure 2.2: Schematic of comet-solar wind interaction and the boundaries of the induced magnetosphere. The boundaries shown here are not to scale (Neubauer 1990).

Cometary magnetospheres come in different sizes. A comet's gas production rate and the ionisation rate play an important role in determining the boundaries and sizes of several sub-structures in the cometary magnetosphere. Much of what we know regarding the structure of the induced magnetosphere is derived from spacecraft encounters with different boundaries and transition regions, as well as those deduced from magnetohydrodynamic models, kinetic models or a hybrid of the two. The locations of these boundaries are often not permanent and clearly-defined. In the sections below, I outline a synopsis of the boundary layers, shown in Figure 2.3, and their properties. This basic summary of the induced magnetosphere is predominantly based on the more comprehensive reviews of Ip (2004), Cravens & Gombosi (2004) and Coates & Jones (2009).

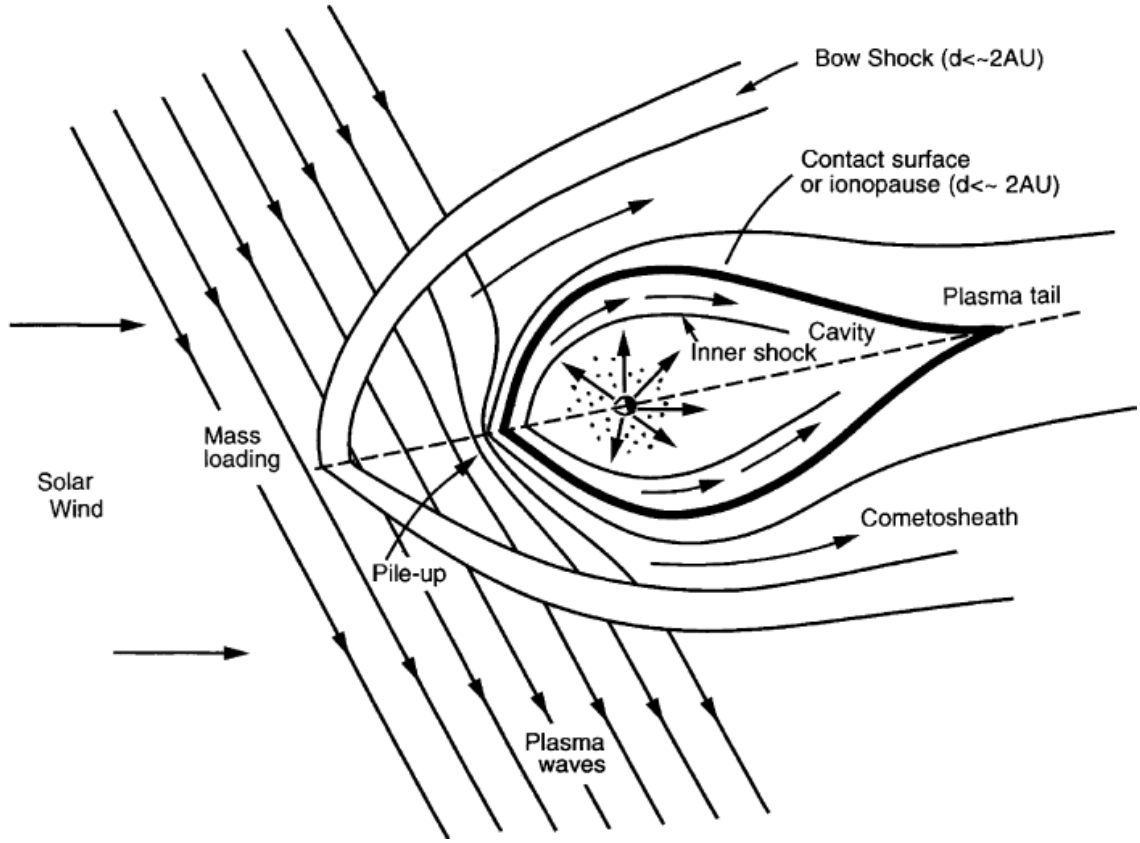

Figure 2.3: The boundaries of the comet-solar wind interaction at a heliocentric distance less than 2 AU (Coates 1997).

2.5.1. Bow Shock

The bow shock is the boundary separating the cometosheath from the solar wind. Cometary bow shocks are weaker than their planetary counterparts as they occur in the mass-loaded plasma where the solar wind flow has slowed down. The deceleration of the solar wind, due to heavy cometary ions being picked up and implanted into the flow, persists until the solar wind eventually reaches a critical mass flux. At this point, a weak bow shock (Mach number ~ 2) arises. Predictions indicated that for one-dimensional scenarios, a cometary bow shock would form when the mean molecular weight of the plasma flow reached 4/3. For two- and three-dimensional simulations, depending on the gas production rate, weak bow shocks were observed to be formed at lower than 4/3 (Coates 2004). This has been confirmed by all spacecraft encounters as a permanent feature of the cometary magnetosphere, albeit with its properties dependent on the HMF orientation upstream of the comet. The bow shock distance (r_{shock}) is determined by the ionisation rate and the comet's gas production rate. For comparison,

$r_{shock} \approx 0.3 \times 10^6$ km at comet Halley, whereas for comet 26P/Grigg-Skjellerup, this was much closer at ~ 25,000 km from the nucleus and for Giacobini-Zinner at 1 AU, it was about 5×10^4 km, which was comparable to the heavy ion gyroradius (Cravens & Gombosi 2004).

2.5.2. Cometosheath

The cometosheath is bounded by the bow shock and the diamagnetic cavity, encompassing the region where the postshock solar wind plasma interacts with the cometary plasma. Downstream of the bow shock boundary, the slowing down of the flow continues, culminating in a stagnation point close to the nucleus (Cravens & Gombosi 2004). Throughout this region, the magnetic field strength increases with decreasing cometocentric distance as the HMF piles up, wraps around the diamagnetic cavity and shapes the magnetotail (Cravens & Gombosi 2004).

2.5.3. Mystery Boundary

Data from spacecraft flybys through 1P/Halley's cometary magnetosphere showed an unexpected double peak in the cometary ion distribution. The origin of this boundary remains unknown, thus giving rise to its name. A possible explanation for this bifurcation could be due to the velocity shear at the bow shock leading to different pickup shell radii (Coates & Jones 2009). This theory does not account for the sudden increase in water group ions nor its bimodal distribution due to a change in solar wind velocity at 500,000 km from the nucleus. The mystery boundary also demarcated a region of significantly enhanced hot electron (0.8 – 3.6 keV) densities and of higher solar density and velocity (Coates & Jones 2009 and references therein).

2.5.4. Cometopause

Situated at a radial distance of ~2×10^5 km from comet 1P/Halley's nucleus, the cometopause is defined as the region where the plasma flow is no longer collisionless. This boundary

separates two regions with different chemistry, with a sudden drop in the proton density and a marked increase in the cometary ion density. Charge transfer between charged solar wind particles and cometary neutrals become important. The charge exchange processes occurring here are thought to be the source of X-ray emissions observed in comets (Cravens & Gombosi 2004). Collisional cooling of electrons and momentum transfer between the ions and neutrals also become evident and influence the formation of the diamagnetic cavity. The debate as to whether the cometopause is a permanent boundary within the cometary induced magnetosphere is ongoing.

2.5.5. Magnetic Pile-up Boundary

Until the recent cometary spacecraft fly-bys, the magnetic pile up boundary had been a theoretical prediction arising from the continuous mass loading of solar wind field lines behind the cometary bow shock. The low velocity of these field lines would inevitably lead to a pile-up of a magnetic barrier on the sunward side of the comet. The magnetic field becomes highly compressed within a region ~45000 km from the nucleus of 1P/Halley and creates a magnetic barrier in the heavily mass-loaded solar wind in the sunward direction. The magnetic field lines drape strongly around the diamagnetic cavity in this region. Inside this region, the magnetic field can reverse its polarity several times due to the varying orientation of the HMF.

2.5.6. Ion Pile-Up Boundary

At 12000 km from the nucleus at 1P/Halley, a peak and subsequent sharp drop in the ion density was registered by both Giotto and Vega. A maximum was concurrently measured in the magnetic field. The most favoured explanation for the density jump has been linked to a drop in electron temperature with decreasing distance to the nucleus. This effectively reduces the rate of recombination of ions and electrons.

2.5.7. Diamagnetic Cavity / Contact Surface

This region was traversed only by the Giotto spacecraft for comet 1P/Halley, but is expected to be encountered by Rosetta at 67P. The diamagnetic cavity is a field-free region of ~4000 km at 1P/Halley, bounded by a 25 km wide contact surface. The dynamic and magnetic pressure outside the contact surface is in approximate equilibrium with the outward collisionally coupled ion-neutral drag (Cravens 1991a). Since the cometary nucleus has no intrinsic magnetic field, there is a purely cometary plasma with no magnetic field within the contact surface.

The current Rosetta mission, which arrived at comet 67P/Churyumov-Gerasimenko on August 2014, will continue to fill in our knowledge gaps for the formation and evolution of these boundaries close to the nucleus, as its heliocentric distance decreases (Nilsson et al. 2015). The Philae lander will remain within the diamagnetic cavity and our current paradigms indicate that it will not contribute information on the solar wind.

2.6. Tails

Comet tails fall in three categories: an ionised gaseous tail, a dust tail and a neutral atomic gas tail. The ion (Type I) and dust (Type II) tails have been well documented but it was not until the end of the 20th century that the first observational confirmation of a neutral atomic tail was obtained.

Sodium and Iron tails

The molecular intensity distribution varies between comets, such that certain comets, rich in metallic compounds, exhibit rarely observed neutral atomic sodium (Cremonese et al. 1997) and iron (Fulle et al. 2007) tails. The neutral source and tail formation for both tails are still undetermined. In the case of the sodium tail, two different sodium sources have been proposed

(Combi & Disanti 1997; Wilson et al. 1998; Brown et al. 1998), though these have yet to be confirmed. I address the two more commonly observed and understood cometary tails below.

Dust Tail

The white and diffuse dust tail consists of micrometre-sized dust grains pushed back from the nucleus and coma by solar radiation pressure (Fulle 2004). With a typical length of 10^4 km, 10^8 km in extreme cases, it opposes the direction of motion of the comet and is slightly curved as its constituent grains gravitationally orbit the Sun. The dust particles are in individual orbit about the Sun. The solar radiation pressure increases the dust particles' heliocentric distance, which causes the curvature of the dust tail.

Anti-tails

Geometrical effects between the observer and the comet can give rise to the visual phenomenon of the anti-tail. This occurs when the observer crosses the orbital plane of a dusty comet, with a sufficiently developed disc of heavy dust particles. The anti-tail is viewed as a spiked dust tail extending from the coma and jutting in the sunward direction. If the comet has a prominent ion tail, the anti-tail will be mirrored to the direction of the ion tail.

2.6.1. The Ion Tail: An induced magnetotail

Studies of the interaction between the solar wind, historically known as solar corpuscular radiation, and cometary ion tails date back to the latter half of the 20th century. In 1951, Biermann studied the properties of cometary ion tails from tail orientation measurements by Hoffmeister (1943), from which he inferred the existence of a continuous outflow of particles from the Sun (Biermann 1957). Often observed remotely as a variable bluish tail, the ion tail is highly responsive to alterations in the HMF orientation upstream of the comet leading to distinct visual clues such as variations in the brightness, size, shape and direction. In the literature, the

tail has been referred to as the Type I tail, the ion tail and the plasma tail. In the context of this thesis, the term ion tail will be used throughout.

Spectroscopic studies of ion tails reveal that their composition is dominated by H_2O^+ and CO^+ ions (Ip 2004; Feldman et al. 2004). The fluorescing carbon monoxide [CO^+] ions give the ion tail its bluish tint. Other observed ionised molecules include OH^+, CO_2^+, CH^+ and N_2^+ (Brandt & Chapman 2004). The visible component of ion tails can reach up to ~10^7 - 10^8 km (~1 astronomical unit) (Brandt 1968), with comet Hyakutake's ion tail reaching up to 3.8 AU (~550 million km) with a minimum tail diameter of ~ 7 x 10^6 km (Jones et al. 2000).

An ion tail tends to be oriented in the anti-sunward direction; however it is always lagging the true anti-solar direction by a few degrees, opposing the direction of the comet's motion. It has been well established that solar wind conditions control and maintain the appearance of the ion tail and that the tail axis is a composite vector of the solar wind velocity vector and the orbital motion vector of the comet. When the projected observing geometry is good, i.e. when the angle between the Sun, target and the observer (S-T-O angle) is large, and that the observer is well outside the comet's orbital plane, i.e. at a large orbit plane angle, we can constrain the solar wind velocity. The ideal geometry for comet observations from Earth would occur when the S-T-O angle and orbit plane angle are both near 90^o. The dynamical variations and the plasma density distribution are controlled by the mass-loading process. Ever-changing, extensive features in the tail such as condensation knots and kinks generally indicate the flow state of the solar wind, whether the comet is surrounded by quiescent fast solar wind or whether it is traversing a turbulent solar wind flow. Kinks in the tail are often clues that the comet may be moving from one solar wind regime to another.

2.6.1.1. Tail Rays

Tail rays, or tail streamers when within the main ion tail, form the fine-scale structure of the ion tail. Typical tail ray lengths are on the order of ~10^6 km (Minami & White 1986) with radii ~ 2000 to 4000 km (Brandt & Chapman 2004). A detailed paradigm for the tail ray formation has not been deciphered yet, though conjectures on the underlying mechanisms range from tail ray

creations due to sector boundary crossings (Ness & Donn 1966) to tangential discontinuities in the HMF (Schmidt & Wegmann 1982) to twisted HMF flux ropes held fixed within the cometary ionosphere by the Kelvin-Helmholtz instability (Wolff et al. 1985). Consecutive photographic evidence of tail rays folding around the main tail axis, suggests that the ionised plasma can be considered as magnetic tracers of the HMF as it drapes around the comet's nucleus (Moore 1991; Watanabe 1991), as seen in Figure 2.4. *Ness and Donn (1966)* proposed that the ion rays can be explained as plasma sheets sandwiched between oppositely directed magnetic fields. This model requires the crossing of the neutral HCS so that cometary ions can collect and drift parallel to the main tail axis. This explanation was rebuffed by Moore's (1991) observations of comet Kobayashi-Berger-Milon (C/1975 N1), whereby a linear fit predicted by the afore described model did not fit well to their measured angular closing velocities. Degroote et al. (2008) invoked the solar wind as the prime trigger for tail rays. They supported this theory with evidence linking a coronal hole flow of fast solar wind as the causal factor for the appearance of tail rays in comet C/2004 Q2 (Machholz). Ip (2004) provides a good review of cometary tail formation mechanisms.

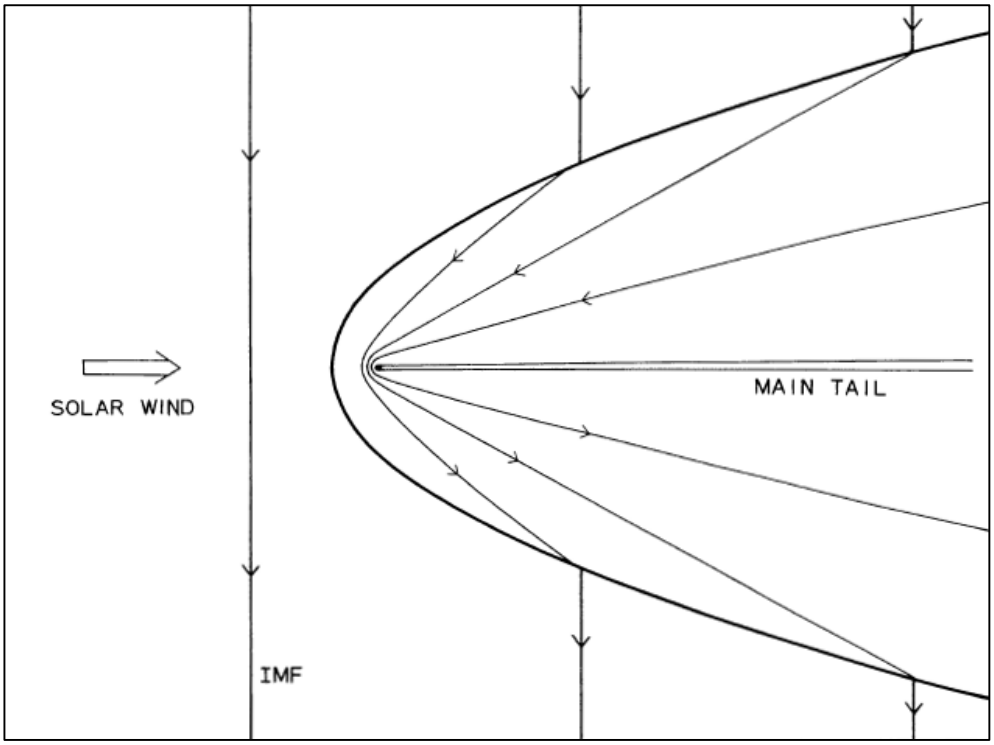

Figure 2.4: Schematic view of ion tail-ray formation and its folding motion (Watanabe 1991). The HMF flows from the left and drapes around the comet's diamagnetic cavity. Pick-up ions in the cometary ionosphere trace the HMF lines and appear as tail rays.

The ion tail ray's velocity within the bow shock decreases on approach to the main ion tail. The section of the HMF outside of the bow shock boundary will flow at the undisturbed solar wind velocity (Siscoe et al. 1986), resulting in a velocity shear along the tail ray. Within the stagnation region, cometary ions are added to the solar wind with the ion tail ray density increasing with respect to the duration that the HMF lines remain within this region (Watanabe 1991). In theory, the folding effect about the main tail axis will be symmetrical, which has been observed remotely. Instances where only one tail ray is observed is likely due to the observing geometry. Hence for consistency, Moore (1991) defined the angle between the main axis to a tail ray as the half angle between two symmetrical rays.

2.6.1.2. Disconnection Events

Amongst the numerous solar-wind driven features, disconnection events are a relatively frequent key phenomenon. The severance of the ion tail from the coma is defined as a disconnection event (DE). DEs occur over a large range of heliocentric distances, heliospheric latitudes and solar cycle phases. The following paradigms have been proposed, however the cause for disconnection events are not fully comprehended yet (Voelzke 2005).

The proposed disconnection models are:

1. Variations in ion production rates, due to changes in the gas production rate or incident EUV radiation, can lead to an increase or decrease of the ionosphere. Significant shrinkage of the ionosphere could lead to the HMF penetrating the cometary atmosphere and induce a tail DE (Wurm & Mammano 1972), though DEs based on ion production effects have not been seriously considered in the last few decades (Voelzke 2005).

2. An increase in solar wind pressure could compress or force the comet's ionosphere off the nucleus, leading to a DE, or a partial one (Voelzke 2005 and references therein; Vourlidas et al. 2007).

3. The third model, concerning magnetic reconnection in the tail, is the most widely-accepted scenario. Magnetic lines of opposing polarity become reconnected either on the sunward side of the comet as the comet crosses the HCS (Niedner & Brandt 1978; Voelzke 2005 and references therein) or on the tailside after encountering a CIR shock front or a high-speed stream and thus a decrease in the Alfvén Mach number (Russell et al. 1986). However, HCS crossings do not necessarily always result in a DE (Delva et al. 1991).

CMEs (Jones & Brandt 2004; Vourlidas et al. 2007; Kuchar et al. 2008; Jia et al. 2009) and HCS crossings (Brandt 1999; Brandt & Snow 2000; Kuchar et al. 2008) are well-known triggers of disconnection events. CIR-related shocks get stronger with increasing heliocentric distance and could potentially cause disconnection events (Wegmann 2000). Disconnection events are easily observable and well documented incidents and are a strong motivator for this research. Where feasible, I aim to identify the sources of DEs.

2.7. Rosetta

Launched in 2004, the ESA-commissioned Rosetta spacecraft and its lander Philae promise a revolution in our current understanding of cometary science. It has since obtained images from two asteroid flybys, entered orbit around Oort cloud comet 67P/Churyumov-Gerasimenko (hereafter 67P) in August 2014 and the Philae landing occurred in November 2014.

The spacecraft's OSIRIS Narrow Angle Camera (NAC) and its navigation camera (NavCam) have delivered the first direct high-quality, high-resolution global map of a cometary nucleus from varying altitudes. Upon approach, it revealed a bizarre two lobed nucleus, joined by a neck. This unique morphology could have arisen from erosion or amalgamation of two different bodies. The mission has provided the most accurate and detailed characterisation of the morphology and evolution of a comet. Some of its main contributions in its first few months are best summarised in Figure 2.5.

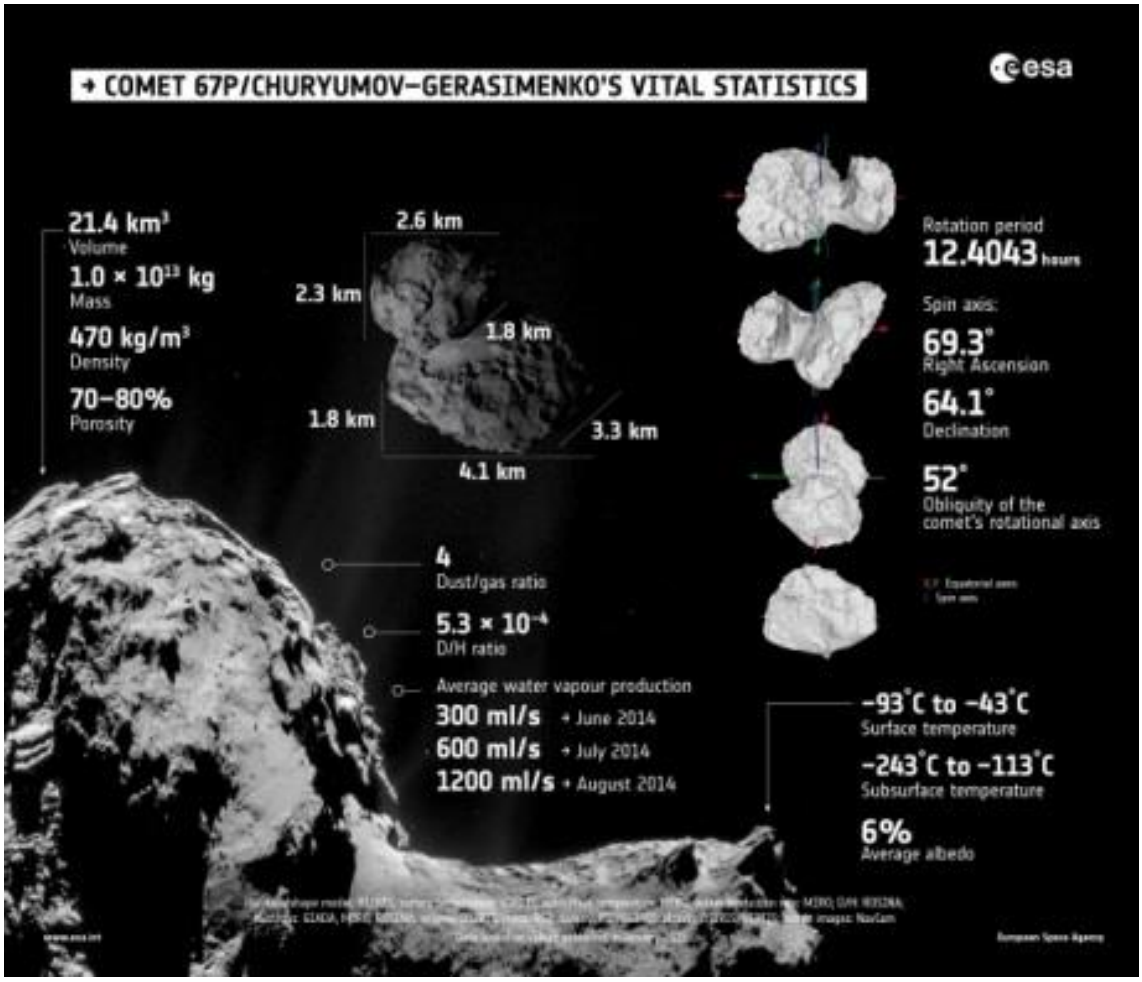

Figure 2.5: Credits for individual results obtained from ESA website: Shape model, rotation properties, volume and porosity: OSIRIS; Mass: RSI; Density: RSI/OSIRIS; Dust/Gas ratio: GIADA, MIRO and ROSINA; D/H ratio: ROSINA; Surface temperature: VIRTIS; Subsurface temperature and water vapour production rate: MIRO; Albedo: OSIRIS and VIRTIS; Comet images: NavCam; Infographic credit: ESA

A series of publications detailing the exciting results were published in January 2015. A summary of these results and the references can be found in Taylor et al. (2015). Below, I highlight and summarise two of the eight principal discoveries, as well as the latest magnetic field measurements of 67P's nucleus.

One of the primary science objectives of the ROSINA instrument's double focusing mass spectrometer (DFMS) was to ascertain whether the composition of water, in particular the D/H ratio of the comet's water was comparable to that of Earth's ocean. A D/H ratio of 5.3 x 10^{-4} from the water vapour outgassing from 67P differed substantially to the measured value of 1.56

x 10^{-4} from Earth's ocean (Altwegg et al. 2015), thus ruling out JFC comets as a likely source of Earth's water.

When Rosetta approached 67P at ~3.6 AU from the Sun, the comet's outgassing rate was low, on the order of ~10^{26} molecules/sec. The relatively thin atmosphere meant that the ion-neutral collisions were an insignificant deterrent to solar wind penetration. This contrasts well with previous in-situ measurements of comets where a substantial ionosphere and magnetosphere were already present. By r_H ~ 3.3 AU and 28 km from the nucleus, a deflection of solar wind, as well as a cometary plasma with a similar number density to that of the solar wind were observed. Nilsson et al. (2015) further reports on charge-exchange collisions becoming apparent in the neutral atmosphere, signalling the initial stages of ionosphere and magnetosphere formation.

It has been proposed that magnetised clumping of metallic, dusty components may occur during the early lifetime of protoplanetary discs (see references in Auster et al. 2015). The existence of magnetic minerals within asteroids suggests that eventual aggregation of the magnetised and unmagnetised building blocks of our solar system could retain its initial magnetic arrangement. However, the latest measurements from Philae's ROMAP magnetometer of 67P's surface, at four different contact points, indicate that the magnetic field of less than 2nT is inconsistent with a magnetised cometary surface (Auster et al. 2015). Corresponding variations in the magnetic field measured by Rosetta's RPC suite, located 17 km above the cometary surface, confirmed that the measured magnetic field is due to the solar wind. ROMAP's spatial resolution is ~1 m. The author concluded that magnetic forces acting upon larger than metre sized magnetised bodies were likely to have been insignificant.

"Puppies are for Christmas but Physics is for life" - Dr Gethyn Lewis.

3. Data Sources And Instruments

The images used in this study were sourced from amateur and professional telescopes, including spacecraft observatories. A brief description of each data source and data required is outlined below.

3.1. Amateur Comet Astronomers

The advent of highly sensitive commercial CCDs coupled with modern telescopes with large fields of view (FOV) has led to the quality of modern comet images being often better than that of professional photographs from a few decades ago. The potential to provide near-continuous monitoring of comets is now a feasible objective with a community of amateur astronomers widely distributed globally. With the ease of online access available today, a dedicated network of comet enthusiasts could be founded with a dedicated website aimed towards amateur astronomy photography. The relatively recent CIOC campaign (2012) (http://www.isoncampaign.org/) for comet ISON also brought together a global network of amateur astronomers and promoted collaboration and discussion through a dedicated Facebook group.

Amateur images for comet Machholz were sourced from extensive online repositories available via Google, Astrobin and Flickr, to name but a few. However, there were drawbacks associated with using images from multiple contributors: there was no conformity or convention for the image formats. This obvious ongoing complication arises from the heterogeneity of astrophotographers' equipment, from their telescopes, CCDs or filters, which leads to different fields of view and image formats [Figure 3.1]. Often, the images were without precise timing or geographic information. Lang & Hogg (2012) found that only ~ 70% of the meta-data supplied by amateur astrophotographers was correct.

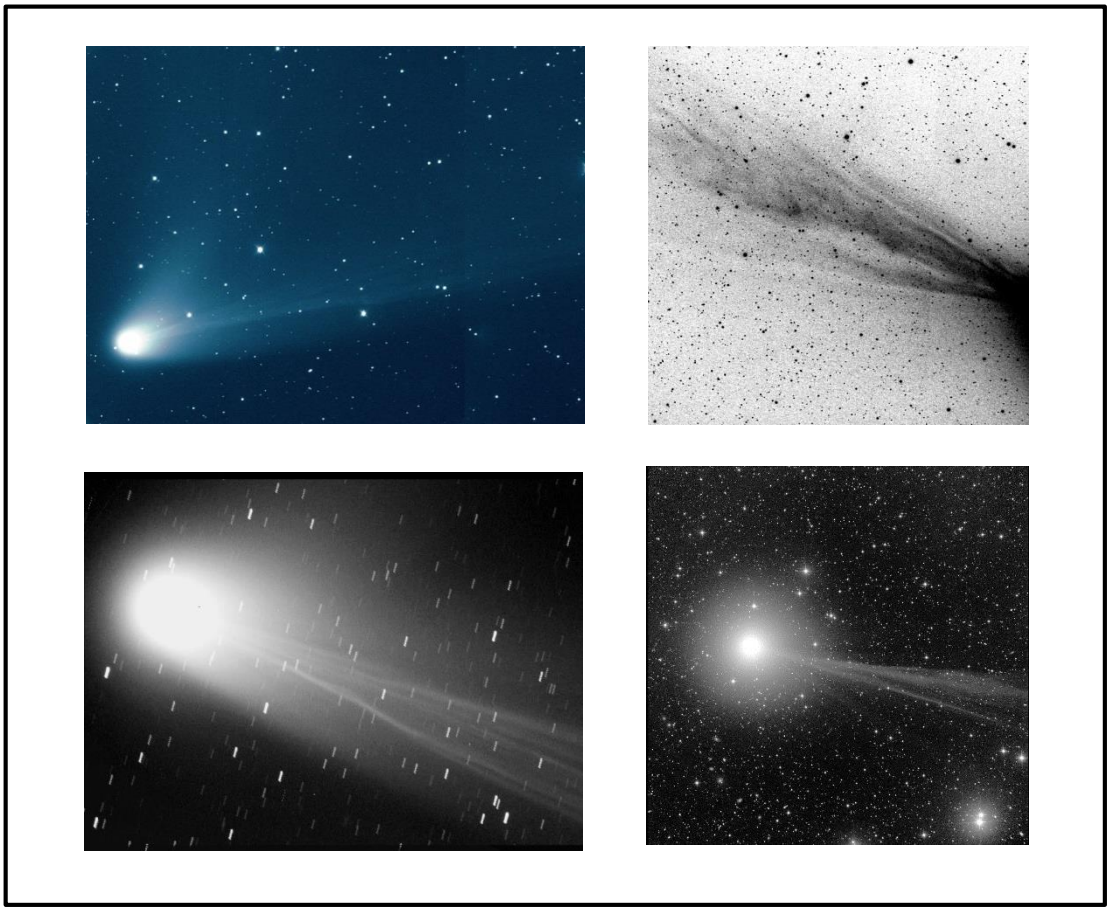

Figure 3.1: The images above show the variation of image formats available in our catalogue. Image credits, from top left to bottom right, are as follows: Mikuz (C/2001 Q4), Holloway (C/2004 Q2), Jäger and Rhemann (C/2001 Q4) and Mobberley (C/2014 Q2)

3.2. Astrometry.net

Astrometry.net (Lang et al. 2010) is a robust astronomical image solver, allowing multiple image formats as input and computing the pointing, plate scale, orientation and field of view (FOV) of the image, assuming a tangent plane (TAN) projection. These are stored under the World Coordinate Systems (WCS) standardised format, which can be used to compute the equatorial coordinates of each pixel in the original image.

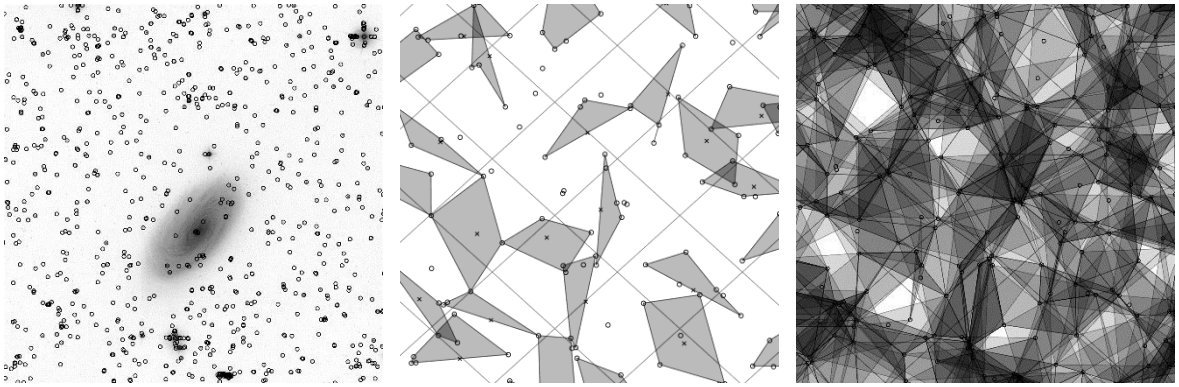

Figure 3.2: Images from Astrometry.net documentation, showing an example reference catalog; image overlaid with a HEALPix grid and quads created, quads repeated till sky is dense with features.

The solver makes use of pre-generated index files, which contain identifiers known as "skymarks", the celestial equivalent of a landmark. The reference catalogue is split into subsections of the sky and the brightest skymarks (stars and sometimes galaxies) are selected so that they provide uniform coverage across the reference image. A HEALpix is short for the Hierarchical Equal Area isoLatitude Pixelization of a sphere and allows the division of a sphere into spherical pixels of equal areas or in Astrometry.net's case, a hemisphere of the sky. A HEALpix grid is overlaid onto the amateur image and a set of overlapping quads are created, with each quad (~4 stars) pointing back to the stars it is composed of [Figure 3.2]. Astrometry.net extracts detected light sources from the input astronomical image into quads and compares their local shape to find the closest match in the index files. The index files are based on 2MASS and Tycho-2 astrometric catalogues. User-specific index files can be custom built, if the current sky catalogues do not provide a sufficiently high solving success rate.

During the early stages of this project, astrometry.net was available with limited functionality. Initially, each image had to be uploaded to and downloaded from astrometry.net individually. This was a vast improvement over identifying each star field by eye, yet the process remained a time-consuming one. There were multiple restrictions regarding the image format to be processed and the image parity, for example the stars had to be white on black background. This has greatly improved over the past few years with batch upload of images under different format being available. Each processed image is available for download under a separate

process log, under a generic filename. Batch download of images with the uploaded filename has yet to be implemented and thus, each image requires user interaction. A local install of astrometry.net resolved this particular problem and has greatly reduced time spent during the preliminary processing stage. Each index file has been designed to solve for images within a set narrow scale range. The FOV of most amateur astrophotographs tend to range from half a degree to a few degrees wide; only index files, designed to solve large angular images, were used in the local install to speed up the computations. As a downside, solving each image took longer and failed more frequently in comparison to its web counterpart. Failed images were reprocessed through the Astrometry.net web server. Astrometry.net was used to compute the astronomical coordinates of each amateur [Figure 3.3], SOHO and INT image.

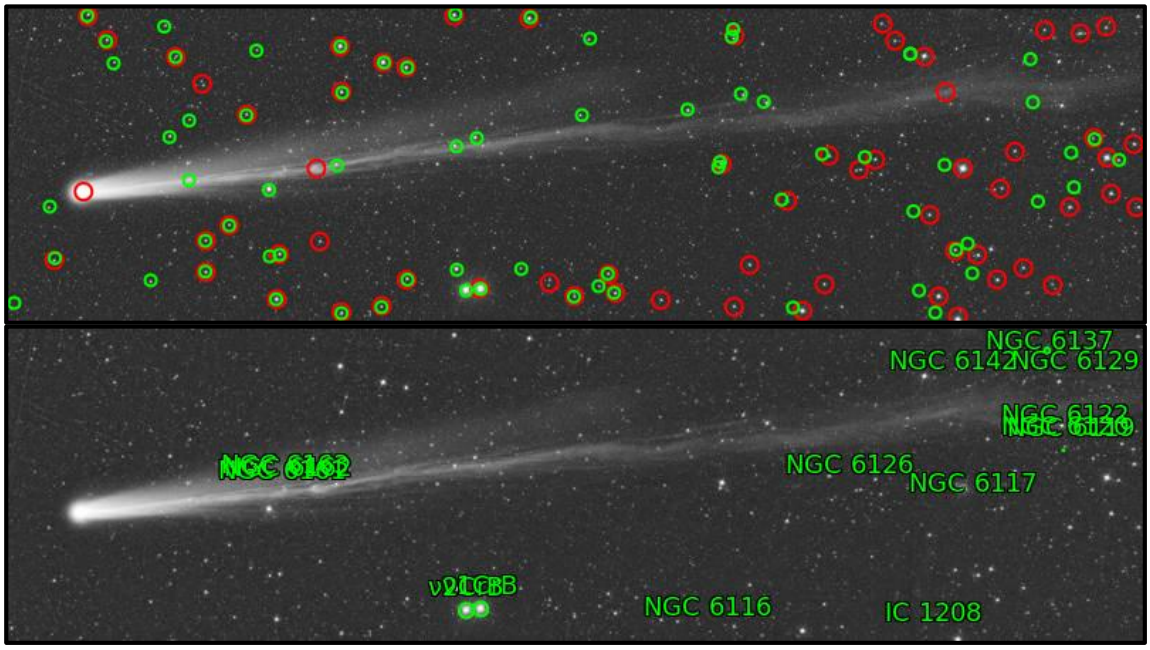

Figure 3.3: Comet C/2013 R1 (Lovejoy) observed by Rhemann [13/12/2013 03:41 UT]. Extracted and resolved sources are in green and unresolved in red. Second image is annotated with known astronomical bodies.

3.3. JPL Horizons

Early during this project, it was determined that the accuracy of the JPL Horizons (Giorgini et al. 1996) orbit data would be greater than any achieved by locally computing the orbit track for each comet. The web interface is easily customised to readily produce any number of data points for the comet, although it is restricted to maximum number of data points to be returned

at any point. A maximum time period of 2 months is chosen to comply with the JPL software restrictions limiting the maximum number of output lines per query, making it necessary to download each orbit data in multiple files. Using the web interface was very time-consuming, especially for targets where a large ephemeris table was required. Querying JPL Horizons ephemerides via their email (batch-brief) method has reduced this considerably. The email procedure is also limited by the maximum file length restriction, although requesting the relevant dataset is much faster.

The software that I have produced requires 4 sets of orbit data: the equatorial coordinates and the orbit plane angle of the target and the 3-vector Cartesian positions and velocity coordinates of the target and the observer. All orbits were downloaded with UTC timestamps and with a timestep of 1 minute for high precision of the comet and observer's location. Distance and velocity units are in Astronomical Units (AU) and AU/day. JPL horizons was also used to determine each comet's inclination and longitude of ascending node, which were used to calculate the normal to the comet's orbital plane [Figure 3.4].

The equatorial coordinates for the target should be set up with the observing origin as the geocentre. This accounts for amateur observers based around the world, for whom it would be tricky to compensate, especially when the geographic location is not available for all images. The heliocentric and geocentric distances and the comet's position angle are not used actively within the code but are useful for understanding the observing geometry. The position angles refer to the extended sun-comet radius vector and are a good approximation of the comet's ion tail in the sky. The orbit plane angle table is produced in the same format with the addition of this parameter on the JPL Horizons interface. The frame of reference is the J2000.0 Geocentric Equatorial Inertial (GEI) with the XY plane defined as the Earth mean equator at J2000.0 and the positive x-axis as the vernal equinox (first point of Aries) at J2000.0 (Fränz & Harper 2002). The astrometric right ascension and declination of the target has been adjusted for light time.

The three-vector Cartesian coordinate system for the comet and observer (Earth, SOHO, STEREO A or STEREO B) positions, has the solar centre at its origin. These denoted the positions and rate of change of the targets, and were used to calculate the image mapping. This required high accuracy and time resolution. The frame of reference was the J2000.0

Heliocentric Earth Ecliptic (HEE) with the XY plane defined as the Earth mean ecliptic and the positive x-axis as the mean equinox of the reference epoch (Fränz & Harper 2002). The vectors have been light time corrected.

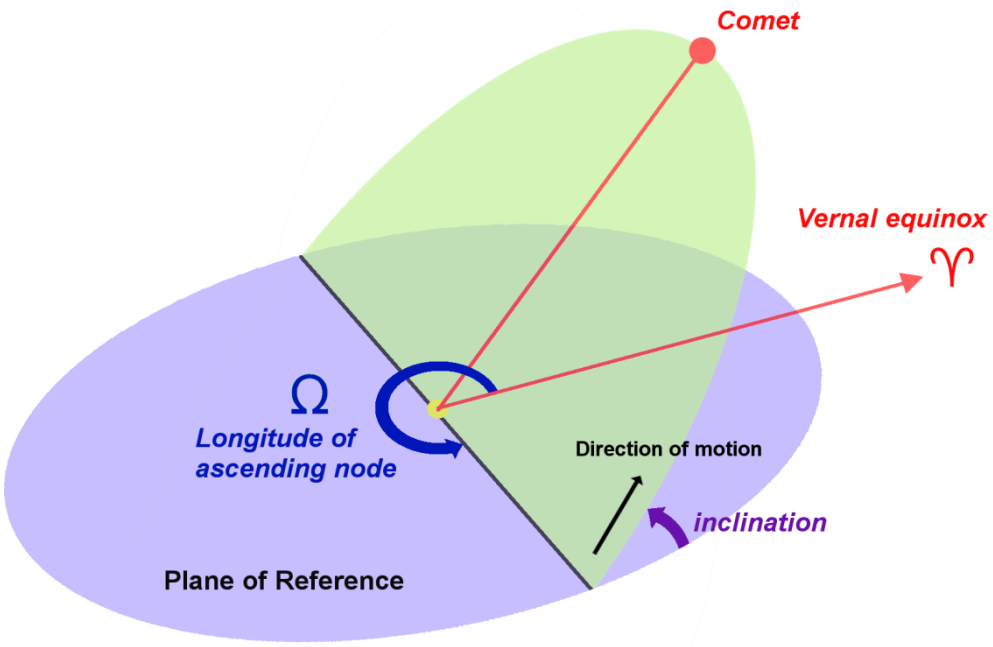

Figure 3.4: Schematic of the longitude of ascending node and inclination required to calculate the normal to the comet's orbital plane.

3.4. ACE/SWEPAM

The Advanced Composition Explorer (ACE) (Chiu & Von-Mehlem 1998) [Figure 3.5] was launched in August 1997 and placed in orbit around the Earth-Sun libration point, L1, roughly 1.5×10^6 km sunward from the Earth. It sits outside of the Earth's magnetosphere in order to investigate the properties of the interplanetary magnetic field, solar wind flow, solar energetic particles and other interplanetary and galactic particles. Its orbit about L1 provides a unique location to measure solar cycle dependent solar wind variations and its relationship with geomagnetic effects.

The Solar Wind Electron, Proton, and Alpha Monitor (SWEPAM) (McComas et al. 1998) is used here as a comparison dataset for the solar wind bulk velocities derived in this thesis. SWEPAM provides detailed real-time sampling of the solar wind plasma as functions of direction and energy. This allows information gathered by the other ACE instruments to be placed in the

context of the varying solar wind conditions upstream of the Earth. There exists data gaps in the SWEPAM dataset and these can be attributed to periods of both high solar energetic particle background and high solar wind speeds.

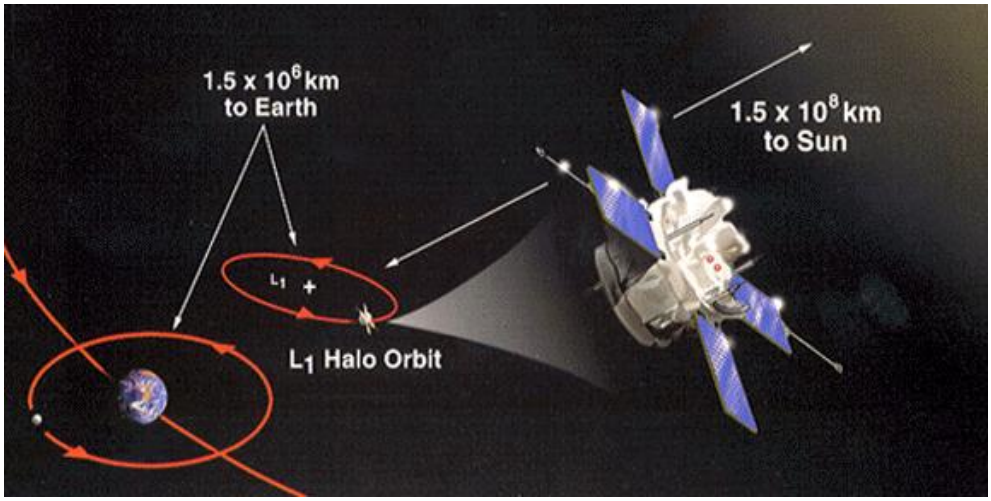

Figure 3.5: ACE in halo orbit around L1, 1.5 x 106 km sunward along Sun-Earth line. Image courtesy of Caltech ACE mission webpage.

3.5. SOHO / LASCO

Launched in December 1995, the NASA and ESA Solar and Heliospheric Observatory (SOHO) (Domingo et al. 1995) spacecraft is currently in a halo orbit around L1. It has not only revolutionised solar-terrestrial relationships and shed light on processes within the solar atmosphere, but has also allowed unprecedented views and discoveries of a subclass of comets, the so-called sungrazing and sun-skirting comets. As of March 2015, the number of SOHO discovered comets stood at 2,891, due largely to the collaborative efforts of amateur astronomers worldwide [http://sungrazer.nrl.navy.mil/]. The primary science objectives of the SOHO mission are to determine the structure, chemical composition, and dynamics of the solar interior, the structure (density, temperature and velocity fields), dynamics and composition of the outer solar atmosphere, and the solar wind and its relation to the solar atmosphere.

SOHO's Large Angle Spectrometric Coronagraph (LASCO) (Brueckner et al. 1995) is an externally occulted coronagraph to obscure the solar disk for stray light rejection (the solar disk outshines the corona by a factor of 10^8 in visible light (Llebaria et al. 2004)); its primary function

being the continuous monitoring of the corona via its white-light coronagraphs C2 and C3. The C2 and C3 [Figure 3.6] coronagraphs provide a field of view coverage of 2.5 – 6.5 (Llebaria et al. 2004) and 3.8 - 32 solar radii (Morrill et al. 2006) respectively. C2 colour filter bandpasses are red, orange and blue (Llebaria et al. 2004) and C3 has broadband colour filters (blue, orange, deep red, infrared and clear) and a narrowband (2nm) Hα filter (Morrill et al. 2006). Image cadences for C2 and C3 are usually approximately 20 and 30 minutes respectively. Its optics are designed to have an occulting disk obscuring the solar disk, thus allowing off-limb detections of faint transient features on the order of 10 to 11 orders of magnitudes fainter.

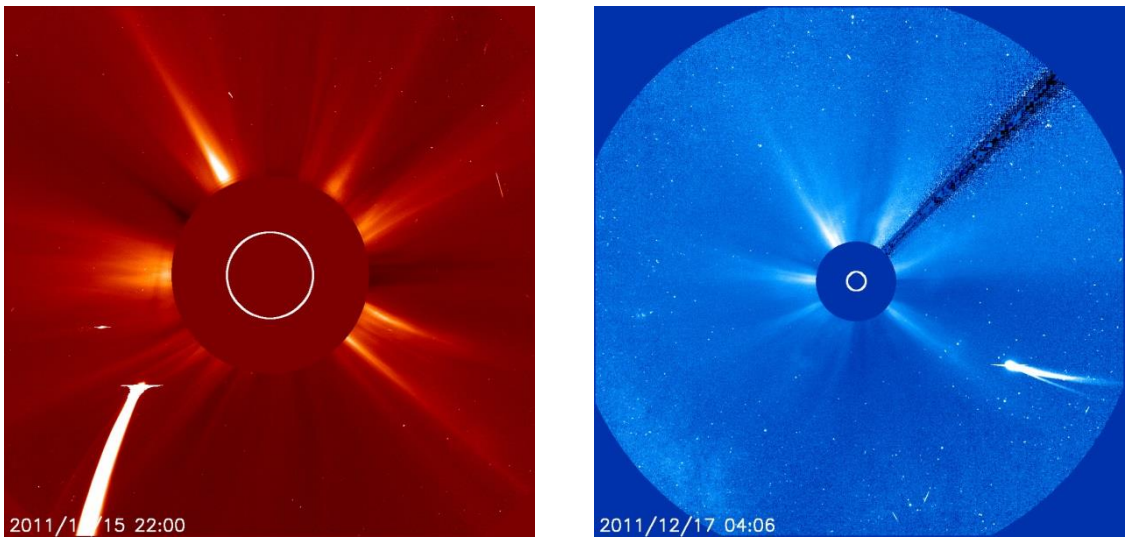

Figure 3.6: Comet C/2011 W3 (Lovejoy) pre-perihelion and post-perihelion as observed from LASCO C2 and C3

3.5.1. CME Catalogue

This CME catalogue is generated and maintained at the CDAW Data Center by NASA and The Catholic University of America in cooperation with the Naval Research Laboratory (Gopalswamy et al. 2009). The catalogue lists all transient CME events from the C2 and C3 coronagraphs [Figure 3.7] and categorises them according to their chronology, position angle, angular width, linear speed, acceleration, mass and kinetic energy. The position angle is measured counter-clockwise from Solar North in degrees. The central position angle (CPA) can be useful in distinguishing between simultaneously occurring CMEs. CMEs with an apparent width of 360^{o} are designated as Halo CMEs. Halo CMEs generally indicate that they could be moving directly towards or away from Earth. Once the CME expansion stabilises in the C2 FOV, a sky-plane

width is measured, when possible. Infrequently, certain CMEs will exhibit significant acceleration or deceleration, thus reducing the linear speed to merely a guide of the average CME speed within the LASCO FOV. Combining the date and time of CME eruption, its linear plane-of-sky speed, width and CPA with the heliocentric distance of our comet and the solar north pole, we can constrain a list of CME candidates likely to encounter the comet for a given date.

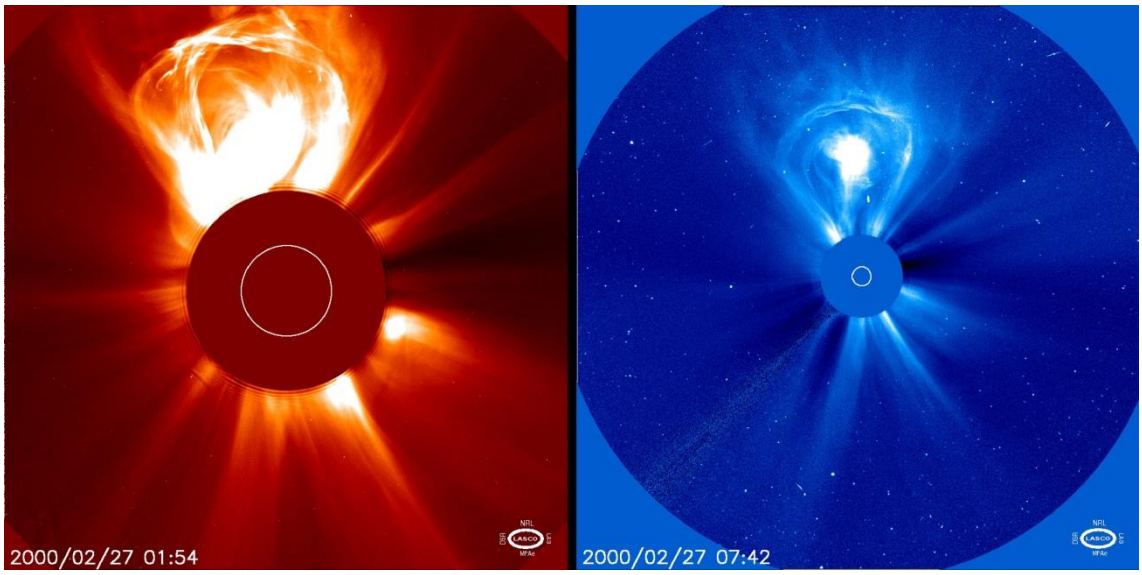

Figure 3.7: Bulb CME observed by C2 and C3 coronagraph on 27th February 2000.

3.6. STEREO A and B Heliospheric Imagers

The Solar TErrestrial RElations Observatory (STEREO) (Kaiser 2005) comprises two spacecraft, Ahead and Behind, both occupying approximately 1 AU orbits around the Sun; one leading the Earth's orbit, whilst the other lags, by a rate of ~22^{o} per year. Launched in October 2006, the twin spacecraft offer a suite of remote sensing instruments, the Sun Earth Connection Coronal and Heliospheric Investigation (SECCHI) (Howard et al. 2008) instrument consisting of 2 coronagraphs (COR1 and COR2) and a pair of heliospheric white-light imagers (HI1 and HI2). The set of telescopes offers the capability of three-dimensional tracking of Interplanetary Coronal Mass Ejections (ICMEs) from their eruption on the Sun through the corona and the interplanetary medium from two different vantage points.

The HI1 and HI2 imagers configuration provide a 20^{o} and 70^{o} FOV of the Sun-Earth line along the ecliptic and are centred off the solar centre by 14 and 53^{o}.7 (Eyles et al. 2008), looking at solar elongations from ~3^{o} to 23^{o}.5 (~12 - 92 solar radii) and 20^{o} to 90^{o} (~ 73 - 318 solar radii) respectively.

Each HI image is the sum of many shorter full-resolution (2048 x 2048) exposures that have been scrubbed for cosmic rays. Images are then binned to 1024 x 1024 pixels (DeForest et al. 2011) and stacked over a period of 40 minutes aboard the spacecraft, thus reducing the signal-to-noise ratio (SNR) and thereby increasing the telescope sensitivity. The increased telescope sensitivity allows observations down to a limiting magnitude of 13. As a trade-off, the HI cameras have no shutters and thus bright planets and stars cause saturation and blooming effects as the images are read off the CCD.

The HI data are available at different processing levels via the UK Solar System Data Centre (UKSSDC) usually with a cadence of 40 minutes. HI1 data is at an angular resolution of 35”/pixel, which allows measurement of fine structures in the cometary plasma tail, whereas the larger angular pixel scale of HI2 images (4’/pixel) means that it is difficult to resolve the ion tail. Only images from HI1 will be used in this thesis.

3.7. Isaac Newton Telescope (INT)

Beginning September 2012, I undertook a 14-month studentship at the Isaac Newton Telescope (INT) as a student Support Astronomer. The INT [Figure 3.8] is a world class 2.5m optical telescope in the northern hemisphere, operated by the Isaac Newton Group of Telescopes (ING). It is collectively funded in different proportions by 3 member organisations: the British 'Science and Technology Facilities Council', the Dutch 'Nederlanse Organisatie voor Wetenschappelijk Onderzoek', and the Spanish `Instituto de Astrofsica de Canarias' (IAC). Located at an altitude of >2400 m above sea-level on the Roque de los Muchachos (Latitude: 28^{o} 45’ 43.4” N, Longitude: 17^{o} 52’ 39.5” W), the INT boasts a median seeing of about 1.2 arcsec, with 20 and 25% of the year lost to inclement weather (clouds, high wind speed, high

humidity, calima or icy conditions). During the dark moon phase, the sky brightness at high ecliptic latitude is V~21.9 mag arcsec^2 (Benn & Ellison 1998).

Consisting of a parabolic primary mirror and a hyperbolic secondary mirror, the INT hosts an imaging camera, with a focal ratio of f/3.3 at its prime focus, and a long-slit spectrograph mounted at its Cassegrain focus, with a longer focal ratio of f/15. This design facilitates focussing of the telescope, simply by moving the small, secondary mirror. The telescope utilises a polar disc, fork type equatorial mount, with its polar axis aligned with the Earth's rotational axis. Its declination axis is kept fixed; this allows for more efficient tracking of targets across the night sky by rotating the polar axis at the Earth's rotational angular velocity. This particular type of telescope mount, coupled with its dome, restricts the INT's operational range to a lowest elevation limit of 20^o, with this lower limit increasing to 28^o at the celestial North pole and ± 6 hours for the hour angle. Declinations lower than -30° 09' 30" are inaccessible with the INT telescope. Certain legacy components of the telescope design have degraded and have not been replaced in over 40 years, making the overall reliability less than optimal. Most technological fallbacks, from outdated mechanical systems to major software crashes, are logged and faults regularly maintained by the ING engineers.

The Isaac Newton Telescope offers a range of handy web applications such as the object visibility tool, allowing for careful scheduling of targets ahead of the observing night and the exposure time calculator, to anticipate the intensity throughput to maximise scientifically useful on-sky observations. Prior to starting observations, calibration frames, the telescope pointing and focussing routines are run to accurately set up and calibrate the observing session. Control of the telescope and dome requires a combination of manual (Engineering rack) and automatic procedures via the Telescope Control System (TCS).

Figure 3.8: 2.5m Isaac Newton telescope. Image credit courtesy of ING webpage.

3.7.1. Wide Field Camera (WFC) and THELI

Comprised of 4 thinned EEV CCD (2048 x 4096 pixels), in a mosaic covering a 34' x 34' field of view, the Wide Field Camera (WFC) [Figure 3.9] is capable of obtaining deep, high-resolution images, which have been useful for large optical imaging surveys, such as the IPHAS survey. Each CCD is separated by ~ 0.5 arcmins from its neighbouring chip, requiring a dither of at least 30 arcseconds in x and y to cover the inter-chip spacing. Each CCD pixel corresponds to 0.33 arcsecs on sky. To fully readout the full 4 CCD mosaic, takes ~42 seconds in slow readout mode and ~23 seconds in fast readout mode. The INT offers a large selection of broadband, Stromgen and narrowband filter sets for use with the WFC's 6 filter wheel. The autoguider CCD is half the size of a WFC CCD and sits behind the filter wheel, which can be problematic when tracking faint targets during poor weather conditions.

I, along with K. Birkett, observed with the WFC during 2nd - 6th January 2014. I had initially proposed to observe comet C/2012 S1 (ISON)'s ion tail, which was anticipated to survive its perihelion in late November 2013. The tail would have been circumpolar towards the latter end of the observing run, with its nucleus below the INT's observing limit for the majority of our observing window. My backup science targets were deep colour images of main-belt comets

(MBC) 133P/Elst-Pizarro and P/2013 R3 (Catalina – PanSTARRS), comets P/2012 T1 (PanSTARRS), P/2013 P5 (PanSTARRS), C/2013 V2 (Borisov), P/2013 V3 (Nevski), C/2012 K1 (PanSTARRS), C/2012 X1 (LINEAR), C/2013 R1 (Lovejoy) [Figure 3.10]. Both C/2013 R1 and C/2012 X1 showed a promising plasma tail. The analysis in this thesis will focus only on C/2013 R1 due to its brighter and more detailed plasma tail. Observations were undertaken with the target's non-sidereal rate for differential tracking. For this particular comet-oriented observing programme, I used a combination of H-alpha, Sloan r and i, Harris B and V filters. The large number of filters meant that we have a very short window to obtain sky calibration flats during astronomical twilight. The bias level for the WFC is ~2000 counts. Dark current is negligible due to the liquid Nitrogen cooled CCDs.

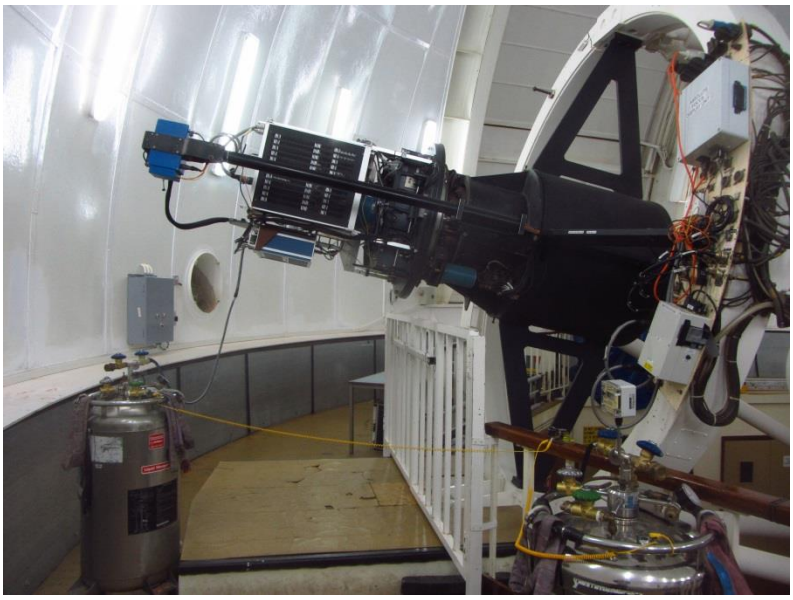

Figure 3.9: Filling the cryostat of Wide-Field camera with liquid Nitrogen to maintain the nominal CCD temperature at 150K.

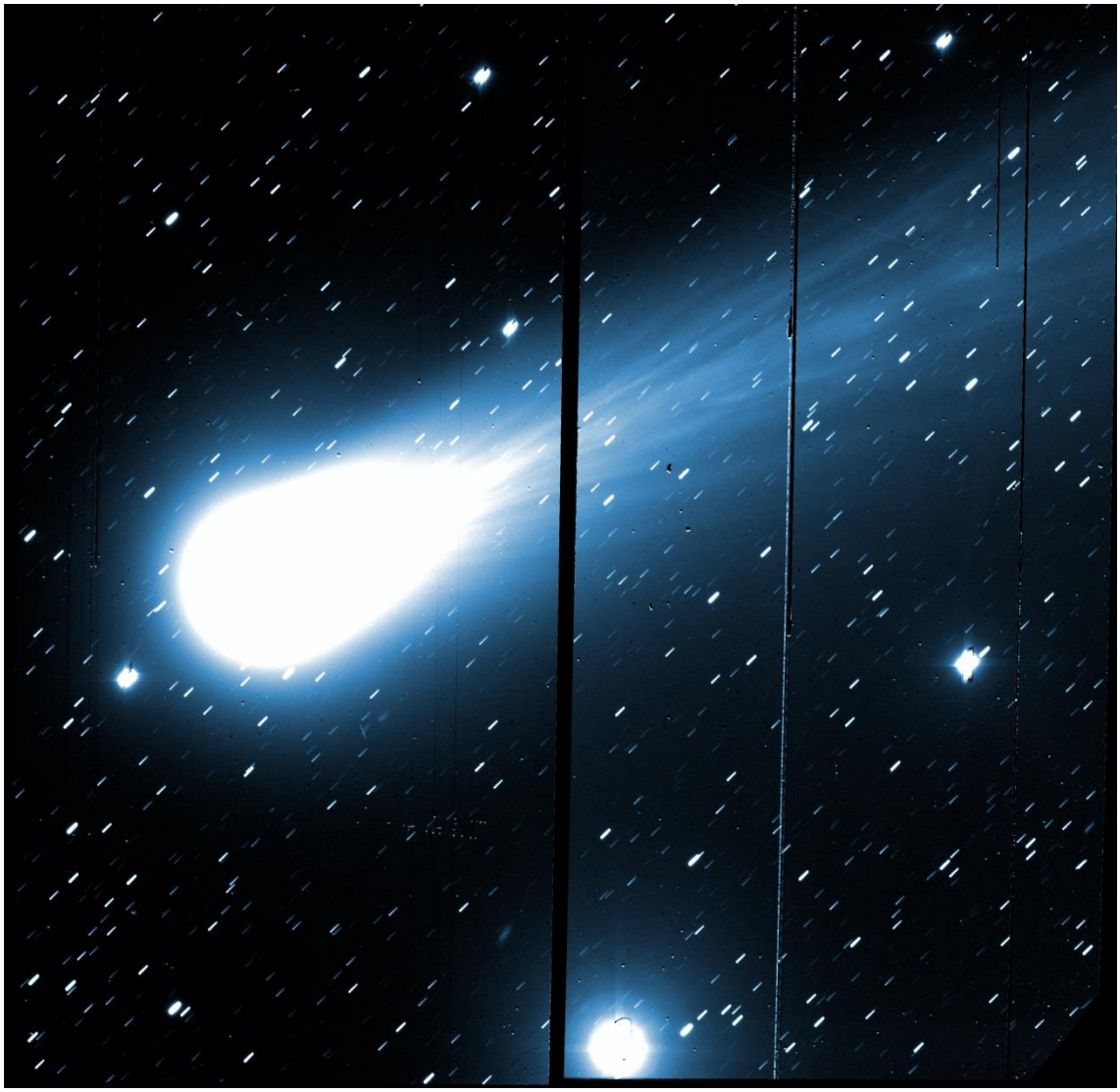

Figure 3.10: THELI reduced and stacked image of Comet C/2013 R1 (Lovejoy) observed with the Isaac Newton Telescope's ~0.5 FOV Wide-Field Camera (CCDs 3 and 4 shown here) on 2nd January 2014 with the Harris B filter. Observer: Yudish Ramanjooloo.

3.7.1.1. THELI

THELI (Schirmer 2013; Erben et al. 2005) is an automated data reduction pipeline for calibration, sky background and optical distortion correction [Figure 3.11] of astronomical images from a number of different telescopes and instruments. INT WFC images are commonly processed through THELI. For more info on how THELI was used, see Appendix B.

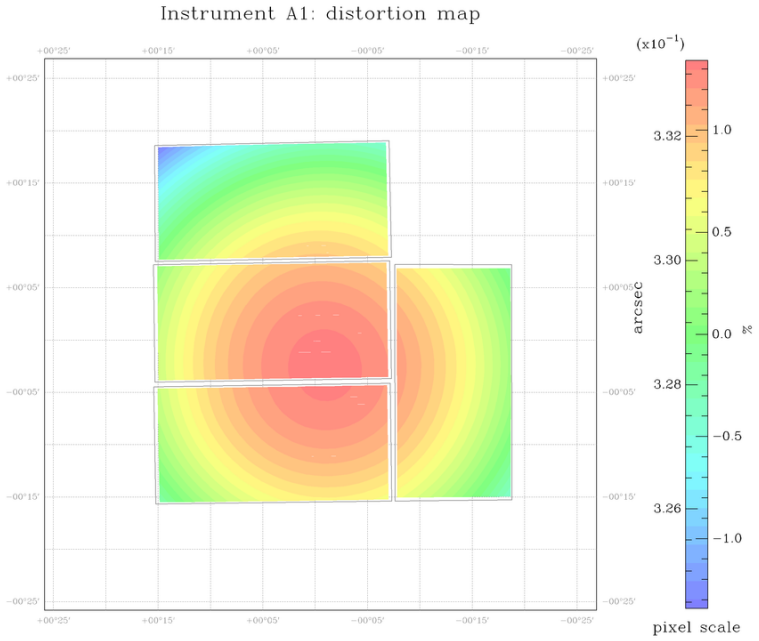

Figure 3.11: Distortion map of C/2012 X1 (LINEAR) taken with the INT on the 2nd January 2014. The symmetrical concentric distortion map here is an example of a good distortion correction to the INT image.

3.7.2. Intermediate Dispersion Spectrograph (IDS) and IRAF

The Intermediate Dispersion Spectrograph (IDS) is a long-slit spectrograph, permanently mounted at the Cassegrain focus of the INT. To alternate between the WFC and IDS [Figure 3.12], the WFC is swapped with a secondary hyperbolic mirror. The IDS is available with a 235 mm focal length camera with a blue-sensitive EEV10 CCD (4096 x 2048 pixels; spatial scale of 0.40 arcsec/pixel) and a red-sensitive RED+2 (4096 x 2048 pixels; spatial scale 0.44 arcsec/pixel) detector. The IDS offers a number of reflective diffraction gratings and CCD combinations allowing dispersions between 0.24 and 4 Å per pixel to vary from low to moderately high resolution. The full unvignetted length of the slit in IDS is 3.3 arcmins (500 detector pixels for EEV10), but its slit width can be altered to vary the amount of light allowed through the spectrograph. The IDS optics, in particular the CCD corrector lens, were not intended for use with the large detectors available for use. This will result in a degradation of the spatial profile towards the top and bottom edges of the CCD, with the target appearing as if it is out of focus in these regions. The thinned EEV10 chip is severely affected by fringing in the red part of the spectrum, thus limiting its utility in this region.

The IDS slit's orientation can be rotated with the Cassegrain turntable. This is of paramount importance in accounting for the atmospheric refraction of starlight which will disperse the light along the vertical direction. This is the parallactic angle. This effect becomes more apparent at low elevations for point source targets. In order to maximise the collection of light from all wavelengths of the target's spectrum, the slit must be aligned to the parallactic angle, so that the slit is oriented perpendicular with respect to the horizon. For extended targets, such as comets, this feature is particularly useful to position the slit either along our line-of-sight from Earth or the comet's position angle from the sun to obtain ion velocities in the anti-sunward direction for the latter. The IDS also comes pre-equipped with neutral density and colour filters. The neutral density filters will attenuate the incoming light across all wavelengths, whilst the colour filters can be used to suppress specific colours within the target's spectrum.

Figure 3.12: Swapping the Wide-Field Camera for the secondary mirror (left). Intermediate Dispersion Spectrograph (right)

Observations:

During discretionary time (D nights) at the INT and during my proposal (7th January 2014), I observed several comets with the IDS. Our observing night, on the 8th January 2014, was cancelled due to snowfall.

Targets observed were: C/2012 K5 (LINEAR); C/2012 X1 (LINEAR); C/2013 R1 (Lovejoy); different latitudes of Ceres to follow up the Herschel telescope's discovery of water vapour; sunward and anti-sunward observations of Ceres in an attempt to detect an induced ion tail;

Europa to track its activity (e.g. enhanced emission from water-derived molecules such as oxygen) near apojove; standard spectrophotometric stars and standard radial velocity stars.

Calibration frames

Spectroscopic copper argon (Cu-Ar) and copper neon (Cu-Ne) arc frames were taken to calibrate the wavelength scale for each science image. A Tungsten lamp was used for our spectroscopic flats. The arc frames were taken before and after our exposures. Long observing programmes, where the target covers a significant portion of the sky, are interspersed with arc frames taken during the science observations. This is to account for flexure in the telescope due to gravity. This effect becomes more pronounced at low elevations. The minimal fringing effects of the blue-sensitive EEV10 IDS detector at the wavelength range we observed means there was no need for flat frames to be taken at different flexures. At the time of commissioning, the worst telescope flexure recorded on the IDS 235 mm camera is about 10 microns/hour. Sky flats of a blank section of the night sky were taken with the largest slit width possible (~9 arcsec) to account for telluric emission lines.

Spectrophotometric and Radial Velocity standard stars

Standard spectrophometric stars were observed to photometrically calibrate the target's spectra, so as to ascertain the atmospheric spectral response and thus remove its contribution from our data. Doppler measurement of ion velocities in the plasma tail requires good weather and seeing conditions and precise spectral calibration. For the latter which can be controlled, it is imperative to obtain observations of a radial velocity standard star, to correct for the relative motion of the star with respect to its observer. In essence, here we are correcting for the Earth's rotation and its orbit around the sun.

Observing log:

During the available D nights and my observing programme, I used the following gratings: H1800V, R1200B, R1200V, R632V. The targets were chosen to be far away from the Moon. This is so that the reflected solar continuum from the Moon and moonshine does not contaminate our spectra. We selected for wavelength ranges which would show these emission lines:

Na: 5896 Å (Brown et al. 1998)

CO+: ~4200 Å (Cochran & Cochran 2002); 3800 – 4800 Å (Ip 2004)

H_2O^+ : 6159 Å (Rauer & Jockers 1993); 5600 – 7000 Å (Ip 2004)

Limited by bad weather conditions on the 7th January 2014, we resorted to a low-resolution grating to maximise the light throughput to the spectrograph. Our aim was to obtain line abundances in comets C/2012 X1 (LINEAR) and C/2013 R1, with peak m_v ~ 8 and m_v ~6 respectively during observations. The INT did not offer differential guiding at the time and differential tracking with the IDS required constant vigilance and periodic, tiny manual adjustments. The IDS spectrograph contains an acquisition camera, which uses light reflecting off the polished metallic slit. This is particularly useful when positioning and orienting the slit onto the target and to maintain the target's position on the slit during non-sidereal tracking. However, the combination of the camera's limiting magnitude (m_v ~ 17), its small FOV of 1.2 x 1.2 arcmins and weather conditions meant that the relative position of the spectra on the chip may be shifted by a few pixels between and during observations. This would have been problematic for radial velocity dispersions but should not be detrimental to the line abundance analysis.

Comet Lovejoy (C/2013 R1), the best candidate for analysis (setup: R632V, wavelength centred on 6200 Å, slit width 1" and fast readout speed), was observed mostly at low elevations (22^o and rising). Measurements were taken along and across the ion tail (slit orientation: 238^o) to obtain abundances along the line-of-sight and along the ion tail (slit orientation: 328^o) in the anti-sunward direction. Measurements were also taken at a slit orientation of 301^o, across the dust tail in an attempt to identify a sodium source for the comet. The spectra will be stacked to increase the signal-to-noise ratio and the dust-reflected solar continuum and the Swings effect

will be subtracted. The Swings effect is defined as the Doppler shifting of Fraunhofer lines with respect to cometary band systems, arising due to the Earth's radial velocity (Brandt & Chapman 2004). This is to determine both abundances and the Doppler velocities along our line-of-sight and along the ion tail for the anti-sunward ion drift velocities (Rauer & Jockers 1993).

3.8. VIXEN 20 cm Telescope

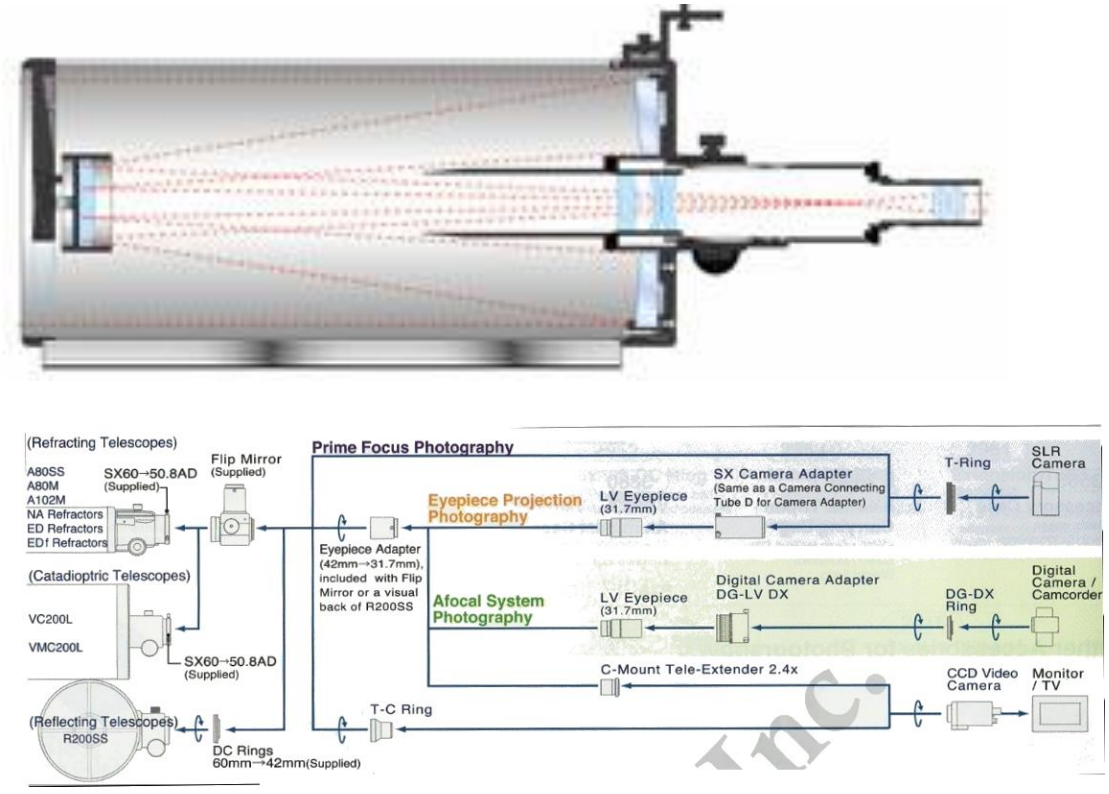

Figure 3.13: Cassegrain Reflector telescope (Top). Vixen set up (Bottom). Images extracted from VC-200L telescope manual by Vixen Optics.

The Vixen 20 cm telescope is a small Cassegrain reflector telescope [Figure 3.13], available for use by Isaac Newton Group of Telescopes (ING) support staff. During late November 2013, along with fellow observer W. Gater, we set out to observe comets ISON (C/2012 S1) [Figure 3.14] and Lovejoy (C/2013 R1). A digital SLR camera attached to a T-ring was mounted at the Cassegrain focus onto the telescope, as shown in the schematic for reflecting telescopes below.

Optical Design	VISAC (Vixen's Six-Order Aspherical Cassegrain) Aspherical Mirror Reflector
Aperture	200mm
Focal Length	1800mm
Focal Ratio	f/9.0
Resolving Power	.58 arcsec
Limiting Magnitude	13.3
Light Gathering Power	816x

No biases, flats or darks were taken as we were limited by a short observing window pre-twilight. The telescope was polar aligned using inbuilt crosshairs within the central leg mount. Tracking was done manually as the telescope's tracking software did not have the comet's non-sidereal information. Hence, exposures were limited to a maximum of 30 seconds as a compromise between capturing enough photons to see the comet's ion tail and reducing star trails for subsequent high-precision astrometry. The images were stacked in sets of 3 and processed through Astrometry.net [Figure 3.14]. It was not possible to obtain solar wind velocities from this series of images but this opportunity allowed me to gain perspective on the observing methods regularly employed by amateur astronomers and the challenges they face.

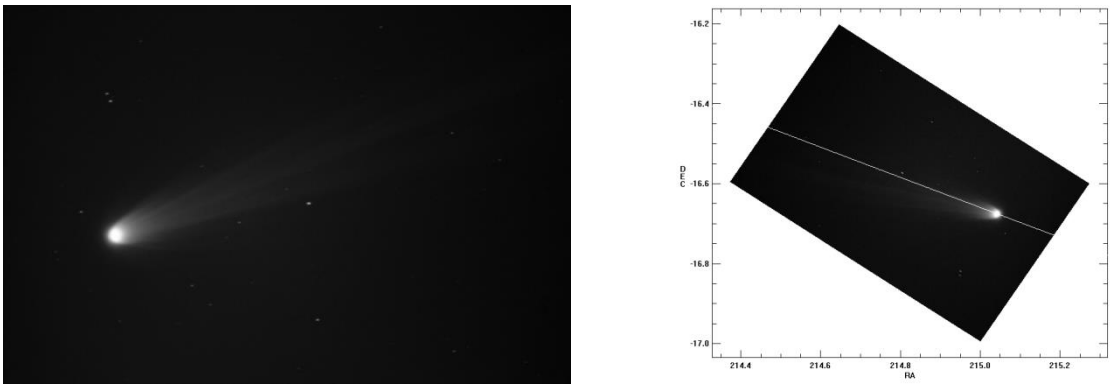

Figure 3.14: *Left*: C/2012 S1 (ISON) photographed 22/11/2013 by W. Gater and Y. Ramanjooloo. *Right*: Images were stacked and intensity stretched with DeepSkyStacker using median Kappa-sigma clipping and mapped onto equatorial plane. The comet's orbit is shown in white.

4. Amateur Observations Of Comets

Remote observations of a comet's ion (Type I) tail can yield extensive information on the solar wind in the comet's vicinity. Past studies (Belton & Brandt 1966; Brandt 1967; Brandt et al. 1972; Brandt et al. 1973; Jockers 1981; Brandt & Snow 2000; Buffington et al. 2008 to name but a few) of the ion tail orientation have successfully constrained the local solar wind velocity. The cometary ion tail is an induced magnetotail structure, pointing approximately along the anti-sunward direction but lags the true anti-solar direction by a few degrees. The aberration angle arises from a combination of the comet's orbital velocity and the local solar wind velocity. With a good observing geometry, comets with a suitably bright ion tail, can contribute towards increasing our understanding of the variability in solar wind velocity.

Of the multiple space probes launched to sample the solar wind in situ, Helios 2 travelled closest to the Sun so far, reaching perihelion at 0.29 AU (Blanco et al. 2013), and successfully measured the solar wind speed to both a high accuracy and high temporal resolution. In situ spacecraft measurements of the solar wind velocity are limited to the position of the spacecraft at the time of observation, and are restricted to the orbits or trajectories that they follow, which in the vast majority of cases are confined to close to the ecliptic plane. An exception is Ulysses which conducted three near pole-to-pole multi-heliolatitudinal scans of the solar wind. In-situ measurements of cometary ion tails however provide information on the solar wind over a wide range of solar latitudes, as this enormous reservoir of objects has orbits with a wide range of periods, eccentricities and inclinations [Figure 4.1]. An extended ion tail also records a time history of solar wind changes over several hours. Therefore, remote observations of the ion tail are key to probe the high spatial variations of solar wind structures across a wide range of heliospheric latitudes [Figure 4.2] and distances and over long timescales with minimal financial investment. If this technique can provide valid estimates of the solar wind velocity in unexplored regions of the inner heliosphere, then this complementary dataset can be used to further refine existing solar wind models.

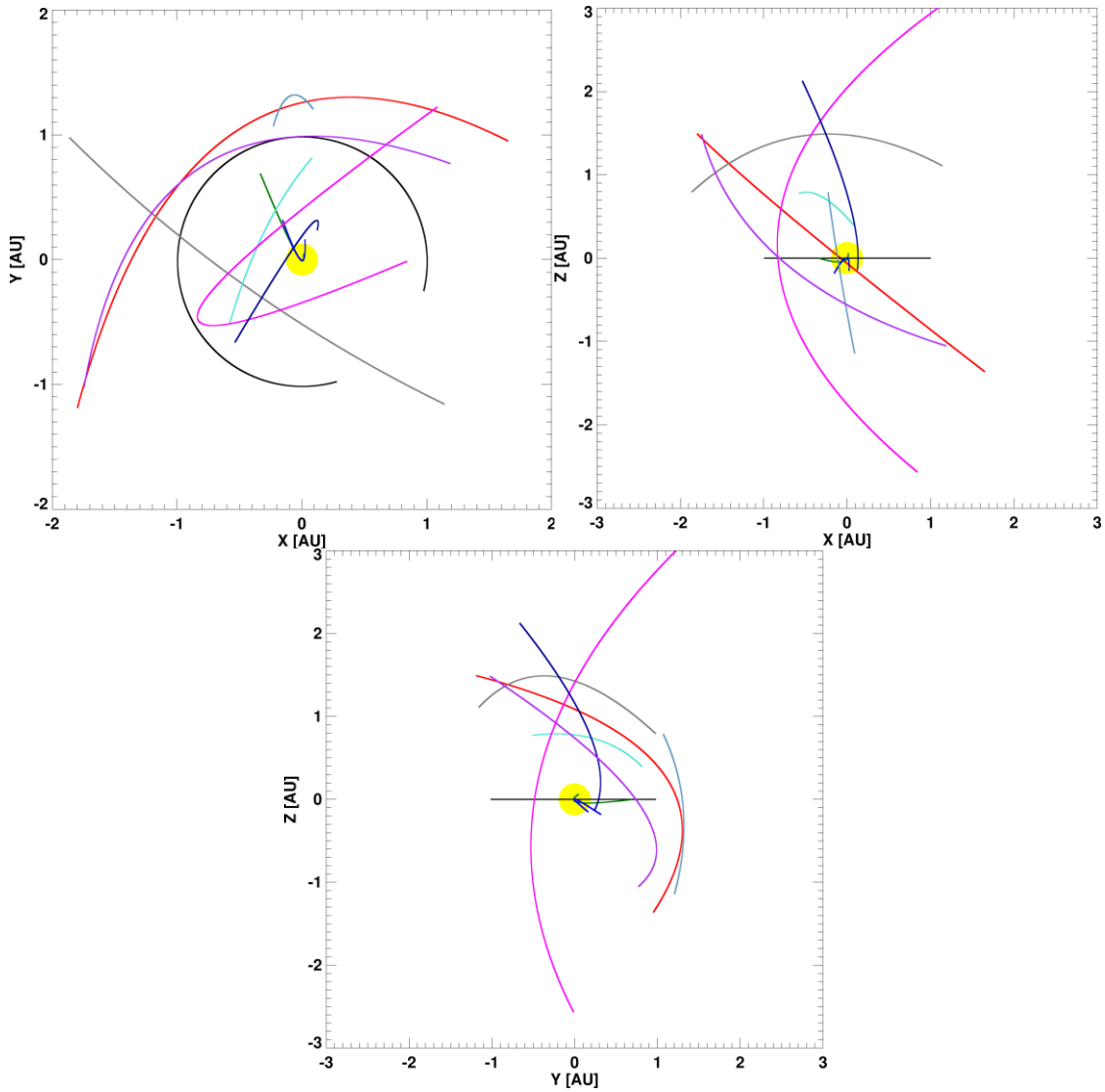

Figure 4.1: Regions of the inner solar system probed by the comets analysed in this thesis. The comets are labelled in the heliographic latitude plot in Figure 4.2 and are similarly colour-coded.

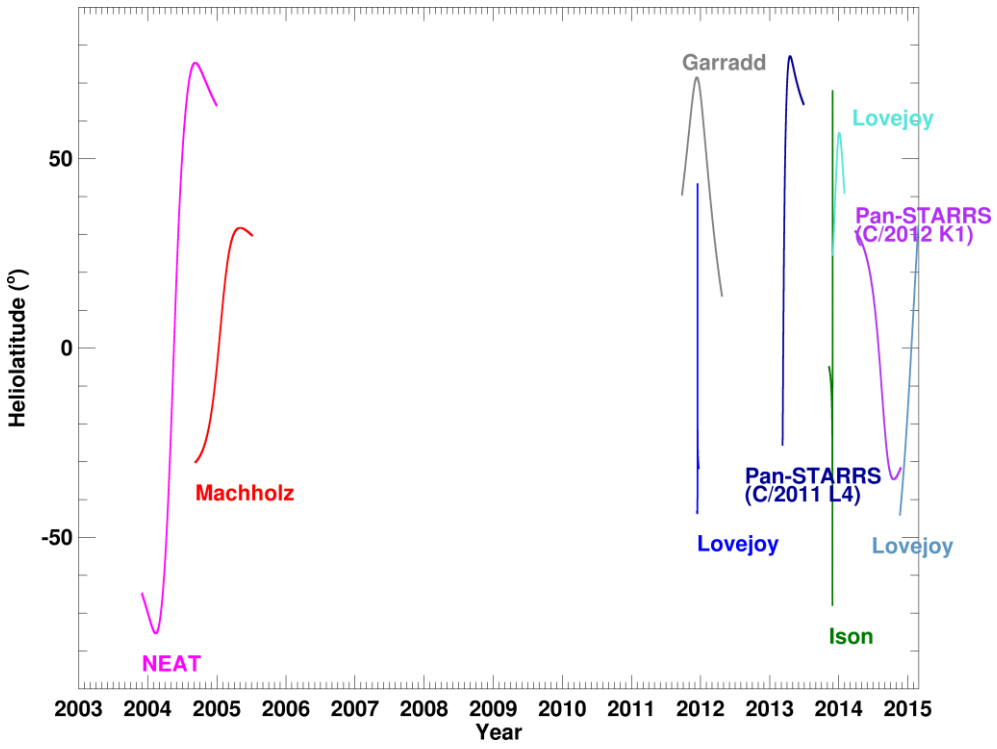

Figure 4.2: Heliocentric latitudes probed by the comets used in this study. Observations of these comets exist outside of the periods shown here but these were not analysed for this study.

Aside from velocity measurements, the continuously varying morphology, dynamics, and orientations of an ion tail, can be used to infer the fluctuations of both large-scale and small-scale structures in the solar wind. Ion tail disconnection events (DEs) are considered to be key markers of solar wind phenomena interactions. Niedner & Brandt (1978) have associated tail disconnections with crossings of the heliospheric current sheet (HCS). Encounters with coronal mass ejections can lead to rapid reconfigurations of tail features and orientations (Jones & Brandt 2004). Furthermore, Vourlidas et al. (2007) linked the first direct observation of an ICME-ion tail interaction which lead to a disconnection of comet 2P/Encke's ion tail. Locations of co-rotating interaction regions (CIRs), where fast and slow solar wind regions interact, and transitions between different solar wind regimes can be accurately identified from kinks in the ion tail, i.e. large and rapid changes in the aberration angle. We have developed a novel system of extracting valid local solar wind velocity estimates, as well as characterising local parameters for transient interplanetary events near comets, allowing us to use comets as solar wind monitors throughout the inner heliosphere.

I will be investigating amateur images of bright comets with a small geocentric distance and good observing geometry from Earth. Using amateur images of comets, I aim to demonstrate that comet observations can provide reliable estimates of the ambient local solar wind velocity at the comet and can lead to the identification of the local parameters of coronal mass ejections (CMEs), the locations of heliospheric current sheet (HCS) crossings, as well as the locations of co-rotating interaction regions (CIRs) during periods of quiescent solar activity. The primary application of this project is to show that comets can be reliable, remote probes of heliospheric conditions.

I used images of comet C/2004 Q2 (Machholz), taken by amateur astronomers, to develop the technique and software to extract multiple estimates of the local solar wind velocity. Amateur images of comet NEAT were used to further validate both the software and the technique described in this chapter. This project is a continuation of a collaboration by G. H. Jones, and J. C. Brandt.

The comets above were chosen as candidates due to their brightness, orbit geometry and the extensive online collection of amateur images. The fortuitous geometry of comet C/2004 Q2 (Machholz) and comet C/2001 Q4 (NEAT) brought them close to the ecliptic plane and within 0.3 AU from the Earth around their perihelion. During comet Machholz's period of maximum brightness and observability, the comet's orbit evolved almost in step with the Earth's motion in both solar ecliptic and heliographic longitudes.

From this unique geometrical arrangement, we assume that:

- local Earth solar wind conditions, as registered by the ACE spacecraft, can be reliably extrapolated to the near-vicinity of the comet and,
- any interplanetary coronal mass ejections would be experienced by both the Earth and the comet.

Estimates of the local solar wind velocity extracted from these images will be compared to values of the solar wind velocity for the inner heliosphere modelled by M. Owens using the ENLIL simulation (Odstrcil 2003). The model was extrapolated to estimate the local solar wind velocity at the comet. This model does not include transient interplanetary events.

Local solar wind velocity estimates, when comet C/2004 Q2 (Machholz) crossed the ecliptic plane and was in step with the Earth's motion will be compared to solar wind velocity measurements by the ACE/SWEPAM instrument. Measurements taken from the ACE spacecraft will need to be offset by ~1.5 to 2 days to account for the time taken for the solar wind structures experienced by the comet to sweep the Earth. Other time periods will not be offset for comparison as ACE will be too far away for reliable comparisons. The SOHO/LASCO CME catalogue will serve as the database to narrow down potential ICME candidates. Polarity reversals in the solar wind are also included and will be compared to images displaying disconnection events.

The results of this project will be used to build a snapshot picture of the solar wind variability in the inner heliosphere, similar to the comet-solar wind paradigm by Brandt and Snow (2000).

4.1. Deriving Solar Wind Velocities

As discussed in chapter 2, the ion tail orientation can be exploited to pin down an approximation of the local radial flow of the solar wind. The aberration angle, Ɛ, is defined by the angle between the comet's heliocentric orbital motion vector and the prolonged radius vector from the sun, i.e. the radial flow of the solar wind.

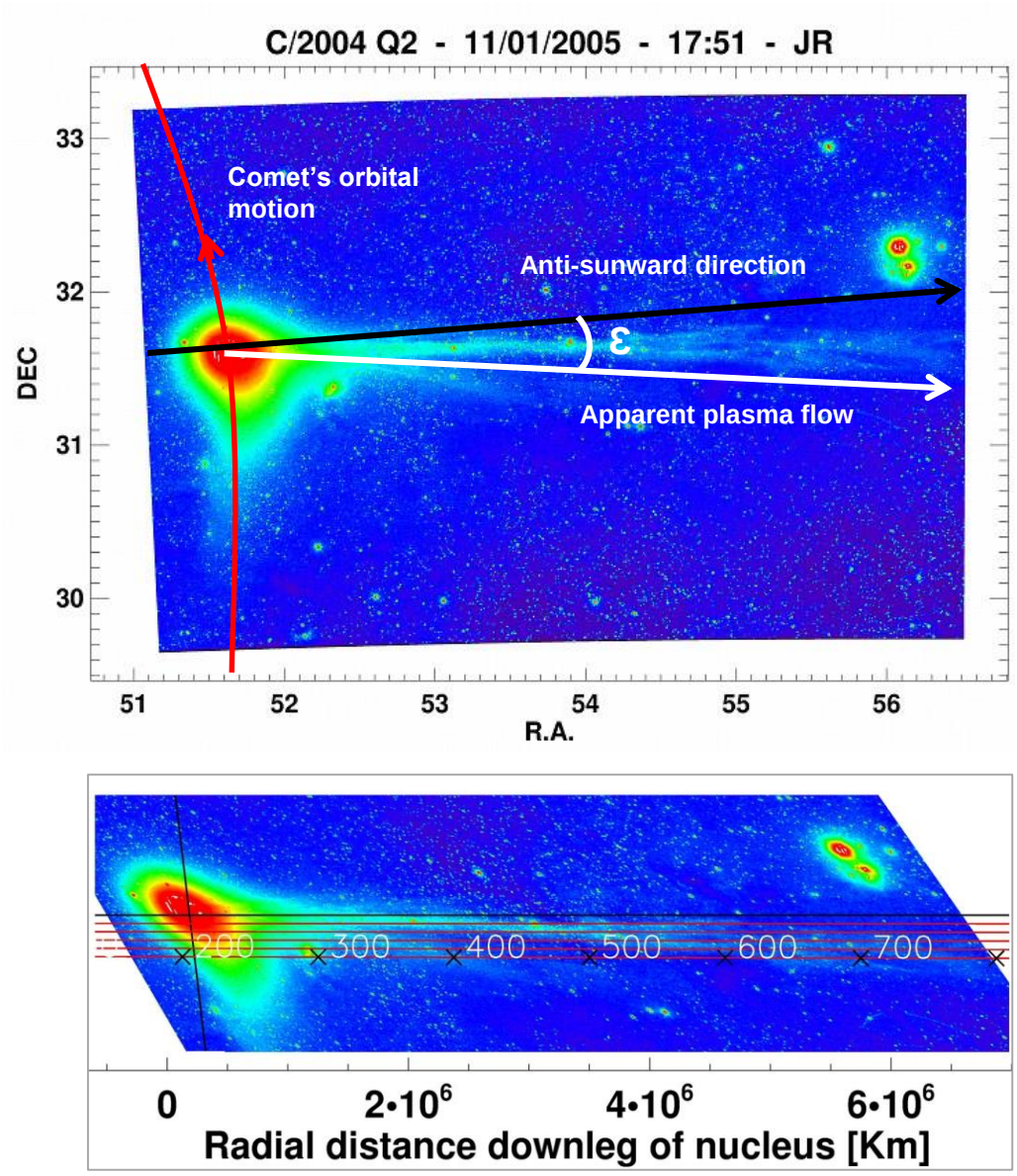

Figure 4.3: Comet C/2004 Q2 mapped in equatorial coordinates and in heliocentric ecliptic coordinates. The second image has been transformed so as to keep the sun-comet line fixed with the predicted comet nucleus location as the origin. The comet's orbit is in red and the sun-comet line in black. The sun-comet line in the first image is a rough approximation whilst in the second image, this is the extended radial vector from the sun.

Figure **4.3** illustrates the slight difference between the two techniques of determining the solar wind velocities. The orientation of the ion tail arises from the combination of the comet's orbital velocity and the local solar wind velocity (Hoffmeister 1943; Biermann 1957). The composite vector equation is given by:

$$\bar{T} = \bar{w} - \bar{V}$$

$\bar{T}$ is flow vector of the ion tail, $\bar{w}$ is the solar wind velocity vector and $\bar{V}$ is the comet's orbital velocity vector. In the top image, it is possible to measure the aberration angle of the ion tail on the plane of the sky. By projecting these vectors onto the comet's orbital plane, as described in Konopleva & Rozenbush (1974), an expression for the aberration angle can be defined. Rearranging the equation for the radial solar wind velocity, we obtain:

$$w_r = \frac{V sin\ \gamma - w_\phi\ cos\ i}{tan\ \varepsilon} + V cos\ \gamma$$

The solar wind velocity vector is resolved into its radial (w_r) and tangential (w_Φ) components. *γ* is defined as the angle between the extended radial vector of the comet and the vector of the comet's orbital velocity, *i* is the inclination of the comet's orbital plane to the solar equator and Ɛ is the aberration angle. The rms error of the radial velocity is given as below. The error on *V*, *i* and *γ* can be ignored since they depend on the accuracy of the orbital elements, which are dwarfed by measuring errors.

$$\sigma_w = \sqrt{\left(\frac{V sin\gamma - w_\phi\ cos\ i}{tan\ \varepsilon^2}\ \sigma_\varepsilon\right)^2 + \left(\frac{cos\ i}{tan\ \varepsilon}\ \sigma_\phi\right)^2}$$

Using my novel technique described in this chapter, the images can be extrapolated along the line-of-sight of the observer and mapped onto the comet's orbital plane. Once the image is mapped onto the comet's orbit a simplified geometry of the system can be extracted. The aberration angle can thus be simplified to the equation below, where $V_\perp$ is the perpendicular component of the comet's velocity to the prolonged radius vector and w_r is the radial solar wind speed.

$$tan\ \varepsilon = \frac{V_\perp}{w_r}$$

The bottom image in Figure 4.3 encapsulates the adopted sampling method for this thesis. With cometocentric distances calculated for the image, multiple cuts are taken parallel to the radial vector with set time steps. Solar wind velocities are then calculated from these known quantities. Since each image is projected onto the comet's orbital plane, the best framework to

estimate the solar wind velocity, all the previous considerations (V, *i* and *γ*) are factored in within the projection mapping. We also compute the solar wind velocity using the simplified equation for the aberration angle. They both produce solar wind velocities within the same range, with some erroneous values produced for very small aberration angles, for instances where the ion tail lies close to the extended radial vector. Even under excellent geometrical scenario, without mapping the image onto the comet's orbital plane, precisely measuring the aberration angle can be difficult as the comet's orbital velocity is generally an order of magnitude smaller than the solar wind velocity (Brandt & Heise 1970).

Alternative techniques

Buffington et al. 2008 used photometric SMEI sky map image sequence of comets C/2001 Q4 (NEAT) and C/2002 T7 (LINEAR) to analyse radial solar wind velocities, once the fisheye geometry was corrected for. SMEI consists of 3 cameras each viewing a 60^{o} x 3^{o} band of sky. The comet tails were seen to extend up to ~0.5 AU (Buffington et al. 2008). A large observed tail extending over a significant fraction of an AU is critical for this technique to work. Here, Buffington assumes that the ion tail has assumed the solar wind speed. By defining a spatially and temporally fixed radial vector from the sun to the comet, the intersection of this fixed line with the ion tail from subsequent images in their time series will thus yield the radial solar wind velocity component. This is repeated for each successive frame in their image sequence to create a grid of solar wind velocities at different positions down the ion tail [See Figure 4.4]. With this technique, Buffington estimated a variable solar wind flow with velocities as low as 200 km s^{-1} and reaching up to 600km s^{-1}. They further report velocity drops of ~100 km s^{-1} during tail disturbances, with these velocities subsequently rising to a higher value than the typical solar wind velocity. Clover et al. 2010 used this similar technique for STEREO HI-A observations inferring that solar wind velocities for the comets observed near perihelion (~0.15 AU for comet 96P/ Machholz and ~0.34 AU for comet 2P/Encke) were highly variable ranging from as low as 200 km s^{-1} for comet 2P/Encke and as high as 670 km s^{-1} for C/2004 Q2 (Machholz). This technique lays a good precedent for our methodology. However, they do not include mapping of

the images onto the comet's orbital plane, which would allow for a true measurement of the purely radial solar wind.

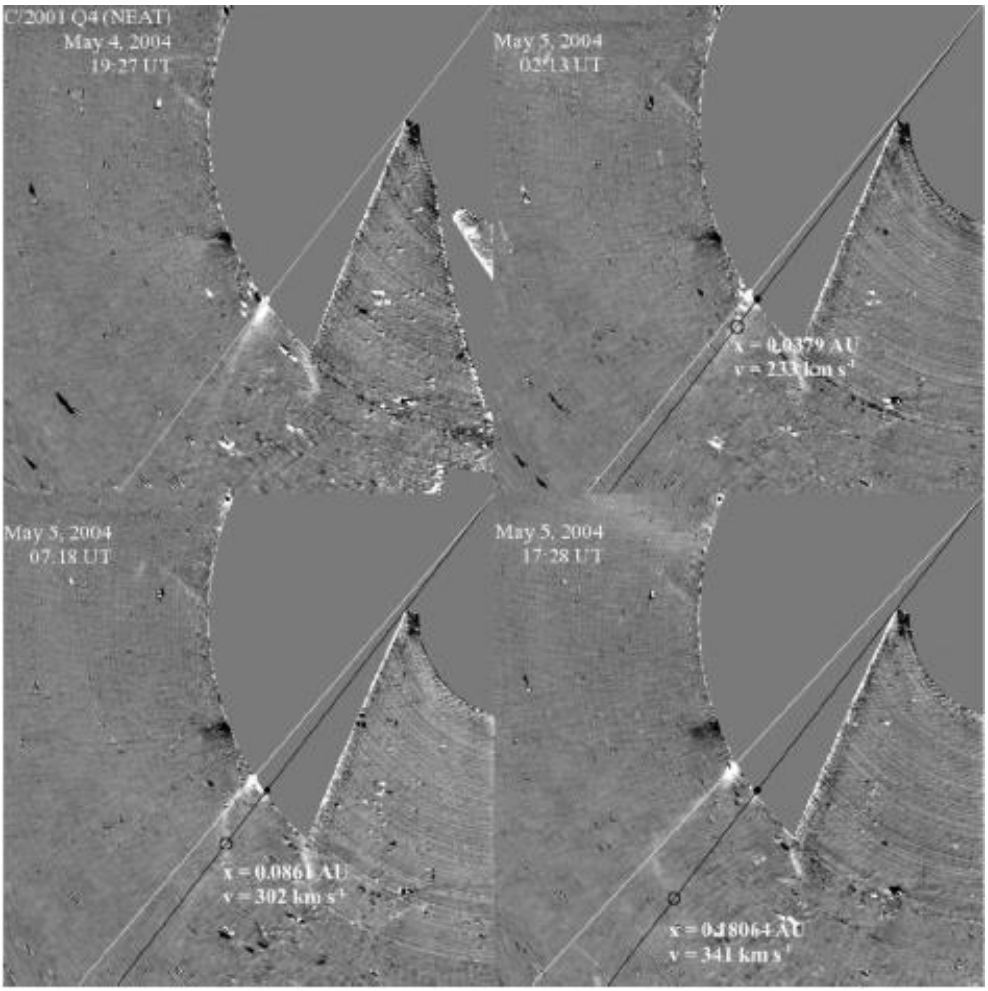

Figure 4.4: Images from SMEI (Buffington et al. 2008). The Sun is in the top right corner of each frame. The white line is the sun-comet line. This line is kept fixed in each subsequent image. The intersection between the comet tail and the black line is recorded. The radial velocity is determined by dividing the distance between this position and the black dot denoting the comet's position in frame 1 by the time.

Doppler velocities

Rauer & Jockers (1993) took Doppler measurements of the H_2O^+ emission lines in comet C/1990 K1 (Levy), previously designated as comet Levy 1990c and Levy 1990XX. By alternating between spectroscopy and narrowband interference filter images of the ion tail, they were able to compare Doppler-shift derived ion drift velocities with the physical evolution of the ion tail. By assuming a stationary ion tail, they used column densities and the velocity field

derived from these measurements to estimate an ion production rate for H_2O^+. Scherb et al. 1990 had previously obtained ion velocities in the ion tail of comet 1P/Halley's 1986 apparition, using a similar technique, but they lacked comparison images for further analysis.

They found the line-of-sight plasma velocities to be variable, ranging from 10 to 70 km s^{-1}, with the velocity vector fields being asymmetrical about the tail axis on two particular nights. During an observed disconnection event, they do not report any sudden acceleration of the disconnected tail with the new tail growth rate showing velocity variations. Using their findings, Rauer and Jockers concluded that plasma motions within the tail were influenced by particle motion rather than a consequence of wave compression.

4.2. Developing The Software

The pointing, field of view, plate scale and orientation of comet images are essential to derive estimates of the solar wind conditions in a comet's vicinity. Historically, deriving the above parameters for amateurs' images' of comets had to be carried out manually. Earlier studies of amateur images were therefore slowed by this analysis stage, which was often further complicated by images from many different amateurs. Astrometry.net (Lang et al. 2010), described in section 3.2, has greatly simplified this process by returning the requisite standards-compliant World Coordinate System (WCS) information almost instantaneously [Figure 4.5]. The success rate of Astrometry.net was found to be >99.9 percent for contemporary near-ultraviolet and visual imaging survey data, with no false positives (Hogg et al. 2008).

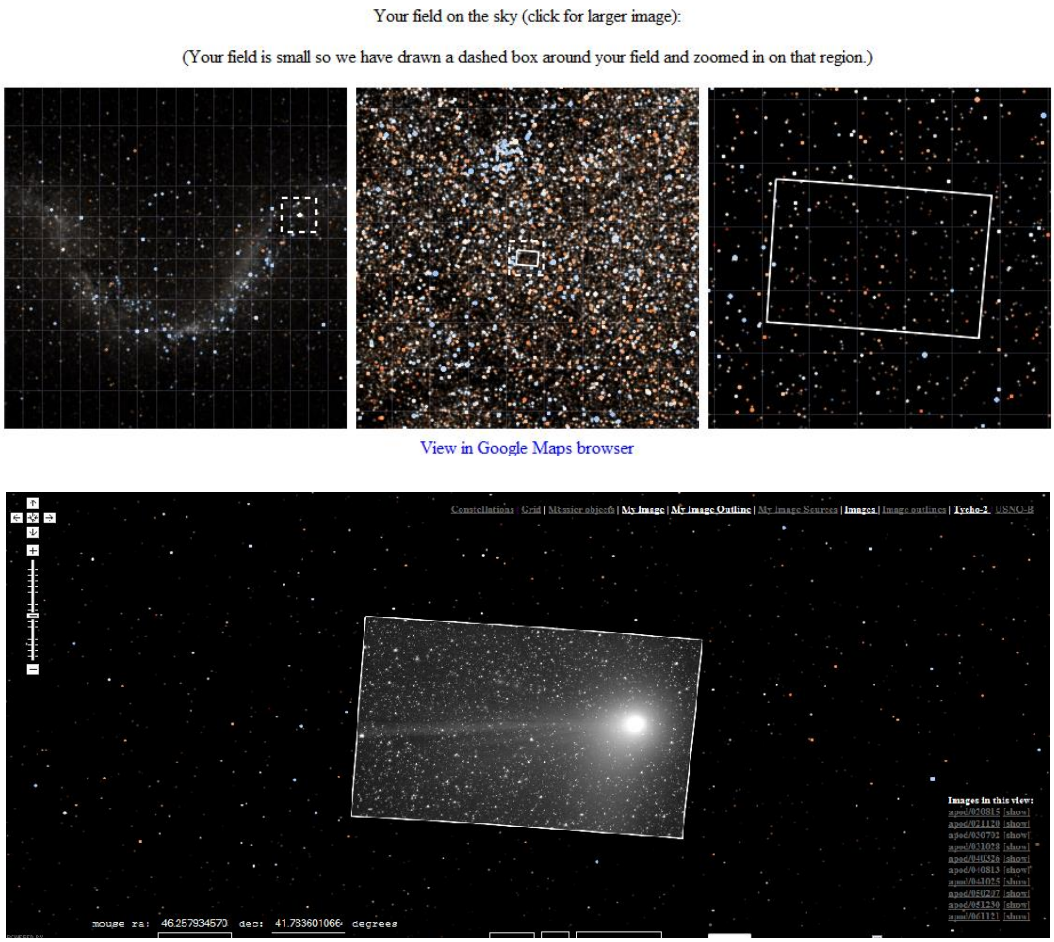

Figure 4.5: Field of view, orientation and platescale of solved image projected onto Google Sky. These were produced during the alpha testing version of the astrometry.net software and are no longer available.

One of the first hurdles during this project was how to rotate and map the amateur images in our catalogue back onto the celestial sphere. Using updated astrometry elements, from Astrometry.net, in the FITS image headers, I computed world coordinates in decimal degrees for each pixel. The rotation and plate scale from each FITS header were extracted and inputted into my software to generate an array representing each pixel in the original image, which was produced with a list of right ascensions (RA) and declinations (DEC). The comet's ephemeris in different coordinate systems (J2000.0) is downloaded from JPL Horizons.

The amateur astronomers are located all around the world. It is not always obvious which time zones were used when they posted the image to an online repository. Moreover, the timing metadata, when provided, is not always accurate. My IDL software applies a median filter to

each image. It then assumes the brightest object in the image is the nucleus and thus deduces an approximate observing time from the comet's orbit. This is not a foolproof method, especially for sequences of images where a large optocentre can cause confusion with determining the correct time for each image. This method relies heavily on an accurate astrometric solution for all images.

Once a time and date of observation for the image has been estimated, the image is then converted from celestial polar coordinates to heliocentric ecliptic longitudes and latitudes to heliocentric ecliptic Cartesian coordinates. Originally, the equatorial coordinates for the Earth's orbit was calculated from known solar positions for the time span of the comet's orbit. However, the conversion into heliocentric ecliptic coordinates was less accurate than required, resulting in a significant offset of the images from the comet's orbital path. It was concluded that downloading the Earth's ecliptic coordinates from JPL Horizons was key to improving accuracy.

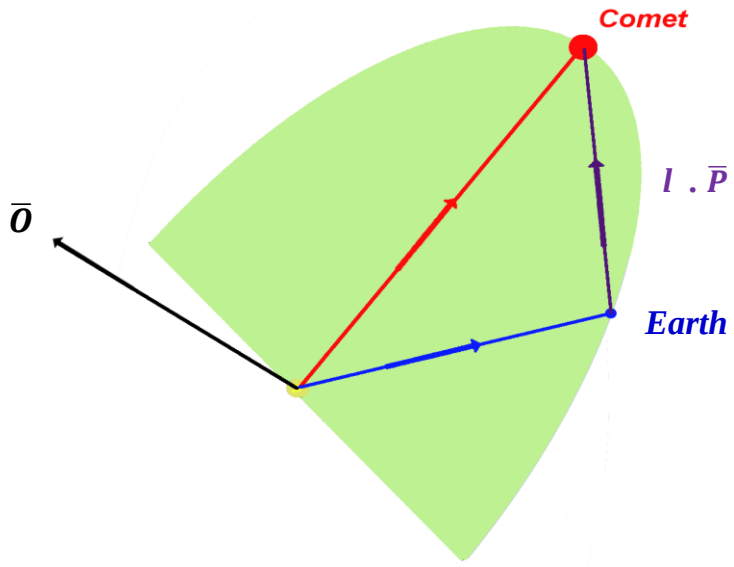

Figure 4.6: Simplified geometry demonstrating the image projection technique from which the projected pixel vector length *l* is derived.

From the ascending node and inclination of the comet's orbital plane, we can define the normal of the comet's orbital plane [Figure 4.6]. The image and orbit coordinates are then converted to ecliptic Cartesian coordinates. The magnitude of the vector to each pixel from Earth, 'l', is then derived from the position of Earth at the time of image exposure and the normal to the comet's orbital plane, using the equation below. Each pixel vector is translated to a new frame of

reference using the Sun as origin. A correction is applied to the magnitude of the radius vector to each pixel to account for light-time travel.

$$\bar{C} = l.\bar{P} + \bar{E}$$

Take dot product with $\bar{O}$:

$$\bar{O}.\bar{C} = l.\bar{O}.\bar{P} + \bar{O}.\bar{E}$$

$\bar{o}$ and $\bar{c}$ are orthogonal, so $\bar{O}.\bar{C} = 0$

$$\therefore\ l = -\frac{\bar{O}.\bar{E}}{\bar{O}.\bar{P}}$$

l is the scalar length of the actual vector of each pixel in the image from Earth. The magnitudes for $\bar{O}$ and $\bar{P}$ are unknown, so a unit vector is assumed for both. $\bar{O}$ is the unit vector normal to the comet's orbital plane, $\bar{P}$ is the unit vector to each pixel from Earth and $\bar{E}$ is the vector of the Earth from the Sun. The projected image is corrected for light time travel from the comet nucleus to the observer location.

The final section of the software computes the vector product of the perihelion vector and the vector perpendicular to the comet's orbital plane to define the x and z axes of a new fundamental plane. Every object in the previous system is mapped with respect to the comet's plane. The multiple translations are a requirement as the comet's orbital plane provides the best framework for estimating solar wind velocity. Each image is plotted with its comet's 'nucleus' defined as the origin of the frame of reference and the comet's orbit is rotated accordingly, so that the Sun is always to the left of the image. Note that this is not necessarily the true location of the nucleus. The brightness of the coma makes it impossible to resolve the comet's nucleus via direct imaging of the comet from Earth. The radius vector from the Sun to the 'nucleus' is extended across the image and is now the x-axis. The z-axis is defined as the normal to the comet's orbital plane.

The ion tail centre at any position lagging the comet's orbit is set as the point where the extended radial vector cuts through the ion tail. Assuming the solar wind is always flowing

radially, the centre of the tail downstream of any position in the orbit that the nucleus has already passed, thus provides the speed when the comet was at that orbit location. The original technique, used herein, to estimate the local solar wind velocity involved measuring the aberration angle by which the ion tail orientation is deflected. This aspect of the technique was fairly difficult and ambiguous since it is difficult to define the tail centre, especially when it's diffuse, not straight and/or disturbed. This yielded erroneously large velocity estimates for ion tails with very small aberration angles.

4.2.1. Selecting Tail Centre

I have devised an alternative method to obtain multiple estimates of the local solar wind velocity from a single image. Similarly to the aberration angle method, this technique requires the image to be projected and mapped onto the comet's orbital plane. This is a similar technique to that used by Buffington et al. (2008) and Clover et al. (2010), although their method did not include a projection of the SMEI and STEREO HI-1 images onto the comet's orbital plane. By taking multiple cross-sections across the ion tail along the radial anti-sunward direction, we consider the ion tail as discrete plasma bundles flowing radially away from the cometary nucleus at the local solar wind velocity. I use this concept to extract multiple cross-sections across the image along the extended radial vector from the Sun.

It was not feasible to design an effective automated method to extract the solar wind velocity. This is the only section where an automatic script could not be accommodated within the code and thus part of the software can be split into a non-interactive routine to produce the images required to run through the tail edge extraction routine. One of the main obstacles to automation was the low relative brightness of the tail with respect to the surrounding sky background. The hump within the brightness slope has a low peak and a gradual smooth decline with no sharp distinction to demarcate the edges of the tail and the sky background.

Multiple tail edge detection methods were investigated. One such solution was to run the image through a high-pass filter followed by a base curve subtraction. To increase the signal to noise ratio (SNR), I combined eleven cross-sections along the prolonged radial vector, five on either

side of the cross-section of interest. A side effect of this step is that small substructures would likely be lost and the overall uncertainty of the tail centre position would increase. Despite these measures, the high-pass filter failed to produce a distinctive feature, which could be isolated as the edges of the ion tail. In effect, the signal gain to noise gain was much less than expected and the resulting brightness profile was noisier. A set of image enhancing and sharpening filters such as the Roberts (Roberts 1965) and the Sobel filter (Sobel & Feldman 1968), typically used to enhance the contrast between adjoining areas with relatively small brightness variations (Hildreth 1985), were tested without a positive outcome.

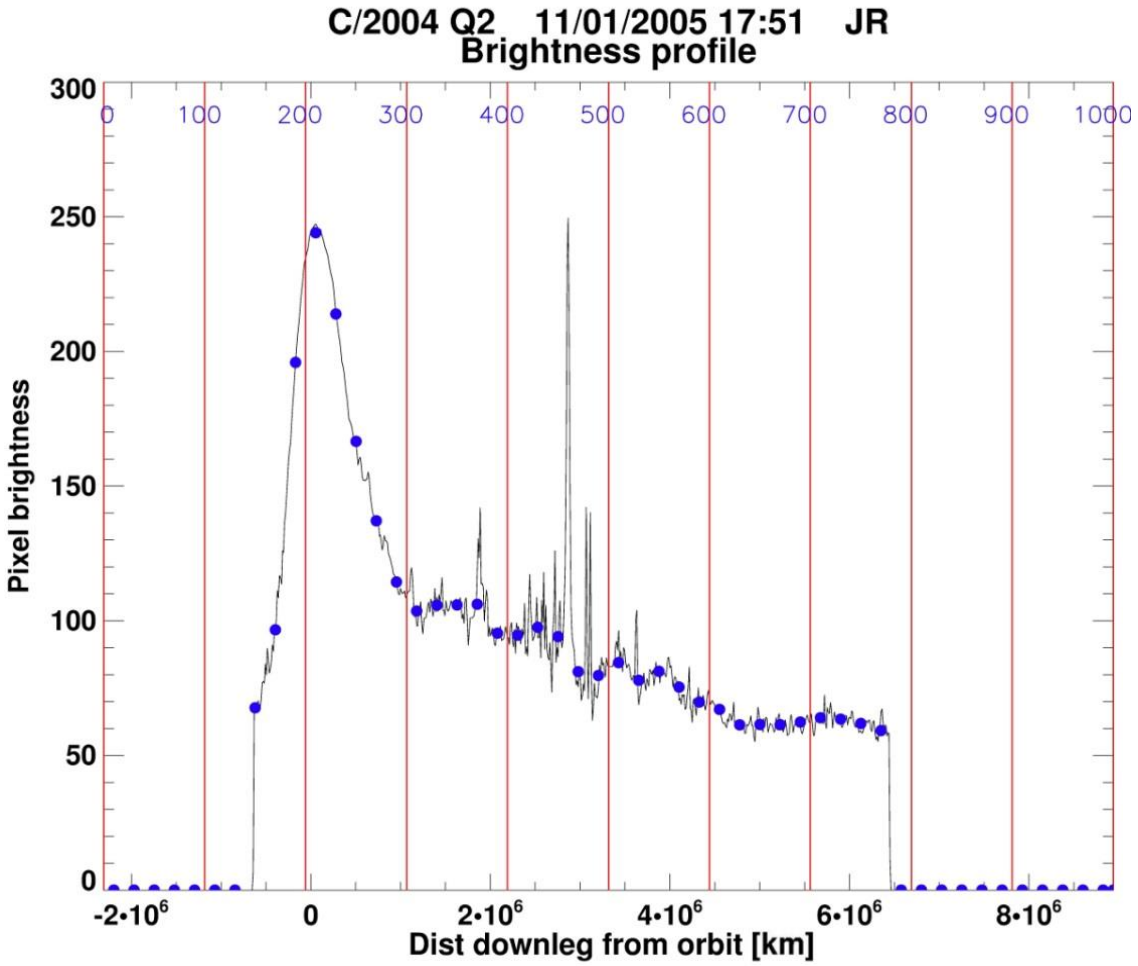

Figure 4.7: Extracted profile across an image. The hump can be seen in the binned data at ~ 3.25 x10^6 km. The brightness data are binned in bins of 20 data. The top label 0 to 1000 is used as a quick comparison with the original image to confirm where the extended radial vector crosses the ion tail.

Figure 4.7 shows the brightness profile extracted along the second cross-section in Figure 4.3. Despite using a median filter, extreme peaks remain in the data due to bright stars. The brightness data are plotted in bins of 20 data points using the median of that bin. The distance along the x-axis is plotted with respect to the comet's nucleus. A slope, derived from the brightness profile, is subtracted from the data and the remaining hump can be used to define the tail centre and the error on the bundle position.

The slope of the brightness profile resembles a skewed Gaussian, however I am only interested in the hump in the downward slope. As my initial curve-fitting program did not yield the best curve fit, I interpolated the data using a least-squares quadratic fit.

Figure 4.8 shows the extracted profile of comet Machholz from the 11th January 2005 by Jäger and Rhemann. This particular cross-section is a better example to illustrate the effectiveness of this first attempt at a base curve subtraction. Here, the red dots are in bins of 10 data points and represents all the data after the brightest peak, which is associated with the nucleus. The black baseline and binned data are computed by manually excluding the hump from the interpolated data set. This, however, defeats the point of finding an automated method since it requires the user to pre-select the hump to calculate a baseline.

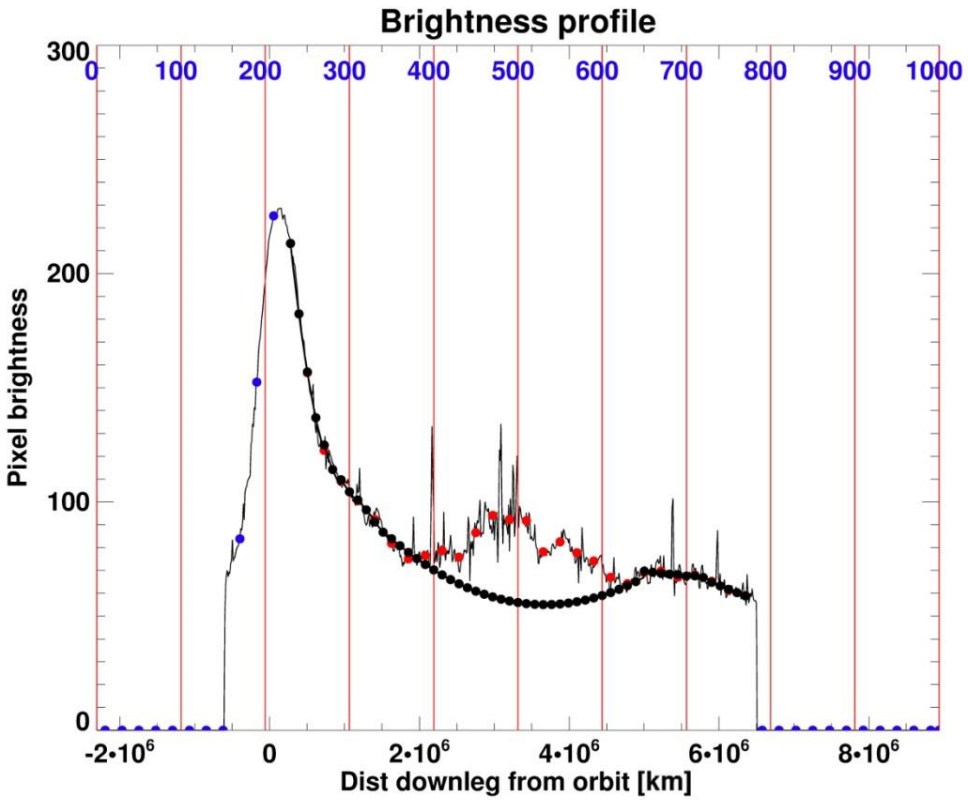

Figure 4.8: Extracted profile across image of comet Machholz by Rhemann and Jäger on 11th Jan 2005. The brightness data, in blue, are bins of 20 data points. The red bins correspond to all data antisunward from the nucleus, and the black binned data are the interpolated base curve from the fall-off from the coma. Individual extreme peaks indicate stellar light contamination.

Subtracting the binned interpolated data from the original curved slope, we obtain the plot in Figure 4.9. I binned the subtracted brightness profile in bins of 10 points (in red). Using the FWHM, the tail centre is defined as the middle of the hump and the error as half of the FWHM. Considering that a cross section is taken along the image, the cut across the tail will actually produce a skewed hump. This means that the true tail centre should be closer to the comet's nucleus than my current estimate. This step was abandoned as it is not a scientifically rigorous method of deducing the tail centre.

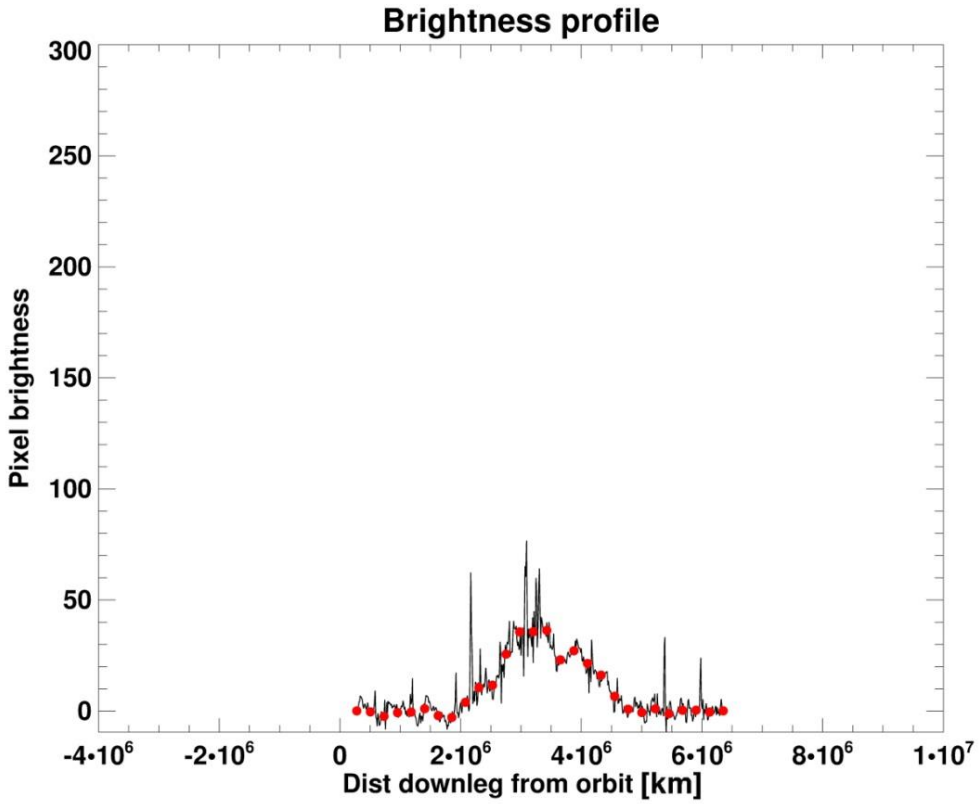

Figure 4.9: Subtracted brightness profile. Hump is used to define the tail centre and its associated error

A curve fitting method was later re-addressed with the expert help of L. Gilbert. A number of graph fits were simulated with varying success as seen in Figure 4.10. Polynomial fits of 4 and 5 terms produced the smallest root-mean-square deviation from the residuals. The final fitting solution adopted was a Gaussian and a 6 degree polynomial. This produced a similar fit to polynomial degree 5 but was a slightly better fit for all profiles.

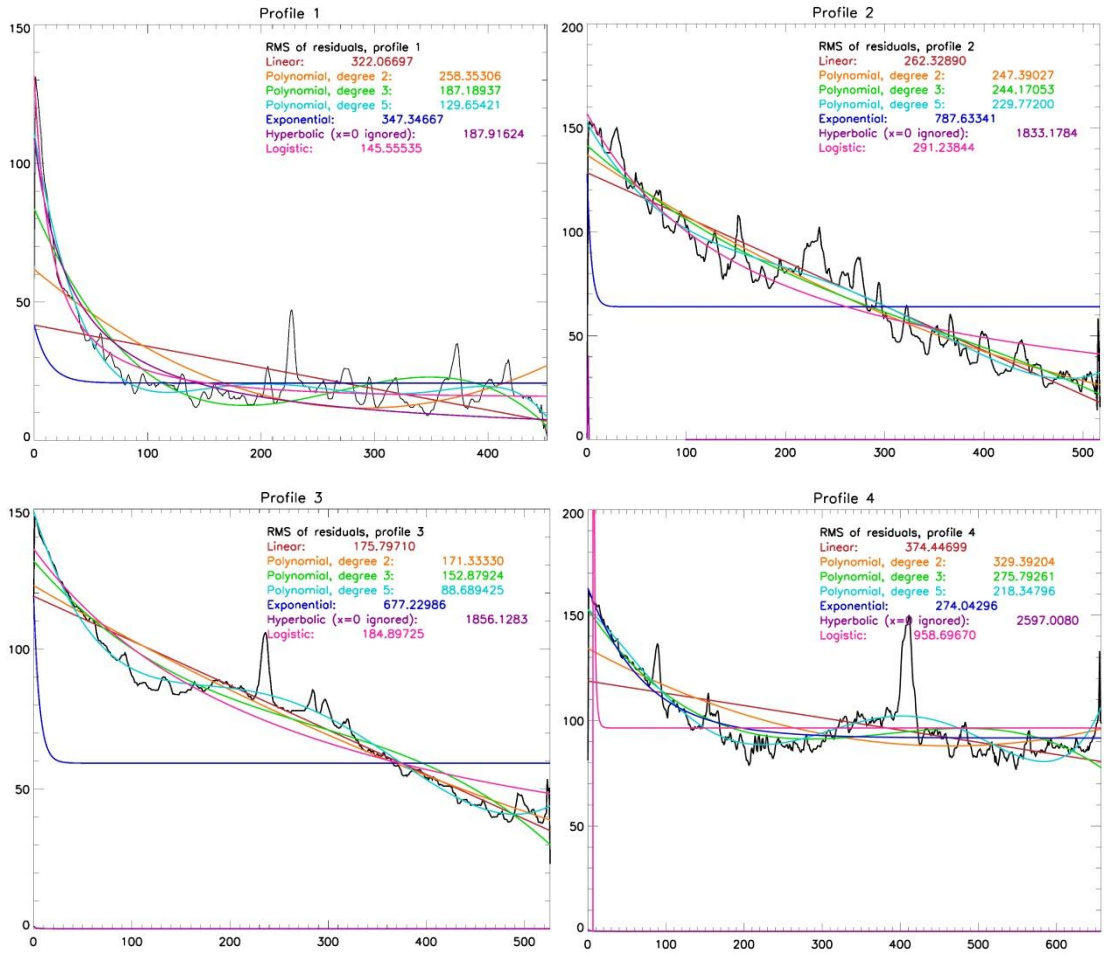

Figure 4.10: These are several types of fitting, by Lin Gilbert, used for 4 cross-section brightness profiles from a set of typical amateur images.

Due to the intrinsic nature of the varying solar wind and the relative brightness of the ion tail as seen by the observer, the shape and size of the decreasing brightness slopes from each image will consequentially vary. Automatically determining the tail centre, from the slopes in Figure 4.10, is further impeded by a non-symmetrical hump in the base curve, which tends to be slightly positively skewed. One further characteristic of note is the low brightness variation between the ion tail and the sky background. The dissimilarity between the profiles for the images in Figure 4.10 indicates the difficulty of automatically spotting the slope hump; though, it is a somewhat easier task by visual inspection. For profiles 1 and 4, the “hump” in the 5th degree polynomial would be situated between the first and third turning points. In plots 2 and 3, where the slope follows a steeper linear-like trend, the turning points are inflection points, making it harder to identify. The profiles are separated in two categories: curved profiles and near-linear

fits. A fitted Gaussian and a polynomial profile is removed from each profile and shown in Figure 4.11. The automatically detected tail sections are marked in red. Profiles 2 to 4 showed a relatively good correlation with the physical location of the tail crossing from the nucleus. However, profile 1 and another similar profile (not shown here) failed in this regard. At a glance, it is easy to determine the futility of producing a generic automation pipeline to determine the tail centre position. For bright tails with counts significantly above sky background, this method would work relatively well.

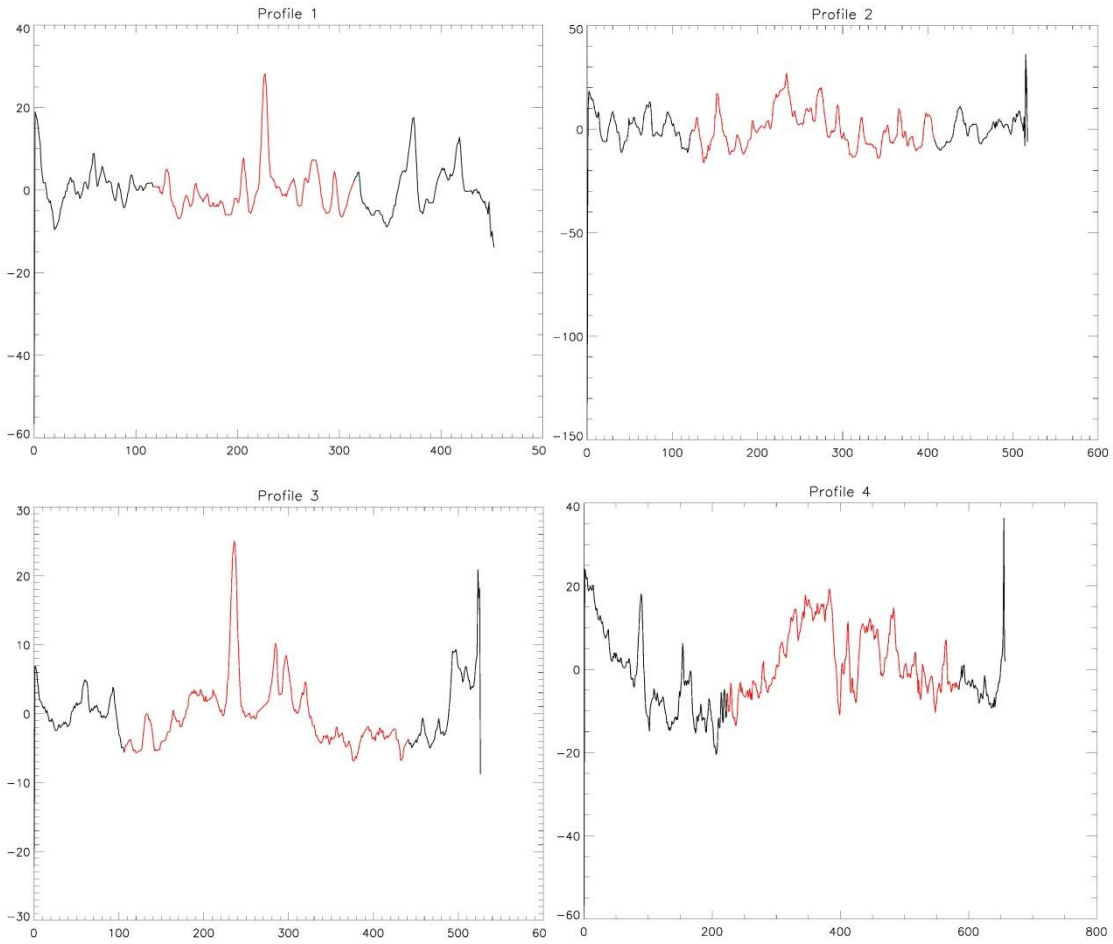

Figure 4.11: Brightness profiles of 4 typical images with a Gaussian and 6 degree polynomial fit subtracted. The automatically detected hump is highlighted in red.

To ensure conformity in the sampling technique, an attempt at devising an automated routine was made with no success. The interpolation technique is a brute force method not ideal for quick and effective automation of the software. With a much less than 100% successful conclusion to the curve fitting routine, it was found that there would be no added benefit of

pursuing an automated solution: we would mostly be forcing the subtracted profile to take a hump-like shape in certain scenarios.

The final implemented solution was to use the advantages of the human eye to better detect the faint features and edges of the ion tail. To further aid in human eye detection of the ion tail, an interactive colour stretching function and a user-friendly Graphical User Interface (GUI) was built into the software, allowing the user to visually and interactively define a new colour palette and manipulate it to accentuate features of interest. Thus, the user can highlight areas of similar brightness in the image to emphasise areas of interest, without requiring an image manipulation software.

The user can then select the extent of the ion tail crossing the extended radial vector. The tail centre is assumed to lie in the middle of the ion tail along the extended radial vector and its error is taken as ±1/6 of the ion tail coincident with the radial vector. Measurements of the tail centre were generally taken from $1x10^6$ km onwards, for no other reason than the edges of the ion tail closest to the nucleus merges with light from the coma and the two components are therefore difficult to separate.

The local solar wind velocity is estimated from the distance travelled by the plasma bundle, from the position where it left the comet's orbit to the ion tail centre, divided by the time difference between the comet's current position in the image and its position when the plasma bundle left the comet 'nucleus'.

The methodology outlined in this report is unique. There is no evidence in the literature that this technique has been previously applied using amateur images.

4.2.2. Using Astrometry.Net

Astrometry.net is available as an online resource (see nova.astrometry.net) or as a local install, which can be tailored to increase solving speed. Since it is not possible to batch-download processed images, the user is required to download and rename each image from a generic filename by hand. This is one of the advantages of locally processing your image catalogue

over the web application. The software accompanying this thesis includes a module to batch download images with the correct filename, however this module is limited to this current version of the web interface (nova.astrometry.net). The Astrometry.net source code is V0.50.

When processing images on a local host, the appropriate index files to use range between 20 arcmins to ~ 11 degrees for the FOV, to achieve the greatest balance between successful solutions vs computing time. The fields of view of most amateur images tend to fall within this range. Images that failed when processed by the local install were reprocessed via the online server.

The WCS transformation matrix of the image, extracted from the astrometric solutions, includes a quadratic SIP (Spitzer Imaging Polynomial) distortion polynomial. Though applied within the mapping software, this does not completely eradicate lens distortion effects. An in-depth analysis of this issue was not undertaken as the relatively small field of views of the amateur images mean that distortion effects are minimal at worst.

4.2.3. Determining the time of observation: Imagetimeheaders

A key part of the comet mapping requires the definition of a point as the ‘nucleus’ in the amateur image. The nucleus is determined as the point at which the comet was imaged from the observer location in universal time (UT). This variable can be obtained from the image headers or the timing metadata when available. The main software relies on the assumption that this nucleus variable roughly corresponds to the comet’s real nucleus in the image. The date and time of observation is also used to find the observer’s position along the Earth’s orbit. This is essential to correctly project the image along the observer’s line of sight and hence to map the projected image onto the comet’s orbital plane.

This step is crucial for images without a recorded time. Furthermore, there is no guarantee that observation times provided by amateur astronomers with their images are accurate. To ensure consistency in the definition of the image times, I developed an algorithm (imagetimeheaders) to automatically determine a date and time for the observation period from the comet’s track as observed from the Earth’s centre. The observer location is assumed to be geocentric as the

actual observer location is rarely provided with the image. Its net effect on the end results would be minimal, except when a comet is exceptionally close to the Earth, where parallax effects would be important.

The comet's real nucleus is assumed to lie within the bright centroid, which I will refer to as the optocentre, and has to coincide with the comet's track as observed from Earth. The image is passed through a median filter, whereby the routine calculates the median of pixels within a moving 15 pixel-wide box. The central pixel of the box is replaced with the computed median. For most instances, this simple blurring technique was adequate to discard most stellar sources, which would have otherwise interfered with this exercise. The image edges were trimmed off as stars along the edges were omitted from smoothing due to the large box width.

With only the centroid remaining in most images, the brightest points in the image were extracted, the brightest 10% of those pixels were chosen and their full width at half maximum (FWHM) computed. A series of test images showed that this corresponded well with the expected nucleus position. Initially the top quartile was chosen to represent the optocentral region, however processing speed varied widely depending on the image sizes. This sub-centroid of the brightest points was compared with the comet's track and the closest point where the comet's track and the sub-centroid coincided, was defined as the optocentre. This is deduced from a plot of the mean distance between each point in the orbit and each point in the sub-centroid. The optocentre is defined as the minimum of the mean distances. This provided both an estimate of the time, where none was available previously, and an estimate of the accuracy of the original timing information, when available.

If the newly calculated optocentre time was significantly different from the old image time, then it is chosen as the new observing time. This time gap was determined from the timing difference between the old and new image times. A minimum time gap of 15 minutes is set as the lower boundary. The heuristic time gap of fifteen minutes is chosen as this timestep is significant enough to result in a mapping with the image nucleus significantly off-orbit from the predicted nucleus position. The original time at which the comet was photographed is retained for later comparison, if it is not used to pinpoint the comet nucleus.

This is not an infallible algorithm. Imagetimeheaders should only be trusted to a certain extent, on the basis of an accurate astrometric solution and the JPL HORIZONS orbits being highly precise. I estimate the percentage of successful solves through this procedure to be >95% after processing over 500 images. My precautionary failsafe was to create a list of processed images with information pertaining to each solution. The user can rapidly double check each result and identify any wrong solution. In cases where the auto-detection routine breaks down, an inbuilt IDL routine has been adapted for manual selection of the centroid region.

There exists a further scenario where the accuracy of determining the timing information is reduced. This arises when the image was taken with long exposure times, usually several minutes in length or when images have been stacked. It is not immediately obvious when this occurs and we can only know of long exposure times for some images if a time range is included in the original image filename. Even when accounted for, images with lengthy exposure times can cause a large projection uncertainty.

4.2.4. Star Removal

Stellar light sources often contaminate the brightness profile extracted along the image cross-sections. This can make it difficult to determine the exact position of the tail centre from the brightness profile. In an attempt to remedy this, I adapted an automatic cosmic ray extraction IDL routine, known as acre, by adjusting its detection threshold. The procedure works by smoothing out the images with a median filter, subtracting the smoothed image from the original and identifying the cosmic ray-induced tracks, or in this case, the stars. This was a critical element of the automatic edge detection algorithm. This technique was more advanced than required and was replaced with the median filter process described previously in section 4.2.3. The software will rid the images of most stars except for a few of the brightest, whose point-spread function have a large FWHM. A notable side-effect of this module will be a moderately aggressive smoothing out of the ion tail. Information on the fine structural features in the tail will be lost but for the particular purpose of measuring the tail centre and its error, this is inconsequential. Therefore, the median filter was only used to find the timing information for the amateur images.

4.2.5. Software Workflow

The correct streamlined workflow for my software is as follows:

- The internet is trawled for suitable images with a fairly bright identifiable ion tail. Amateur astronomers have also donated images to this project.
- The images are then processed through astrometry.net.
- Download the highly precise orbit data from JPL Horizons. Use the email interface to reduce download times.
- Use orbit plane angle to ascertain whether images will be projected accurately.
- Process all images through ‘Imagetimeheaders’.
- Projection mapping of images onto the comet’s orbital plane.
- Tail centre selection
- Solar wind calculation
- Concatenate all values and create the solar wind plot.

4.3. Errors

The entire aim of this technique is to produce estimates for the purely radial local solar wind velocities. These velocities are calculated under the assumption that there are no non-radial components to the solar wind flow. Every object in this defined system (sun, earth, and comet) is projected onto the comet’s orbital plane, which will arise in projection uncertainties, as some parts of the comet’s ion tail may be outside the orbital plane, especially in the case of a strongly non-radial solar wind flow. Any calculations such as the distance between ion tail features, as well as their evolution speed, are subject to these large uncertainties. The projection and mapping of the images onto the comet’s orbital plane can provide a good estimate of the local solar wind velocity but these sources of uncertainty must be borne in mind.

Errors for the solar wind velocity arise from the multiple coordinate transformation, the errors associated with the projection and mapping onto the comet's orbital plane and errors due to the assumption that there is only a radial component to the solar wind. There is also a human error element to the project that I had attempted to minimise by extracting the profile brightness of each pixel along the extended radial vector. In addition, the preparatory steps prior to the use of this software bear their own set of uncertainties.

I treat each identified source of uncertainty as its own mini case study. I will then attempt to demonstrate that certain error sources are negligible, such as choosing the Sun's body centre instead of the solar system barycentre to define the comet's and the Earth's orbits in heliocentric ecliptic Cartesian coordinates.

Source: Astrometry.net

Astrometry.net has greatly reduced the amount of time required to analyse an amateur image of a comet to determine its field of view and its equatorial coordinates, amongst other parameters. Despite its usefulness, it does not compute an error on the image position. The sole method available to determine the error on each pixel position in right ascension and declination would be to manually identify the coordinates of each star in the image from known stellar catalogues and compare these to the positions computed by Astrometry.net [private discussion with D. Lang]. This would be a laborious task. The current return on time invested for this task would be minimal. With a >99.9% reported solving accuracy for astrometry.net, I thus assume that the errors on the pixels positions are negligible. It is important to note that the error on the pixel positions will be dependent on the quality of the original image.

Error source: Error on orbit and geocentric assumption

The error on the heliocentric ecliptic Cartesian coordinates of both the comets' and the Earth's orbits is unavailable from JPL Horizons. Due to the high temporal resolution and precision of the ephemerides, I assume the error on these positions to be negligible in this circumstance and

the error on the Earth's position to be ±1 Earth radius (R_E). This error estimate is also based on the assumption that the observer location is geocentric. A topocentric reference point is available for a significant proportion of observers, however this complicates the process for minimal improvement.

As a worst case scenario, we hereby consider that two consecutive images in our archive could have been taken at antipodes to each other. This error will contribute to the error in the observation time. From the Earth's orbital velocity and its radius, the positional error on the observer's location (σ_R) is converted to an error in time of ± 3.5 minutes along the orbital track, based on how rapidly the Earth would cross one Earth radius.

Error source: Error on observation time

Determining the errors on the observing time (σ_t) is hindered by two setbacks. The first is that a significant number of images available either online or directly from the amateur astronomers lack a timestamp for the photograph. The issue is further compounded by the inaccuracy of the reported times for a few images. The sole evidence of this timing inaccuracy can be found in the discrepancy between the image position, once mapped onto the celestial sphere, and the comet's track in equatorial coordinates. The imagetimeheaders procedure revealed that the timing discrepancy could range from a few minutes to a few days. Imagetimeheaders was thus adopted as a consistent method of estimating a timing uncertainty for each amateur image. Errors associated with the observing time for amateur images are dependent on the field of view of the image, the size and shape of the centroid, whether it is saturated and a correct astrometric solution.

As a test, I mapped multiple images with known timing discrepancies onto their orbital plane to determine the effects of using an 'inaccurate' date and time of observation. The mapped images [Figure 4.12 and Figure 4.13] were observed on the 12th December 2004 at 01:15, as recorded by the observer. The time computed by the 'imagetimeheaders' module placed the observing time and date at 23:01 on the 11th of December. As can be seen from Figure 4.13, the bright

centroid falls short of the comet's orbit when compared with the expected image seen in Figure 4.12. The timing information provided in the image filename is thus deemed to be inaccurate.

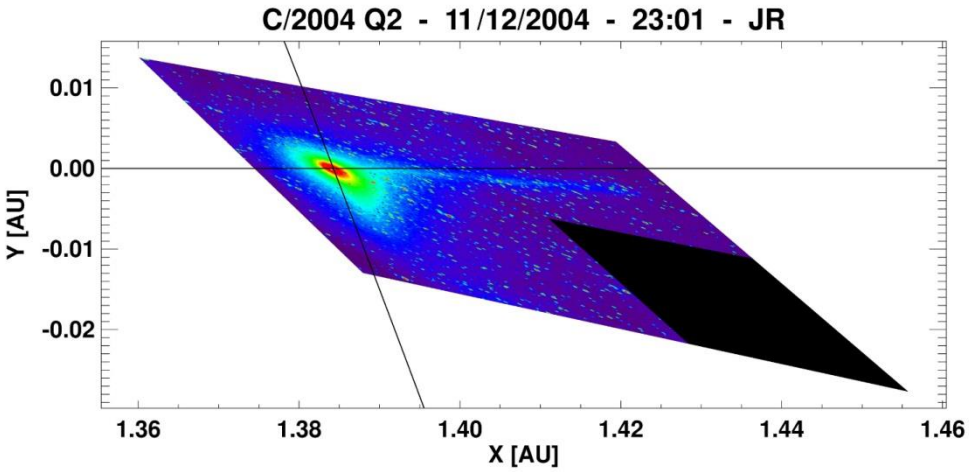

Figure 4.12: Projected image of comet Machholz mapped onto the comet's orbital plane using the observer location at 23:01 on the 11th December 2004 (defined by 'imagetimeheaders'). Image observed by Candy.

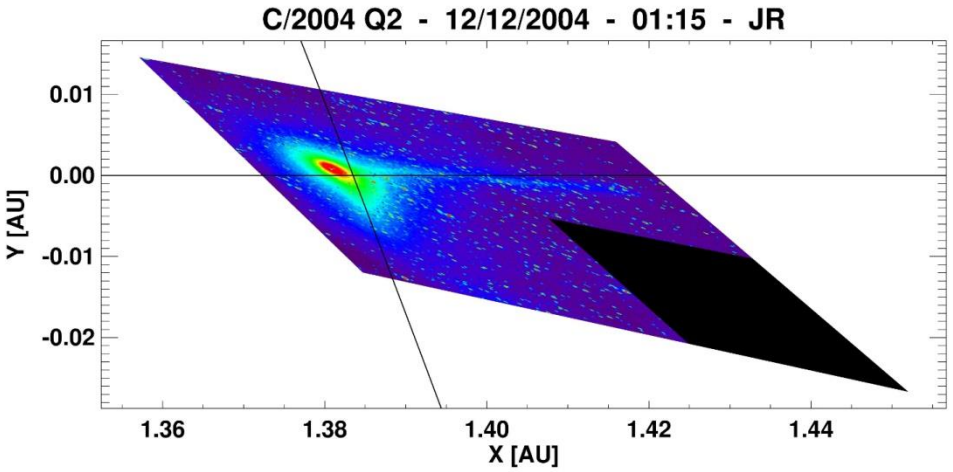

Figure 4.13: Image of comet Machholz is now projected and mapped onto the comet's orbital plane using the Earth's location defined by the time provided by observer. Image observed by Candy on 01:15 on the 12th December 2004.

To rule out an incorrect astrometry.net result, I overlaid the solved image on an optical Digital Sky Survey (DSS) sky background in Aladin [Figure 4.14].

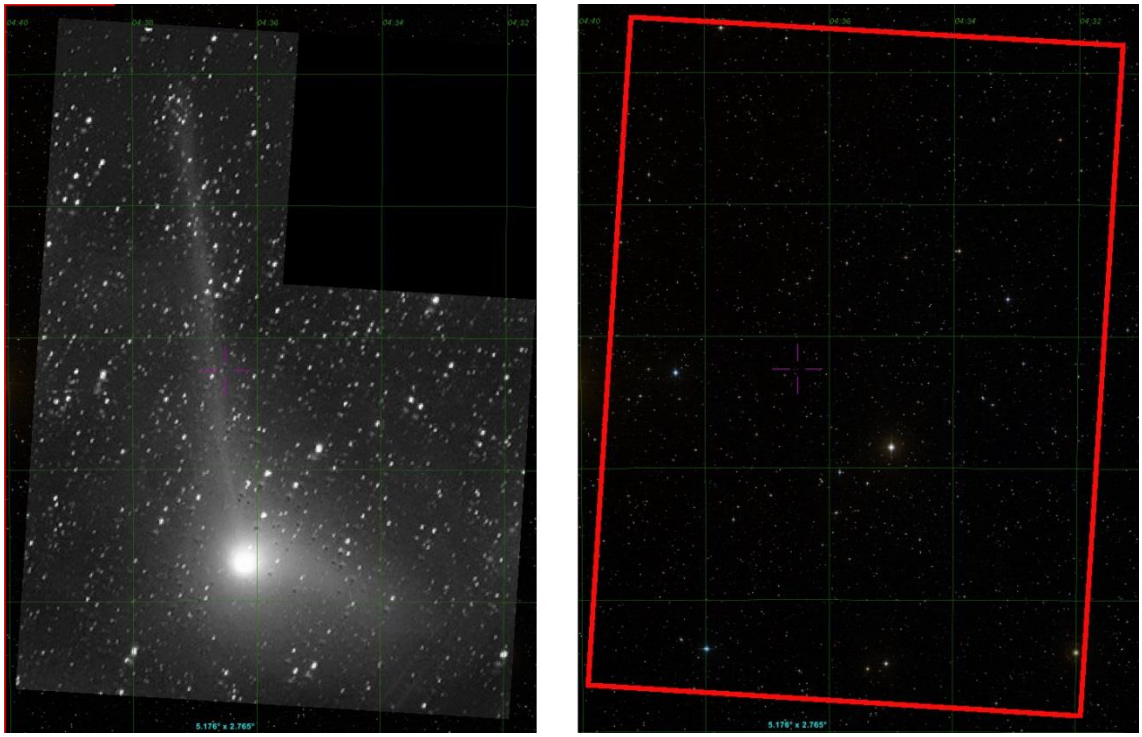

Figure 4.14: Astrometry.net solved image of comet Machholz observed by Candy on 11th December 2004, overlaid in Aladin. Image on the right is the FOV of the sky background. The stars match perfectly.

The new date and time of observation is shown by the blue crosshairs in Figure 4.15. The black squares show the top 10% brightest points in the centroid. Its FWHM is plotted in red. The orbit coinciding with the centroid is plotted in black and the error is in yellow. In order to quantify an error on the timing information, I assume that all timing information provided with the image is inaccurate and the optocentre date and time correspond to the 'true' observer location. Therefore, the uncertainty on the timing information can now be assumed to lie somewhere in the region where the bright sub-centroid and the comet track coincide. I estimate this error to be $\pm \frac{1}{6}$ of the comet track on either side of the optocentre, so that the error is one-third of the comet track overlaying the bright sub-centroid.

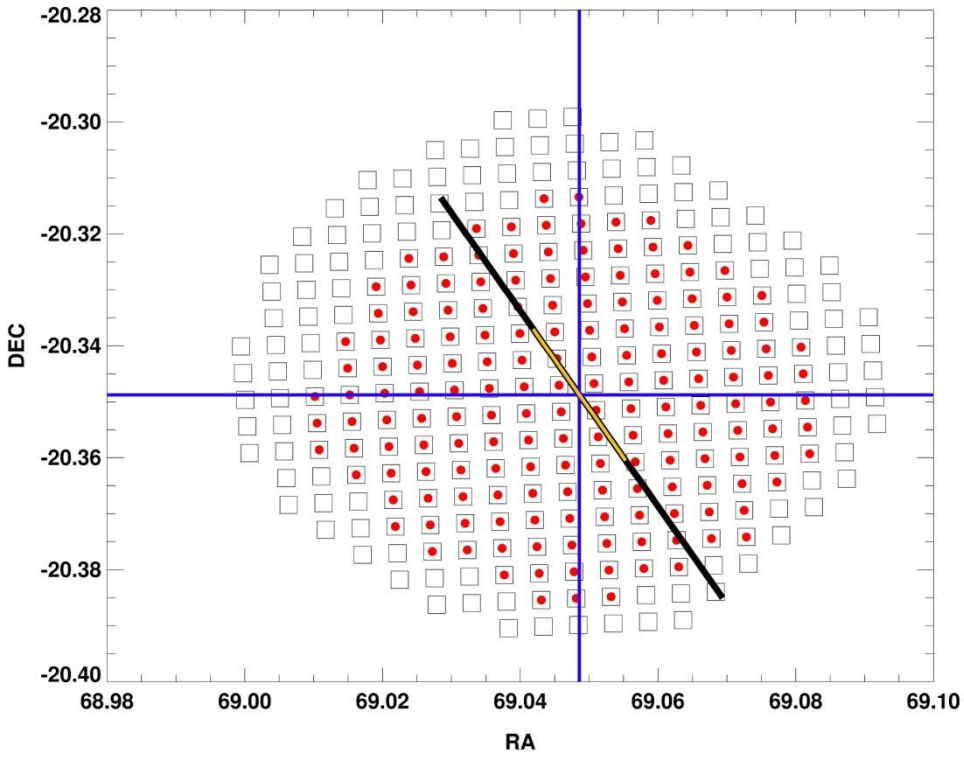

Figure 4.15 shows the centroid (black squares) for comet Machholz observed by Candy on 12/12/2005 at 01:15. The red dots correspond to the FWHM of the centroid. The orbit is in black, the errors in yellow and the blue crosshairs pinpoint where the sub-centroid is closest to the comet track.

I investigated the effect of using different box sizes when determining the bright centroid from the images, when manually determining the coinciding regions. The sizes of the box showed no significant effect for images with large centroids. However, the disparity between the optocentre times estimated for smaller centroids is correlated with the box size, although the error on the timing information remains relatively similar. For consistency and efficiency, I decided to use a box whose edges can be interactively constrained by the user to the outermost contour of the centroid. In the error propagation section below, it will become apparent that the error on the observing time can have a large effect on the projection mapping uncertainty and thus the solar wind velocity uncertainty. Therefore, it is important to correctly calculate the observing time and its error.

Light time correction

The position of the nucleus on the comet's orbit was corrected for light time travel from the comet to the Earth. A comparison of an uncorrected and a light time corrected image is shown in Figure 4.16. This provided a rough indication of the 'true' location of the comet's 'nucleus' when the light observed was reflected off the target. As the position of the comet along its orbit from Earth is known to a resolution of 1 minute, the light travel time from the comet to Earth is rounded to the nearest minute, the smallest time step available in the orbit dataset. I assume the error on this light time correction (σ_{LT}) to be ± 0.5 minutes.

Each projected image pixel is also corrected for light travel time. The light time correction is computed as follows:

$$\delta t = \frac{l \ . \ P_{(x/y/z)_i}}{c}$$

$$\delta R = \delta t \times \bar{v}_c$$

δt is the time correction due to light travel time, l is the magnitude of the projected vector to each pixel, $P_{(x/y/z)_i}$ are the pixel positions along each axis and i refers to the pixel index. δR is the correction to be applied to each pixel and $\bar{v}_c$ is the comet's orbital velocity. The light time correction is iterated ten times to obtain an estimate of the 'true' position of the image on the comet's orbital plane.

Therefore, the error due to light time correction ($\sigma_{\bar{P}_{LT}}$) is:

$$\sigma_{\delta t} = \left(\frac{\sigma_l}{c}\right)^2$$

$$\sigma_{\bar{P}_{LT}} = \bar{v}_c^2 \times \sigma_{\delta t}$$

The errors on the pixel positions were assumed to be negligible as described in '**Error Source: Astrometry.net**'. The errors on the light time corrected pixel positions were also negligible and

thus not included in future calculations. The comet's mean velocity was ~32 km s^{-1}. This yielded the following uncertainties: $\sigma_{\delta t}$ ~ 10^{-9} s and $\sigma_{\bar{P}_{LT}}$ ~ 10^{-6} km.

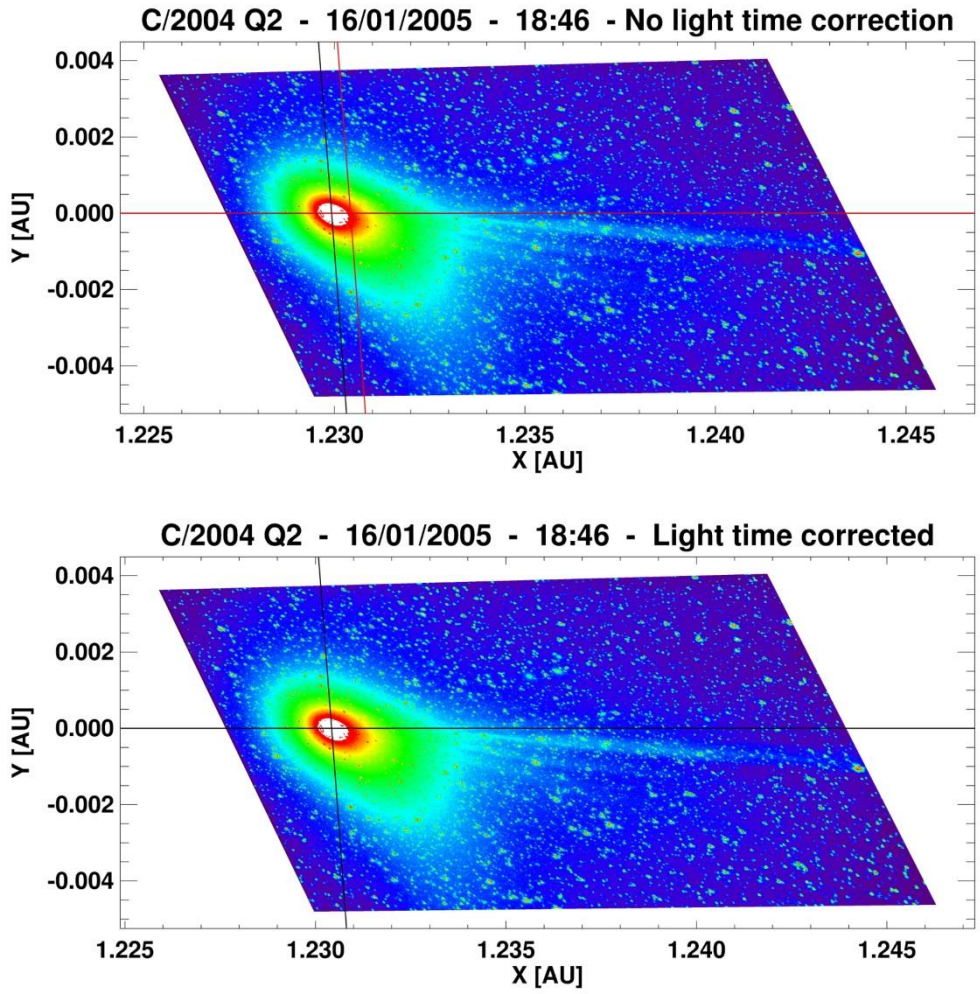

Figure 4.16: Top image shows the original image mapped onto the comet's orbital. The extended radial vector and the comet's uncorrected orbit is marked in black. In red, we have the light-time corrected position of the nucleus as per JPL Horizons. The bottom image is light-time corrected and the nucleus aligns well with the predicted position.

Error source: Inclination and Ascending node

The inclination and the ascending node of the comet's orbital plane are used to define the normal to the comet's orbital plane. I estimated an error on the inclination and ascending node of the comet's orbital plane by calculating the mean and the standard deviation of both variables over the 9-month period that comet Machholz was extensively observed by amateurs (Sep 2004 to Jul 2005). The error on both variables will be directly reflected in an error on the azimuth and

the elevation of the comet's orbital plane. The relative error on the inclination is 0. 07 % and the relative error for the ascending node is 0. 2 %.

This does not tell us a lot about its effect on the projected image. We can test how significant an effect the variation in both the inclination and ascending node will have on the projection and mapping of the image by using the inclination and ascending node value 3 months on either side of an image. We can thus assess the change in the magnitudes of each pixel vector from the Sun and the Earth by taking 3 values for the inclination and the ascending node over a period of 6 months.

The range of inclination and ascending node values were obtained from JPL Horizons (J2000.0), which includes planetary gravitational perturbations. The test image was taken by Rhemann and Jäger on the 16th of January 2005 at 18:46. The two test values of inclination and ascending node are taken 3 months either side of this date and are given in Table 4-1.

Table 4-1: Inclination and ascending node values for comet Machholz over a period of 6 months. Values are from JPL Horizons.

Date	16th Oct 2004 (- 3 months)	16th Jan 2005	16th April 2005 (+ 3 months)
Inclination	38.589	38.589	38.589
Ascending node	93.625	93.624	93.622

I projected the image onto the comet's orbital plane using the values above and determine the distance by which each corners of the image and the distance of the nucleus from the Sun are shifted. This works out as a maximum shift of ± 3500 km along the comet's orbital plane. This error is ignored as its effect would be imperceptible when we consider that the nucleus is ~1.85 x 10^8 km from the Sun on the 16th January 2005.

Error source: Solar system barycentre vs Sun body centre

A source of error I considered early on during the project was the error arising from the basic assumption that the Sun's body centre is the origin of both the comet's and Earth's orbits, instead of the solar system barycentre (SSB).

The first step was to compare the two orbits against each other, as shown in Figure 4.17. Over the last century, on average, the solar system barycentre was ~ 8 x 10^5 km from the solar centre (JPL Horizons).

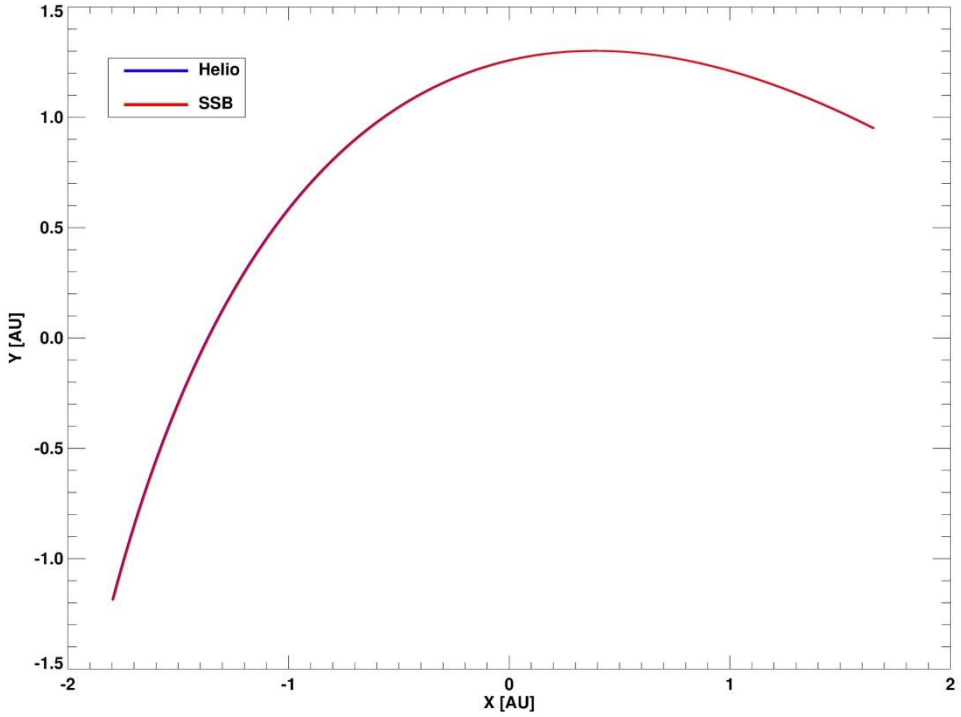

Figure 4.17: Orbit of comet Machholz from Sep 2004 – Jul 2005 using different frame origins. Units are in AU. The red and blue tracks are overlapping in this picture. The two lines are separated by a maximum of 8500 km.

The maximum discrepancy due to the different origins is ± 8500 km for the comet's orbit and the Earth's orbit. A better test to understand the significance of using a different origin would be to project the image onto the comet's orbital plane by using the SSB as the origin. Figure 4.18 is the projected image and orbit onto the comet's orbital. It is clear that using the SSB produces a significant discrepancy between the expected positions of the comet nucleus and the orbit. As can be seen from the figure below, any measurements on the tail centre and any estimates of the solar wind velocity would be impossible. The Sun's body centre is deemed to be the more accurate origin for the frame of reference.

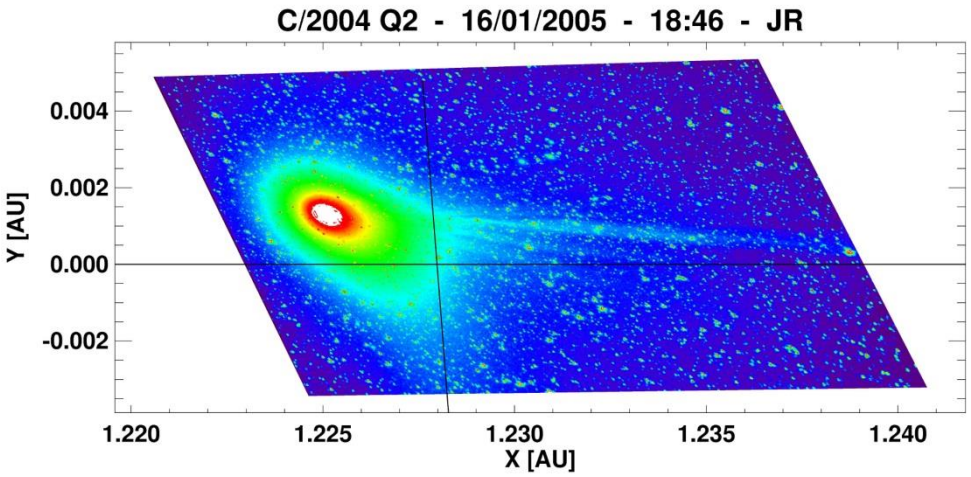

Figure 4.18: Projected image of comet Machholz on the 16th January 2005 using the SSB as origin. Image is taken by Rhemann and Jäger.

Error source: Error on the tail centre.

As mentioned previously, the radial position error of the tail centre (σ_{tail}) is assumed to be ± 1/6 of the ion tail crossing the radial vector.

Error source: Projection effects – line of sight issues

Another important and potentially large contributor to the net errors is the error due to line of sight projection effects. When the image is projected along the line of sight from Earth, the tail centre, as I measure it, is labelled M in Figure 4.19. Due to the projection effects, we cannot know where the 'true' tail centre is. For example, the tail centre could lie anywhere along the line of sight from Earth between P1 and P2. This source of error is ignored as we cannot quantify this value, due to the lack of information. This would only be possible if the comet was imaged by an observer from two different angles at the same time. The angular separation between the observers would need to be sufficiently large for this to be possible.

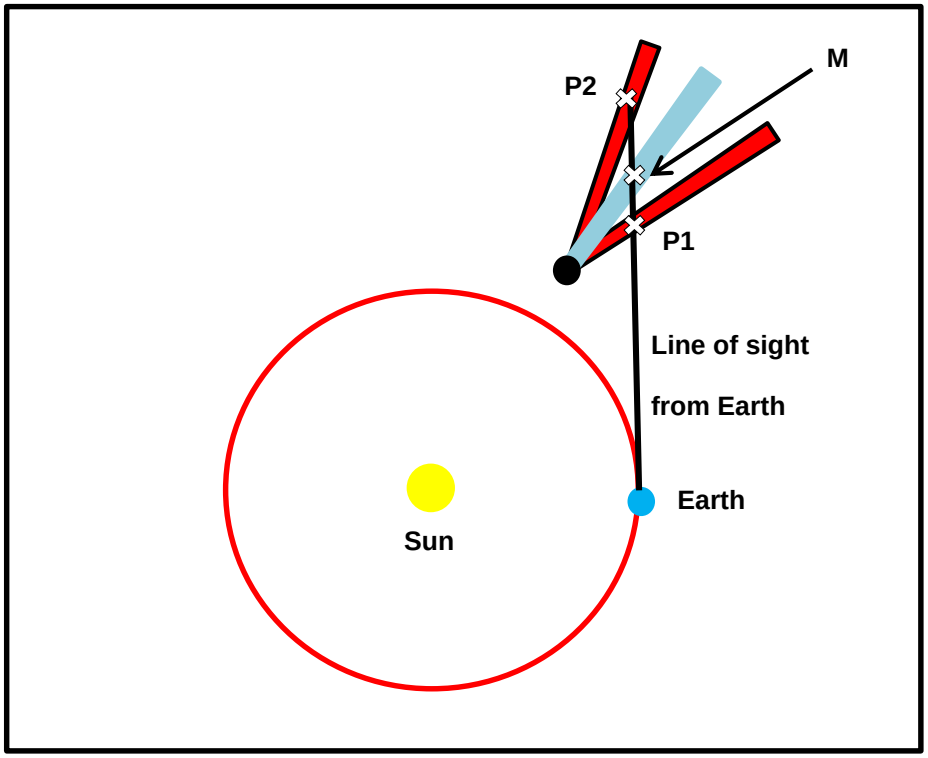

Figure 4.19: Top view cartoon of comet Machholz as observed from the Sun.

Error Propagation

The error on the observer location (σ_{OBS_t}) is found in terms of time, as it is easier and more accurate to refer to each point along the orbits using its corresponding date and time. The time resolution of each orbit is known to the nearest minute. Therefore, the value for σ_{OBS} is rounded to the highest closest integer minute. This is then used to find the observer location, $OBS_{(x/y/z)}$. The error on the observer location along each direction is found from the maximum between ($OBS_{(x/y/z)} \pm \sigma_{OBS_t}$). Note that $OBS_{(x/y/z)}$ refers here is also in terms of time. The value of ($OBS_{(x/y/z)} \pm \sigma_{OBS_t}$) is converted to a measure of distance from the orbit data. σ_{OBS_t} is calculated thus:

$$\sigma_{obs_t} = \sigma_t + \sigma_R$$

The projection mapping is built upon the premise that the timing information was calculated correctly from 'imagetimeheaders'. For instances where the error on time is inaccurately large, this will cause the error on the mapping to be exceedingly large and will produce large erroneous error values for the solar wind.

$$\sigma_{l_{(x/y/z)}} = OBS_{(x/y/z)} \times \sigma_{OBS_{(x/y/z)}}$$

The error along each projected pixel vector from the Sun is then:

$$\sigma^2_{S_{(x/y/z)}} = \sigma^2_{l_{(x/y/z)}} + \sigma^2_{OBS_{(x/y/z)}}$$

The mapped, projected vector to each pixel, $\widehat{S'} = [\ S'_x, S'_y, S'_z\ ]$ where

$$S'_x = \widehat{S}.\widehat{N}$$

$$S'_y = \widehat{S}.\widehat{Y}$$

$$S'_z = \widehat{S}.\widehat{O}$$

$\hat{S}$ is the projected vector for each pixel, $\widehat{N}$ is the vector to the nucleus, which is defined as the new x-axis for the comet's orbital plane, $\hat{O}$ is the normal to the comet's orbital plane, which is used to define the new z-axis for the comet's orbital plane and $\hat{Y}$ is the orthogonal vector to the new x and z axes.

$$(\sigma S'_x)^2 = (N_x.\sigma_{Sx})^2 + (S_x.\sigma_{Nx})^2 + (N_y.\sigma_{Sy})^2 + (S_y.\sigma_{Ny})^2 + (N_z.\sigma_{Sz})^2 + (S_z.\sigma_{Nz})^2$$

$$(\sigma S'_y)^2 = (Y_x.\sigma_{Sx})^2 + (S_x.\sigma_{Yx})^2 + (Y_y.\sigma_{Sy})^2 + (S_y.\sigma_{Yy})^2 + (Y_z.\sigma_{Sz})^2 + (S_z.\sigma_{Yz})^2$$

$$(\sigma S'_z)^2 = (O_x.\sigma_{Sx})^2 + (O_y.\sigma_{Sy})^2 + (O_z.\sigma_{Sz})^2$$

Errors on the normal to the comet's orbital plane ($\sigma_{\hat{O}}$) are assumed to be negligible [see error source: **Inclination and ascending node**], which is why the terms $(\hat{S}.\sigma_{\hat{O}})$ are dropped from the equation for $\sigma S'_z$.

The errors are converted into errors as mapped onto the comet's orbital plane and the largest error between that of the transformed pixel vector and the transformed orbit is taken as the error for the projected mapping. The reasoning behind this is that the error on the orbit will directly translate to an error on position of the tail centre. The error on the mapped image along the x-axis ($\sigma S'_x$) is combined with the error on the tail centre (σ_{tail}) to find the error on distance that the plasma bundle has travelled (σ_{dist}). The error on time is found from:

$$\sigma_{time} = \sigma_t + \sigma_{LT}$$

The error equation for the local solar wind velocity is given below. t_{plas} is the time difference between the nucleus and the orbit position when the plasma bundle left the nucleus. There is an error on the extended radial vector used to sample the image. The effects of this error were not explored quantitatively as the radial cross sections of the image will be relative to the position of the nucleus, from which it is found. Therefore, the error on the nucleus position will be reflected in a similar shift in the image and the extended radial vector, thus cancelling out.

$$\sigma_w = \frac{\sigma_{dist}}{t_{plas}}$$

Errors on the obliquity of the ecliptic and the galactic longitude of the ecliptic equator could also be used to compute an error for the comets' and the Earth's orbital plane. These errors have been ignored for this project as they would be tiny. Their magnitudes would be dwarfed by the larger errors associated with non-radial solar wind flows and intrinsic solar wind structures.

It is important to note that my treatment of the errors in this context pales in comparison to the contribution of uncertainties from error sources such as projection effects and non-radial flows. Unfortunately, there is no way to quantify the error associated with the error sources listed above.

4.4. Tracking Fast Moving Sub-Structures

An alternative method of quantifying the solar wind speed is to visually track dominant features in consecutive images. These include identifiable kinks, condensation knots or disconnections and tracking these features, being entrained downtail of the nucleus by the solar wind.

Flow vector maps (hereafter vector maps) are not new in the study of cometary features. For example, using a time series of narrow band dust continuum subtracted images of comet Liller (C/1988 A1), Rauer & Jockers (1990) tracked three tail structures over the course of several images and derived speeds of 20km s^{-1} at 1-2 x 10^5 km from the nucleus and 100 km s^{-1} at 1 x 10^6 km from the nucleus. Yagi et al. (2014) also used this concept to obtain short temporal

variations of the plasma features near the nucleus (<10^6 km from nucleus) of comet C/2013 R1 (Lovejoy). They report slow speeds compared to previous similar studies on the topic. The results from the Yagi paper were not used for comparison of comet C/2013 R1 (Lovejoy) due to the differing scale lengths at which the features were identified.

As far as I am aware, my project is the first to use the comet's orbital plane to measure the temporal modulations in the tail. The criteria employed for amateur data is that the images had to be observed during the same observing night, regardless of location, and with an adequate time separation in between to ensure that we are looking at the same evolving structure and to compensate slightly for errors in the image time.

Aside from a series of images, for e.g. comet C/2004 Q2 on the 7th January 2005, the vector maps were used to calculate the non-radial solar wind flow velocity in the comet's orbital plane. The non-radial flow measurements were used for the rest of images, which provided a better estimate, however it still cannot account for deviations of the ion tail out of the comet's orbital plane. For images on the 7th January 2005, only the radial flow of the plasma structure was analysed.

Application of vector maps to cometary ray closing rates

As expounded in Chapter 2, it is possible to assume a simple model of symmetrical pairs of folding rays as representative tracers of the mass-loaded draped IMF. Thus, measurement of rays' angular closing rates can be reliably used as a means to constrain the velocity of the mass-loaded solar wind. If multiple rays are visible in consecutive images, we can derive an acceleration of the solar wind velocity near the comet head. As with most studies on the topic, this technique is limited to the region close to the nucleus, ~1 x 10^5 – 10^6 km and requires an adequate spatial and temporal resolution.

The earliest technique was investigated by Schlosser (1966), who remarked that the tail rays could not only close in except in certain circumstances, they were observed to open out, become stationary, and ultimately resume their normal behaviour. He concluded that the tail

rays were travelling in the region of 120-170 km s^{-1} by measuring the centres and diameters of tail rays in consecutive images of comet C/1908 R1 (Morehouse), simultaneously observed from two observatories.

The technique employed by Watanabe (1991) unfolds the comet-solar wind geometry by defining a new coordinate system, with the comet at its origin and the IMF plane containing the X-Y axes. They estimate a stand-off distance of the bow shock boundary by comparing the magnetospheres of comet 1P/Halley and 21P/Giacobini-Zinner to their total visual magnitudes and extrapolating this to deduce a value for comet P/Brorsen-Metcalf 1989o. They further assume an idealised model of a zero-velocity magnetic field at the stand-off point and that the ion tail rays were created by the undisturbed solar wind. Though it purports to be a solar wind velocity measuring technique, this paper provides estimates of the mass-loaded solar wind as it folds and accelerates to the ambient solar wind velocity and is therefore not as good a representation of the local solar wind velocity as the main tail itself. They report a 20% lower velocity than that derived by radio scintillation observations for this comet, which they attribute to the aforementioned reason.

Moore (1991) developed a fairly similar technique although they stopped at projecting the images onto the plane of the sky at the comet. The tail rays were then measured as they folded about the main tail axis, though no attempts were made at producing a solar wind velocity.

In my study, I utilised a customised version of my velocity vector maps by overlaying two consecutive images and tracking how the tail ray folds. In contrast to the previous techniques, I did not quantify the angular closing rates but rather identified and followed sections of the tail ray as it approached the main tail. We can thus measure the radial velocity shear across the tail ray. I expect that as the tail rays curve and lengthen, as they merge with existing plasma along the main tail axis, measurements taken near the nucleus will yield slower velocities than further down the tail streamer.

Errors

The vector map technique suffers from imprecise astrometric mapping. Due to large optocentres, times derived from imagetimeheaders will be slightly limited in precision. The

relatively high velocities of the bulk solar wind and the large field of view of most images drown out the timing uncertainty. For the vector maps and tail ray methods, when two consecutive images are considered from different observers, and for small FOVs, this effect becomes considerable as the timing uncertainty will be compounded and cannot be knowingly accounted for. The feature-tracking velocities are calculated from Δr/Δt, where Δr is the distance that the feature has travelled between subsequent images and Δt is the time range between the two. The error is thus given by:

$$\frac{\sigma v_{feature}}{|v_{feature}|} = \sqrt{\left(\frac{\sigma_r}{r}\right)^2 + \left(\frac{\sigma_t}{t}\right)^2}$$

For the feature tracking, the features were composed of a series of expanding amorphous blobs of varying shapes and sizes and their location is measured by a single position estimated as the feature's centre. The error is assumed to be the distance error of the projected pixel vector. The same process was adopted for the tail rays.

The error on Δt is given by:

$$\sigma_t = \sqrt{\sigma_{t_1}^2 + \sigma_{t_2}^2}$$

The distance error between feature motions in consecutive images can be simplified to the equation below, where σ_x and σ_y are the pixel distance errors:

$$\sigma_r = \sqrt{\sigma_{\Delta x}^2 + \sigma_{\Delta y}^2}$$

Where $\sigma_{\Delta x/y}^2 = \sigma_{x/y1}^2 + \sigma_{x/y2}^2$

Vector map analysis was performed on these comets:

- C/2001 Q4
- C/2004 Q2

- C/2009 P1
- C/2011 L4 (STEREO HI-1 B)
- C/2012 K1
- C/2012 S1 (STEREO HI-1 A)
- C/2013 R1 (Amateur and INT observations)
- C/2014 Q2

The folding tail rays methodology was applied to these comets:

- C/2004 Q2
- C/2011 W3 (STEREO HI-1 A)
- C/2013 R1 (Amateur and INT observations)
- C/2014 Q2

4.5. Orbit Plane Angle

An aspect of the comet-sun-Earth geometry that I had not initially considered is the orbit plane angle. This is the angle between the line of sight from the observer (at Earth) to the comet, and the latter's orbital plane [Figure 4.20]. A non-zero value indicates that the observer is viewing from a position that is not in the comet's orbital plane. The resulting over/under-estimation of the ion tail's true location will be dependent solely on the magnitude of the angle and whether the observer is leading or lagging the comet's motion.

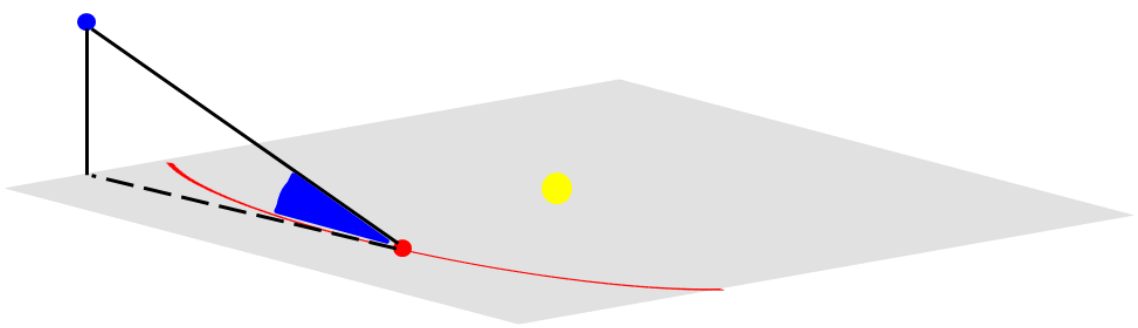

Figure 4.20: Cartoon illustrating the orbit plane angle (blue). The comet is in red and the observer in blue above the comet's orbital plane in grey.

Figure 4.21 and Figure 4.22 are plots of the absolute value of the orbit plane angle plotted against time from the 8th September 2004 to 8th July 2005 for comet Machholz and from the 1st December 2003 to the 31st December 2004 for comet NEAT. As can be seen from the figures below, the orbit plane angle is equal to zero, every 6 months, as the Earth crosses the comet's orbital plane. We are particularly interested in these periods where the orbit plane angle nears 0, as the geometry of the two orbits during these time periods prove problematic for the mapping technique I use. When the orbital planes coincide, images taken during this period become widely stretched when mapped onto the comet's orbital plane. The projection mapping technique is a strong function of the orbit plane angle and the distance between the observer and the comet. Extreme scenarios when the observer is far from the comet and the orbit plane angle is low, the pixel vector extrapolation breaks down and results in extremely lengthy vectors stretching out in all directions. Thus, any radial estimates derived from these images would be unreliable and unrealistic.

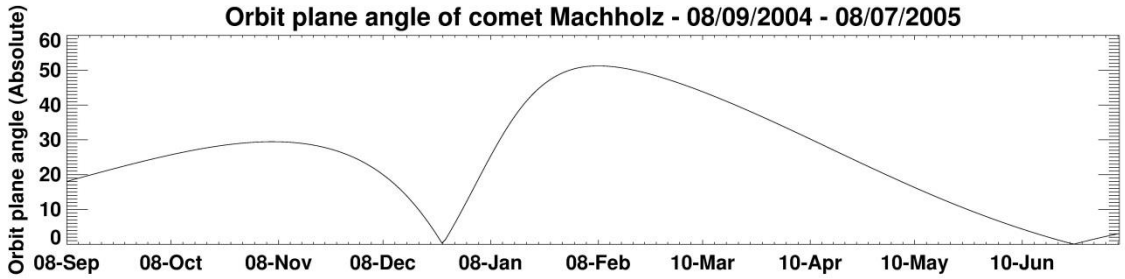

Figure 4.21: Plot of orbit plane angle for comet Machholz. Angle is in degrees.

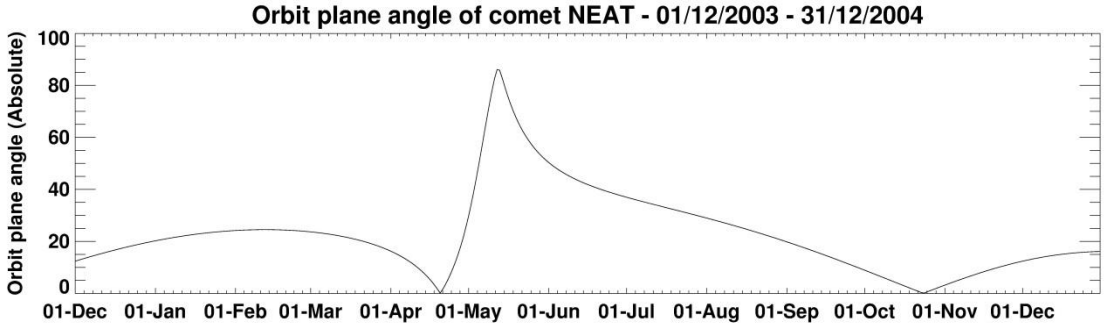

Figure 4.22: Plot of orbit plane angle for comet Machholz. Angle is in degrees.

The vital plasma information we seek is actually hidden where the vectors coincide. By zooming in, we can sometimes resolve the images. Figure 4.23 clearly shows that the mapping technique sometimes “works”. However, images taken during this time period will be recording deviations of the comet along the z-direction. This provides us with a unique opportunity to measure the deviation angle of the comet’s ion tail from its orbital plane due to the non-radial flow of the solar wind. This is a new aspect of the project that I had not encountered or considered thus far, which will be an interesting addition to our version of the comet-solar wind paradigm. The downside is that only a small proportion of images can be used for this.

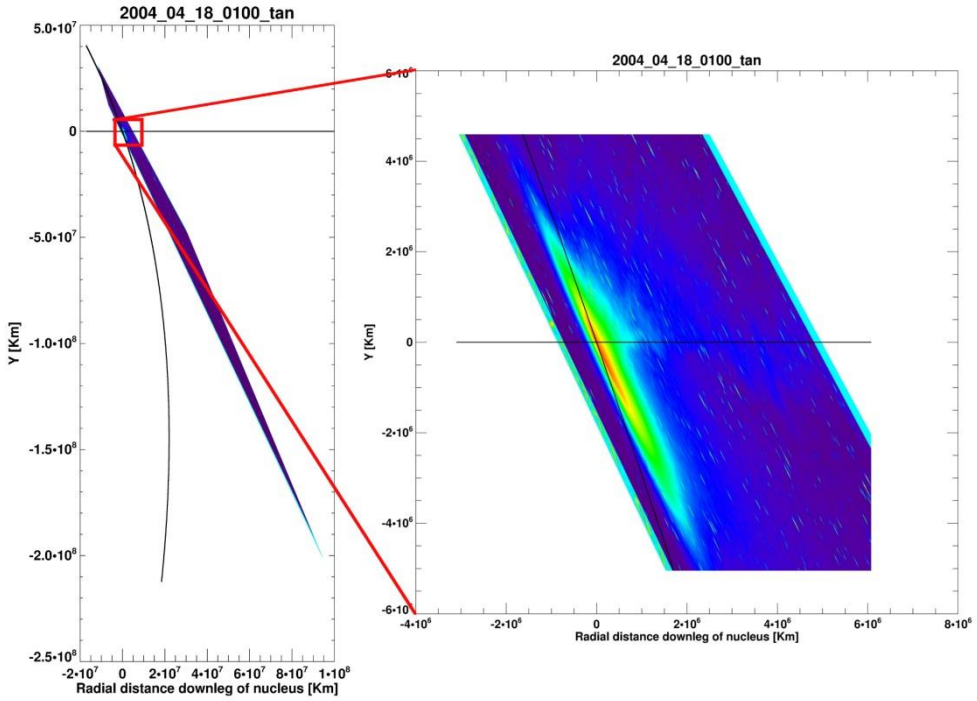

Figure 4.23: Mapped image of comet NEAT by Tan taken on the 18th April 2004. Orbit plane angle is ~ 0º on 20th April 2004. The image on the right is zoomed in onto the nucleus and shows a very faint ion tail close to the radial vector.

On inspection of the original image of comet NEAT taken during this period [see left image of Figure 4.24], we can notice a slight kink in the comet tail. Another image taken on the 19th April 2004 [right image of Figure 4.24] shows a prominent kink. Note that this is not the same kink seen in the image taken on the 18th April 2004. Both images were taken by Tan, an amateur astronomer. During my original analysis of the images, I assumed that the kink might pinpoint a transition region between the slow and fast solar wind. The mapped images coupled with the orbit plane angle seem to suggest that this it is better to attribute this kink feature to a non-radial

flow of the solar wind. This ‘problem’ mandates more attention, especially if it is possible to extract information of non-radial flows from these images. More extreme examples for unresolvable ion tails will be given in chapter 6.

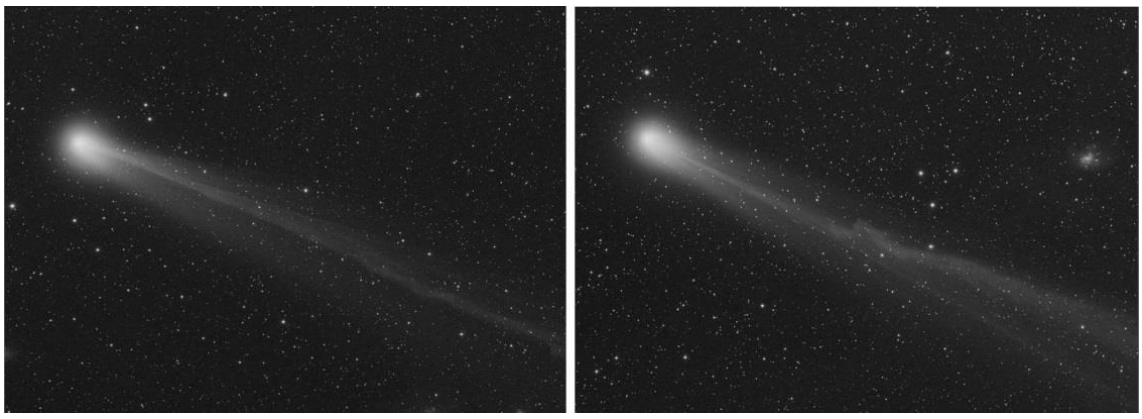

Figure 4.24: Original images of comet NEAT on the 18th and 19th of April 2004 respectively. Images were taken by Tan.

4.6. Mercator Map

The heliocentric coordinates of each sampled plasma bundle can be corotationally traced back along the Parker spiral to its origin on the solar wind source surface. Its cometocentric coordinates are first converted back into heliocentric rectangular coordinates, then into heliographic spherical coordinates (Carrington rotation system). Knowledge of the inclination and the longitude of ascending note of the Sun’s equatorial plane to the ecliptic plane is required to perform the heliographic transformation (Hapgood 1992; Fränz & Harper 2002). Using the mean sidereal Carrington rotation rate of the sun, we can thus map the plasma bundles back to its source longitudes for the slow (400 km s^{-1}) and fast (800 km s^{-1}) solar wind back to the solar wind source surface (~2.5 solar radii above the photosphere) and the time at which it left the Sun. Here, I assumed typical slow and fast solar wind speed without knowing their true value. I also assume that they remain at this same speed on their path from the Sun to the comet, although this is a simplification as the solar wind speed could potentially change between the Sun and the comet.

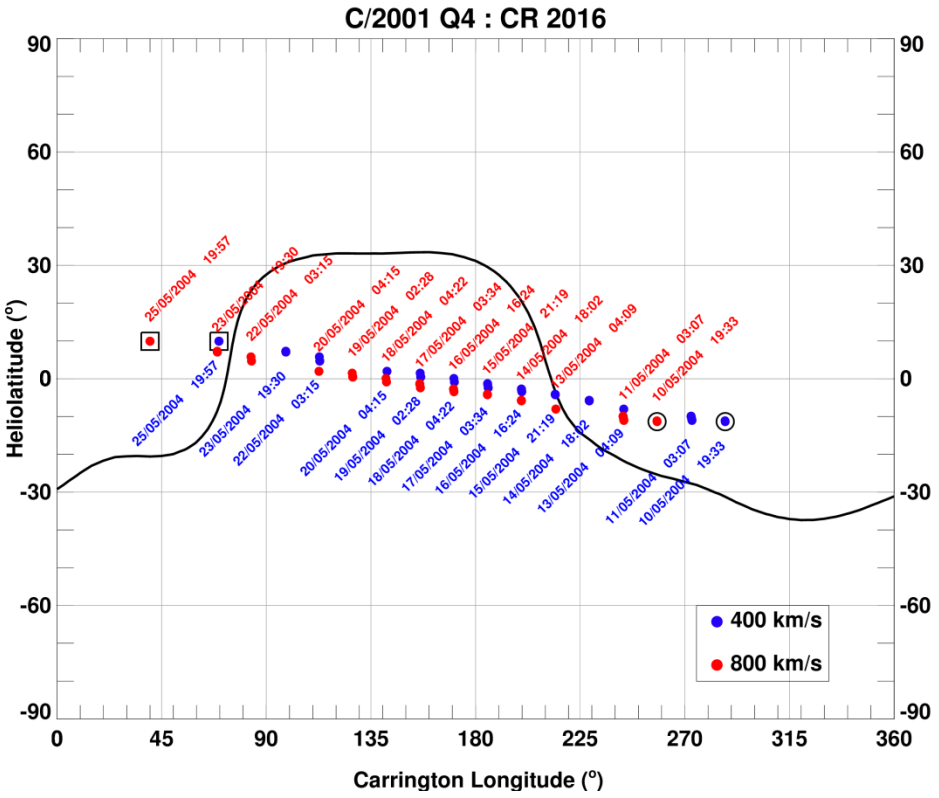

Figure 4.25: Mercator map for comet C/2004 Q2 (Machholz) for Carrington rotation 2016. The slow wind (400 km s^{-1}) is in blue and fast solar wind sources are in red (800 km s^{-1}). See text for explanation.

Figure 4.25 shows the sources for the slow solar wind in blue and the fast solar wind (in red). Only the first date and time for a range of plasma bundles are plotted for each day. Data points within the black circle represent the first date sampled for this Carrington rotation and the last data points are enclosed in a black square.

The black solid line is the approximate position of the neutral line on the solar wind source surface as calculated by the Wilcox Solar Observatory research team (Schatten et al. 1969; Altschuler & Newkirk 1969; Hoeksema 1991). This is a good, but not absolutely reliable indicator of the heliospheric current sheet source. From a combinative analysis of the photospheric magnetic field observations and a potential field model, the coronal magnetic field is calculated and forced to be radial at the source surface. The 2.5 $R_{\odot}$ radial solution was chosen out of the available computations. This form of the solution assumes that the field in and above the photosphere is radial and requires no polar field correction to match HMF observations at Earth, as the classic computation does. The latter solution assumes that the

photospheric magnetic field contains a meridional component. There is a 3.25 $R_\odot$ calculation available, though the smaller source surface radius provides a better overall match to the structure of the inner corona and the HCS's maximum inclination to the ecliptic.

Theoretically, we would anticipate a disconnection event at the comet as it crosses the heliospheric current sheet. The image archives will be compared against the Mercator map and a model of the solar wind at the comet to determine whether a disconnection event was observed at these crossings.

4.7. Data Rejection

The primary reasons for rejecting images were as follows:

- Image is of poor quality, e.g. star trails, saturated image or incorrect astrometric solutions.
- Ion tail is too faint to resolve or its edges are poorly defined against the sky background.
- The image FOV is too large to resolve ion tail.
- In certain instances, the first solar wind velocity measurement was discarded. The proximity of the ion tail to the coma made determining the tail centre unreliable.
- Mapped image shows ion tail lying on extended solar radial vector. Often, images had part of their tail on the extended radial vector. Those data points were not rejected although under more stringent conditions, these should be excluded as they would yield very high radial velocities.
- The last 2 rejection criteria are only applicable to comet NEAT. The dust tail and the ion tail overlapped making any estimates impossible or highly unreliable.
- Inaccurate image mapping due to ~ 0^o orbit plane angle.

A final rejection analysis is run through before plotting the final solar wind velocity results. The solar wind results are compared with image comments noted during the data extraction process and the mapped images to identify where the analysis may have gone wrong or if unreliable measurements were taken. Images showing atypical solar wind structures are also highlighted.

The same rejection criteria will be adhered to for all future analyses including professional observatory and spacecraft observations.

5. Snapshots of the Inner Heliosphere

I will demonstrate in this chapter that the image analysis technique and software can be reliably used to constrain the local solar wind velocity at a comet for calm solar wind flows. During other periods, the mapping technique can be used to show rapid changes in the ion tail morphology due to transient solar wind phenomena such as coronal mass ejections, co-rotating interaction regions and heliospheric current sheet crossings.

I also attempt to construct a comprehensive picture of solar wind interactions with the ion tail of comets, over a period of 11 years from 2003 to early 2015, by using the numerous amateur images of comets available online. I supplemented the amateur observations of comet C/2013 R1 (Lovejoy) with images I acquired at the Isaac Newton Telescope.

5.1. Comet C/2004 Q2 (Machholz)

A relatively bright comet (m_v ~+3.5), Comet Machholz [Figure 5.1] proved to be a near-ideal probe of the solar wind due to a fortunate alignment with the Sun-Earth line. At perihelion, comet Machholz was 1.12 Astronomical Units (AU) from the Sun on the 25th January 2005. At its closest, comet Machholz was within 0.35 AU of the Earth on the 5th January 2005. This geometry provided a unique opportunity to reliably map near-Earth solar wind conditions out to the comet. The comet's J2000.0 orbital elements were inclination (*i*) = 38^{o}.6; eccentricity (e) = 0.99; Perihelion date (T) = 25/01/2005, 21:52 UT.

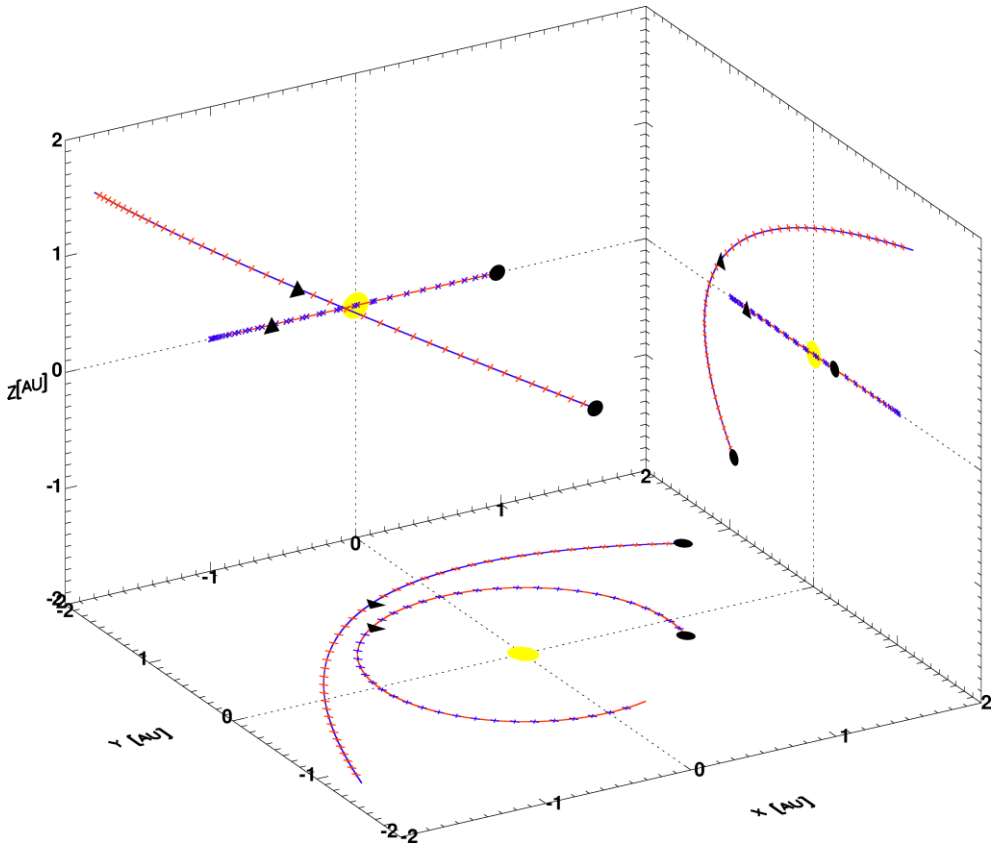

Figure 5.1: Heliocentric ecliptic coordinates of comet C/2004 Q2 (Machholz). Black circles represent the start of the orbits and black triangles show the positions of the comet and the Earth at the comet's perihelion.

Figure 5.1 shows the span of the comet's orbit over which it was studied, starting in early September 2004, denoted as a black circle, continuing until July 2005. Each cross on the orbit represents a time step of 1 week. The orbits are in heliocentric aries ecliptic (HAE) coordinates with the heliocentric distances given in astronomical units (AU). The black triangles show the relative positions of the comet and the Earth as comet C/2004 Q2 approaches perihelion.

Data coverage

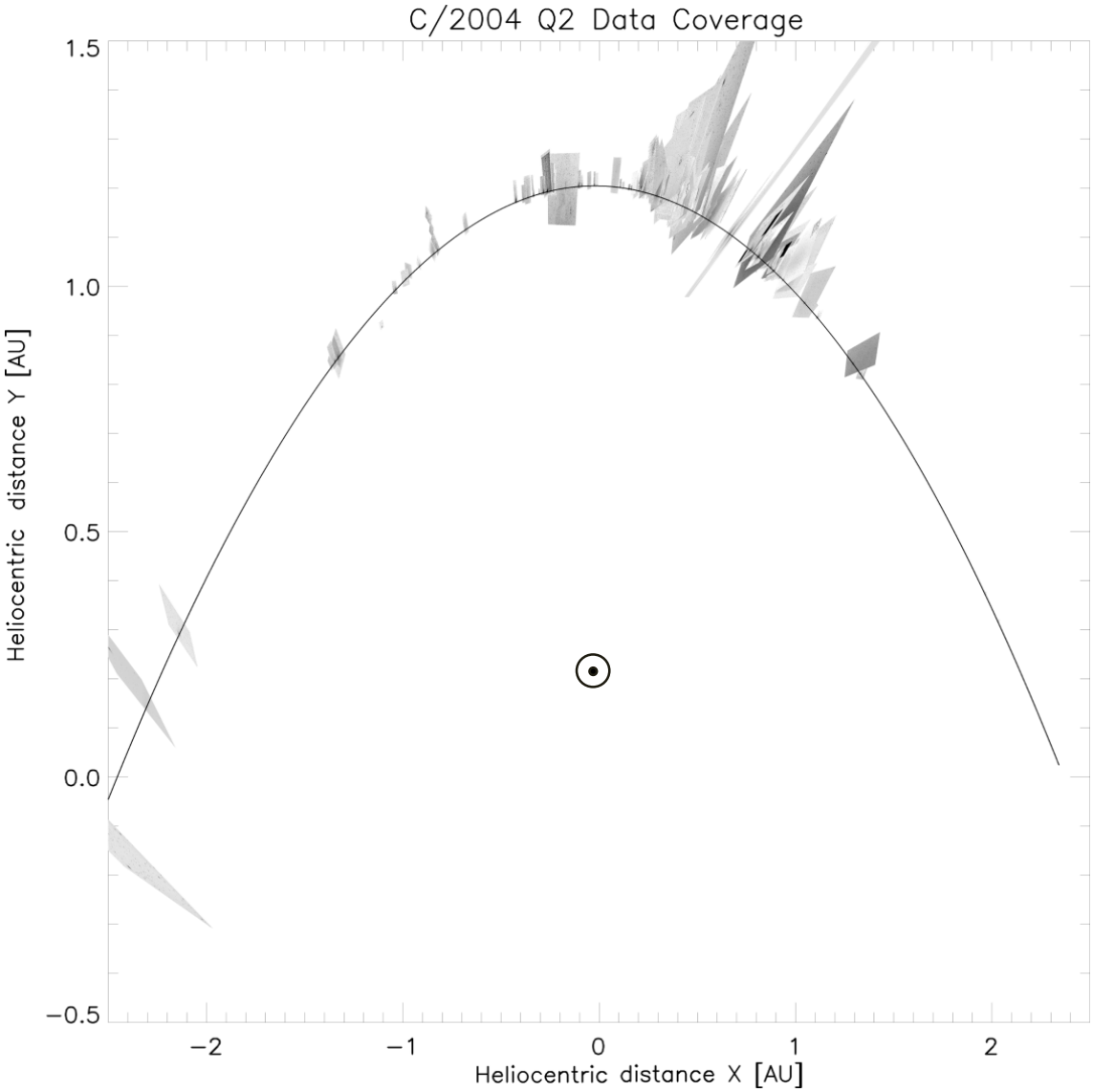

Figure 5.2: Most of the amateur observations were concentrated prior to perihelion, with some observations dating up to a few months afterwards. The images and the comet's orbit have been mapped so that the y-axis is defined as the direction to perihelion. Earliest image is to the right of the data coverage plot, increasing chronologically towards the left.

Figure 5.2 shows the time span over which comet Machholz was monitored, with the highest observing frequency centred a few days prior to its perihelion. The density of images is such that the overlapping images will hide other images underneath. This coincides with a period when the ion tail likely encountered a heliospheric current sheet crossing and an ICME on ICME

interaction. These features were easily identifiable from the image catalogues and the extreme solar wind velocities registered at ACE and through this technique. The images shown here are those that were successfully processed through all stages of the data reduction and analysis pipeline prior to extracting the solar wind information.

Image statistics

Out of 752 amateur images forming the initial catalogue, 551 images were processed successfully through astrometry.net. 380 of those had no visible ion tail once mapped onto the comet's orbital plane or contextually poor data quality. Of those 170 remaining images, 497 solar wind velocity samples were extracted, of which 45 were deemed unreliable, 62 were from images that exhibited turbulent ion tails, large orientation changes or atypical ion tail behaviour and 29 came from images where the early segment of the tail lay on the Sun-comet line.

5.1.1. ACE Offset

Comet Machholz was fortuitously well located near the ecliptic plane for a short period in the midst of the terrestrial observations. Its relatively small geocentric distance meant that solar wind velocities measured in the circumterrestrial space could be reliably extrapolated along the Parker spiral as an approximator of the comet's ambient solar wind conditions. This can only work for near-Earth candidates when they are near the ecliptic plane and for a short time range due to the high spatial and temporal variability of the solar wind [Figure 5.3]. Theoretically, if the comet is moving in step with the Earth, then it should be experiencing the same solar wind structure as the plasma flux tubes expand radially outwards. The caveat here is that the solar wind is assumed to be flowing radially from an unchanging source.

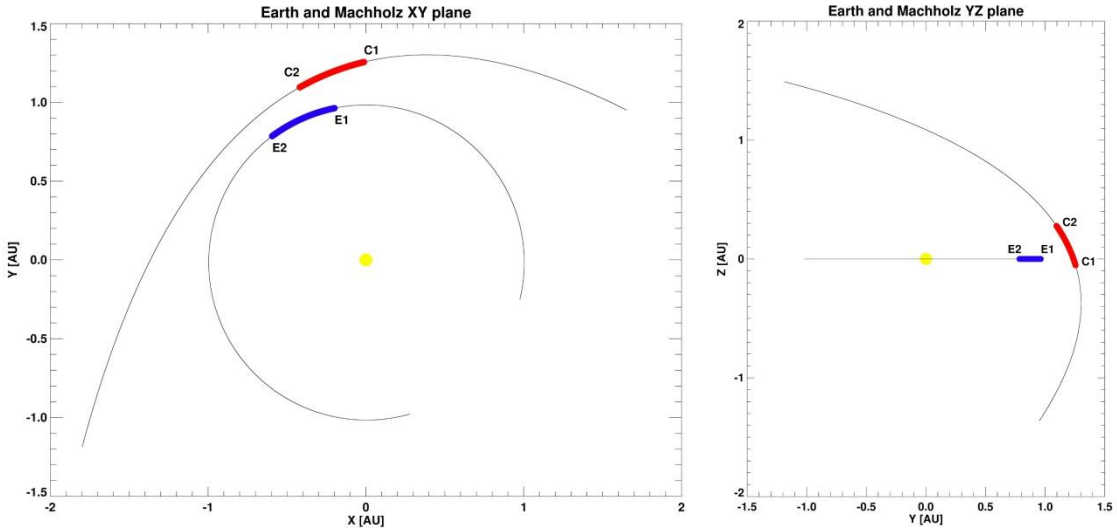

Figure 5.3: Comet Machholz's geocentric distance and its position relative to the ecliptic plane. C1/C2 and E1/E2 represent the start and end date of the comet's and the Earth's orbit during the period where the comet is within -5 and +10 degrees of the ecliptic plane.

A time lag (hereafter offset or ACE offset) between the solar wind arriving at ACE and of the same solar wind parcels arriving at the comet, is computed and compensated for. Initially the solar wind data was offset for the duration when the comet is close to the ecliptic, from the 19th December 2004 to 21st January 2005. This agrees with the period chosen in past studies. After assessing the comet's orbital evolution in solar ecliptic coordinates [Figure 5.4], I restricted this period to when the comet is within ~5° of the ecliptic plane, as the Earth's faster relative motion will mean that the comet will likely not encounter the same solar wind streams outside of 5° from the ecliptic. A timing correction is applied to the ACE/SWEPAM sampled data from the 28th December 2004 18:00 UT until the 13th January 2015 23:00 UT. We expect the comet to have experienced the same solar wind spiral structure as encountered by ACE. The date range chosen differs from that presented by Sizonenko (2007) and Degroote et al. (2008). This is mainly due to the date flexibility allowed by the semi-completeness of our amateur images dataset in comparison to allocated professional observing schedules.

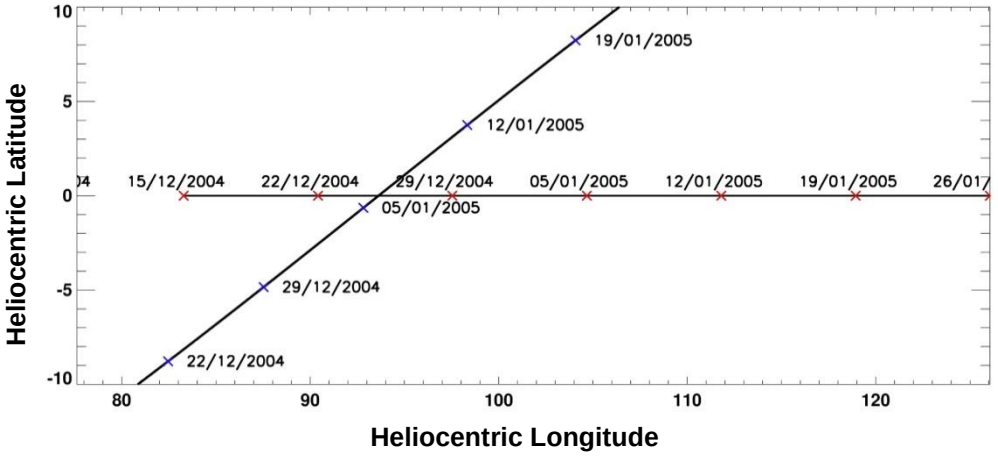

Figure 5.4: The solar ecliptic longitude and latitude of comet Machholz and Earth are shown for the period when comet Machholz remained close to the Earth's orbit and within 5º of ecliptic.

To extrapolate the solar wind data out to the comet's position, Neugebauer et al. (2000) proposed the following correction, comprising a radial and an angular offset.

$$\Delta t = \Delta t_{rad} + \Delta t_{rot}$$

$$\Delta t_{rad} = \Delta r / (v_{sw} + v_{comet})$$

$$\Delta t_{rot} = \Delta_{lon} / \Omega_{\odot}$$

The radial velocity component of the offset can be determined from the difference between the heliocentric distance between the Earth and the comet's position and the solar wind velocity, as measured by ACE. A relative velocity component of the comet with respect to the Earth can also be accounted for. The maximum relative velocity of the comet is ~ 2km s^{-1}. Similarly to Degroote, I set the comet velocity term to 0 since the comet's relative velocity is much less than the solar wind velocity. The rotational correction is computed from the longitudinal difference between Lagrangian point (L1) and the comet's position. $\Omega_{\odot}$, the solar rotation frequency, is given by $2\pi/T_s$, where T_s is the Sun's synodic rotation period (27.3 days). Based on this correction, the comet should thus be experiencing the same structure as the ACE data a few days later.

Using the methodology above as set out in Degroote (SOHO/CELIAS velocities) and Sizonenko (OMNI velocities), I could not replicate the timing offset demonstrated in their velocity plots for our overlapping periods. Though there is a fairly strong correlation between the Neugebauer computed offsets and that of the Owens model [Figure 5.5], the lag is still significant. Both papers show the solar wind transition region on the 11th January falling on the 12th January.

To cross check the timing offset, I developed my own ACE offset. The Sun rotates in a counter clockwise direction as viewed from above the north pole and with its rotational axis tilted by an inclination of 7.25^{o} to the vector perpendicular to the ecliptic plane. The solar wind emerges from the Sun and propagates radially outwards, with the HMF following the Parker spiral in a clockwise direction with respect to solar system objects. In the inertial reference frame, the comet and the Earth both have prograde orbit, and during the period of interest move almost in-step with each other. From the Earth's vantage point (with the Sun-Earth line fixed), the comet will appear to move from left to right and from south to north. I used the synodic solar rotation rate (~27.3 days) to extrapolate each radial solar wind velocity data point from the ACE/SWEPAM instrument, measured upstream of the Earth, to the comet's orbit using the known solar wind velocity and the difference between ACE and the comet's heliocentric distances. Thus, the heliospheric longitudinal difference between the Earth-experienced solar wind on the comet's orbit and the comet's current longitude were converted into a timing offset.

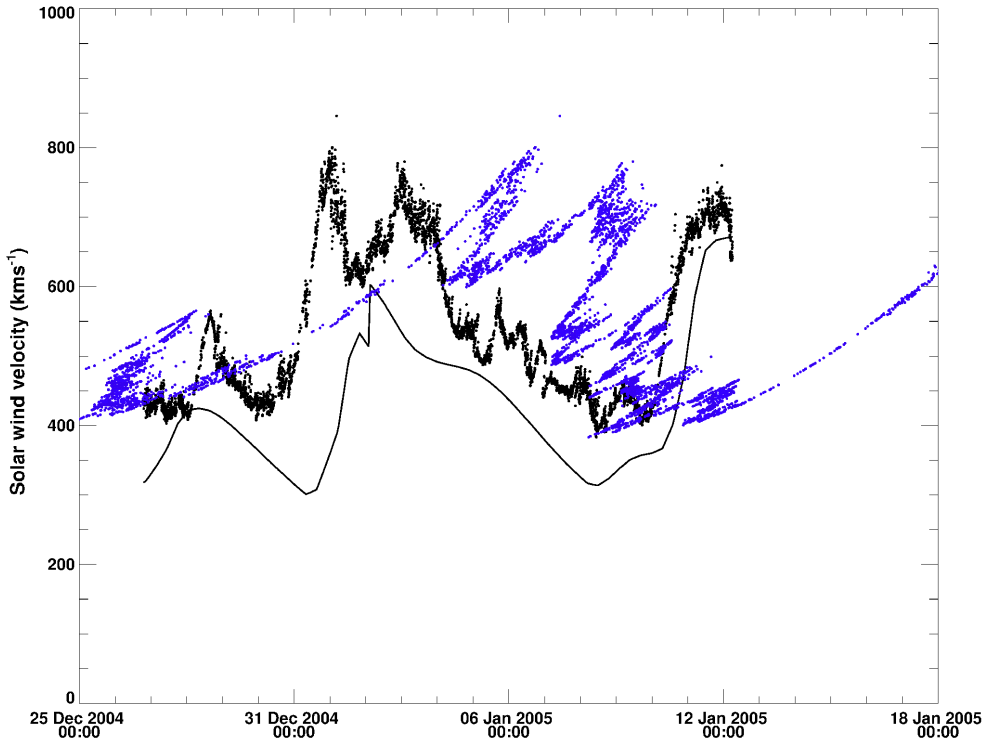

Figure 5.5: The above shows the solar wind velocities from the ACE data as corrected by the Neugebauer method (in black) and as extrapolated by my technique (in blue). The data plot extends for the period that this near-Earth comet should be experiencing similar solar wind phenomena to those at Earth. The solid black line is the modelled solar wind velocity at the comet from a run of the ENLIL model of the quiet solar wind by M. Owens.

Initially, the comet is ahead of the Earth in terms of heliospheric longitude and will experience the solar wind flux tubes slightly before ACE senses it in-situ. The radial solar wind velocity will modulate the Parker spiral shape causing it to wind up more tightly or straighten. The ACE offset computed from the Neugebauer model fits the ENLIL model well [Figure 5.5], aside from a small time discrepancy for the comet's encounter with the solar wind transition region. The Degroote and Sizonenko ACE offset used the same equations and yet produced very different results [Figure 5.6], prompting me to develop my offset correction.

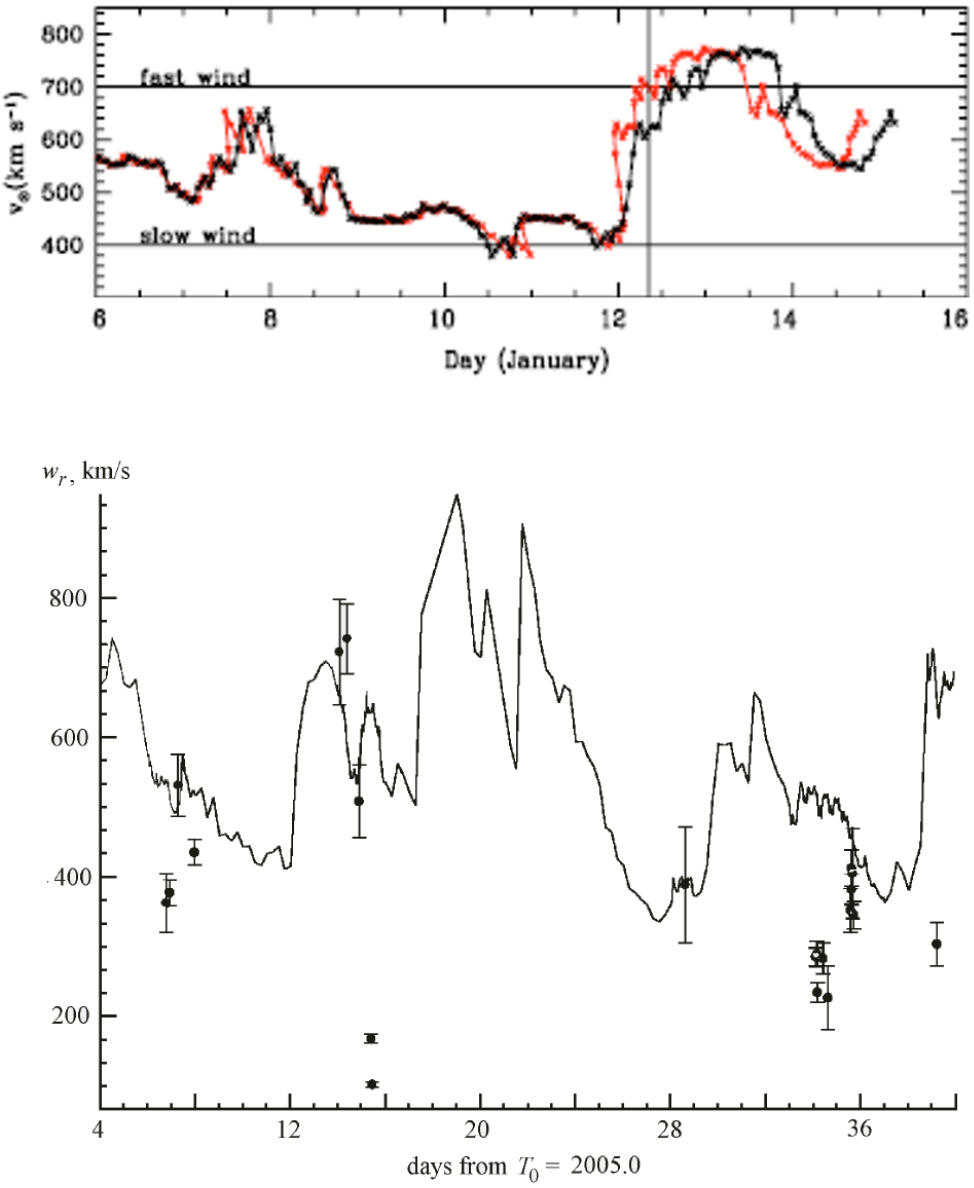

Figure 5.6: Corrected solar wind velocities from SOHO/CELIAS (top) from Degroote et al. (2008) and OMNI (bottom) from Sizonenko (2007) showing very solar wind velocities at the comet during the same period. Note that the timeline is different for both plots. The expected date for the transition region matches for both Sizonenko and Degroote (12/01/2005) but still do not match the Neugebauer or Owens model.

My method of extrapolating the solar wind velocity to the comet's orbit is clearly unphysical as there are multiple values of the solar wind occurring simultaneously at the comet's orbit. Solar wind streams of different velocities would lead to interaction regions rather than overtake each other, which is what the plots in blue suggest. Hence, I conclude the timing offset calculated with the Neugebauer methodology to be valid for the period when the comet and ACE should be

experiencing the same solar wind structures. The assumption here is that the plasma observed at the comet's heliocentric latitude is the same as that of ACE, which is not strictly true.

5.1.2. Radial Solar Wind Speed

The solar wind plots below [Figure 5.14, Figure 5.16, Figure 5.22, Figure 5.32 and Figure 5.37] show a comparison of the local solar wind velocity estimates derived with this technique for comet Machholz (**blue dots**), with the offset measurements from the ACE/SWEPAM instrument (**red**) and a model of the inner heliosphere by M. Owens (**black solid line**). The solar wind velocity estimates, derived from amateur images, span 6 Carrington rotations (CR 2023 – CR 2028). The ACE data and Owens ENLIL model are not available for all Carrington rotations. The error bars for the solar wind velocity are given in red. Errors in time are very small and can seldom be seen when the derived timing error is large. Spikes in the original SWEPAM data indicate when the instrument was overwhelmed and these have been removed from the final plots. The top abscissa values represent the heliocentric distance range for each sampled plasma bundle. The heliocentric distance on the top axis does not retain the same tickmark scale throughout as the comet sweeps different heliocentric distances over time.

The modelled solar wind velocities (solid black line for CRs 2024 - 2027) were computed by M. Owens for the inner heliosphere based on the coupled ENLIL-CORHEL model (Odstrcil 2003). The corona and heliosphere are simulated using two different models to produce a more realistic extrapolation of the neutral line and solar wind velocity from 2.5 $R_{\odot}$ to the comet's heliocentric distance. This model does not include transient interplanetary events. The polarity reversals in the solar wind at the comet are indicated in black and white at the top of each plot for Machholz. The sharp jumps in the solar wind velocity at the beginning of CRs 2026 and 2027 are artefacts arising from the manner in which the simulation was processed and where the CRs were compiled together. Each CR were solved independently and then concatenated.

The coronal field is based on the Magnetohydrodynamics Around a Sphere (MAS) 3D MHD model (Linker et al. 1999; Mikic et al. 1999) model. The initial boundary conditions are set using observations of the photospheric magnetic field from the National Solar Observatory at Kitt

Peak and deriving a potential magnetic field solution outwards to the photospheric radial field, a uniform boundary density and a Parker spiral solar wind outflow.

The heliosphere is simulated by 'ENLIL', a 3D MHD time-dependent model of an ideal fluid. Boundary conditions were set by the MAS coronal solution. The simulation for the global behaviour of the solar wind plasma, is bounded from 30 $R_{\odot}$ to 2 AU, covering 360 degrees in azimuth and -60° to +60° in solar latitude.

In addition to the Owens computed solar wind model at the comet's location, I have elected to use the visualisation tools, available at the CCMC (http://ccmc.gsfc.nasa.gov/index.php), for ENLIL (resolution: 512x60x180) with MAS (CORHEL) using National Kitt Peak observatory magnetograms as my time-independent inner boundary condition. Multiple plane cuts were taken along the longitude, latitude and heliocentric distance at the comet to provide visual aid of the MHD solar wind behaviour and thus, some context to the radial velocities. Runs have been requested for CRs: 2015 - 2017, 2024 – 2027, 2115, 2116, 2119 - 2121, 2134, 2144 – 2145, 2150, 2155 - 2159. An 'ENLIL with cone' model, for ICME replication within the MHD simulation, was found in the published runs for CR 2025. These are included as independent verification of an ICME interaction with the comet.

After a careful point-by-point analysis, I determined special cases where the comet-derived solar wind velocities may be misrepresented. The data points in green are where a significant portion of the ion tail (~1-2 x 10^6 km) lies on radial vector. The latter could be considered unreliable as this suggests infinite solar wind velocity for this period and will cause an overestimation of the solar wind velocity for subsequent estimates of the solar wind from the same image. Points in purple [Figure 5.14, Figure 5.16, Figure 5.22, Figure 5.32 and Figure 5.37] indicate atypical plasma flows, i.e. any instances that deviate from a straight tail as a result of a smooth solar wind flow. This can be due to transient solar wind phenomena or turbulent equatorial solar wind flow. The blue dots are thus a better indicator of quiescent, radial solar wind speeds in the comet's local environment and will be the main point of focus for comparisons with modelled values. Note that each plot has its own timescale.

Solar wind velocities for comet Machholz ranged from ~120 to 1800 km s^{-1} [Figure 5.7]. Often, these extremely high velocities are indicative of deviations from quiescent surrounding solar wind conditions and/or non-radial flow. These will be addressed in detail later as the main focus is the comparison of the ambient radial solar wind flow. Images of the ion tail from multiple observers provide corroborating evidence of non-radial transient solar wind phenomena.

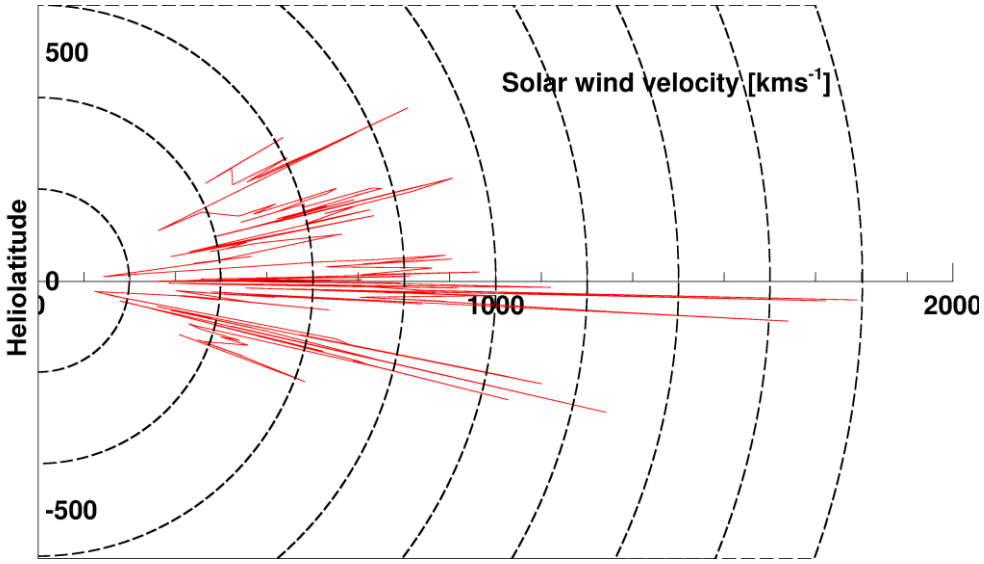

Figure 5.7: Solar wind velocity against heliolatitudes for comet C/2004 Q2 for the duration that it was observed. High velocities are discussed thoroughly during their respective Carrington Rotation analysis. The circles represent isovelocity contours for a fixed radial solar wind velocity at increments of 200 km s^{-1} from -90° to +90° in heliographic latitudes.

The inclination of comet Machholz's orbit to the ecliptic means that it only experiences the local solar wind velocity as measured by ACE/SWEPAM for a short period of time. ACE data should be in best agreement in the first half of January 2005 when comet Machholz crossed the ecliptic plane and was closest to Earth. ACE data was offset for a segment of two Carrington rotations to account for time lag between the comet and ACE experiencing the same solar wind conditions. The extrapolated solar wind data is a relatively good match to the measured solar wind velocities between the 8th and 12th January 2004, with turbulent flow measured at L1 overlapping well with the ion tail's. Unfortunately, observational data gaps render direct comparison more difficult as we cannot predict the behaviour of the solar wind during these "dark" periods. Periods of poor correlation around the 29th December may be due to the fact that

cometary measured solar wind velocities tend to be generally poorer during this period. The orbit plane angle is near 0^{o} on the 24^{th} of December and steadily rises over the next few days.

Solar wind estimates during CRs 2026 and 2027 [Figure 5.32 and Figure 5.37] are in good agreement with the modelled solar wind velocity at the comet. This indicates that this technique is ideal to sample the solar wind during quiescent solar wind conditions. Solar wind plots are capped at 1000 km s^{-1} to facilitate comparison of the quiescent solar wind speeds. For C/2004 Q2, there were 17 data points with velocities higher than the cap. During periods when the scatter plot deviates from the model of the inner heliosphere, we observe rapid and chaotic changes in both morphology and orientation of the ion tail. These likely include highly non-radial plasma flows and are seen as a sharp increase/decrease of solar wind velocities over short time steps. Comparisons between amateur images and polarity reversals in M. Owens' model have not shown any evidence for disconnection events associated with heliospheric current sheet crossings, although we do see a globally well-observed kink structure during the period when we expected a crossing.

In chapter 2, I introduced various tail features that can be detected in the ion tail such as dense condensation clouds, kinks, disconnection events and how these may arise. For each Carrington Rotation, I will attempt to explain the non-quiescent solar wind velocity estimates and discuss how the images available can be used to identify the ion tail interactions with ICMEs, HCS crossings and CIR location, which can dominate the structure and evolution of the ion tail. A comparison of each CR with the comet's orbital plane angle, a Mercator map of the measured plasma bundles mapped back to the solar wind source surface and the original and mapped images will aid in building a complete view of the comet-solar wind interaction in the inner heliosphere.

I also resort to the visualisation tool of the ENLIL data for this CR from recently requested runs from the Community Coordinated Modeling Center (CCMC) as an additional resource for the solar wind variation at the comet. Previous published runs by other authors, which includes a cone model run for a fast Halo ICME on the 17^{th} January, will be used to supplement the repertoire of MHD predictions.

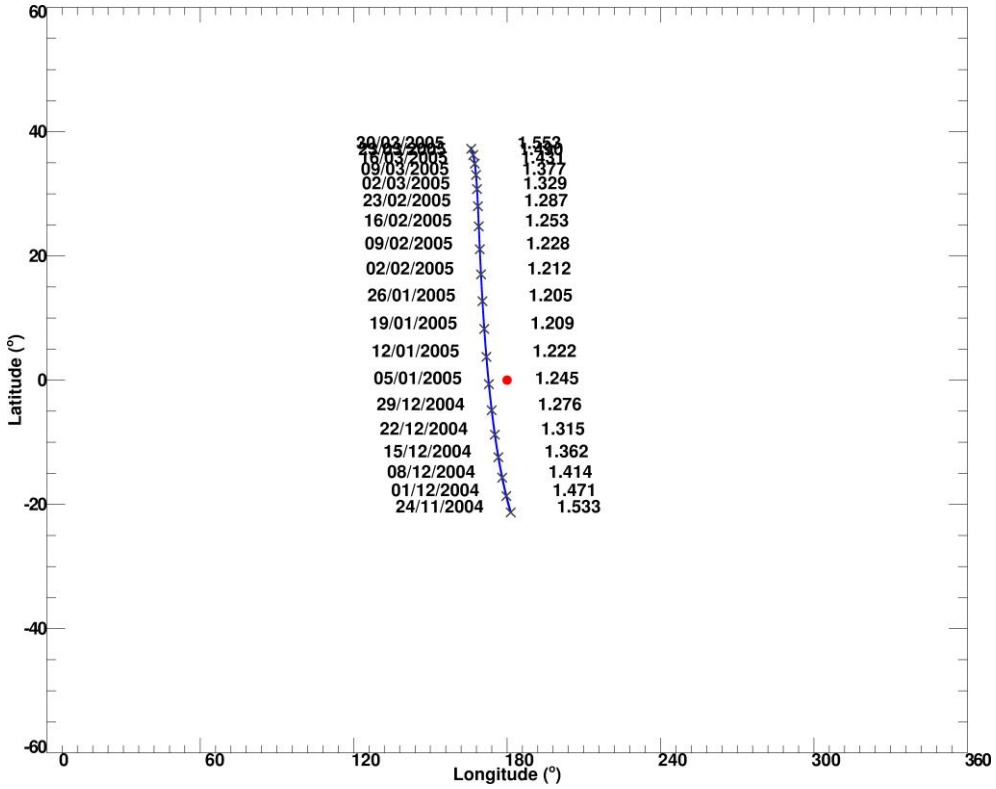

Figure 5.8: Heliocentric ecliptic orbit of comet C/2004 Q2 with the Sun-Earth line fixed. The orbit has been limited to 24th November 2004 to 1st April 2005 to cover the time span over which the solar wind velocity has been sampled (CRs 2023 to 2028). The heliocentric distances are marked on the right hand side.

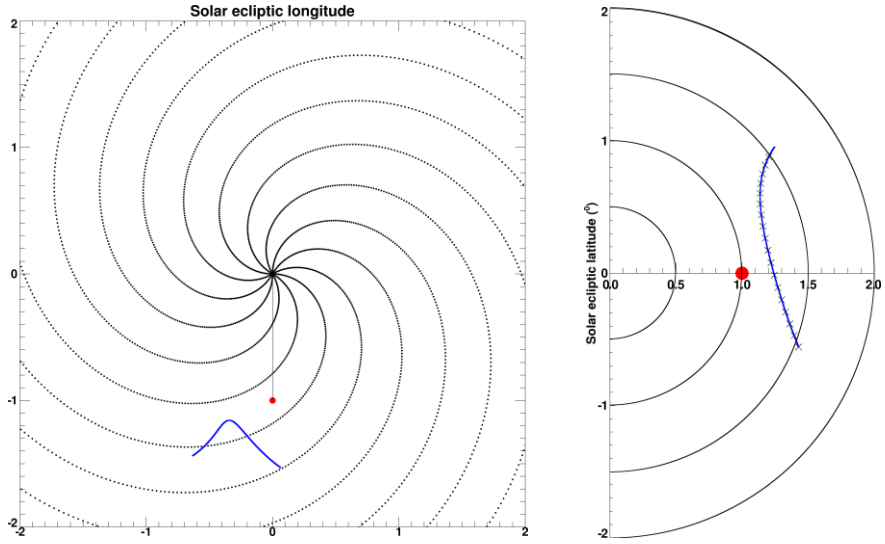

Figure 5.9: Comet's ecliptic longitude and latitude against its heliocentric distance from 24th November 2004 to 1st April 1005. The Sun-Earth line is kept fixed. These plots are useful for an approximate comparison with the ENLIL model (heliographic coordinates) for all CRs. Orbit starts from right with respect to Sun-Earth line in the left-hand panel. The left hand plot shows the slow solar

wind Parker spiral as the solar wind propagates radially outwards. Axes are in AU.

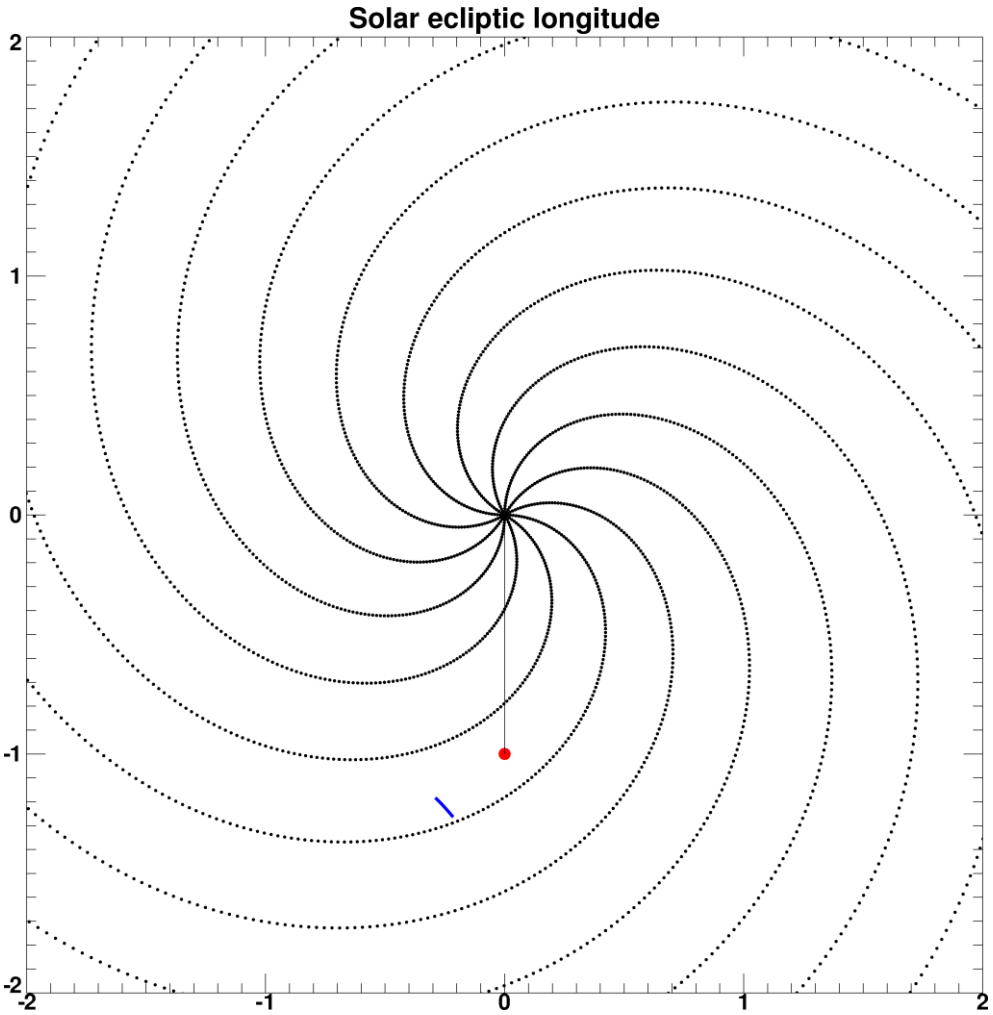

Figure 5.10: Slow solar wind parker spiral structure shown above. Sun-earth line is kept fixed. Comet (blue) is within ±5 degrees of ecliptic. Earth is shown in red. This plot is useful for an approximate comparison with the ENLIL model output for the period that the comet is closest to Earth. The comet's orbit starts from the bottom right. The comet's orbit is given for the brief period where ACE data can be reliably offset.

Figure 5.8, Figure 5.9 and Figure 5.10 plot the comet's heliocentric ecliptic orbit with respect to the Sun-Earth line and allows a simple and quick comparison with the visual tools from the ENLIL MHD predictions. The plot of the expected positions of the comet with respect to the Sun-Earth line should be considered with cutplanes of the longitude and latitude, with r kept constant, for different heliocentric distances. Note that the dates given in the MHD colour contour plots are in American style (mm-dd-yy).

Observing Geometry

The observing geometry between the observer and the comet is fairly poor during early observations [Figure 5.11]. The observer's position projected onto the comet's orbital plane rapidly crosses the comet's orbit over a period of 2 months. The comet is close to the Earth when its orbit plane angle is near 0^o. The rapid relative motion of the comet as it approaches its perihelion means that the observing geometry is good enough for ACE comparison, with the slight discrepancy in time between the Owens' model and the offsetted ACE data easily explained due to the low orbit plane angle. The orbit plane angle is at its peak when the comet is at perihelion on 25/01/2005. Unfortunately, we have very few images to analyse during this period. The observing geometry remains relatively stable and high for CRs 2026 to 2028 [Figure 5.12], accentuating these CRs as the best examples for comparing our velocities with the modelled values.

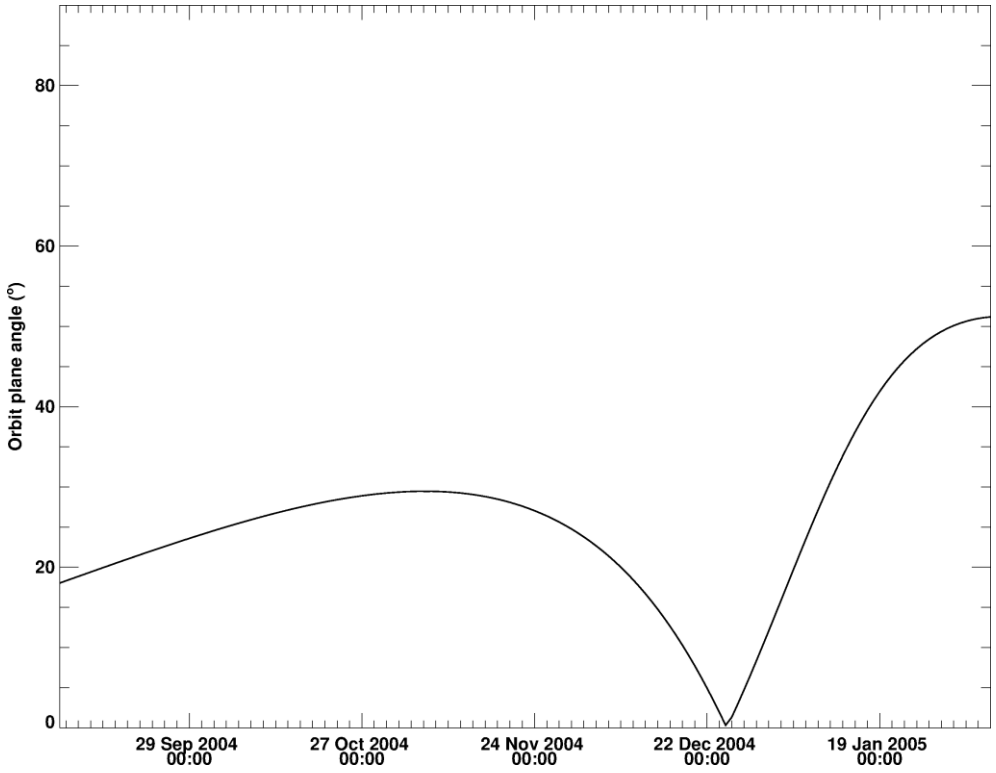

Figure 5.11: Orbit plane angle of C/2004 Q2 from 8th September 2004 to 6th February 2005. Minor tickmarks represent every 2 days.

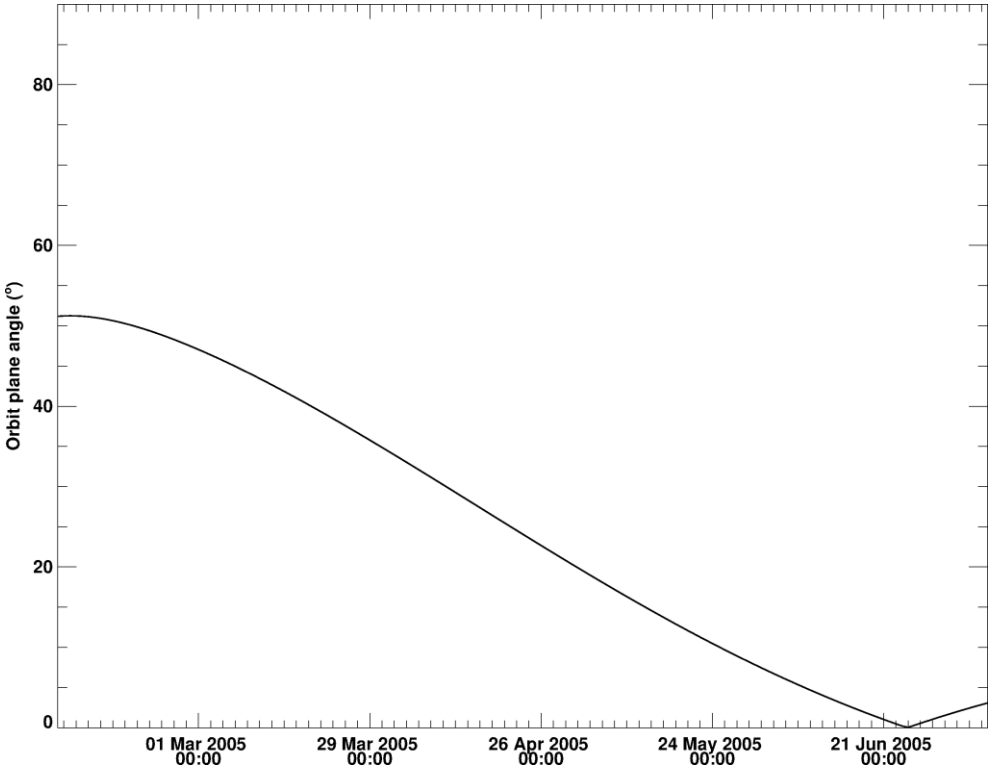

Figure 5.12: Orbit plane angle of C/2004 Q2 from 6th February 2005 to 8th July 2005. Minor tickmarks represent 2 day intervals.

CR 2023

Figure 5.13 shows the Mercator map for CR 2023 with the average speeds for the slow (blue) and fast solar wind (red) mapped back to the solar wind source surface (2.5 $R_{\odot}$). The first and last data points are marked with a circle and a box respectively. The comet was at low equatorial latitudes and experienced low solar wind velocities as seen in Figure 5.14. There were no turbulent events recorded in the image archive.

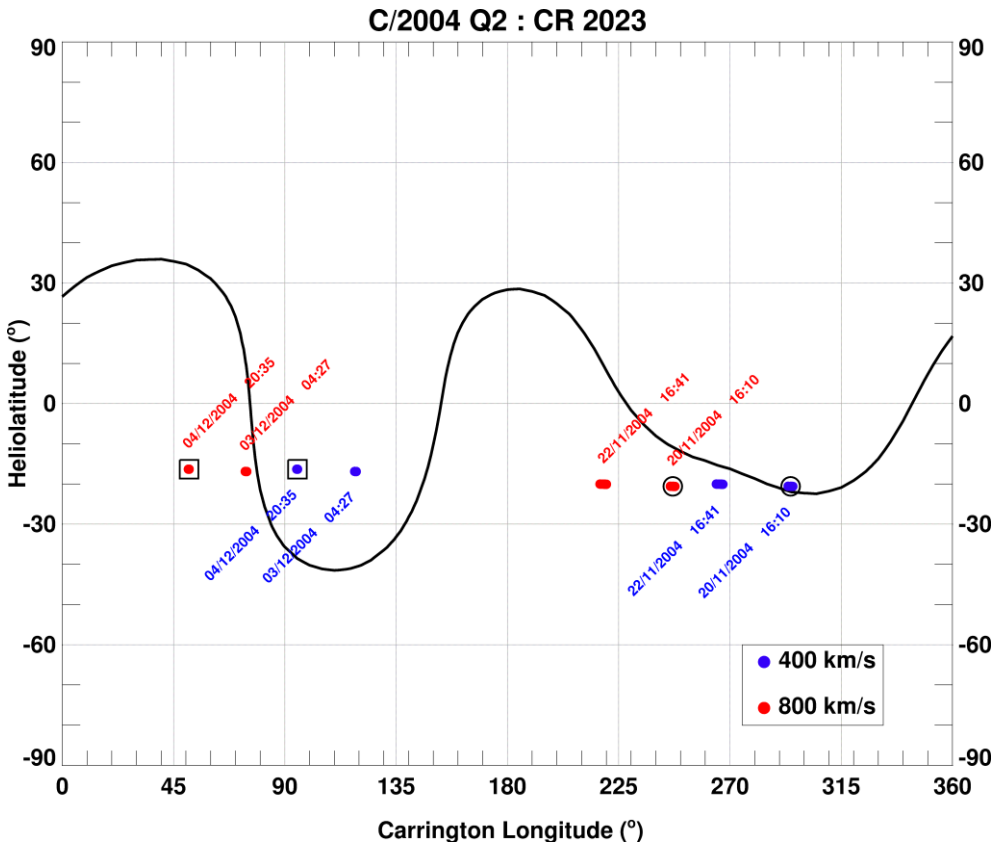

Figure 5.13: Mercator map for CR 2023 for comet C/2004 Q2.

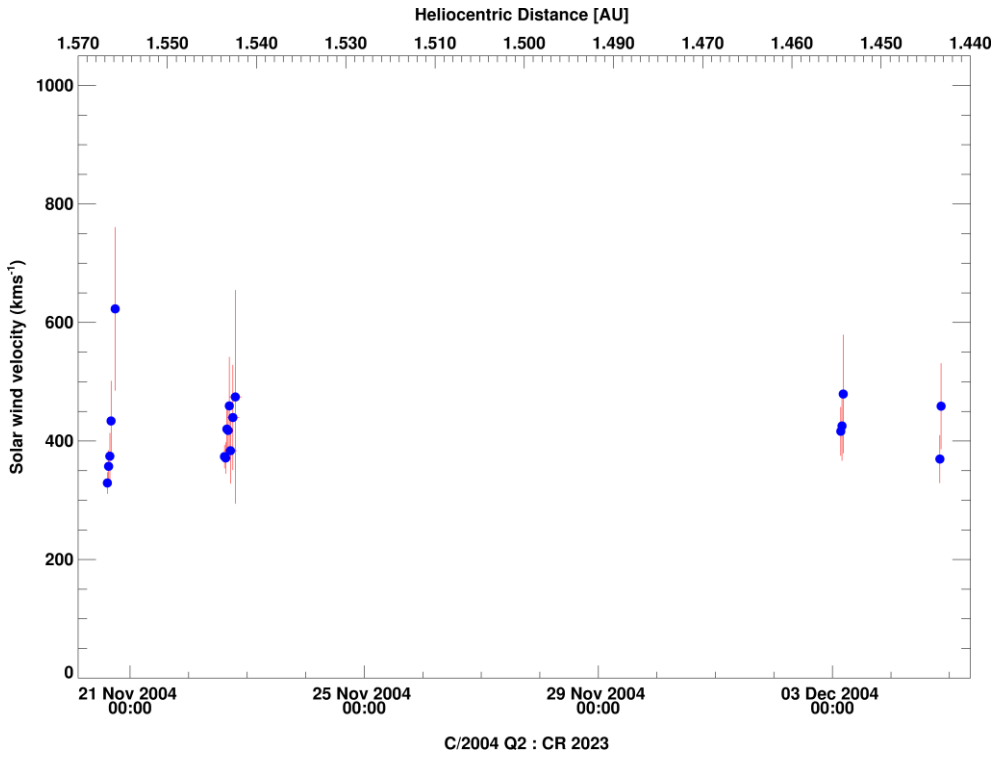

Figure 5.14: Solar wind velocity for comet C/2004 Q2 during CR 2023.

CR 2024

There are a series of images on the 6th December showing a disconnection event. Solar wind estimates could not be extracted from any images, expect for one, due to the faintness of the ion tail once mapped onto the orbital plane. Figure 5.15 indicates that if the comet was experiencing slow solar wind speeds, it would have likely traversed the HCS on the 6th December. A Mercator map using the measured velocities at the comet traced back to the solar wind source surface is included in Figure 5.15. We can easily see the range of possible heliolongitudes and latitudes for the solar wind source lying between the 400 and 800 km s^{-1} data point.

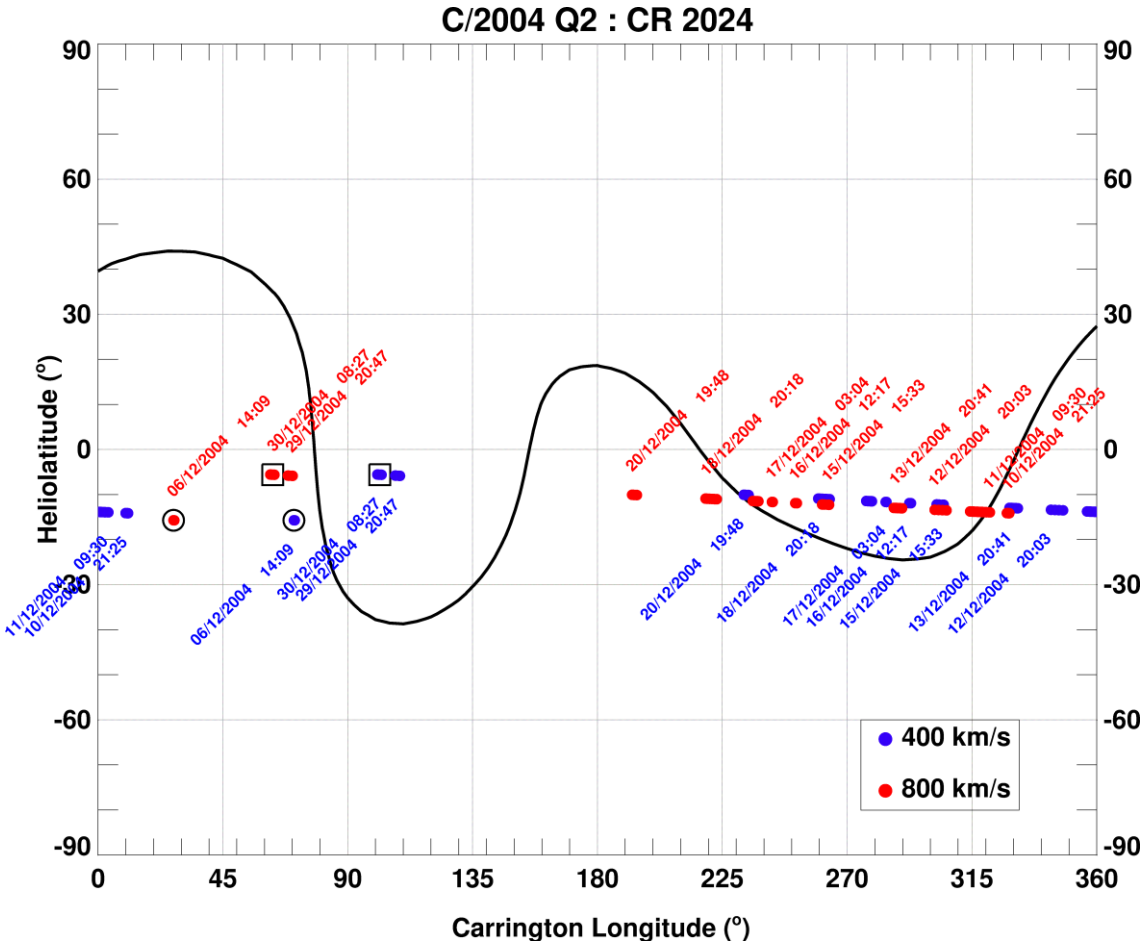

Figure 5.15: Mercator map for CR 2025. Dates and times are plotted only for the first sample of each day for a slow and fast solar wind.

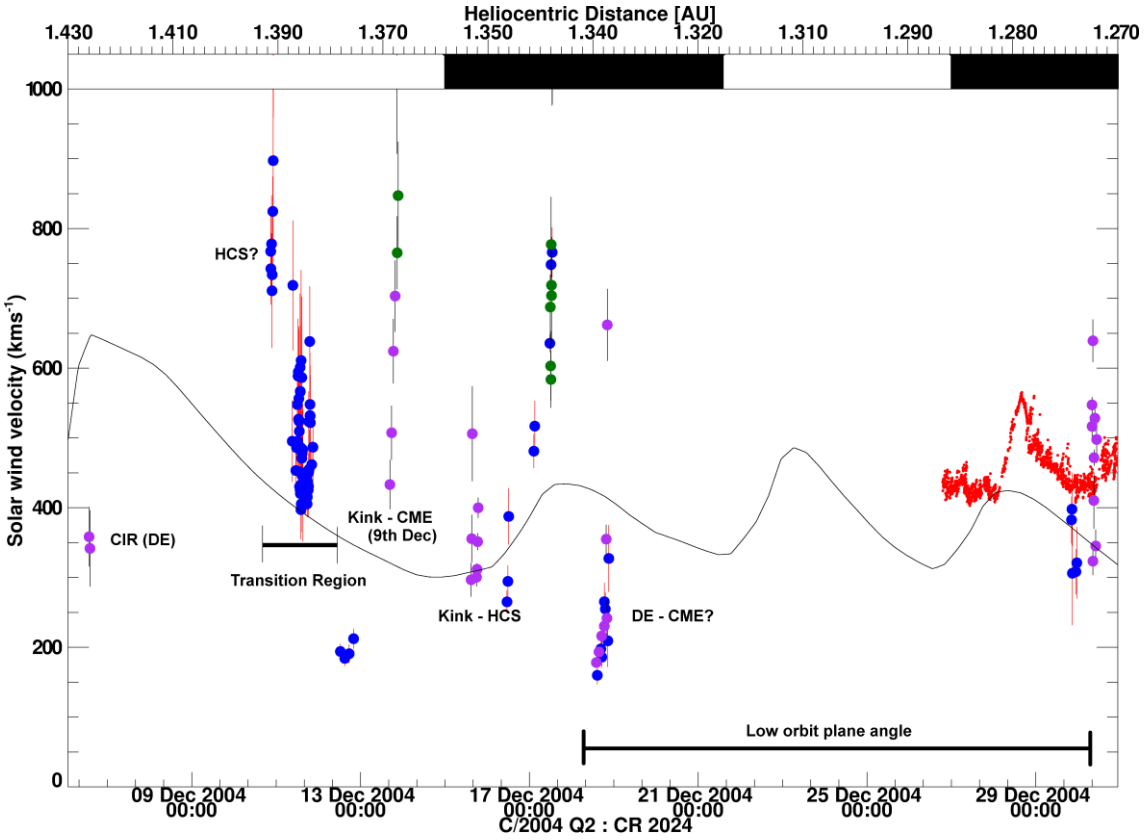

Figure 5.16: Solar wind velocity for comet C/2004 Q2 during CR 2024. ACE data is in red.

There is no HCS crossing expected during this period, according to the Owens ENLIL MHD predictions. Comparison of plane cuts at the comet's location revealed that it encountered shocked slow solar wind preceding a CIR.

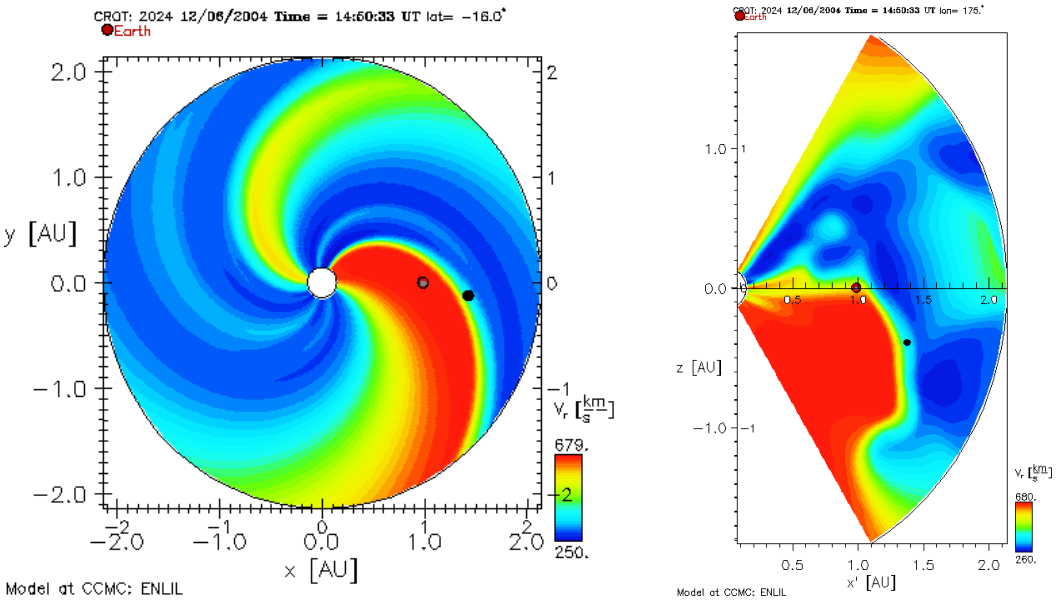

Figure 5.17: Radial velocity at the comet. The comet's position has been overlaid on the ENLIL plots at the closest time available to observations of a kink and eventual DE in the ion tail. Images are for modelled solar wind on 06/12/2004 at 14:50 UT.

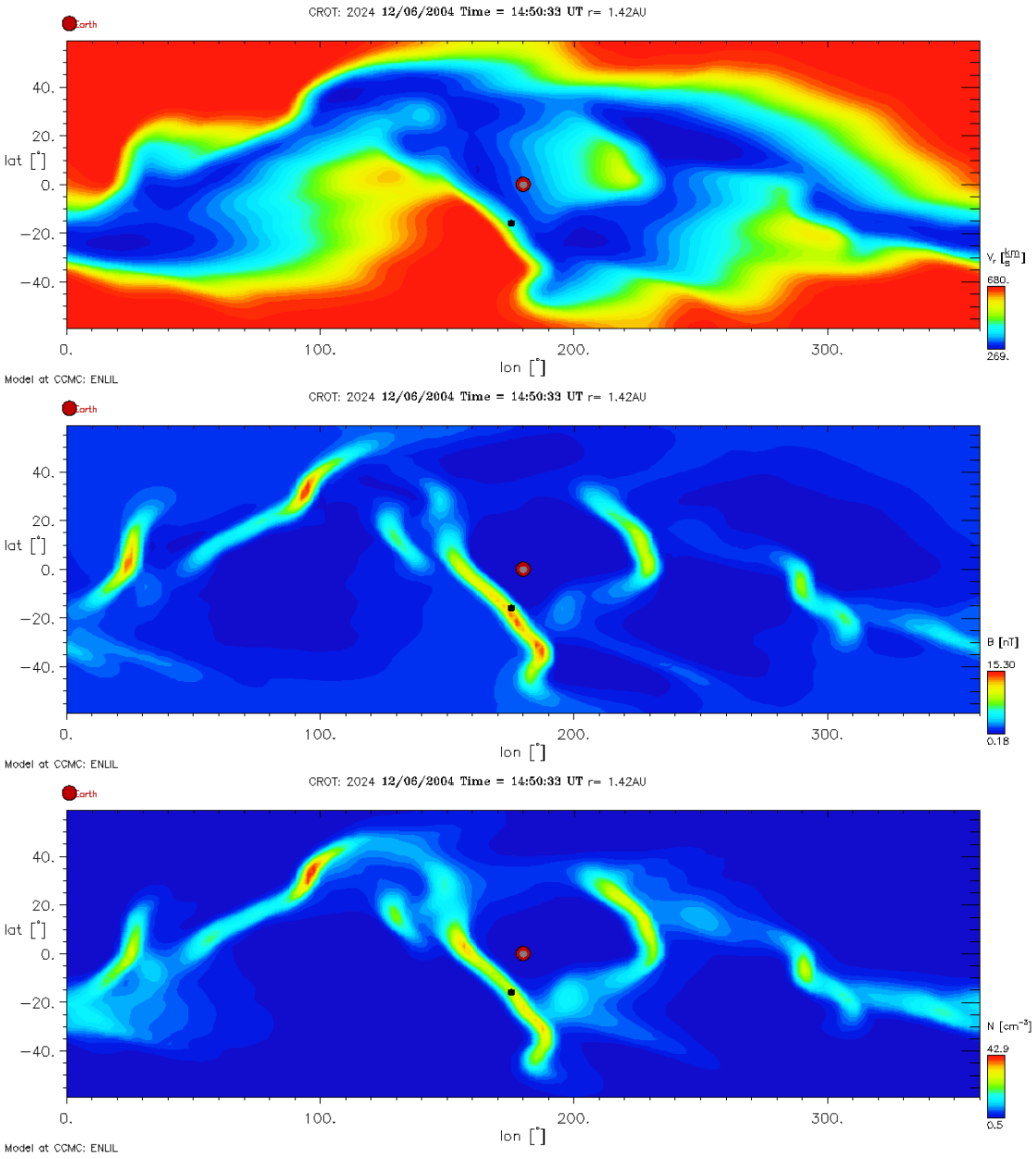

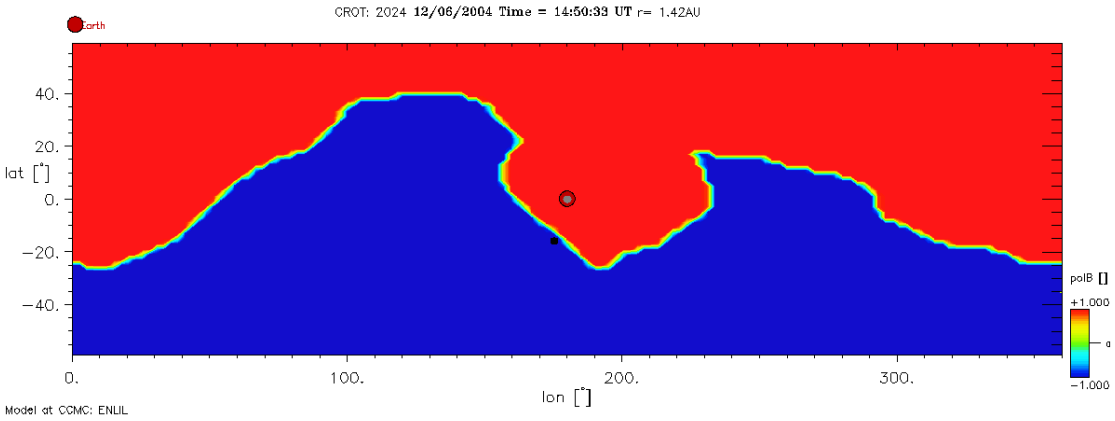

Figure 5.18: The comet is clearly trapped in shocked solar wind in a region with a clear peak in magnetic field (B) and particle number density (N). The comet also encountered a polarity reversal at this position. Images are for modelled solar wind on 06/12/2004 at 14:50 UT.

According to the Mercator map [Figure 5.15], a second HCS crossing is expected in the days leading up to the 14th December. The Owens modelled polarity reversal at the comet puts this event sometime during the 15th and 16th December. Thus a HCS crossing is dismissed as the reason for the large velocity variation on the 10th and 11th December.

According to the 'ENLIL with cone' model output presented in Figure 5.19, there are no expected ICME interactions or peaks in the B field strength, the particle density or polarity reversals. The comet should be experiencing 500-600 km s^{-1} winds and decreasing. This is slightly higher than the Owens model though still below my measured values [Figure 5.16]. The expected decrease in solar wind velocity is noted in Figure 5.16.

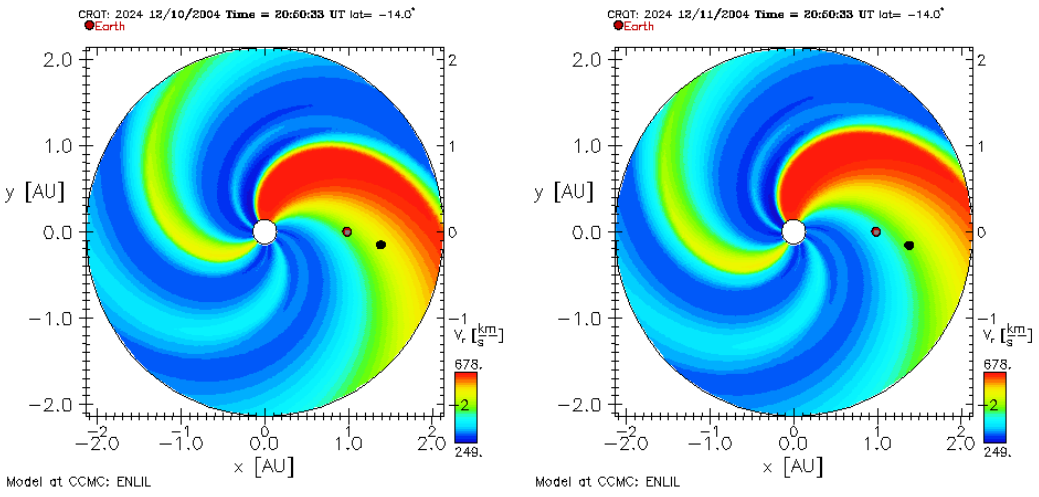

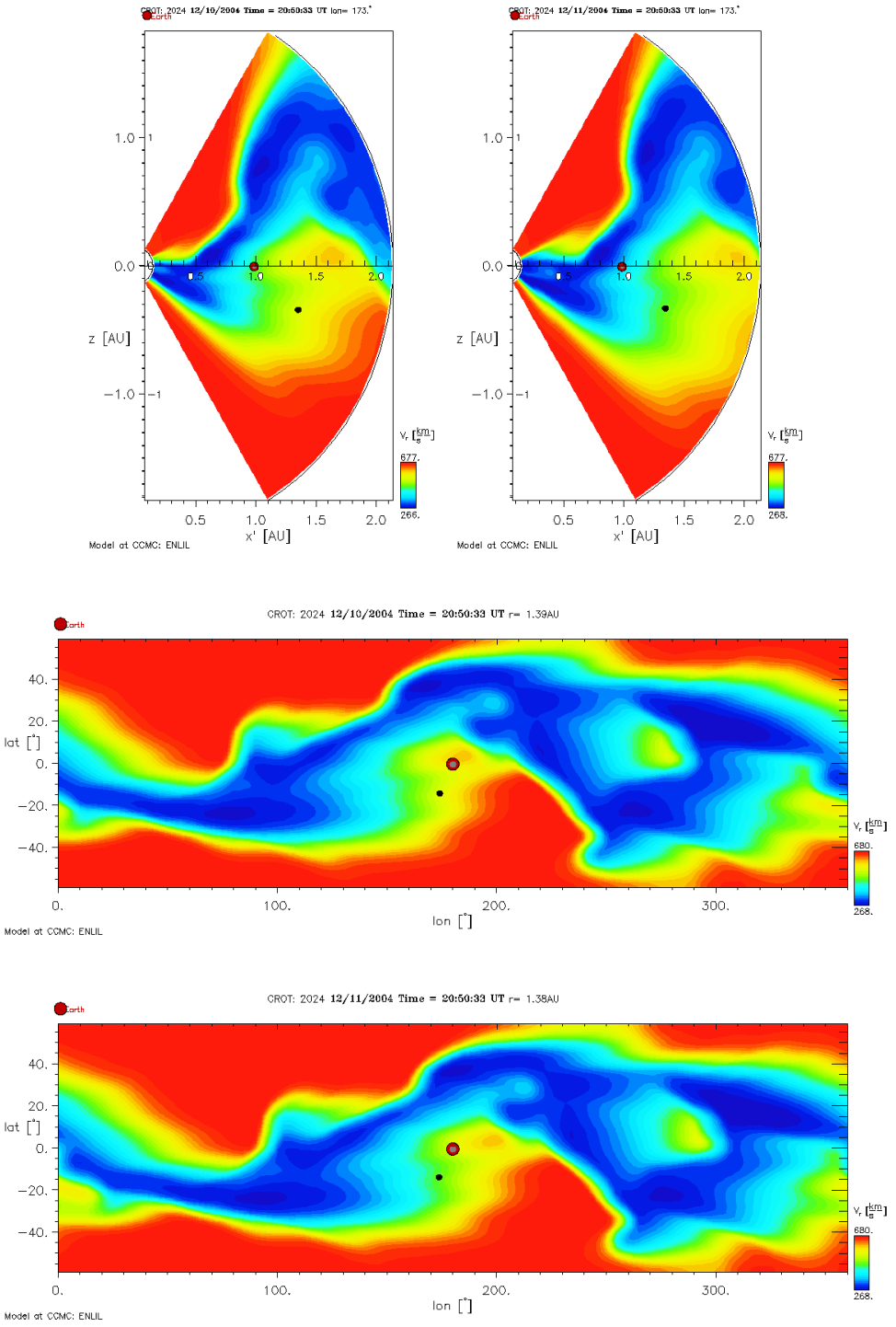

Figure 5.19: C/2004 Q2 experiences slower solar wind velocities between 10/12/2004 20:50 UT and 11/12/2004 20:50 UT as it enters a transition region between the fast and slow solar wind.

In reality, measurements taken at the comet, assuming they are correct, revealed a much more complex picture. This is supported by imaging of a turbulent ion tail and a faint DE. Contrary to my initial statement regarding atypical data points, the turbulent events in this sequence are not

marked as purple in the solar wind plots as the ion tail remained near-straight with only a slight curve for most of the images**.** Furthermore, the faintness of the ion tail added to the ambiguity of identifying the solar wind conditions.

The role that large, i.e. poorly-defined optocentres play in identifying the nucleus position in my software is one of the primary reasons for my data scatter. This is addressed in greater detail in the 'Discussion' chapter. In brief, large optocentres, for images with unknown times, yielded a wide range of potential observing times. This uncertainty will trickle through the software, so that the end mapping may be slightly off due to a poorly-defined nucleus position and observer location. Thus, this had a larger impact on the calculated solar wind velocity than I had previously anticipated**.** For example in CR 2024, from 12:00 UT on the 11th December 2004 to midnight on the 12th December 2004, we have a large velocity range of ~250 km s^{-1} determined for this half day period. This accounts for 57 estimates from 17 images, most of which show a large optocentre. The image mapping requires precise knowledge of the Earth's location to accurately extrapolate the images along the observer's line of sight. Choosing an earlier time than the comet was actually observed will have the comet's ion tail lying mostly on the prolonged radial vector. This could be the alternative to the aforementioned HCS and CIR explanation. This image timing problem cannot be minimised without the actual times being correctly recorded and supplied by the observer. In all likelihood, the large data scatter for CR 2024 is predominantly associated with this timing uncertainty coupled with low orbit plane angles towards the middle of this CR.

Images during CR 2024 are complicated to interpret. Most of the data during this period showed atypical solar wind flow. With decreasing orbit plane angle, we expect the projected ion tail to lie along the extended radial vector with dispersions off the orbital plane associated with non-radial outflow of solar plasma. However, this alone cannot explain the aberrant tail features between the 13th and 19th December, when the orbit plane angle is above 10^{o}. The ion tail consists of large kinks on the 14th, typically evidence of a CIR or a transition region. However, these images also show the ion tail leading the comet's motion. Similar outflows are seen on the 15th December including a bifurcating ion tail. The high radial velocities, the rapid reorientations of the ion tail and the large-scale plasma clouds suggest that the comet may have encountered a

halo ICME on the 14th (observed at 08/12/2004 09:36 UT; Speed: 611 km s^{-1}) and the HCS crossing on the 15th, which is seen as a kinked ion tail leading the comet's motion.

A major ion tail disruption is prevalent in a series of images on the 18th December with the ion tail leading the comet's motion [Figure 5.20]. The tail is a quintessential example of a disturbed solar wind flow, displaying large orientation changes, multiple folding ion rays, scalloped ionic features, condensation clouds and a disconnection event, which is only seen once the ion tail regains its normal orientation. In spite of the low velocities, this flow is most likely due to an ICME rather than turbulent equatorial slow solar wind flow.

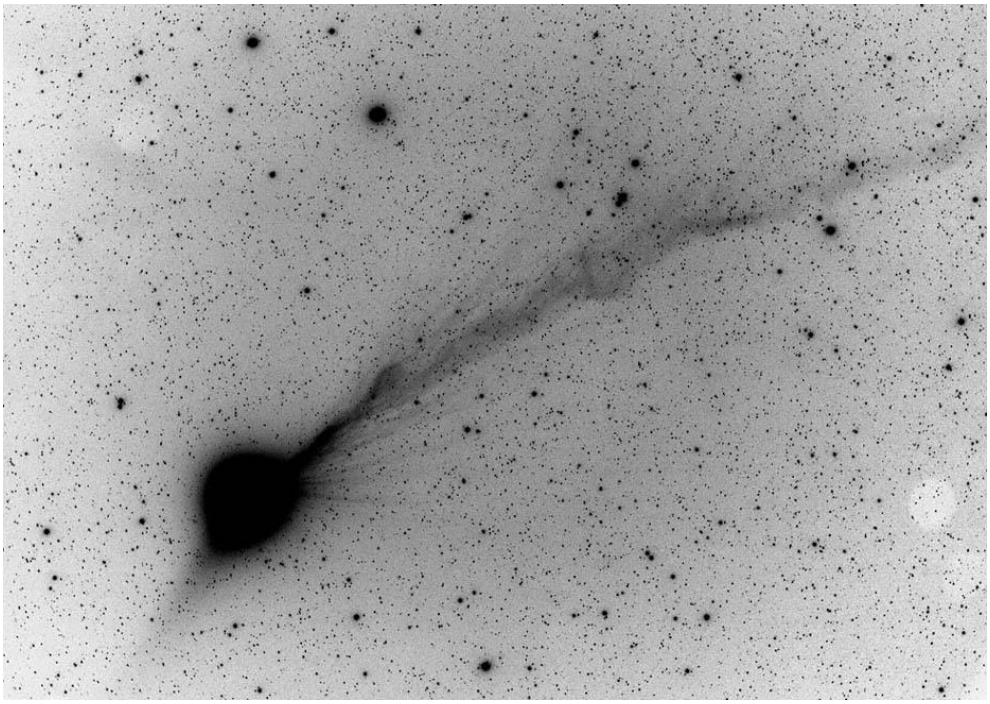

Figure 5.20: ICME induced disturbance in the ion tail of comet C/2004 Q2. Observations were undertaken by Hayakawa on 18/12/2004 at 23:13 JST. DE and scalloped ionic features are seen propagating over a period of 8 hours. Last image was obtained by Hayakawa.

On 30/12/2004, images from Japanese observer Kurita show an ion tail seemingly originating from a tail ray rather than the nucleus. Without more images, it is impossible to say whether this is a DE. It is difficult to pin down the causal factor here due to the low orbit plane angle. The range of velocities could point to a CIR originating from regions of opposite polarity.

The extrapolated solar wind velocities before 28th December 2004 at 18:00 UT and after 13th January 2005 at 23:00 UT should show less correlation with the solar wind samples extracted with this study due to the latitude dependency and the increasing geocentric distance. It is important to note that the ACE extrapolated solar wind velocities are within range of the solar wind velocities measured locally at the comet. For CR 2025, the comet is undergoing atypical solar wind flow, providing an indication of the reasons for the discrepancy between the two.

CR 2025

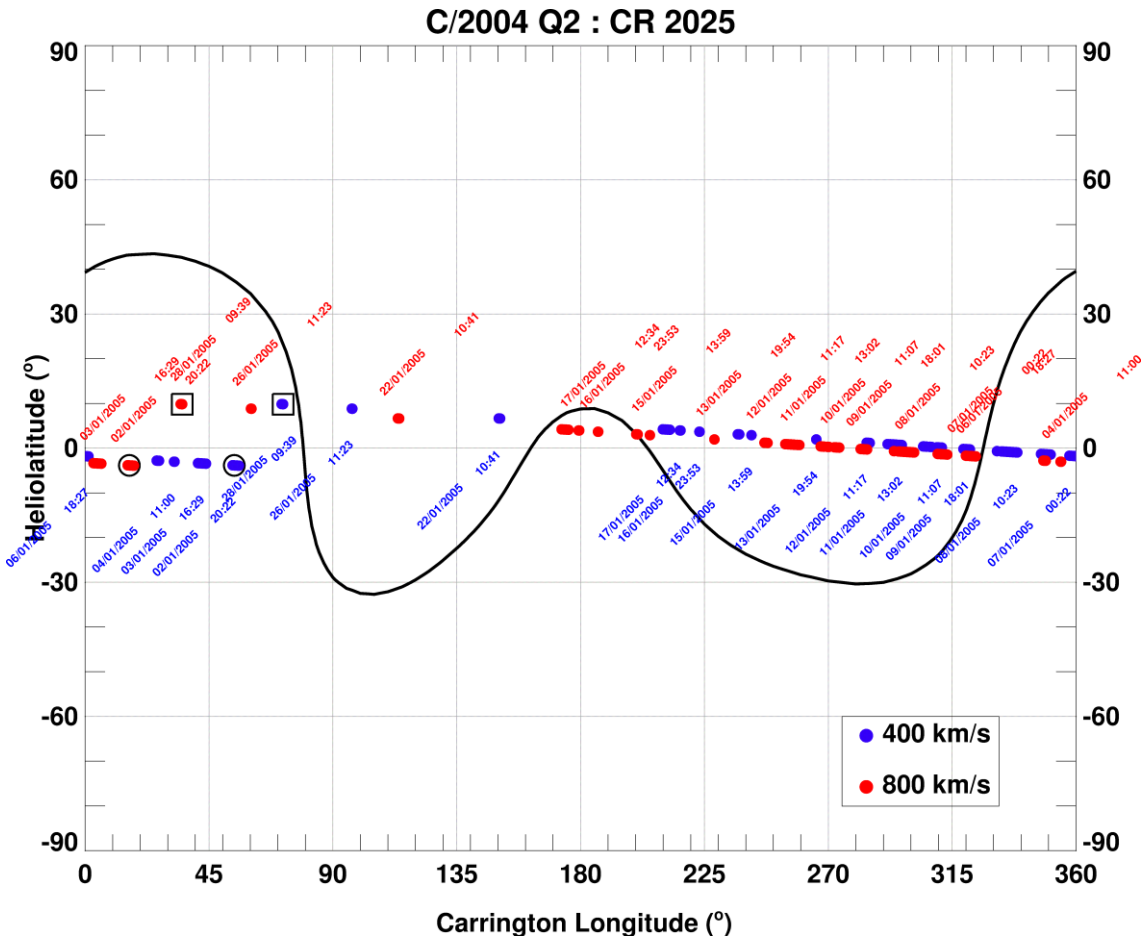

Figure 5.21: Mercator map for CR 2025. Dates and times are plotted only for the first sample of each day.

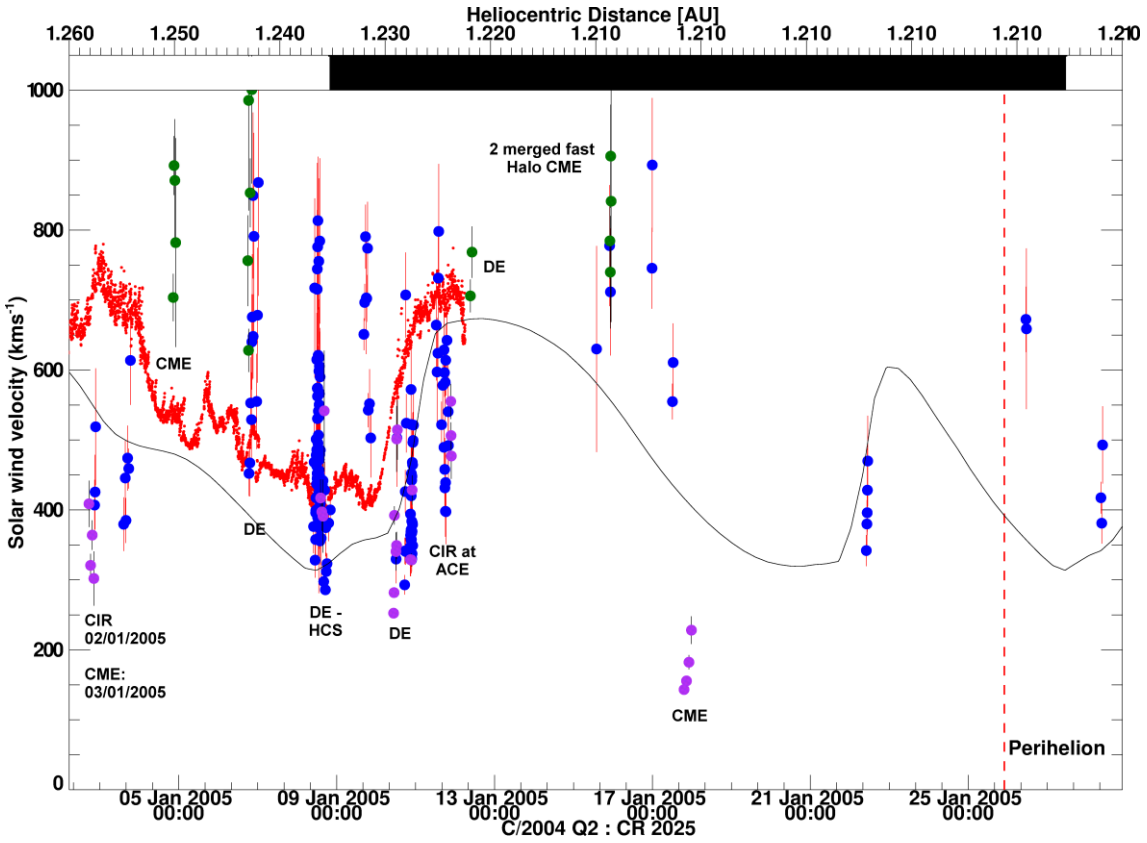

Figure 5.22: Solar wind velocity for comet C/2004 Q2 during CR 2025. ACE/SWEPAM measured solar wind (in red) has been extrapolated to the comet's orbit. Longitudinal difference between the comet and the extrapolated solar wind is converted into a timing offset for the solar wind data.

Overall, the extrapolated ACE solar wind velocities and the velocities recorded at the comet are in relatively good agreement, and especially so with the MHD model at the comet during turbulent solar wind periods. The blue points are strongly correlated with the M. Owens ENLIL MHD data for most of the predicted velocities during normal solar wind activity. My measured solar wind velocities also show a strong correlation with the MHD modelled values during the CIR.

Turbulent events:

Radial expansion of a plasma knot into a wide and diffuse ion cloud

A tail disruption occurred on 2nd January 2005 at the start of CR 2025, first captured by Asian astronomers at 11:00 UT till 13:00 UT until further monitoring of the comet was independently

contributed by their European counterparts. It is clear from the cut planes [Figure 5.23] at the comet that a change in the underlying solar wind regimes was the inherent cause for the density enhancements in the ion tail.

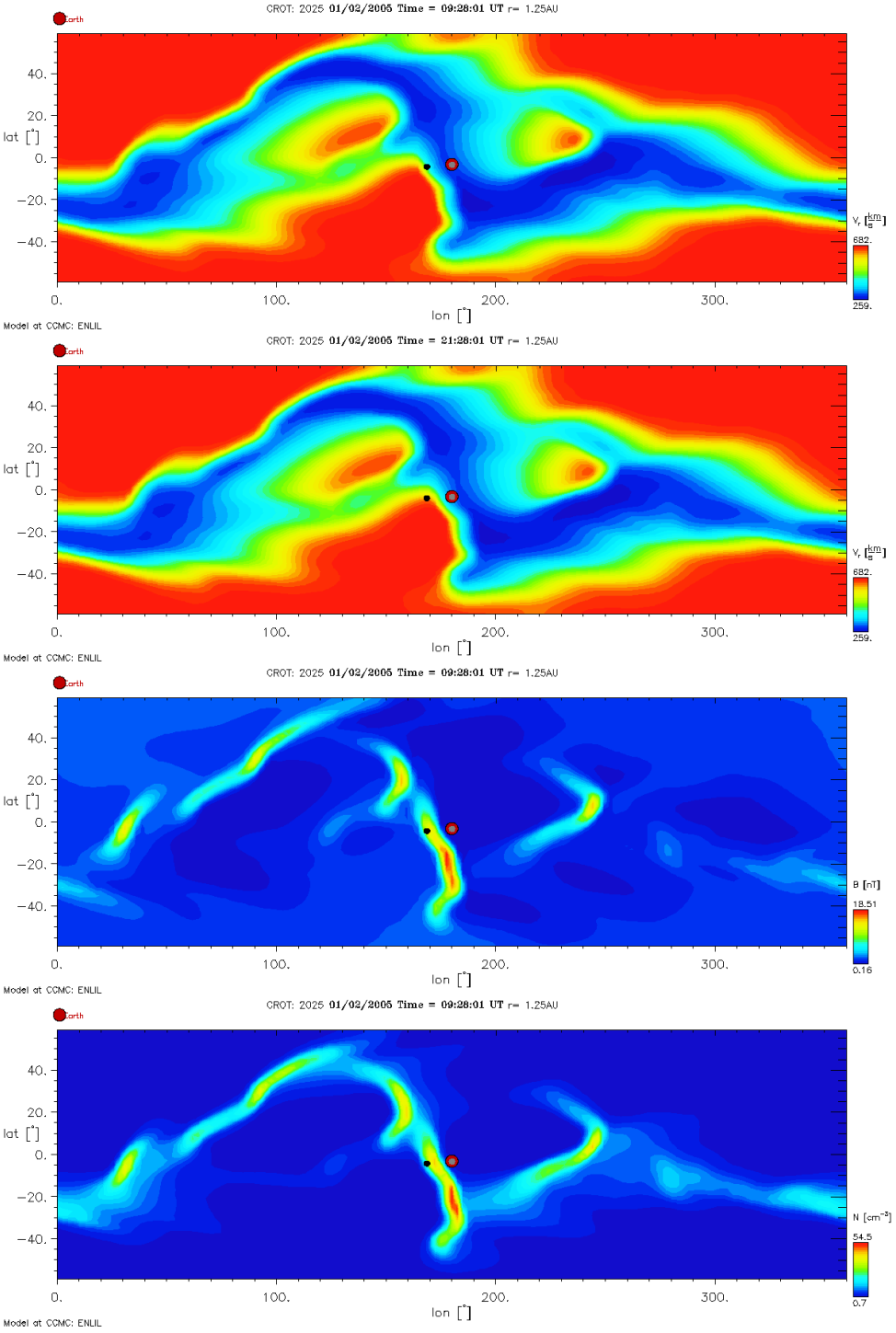

Figure 5.23: Cut plane of MHD prediction for r = 1.25 AU. The comet is around (169º, -2º) heliographic longitude and latitude and encounters shocked slow solar wind ahead of a CIR before experiencing slowly increasing solar wind

speeds. Modelled run for 2nd January 2005 at 09:28 UT and 21:28 UT for second v_r plot.

The orbit plane angle was very low, which thwarted my attempts to investigate the radial solar wind; however the fact that the projected tail lay on the radial vector and spread out symmetrically indicates slight non-radial flows at this point. A trail of condensation knots can be tracked downstream of the comet head streaming along the radial vector, resulting in a large scale plasma cloud lagging the comet motion, as seen in images 6 hours later [Figure 5.24]. Low radial velocities were recovered from the image by Jäger and Rhemann corresponding to the velocity dip below the MHD predictions. The ion tail reverted back to its original position, fanning either side of the Sun-comet line with multiple tail rays seen on the 3rd January. Three ICME candidates from the CDAW catalogue were also identified [see section 5.1.3.2], though a CIR was expected to be encountering the comet at the time, and may be the cause. The solar wind velocities match exceedingly well those expected from Figure 5.23.

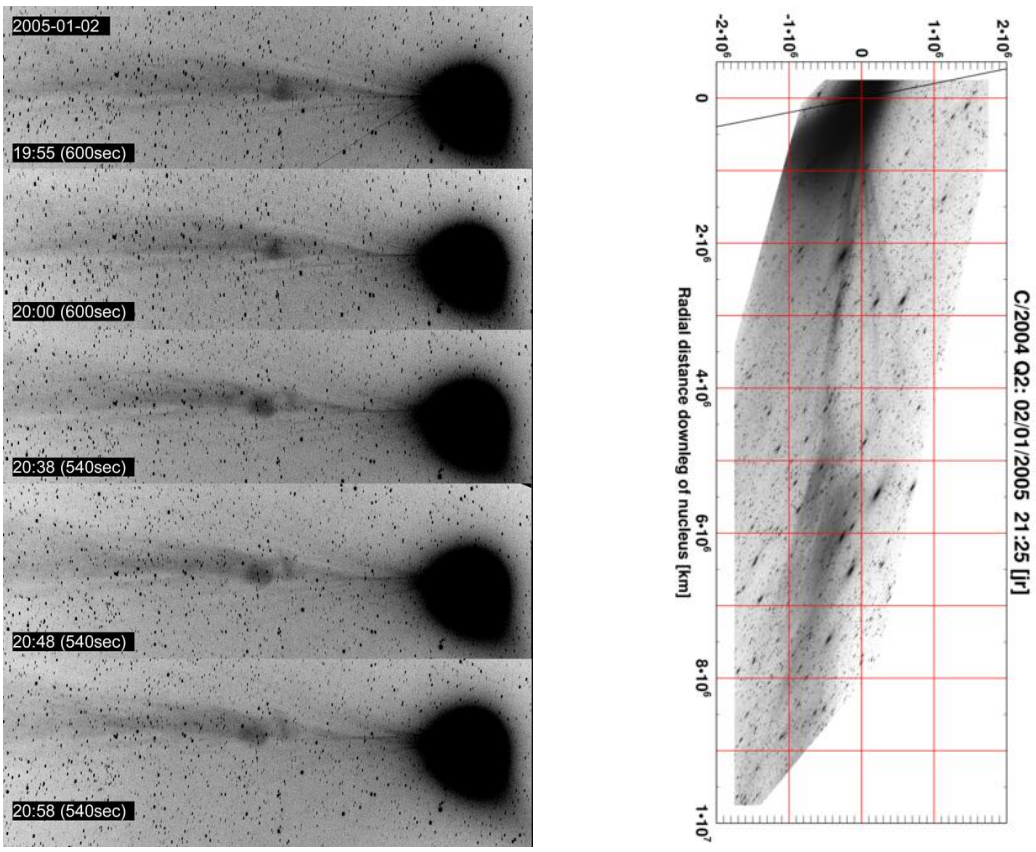

Figure 5.24: Tail streamers and a large disrupted tail observed by Jäger and Rhemann (JR). This follows a series of images showing the plasma cloud as small density enhanced knots within the ion tail several hours earlier.

Images taken between the 4th and 6th January showed a thin ion tail, lying close to the extended radial vector. These produced extremely high solar wind speeds (~1650 km s^{-1} and 1300 km s^{-1} taken from a single image). These are likely erroneous due to the tail-radial vector geometry. The ion tail during the second half of this period shows a propensity for widening as it curves off the radial vector, resulting in a large scatter in implied solar wind speeds.

Four DEs and a forked tail

Four DEs, two occurring on the 7th and one on the 8th and 10th January, occurred during the period of most intense observation of the 6 CRs: the images taken during this time constitute ~30% of the Machholz image archive. There are clearly two DEs based on the kink location on the 7th with the first event captured by Japanese astronomers and the second by the European astronomers. This period is an obvious candidate for the vector maps technique with clear dominant structures to track. The ion tail is sitting on the projected radial vector and occasionally deviates forwards of the radial vector. These spurious contradictory motions suggest that the deduced observing times are sufficiently inaccurate so as to render the feature tracking techniques ineffective. A tentative attempt is made at determining the radial flow of the two DE connected tail kinks in section 5.1.3.2. Images on the 10th January are arguably the most dramatic, with a prominent kink and a bifurcating ion tail leading the comet's motion as seen in [Figure 5.26]. The tail eventually undergoes a disconnection event, with the disconnected tail propagating radially along the Sun-comet vector.

Crossings of the heliospheric current sheet can cause field lines of opposite polarity to reconnect, thereby severing the ion tail from the nucleus. The CCMC ENLIL model predicts that the HCS would encounter the comet's ionosphere between the 9th and 10th January 2005, with the comet experiencing low velocities prior to disconnection Figure 5.25. The HCS is steeply inclined and thus it is expected that only one of the DEs could be related to a HCS crossing. The velocity dispersions at the comet were initially intriguing though the velocity range is well explained in comparison with the ACE data, especially when considering that the velocity

samples are often taken over an average range of 1 x 10^7 km downstream of the nucleus, meaning that they are far away enough to be at ambient solar wind speed.

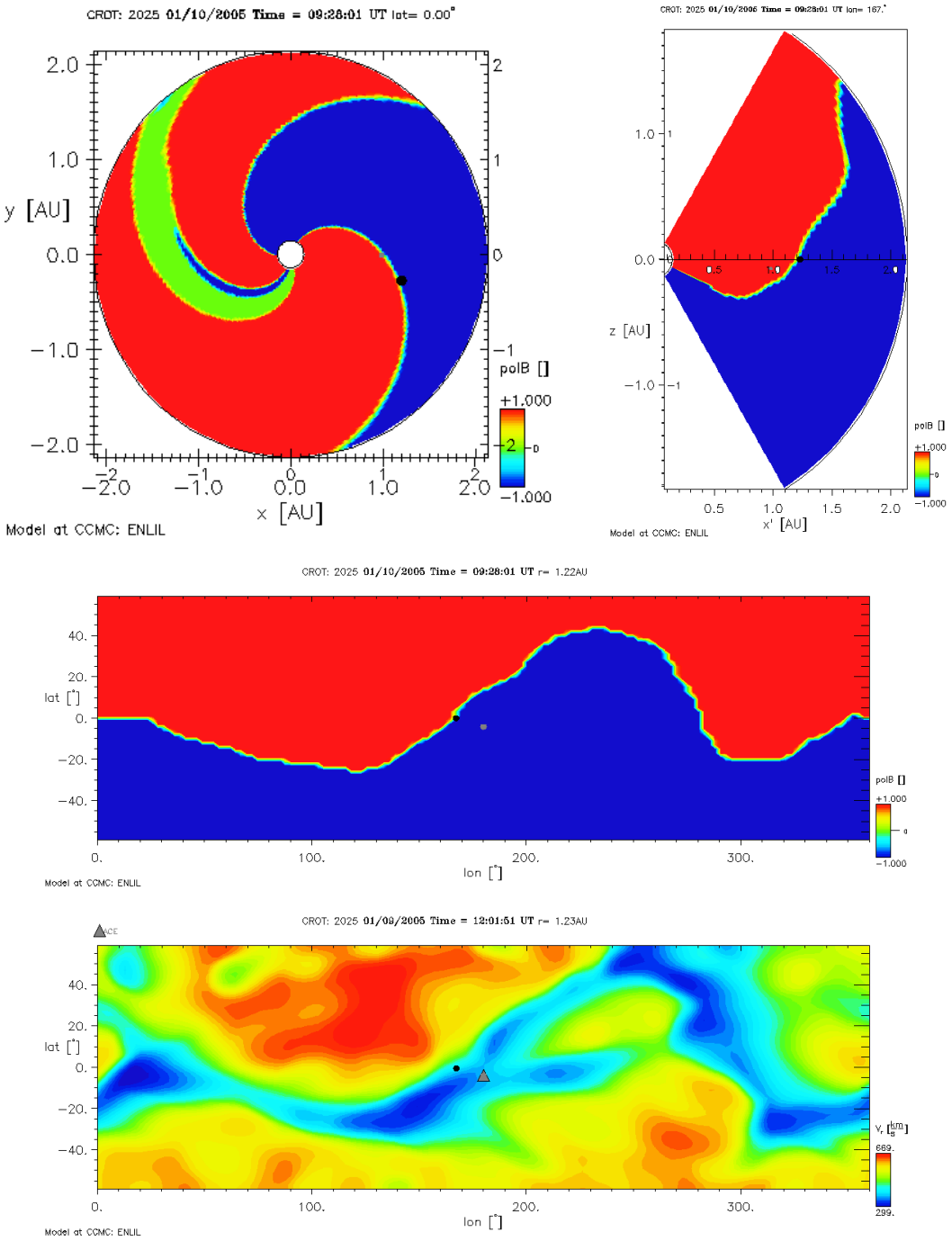

Figure 5.25: Predicted HCS crossing and low solar wind velocities at the comet's heliographic coordinates. Cutplanes were obtained the CCMC ENLIL MHD runs.

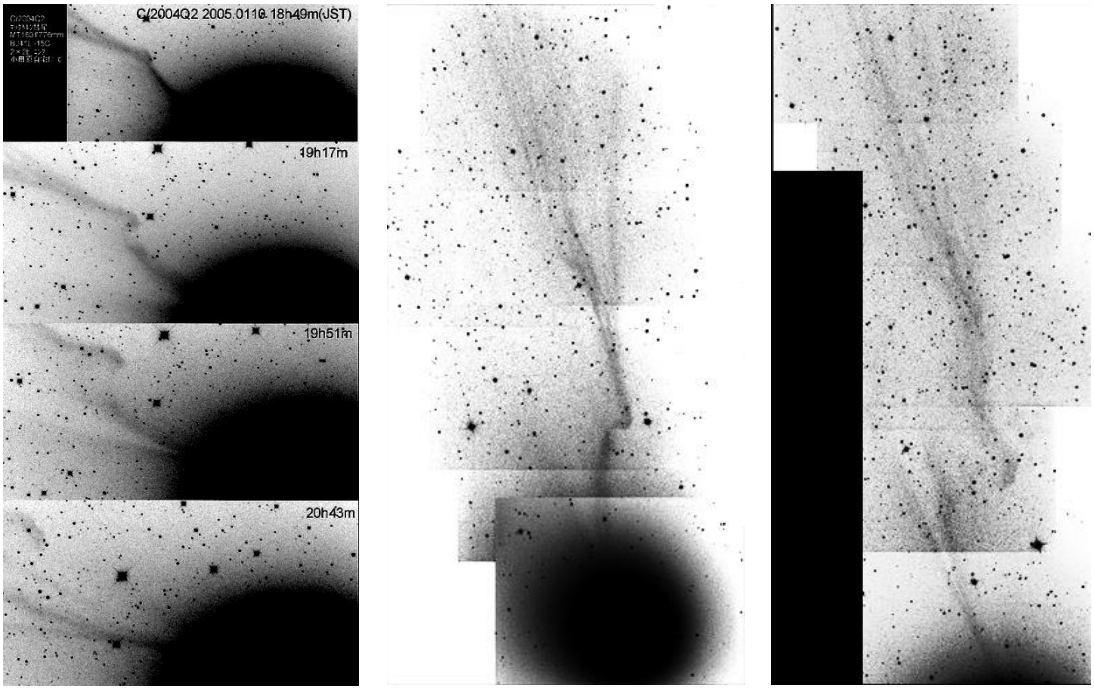

Figure 5.26: Image sequence (left) of comet C/2004 Q2 captured on 10/01/2005 by Japanese observers, Kubotera and Akutsu (middle and right). The sequence on the left was observed from 09:49 - 11:43 (UT), middle image is a contrast enhanced composite of images observed between 09:58 and 10:10 (UT) and last image shows the disconnection event observed between 11:20 and 11:29 (UT). The motion of the large kink (eventual DE) and a forked tail can be traced in a vector map of the image sequence.

Fast changing orientations of the ion tail provide visual evidence of large abrupt changes in the solar wind flow over a short period of time. CIRs can also lead to increases in magnetic and dynamic pressure, ultimately disconnecting the ion tail from the nucleus. Such events in comets can therefore be used to deduce the location of CIRs. This scenario is not immediately obvious, but in the absence of predicted ICME collisions or HCS crossings, CIRs are the most likely cause. As Sizonenko (2007) reported, comet Machholz's perihelion passage occurred during the declining phase of solar activity when fast and slow solar wind streams are often seen to alternate in the interplanetary medium. Rapid tail orientation changes in amateur images of comet Machholz, by different observers, on the 7th to the 9th January 2005 suggest that comet Machholz may have interacted with the shock preceding a co-rotational interaction region. This is supported by the graphical output of the MHD model.

There is no evidence of an ICME interaction during this period; however, the images show evidence of a large-scale solar wind event. The tail morphology and orientation change rapidly

during this period. The ion tail crosses the Pleiades cluster during this period, making it difficult to estimate the local solar wind velocity due to the background nebulosity.

The exact cause for the velocity scatter on the 8th January 2005 (CR 2025) is difficult to identify. The comet should be experiencing a variable mix of solar wind velocities if it encountered the forward shock of the CIR. It is likely that it transitioned from a smooth ~600 km s^{-1} solar wind flow to being caught in the slow wind within which the HCS is immersed and then becomes trapped between the ensuing compressed region of a CIR, eventually traversing into a region of enhanced solar wind velocity on the 12th January. The latter supposition is backed up by Degroote et al. (2008), based on a sudden peak in the proton flux, measured by SOHO/CELIAS and a drop in the O^{7+}/O^{6+} in ACE/SWICS [Figure 5.27].

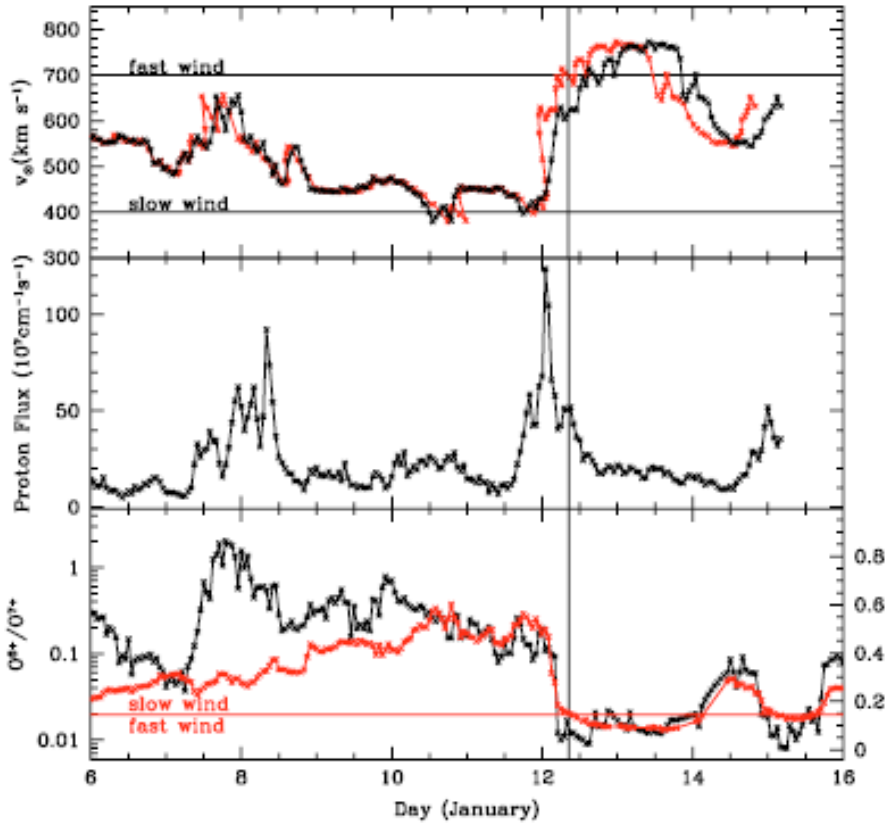

Figure 5.27: (Caption from Degroote 2009) *Upper panel*: Measurements of the solar wind velocity from SOHO/CELIAS (black line) and a corotational mapping (red line) at the location of C/2004 Q2 (Machholz). *Middle panel*: the proton flux from SOHO/CELIAS Proton Monitor at L1. The solar event on 12 January was due to a CIR, which is typically preceded by a sudden peak in the proton flux. *Lower panel*: ratio of O^{7+}/O^{6+} from ACE/SWICS. The red line represents the results from an empirically deduced formula (Zurburchen & Richardson 2006), for which a low value (horizontal red line) indicates a fast, cold solar wind. The vertical black line denotes the first observation on 12 January.

18th January: The Koprolin sequence

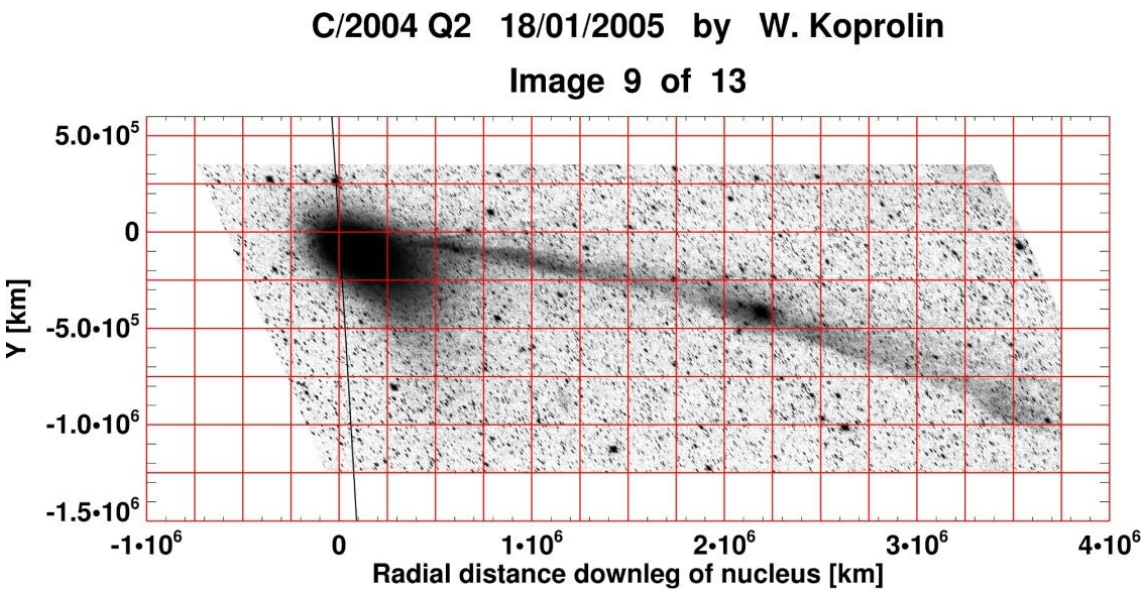

Figure 5.28: Unusual behaviour of the ion tail as evidence of ICME interaction for comet C/2004 Q2. This is a projected frame from the image sequence by W. Koprolin, which is presented in Figure 5.42.

Few full length interactions connecting ICMEs to tail disruptions have been recorded. Of these, a 13 image sequence captured by W. Koprolin on the 18th January 2005 [Figure 5.28 and Figure 5.42] shows a clear cut case of an ICME-induced change in morphology and non-radial dynamical orientation to a comet's ion tail. This opportunity coupled with the mapping technique allows a constraint to be set on the acceleration of the ion bundles by means of tracking density enhancements with a vector flow map. This is an interesting case study that will be discussed in section 5.1.3.2.

Our initial candidate for this unique interaction was the eruption of a powerful, fast halo CME on January 17 2005, shortly before its observation time at 09:54 UT. SOHO LASCO observed the earthward propagation of the ICME at a linear plane-of-sky speed of 2547 km s^{-1}. Another fast halo CME was also released half an hour earlier with a linear speed of 2094 km s^{-1}. The comet's position angle was at 87.3°, its heliocentric longitude and latitude at 15° leftwards of the Sun-Earth line and 8° - 12° above the ecliptic plane during the time taken for the ICME to reach the comet at 1.2 AU.

Determining the radial plasma velocity for this event would be meaningless, as a strong non-radial flow is so evident from individual tail features, hence only the first image was sampled and included in the radial velocity study [marked purple on 18th January in Figure 5.22]. The local radial velocity profile ranged from 230 km s^{-1} near the comet head, decreasing to 140 km s^{-1} by the tail end. These are improbably low velocities, even for a mass-loaded ICME and considering drag forces acting upon the ICME's motion. Later images show a curving near-parallel ion tail implying near-infinite radial velocities. The SWEPAM instrument is overwhelmed between 17/01/2005 ~12:00 UT to 19/01/2005 ~00:00 UT resulting in a data gap in solar wind conditions near the Earth.

The MHD cone model replicating the ICME places its footpoints slightly above and below ACE, such that the leading edge of the ICME is expected to pass over ACE's position. Though I do not expect the ICME itself to have caused the disturbance on the 17th nor the slow speeds on the 18th, its forward shock would have disrupted the ambient solar wind flow and accelerated the surrounding medium. ACE will have experienced a period of enhanced solar wind velocities (~600 km s^{-1}) thus explaining the discrepancy of the extrapolated solar wind velocities (~600 km s^{-1}) with the lower speed MHD predictions by M. Owens.

Using cutplanes of the simulation [Figure 5.29], I expect the comet to have encountered the fast ICME by the evening of the 18th and morning of 19th. The comet's position has been overlaid, although the axes differ slightly. Plane cuts were taken at 165° longitude, 10° latitude, and at r=1.2 AU. The images confirmed the large observed deflection of the ion tail to the opposite side of the Sun-comet vector. It doesn't explain all aspects of the Koprolin sequence but it does account for the enhanced velocities observed at ACE. Assuming a linear regression model [Figure 5.43], the ICME candidate for an ICME-ion tail impact was narrowed down to three halo ICMEs. The CMEs were observed on 13/01/2005 17:54 UT, 15/01/2005 06:30 UT and 23:06 UT travelling at 495 km s^{-1}, 2049 km s^{-1} and 2861 km s^{-1} respectively. Factoring in ICME deceleration in the inner heliosphere, the last two ICMEs are more likely to have interacted with the comet.

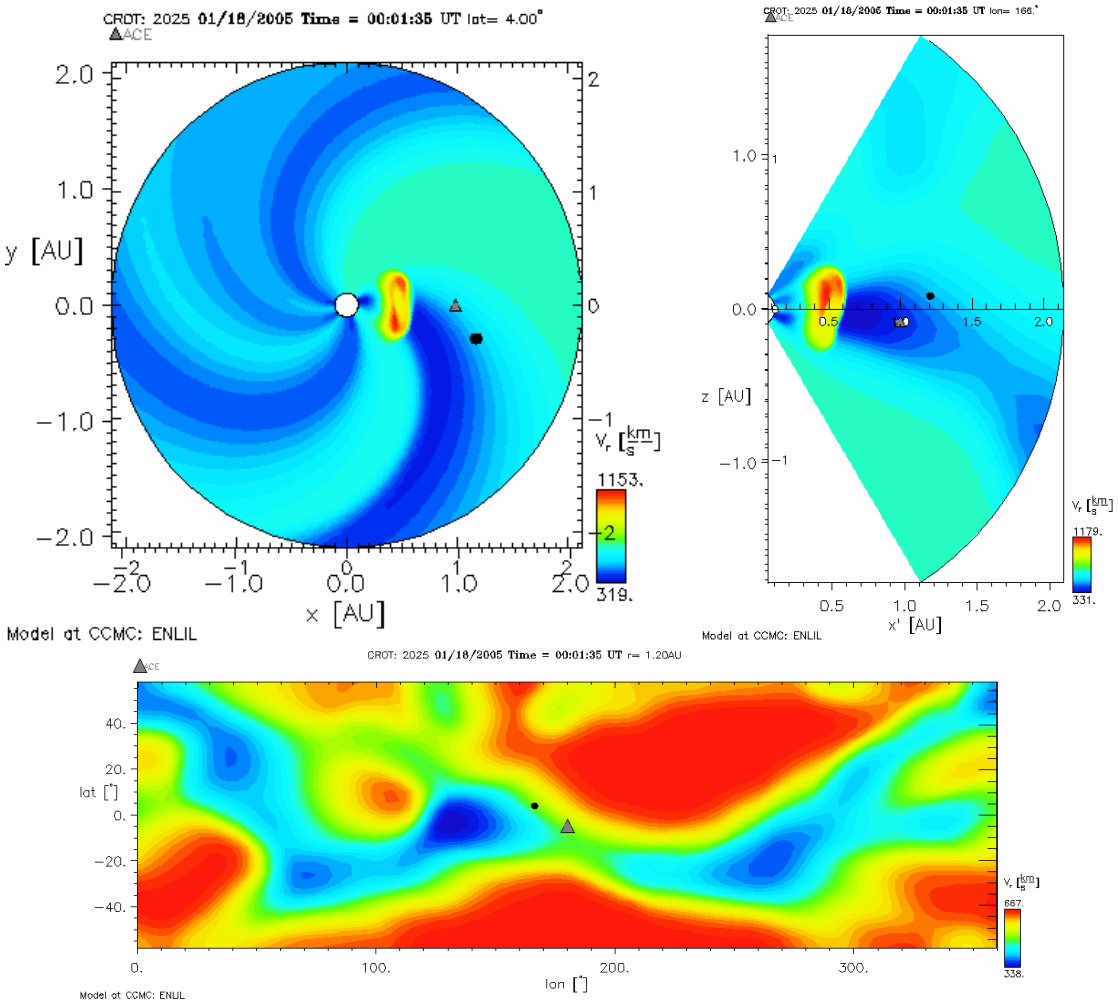

Figure 5.29: Plane cuts taken along 7.6º latitude, 165º longitude and 1.2 AU to coincide with comet's location between 18th 00:01 UT and 19th January 2005 00:00 UT (see following images). The comet's location has been overlaid (black dot). Figures continue overleaf.

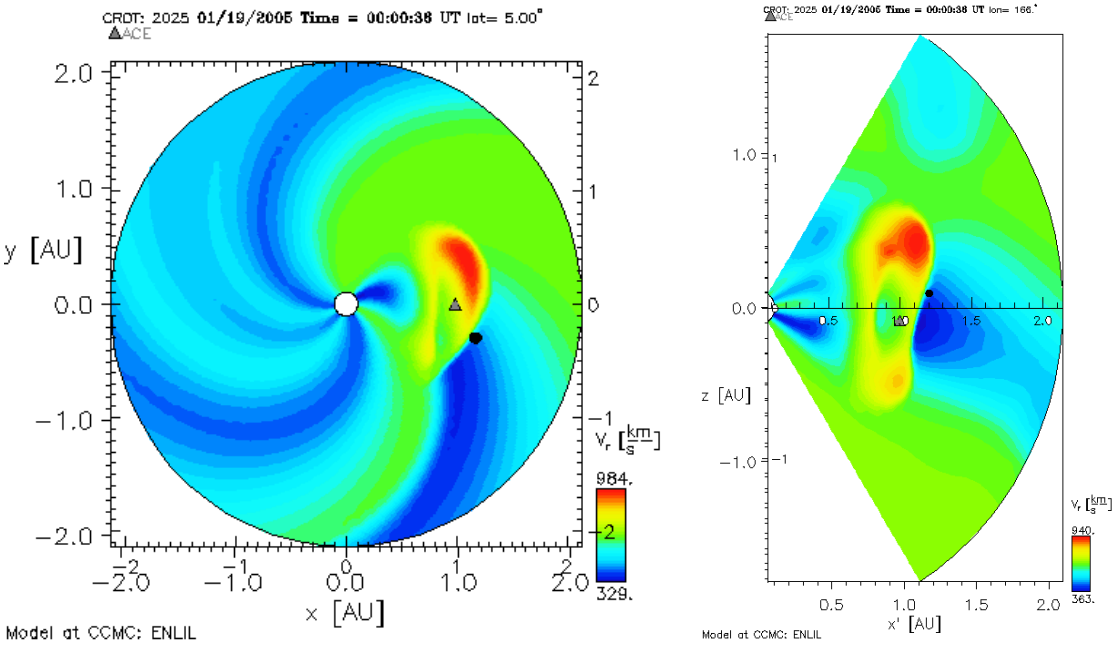

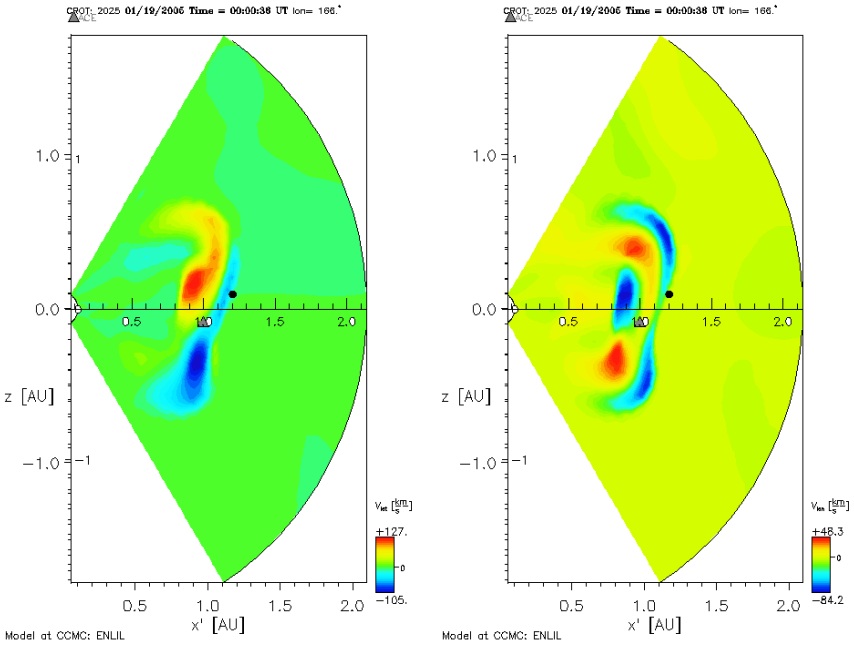
CROT: 2025 01/19/2005 Time = 00:00:36 UT lon= 166.°
ACE
1.0
0.0
−1.0
z [AU]
0.5
1.0
1.5
2.0
x' [AU]
Model at CCMC: ENLIL
+127.
−105.
+48.3
−84.2

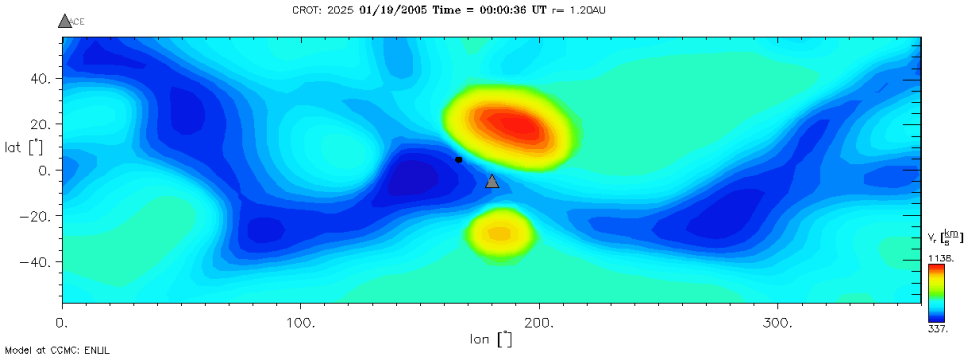
CROT: 2025 01/19/2005 Time = 00:00:36 UT r= 1.20AU
ACE
40.
20.
0.
−20.
−40.
lat [°]
0.
100.
200.
300.
lon [°]
1138.
337.
Model at CCMC: ENLIL

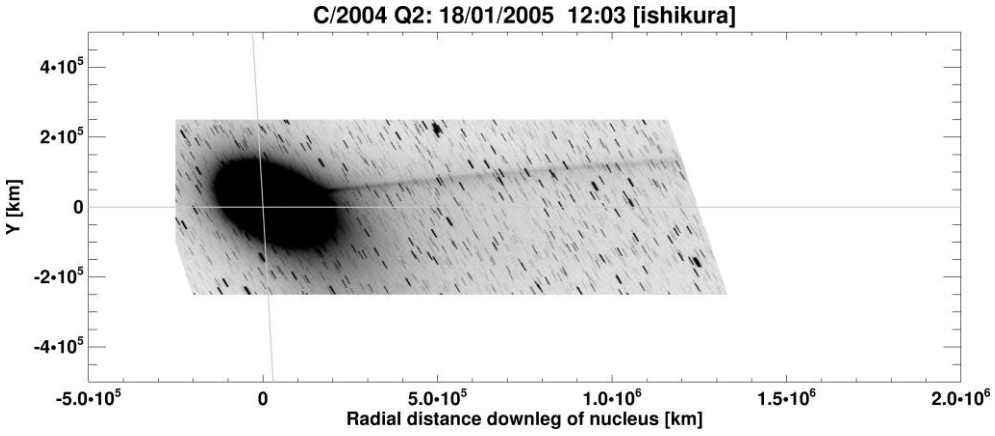
C/2004 Q2: 18/01/2005 12:03 [ishikura]
4•10^5
2•10^5
0
-2•10^5
-4•10^5
Y [km]
-5.0•10^5
0
5.0•10^5
1.0•10^6
1.5•10^6
2.0•10^6
Radial distance downleg of nucleus [km]

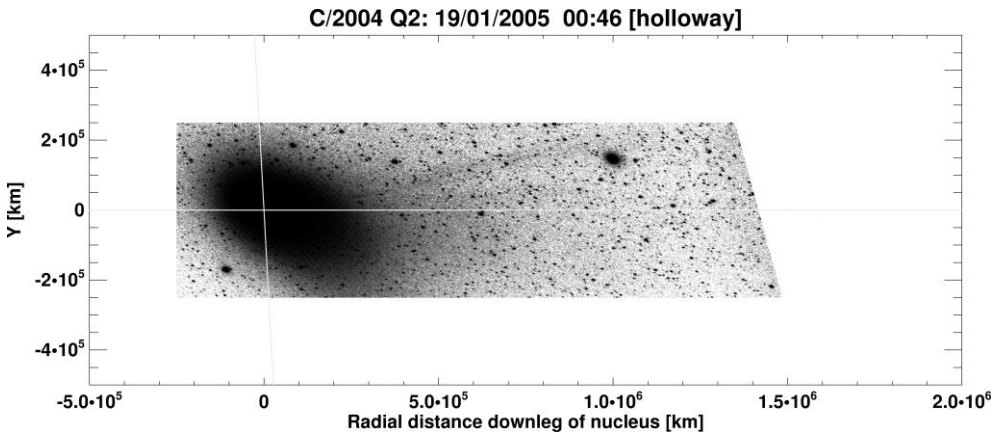

Figure 5.30: Observations of comet Machholz, by Ishikura and Holloway on 18th and 19th January 2005, showing a large deflection of ion tail due to an ICME interaction.

CR 2026

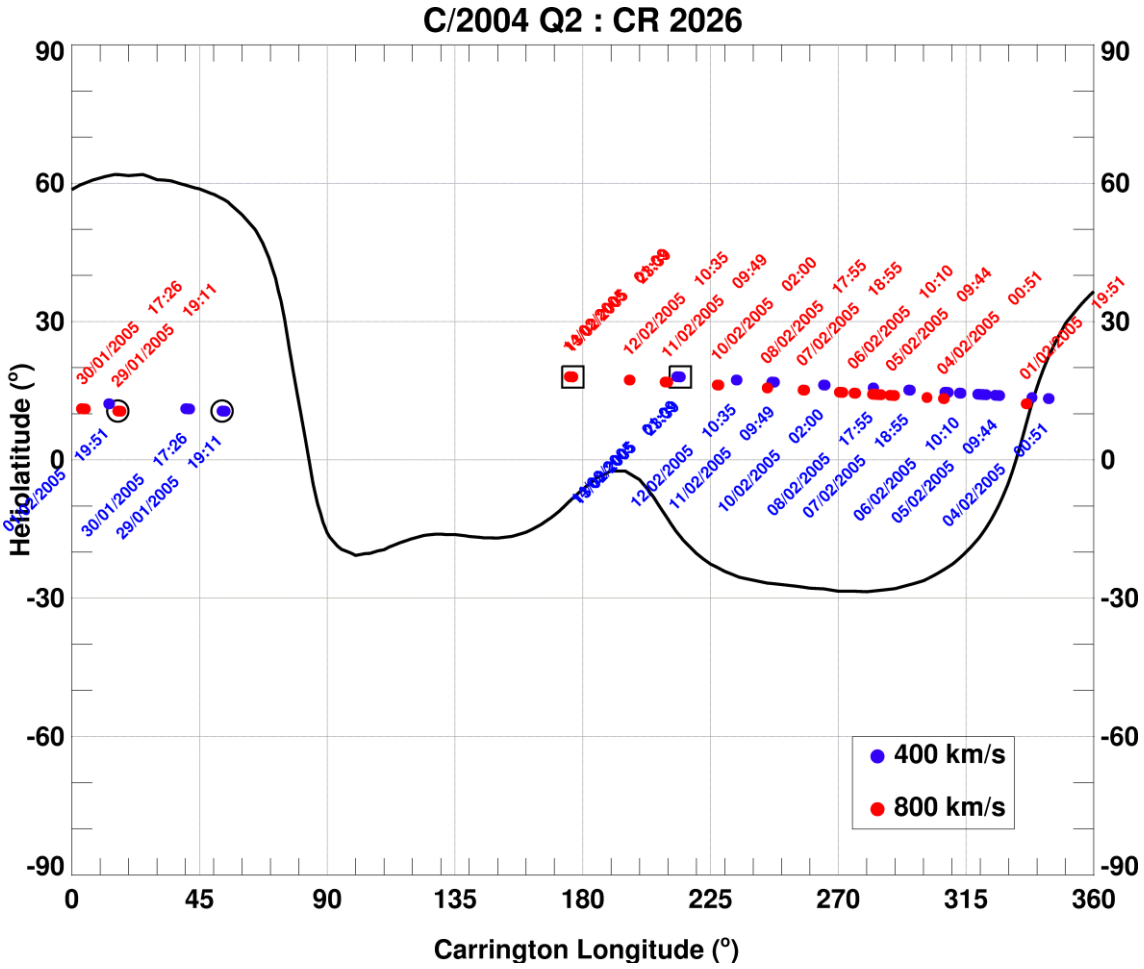

Figure 5.31: Mercator map for CR 2026.

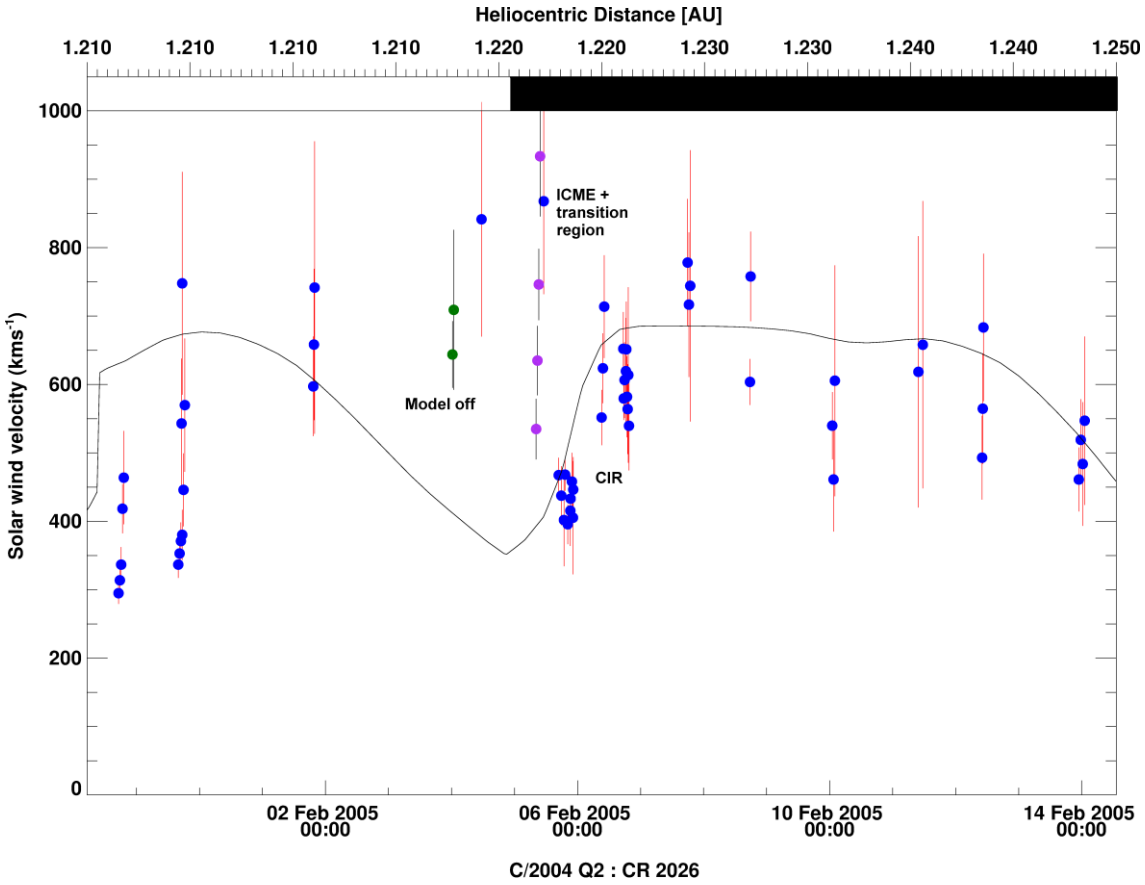

Figure 5.32: Solar wind velocity for comet C/2004 Q2 during CR 2026.

During the second half of CR 2026, the comet-solar wind velocities match well with the predicted values, whilst the comet is within quiescent, unipolar solar wind flow. The prominent feature for this CR is the consistent underestimation of the solar wind velocities with respect to the Owens' model. The discrepancy seems to be generally insensitive to the observer's location along the z axis with respect to the comet's orbital plane though I have noticed a correlation between the over/under-estimation of the solar wind velocities with diminishing orbit plane angle.

There are no ICME interactions expected between the 29th and 31st of January. The ENLIL visualisations predict that the comet should be within a pocket of fast solar wind from a coronal hole in the equatorial region. A polarity reversal in the HMF was expected two days prior and thus should not have interacted with the comet. The velocity jump at the start of a CR is a known artefact of the Owens MHD predictions when aggregating two independently solved CR

runs, though it does seem that the comet would have encountered a CIR 0.5 days earlier. The relatively large discrepancy at the start of the CR cannot be explained from the images either, which show a long thin ion tail with no outstanding features.

On 04/02/2004 00:00 UT, the morphology of tail suggests a sudden acceleration of the ion tail from a slow solar wind flow. One potential ICME interaction was identified, though the probability of interaction is quite low. The latest ENLIL visualisations [Figure 5.33] are also at odds with the Owens' results, predicting a higher velocity range of 500-600 km s^{-1} at the comet's location and thus I conclude that my inferred comet- solar wind velocities are generally accurate.

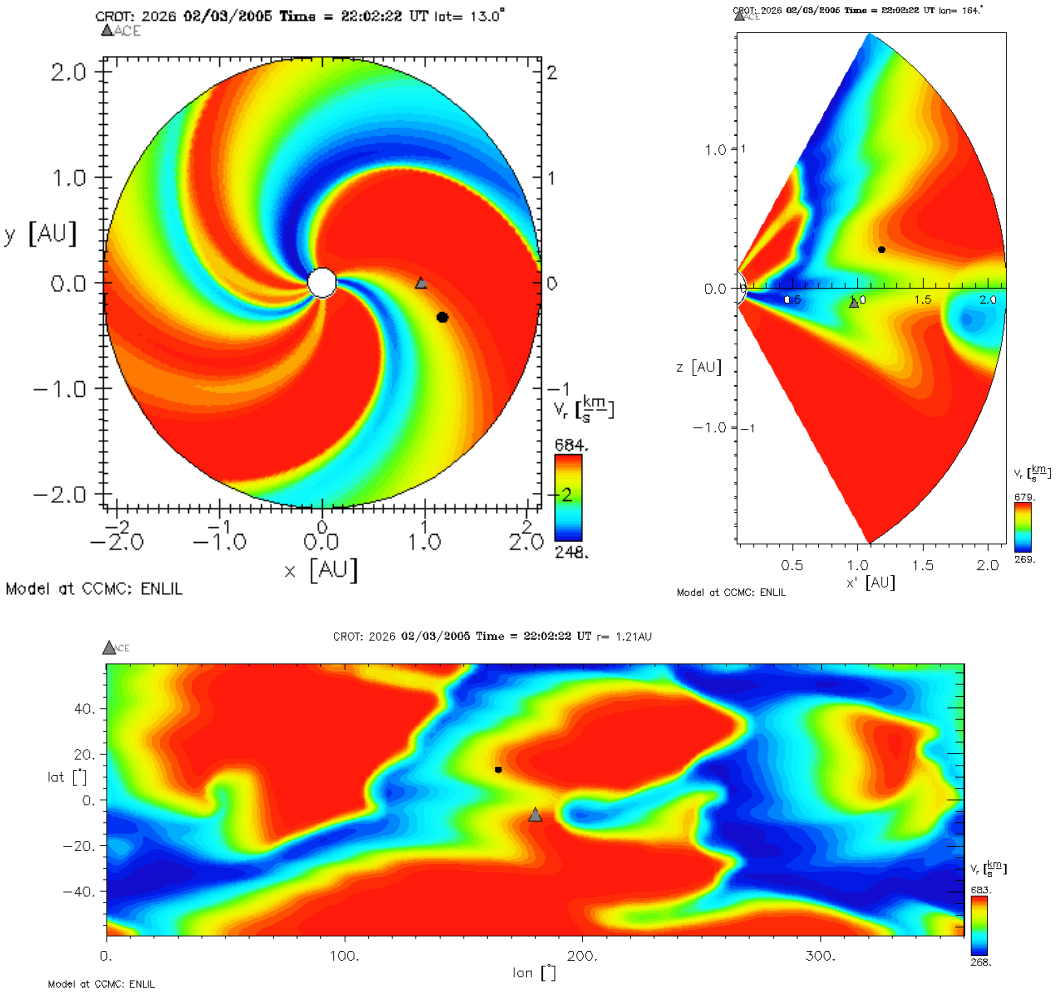

Figure 5.33: CCMC ENLIL visualisations for transition region on 03/02/2005 at 22:02 UT.

The large tail kink in Figure 5.34 supports the idea that the comet is travelling through a region of slowly decreasing solar wind velocity. The tail experiences a short burst of enhanced velocity apparently tending towards infinity before reverting to the original surrounding flow. A CME was observed by the SOHO C2 coronagraph on 01/02/2005 at 17:54 UT (Position angle: 98^{o}; Angular width: 46^{o}; solar pos. ang.: -13^{o}; comet position angle: 80$^{o;}$ CME speed: 463 km s^{-1}). Based on the visualisations [Figure 5.35], it is feasible that the comet encountered an ICME embedded within the transition region solar wind regime, with the relatively slow ICME having undergone acceleration. The image catalogue is sparse for this time period making the transient phenomena difficult to identify.

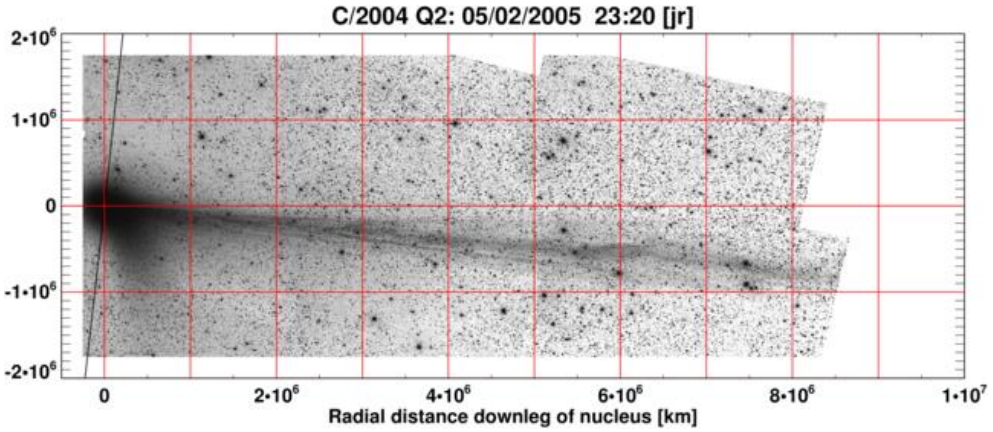

Figure 5.34: Image of C/2004 Q2 by Jäger and Rhemann showing a velocity change from slow to fast, and then back to slow winds.

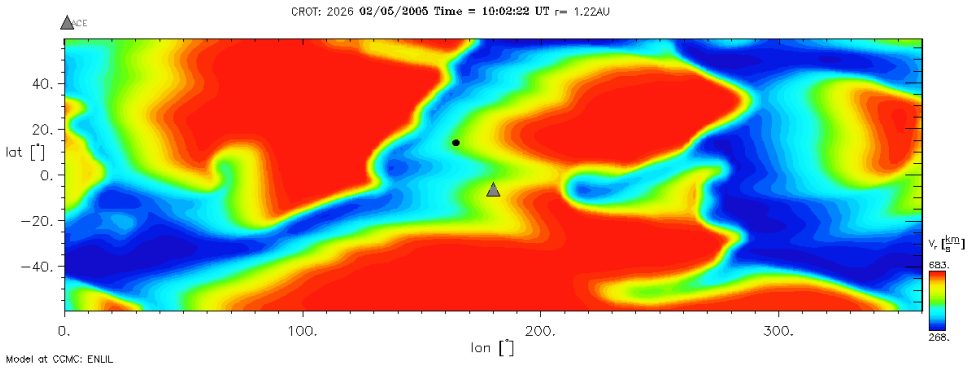

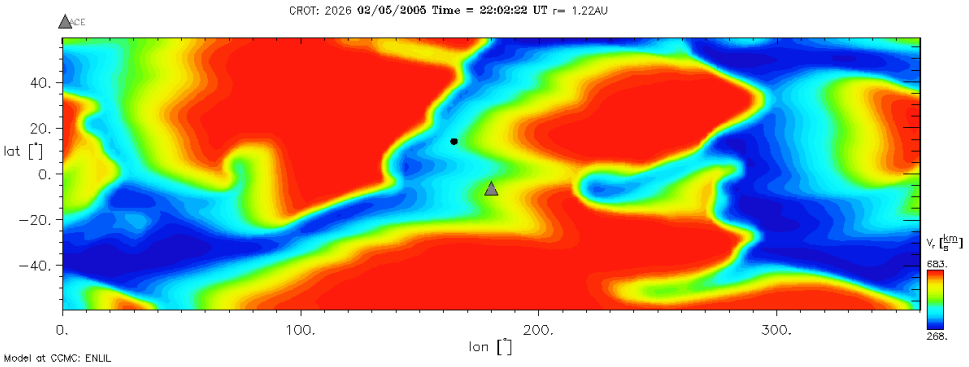

Figure 5.35: ENLIL 3D visualisation of the radial solar wind velocity 13 hours and 1 hour before JR image above.

Good agreement between my solar wind data and the MHD model for the second half of February is attributed to a favourable combination of the best orbit plane angle for this comet (~50º) and smooth, fast solar wind flow.

CR 2027

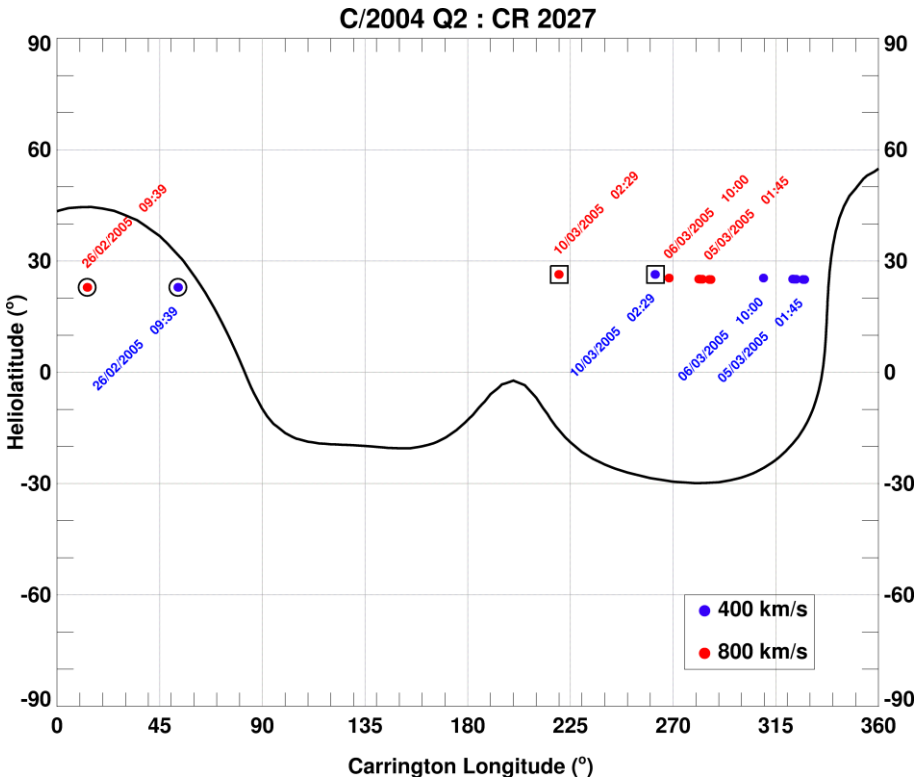

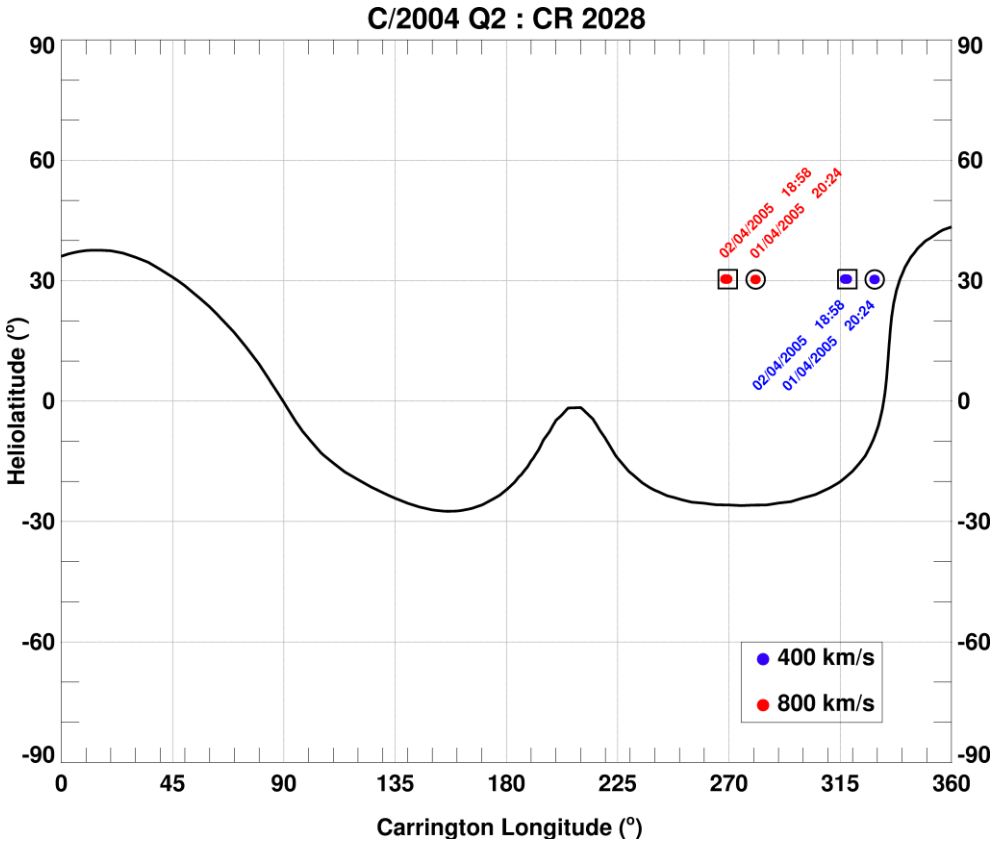

Figure 5.36: Mercator maps for CRs 2027 and 2028.

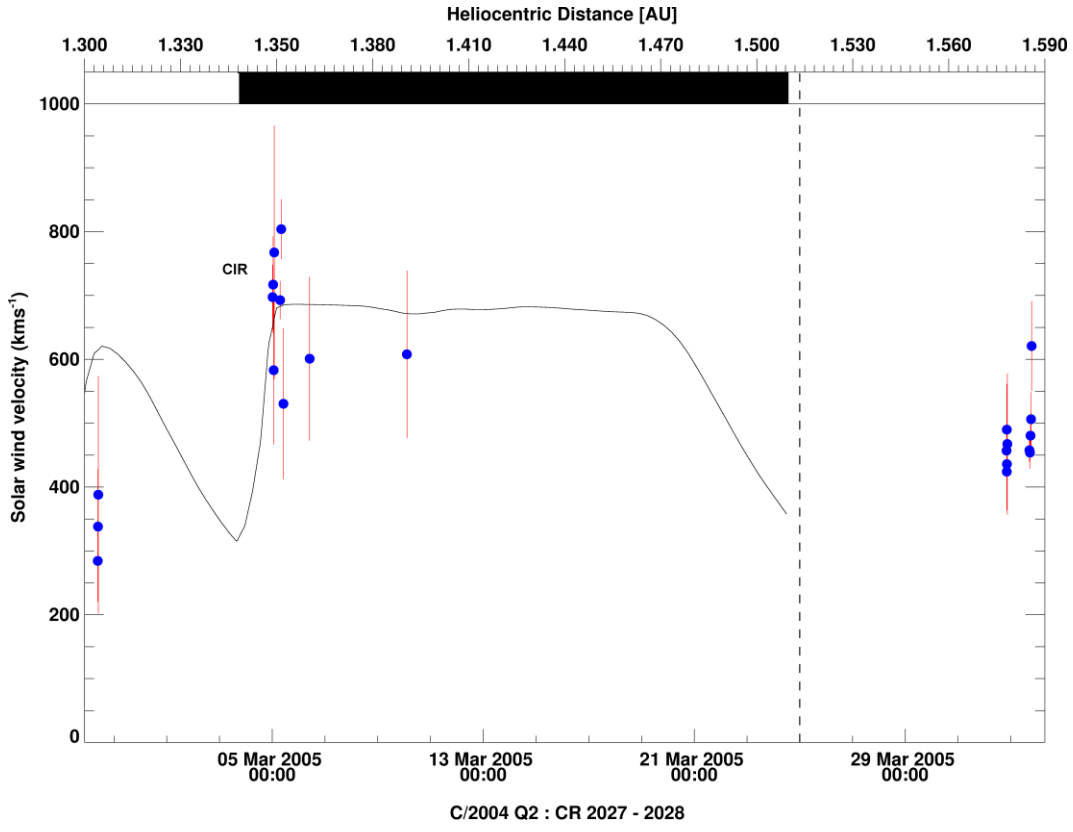

Figure 5.37: Solar wind velocity for comet C/2004 Q2 during CR 2027 and the beginning of CR 2028. Dashed line marks the end of CR 2027. Note that each timestep is equal to 2 days.

CR 2027 further reinforces the concept that this technique produces reliable estimates of the solar wind velocity, within reasonable uncertainties, during the quiet solar wind and high orbit plane angles. A comparative analysis of modelled values at the comet's location was not available for CR 2028. The velocity discrepancy at the start of this CR is related to an artefact when collating modelled velocity values from distinct runs. Comparison with visualisation cut planes indicates that the comet was expected to be experiencing fast solar winds.

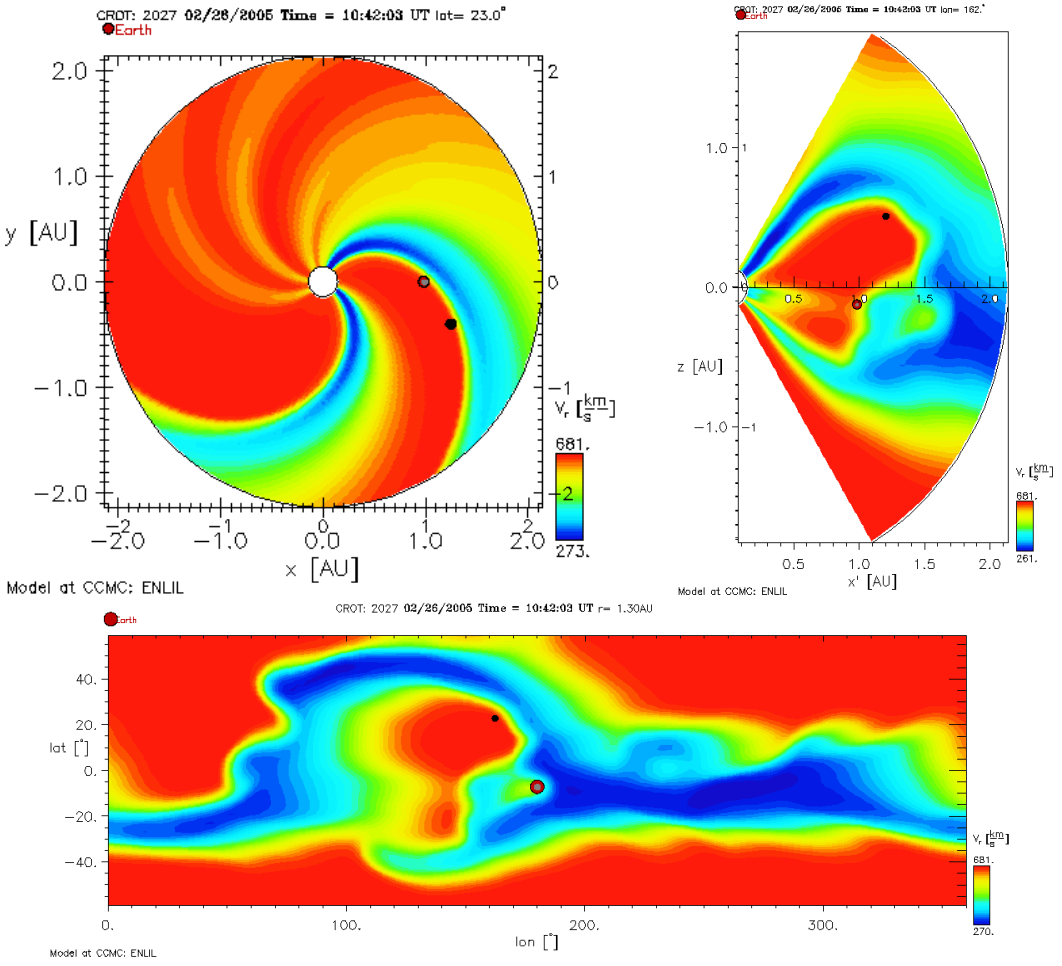

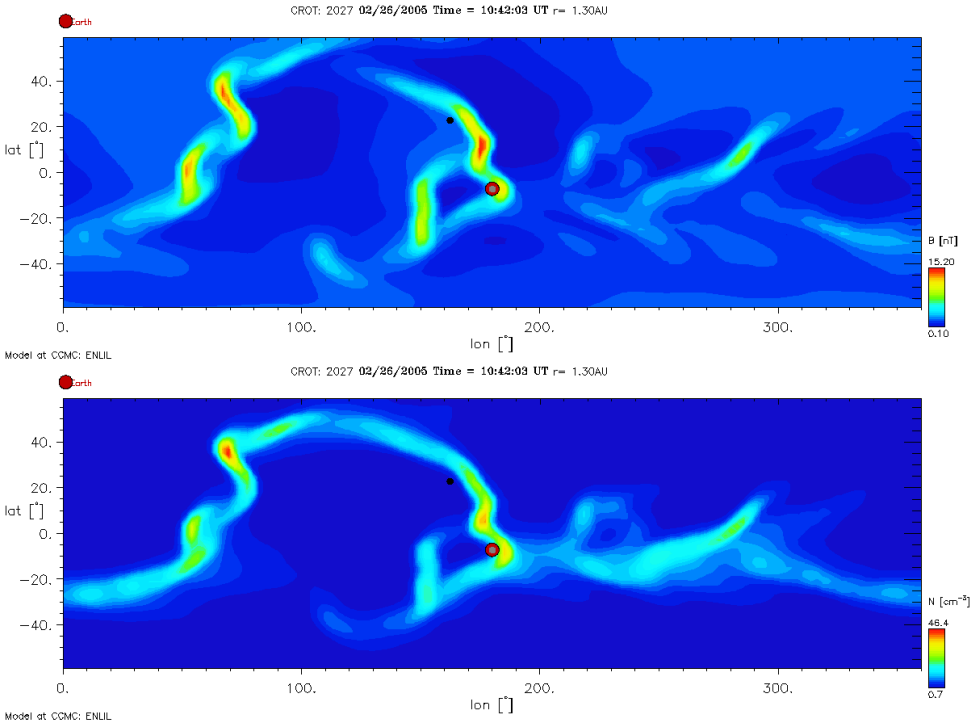

Figure 5.38: MHD visualisation of C/2004 Q2 (heliographic lon = 162°; lat = 23°; r= 1.3 AU) on 26/02/2005 at 10:42 UT. According to this model, the comet should be experiencing fast solar wind post-CIR.

Data on the 5th March correspond to images taken 3 hours before and 7 hours after Figure 5.39. Images from 11:00 UT exhibit a kink in the ion tail and it is clear that the comet is on the leading edge of a CIR, thus accounting the range of velocities recorded.

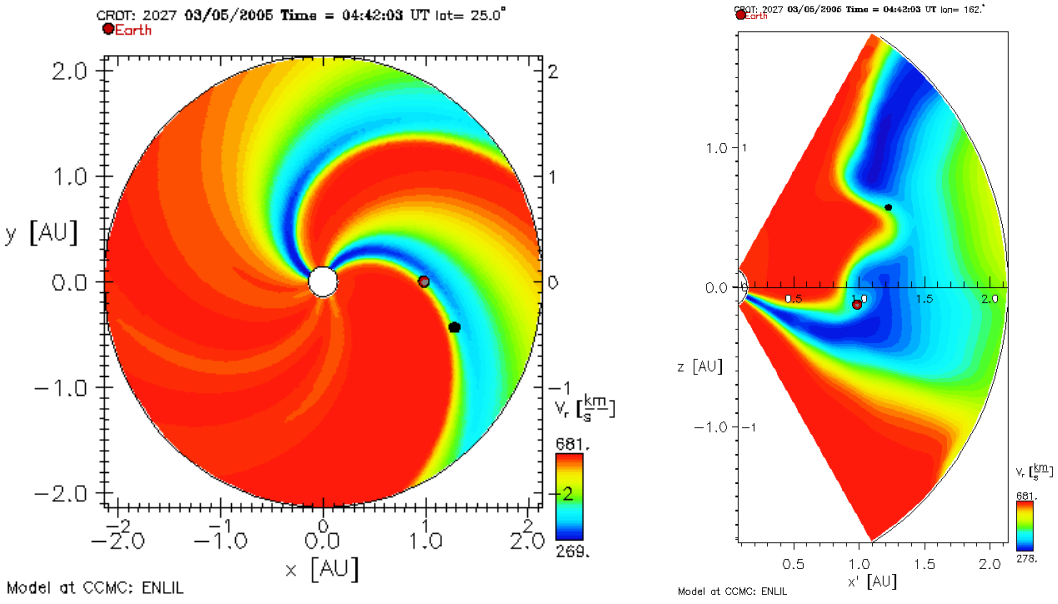

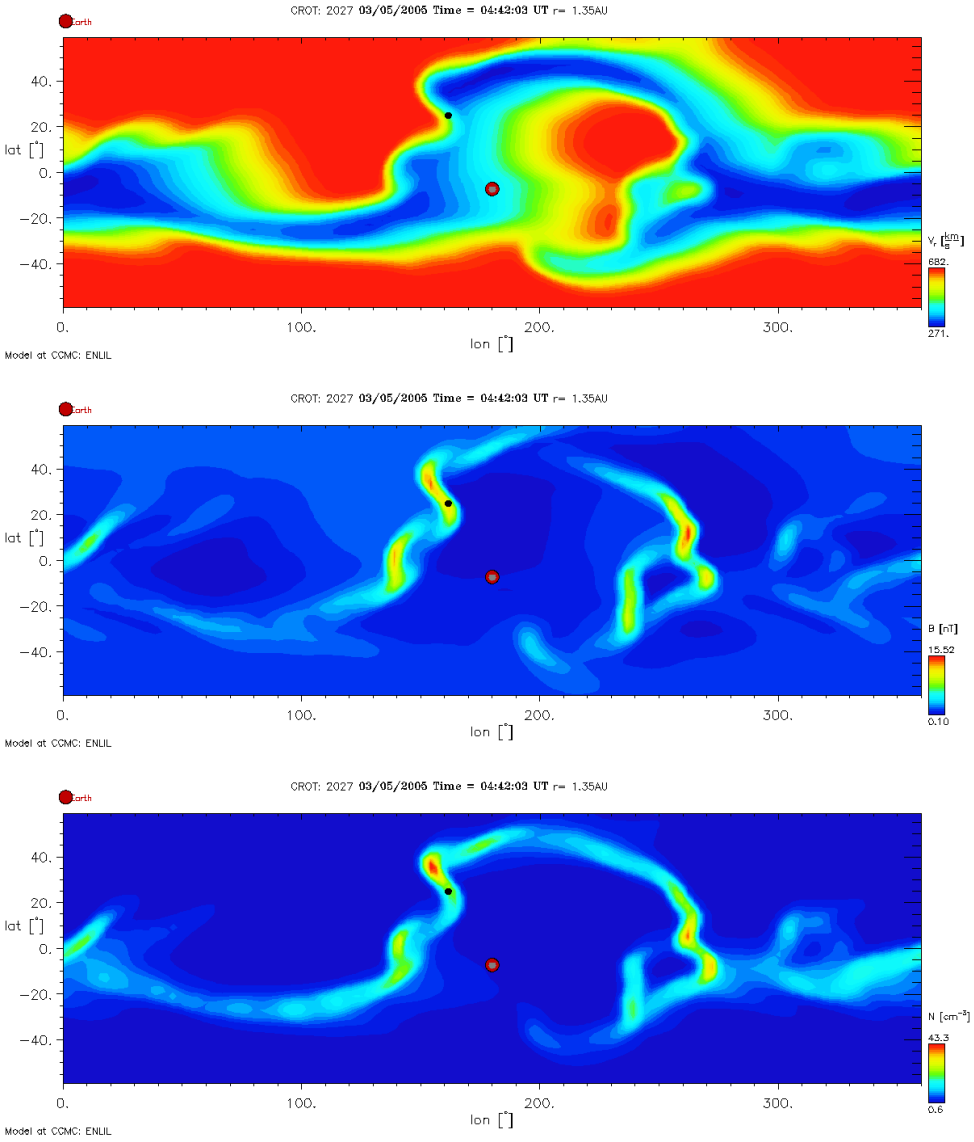

Figure 5.39: MHD visualisation of C/2004 Q2 (lon = 162°; lat = 25°; r= 1.35 AU) on 05/03/2005 at 04:42 UT. Comet is experiencing shocked slow solar wind at a CIR transition region from slow to fast solar wind.

The last set of 5 data points on 2nd April 2005 at ~ 19:00 UT were all calculated from one image that display a kinked ion tail. The orbit plane angle begins to decrease here. The solar wind model does not stretch until this date. According to the Mercator map [Figure 5.36], the comet should be experiencing slow solar wind speeds, as reported in Figure 5.37.

5.1.3. Alternative Methods to derive Solar Wind Velocities

5.1.3.1. Low Orbit Plane Angle

The orbit plane angle of comet C/2004 Q2 was below 10 degrees between 17th December 2004 and 1st January 2005, covering half the span of CR 2024 and the initial phase of CR 2025. The ion tail sits on the radial vector for most of this period though this is a consequence of our geometrical perspective. Radial measurements of the ion tail should be considered spurious. Despite this, this does pose a unique opportunity to measure the non-radial dispersions of the ion tail off the comet's orbital plane. Furthermore, radial propagation of turbulent events in the ion tail, when lying on the Sun-Earth line, will act as a good estimator of the radial velocities.

The comet encountered an ICME between 17th and 18th December, so a period with less turbulent flow and with a distinguishable ion tail from the sky background was chosen as my test images. This limits the observing period to the 29th December 2004 to 1st January 2005, when the orbit plane angle was between 6 to 12 degrees. Additionally, these off-orbital plane flows can only be measured when the flow is lagging the comet's motion in order to have an estimate for the original time the bundle left the comet head. The counter-scenario where the flows are seemingly leading comet motion from our perspective, the only technique that can be used to estimate non-radial velocities is to build a flow vector map from consecutive images.

Errors

A box is fitted to the ion tail along the radial vector to determine the measurement error in y, as we are only interested in the displacement from the orbit in y. The measurement error of the bundle centre is taken to be ±1/6th of the distance between the edges of the box in y. Combined with the uncertainty on the projected image, an uncertainty for the non-radial solar wind velocity can be determined. The error on the non-radial velocity will be comparatively large but this is mostly due to the uncertainty on the projected image.

Results

In spite of the small image set available, I determine the non-radial velocities to be ~40 km s^{-1}, as seen in Figure 5.40. This is comparable to the average non-radial component of the solar wind velocity as measured by ACE over a period of three and a half years [Figure 5.41]. The average non-radial velocity as measured by ACE was ~ 30 km s^{-1}.

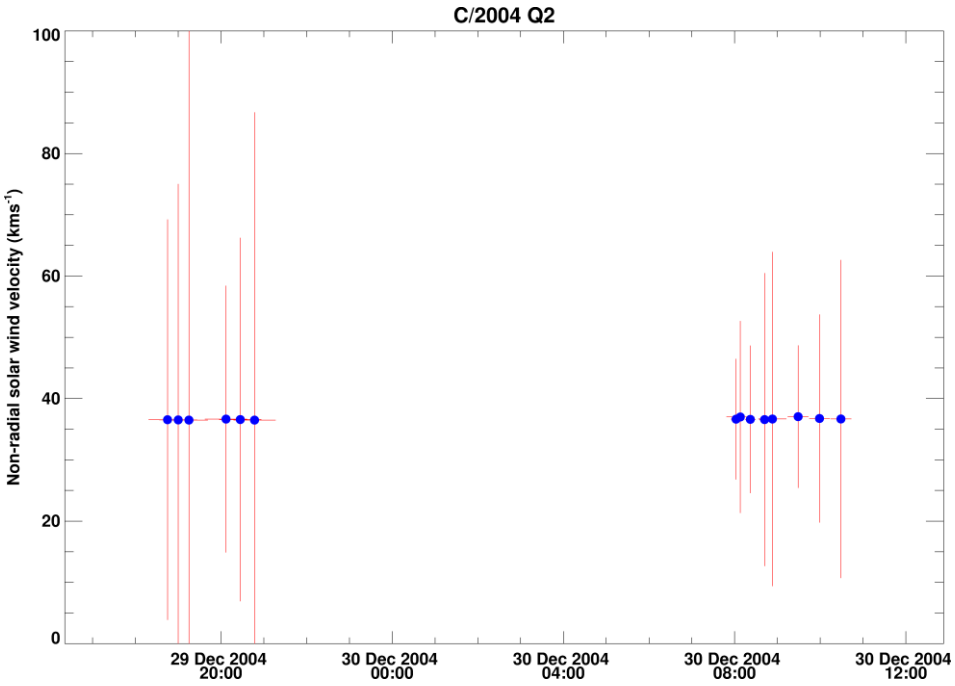

Figure 5.40: Non-radial velocities for C/2004 Q2 obtained during periods of low orbit plane angles and when the ion tail was inclined out of the comet's orbital plane.

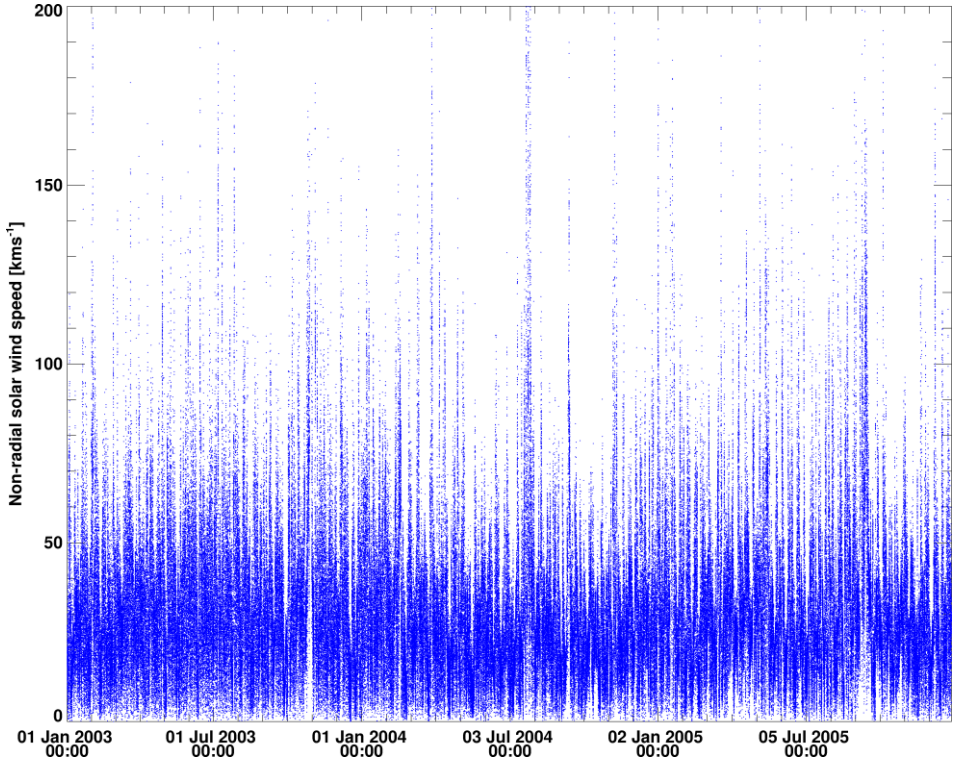

Figure 5.41: Non radial velocities as measured by ACE/SWEPAM at L1 over 3.5 years. The mean non-radial velocity component of the solar wind velocity is ~30 km s^{-1}. These non-radial velocity variations can arise from CIR or ICME interactions with the solar wind.

5.1.3.2. Vector Maps

Rare opportunities, such as capturing the entire duration of an ICME-influenced tail disruption, provide unique insight into the non-radial expansion of the ICME and the subsequent acceleration of individual plasma bundles within the tail. Other events such as DEs, whereby the tail may appear to lead the comet motion, can be tracked to determine its velocity. An important caveat to note is that the flow vector maps are a good estimate of the non-radial component of the solar wind in the comet's orbital plane, though it is likely to have a tangential component. The remaining component can only be determined from three dimensional triangulation of the ion tail when stereoscopic observations are available.

Errors:

Since the ion tail features are chosen by clicking on areas of interest in the images, the positional error of both measurements will be the same, as the uncertainty translates to a

relative shift of the projected image. Therefore, the relative error on the feature's velocity is much smaller than the uncertainties given below. Factoring out the projected image uncertainties, the dominating component is then the timing error.

The observing time and its error were inferred from the size of the optocentre for each image with unknown times. The Koprolin image sequence ranks amongst the few groups of images where the observing time is known to be exact. Despite this, since the number of stacked images and their exposure time is unknown, I defaulted to my 'imagetimeheaders' software to determine the uncertainty based on the size of the optocentre, thus massively overestimating the error in time. I elected to adopt a conservative approach towards the uncertainties calculated for this study as the true timing uncertainty cannot be determined.

Case study: The tale of an ICME's interaction with a comet's tail

Image sequence by W. Koprolin

When positioned 15 degrees leftwards of the Sun-Earth line and travelling between 8 and 11 degrees northwards of the ecliptic plane, comet C/2004 Q2 experienced at least one extreme ICME interaction, at ~1.2 AU of the Sun. The sequence captured by W. Koprolin [Figure 5.42] demonstrates the extent to which ICMEs influence and dictate the structure and evolution of a cometary ion tail. Analysis of the movie animation suggests that the ICME may have collided with the ion tail without interacting with the comet head to a significant degree. The trailing end of the ion tail becomes disconnected from the main ion tail, even forming multiple mini ion tail-like structures within the trailing end, as the embedded B field of the ICME reconfigures that of the ion tail. The images in Figure 5.42 are an extract of a 13 image sequence by W. Koprolin on the 18th of January 2005. The exposure time for each is ~10 minutes. The radial solar wind velocity approach is incongruous in this instance.

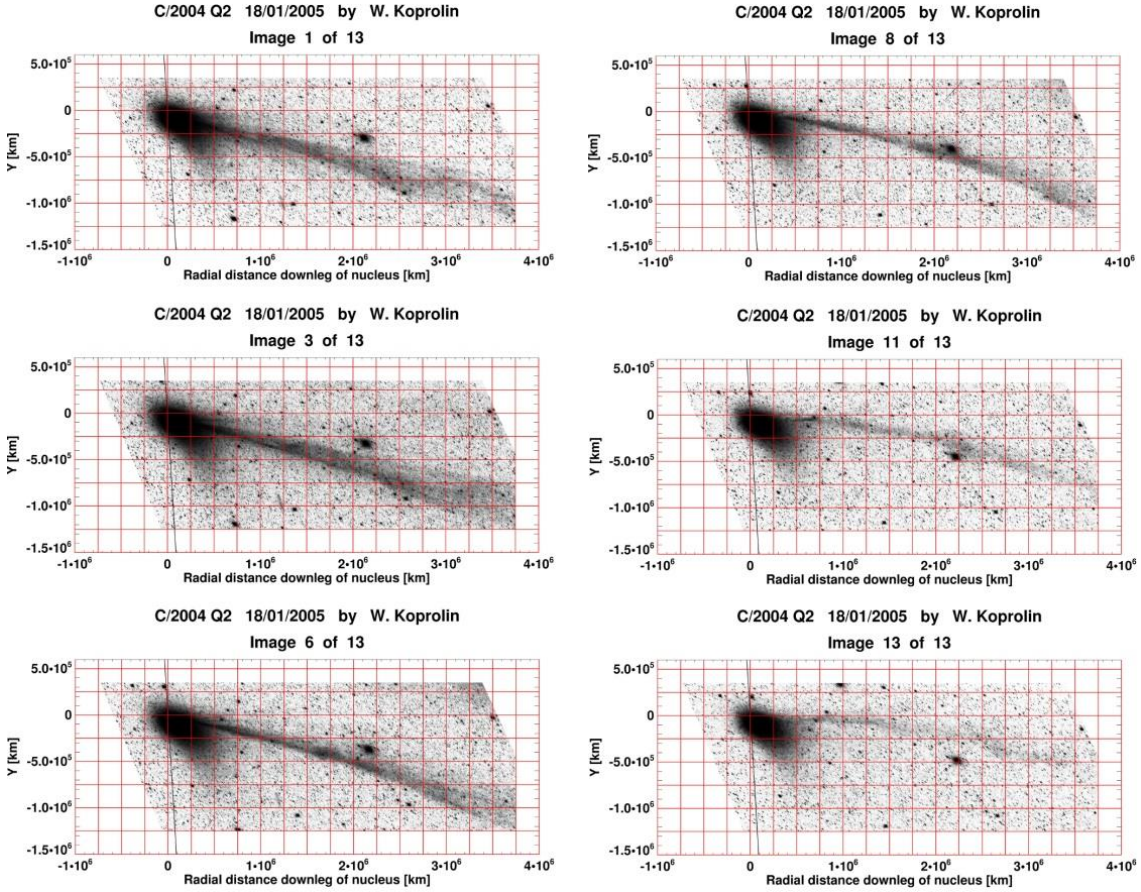

Figure 5.42: Excerpts from the 13 image sequence by W. Koprolin on 18/01/2005. Each image was mapped using a cometocentric frame of reference. Non-radial disturbances in the ion tail can be tracked as the ion tail begins to curve and dissipate.

Two high-velocity ICME eruptions, observed by LASCO, at 09:30 and 09:54 UT on January 17,2005, were first suspected as likely candidates, which merged prior to arrival at the comet. A rough linear speed was calculated from the comet's heliocentric distance and the time taken between the eruption and when the disturbance was detected at the comet. This implied an extremely high (and, to some, controversial) velocity upwards of ~2500 km s^{-1}. The ACE plasma instrument became overwhelmed during this time as it experienced an energetic particle storm probably related to the ICME. The estimated velocity correlates well with the measured plane-of-sky velocity, which registered at 2094 km s^{-1} for CME1 and 2547 km s^{-1} for CME2, though this requires an acceleration of the first CME by CME_2. Bouratzis et al (2010) reports that CME1 would have reached CME2 at 12:45 UT on the same day, at approximately 37 $R_\odot$.

High ICME speeds exceeding 3000 km s^{-1} (Gopalswamy 2005) have previously been measured, though these velocities were observed close to the solar surface. Empirical evidence and the literature suggest that the fast ICMEs will have undergone rapid deceleration to ambient solar wind speeds due to frictional drag effects and imparting momentum to the surrounding medium (Shen et al. 2012). The forces acting upon the ICME, in different combinations depending on location within the CME, are the magnetic pressure term of the Lorentz force and the pressure gradient for the accelerating force and solar gravitational pull, aerodynamic drag and the B field tension as the retarding force.

For simplicity, I assumed a linear propagation model for the ICMEs' propagation [Figure 5.43]. Thus, I identify a series of ICMEs and their induced Shock Arrival Time (SAT) at Earth and the comet's environment. The ICME list is compiled by comparing their central position angle, the Sun's position at time of eruption and the ICME's angular width with the comet's position angle. Halo ICMEs were also included due to C/2004 Q2's proximity to Earth and the ecliptic plane. Note that the ICMEs observation times were used instead of their eruption times. They were observed at different solar heights, however they were assumed to have left the solar surface at their observation time, which is a reasonable approximation at this scale.

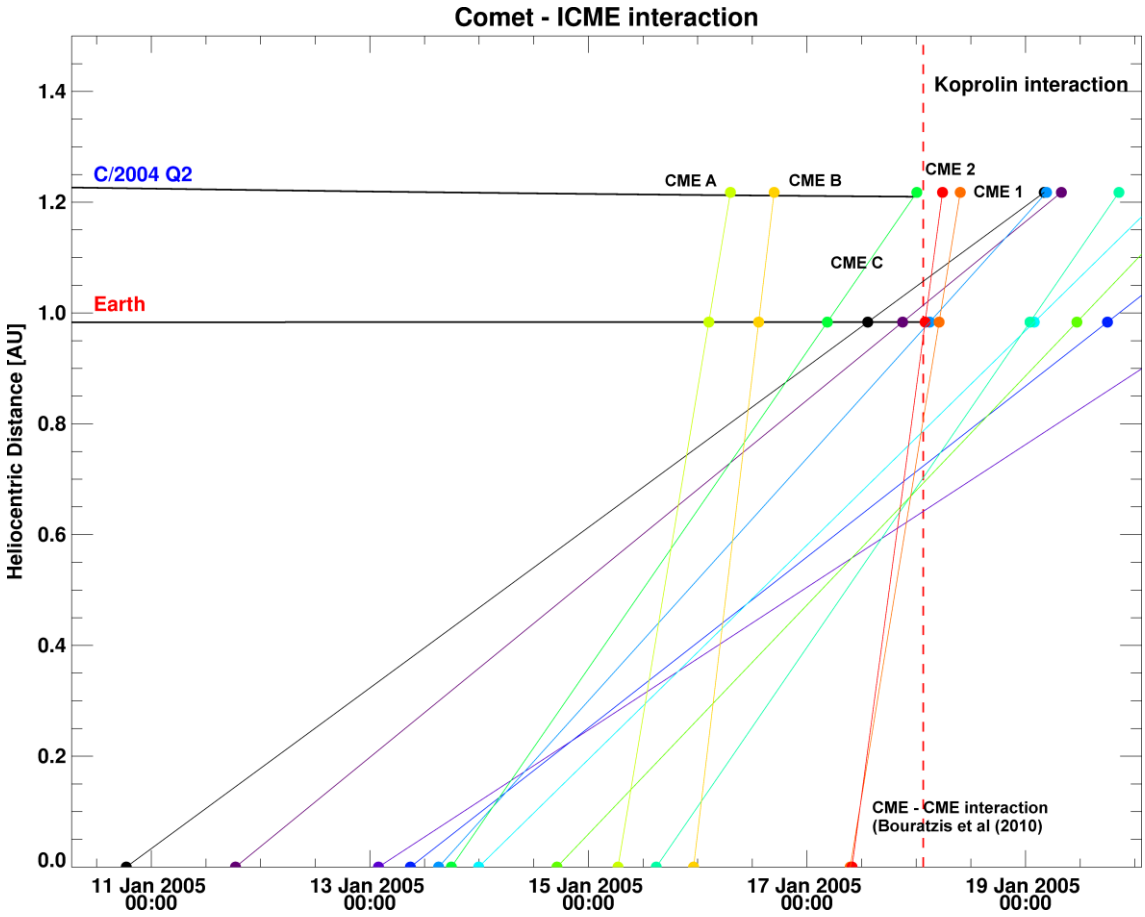

Figure 5.43: Distance-Time graph showing linear propagation of ICME and expected interaction points at Earth and comet C/2004 Q2. This is a basic tool for estimating arrival times and is not a realistic relationship of the ICME velocity with increasing heliocentric distance. The Koprolin interaction is marked with the dashed line (red) providing a cutoff for potential comet-ICME candidates.

This method is inherently flawed but it is a good approximation for the minimum SAT at the comet. Based on this, I conclude that it is unlikely for the fast ICMEs to have been the originator of the Koprolin event, but rather ICMEs A, B, C.

ICME2 will expand into a disturbed, less dense, faster and more magnetised medium in the wake of ICME1. It will eventually catch up and cannibalise ICME1 to form a complex combined transient structure before reaching the comet. There are only two images taken overall on the 18th and 19th, with the first sign of disturbance noted at 12:00 UT on the 18th and lasting at least 0.5 days. This implies a combined minimum speed of 1833 km s^{-1} to travel from 37 $R_{\odot}$ to 1.2 AU in 23.3 hours. The MHD visualisation shows that the compound magnetic cloud will miss the comet but the converged shock of the two ICMEs will reach the comet [Figure 5.29], resulting in

a sustained period of high velocities. Moreover, this neatly explains the discrepancy between the MHD predicted velocities (solid line in radial velocity plots) and my extrapolated ACE values for this period.

Results

Distinguishing features were tracked in consecutive Koprolin images. In my software, the user is provided a pair of images from which the bundles can be chosen from image 1 and 2. Ideally, the chosen positions in image 2 of image pair 1&2 should match the positions of image 2 in pair 2&3. This is not always the case, since the positions are determined by eye, though the code attempts to minimise human error. Figure 5.44 shows the distances of each measured feature downstream of the nucleus in a cometocentric frame. Each column consists of pairs of measurements representing the motion of features between two images. For example, the pairs in column 1 corresponds to the motion of the ion bundles between image 1 and 2 and so on. Features tracked in multiple images, were then connected and plotted in the same colour. Most of the ion bundles propagate near-linearly. The previous step of identifying unique features allows us to link the velocities together to understand the velocity variations across the tail [Figure 5.45]. Since the velocity uncertainties are large and would impede viewing of the values, I have included a second plot [Figure 5.46] with the timing uncertainty plotted in red and the velocity uncertainties are appended next to their value.

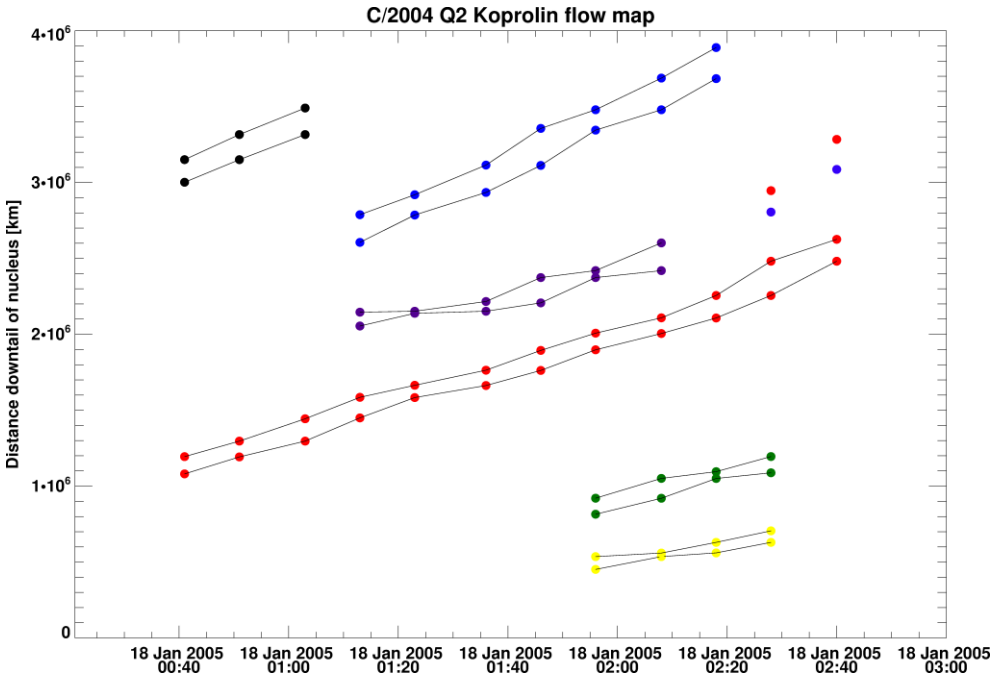

Figure 5.44: The distances of all the selected features. Each column refers to a pair of image. Features tracked between images have been identified and linked together. In the last images, the bundles have grown tremendously in size. The last two data points are unconnected as different regions of the plasma bundle was chosen.

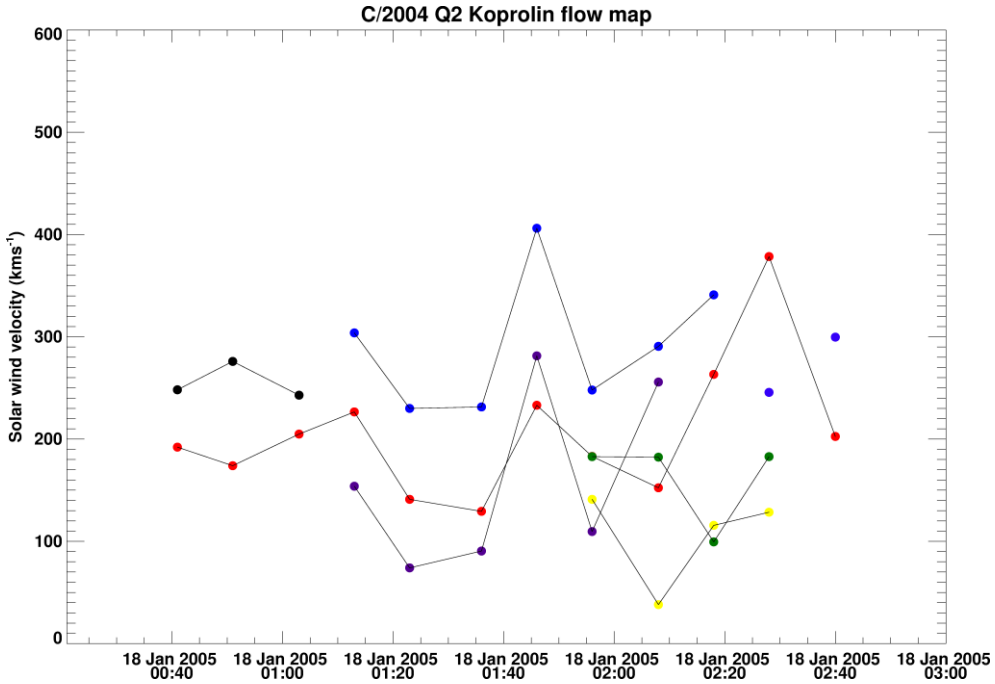

Figure 5.45: Non-radial velocities, in the comet's orbital plane, derived from Koprolin image sequence. The large mix of velocities within a short period is clearly a sign of ongoing disruption.

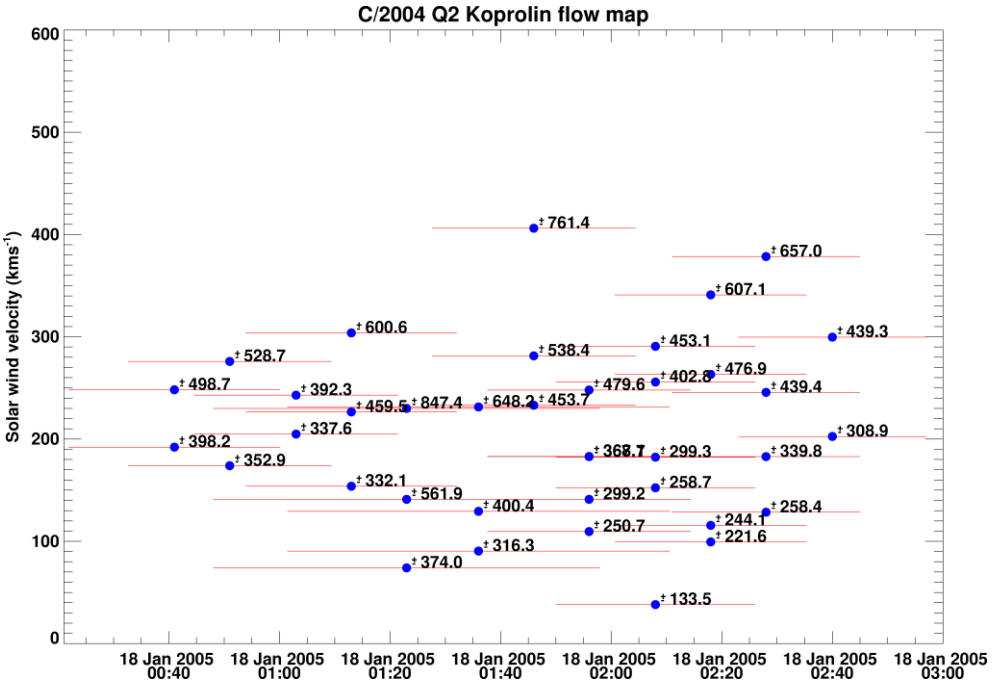

Figure 5.46: Solar wind velocities with errors derived from vector maps. The errors are large due to the projections uncertainty along Y. All images share a similar error. Uncertainty on the velocities will be minimal in comparison.

We can compute the acceleration profile [Figure 5.47] across the tail from the large range of velocities. We notice a similar trend across the tail, with the acting forces fluctuating between accelerating and decelerating the ion tail. The ion tail was also observed to decelerate upon impact. Over an interaction scale length of 4 x 10^6 km, the ion tail undergoes accelerating and decelerating forces as it is impacted by different regions of the ICME.

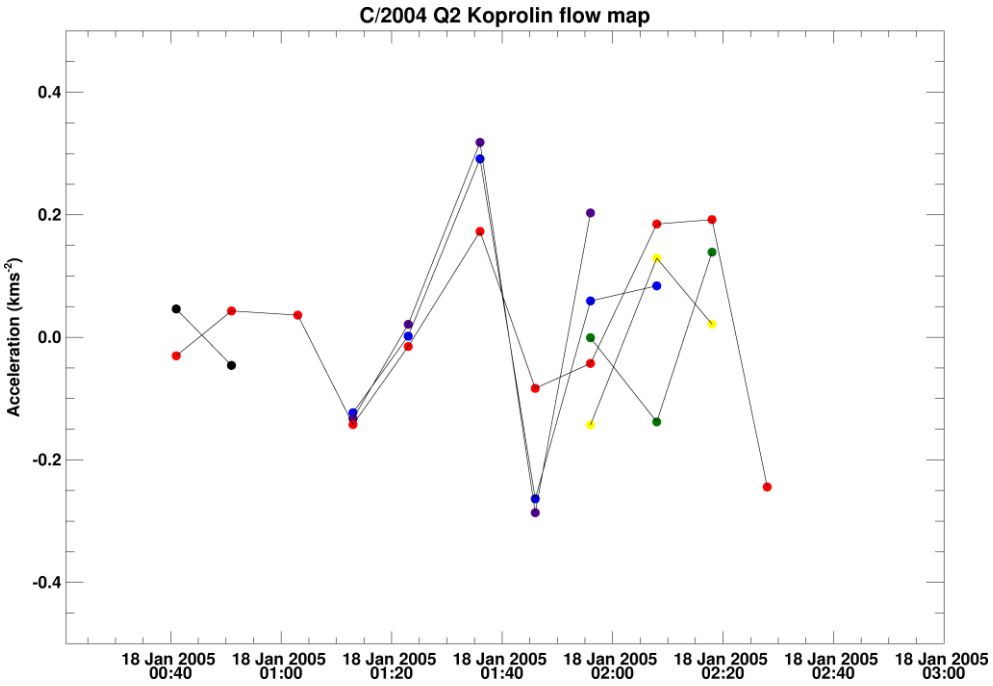

Figure 5.47: Acceleration of identified features as tracked in multiple images. Identified features are plotted in the same colour and linked.

CASE STUDIES: Compiled animations from a global network

December 15, 2005

The HCS-related DE on 15th December yielded low non-radial velocities near the comet head, covering ~ 0.5 x10^6 km in one hour. The head of the disconnected tail and the fork were tracked at 109.9 ± 123.7 and 116.2 ± 123.7 km s^{-1} respectively.

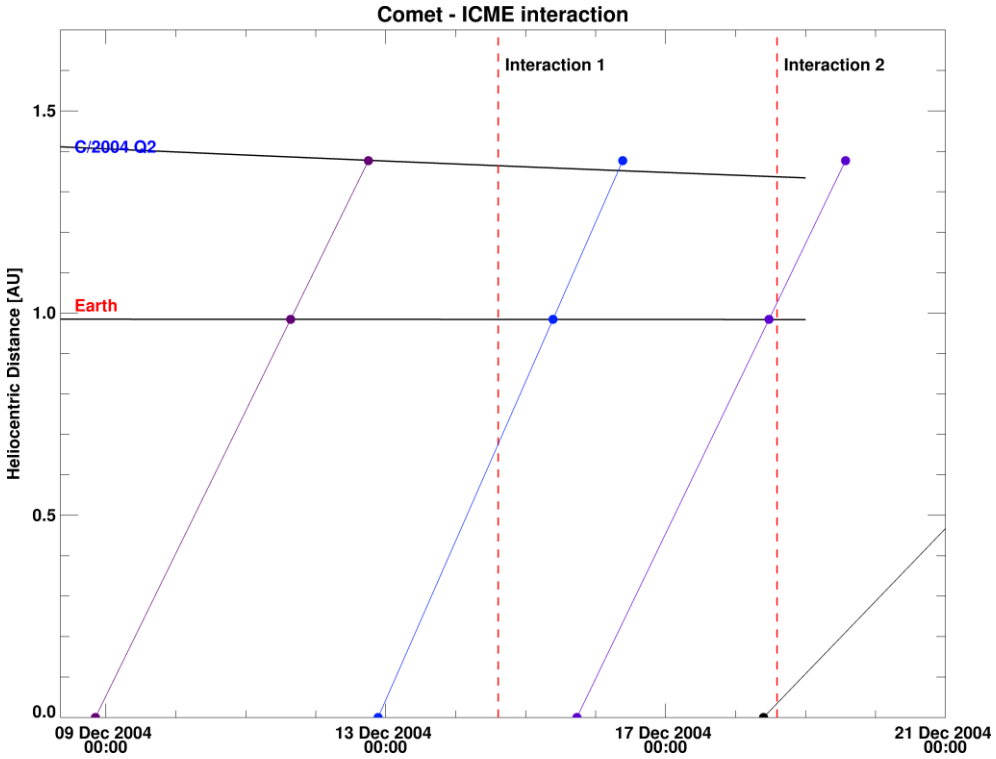

Figure 5.48: Estimated minimum Shock Arrival Times (SATs) of ICMEs at comet C/2004 Q2. The dashed lines, labelled Interaction 1 and 2, refer to the time of the first image in which the turbulent event was observed.

Figure 5.48 provides a quick overview of the minimum SATs for ICMEs launched in the general direction of comet C/2004 Q2 in December 2004. The comet's position angle varies from 18 to 29 degrees. Compensating for the lag in expected arrival time at the comet, the Halo ICME erupting around 08/12/2004 09:36 UT (Speed: 611 km s^{-1}), is the most promising candidate for the cause of the phenomena observed at the comet on 14/12/2004. Factoring in the solar position angle (~12^{o}), the ICME observed on the evening of 12/12/2004 at 21:24 UT (Speed: 682 km s^{-1}; CPA: 312^{o}; Angular width: 79^{o}) will miss the comet by ~10^{o} on 18/12/2004. The turbulent events described below are unlikely to have resulted from phenomena other than an ICME interaction.

December 18, 2004

This period showed signs of an intense ICME interaction with the ion tail [Figure 5.49]. The ion tail was wide, distorted and leading the comet motion (early measurements in Figure 5.50)

before disconnecting from the main tail in the later observations. The ion cloud forms a U-bend shape, which was tracked at its forming points. The U-bend shape undergoes the same initial decelerating force slowing down to extremely low velocities before the net force acting upon it flips and the feature begins to accelerate in later images.

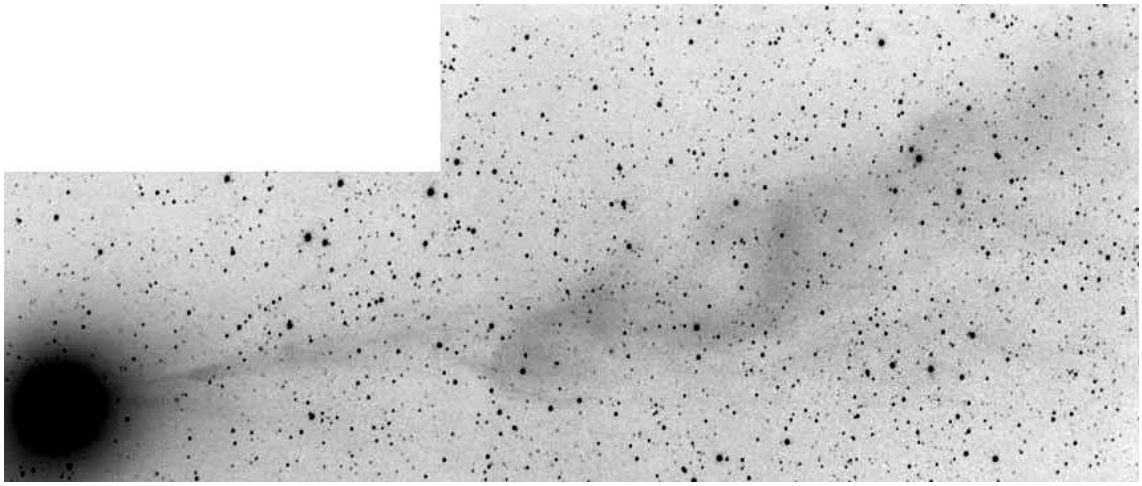

Figure 5.49: Evidence of an ICME interaction leading to a DE. Image captured by Jäger and Rhemann on 18/12/2004 22:10 UT.

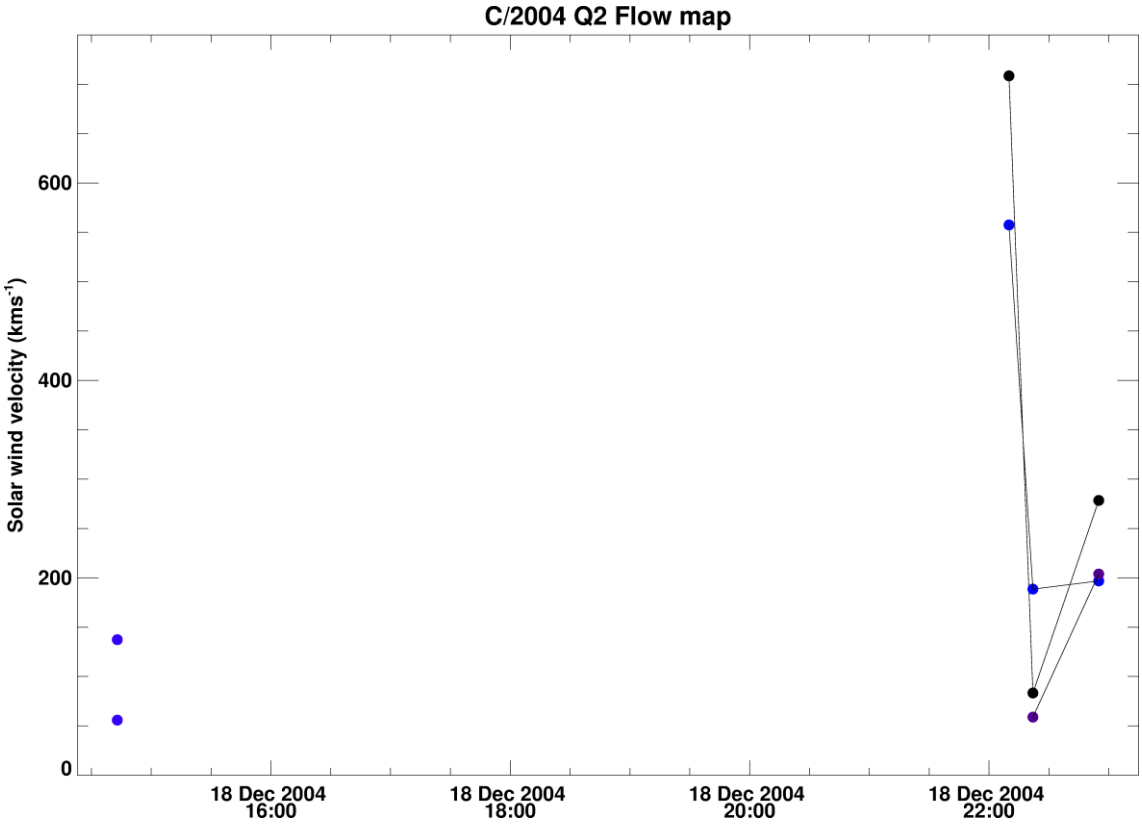

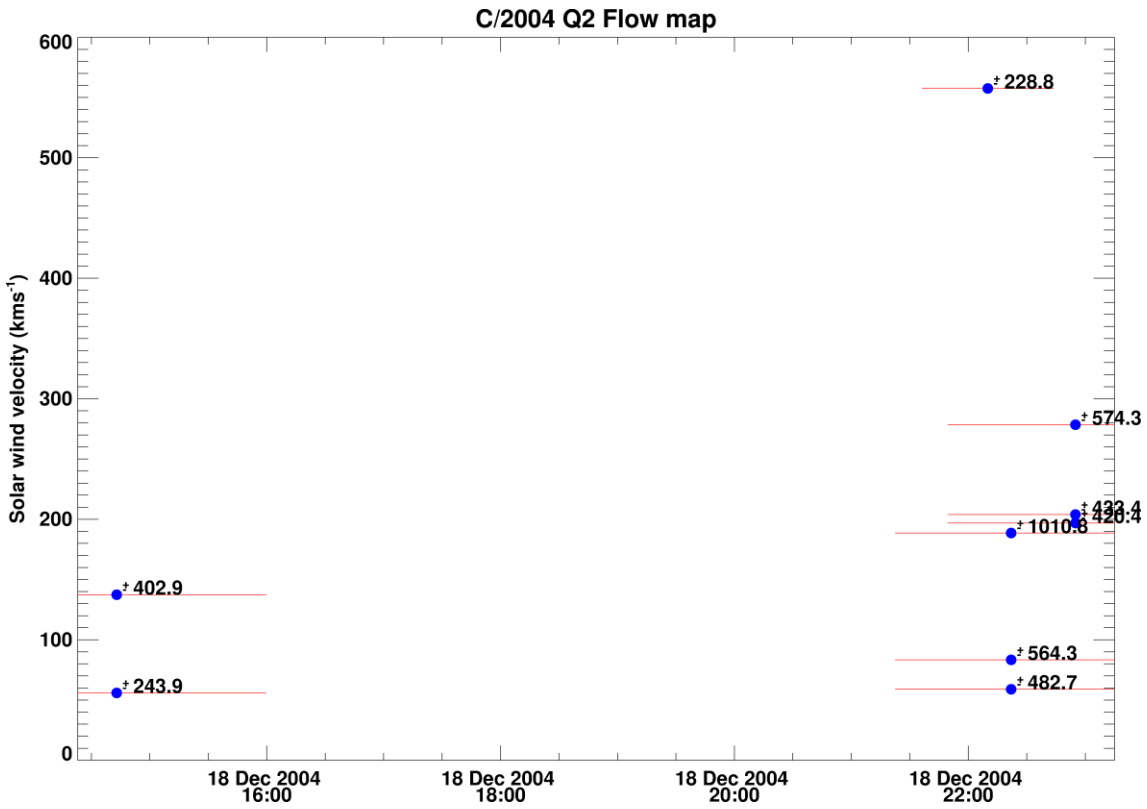
C/2004 Q2 Flow map
Solar wind velocity (kms-1)
600
500
400
300
200
100
0
228.8
574.3
423.4
420.4
1010.8
402.9
564.3
243.9
482.7
18 Dec 2004 16:00
18 Dec 2004 18:00
18 Dec 2004 20:00
18 Dec 2004 22:00

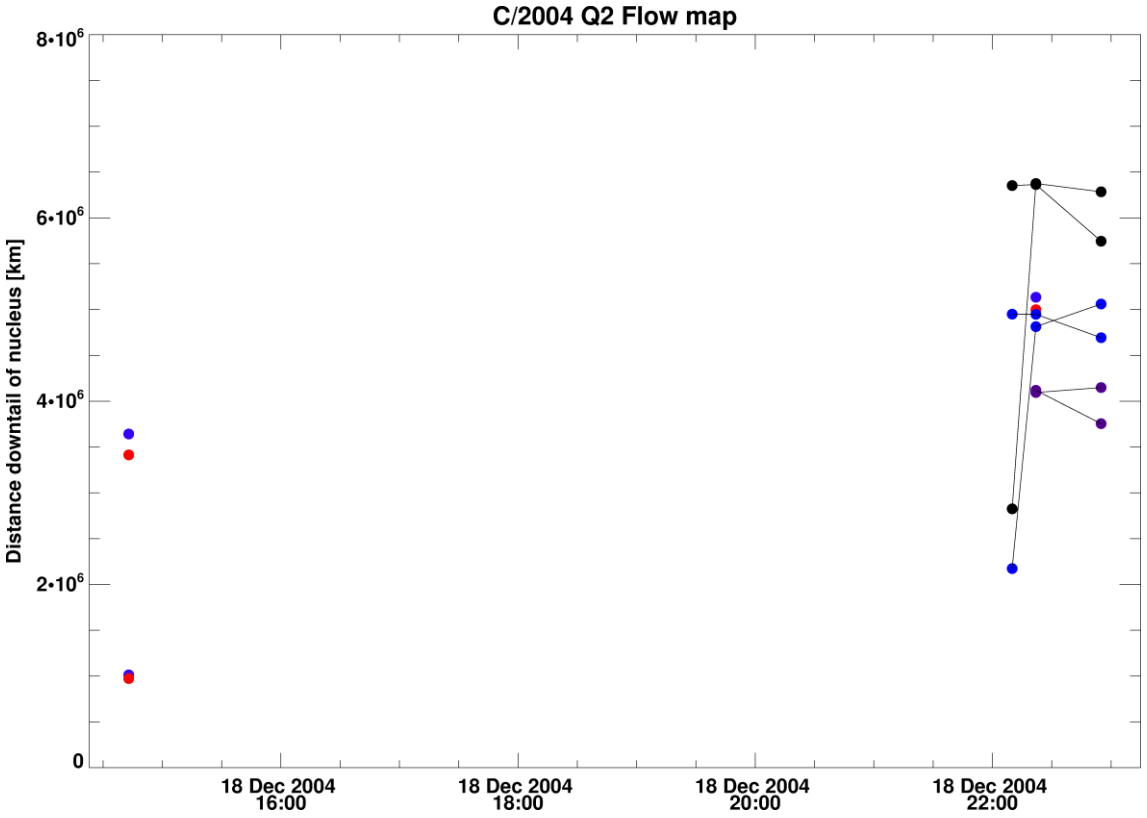
C/2004 Q2 Flow map
Distance downtail of nucleus [km]
8•10^6
6•10^6
4•10^6
2•10^6
0
18 Dec 2004 16:00
18 Dec 2004 18:00
18 Dec 2004 20:00
18 Dec 2004 22:00

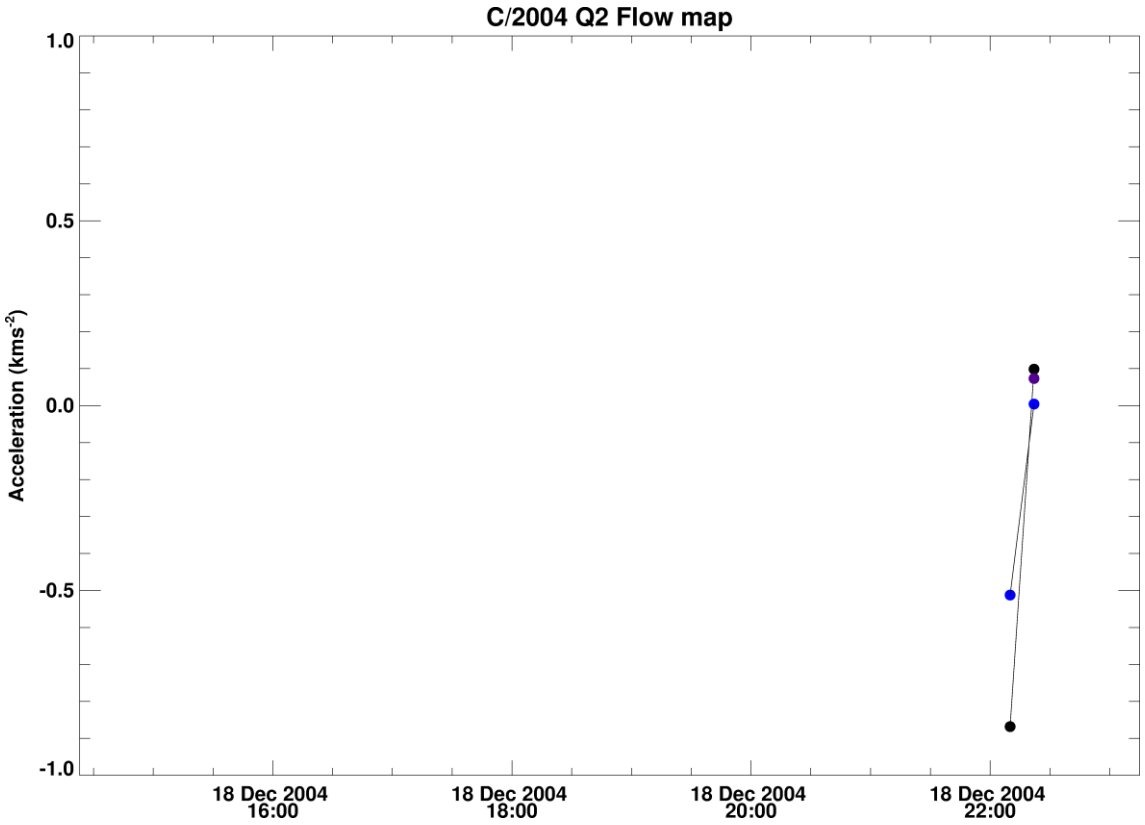

Figure 5.50: Each column of data was extracted from the same image. The U-bend shape was tracked from ~21:00 UT on 18/12/2004. The numbers next to the data points in the second plot are the uncertainties on the solar wind velocity derived with this method. The large uncertainties are due to uncertainties arising from the projection mapping and not due to the flow vector map technique.

January 2, 2005: ICME or HCS combined with low orbit plane angle

Images by M. Holloway on January 2, 2005 revealed an ion tail with multiple streamers and harbouring scalloped features within. The tail initially led the comet's motion, however there aren't any features that can be tracked in subsequent images to calculate the non-radial velocity. Moreover, it was not possible to determine the accuracy of the deduced observing times or whether the images had been successfully plate solved. Images from Japanese observers later during the day present a density enhancement travelling anti-sunward. These Holloway images were excluded from the vector maps technique though they hint that the comet may have encountered an ICME. The transient interaction [Figure 5.51] was inferred to be ICME-related, however a HCS crossing, expected around the 1st January, cannot be ruled out with the unusual ion tail orientation easily explained due to the low orbit plane angle. The

ensuing density enhancement and eventual DE in later images are likely unrelated to the Holloway images due to the different morphology, tail orientation and direction of motion.

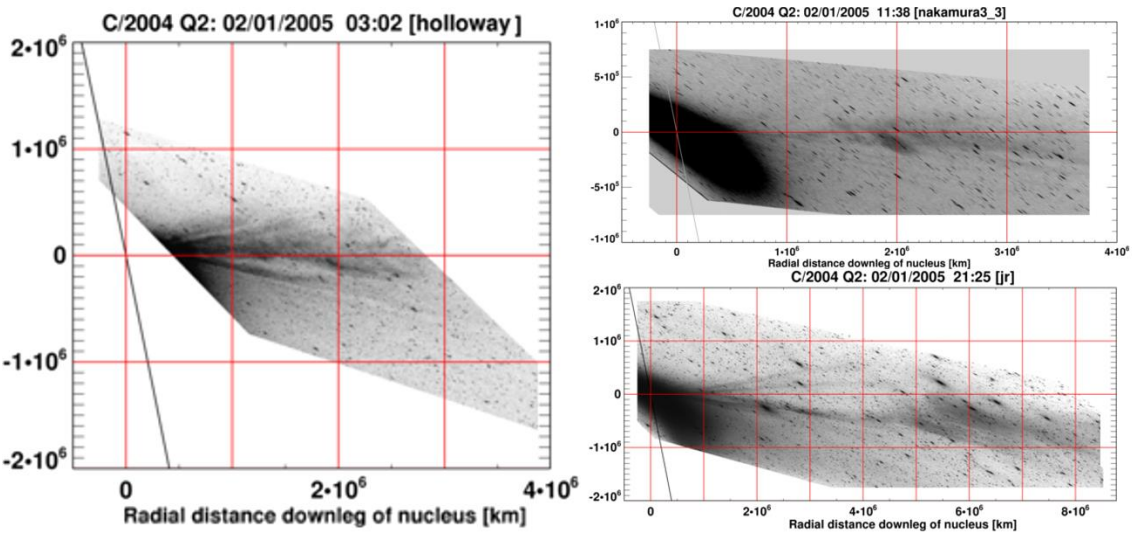

Figure 5.51: Image sequence from 02/01/2005. The image time for image on the left should be considered unreliable due to cut off optocentre.

Only the first and third Nakamura images were successfully solved. The knot within was identified to be travelling at 72.9 ± 212.6 km s^{-1} along the Sun-Earth vector, whilst the comet is at a low orbit plane angle. The plausibility that the massive ion cloud in the 21:25 UT JR images is the expanded Nakamura knot is moderately high due to its low velocity. This sets the feature's velocity at 115.8 ± 14.3 km s^{-1} in the JR images. The extremely small velocity uncertainty for this feature is due to the low pixel projection uncertainty and small FOV for this image.

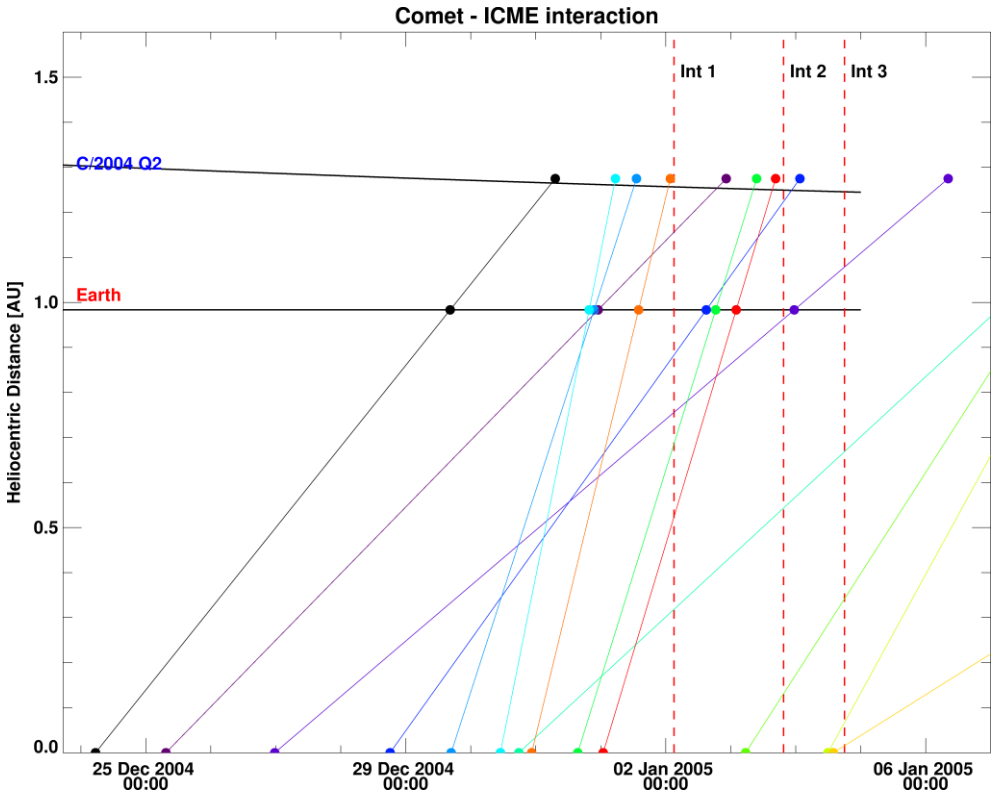

Figure 5.52: Estimated minimum SATs of ICMEs at comet C/2004 Q2. Interaction period marked in red is chosen for the first sign of a clear interaction in the image catalogue.

Likely candidates for the interaction periods observed in the image catalogue are fairly evident if a linear velocity is assumed. The comet's position angle was 70º - 75º for this period.

ICME Candidates:

Date	Time	Linear speed	CPA	Angular width	Interaction	Remarks
28/12/2004	18:12	350	78.21	110	3	
29/12/2004	16:45	774	74.21	140	1	Partial Halo
30/12/2004	10:57	1247	75.21	176	1	Partial Halo (uncertain width)
30/12/2004	22:30	1035	170.2	360	2 or 3	Halo
31/12/2004	15:30	802	64.21	143	2 or 3	Partial Halo
01/01/2005	00:54	832	170.2	360	3	Halo

January 3, 2005

The images on this date are outstanding, mostly in the number of tail rays observed. The sunward tip of the plasma bundle [Figure 5.53] was the only feature tracked.

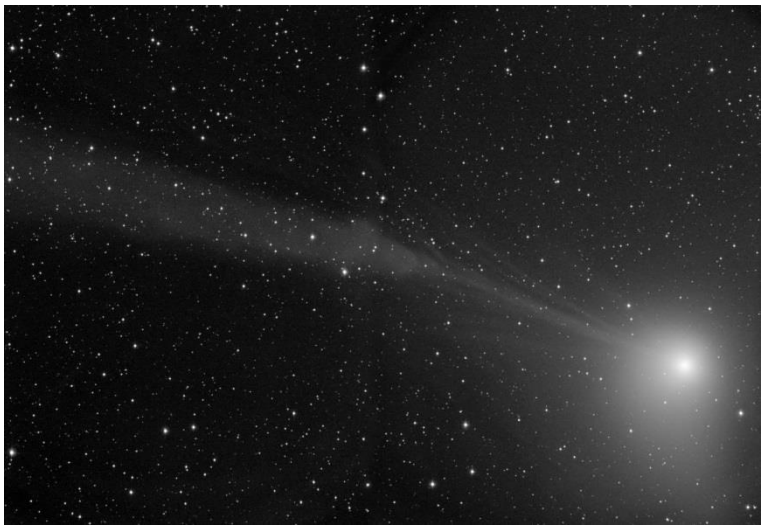

Figure 5.53: Comet C/2004 Q2 captured by Schedler on 03/01/2005 at ~19:30 UT.

The results suggest that the plasma bundle is slowing down to a standstill. These images were split up from an animated GIF file and the resulting data quality was in the low-to-medium range. This would at most cause tens of km s^{-1} variation in the derived solar wind velocity, which is significantly large for the values given in Figure 5.54.

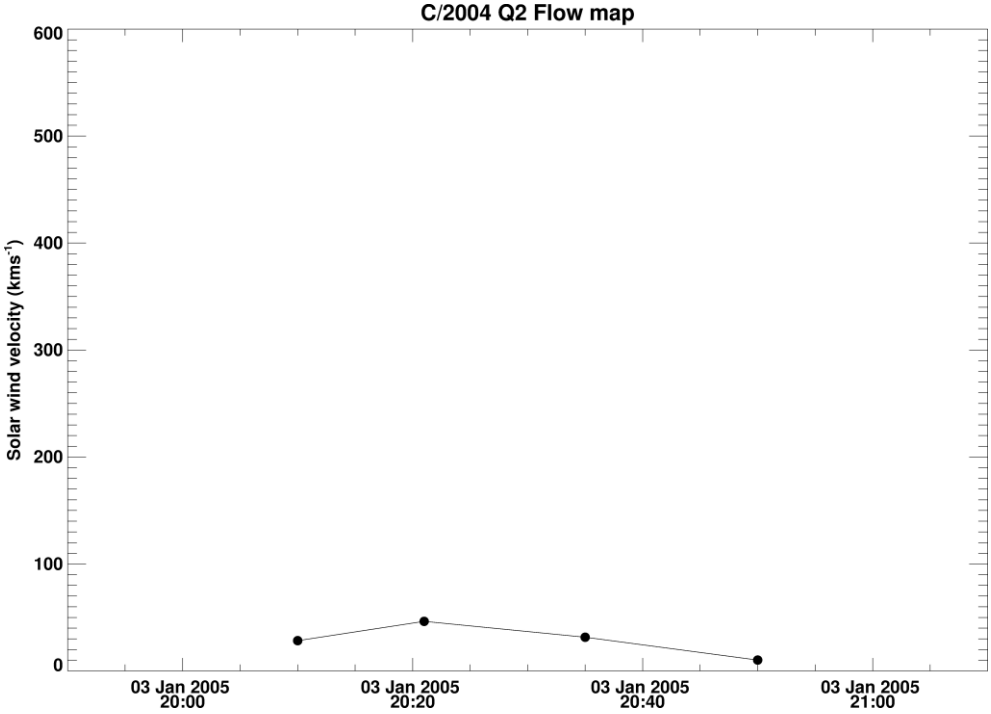
C/2004 Q2 Flow map
Solar wind velocity (kms-1)
600
500
400
300
200
100
0
03 Jan 2005 20:00
03 Jan 2005 20:20
03 Jan 2005 20:40
03 Jan 2005 21:00

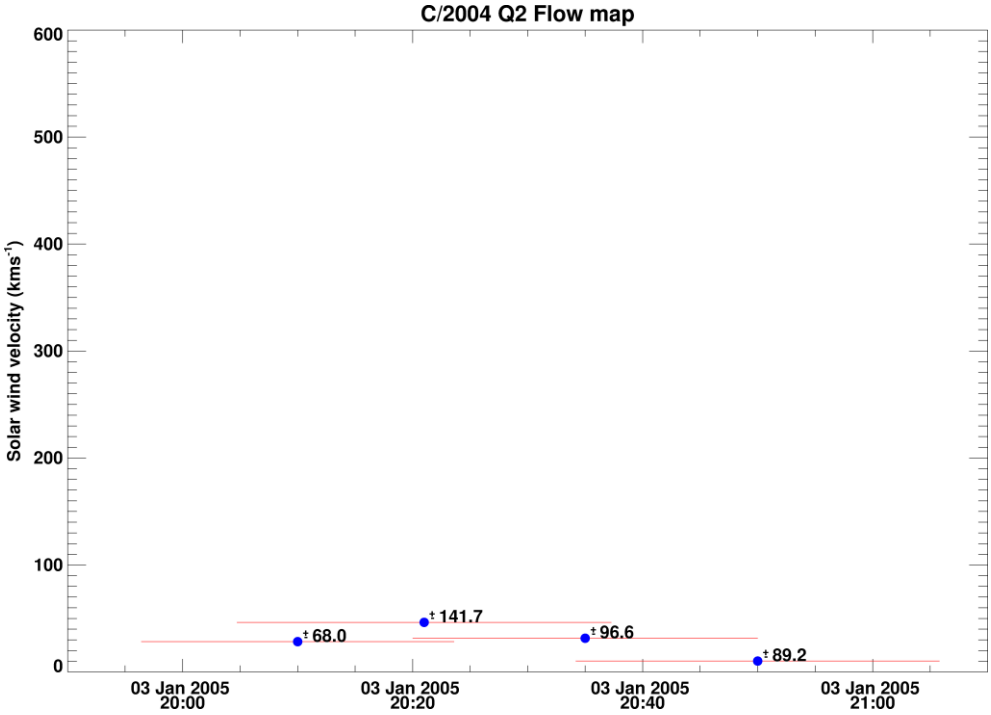
C/2004 Q2 Flow map
Solar wind velocity (kms-1)
600
500
400
300
200
100
0
± 141.7
± 68.0
± 96.6
± 89.2
03 Jan 2005 20:00
03 Jan 2005 20:20
03 Jan 2005 20:40
03 Jan 2005 21:00

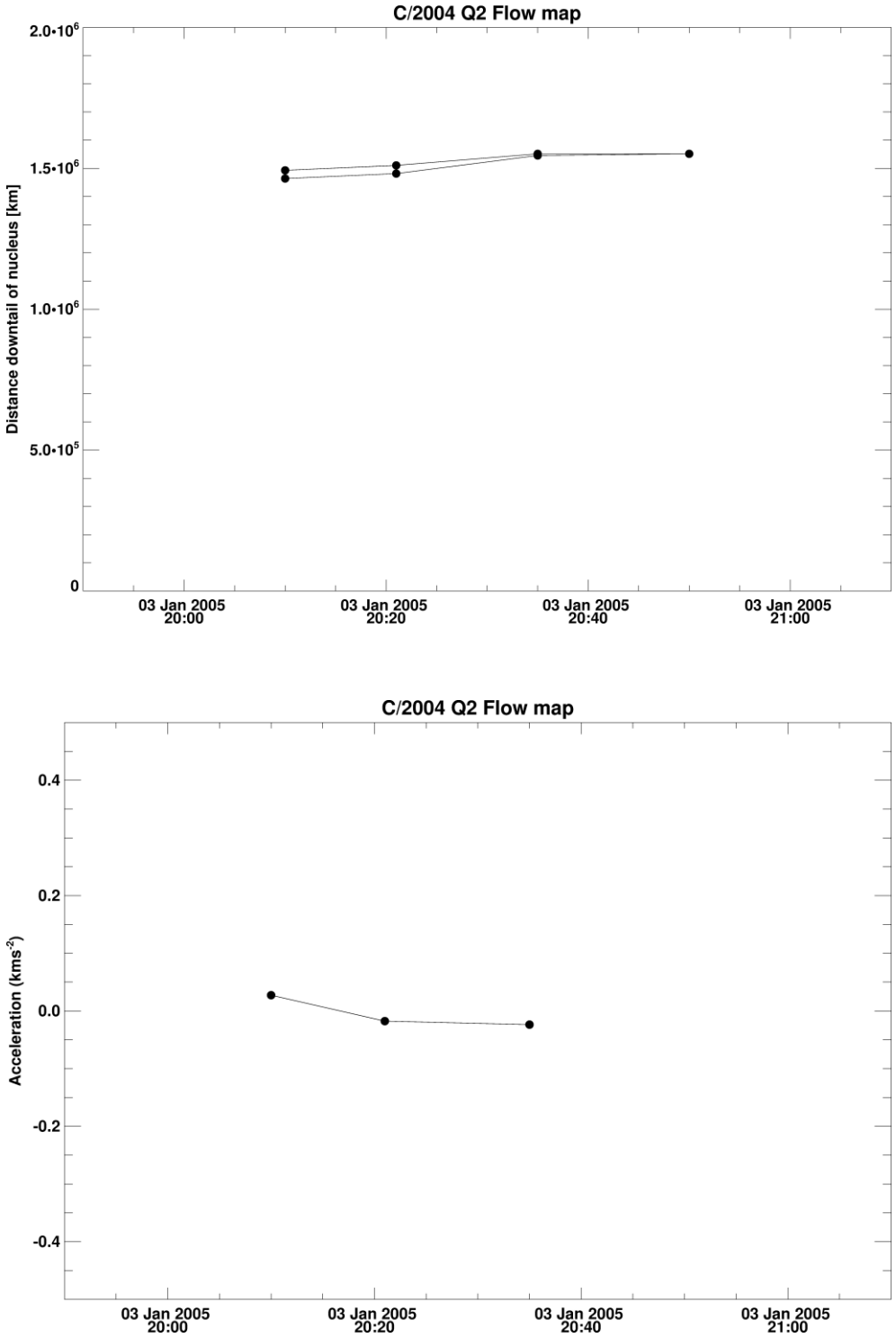

Figure 5.54: Each column of data was extracted from the same image. The central plasma bundle shows a slight deceleration in subsequent images.

January 4, 2005

With 4 ICMEs identified as potential interactors, the undulating tail consisting of multiple density enhancements and kinks is inferred to be affected by at least one ICME. There also exists the

possibility that the kinks could be formed via rapid HMF reorientations upstream of the comet, leading to thin-to-wide-to-thin views of the ion tail.

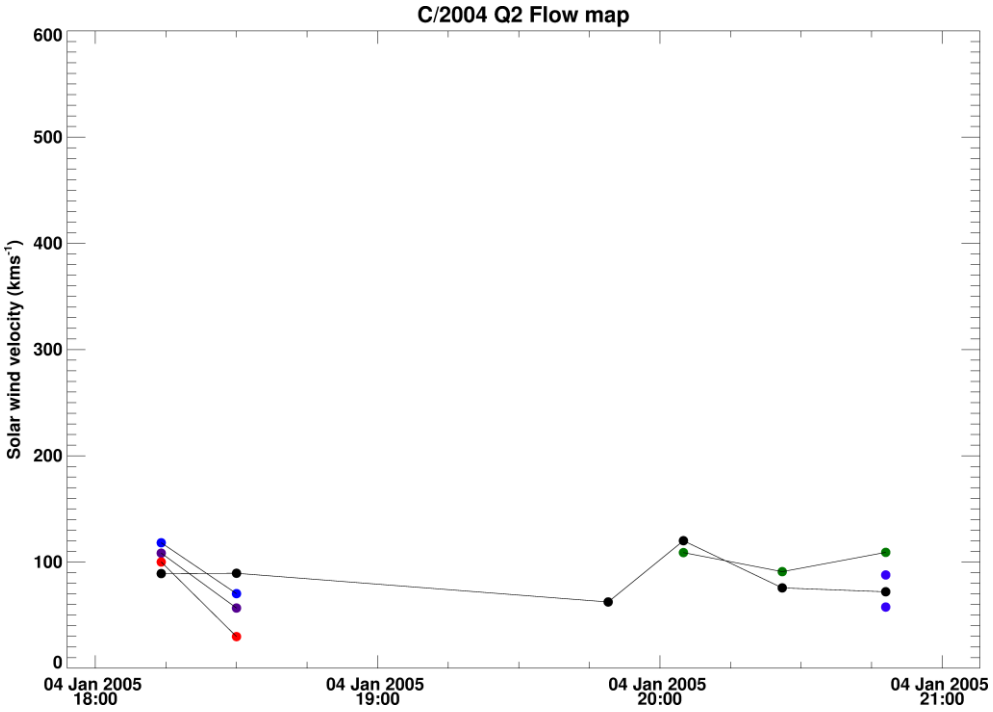

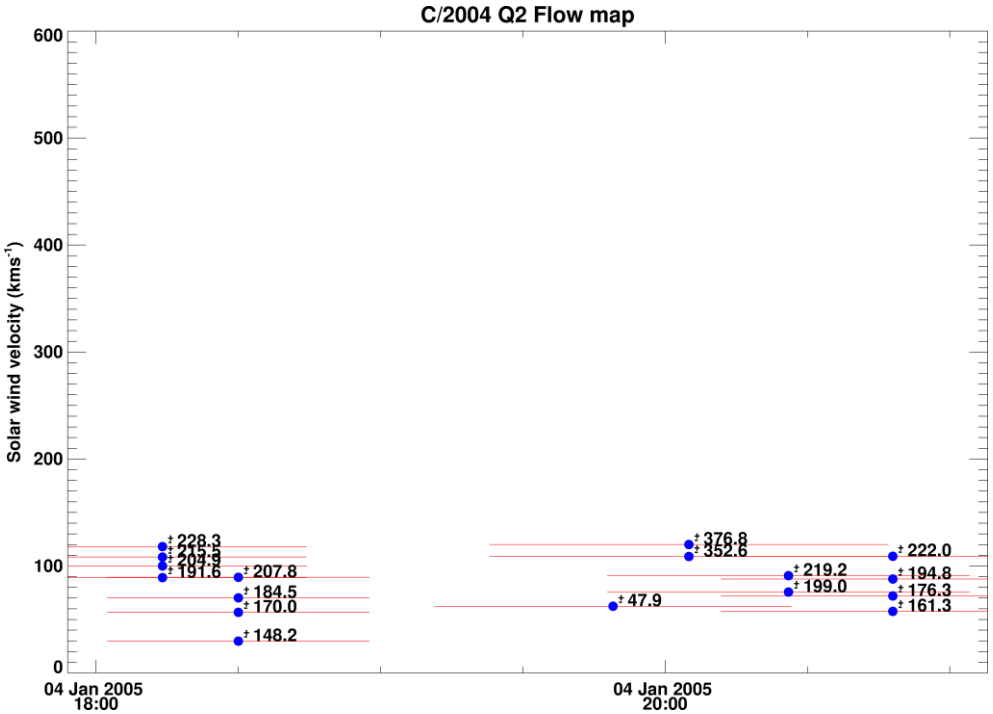

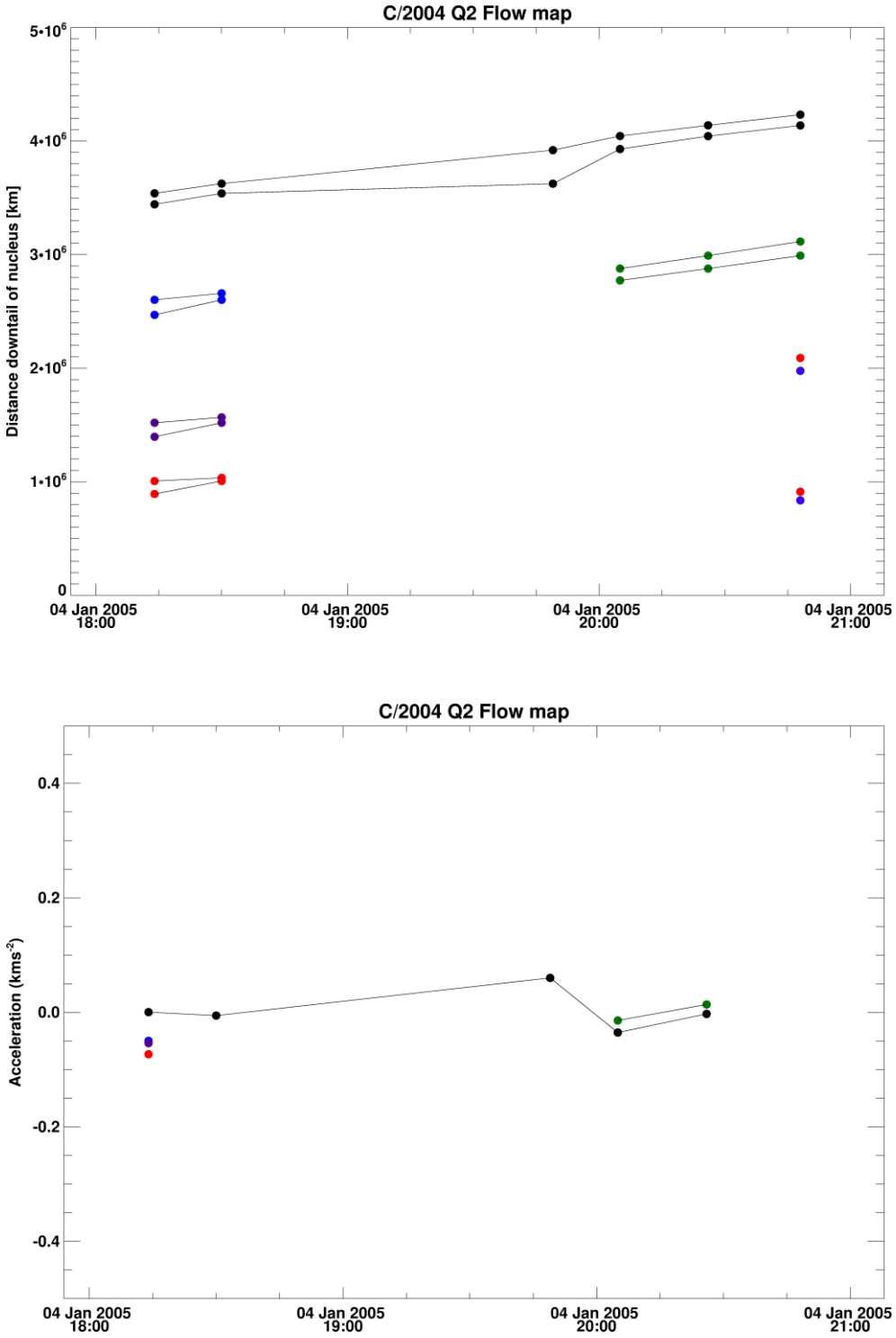

Figure 5.55: Each column of data in individual plots was extracted from the same image. Variations in the solar wind velocity are small enough to infer that the plasma bundles are moving downstream at a steady pace.

The derived velocities remain fairly stable showing no signs of acceleration. The outlier at 19:45 UT [Figure 5.55] producing a peak in the velocities is due to choosing a different section of the large plasma bundle to track.

January 7, 2005 – Multiple observations of two DEs

Images on the 7th January are split into two DE observations. The first was actively monitored by Japanese observers, but unfortunately the image of the tail was too faint to process. The European images yielded low solar wind velocities fluctuating about 100 km s^{-1} [Figure 5.56] for the near-radial propagation of the ion bundle. This implies that the kink may be influenced by a non-radial component of the solar wind. Data outliers are most probably linked to the timing inaccuracy and thus a larger velocity might be derived for an image falling in the wrong chronological order in the image sequence.

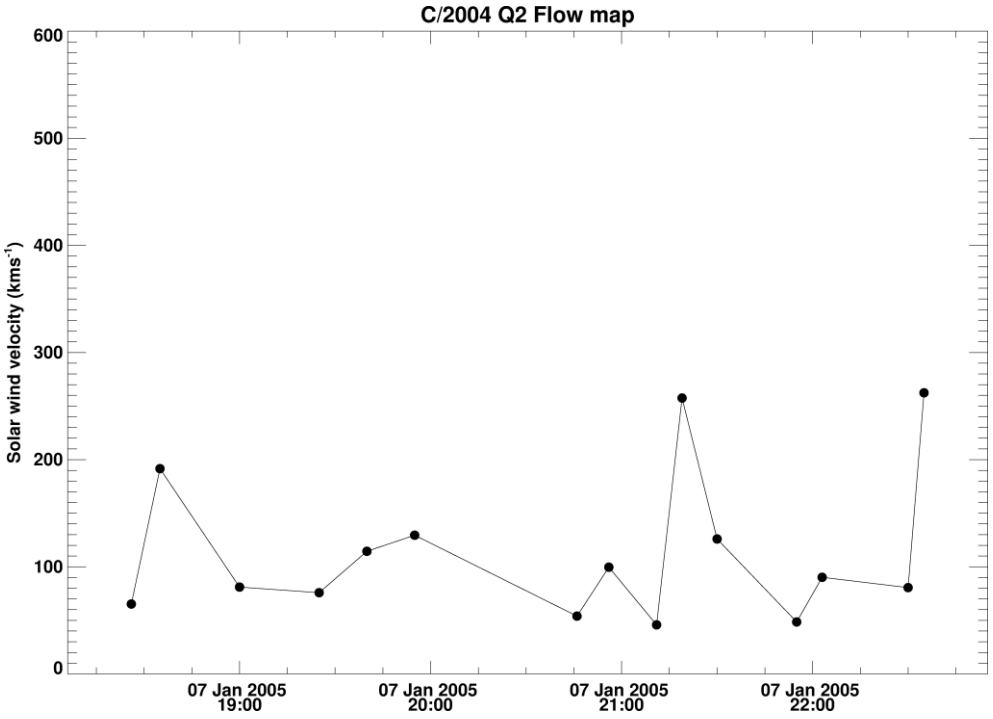

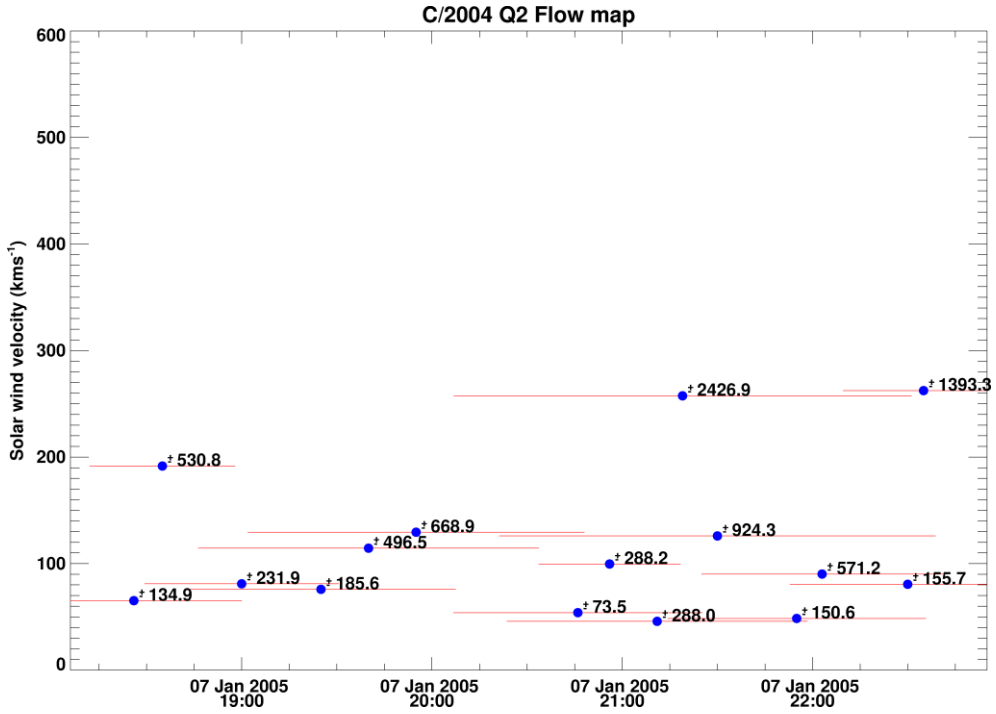
C/2004 Q2 Flow map
Solar wind velocity (kms-1)
600
500
400
300
200
100
0
± 2426.9
± 1393.3
± 530.8
± 668.9
± 924.3
± 496.5
± 288.2
± 571.2
± 155.7
± 231.9
± 185.6
± 134.9
± 73.5
± 288.0
± 150.6
07 Jan 2005 19:00
07 Jan 2005 20:00
07 Jan 2005 21:00
07 Jan 2005 22:00

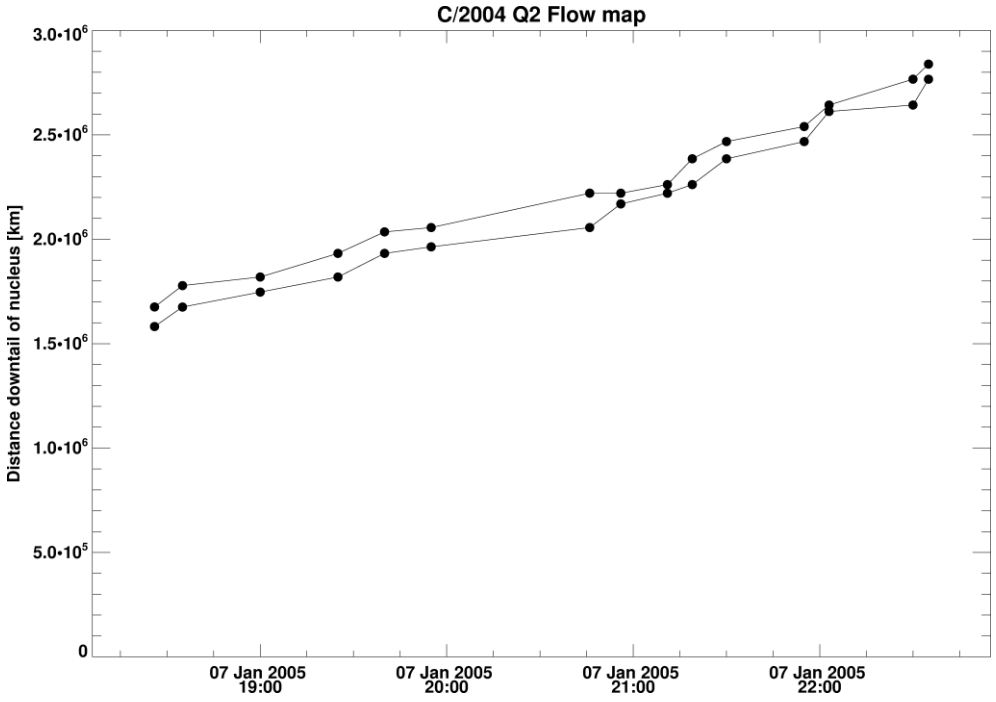
C/2004 Q2 Flow map
Distance downtail of nucleus [km]
3.0•10^6
2.5•10^6
2.0•10^6
1.5•10^6
1.0•10^6
5.0•10^5
0
07 Jan 2005 19:00
07 Jan 2005 20:00
07 Jan 2005 21:00
07 Jan 2005 22:00

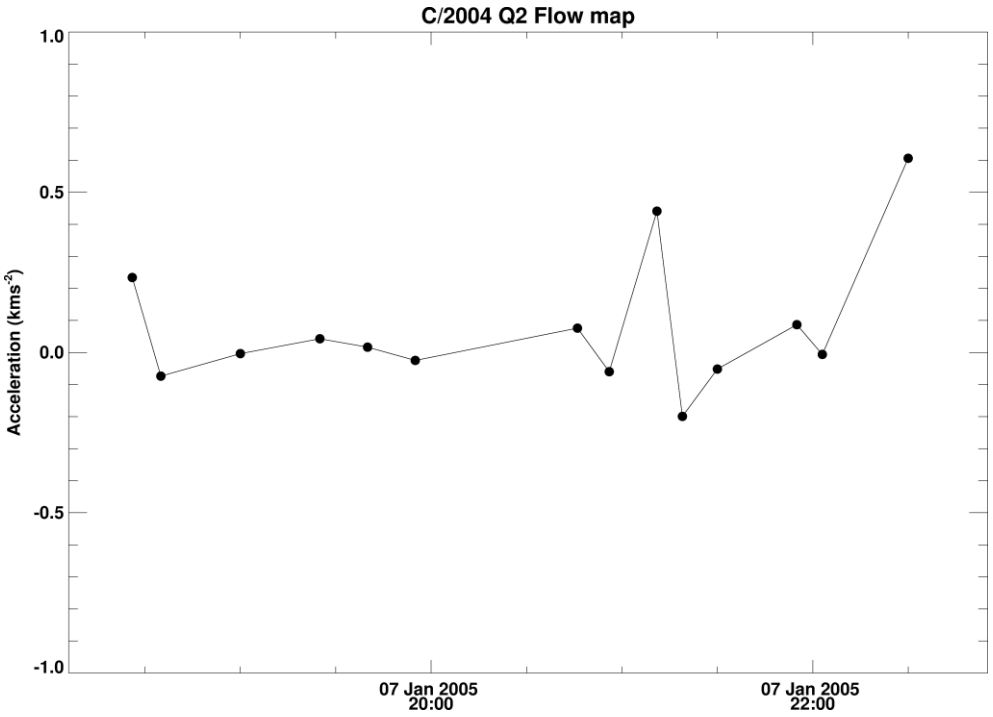

Figure 5.56: Each column of data was extracted from the same image. The kink moved near-radially along Sun-comet vector with little deviation along the y-axis.

January 10, 2005 – A kink and a forked tail

A large kink and a forked tail protruded in the opposing direction to the expected ion flow. The kink eventually evolved into a DE. The disconnected tail traced the Sun-comet vector as the main ion tail regained its usual state. The feature in black is the fork in the tail, believed to be formed from a folding ion ray and the disconnected tail. As seen, the forked tail is slowly undergoing acceleration, probably under the influence of the surrounding medium. The disconnected tail, in blue, remains close to the nucleus with most of its displacement along the y-axis.

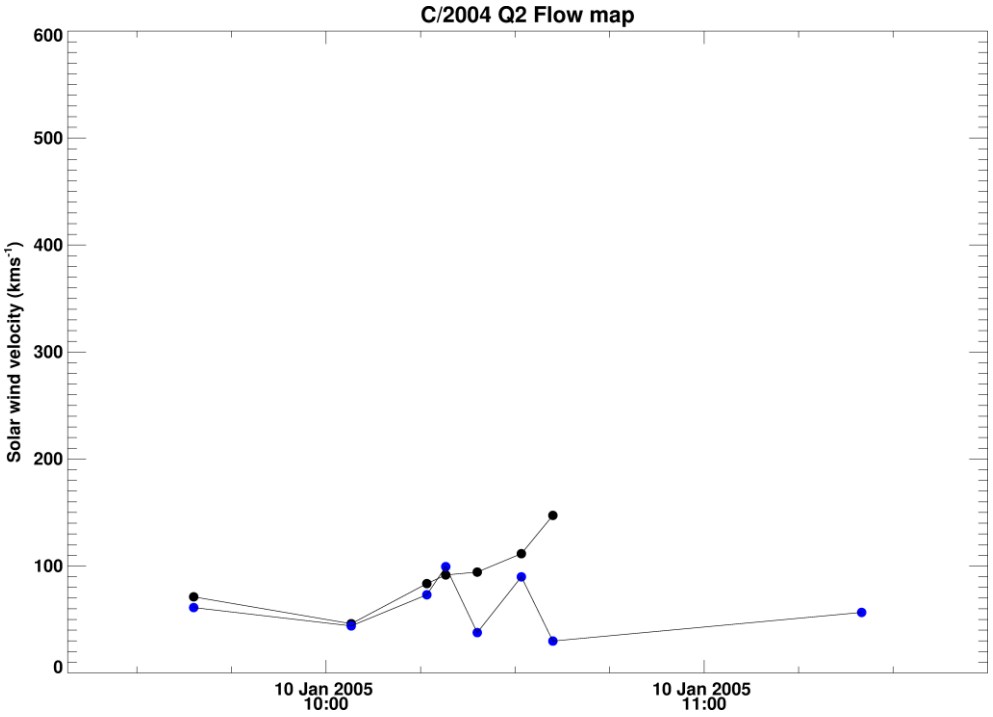
C/2004 Q2 Flow map
Solar wind velocity (kms-1)
600
500
400
300
200
100
0
10 Jan 2005
10:00
10 Jan 2005
11:00

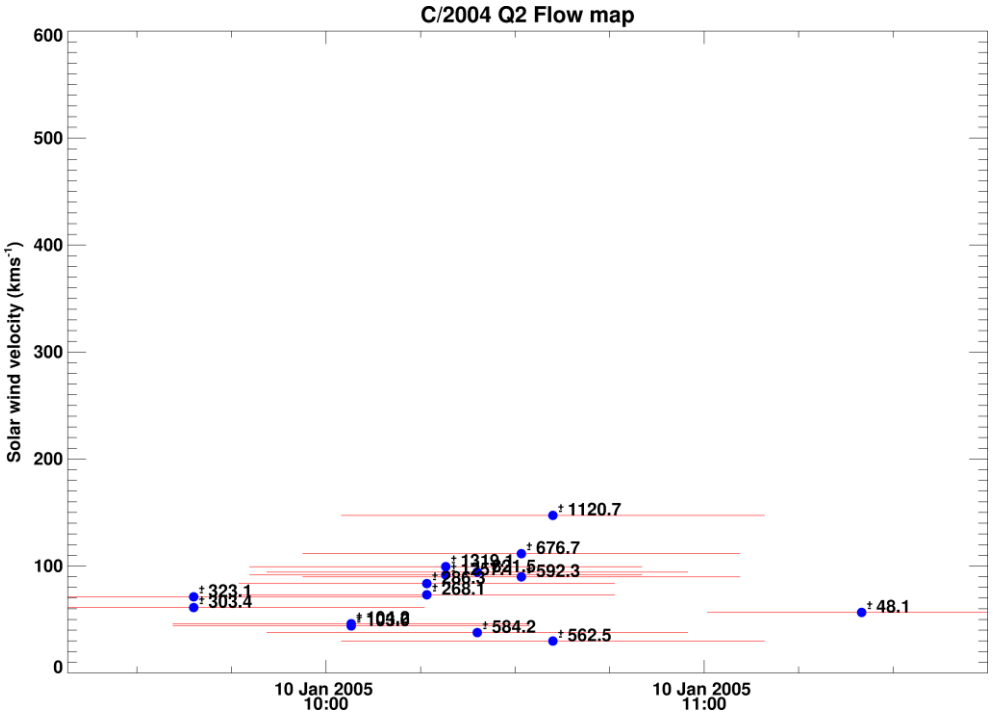
C/2004 Q2 Flow map
Solar wind velocity (kms-1)
600
500
400
300
200
100
0
1120.7
676.7
592.3
323.1
303.4
268.1
584.2
562.5
48.1
10 Jan 2005
10:00
10 Jan 2005
11:00

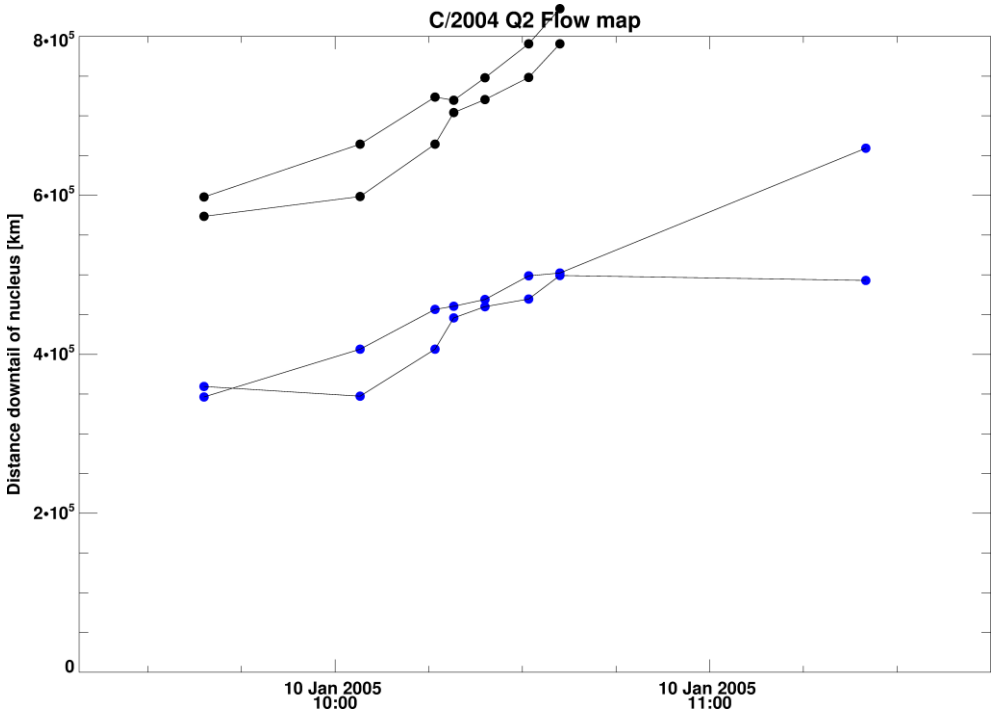

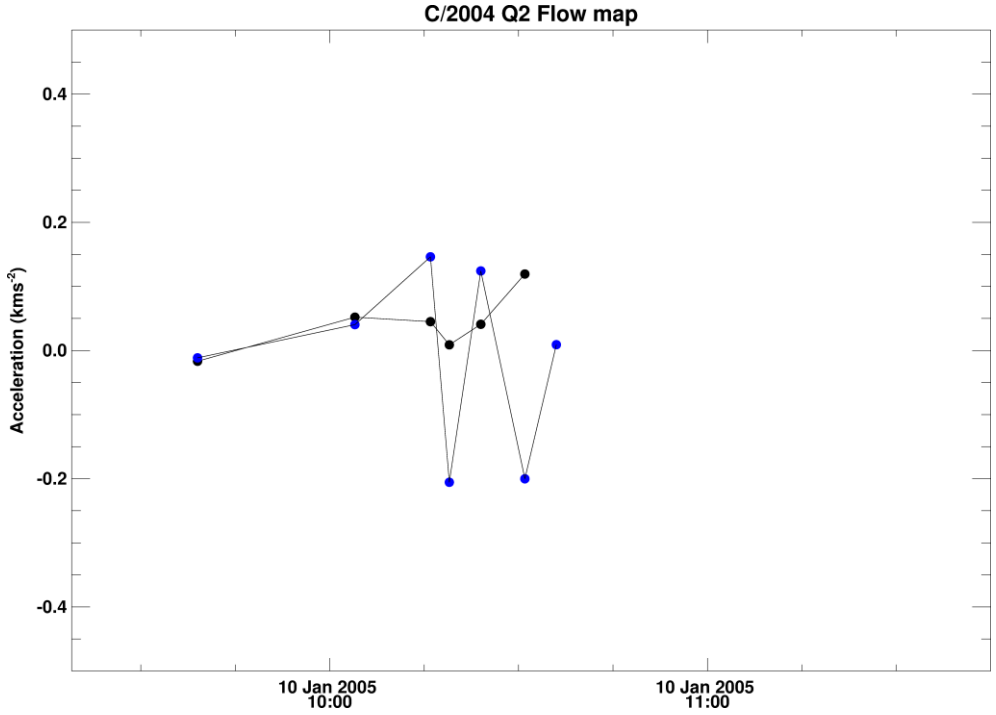

Figure 5.57: Each column of data was extracted from the same image. The forked tail (in black) accelerates to slow solar wind speeds towards the end of observations. The disconnected tail alternates between accelerating and decelerating over a short space and time.

It is clear that complex ICMEs act as a major tail disruptor. If identification of ICME interaction with ion tails and the flow vector map constraints prove useful to the solar physics community, then a more intricate treatment of the ICME SAT will be required in each instance. So far, the velocity vector maps have not yielded any interesting results aside from the Koprolin feature maps. In fact, the low velocities derived for most of the images are intriguing. This would imply that velocities derived via the flow vector maps underestimate the solar wind velocity, though the radial velocities aligned well with the extrapolated ACE solar wind measurements. Thus, the radial velocity technique is a better measure of the global bulk plasma speed and the vector maps provide a better estimate of condensation knot/kink/DE velocities in the orbital plane of the comet.

5.1.3.3. Folding Ion Ray Velocities

A handful of images were chosen from a series of animations to determine the radial closing rates of folding ion tail rays. These studies had previously been undertaken solely looking at the angular closing rate per hour without comparison to the local solar wind velocities. The heavily mass loaded solar wind velocities reported will be in the conventional km s^{-1} units. These will typically be much lower than the radial velocity estimates as the tail rays are still undergoing acceleration.

January 3, 2005

The image sequence on the 3rd January shows a DE with well-formed symmetrical pairs of ion folding rays merging to form a new ion tail, shortly after disconnection. Figure 5.59 shows a recreation of the ion tail rays from 3 samples taken at the start, middle and end of each tail ray. The tail ray is expected to move radially and thus the location where the ion tail ray and the radial vector coincide are measured in consecutive images. The top and bottom tail rays in the first set of images are given in red and blue respectively and the new locations of the top and bottom tail rays are in black and blue respectively. The velocity plots show the tail ray velocities with respect to time and their radial distance from the nucleus. Measurements are ordered by

colour, with blue, purple and red referring to the first, second and third sample. We would expect the velocity measurements at the far end of the tail ray to be larger than the first measurements.

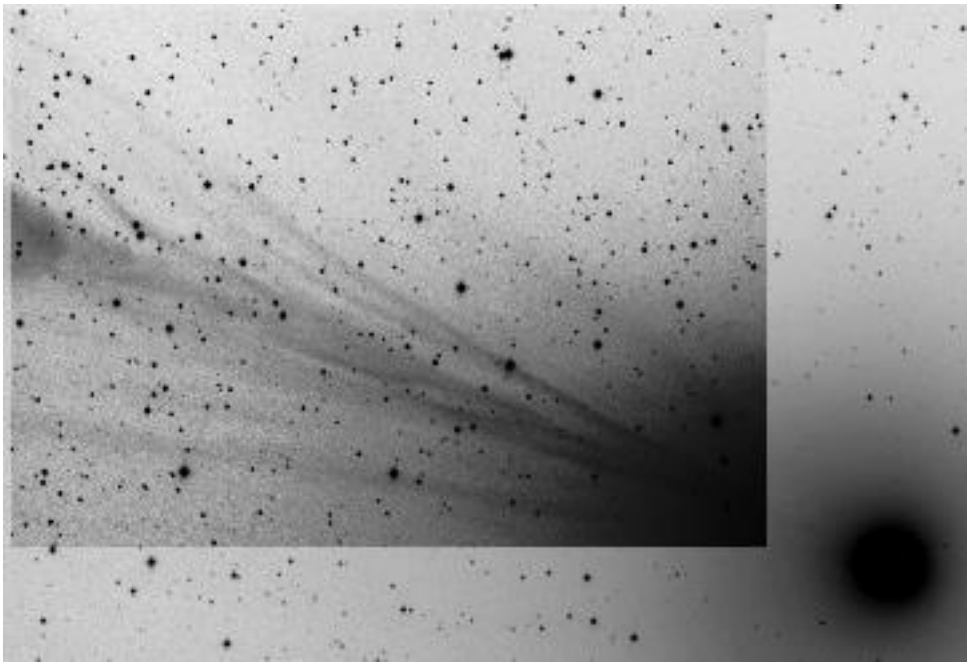

Figure 5.58: Sample of Schedler animation of comet C/2004 Q2 on 03/01/2005 19:30 UT. A folding ion ray changes orientation in response to the solar wind upstream of the comet head.

A contrast-enhanced image of the ion tail on 03/01/2005 shows the meandering nature of the folding ion rays as they dynamically respond to the HMF orientation upstream [Figure 5.58]. Due to the curving nature of the folding rays, the velocity profile down the tail ray axis for half of the top tail rays is contrary to theoretical expectations [Figure 5.60], with tail end velocities decreasing with increasing distance and time. Ion tail rays have been previously observed to curve and lengthen as they fold about the main tail axis, though in the inverse sense to the Schedler tail rays.

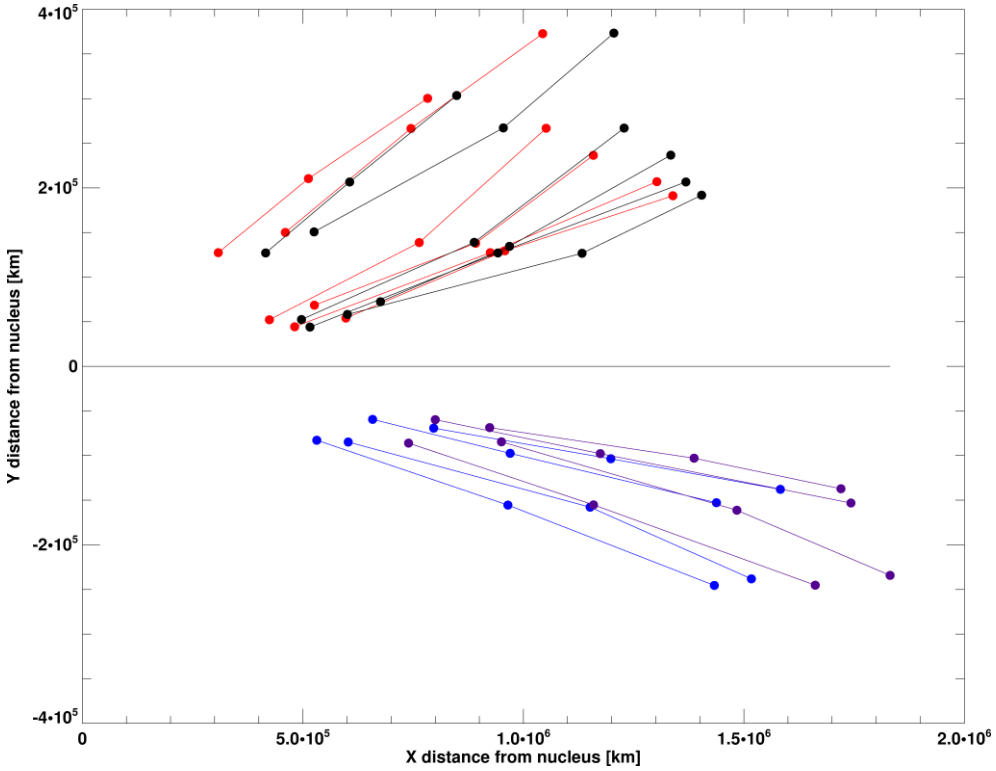

Figure 5.59: Recreation of ion tail rays sampled from animation sequence. Red and blue lines are folding rays sampled in first image. Black and purple lines are their new positions in the second image.

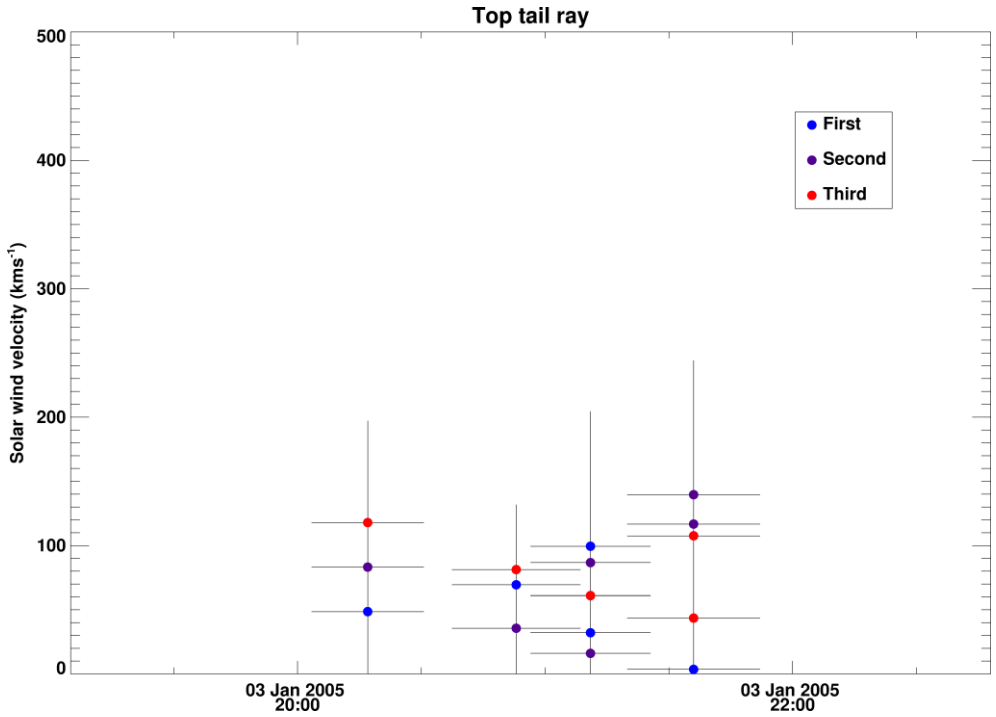

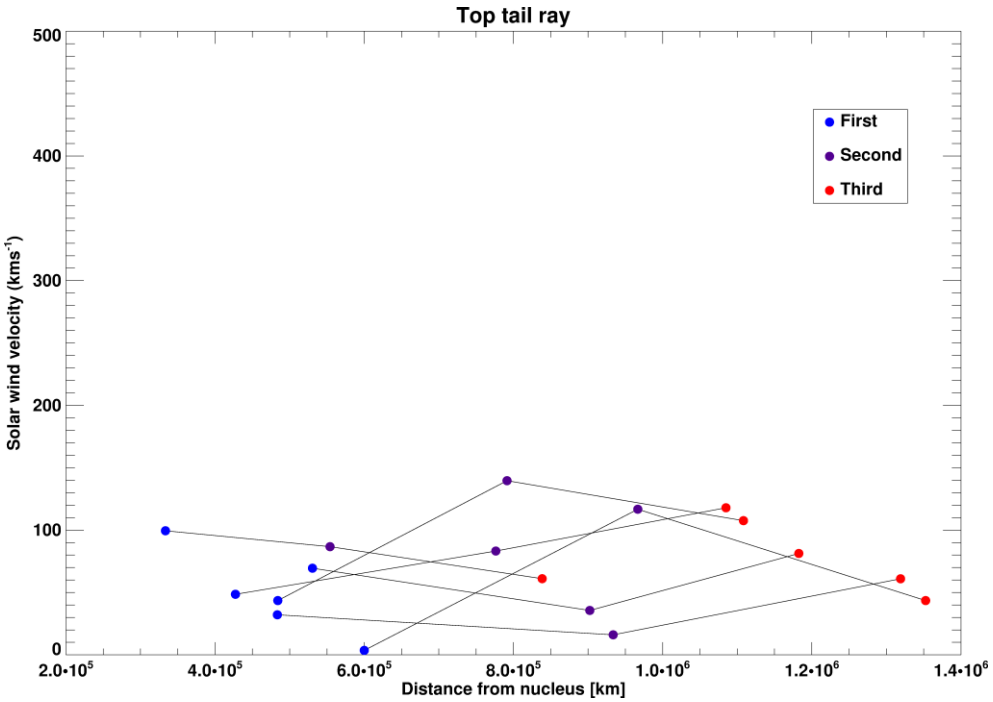
Top tail ray
Solar wind velocity (kms^{-1})
Distance from nucleus [km]
First
Second
Third
500
400
300
200
100
0
2.0•10^5
4.0•10^5
6.0•10^5
8.0•10^5
1.0•10^6
1.2•10^6
1.4•10^6

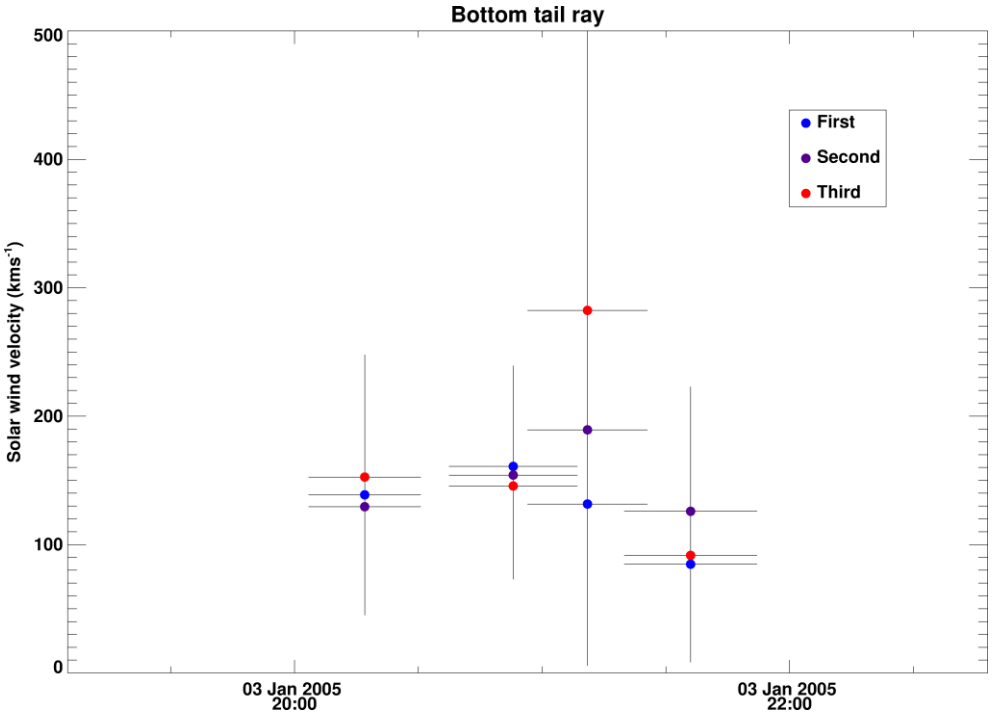
Bottom tail ray
Solar wind velocity (kms^{-1})
First
Second
Third
500
400
300
200
100
0
03 Jan 2005
20:00
03 Jan 2005
22:00

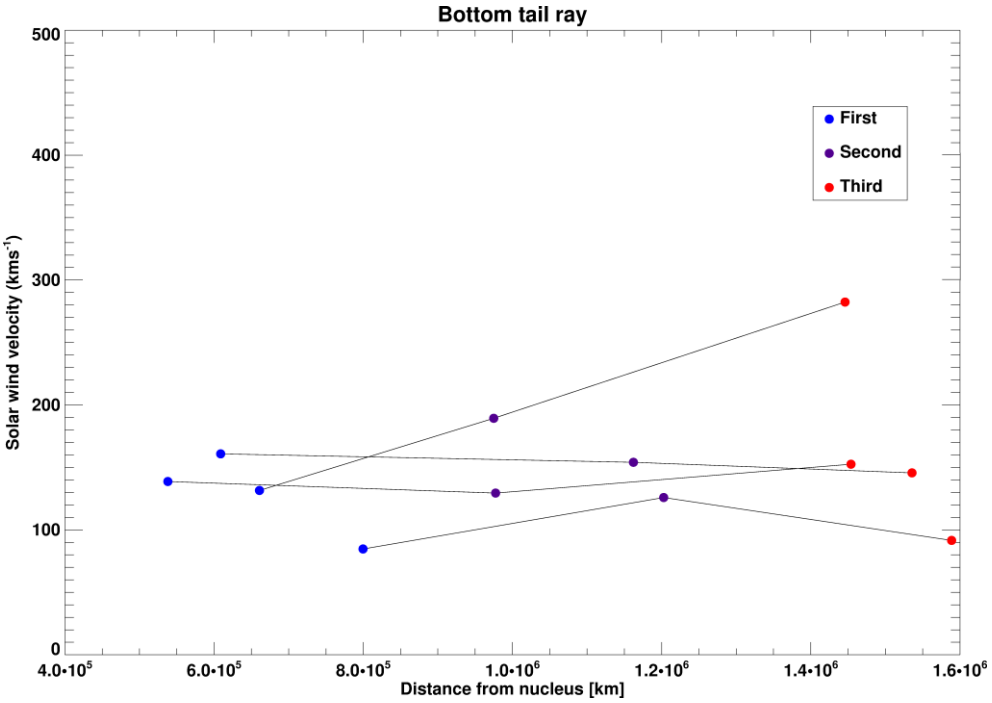

Figure 5.60: Tail ray velocities for bottom and top tail rays. Left plots show their variation in time. Plots on the right show their variation with increasing distance from nucleus. The legend 'First, Second and Third' indicate the first, second and third measurement taken along the tail ray.

January, 4, 2005

Figure 5.61 is a recreation of the tail rays sampled on January 4, 2005. As seen in Figure 5.62, the velocities increasing with distance along the folding ray axis match well with our current paradigms. The folding ion tail rays were straighter for this period.

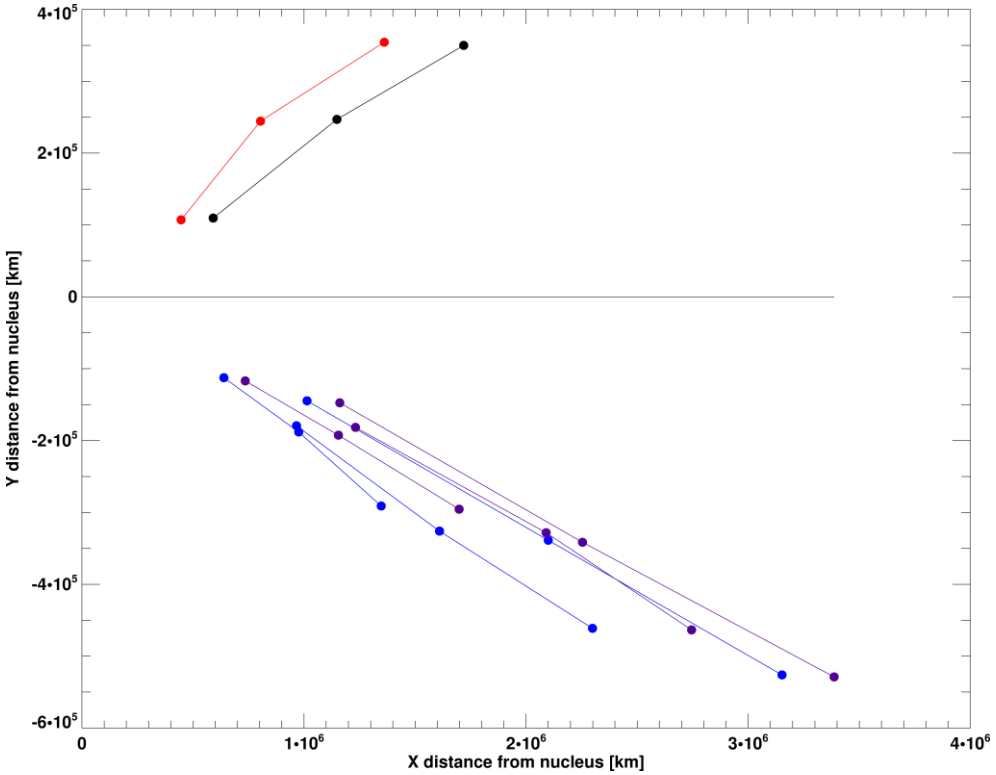

Figure 5.61: Recreation of ion tail rays sampled from animation sequence. Red and blue lines are folding rays sampled in first image. Black and purple lines are their new positions in the second image.

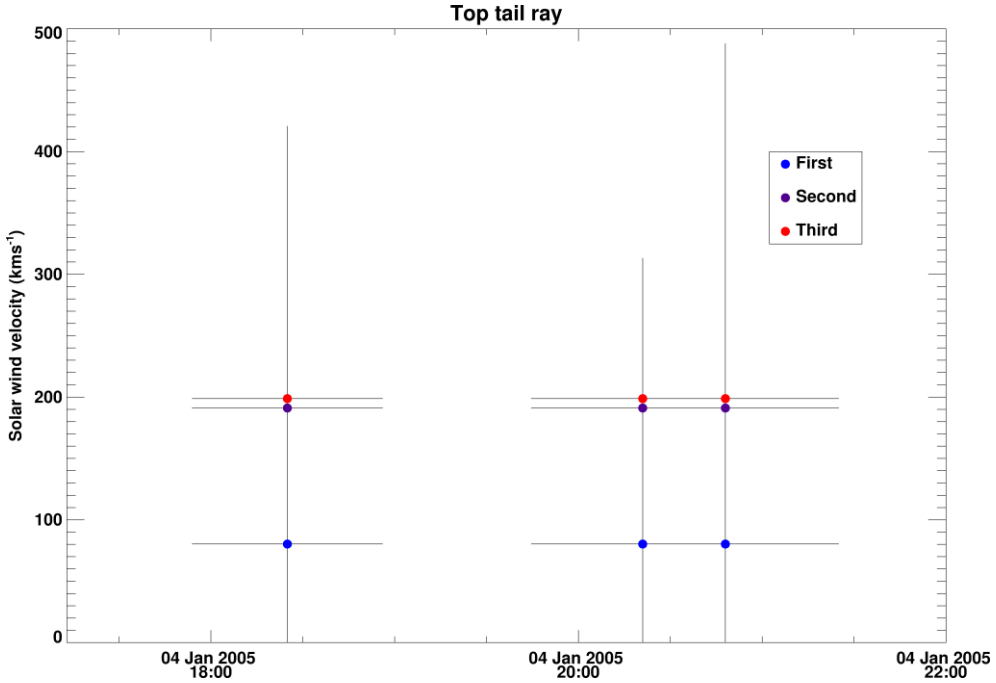

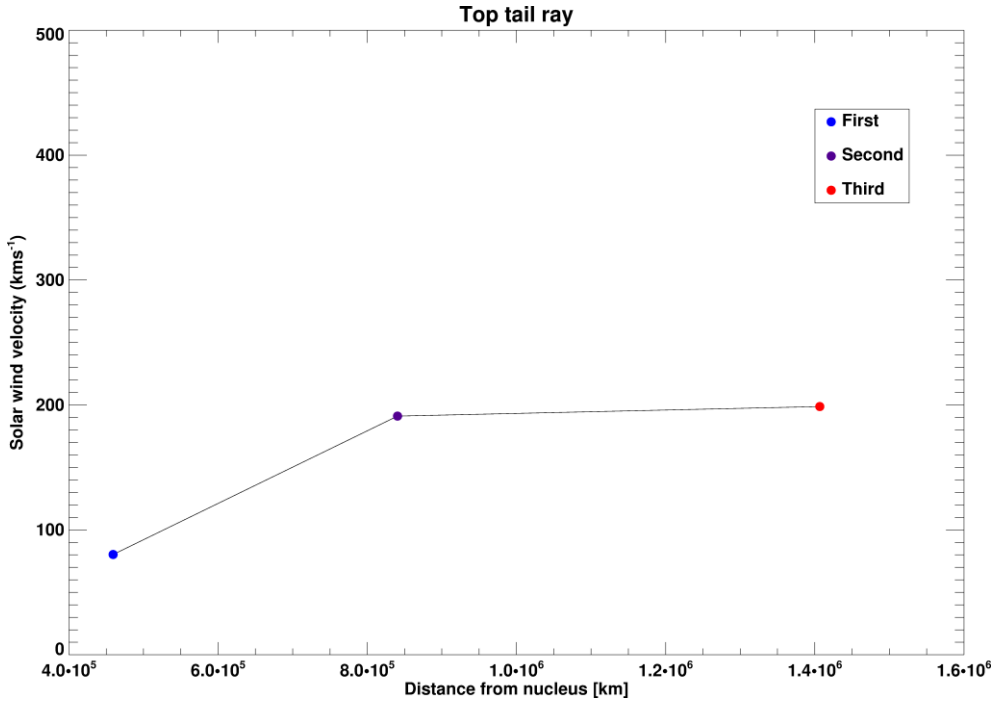
Top tail ray
Solar wind velocity (kms^{-1})
500
400
300
200
100
0
First
Second
Third
4.0•10^5
6.0•10^5
8.0•10^5
1.0•10^6
1.2•10^6
1.4•10^6
1.6•10^6
Distance from nucleus [km]

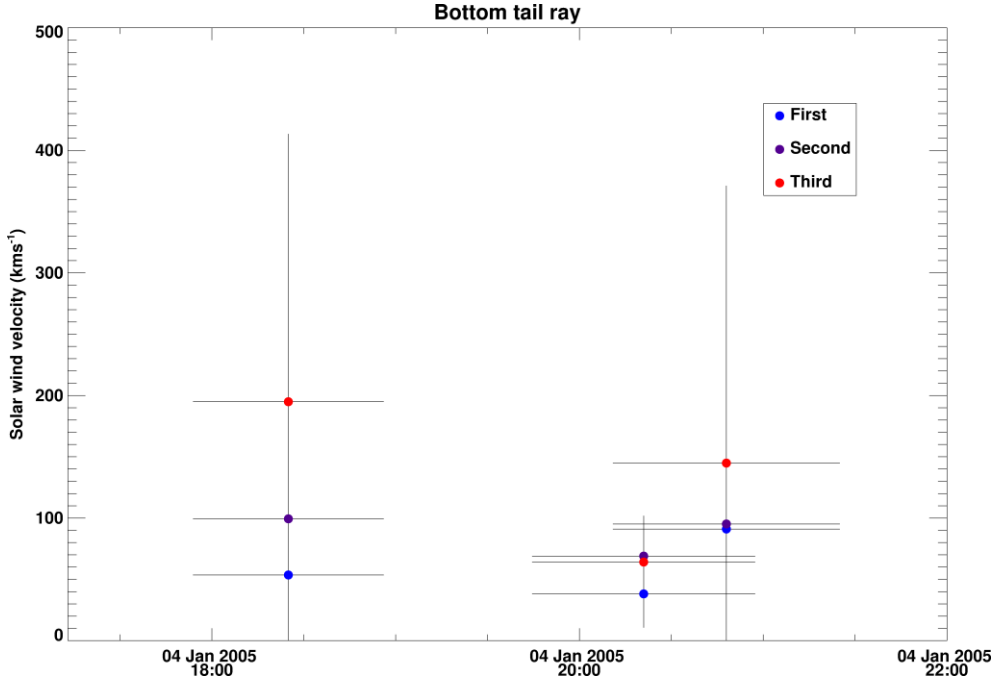
Bottom tail ray
Solar wind velocity (kms^{-1})
500
400
300
200
100
0
First
Second
Third
04 Jan 2005
18:00
04 Jan 2005
20:00
04 Jan 2005
22:00

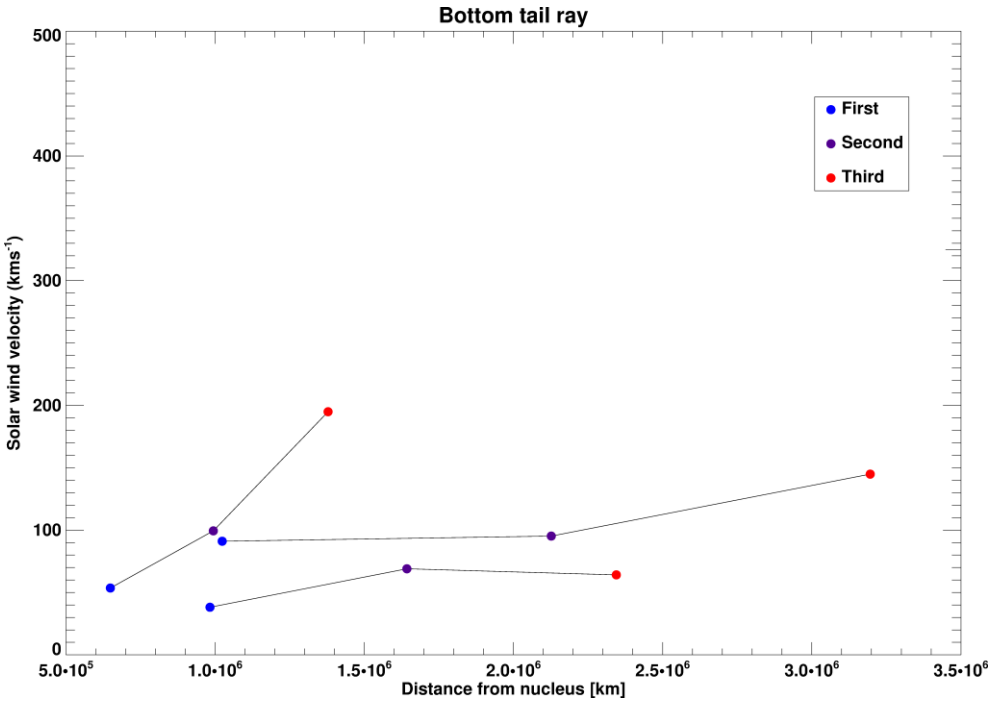

Figure 5.62: Tail ray velocities for bottom and top tail rays. Left plots show their variation in time. Plots on the right show their variation with increasing distance from nucleus.

Degroote et al. (2009) reports tracking the evolution of two ion tail between two observations taken with a U-band filter on January 12, 2005, deducing the structure's velocity to be ~235 km s^{-1} at about 3000 km from the nucleus. Distances derived with my technique are lower at a larger distance from the comet head.

5.1.4. Conclusion

Comet Machholz was a complicated comet combining a fortuitous geometry, with some tricky elements, with extensive periods of turbulent solar wind activity, the nature of which has been successfully identified in many cases. The alternative flow vectors technique is useful in elucidating non-radial components of the solar wind and its transient events, albeit yielding lower than expected velocities. It is especially useful in tracking the expansion and acceleration of ICME-comet ion tail interactions. Constraining the list of ICME interaction candidates is a useful exercise although determining a linear speed from the Sun to the comet is not a realistic method of interpreting this transient structure, as these structures are expected to change in

speed. A deeper study involving all the forces acting upon the ICME is required before an interaction candidate can be determined for each event.

5.2. Comet C/2001 Q4 (NEAT)

Comet NEAT, the second near-Earth comet that I studied, reached perihelion in 2004 with a peak m_v of >~+3. With a large orbital inclination, comet NEAT was a good candidate to probe the heliolatitudinal variations of the solar wind and identify the latitudinal boundary between the fast and slow solar wind regions. Similarly to comet Machholz, comet NEAT came within 0.321 AU of the Earth near its perihelion. The comet crossed the region within 10^o of the ecliptic in only a few days. Coupled with its longitudinal separation from the Earth, the comet's path did not allow for reliable extrapolation of near-Earth solar wind data to its vicinity. The comet's orbital elements were Inclination (*i*) = $99^o.6$; eccentricity (e) = 1.00; Perihelion date (T) = 15/05/2004, 23:10 UT.

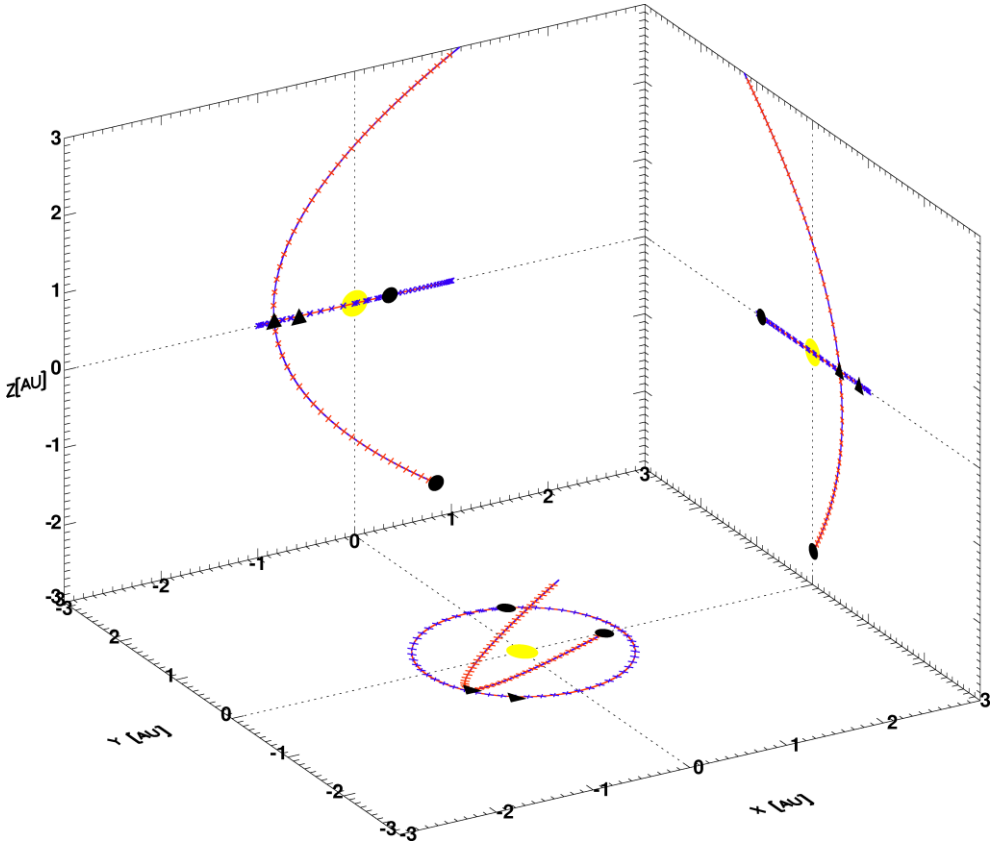

Figure 5.63: Heliocentric aries ecliptic coordinates of comet C/2001 Q4 (NEAT). Black circles represent the start of the orbits and black triangles show the positions of the comet and the Earth at the comet's perihelion.

Figure 5.63 and Figure 5.64 here show the orbit and data coverage of comet C/2001 Q4 (NEAT) when most of the observations, analysed here, were undertaken. In Figure 5.63, starting in early December 2003, the orbits have been dissected into weekly time steps until late December 2004. As used previously for comet Machholz, the black circles represent the first data point of each orbit and the triangles are the positions of the Earth and the comet at comet NEAT's perihelion. Most of the observations were centred around perihelion.

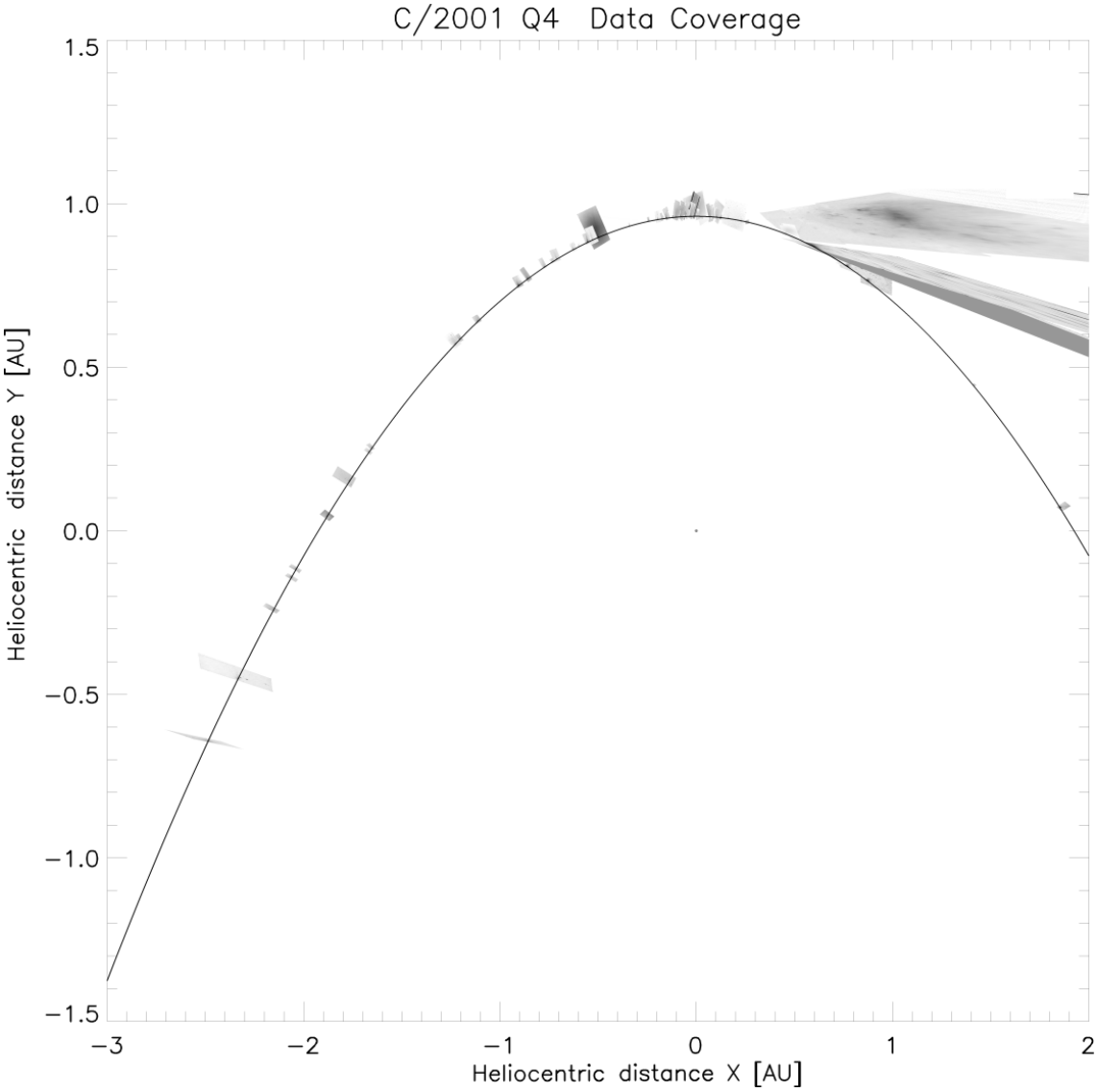

Figure 5.64: The images and comet NEAT's orbit projected and mapped onto the comet's orbit in heliocentric aries ecliptic coordinates. The plot above was transformed so that the positive y-axis is defined as the direction to perihelion. Chronologically, observations begin from the right and move leftwards.

Image statistics

250+ images are available in my catalogue. Of those, 167 images were successfully plate solved. 38 images were rejected due to poor astrometry. 66 of the remaining images were excluded for reasons that included a lack of a visible ion tail or low data quality. Ultimately, 64 images were successfully processed through the entire pipeline with a total of 211 solar wind velocity estimates. 7 samples were rejected as unreliable due to the faintness of the ion tail in

some of the images and one set of measurements was taken from a tail ray system. 103 samples were taken during periods of disturbed solar wind.

5.2.1. Radial Solar Wind Speeds

In Figure 5.68, Figure 5.73 and Figure 5.83, I also mark the data acquired during low orbit plane angle in purple since they are a geometrical happenstance and an unavoidable element of this technique. These should still show radial velocities though if we are looking along XZ plane, instead of XY. In green, I include image-related issues, such as where the ion tail and dust tail overlap and faint images in addition to show where the ion tail straddles the radial vector. Only instances where these were problematic but not impossible to derive a solar wind velocity estimate were highlighted.

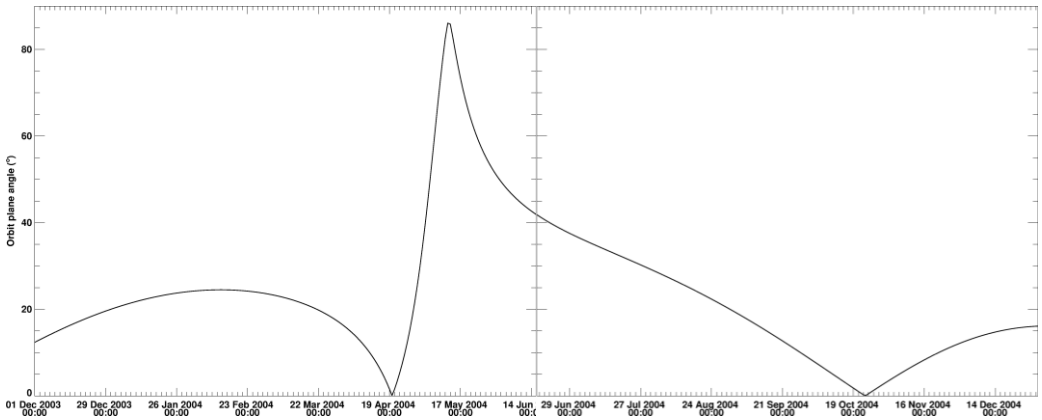

Figure 5.65: Orbit plane angle for comet C/2001 Q4. Minor time steps are for every 2 days, running from 1st December 2003 to 31st December 2004.

For most of the observing period when the orbit plane angle was small [Figure 5.65], comet C/2001 Q4 (NEAT)'s ion tail was embedded within the dust tail from our perspective. What we see here is the thickness of the dust tail as it lies on the comet's orbital plane. Thus, estimates of the local solar wind velocity for that time period were considered unreliable and not included in the samples shown below. This effect was further enhanced as the comet was particularly dusty: its large diffuse dust tail often obscured the ion tail [Figure 5.66]. This made accurate determination of the solar wind velocity trickier than with comet C/2004 Q2 (Machholz). The inbuilt contrast enhancement within my software could not resolve the structures close to the ion

tail as well for the image shown in Figure 5.66. Every image was not manually enhanced prior to processing due to the large size of the image catalogue. Comet NEAT is on a highly inclined orbit (~100^{o}) to the ecliptic, so it will only experience the same solar wind structure as the Earth for a very brief period around the comet's perihelion (15th of May 2004).

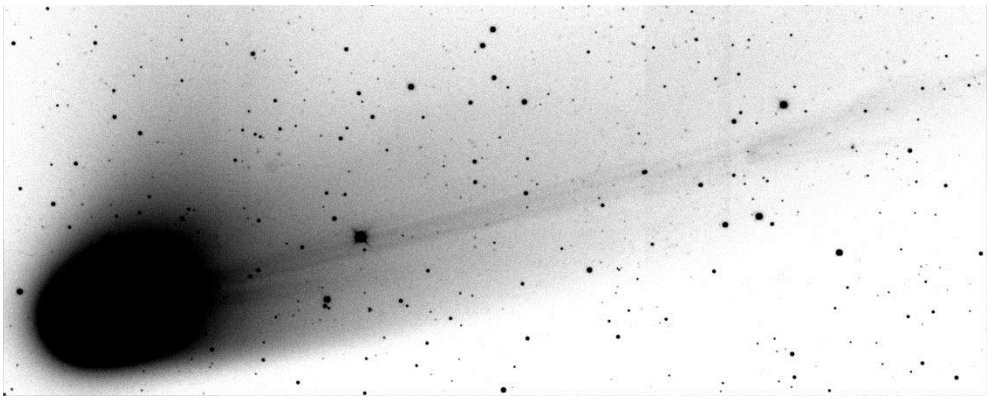

Figure 5.66: High contrast image of C/2001 Q4 (NEAT) by Mikuz taken on 23/05/2004 at 20:40 UT at peak orbit plane angle. The image was contrast enhanced using commercially-available software. A rudimentary contrast enhancing feature was combined with the IDL software though the level of detail is not as easy to achieve.

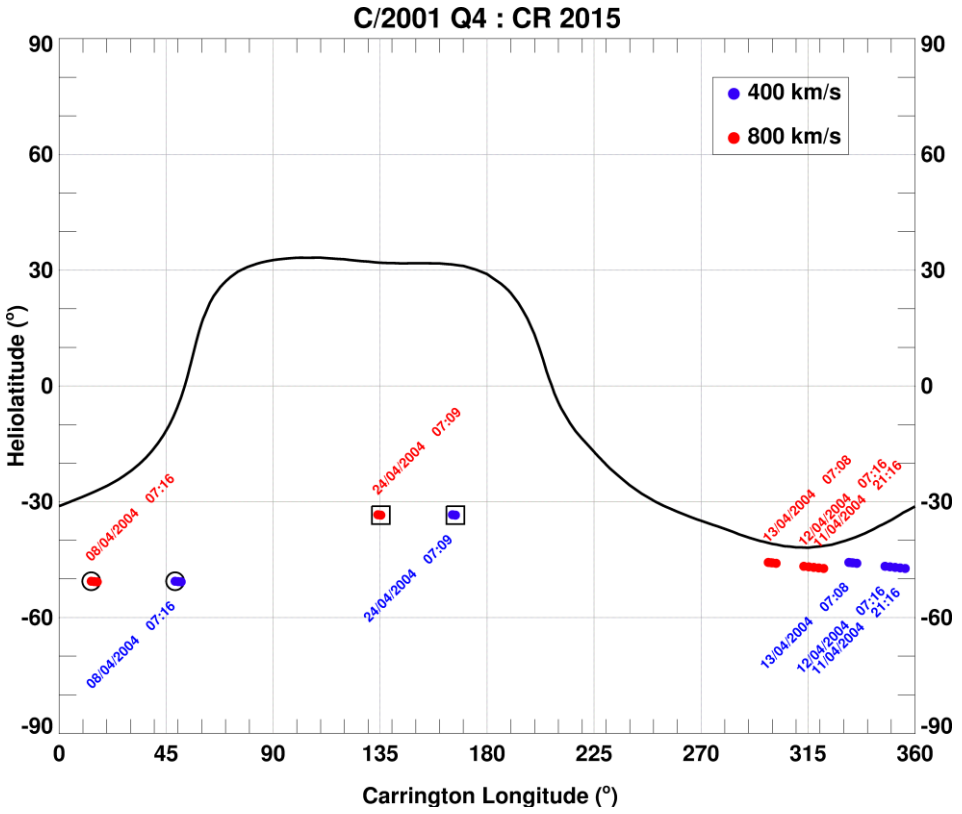

Figure 5.67: Mercator map for CR 2015.

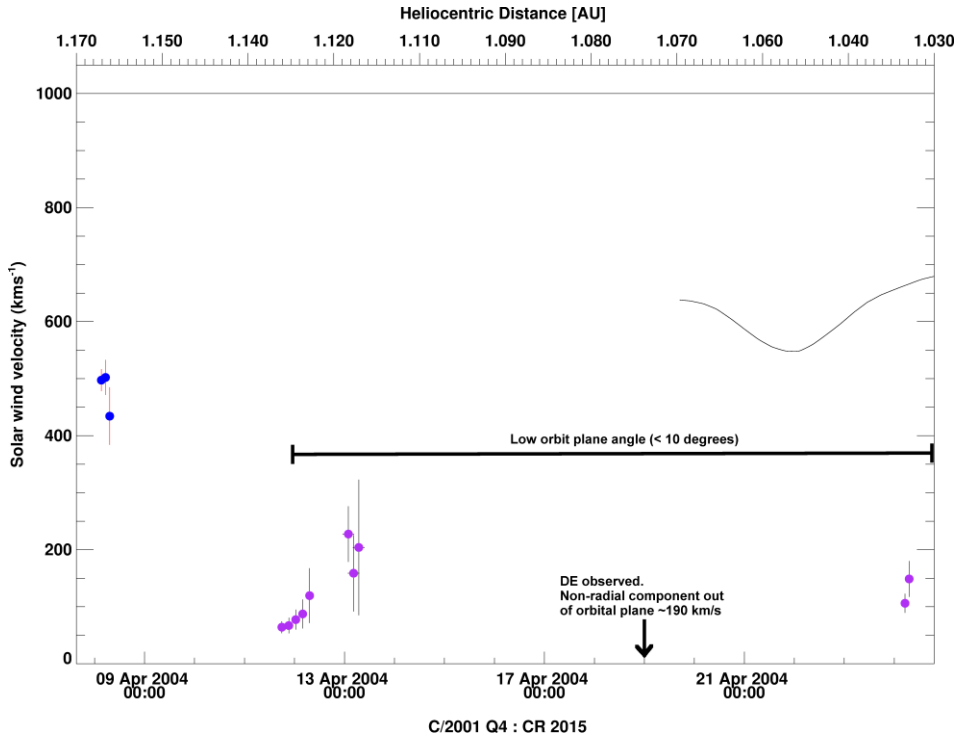

Figure 5.68: Solar wind velocities for C/2001 Q4. Most of the velocities in this CR were taken whilst the orbit plane angle was low.

For CR 2015, the comet was encountering very slow solar wind velocities originating near the approximated neutral sheet on the solar wind source surface. By the 24th April, comet NEAT should be experiencing high solar wind speeds since the sources are far from the neutral line, however my inferred speeds remain around 100 - 150 km s^{-1} [Figure 5.68]. The very large tail aberrations observed during this epoch are due to non-radial flows out of the comet's orbital plane and are not a good measure of the radial solar wind velocity. The velocity estimates from the 12th to 13th April were extracted from only two images. It bears repeating that images with a strong dust component that are extrapolated at low orbit plane angles deteriorate rapidly and become increasingly unreliable. This makes it hard to demarcate the ion tail from the general background [Figure 5.69].

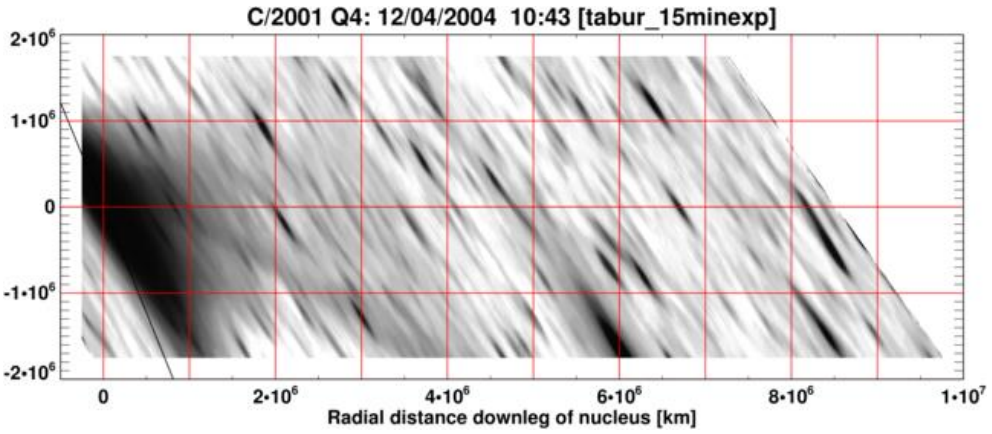

Figure 5.69: Best mapped image of comet NEAT at low orbit plane angles. This is a 15 minutes exposure by Tabur on 12/04/2004 10:43 UT.

The large aberration angle here implies a 40 km s^{-1} non-radial flow of the solar wind, which is within the scale deduced for comet C/2004 Q2 and C/2001 Q4 (§ 5.2.2.1).

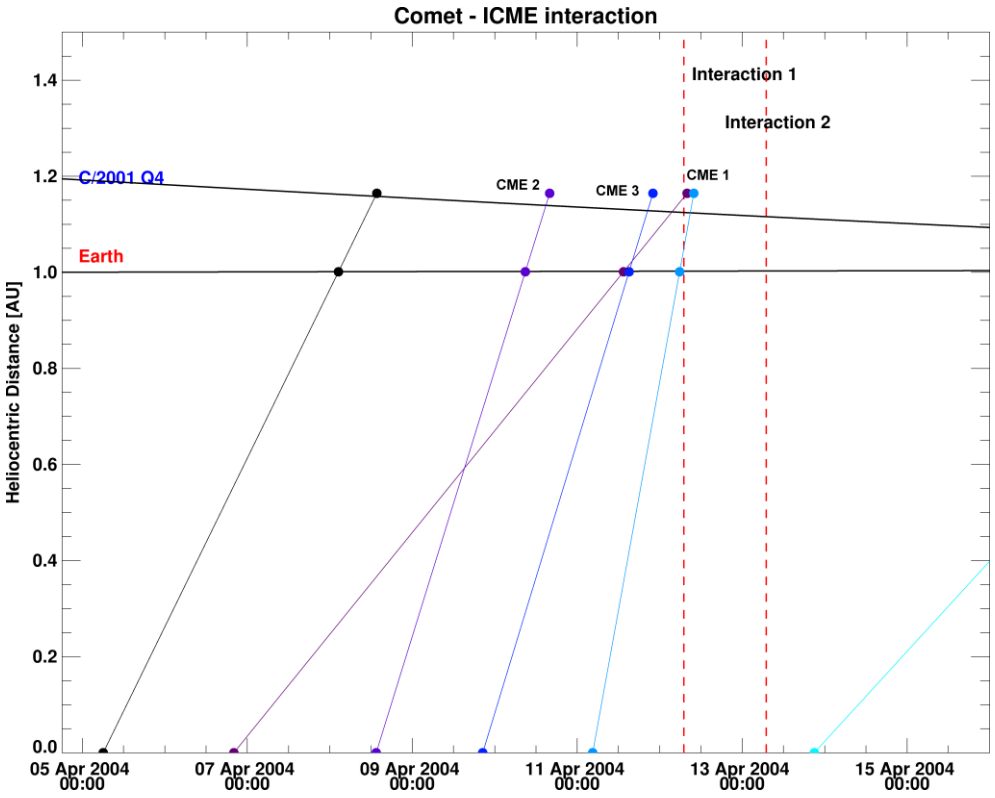

Figure 5.70: ICME SATs at C/2001 Q4. Interaction 1 and 2 mark the two images measured on 12th and 13th April 2004.

The ENLIL MHD model for CR 2015 had been requested, though an incorrect input magnetogram meant that it was unusable. This analysis is therefore supplemented with a high resolution simulation model using a magnetogram from Mount Wilson Observatory. The inner boundary condition is set by the WSA model and its outer boundary limited to 10 AU. The larger than usual outer boundary does not affect the MHD solution computed at 1 AU. The lower and upper bounds for the latitudinal grid are set to ± 44^{o} and thus comparisons could not be drawn for the 12th and 13th April 2004, where the comet was at heliographic latitude ~ -47^{o}. Time being a limiting factor, a new run was not requested for these two events when it is obvious that the low orbit plane angle is the primary influence for the low velocities recorded. An ICME linear traveltime map [Figure 5.70] is considered as an alternative approach to determining the solar wind conditions; CMEs 1, 2 and 3 are identified as potential interaction candidates and could induce a tangential component in the surrounding plasma flow, with the last two ICMEs being far more likely candidates when factoring in the non-linear propagation of ICMEs.

A DE was observed when the observer crossed the comet's plane between the 18th and 19th April 2004. The new ion tail and the disconnected tail are both leading the comet's motion. There are no ICME impactors predicted to arrive at the comet in time. There are no enhancements in the magnetic field or the number density of the solar wind from the ENLIL model output at the comet's location. At most, the non-radial longitudinal component of the solar wind at the comet would be ~ 5-10 km s^{-1} and cannot explain the disturbed tail morphology. Without further evidence, the exact cause of the DE could not be determined. Despite the blurriness of the extrapolated images, a rudimentary tracking of the DE yielded a surprisingly large non-radial velocity component out of the comet's orbital plane of 193.9 km s^{-1} and 189.4 km s^{-1} for the top and bottom end of the DE [Figure 5.71]. The formal uncertainties on these errors were enormous, in the range of 10^5 km s^{-1}, and almost undoubtedly exaggerated due to the extreme observing geometry. This stems from the large projected image size (~10^{13} km) when extrapolated along our line-of-sight.

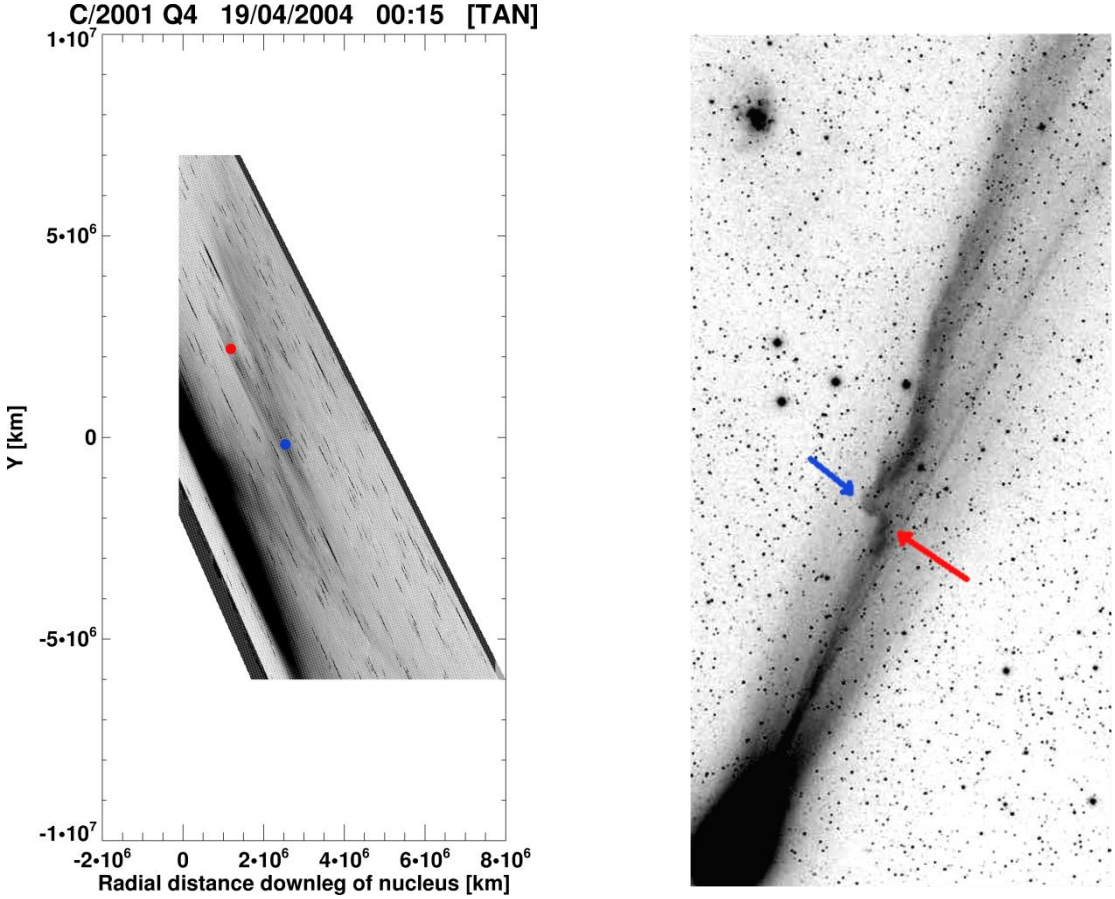

Figure 5.71: Contrast enhanced image of C/2001 Q4 depicting a DE captured by Tan on 19/04/2004 at 00:15 UT. The mapped image is shown on the left with the top (red) and bottom (blue) sampled locations marked.

CR 2016

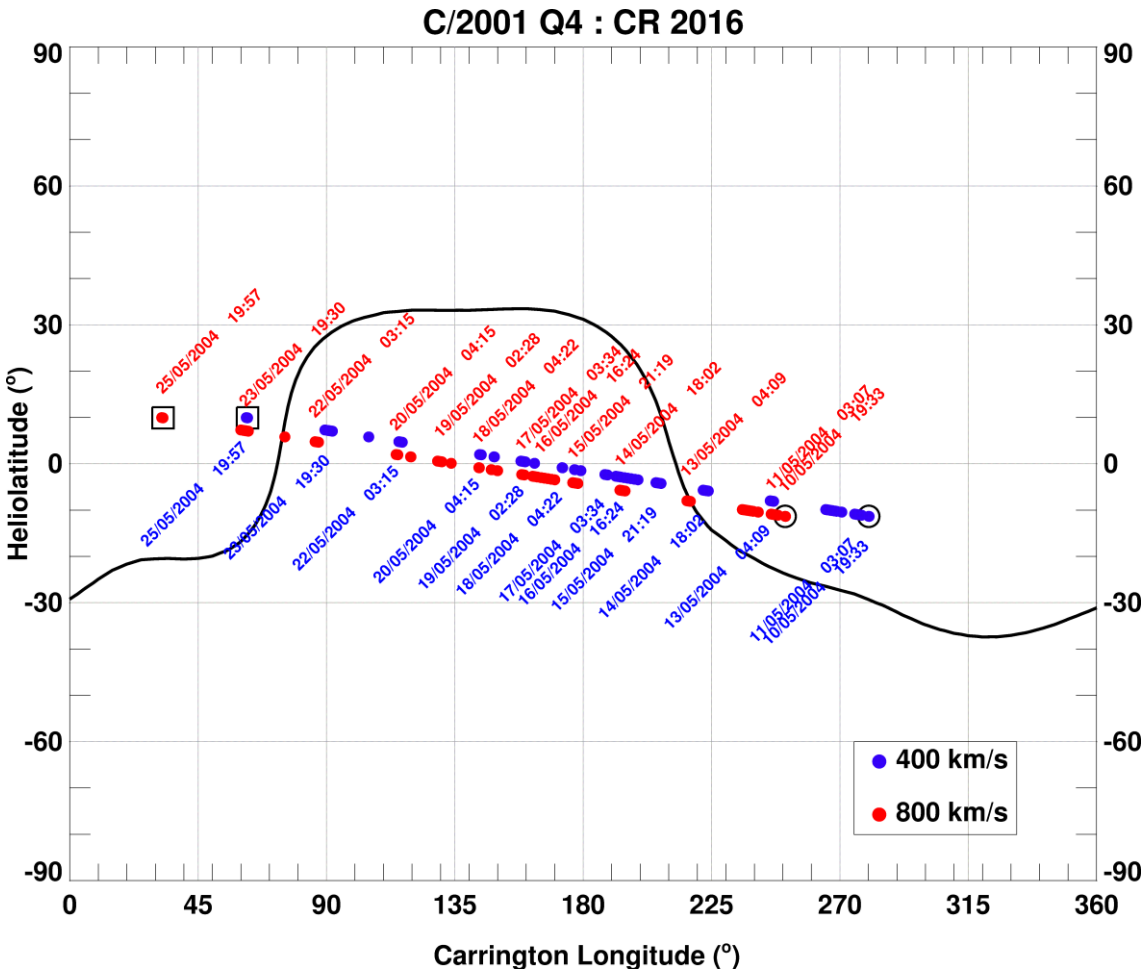

Figure 5.72: Mercator map for CR 2016.

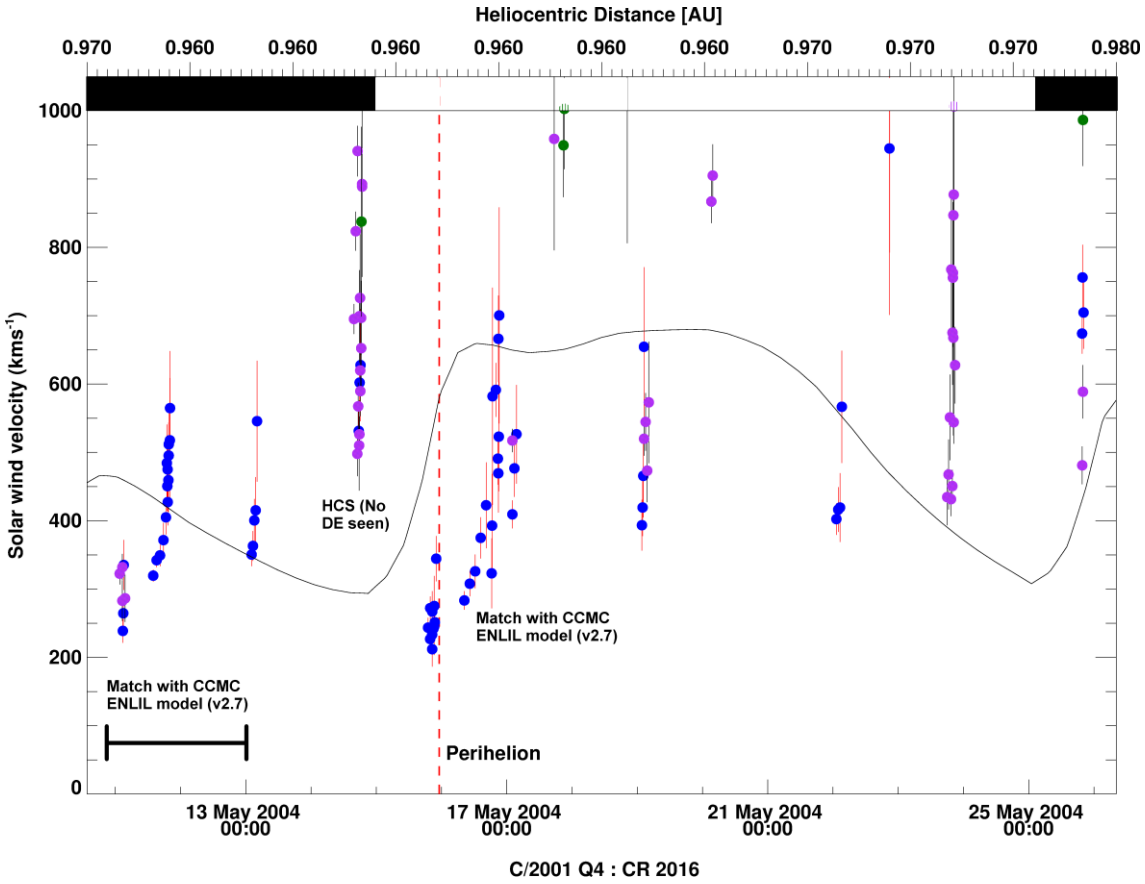

Figure 5.73: Solar wind velocity for C/2001 Q4 for CR 2016. The data shows 5 periods of atypical ion tail flow. The black and white panels at the top of the plot show the expected magnetic polarity at the comet's location. ENLIL modelled solar wind velocities (Owens) at the comet's location are shown as the solid black line.

The orbit plane angle improves drastically during May, peaking at around 85^{o} mid-May. The comet is within 10^{o} of the ecliptic plane between 03/05/2004 to 31/05/2004 and experienced high solar wind velocities peaking above 1000 km s^{-1}, calculated from 8 separate images between 17/05/2004 and 23/05/2004. There are mini data gaps in the ACE/SWEPAM data on the 17th, 19th and 28th May 2004, which can correspond to periods where the instrument is overwhelmed. Each of the velocity spikes is attributed to a significant extent of the tail lying on the radial vector, implying infinite radial solar wind velocities. Estimates taken further down the tail yielded larger values than expected.

Images taken in the evening of 11th May have an ion tail close to the radial vector near the nucleus. The ion tail in each image is initially thin, then rapidly widens with increasing distance from the nucleus. The range of velocities is reminiscent of transition regions encountered by

C/2004 Q2. The ENLIL visuals from CCMC [Figure 5.74] predict that the comet experienced a period of slow solar wind ~400 km s^{-1}, accounting well for the lower than predicted ENLIL MHD model (Owens) during the early half of May 11, 2004 [Figure 5.73].

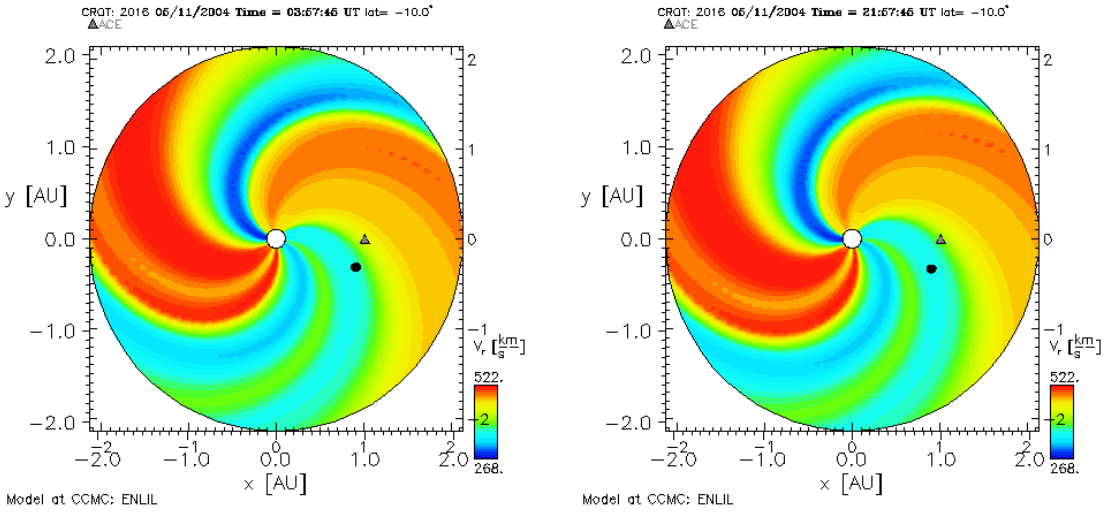

Figure 5.74: Comet's location (circle) within a slow solar wind stream for an extended period with a small peak in the velocity space. The above MHD model was produced in 2013 from the latest version of ENLIL (v2.7).

No solar wind phenomena could be pinpointed to explain the velocity range on the 11th May, though the latest MHD model implies that the comet drifted through a phase of slow solar wind velocity, with a small temporary peak in the velocity at the comet halfway through. This matches my data trend and accounts for the array of velocities several hours later, though it fails to explain the mismatch in velocity peaks. A CME, tentatively linked with interaction 2 [Figure 5.75], was observed with a linear speed of 469 km s^{-1} at 07/05/2005 10:50 UT with a CPA of 115º and angular width of 94º. The comet's position angle is ~110º. The low ICME speeds indicate that the high radial velocities measured at the comet are incorrect. If the technique is considered to work accurately, it implies there was a large tangential component in a disturbed ICME-solar wind medium which introduced geometrical perspective complications along our line of sight.

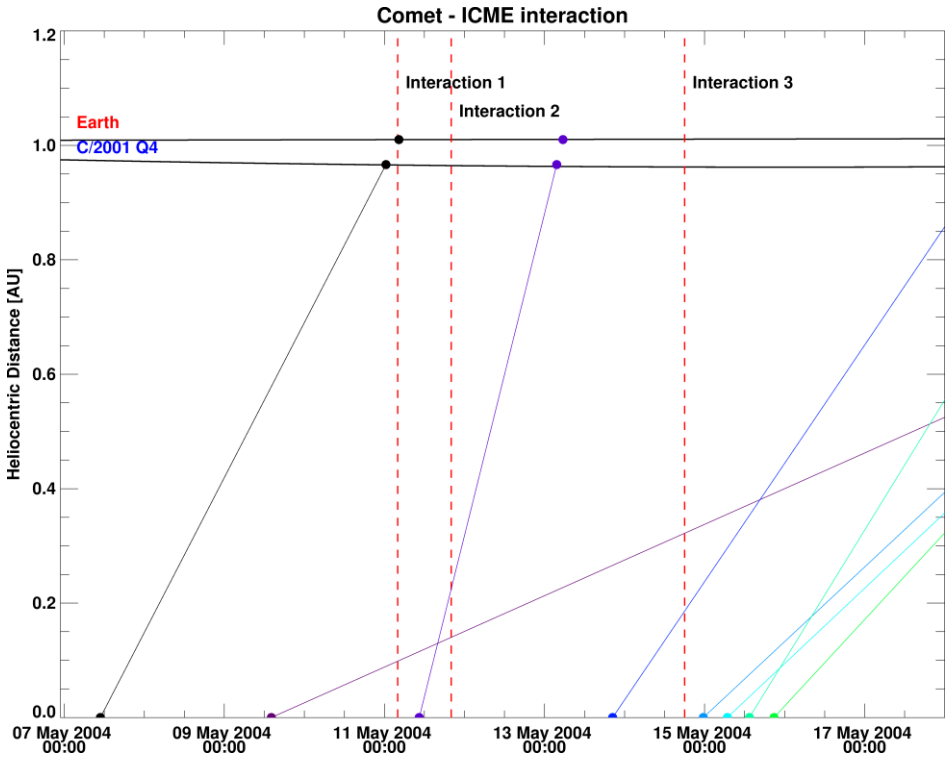

Figure 5.75: ICME SATs at C/2001 Q4, reaching the comet shortly before Earth.

The Owens MHD model and the Mercator map [Figure 5.72] both predict a HCS crossing with slow solar wind speeds on the 15th at ~ 00:00 UT. No such events were observed in the image catalogue, though multiple tail rays, often associated with DEs, were prominent 6 hours earlier. The tail orientation changed multiple times and formed a kink parallel to the radial vector [Figure 5.76].

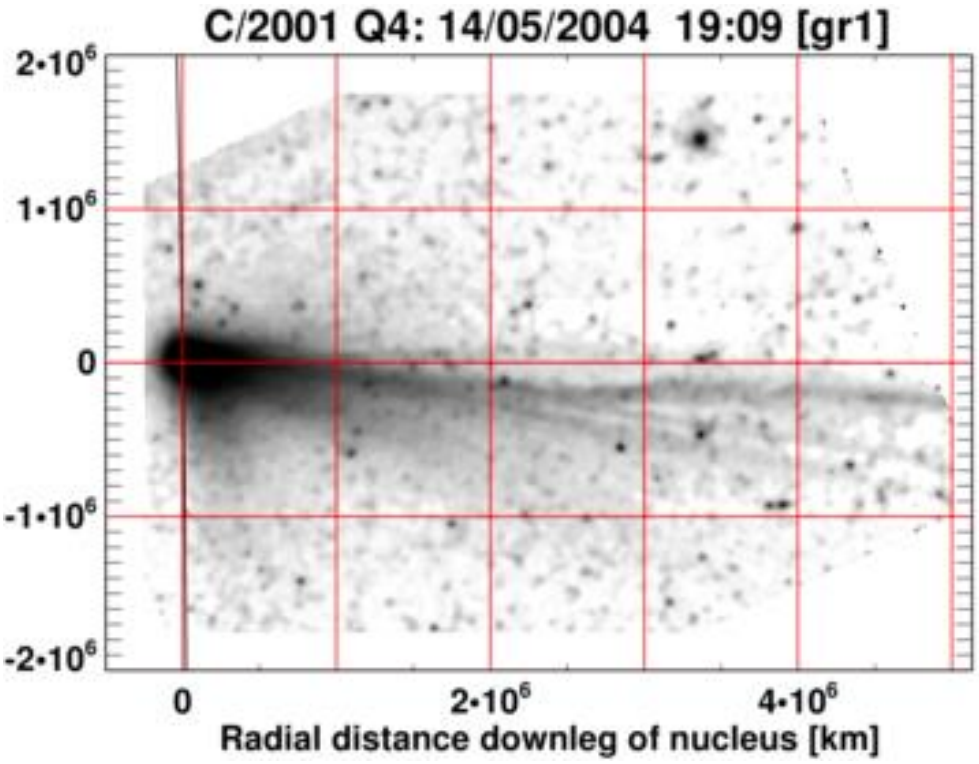

Figure 5.76: Contrast enhanced mapped image by Rhemann showing multiple ion tail orientations of C/2001 Q4.

The paucity of observations during the expected HCS crossing means we cannot confirm a HCS crossing from observations. From Figure 5.75, we can infer that the comet could have interacted with the ICME observed on 11/05/2005 10:26 UT, travelling with a plane-of-sky speed of 974 km s^{-1}. The CME's CPA was 115^{o} and had an angular width of 66^{o}.

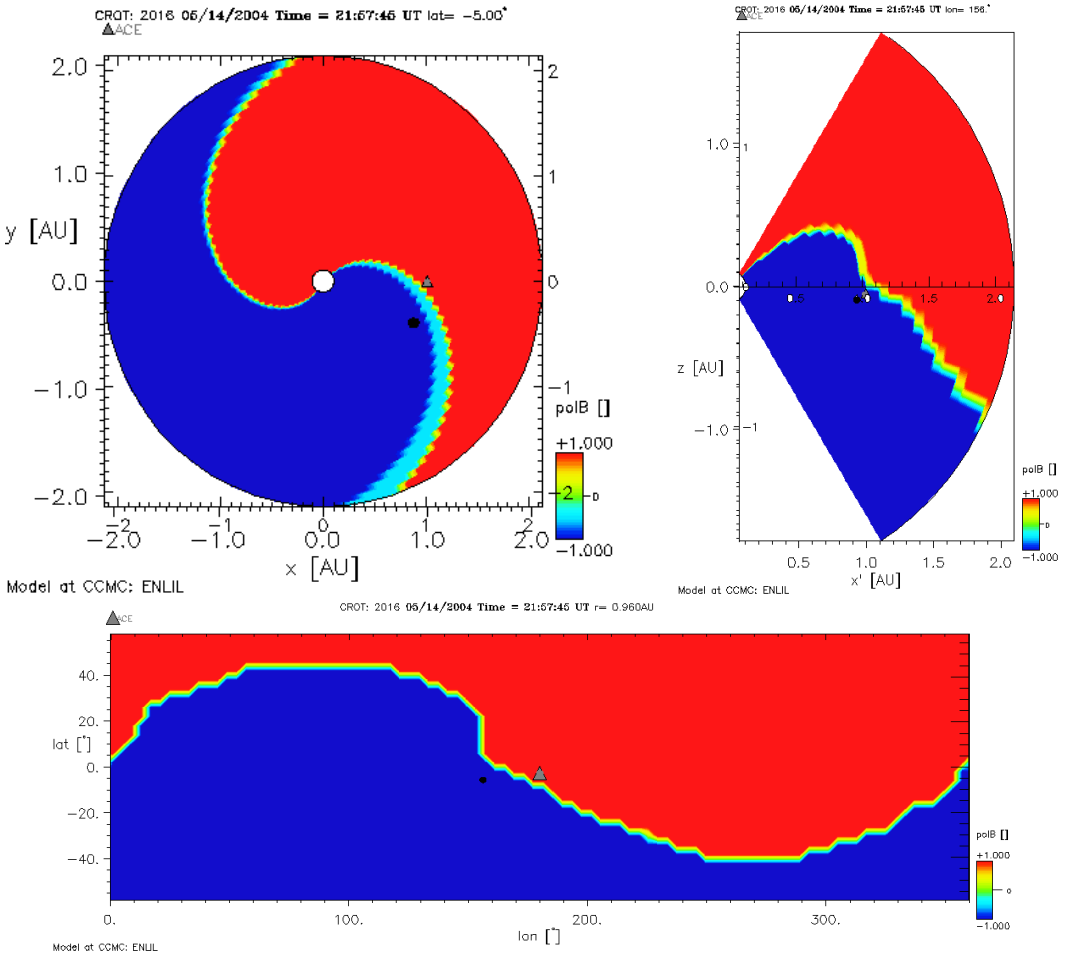

Figure 5.77: ENLIL model run (from 2013) implying that the comet encounted the HCS earlier than predicted by the Owens model.

If the comet encountered the HCS, as supported by Figure 5.77, this could explain the discrepancy with the MHD model. It was often observed that the detached tail did not follow its original trajectory when connected to the ion tail. This will result in inaccurate estimates of the solar wind velocity. A large orientation change, from a fast to slow plasma flow, was tracked between two subsequent images on 14th May 2004. The fast moving section of the ion tail is near-parallel to the radial vector suggesting infinite solar wind speeds. The vector map solution is 67 ± 310 km s^{-1} in the comet's plane.

The Owens model predicts a dip in velocity down to 300 km s^{-1} before a steady increase. The comet velocities replicate this transition region though offset by a day. According to my data, the transition region ends in the early hours of the 17th May. This matches conveniently with multiple tail orientations on the 16th and a kinked tail, followed by a DE between the 17th and 18th May.

Up to two-thirds of the ion tail often coincided with the Sun-comet line. This period, including the extremely high solar wind velocities, could not be related to a known ICME or HCS crossing. Evidence of a transition region in the ENLIL visuals from CCMC supports my results [Figure 5.78]. It bears noting that around this point, we are mostly looking straight down onto the comet's orbital plane, so what we should be seeing is a purely radial projection of the ion tail with minimal line-of-sight geometrical inaccuracies. From the evening of the 19th to morning of the 20th, a series of high velocities was determined. The ion tail remained close to the radial vector. A forked tail, formed with a tail ray and a large kink proved that the comet had encountered disturbed solar wind flow. Over the following days, both versions of the ENLIL models agree on the expected solar wind streams. A list of potential ICME impactors were identified and presented in Figure 5.79 and Table 5-1 to explain the unexpected velocities measured at the comet. No strong conclusions were drawn for the perplexing behaviour of C/2001 Q4's ion tail in this period.

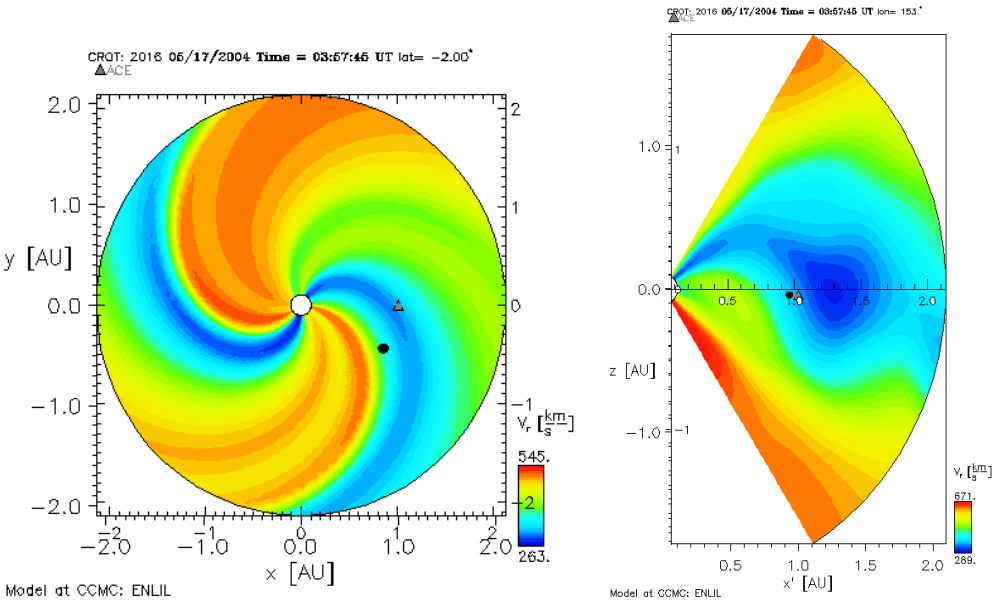

Figure 5.78: ENLIL image set showing the comet encountering gradually increasing speed on the 17th May 2004. Solar wind velocity at the comet is ~400 km s^{-1}.

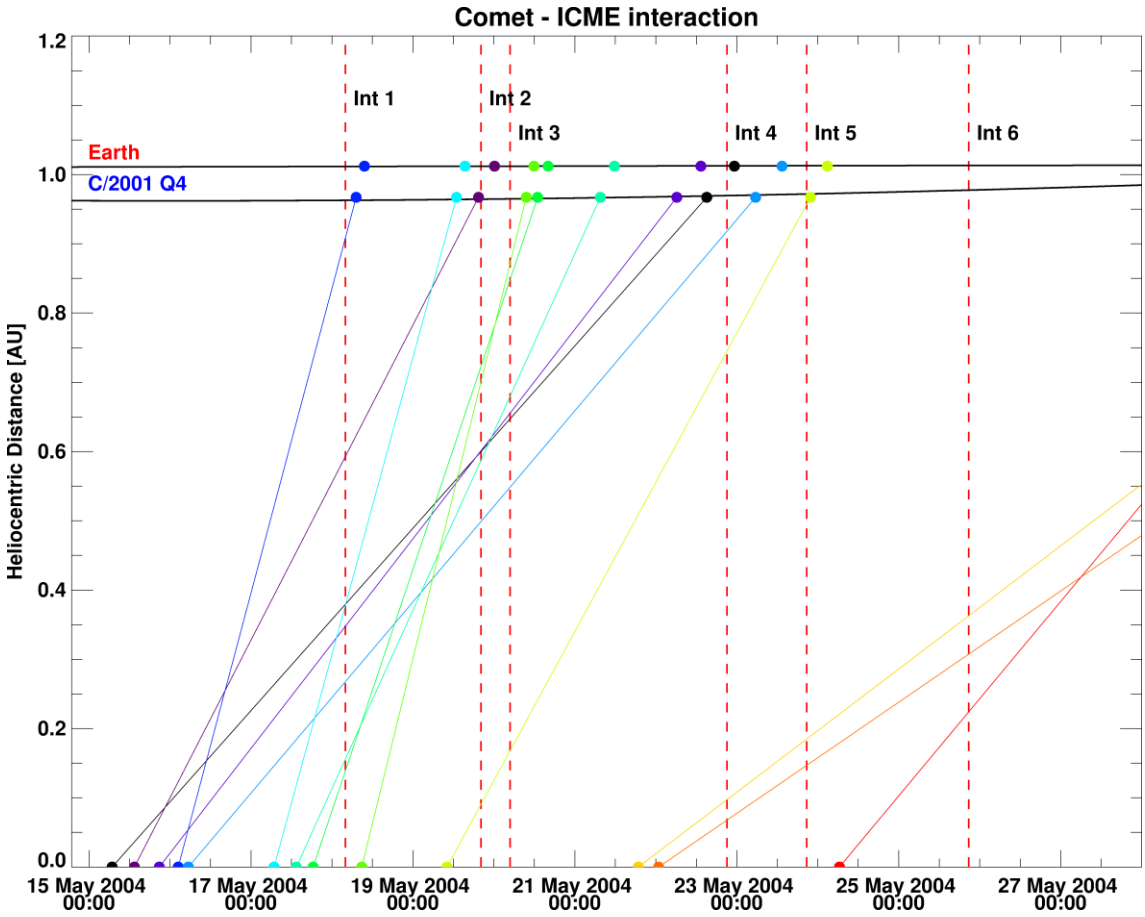

Figure 5.79: ICME SATs at C/2001 Q4 assuming a linear plane-of-sky speed.

Potential ICME impactors:

Table 5-1: List of ICME interaction candidates with C/2001 Q4. As discussed previously, these should be considered as an approximation for the SATs at the comet. The comet's position angle was ~ 102º and the position angle of the solar rotation axis was -19º.

Date	Time (UT)	Linear Speed (km s^{-1})	CPA (º)	Angular width(º)	Interaction
15/05/2004	06:50:06	228	135	76	4 or 5
15/05/2004	13:27:12	394	115	156	3
15/05/2004	20:50:05	262	133	115	4 or 5
16/05/2004	05:26:05	239	122	118	5
17/05/2004	06:50:07	743	117	34	2 or 3
19/05/2004	10:06:05	373	145	64	6

The evolution of a fuzzy zigzag kink into a DE is followed through 4 images on the 23rd May 2004, where it was most distinct. Once the zigzag feature could be resolved, the DE was

tracked in three separate locations. The tail was almost at a standstill after disconnection before getting accelerated in the last image [Figure 5.81 and Figure 5.82].

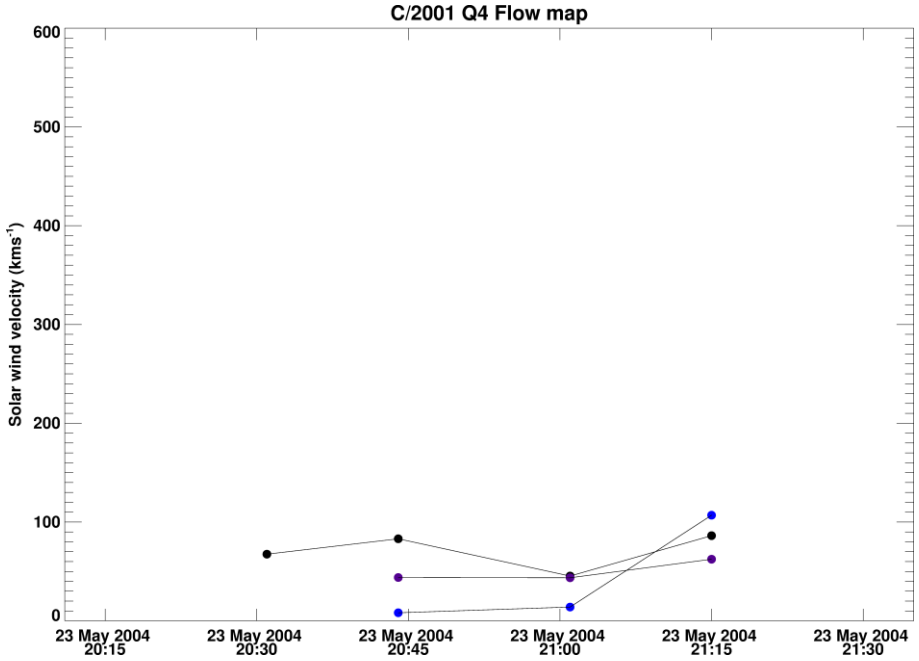

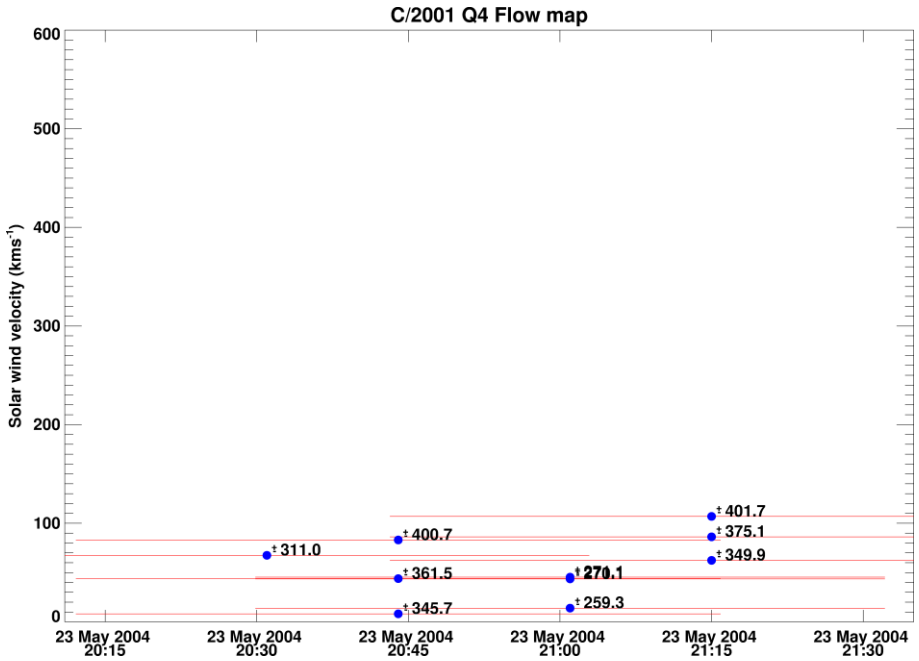

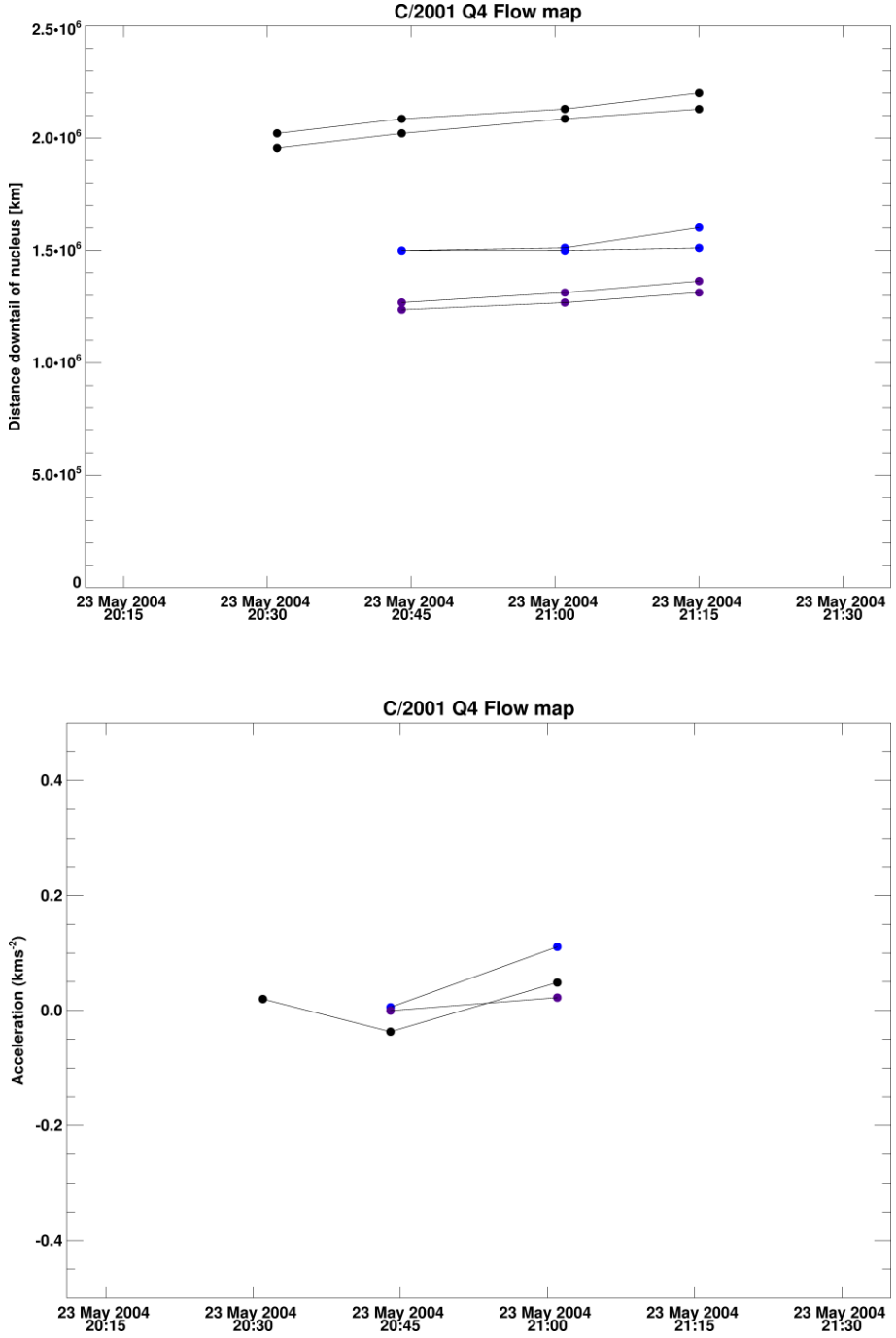

Figure 5.80: Velocity, distance and acceleration against time plots for zigzag DE. Observations of C/2001 Q4 were undertaken by Schedler on 23/05/2004.

Near the end of CR 2016, the comet crosses the HCS, bounded by a CIR. This is predicted by both ENLIL models and a large kink in the ion tail was observed at this time.

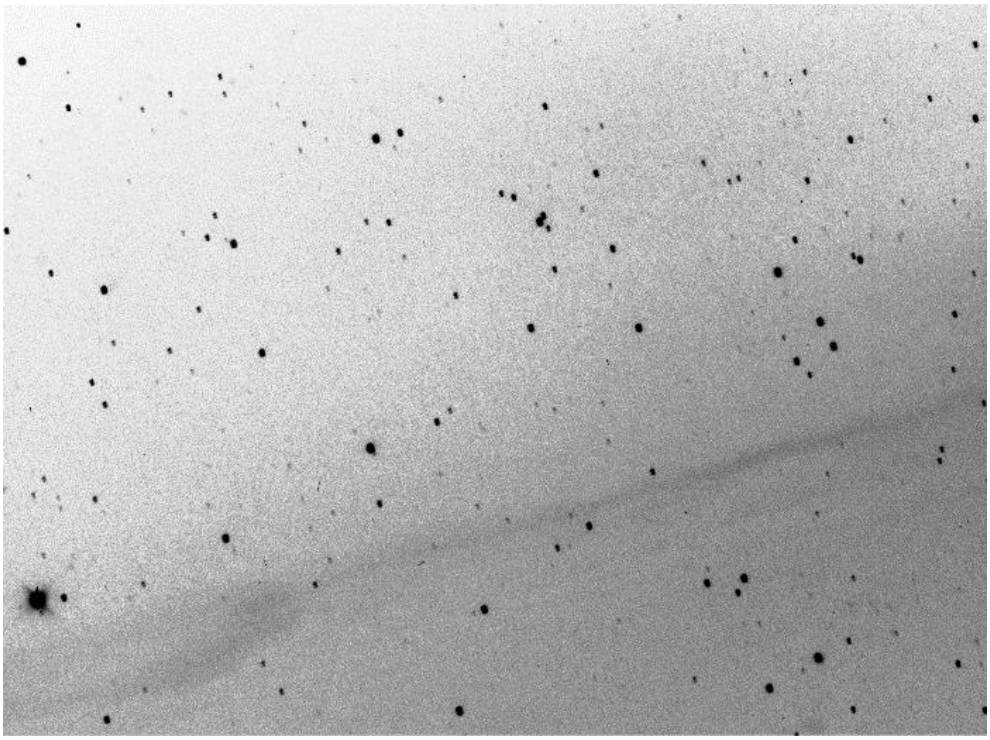

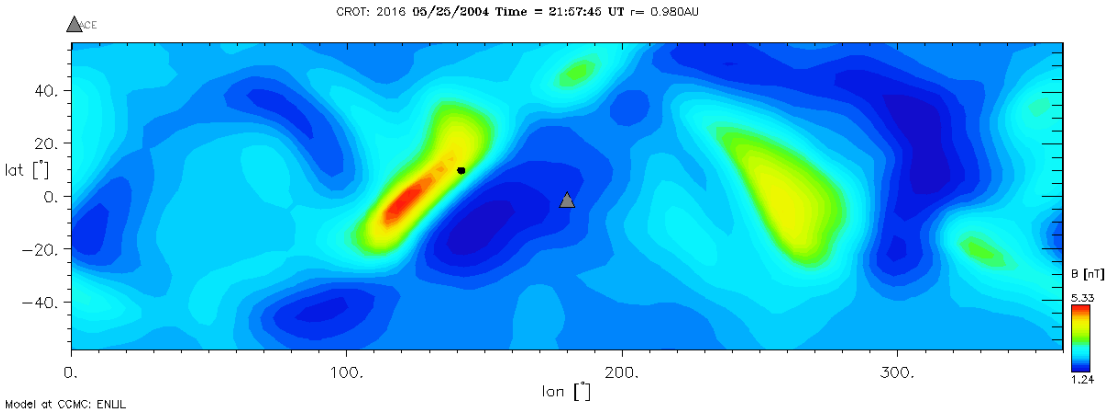

Figure 5.81: Large kink in ion tail observed on 25/05/2004 at 20:46 UT post-HCS crossing and during CIR. The nucleus is out of the image and is in the upper right corner of the top image.

CR 2017

The Owens MHD model does not cover the entire Carrington Rotation [Figure 5.83]. Similarly to previous CRs for this comet, my velocities do not match those predicted at the comet's location.

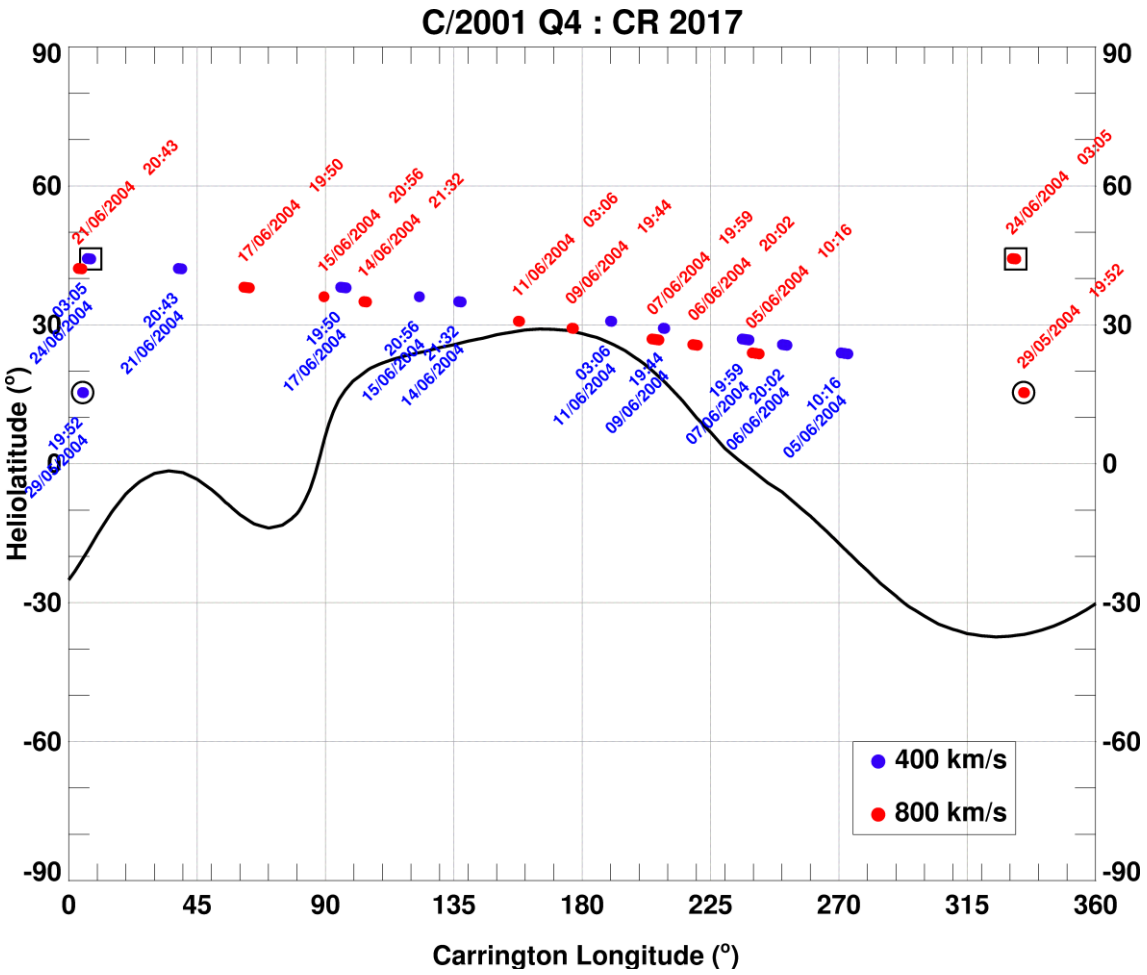

Figure 5.82: Mercator map for CR 2017 for comet C/2001 Q4. No HCS crossing expected during this period. The comet is anticipated to experience fast solar wind speeds as it reaches higher latitudes towards the end of this CR.

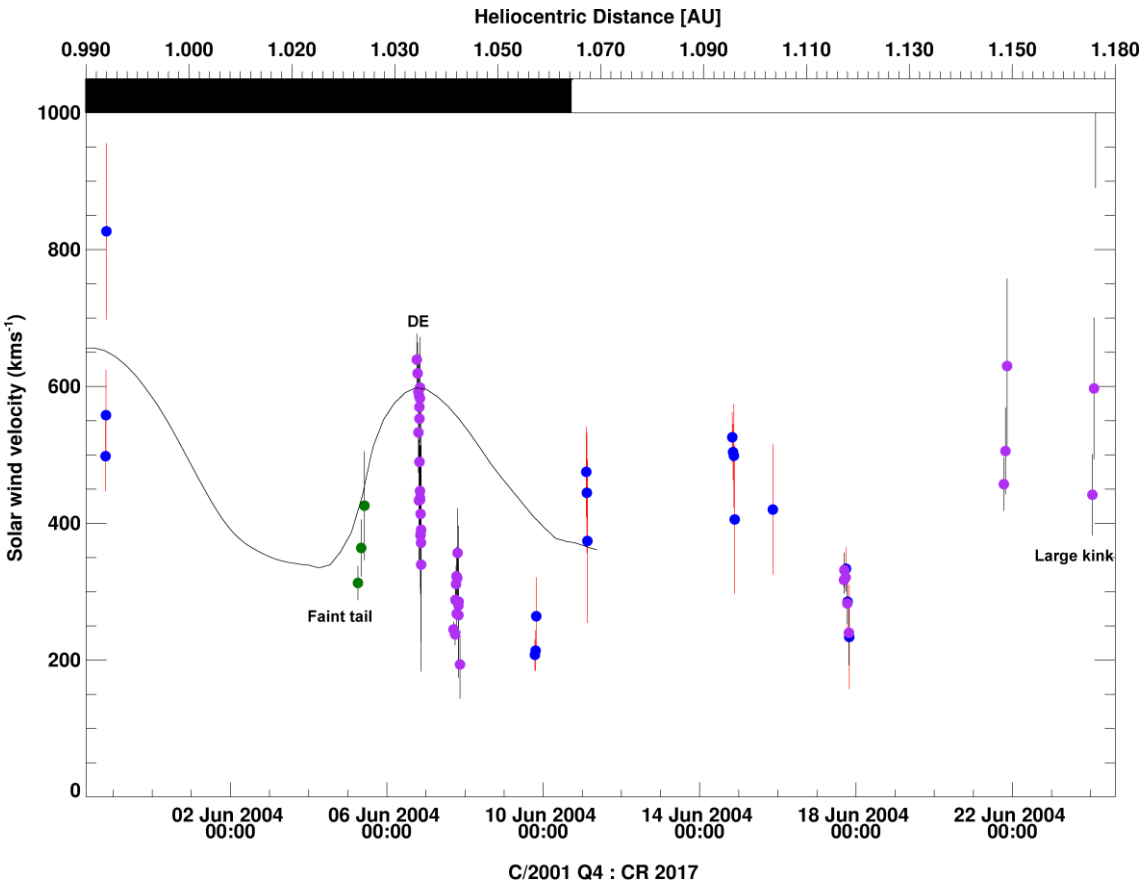

Figure 5.83: Solar wind results from C/2001 Q4 for CR 2017. The Owens ENLIL-based MHD model stops mid-way through the CR. Ion tail images taken during this CR were fainter and thus harder to analyse.

33 estimates were obtained within 1.5 hours of each other from 8 images on June 6, 2004. The images captured a DE with the detached tail sitting closer to the radial vector, resulting in a range of velocities in a short time period. Here, the new ion tail has slower velocities than the disconnected tail, with the overall tail being inversely curved to expectations. The detached tail was observed to decelerate by -0.03 km s^{-2} over the course of 26 minutes from 58.1 ± 119.1 km s^{-1} to 12.9 ± 135.0 km s^{-1} after disconnection. The high density of low values is due to 4 images taken within 4 minutes of each other by the same observer. Despite the match with the modelled values, the data points marked in green are due to the extreme faintness of the ion tail, once mapped.

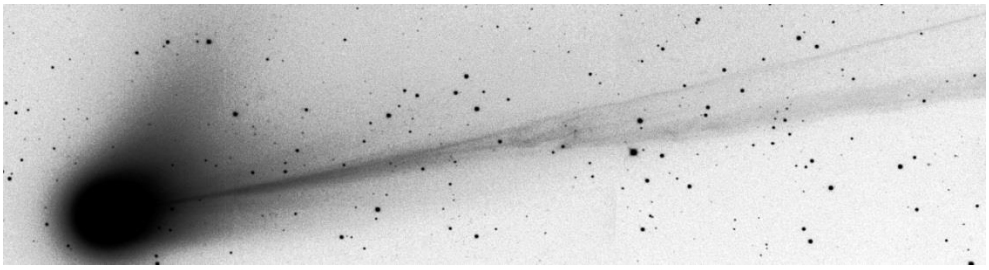

Figure 5.84: Image by Mikuz observed on 06/06/2004 at 21:27 UT, showing a DE.

In the absence of a predicted HCS crossing, I look to the CCMC visualisations [Figure 5.85]. The plasma bundles are expected to have left the comet head between 1830 UT and 2100 UT. With considerations of the comet's fast motion across heliospheric latitudes between 6th and 7th, it is inconceivable that the comet crossed the solar wind transition region that rapidly, resulting in a velocity range of 300 km s^{-1}.

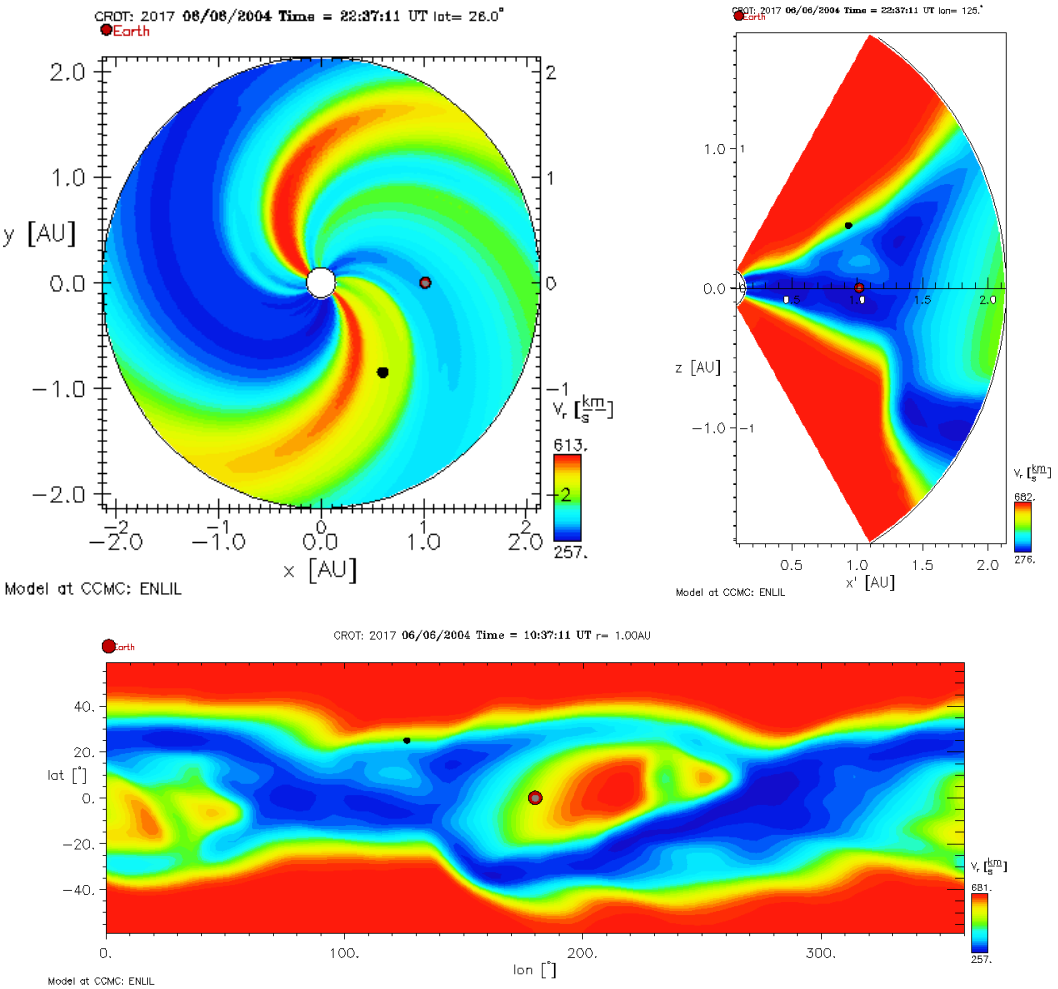

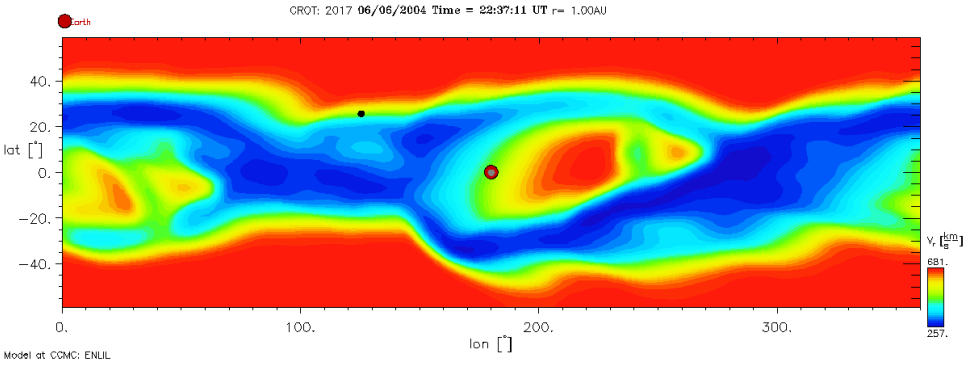

Figure 5.85: ENLIL MHD model for CR 2017. The comet is expected to encounter a transition region.

With no change in polarity, magnetic field strength or number density, it is unexpected for a DE to occur at the transition boundary and thus the remaining possibility is that of two potential ICMEs causing a polarity reversal at the comet [Int 1 in Figure 5.86]. The first (CME1) was observed on 29th May 2004 15:06 UT headed towards the comet (position angle ~96°) at 164 km s^{-1} with a CPA of 108° and CME width of 17°. The solar axial tilt's position angle was -15°. The second (CME2), observed on 03/06/2004 at 12:06 UT, had a linear speed of 573 km s^{-1}, CPA of 94° and angular width of 69°. Both ICMEs will encounter the fast solar wind, with the second ICME partially bathed in a slow solar wind flow. The first will be accelerated to ambient solar wind speeds. It is more likely that the second ICME will have interacted with the ion tail and caused the disturbance reported earlier.

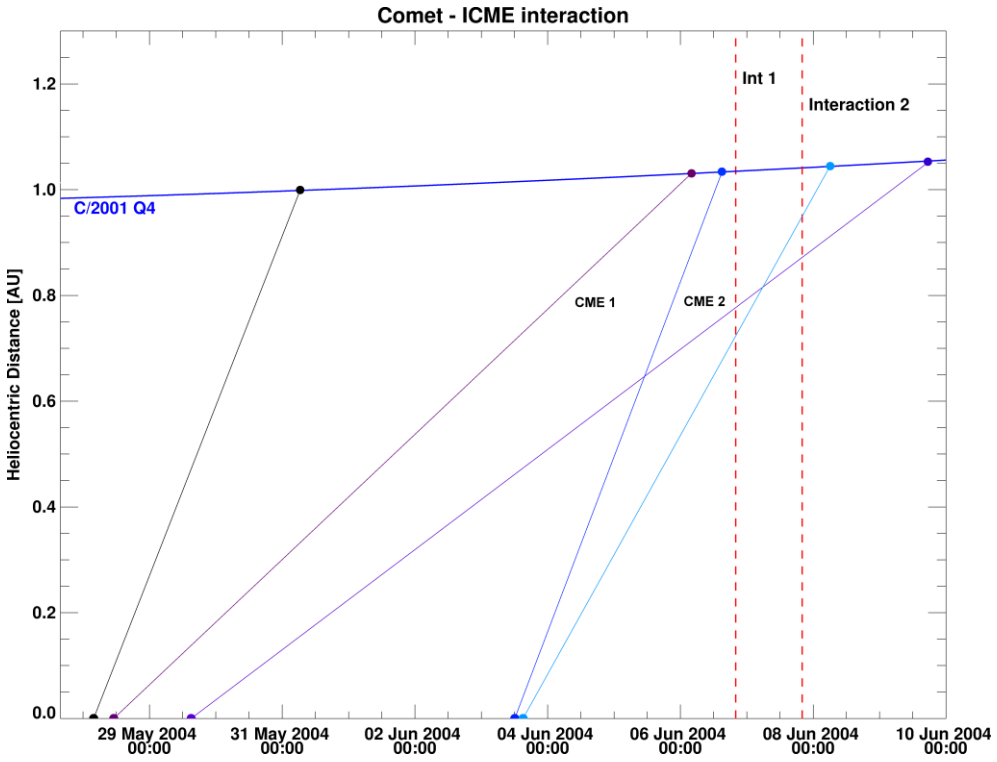

Figure 5.86: Estimated SATs at the comet assuming a linear speed.

The range of velocities on the 7th June corresponds to a kinked ion tail. The velocity profile increases down the tail, similarly to the 6th June, during this period. With the Vector maps technique, the kink within was observed to travel at 31 ± 65 km s^{-1}.

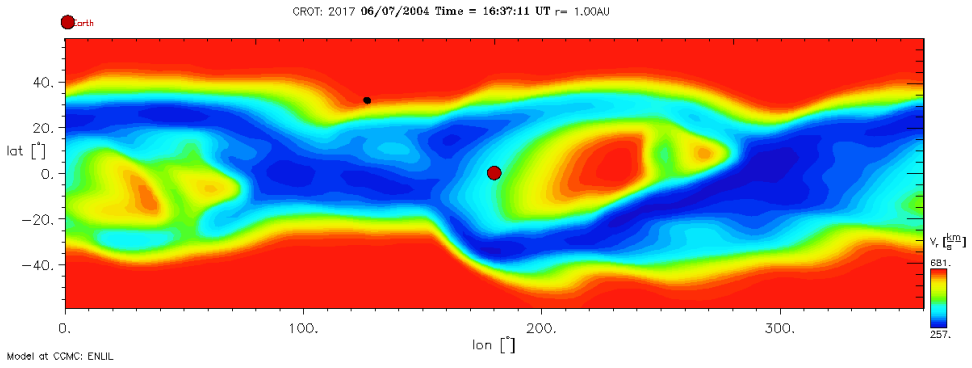

Figure 5.87: Plane cut of MHD model at 1AU showing that the comet is expected to be experiencing fast solar wind speeds.

Aside from the two ICME interactors predicted in Figure 5.86, there are no peculiarities in the solar wind stream [Figure 5.87] to guarantee a DE. Without a modelled transient explanation

available, CMEs 1 and 2 [Figure 5.86] are considered to be the most likely candidates to have caused the observed kink.

The ion tail becomes dimmer towards end of June during the comet's egress. Events of the 17th detail a quadruple orientation change in the ion tail, with low radial velocities, in spite of predicted smooth, high speed solar wind outflow due to its high heliospheric latitudes. No ICMEs are expected to have interacted with the comet.

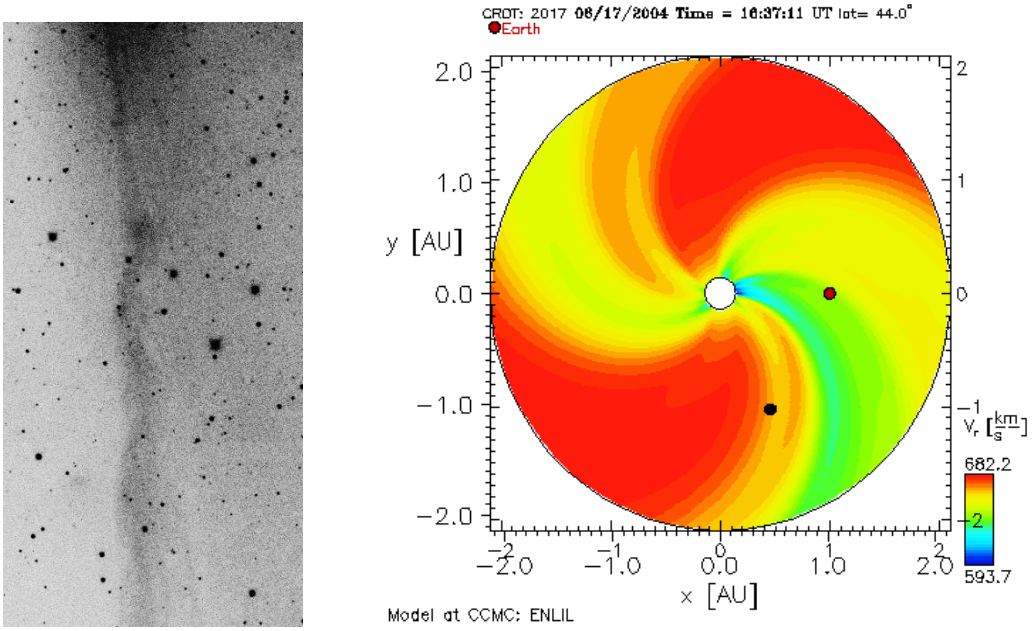

Figure 5.88: *Left*: **Comet C/2001 Q4 showing a quadruple kink. The nucleus is out of the image frame at the top. This image was observed on 17/06/2004 at 21:04 UT by Mikuz.** *Right*: **Polar cut of the radial solar wind velocity at the comet's heliographic latitude (44º).**

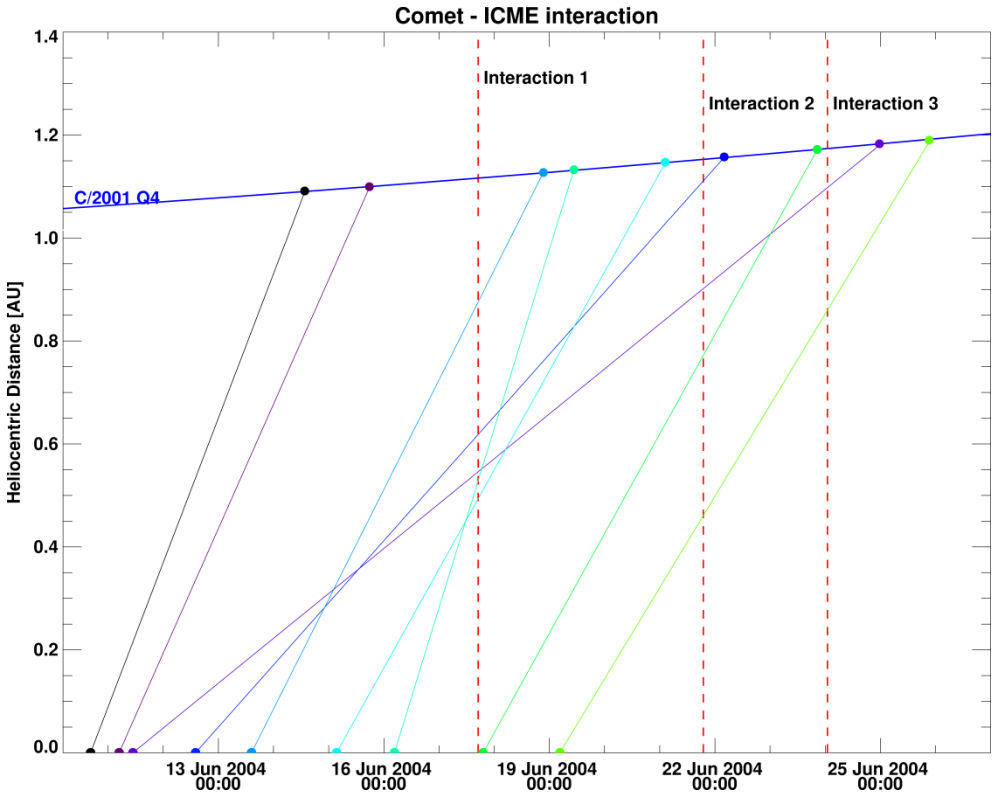

Figure 5.89: CME travel time to comet's location predicted from its linear plane-of-sky speed as measured by SOHO.

The last two events have been highlighted as atypical cometary ionic flow. Images on the 21st show a bend in the ion tail suggesting a transition from slow to fast ambient plasma flow, whilst those on the 24th exhibit a large kink in the ion tail, akin to previously observed ICME interactions [Figure 5.90 and Table 5-2], possibly the result of a DE. Much of the ion tail was close to the radial vector with a derived velocity peak of 1073 km s^{-1}. The CCMC ENLIL model predicts solar wind velocities > 600 km s^{-1}.

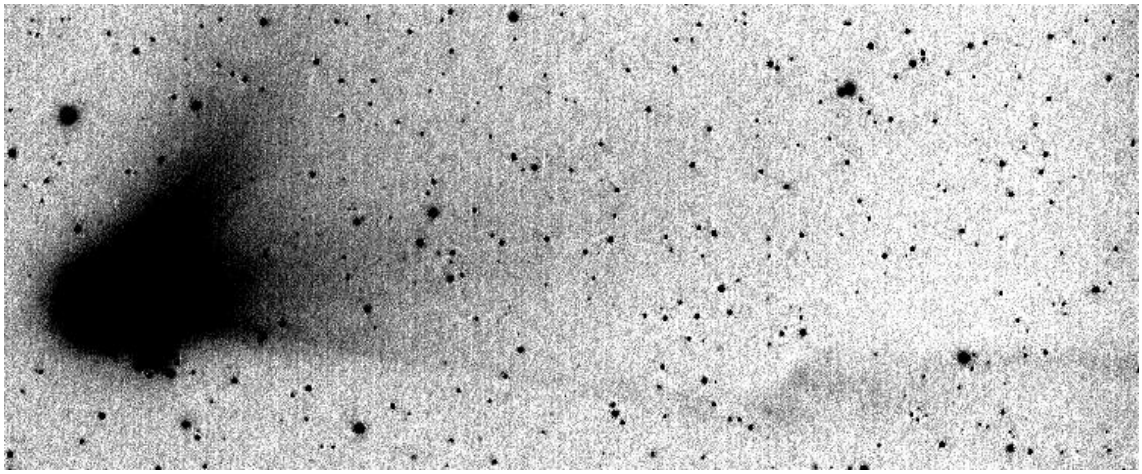

Figure 5.90: C/2001 Q4 on 24/06/2004 by M. Holloway. A large kink and a thin ion tail hint at a DE.

Table 5-2: Potential ICME candidates. It is difficult to infer which of these ICMEs interacted with the comet. The comet's position angle was ~86º and the solar axis's position angle was -8.5º.

Date	Time	Linear Speed (km s^{-1})	CPA (º)	Angular width (º)	Interaction
10/06/2004	16:26:22	486	95	23	1?
11/06/2004	04:50:06	419	124	78	1?
12/06/2004	14:06:05	209	73	48	3
13/06/2004	14:26:05	369	98	34	2
15/06/2004	03:26:05	333	68	114	2
16/06/2004	04:36:05	603	72	127	2
17/06/2004	19:12:05	335	112	42	3

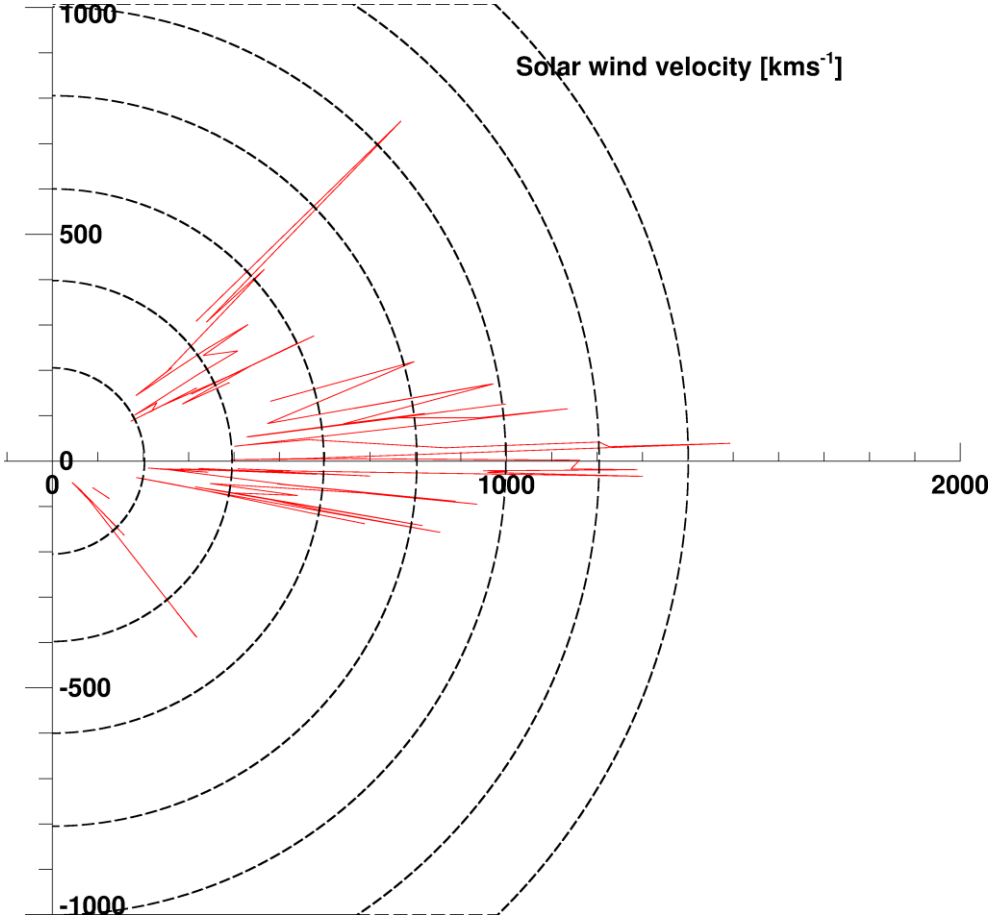

Figure 5.91: Heliospheric latitudinal variations of the remote-sensed local, radial solar wind velocity as measured at comet C/2001 Q4. The circles represent isovelocity contours for a fixed radial solar wind velocity at increments of 200 km s^{-1} from -90º to +90º.

My initial objective of pinpointing the latitudinal boundary between the fast and slow solar wind was not achieved, largely due to high velocities calculated in the equatorial regions, many of which may have been due to ICMEs. Although the comet almost certainly crossed a boundary between slow and fast winds, the effect of that boundary crossing was not unambiguously noted in the velocity distribution in the ion tail. The peak in solar activity for cycle 23 was in March 2000, so we should be expecting solar activity to be winding down during this period. Unlike C/2004 Q2, the behaviour of C/2001 Q4 was difficult to interpret. As it stands, the underlying cause of a large number of outflow variations in the ion tail remains debatable. Notwithstanding the seldom good agreement between the trend in my solar wind velocities and the latest MHD model, it appears that the technique cannot be used to predict the solar wind velocity at comet C/2001 Q4's location. Incidentally, the velocity matches occurred in CR 2016, the period with

the least identified turbulent velocities. Further comparison of CR 2016 with cometary derived velocities from Sizonenko (2007), are in good agreement during observations overlap, as seen in Figure 5.92, aside of the period extending 1 day on either side of 19th May 2004.

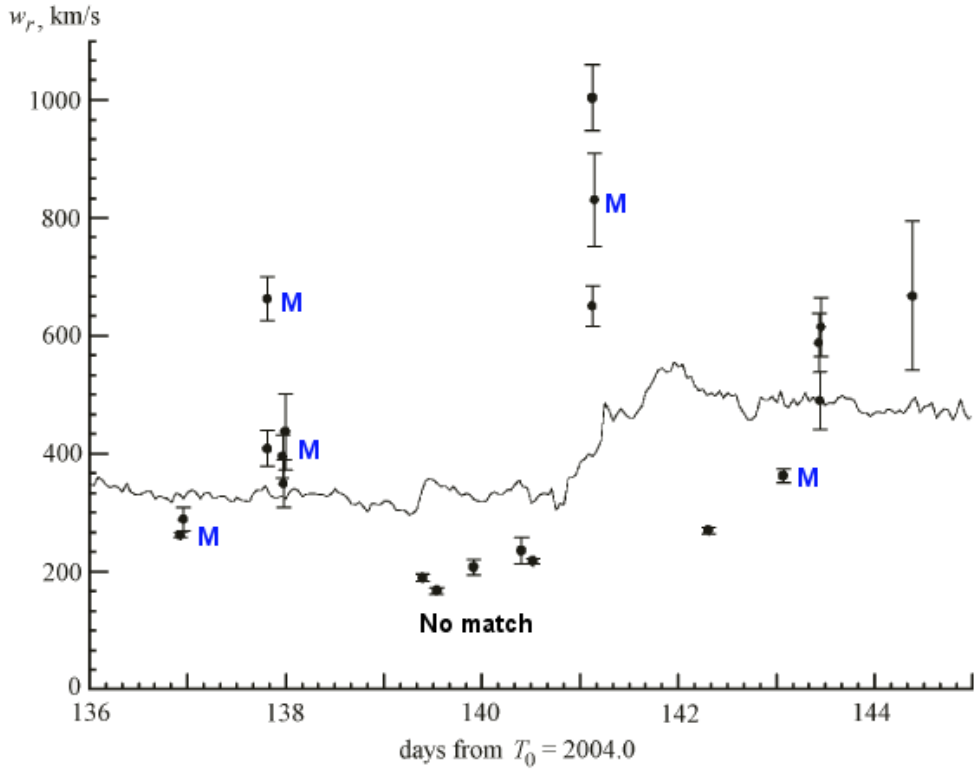

Figure 5.92: Solar wind velocities by Sizonenko (2007). The velocities are determined from direct measurements (OMNI data - solid curve) and observations (dots) of the ion tail for C/2001 Q4. Data matches with our velocity measurements for CR 2016 are labelled with 'M'. The measurements span from 15/05/2004 to 24/05/2004.

5.2.2. Alternative Methods to derive Solar Wind Velocities

5.2.2.1. Low Orbit Plane Angle

At low orbit plane angles, displacements along the y-axis, in the cometocentric reference frame, can only be due to the non-radial component of solar plasma flow. Similarly to comet C/2004 Q2 (Machholz), the non-radial component of the solar wind velocity fluctuated by around 40 km s^{-1}

[Figure 5.93]. The data were collected from a limited dataset as it is not always possible to resolve the extrapolated images at low orbit plane angles.

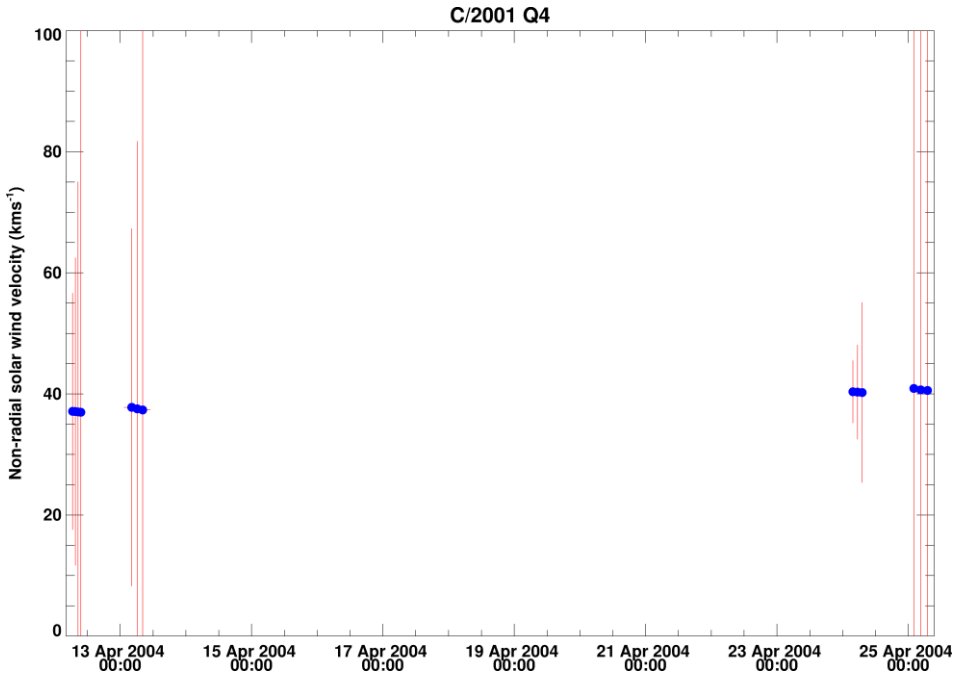

Figure 5.93: Non-radial solar wind velocity derived during low orbit plane angles.

5.2.2.2. Folding Ion Ray Velocities

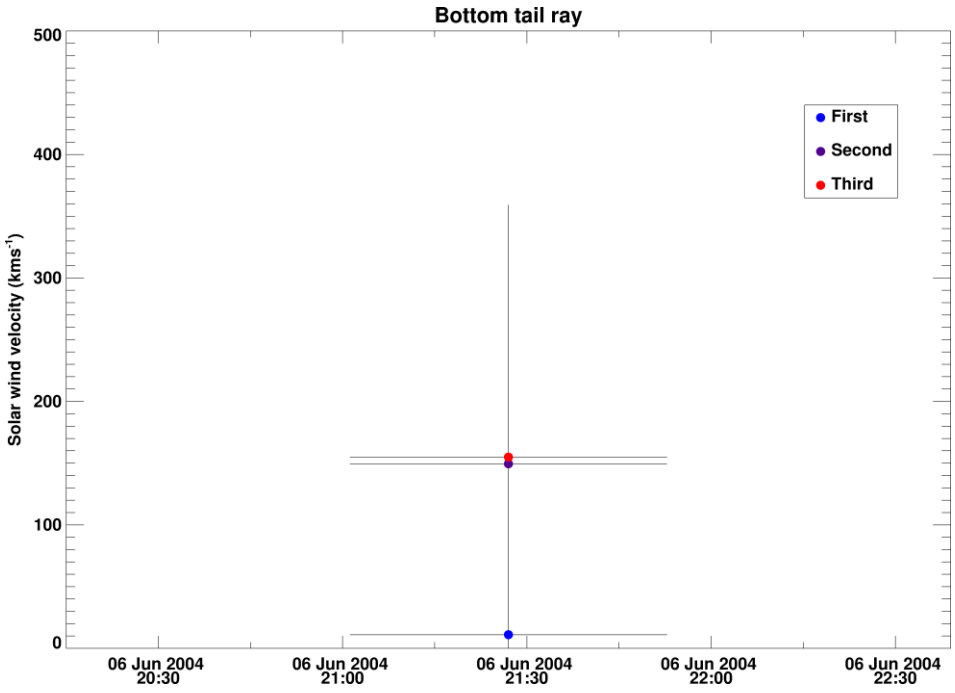

Figure 5.94: Solar wind velocity variation with time and distance from nucleus.

Comet C/2011 L4 was not rich in its folding tail rays, though the one measurement follows expectations of a proportional increase in solar wind velocity with both time and distance from nucleus.

5.3. Comet Garradd (C/2009 P1)

C/2009 P1 (Garradd) is an Oort cloud comet on a hyperbolic orbit (Gicquel et al. 2014), that probed the inner solar system to high heliographic latitudes of ~50^{o} at a minimum heliocentric distance of 1.55 AU around its perihelion on December 23, 2011. It reached a minimum geocentric distance of 1.27 AU on March 5, 2012. It reached a minimum solar elongation of 45^{o}, during the observing period I analysed, on December 5, 2011, shortly before its perihelion. The comet peaked in brightness attaining an approximate apparent m_v of +6 in February 2012, according to Aerith.net (Yoshida, S.) and +10.6 according to JPL Horizons (Giorgini et al. 1996). Inclination (*i*) = 106^{o}.2; ascending node = 326^{o}.0, eccentricity (e) = 1.00; Perihelion date (T) = 23/12/2011, 06:14 UT

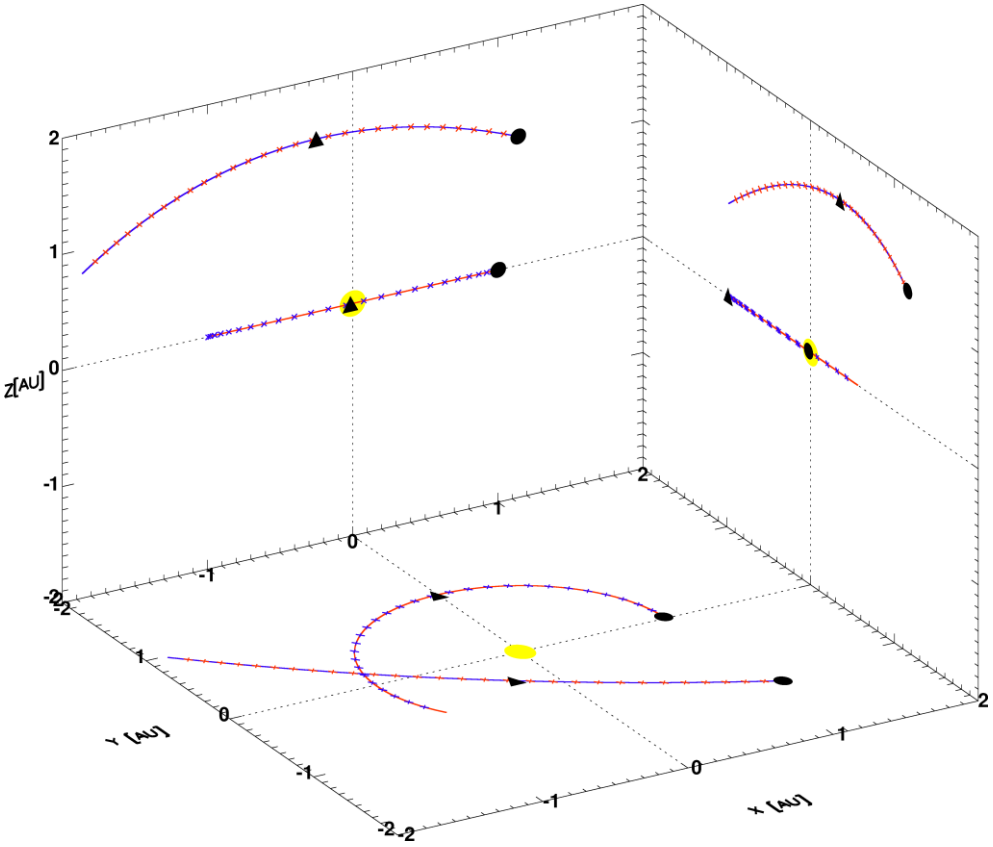

Figure 5.95: Heliocentric ecliptic coordinates of comet C/2009 P1 (Garradd). Black circles represent the start of the orbits and black triangles show the positions of the comet and the Earth at the comet's perihelion.

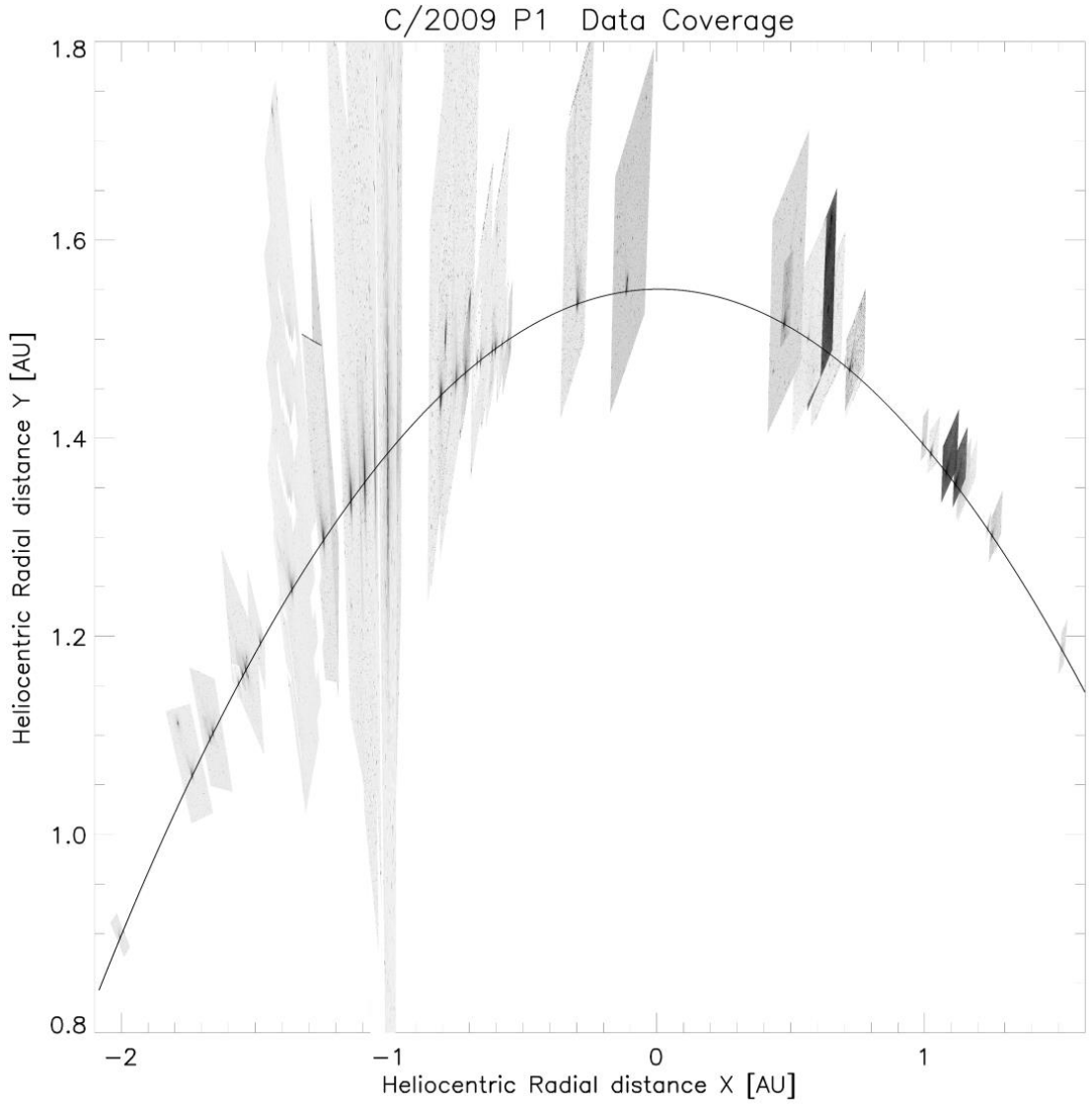

Figure 5.96: Data coverage for comet C/2009 P1 (Garradd). The images and the comet's orbit have been mapped so that the y-axis is defined as the direction to perihelion. Earliest image is to the right of the data coverage plot, increasing chronologically towards the left.

Figure 5.95 shows the heliocentric ecliptic coordinates of C/2009 P1 over a time span of 7 months. Solar wind velocities were only extracted from images between 2011/10/17 and 2012/03/25 due mainly to the high visibility of the ion tail during this period.

Image statistics:

90 images were processed through Astrometry.net with a high solve rate. Of 79 images processed with my software, I successfully extracted 90 solar wind velocity estimates from 27 images interspersed over seven Carrington rotations. The data points only cover a short time period from each Carrington rotation. The CRs were collated into two periods for CRs 2115 to 2117 and 2118 to 2121. Three measurements were rejected as unreliable. 38 data points were highlighted in purple as showing a deformed ion tail and 8 measurements, marked in green, were taken during periods where a section of the ion tail overlapped with the Sun-comet radial vector.

5.3.1. Radial Solar Wind Speeds

Analysis of this comet was negatively impacted by a faint ion tail observed during its first apparition and low orbit plane angle (< ~20^{o}) throughout the observations [Figure 5.97]. Comet C/2009 P1 is the first of the non near-Earth comets to be presented in this study. These comets all shared a relatively low orbit plane angle. Earth crossed the comet's orbital plane on 15/02/2012 at 07:57 UT. Only two images were available for estimation of the non-radial velocity components.

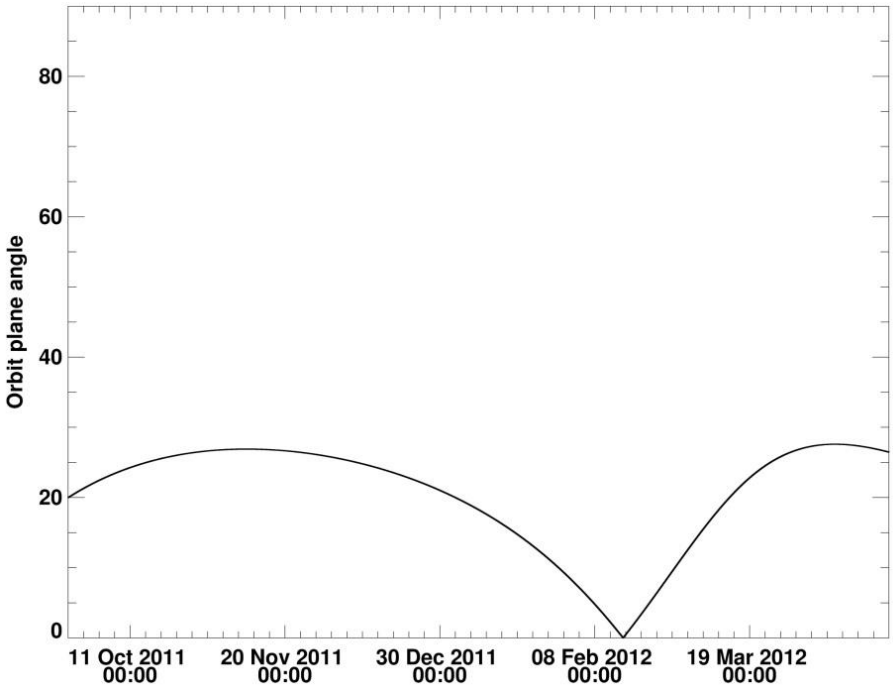

Figure 5.97: Orbit plane angle of Earth with C/2009 P1 from CR 2115 to 2121.

During its apparition, Garradd showed dynamic tail motions including multiple instances where the ion tail preceded cometary motion. Despite this atypical ion tail behaviour, no consecutive images of tail rays or prominent, distinguishable moving features were available to track. A peak velocity of 850 km s^{-1} was derived whilst the rest of the estimates correspond to values more typical of the slow solar wind. There are no Owens modelled solar wind velocities at the comet's location. ENLIL model runs were collated from multiple previous runs available at CCMC, and one of my recently requested run for CR 2116.

CR 2115 – 2117

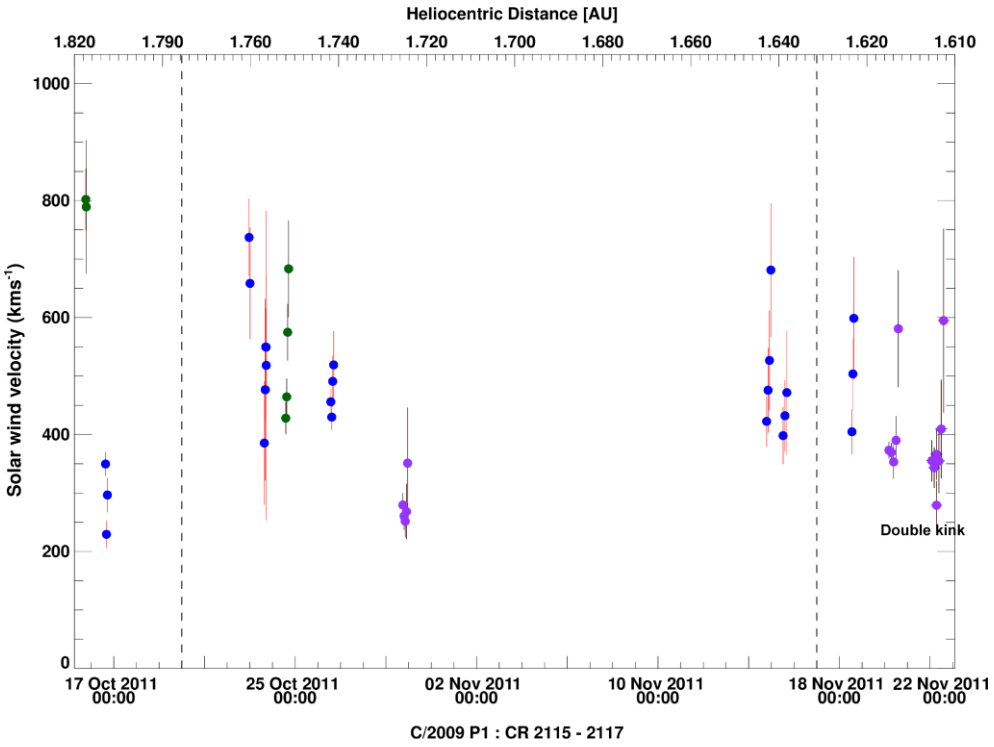

Figure 5.98: Solar wind velocity for three Carrington rotations

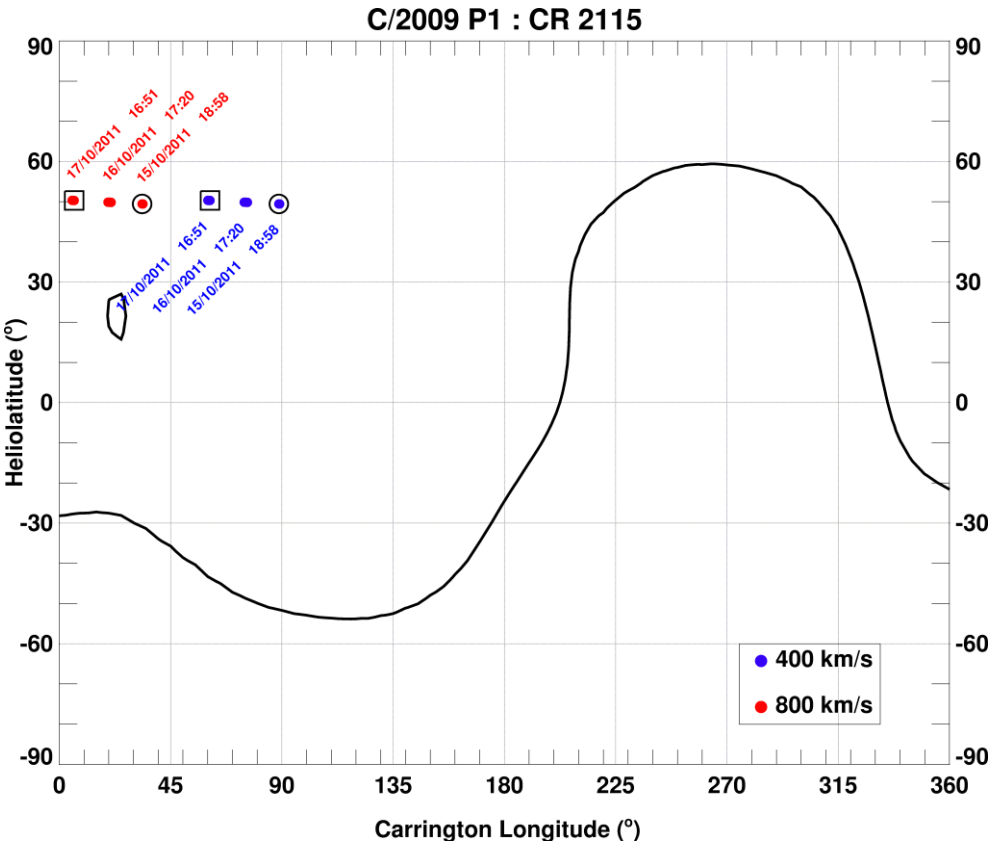

Figure 5.99: Mercator map for CR 2115. Comet should be experiencing fast solar wind streams due to its high heliographic latitude. The HCS is shown at 60°,

however the potential field source model is generally considered to be unreliable at heliographic latitudes greater than 45°.

The high heliographic latitudes of C/2009 P1 loosely predict fast solar wind velocities at the comet during CR 2115, if the solar wind source is clear of the HCS [Figure 5.99]. Comparison with Figure 5.98 contradicts this prediction for the regular data points. The high velocities on 15/10/2011 are obtained from a very faint ion tail and should be treated as unreliable. Data points from 17/10/2011 were rejected based on an observed bifurcating ion tail. Whilst the primary ion tail is coincident with the Sun-comet line, the curved secondary ion tail, likely an asymmetrical folding tail ray, revealed a slow plasma outflow in the vicinity of 200 km s^{-1} along the tail and 300 km s^{-1} near the comet head.

A low resolution (256x30x90) ENLIL model (v2.7 from 2012), with Wang-Sheeley-Arge (WSA) model input as its inner boundary condition, was used for CR 2115. The WSA model is an alternative method for computing a potential-field model of the current sheet from 2.5 to 5 $R_\odot$, from ground-based magnetograms of the photospheric magnetic field. More recent runs were available, though none covered the temporal or latitudinal extent required to predict modelled values at the comet. Comparison of the model between 15/10/2011 16:00 UT and 17/10/2011 16:00 UT shows that the comet will experience ~400 km s^{-1} winds, higher than my reported 200 – 350 km s^{-1}. There are no ICME interactions expected during this period.

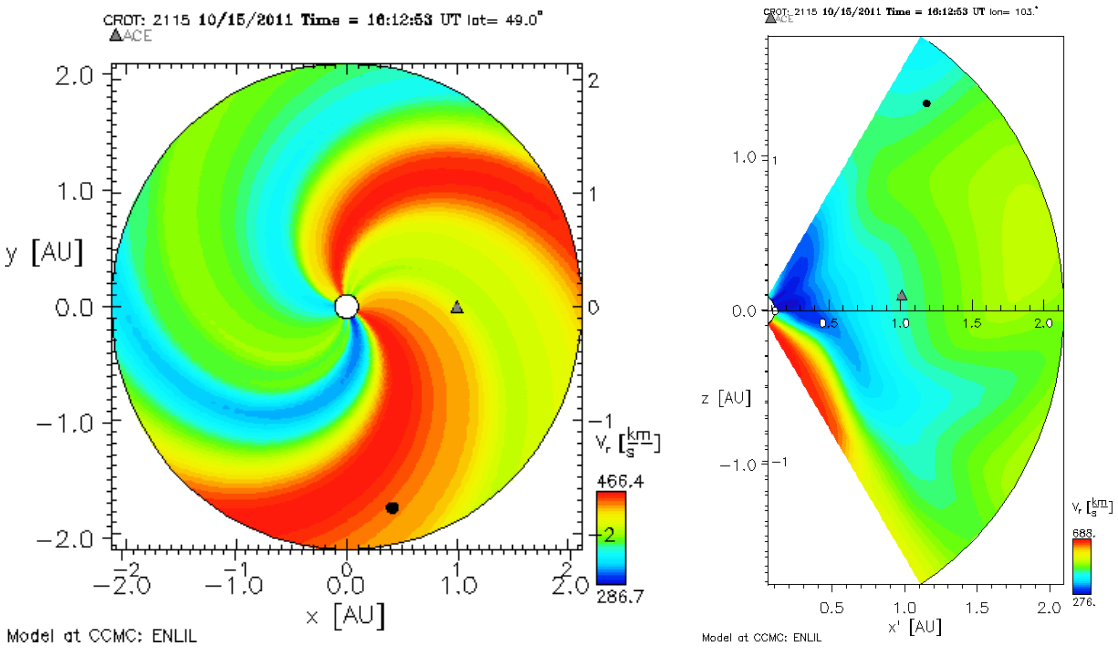

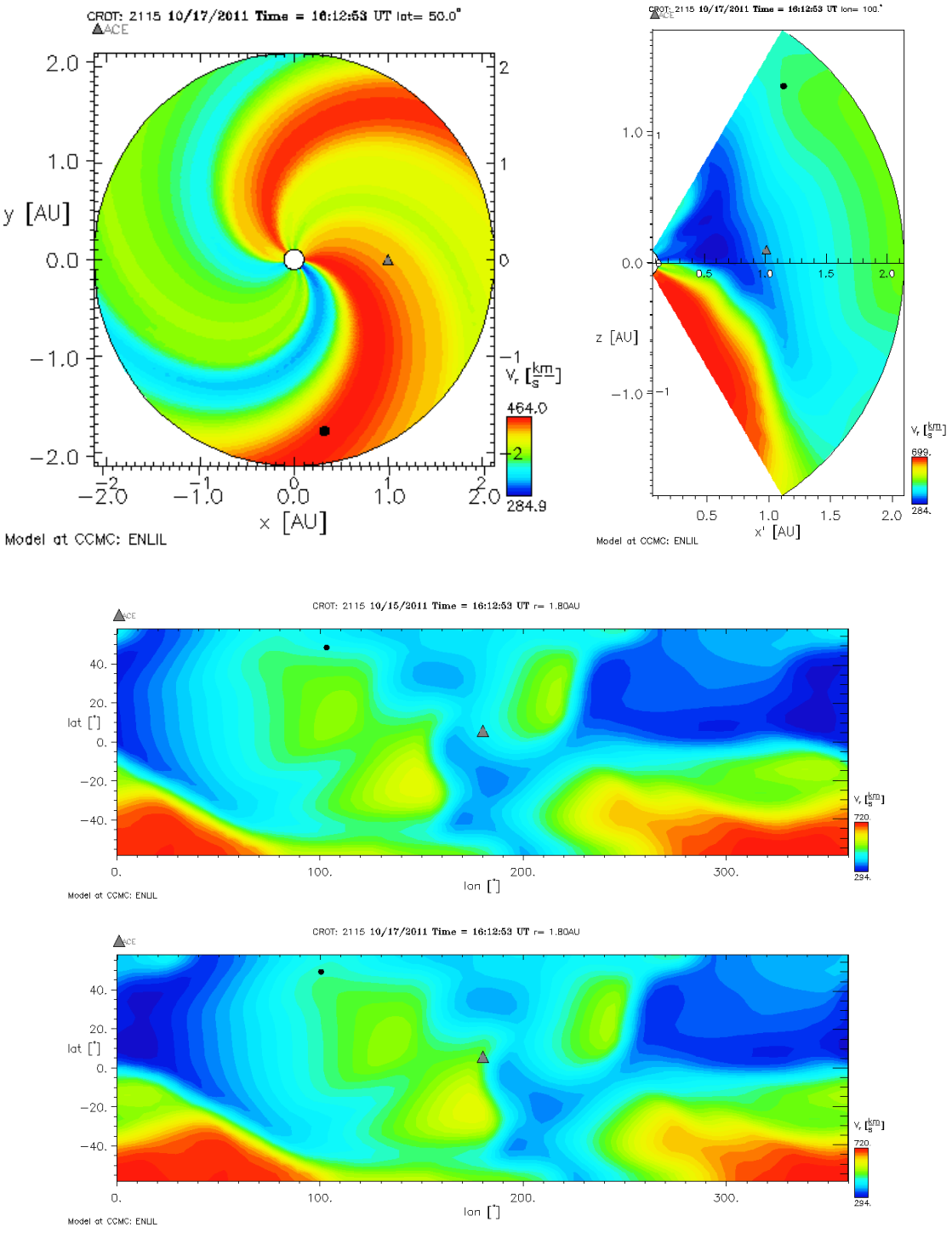

Figure 5.100: CCMC ENLIL model predicts slow solar wind speed at the comet's location.

CR 2116

To avoid labelling congestion, the dates and times for each bundle were set out in a table in Figure 5.101. The encircled data point corresponds to the first sampled data point for this Carrington rotation. The last date is enclosed within the black box.

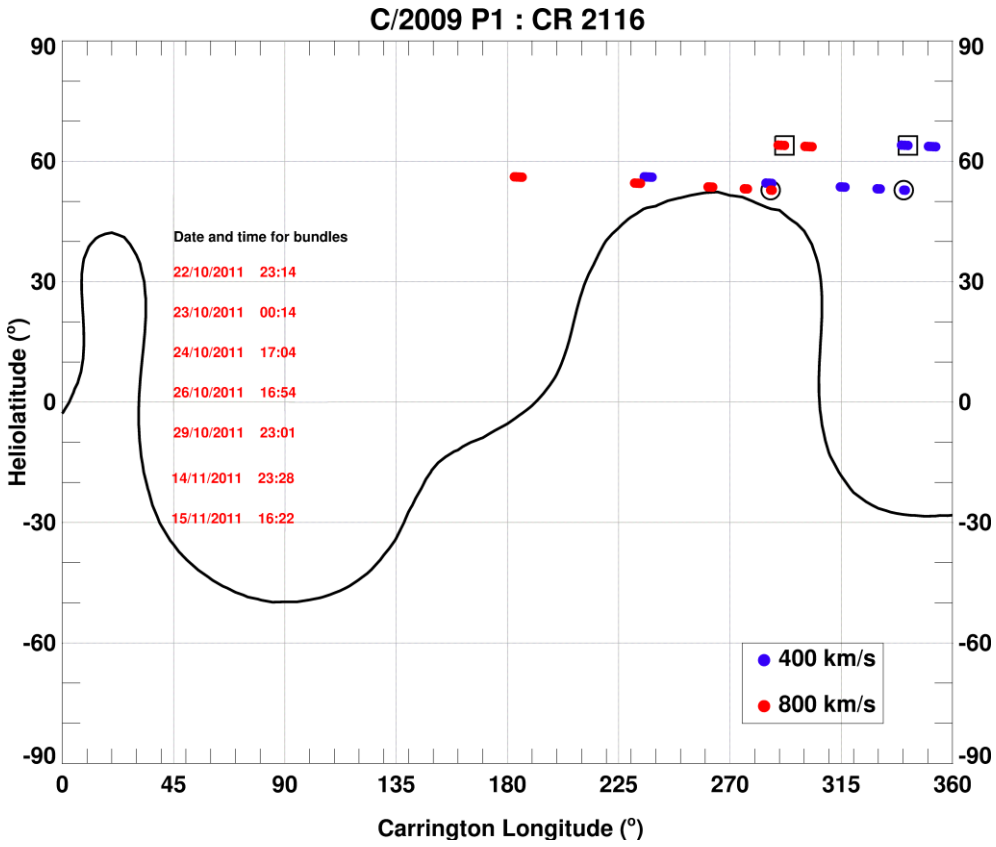

Figure 5.101: Mercator map for CR 2116 showing expectations of slow solar wind speeds near the neutral line. The first data point is circled and the last data point is enclosed in a square.

The comet is expected to experience slow solar wind streams close to the neutral line according to Figure 5.101. This agrees well with the MHD predictions whereby the comet encounters ~350 km s^{-1} flows and decreasing to ~ 250 km s^{-1}. This downward trend is seen in the data though the reported velocities. However, the measured solar wind velocities indicate a fast solar wind stream from 700 km s^{-1} down to 450 km s^{-1} on the 27th October 2011. Velocities taken in the 'turbulent' period leading up to the 30th matches the predicted solar wind values almost exactly. Data from the 29th October is highlighted due to a small kink in the ion tail, which may be due to an HMF orientation change in the flow upstream of the comet. Comparison for the 14th and 15th November were impossible as the comet's progress towards high heliographic latitudes (> 60^{o}) placed it outside the scope of the ENLIL model, which is limited to 59^{o} heliographic latitude. The

images show a widening ion tail as it curves away from the extended radial vector. The cometary derived solar wind velocities match well with expected values for a slow solar wind.

A recurring trend has been noticed for all analysed comets, which accounts for the 200 km s^{-1} discrepancy between the first and last estimate on the 14th November. The first solar wind estimate, sampled near the comet head, has tended to be significantly higher than the speeds implied by the rest of the ion tail. This behaviour could be explained if the comet encountered a transition region; however, this systematic range of values has been noted previously due to a curving ion tail towards the dust tail. This implies that the tail curvature is either a feature of this technique or the dust tail is also acting as a source of pick-up ions into the mass-loaded solar wind, giving an asymmetric ion source.

CR 2117

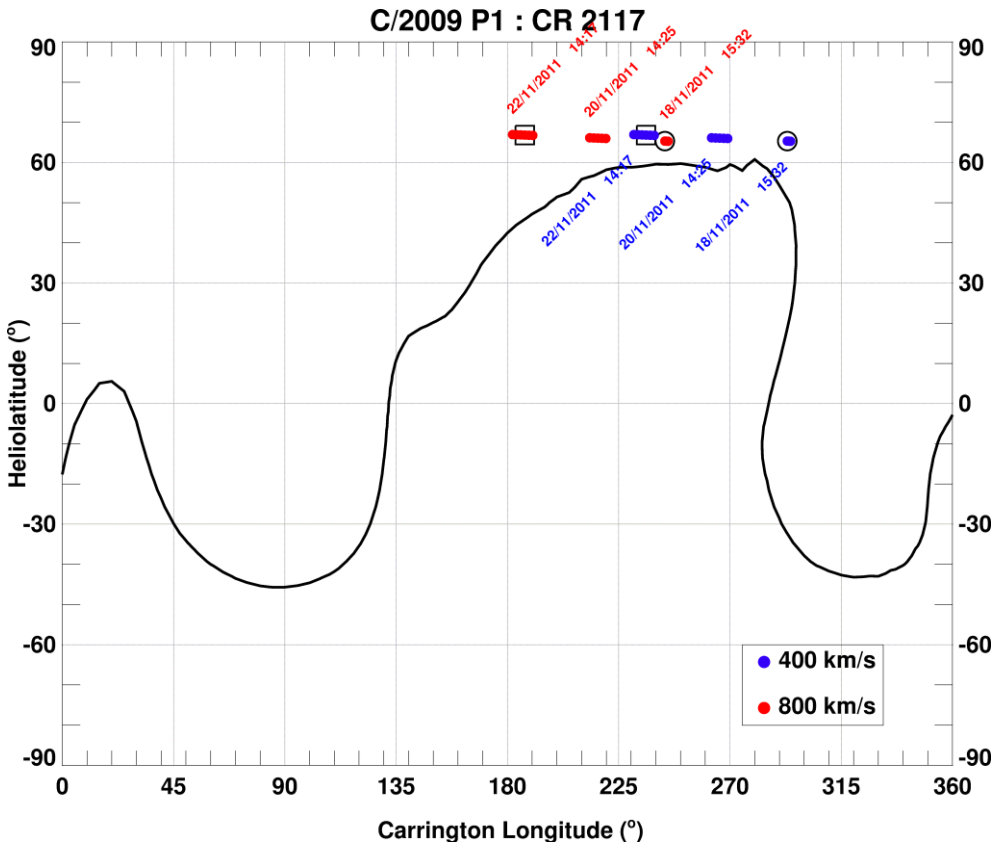

Figure 5.102: Mercator map for CR 2117 predicting slow solar wind speeds at the comet from its proximity to the neutral line at high heliographic latitudes.

No comparison models were available for CR 2117. The solar wind velocity measurements match expectations for a slow solar wind. Measurements from the 20th and 22nd November are taken from two images with an extensive, curving ion tail with samples taken over a 8-10 hour period from both images. There is a double kink in the ion tail on the 22nd November, suggesting a DE may have occurred [Figure 5.103]. Measurements of first and second kink along the same radial vector show that they are travelling at ~280 and ~370 km s^{-1} respectively. The high heliolatitudes of the HCS mean that it could be the cause of the DE. Two ICMEs were tentatively linked to this disruption event [Figure 5.104]. The comet's position angle was ~35° and the solar axial tilt position angle at 20°. The first was observed at 14/11/2011 15:48 UT with a linear speed of 421 km s^{-1}, CPA of 25° and angular width of 61°. The second was a partial halo CME, observed at 15/11/2011 05:24 UT, travelling at 523 km s^{-1} with a CPA of 60° and angular width of 198°.

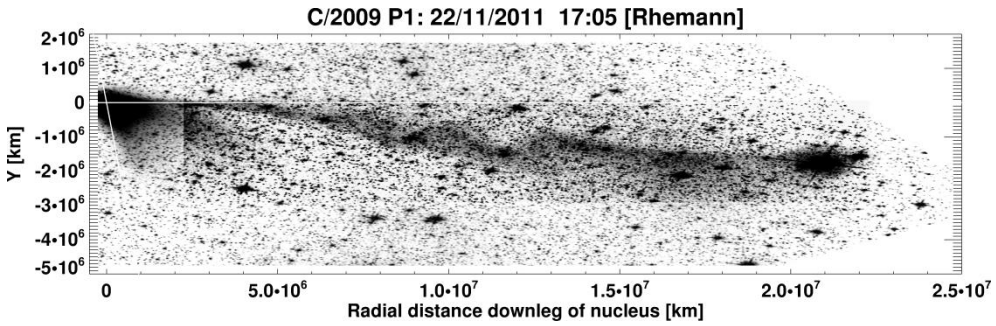

Figure 5.103: Mapped image of C/2009 P1 by G. Rhemann on 22/11/2011 17:05 UT showing a large double kink in the ion tail. Image has been contrast enhanced with IDL and other imaging software.

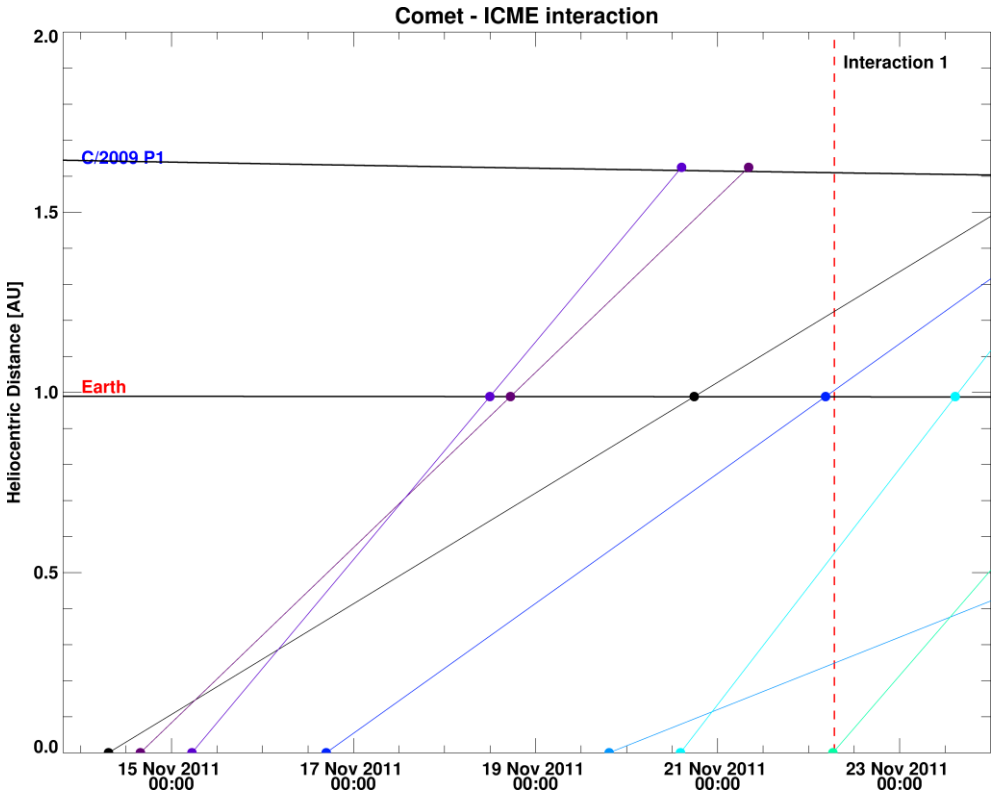

Figure 5.104: ICME Shock Arrival Times (SATs) at Earth and the comet's location for interaction occurring on the 22nd November 2011. The first and second kink were measured at 06:47 UT (dashed red line) on 22/11/2011.

Two further ICMEs observed on 20/11/2011 at 14:12 UT (linear speed: 567 km s^{-1}; CPA: 37°; Ang. width: 120°) and 22/11/2011 at 06:24 UT (partial halo CME; linear speed: 506 km s^{-1}; CPA 96°; Ang. Width: 192°) are expected to cause a disturbance at the comet. Two images taken half an hour apart show a large bend in an ion tail, which is leading comet motion. This indicates a large non-radial component in the solar wind. The bend does not display any distinguishing features to track with my flow vector maps. The sun's tilt axis is at a position angle of 18° and the comet was at a 25° position angle.

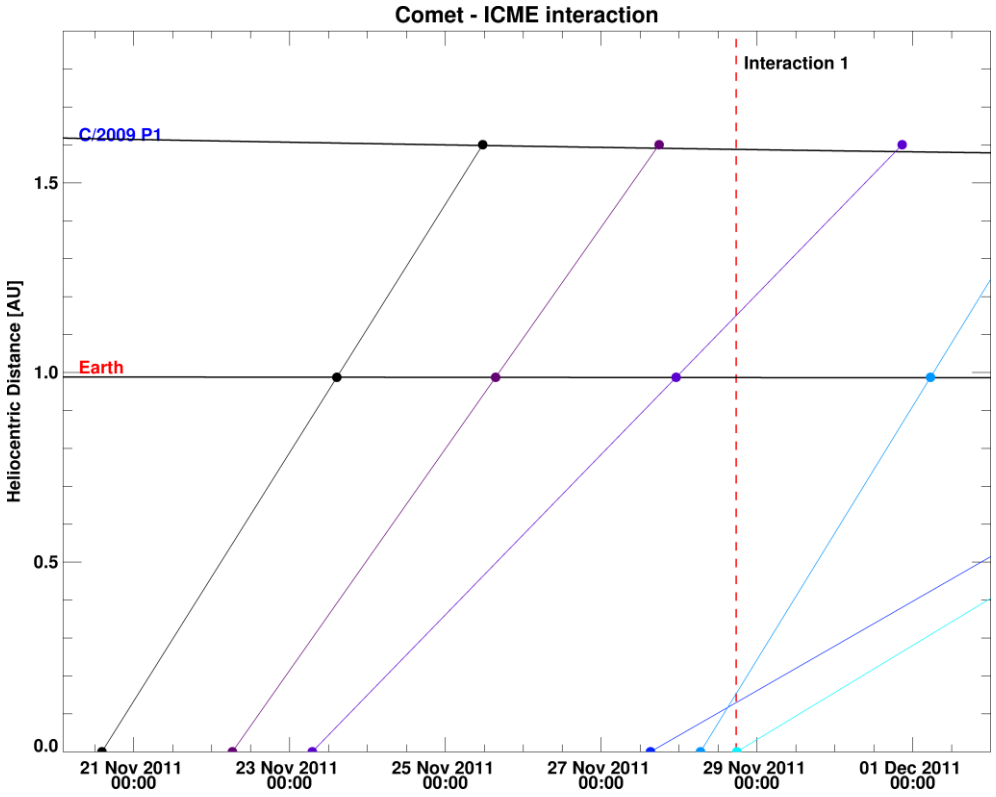

Figure 5.105: With considerations to external forces acting upon an ICME's motion in the interplanetary medium, the first two ICMEs are likely candidates to have caused a large bending and non-radial motion of the ion tail.

CR 2118 – 2121

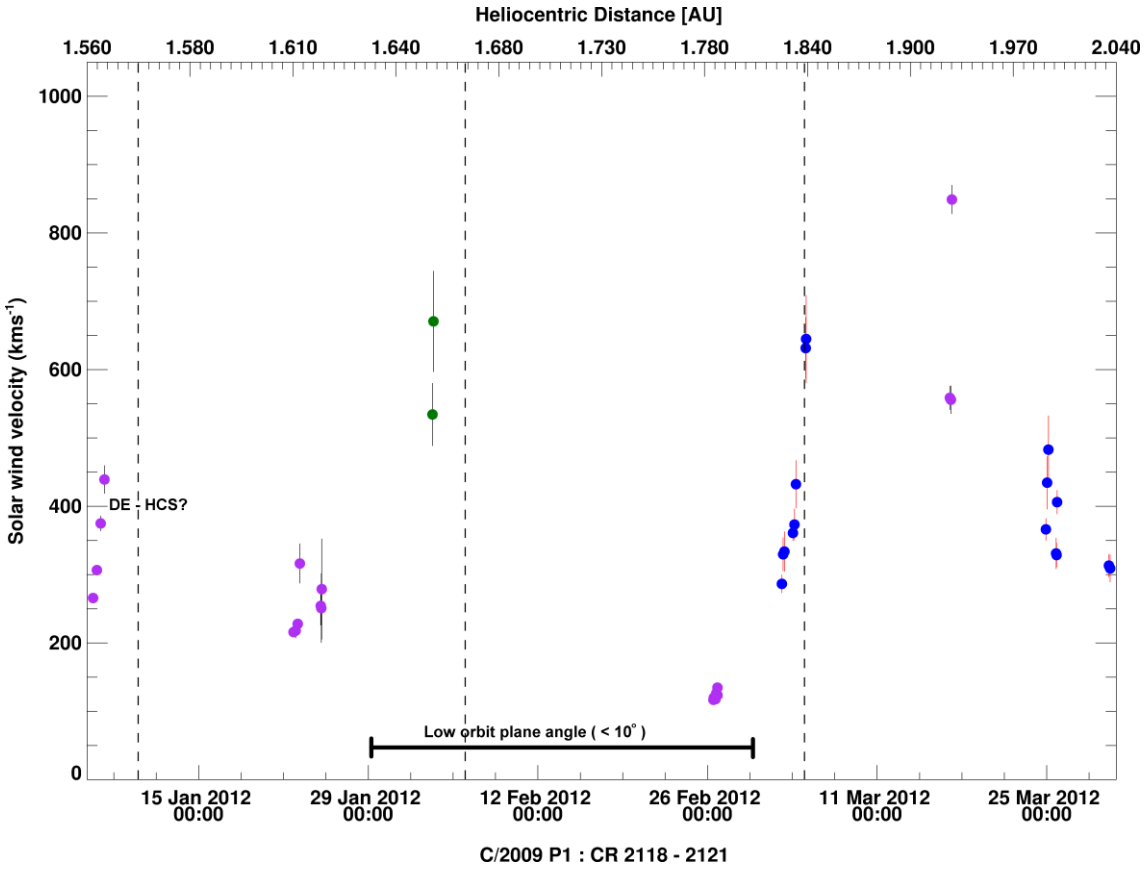

Figure 5.106: Solar wind velocities measured from observations for CR 2118 to 2121.

From Figure 5.106, we expect the comet to encounter two transition regions, during CRs 2120 and 2121. The orbit plane angle was below 10° throughout CR 2120.

CR 2118

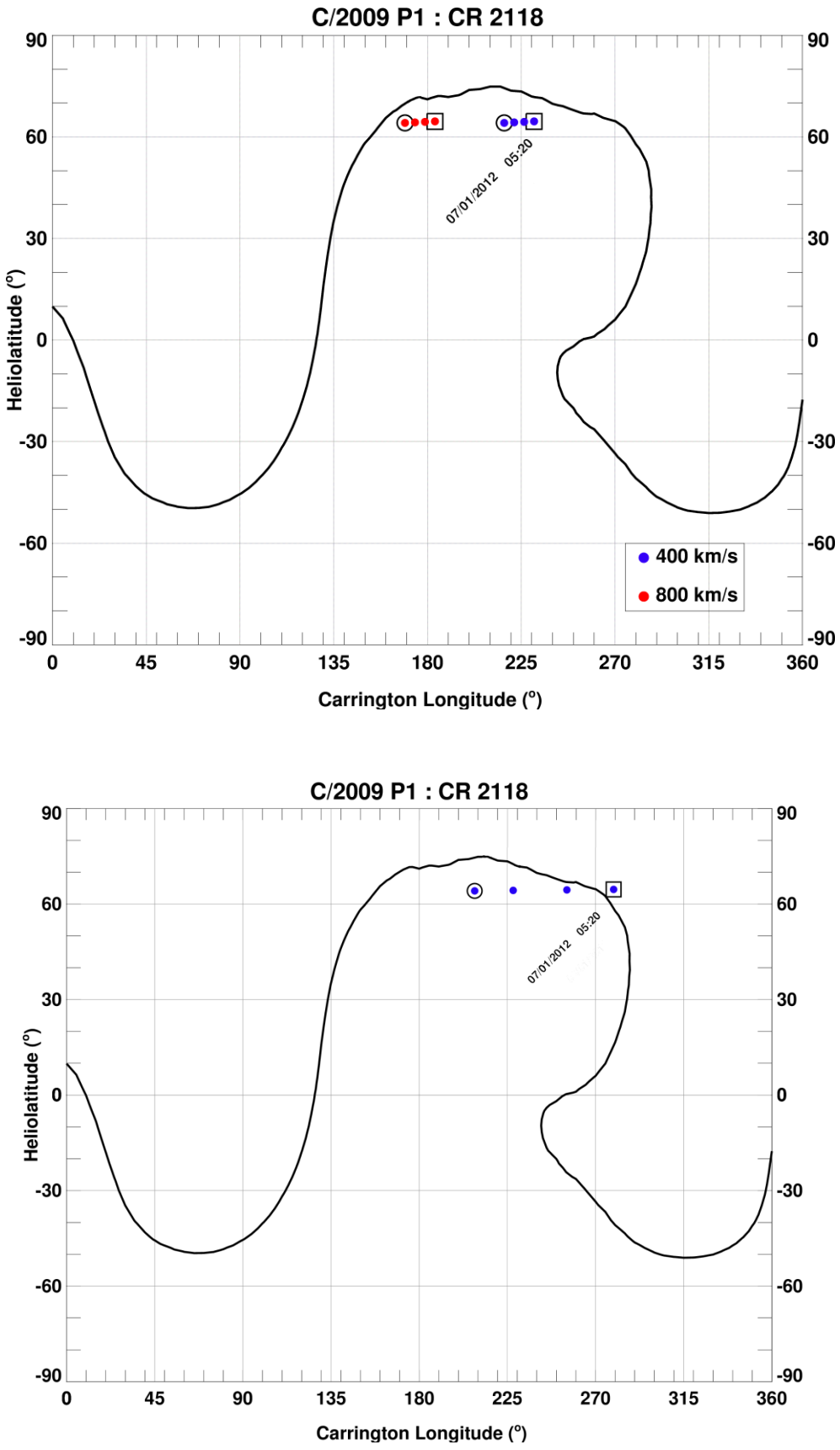

Figure 5.107: Mercator maps for CR 2118. Top plot shows the sources mapped to the solar wind source surface assuming a 400 km s^{-1} and 800 km s^{-1} solar wind velocities. The bottom plot shows the samples mapped back using solar wind velocities calculated with this technique.

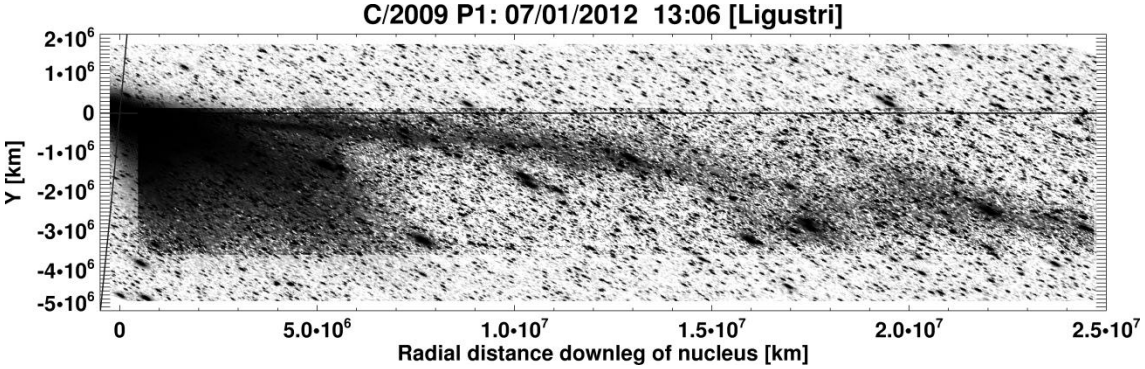

Figure 5.108: A DE is clearly seen in a contrast enhanced image of Ligustri. The image was observed on 07/01/2012 at 13:06 UT.

If the radial velocities, sampled from 06/01/2012 06:50 UT to 07:01/2012 05:20 UT, are assumed to be correct, the comet will have encountered a sector boundary in the solar wind as it crossed a warped HCS, as per Figure 5.107 and leading to the DE observed in Figure 5.108. The first measurement is of the new ion tail, which is travelling slightly faster than the disconnected tail. An alternative explanation is a halo CME arriving at the comet shortly before the expected interaction. The dashed line [Figure 5.109] marks the halfway point between the times at which the samples were taken. The comet's position angle was 339^{o} and the solar rotation axis at 2^{o} position angle. The CME's CPA was 297^{o} with an angular width of 215^{o}. The CME was observed to travel at 639 km s^{-1} on 01/01/2012 at 12:36 UT.

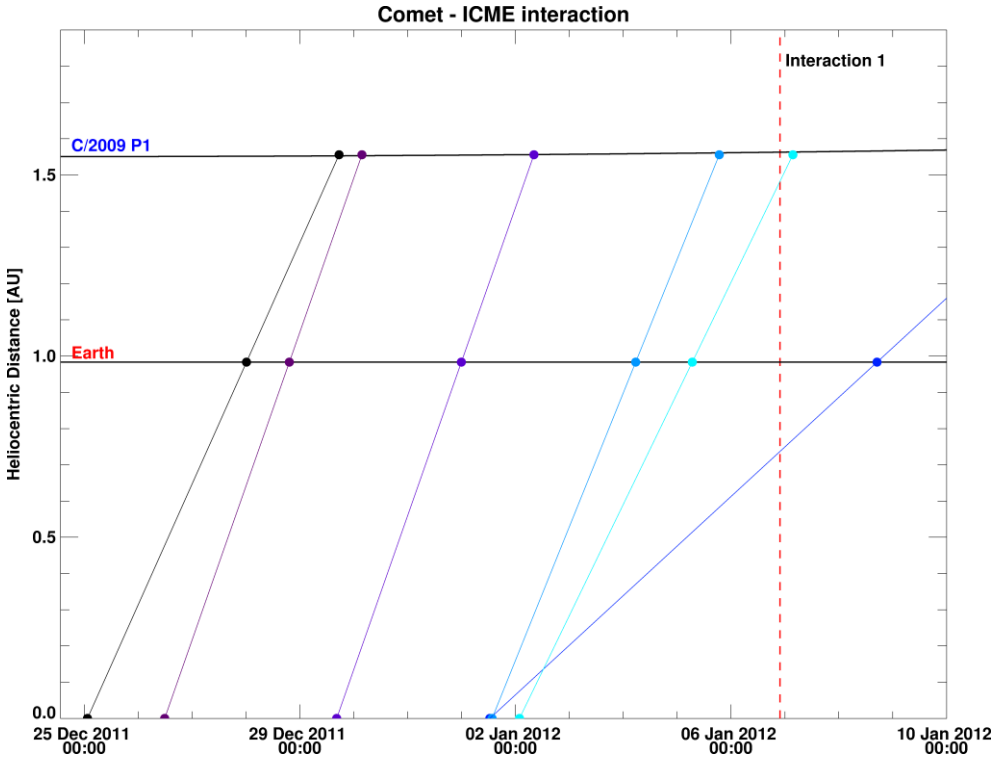

Figure 5.109: ICME shock arrival times at C/2009 P1 assuming a linear plane of sky speed.

CR 2119

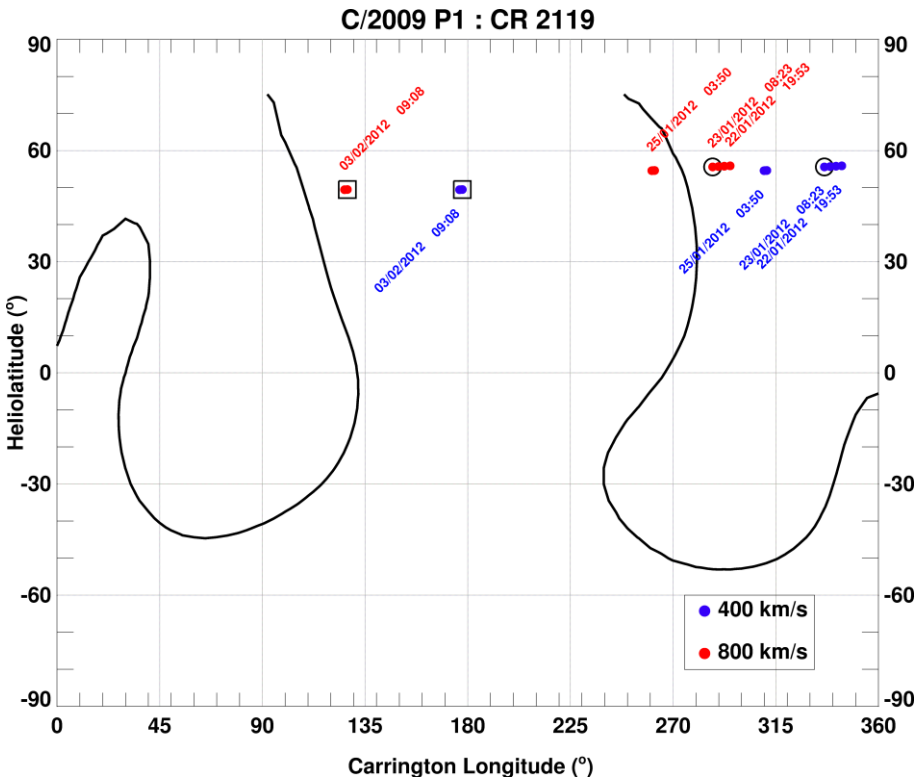

Figure 5.110: Mercator map for CR 2119. The comet will be experiencing slow solar winds due to the proximity of the mapped source bundles to the expected position of the neutral line.

The comet's descent towards lower heliographic latitudes during CR 2119 means we can once again anticipate solar wind streams interacting with the comet. It was not possible to compare solar wind velocities for higher latitudes due to the latitudinal limitations of the ENLIL MHD model from CCMC [Figure 5.111]. The MHD model predicts that the comet will traverse fast wind streams of ~600 km s^{-1} and decreasing [Figure 5.111]. By February 3, 2012, it is entrapped in a pocket of ~500 km s^{-1} surrounded by slightly slower 400 to 300 km s^{-1} radial plasma velocities. This conflicts with the solar wind velocity reported in Figure 5.106. In 12 images over the course of 9 days from 26/01/2012 to 03/02/2012, the ion tail lead the comet motion. It is highly likely that we were witnessing the non-radial velocity components out of the orbital plane. The orbit plane angle was ~10^{o} for this period and slowly decreasing. Thus, the last estimates, marked in green in Figure 5.106, should be considered erroneous due to the faintness of the ion tail and that the observed ion tail orientation is not due to the dynamical aberration from a radial solar wind. An interesting geometrical phenomena known as the anti-tail, arising when the observer crosses the comet's orbit, was readily visible for comet Garradd during this period. The large kink in C/2009 P1 is likely due to the geometrical perspective rather than a transient solar wind event.

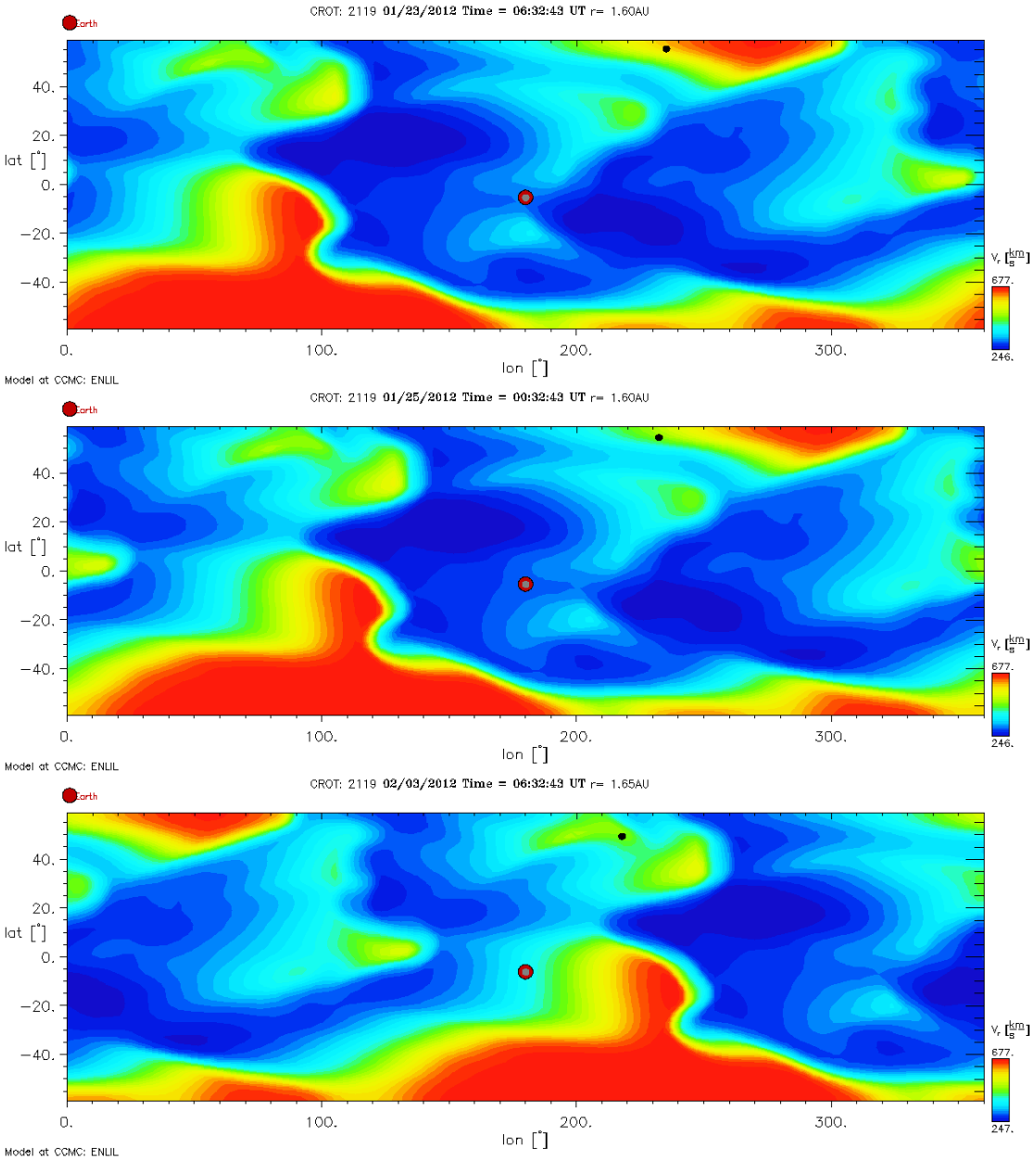

Figure 5.111: The comet is predicted to encounter fast solar wind speeds of ~600 km s^{-1} and decreasing to ~ 400 km s^{-1}.

CR 2120

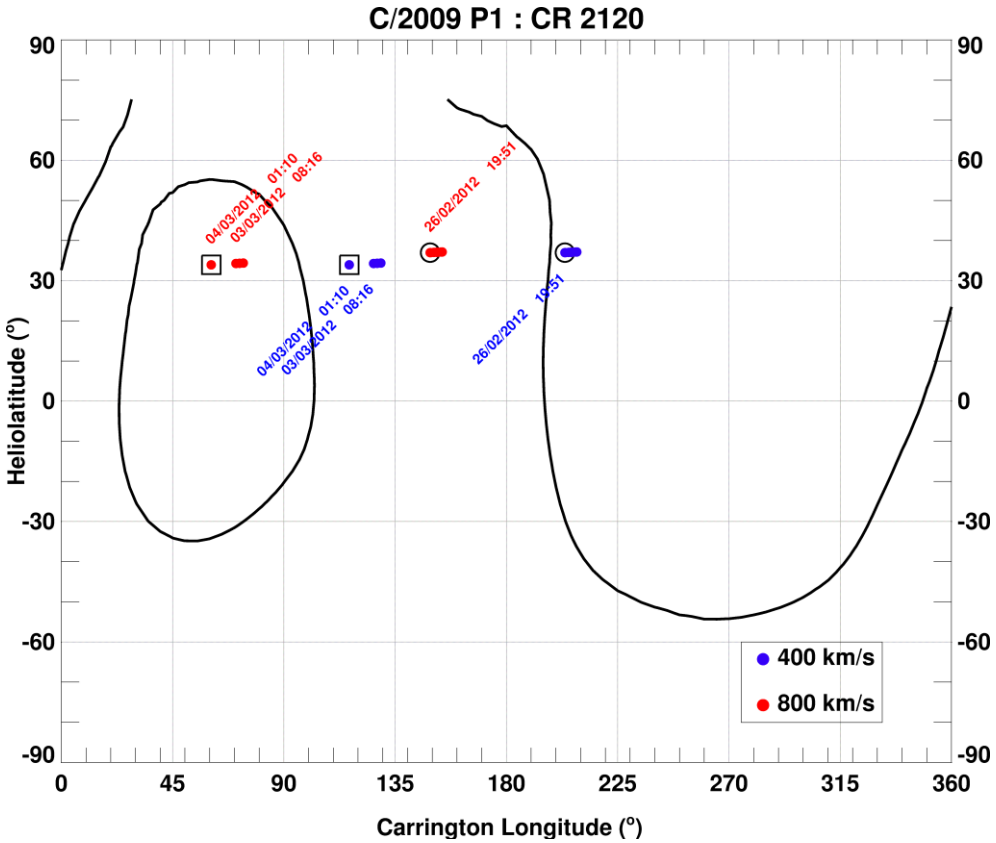

Figure 5.112: The comet is expected to encounter two HCS crossings if it initially encountered slow solar wind, followed by fast solar wind streams from the magnetic island.

Images gradually became distorted as the Earth crossed the comet's orbital plane. Comet Garradd during CR 2120 exhibited one of the most spectacular anti-tails [Figure 5.113] to be recorded in photographic history. As the orbit plane angle gradually increases, the ion tail is once again seen leading comet motion in late February.

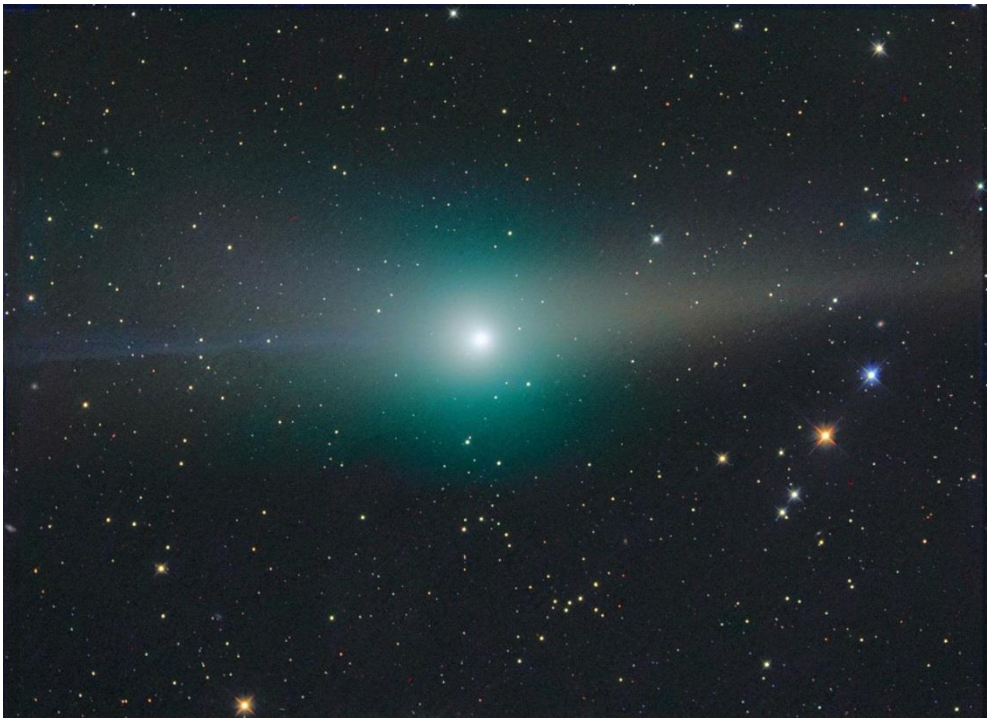

Figure 5.113: The anti-tail (heavy dust grains) of comet C/2009 P1 apparently pointing sunward in the direction opposite to the ion tail. Image observed by Jäger on 2012/02/20 at 21:50 UT.

By February 26, 2012, the geometry is again adequate for radial sample extraction. The comet, however, is still at low orbit plane angles and extremely low velocities were derived. Non-radial velocities were derived and presented in Figure 5.115. The images, example given in Figure 5.114, show a DE occurring on this day. Considering a 400 km s^{-1} solar wind speed, the comet is expected to cross the HCS according to Figure 5.112. The ENLIL simulation counters that argument, predicting a HCS crossing a few days later. The comet should also be immersed in 350-400 km s^{-1} solar wind streams.

Assuming that the Mercator map is a better match for solar wind conditions at the comet, which is not necessarily the case, and knowledge from prior observations that HCS crossings produce unreliable solar wind velocities, the DE could have been caused by a HCS crossing. In the absence of a modelled CIR and empirical evidence for an ICME interaction, a HCS crossing is the most plausible scenario.

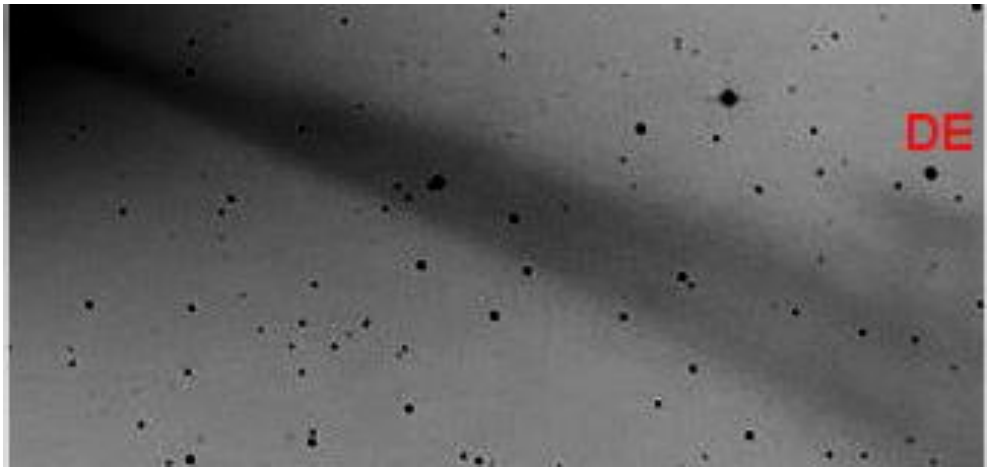

Figure 5.114: Contrast enhanced image of a DE captured by Rhemann on 26/02/2012 at 23:02 UT. The comet's nucleus is towards the upper left of image.

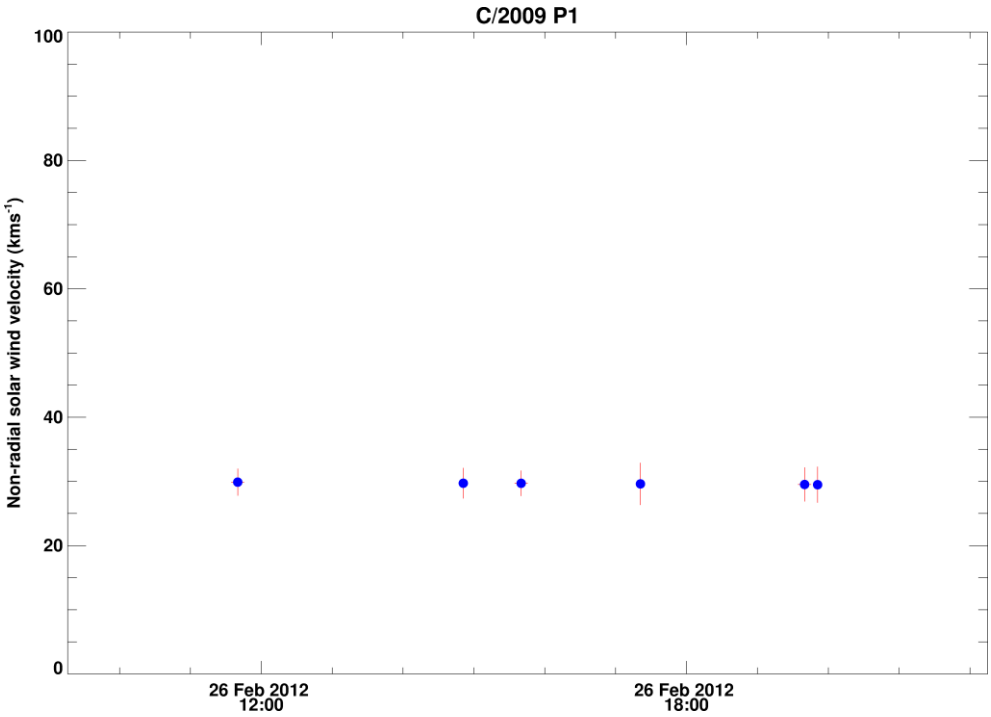

Figure 5.115: Non radial velocities derived from two images on 26/02/2012.

CR 2121

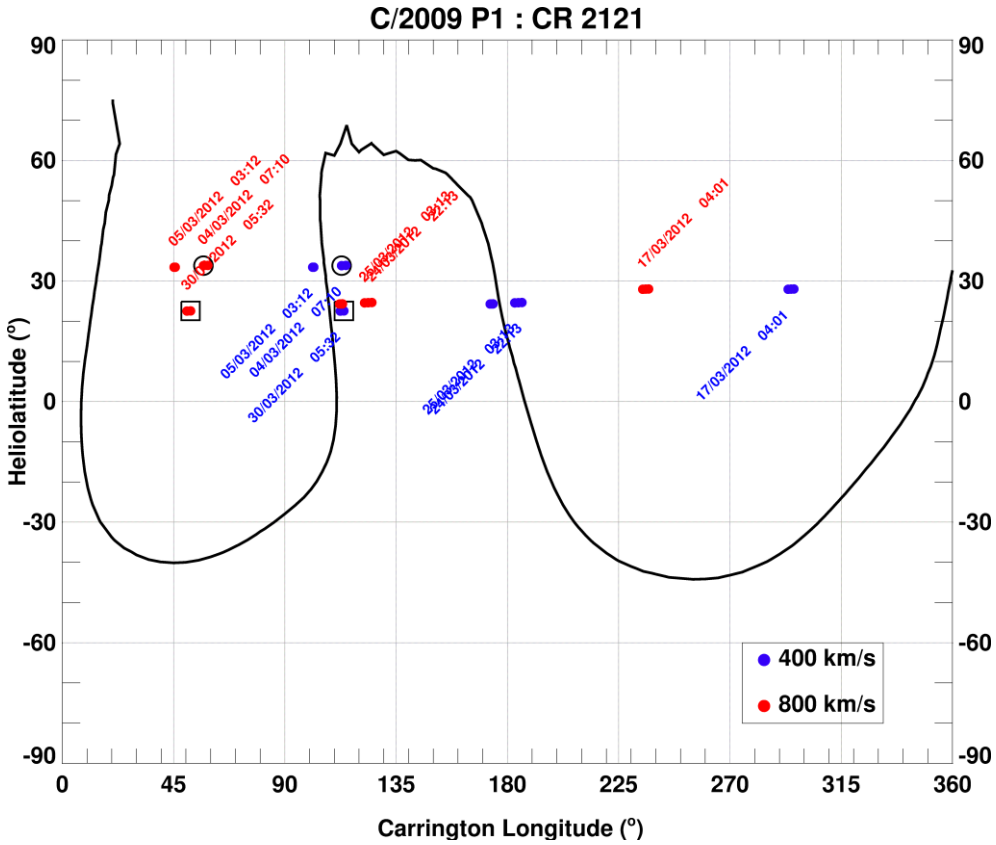

Figure 5.116: Mercator map for CR 2121 for comet C/2009 P1.

CR 2121 may have proven dramatic for the comet. Multiple ENLIL runs modelling CIRs and CMEs were requested for this time period with different inner boundary conditions set using magnetograms from different observatories. For consistency, a model from 2012, using Kitt Peak magnetograms with inner boundary conditions set by the WSA model, was used to predict MHD values at the comet. The model was initially compared alongside a more recent one from 2014 using magnetograms from the GONG observatory. They were both found to simulate similar velocities at the comet's location. However they differ very slightly in terms of the solar wind structure in the inner heliosphere at the comet's latitudal plane. The magnetogram source from the Gong observatory is provided with a warning that there are known issues with polar fields and that the data source is still under trial. Thus, only the WSA and Kitt Peak models are presented here.

My solar wind velocities match closely the predicted values on the 4th and the peak in velocity on the 5th is within the bounds of the predicted MHD values, which also computes a small bump in velocity at the comet [Figure 5.117]. The ion tail is observed to lead the comet motion. No intrinsic transient properties of the solar wind were identified as the cause. Erring on the side of caution, I speculate that the CME observed on 29/02/2012 12:00 UT with a CPA of 249°, angular width of 85° and travelling with a linear speed of 675 km s^{-1} could induce a non-radial flow of the ion tail [Figure 5.118]. This is contingent on the ICME decelerating to the slow solar wind speeds it is expected to encounter prior to interaction at the comet. The comet's position angle is 243° and the sun's rotational axis at a position angle of -21°.

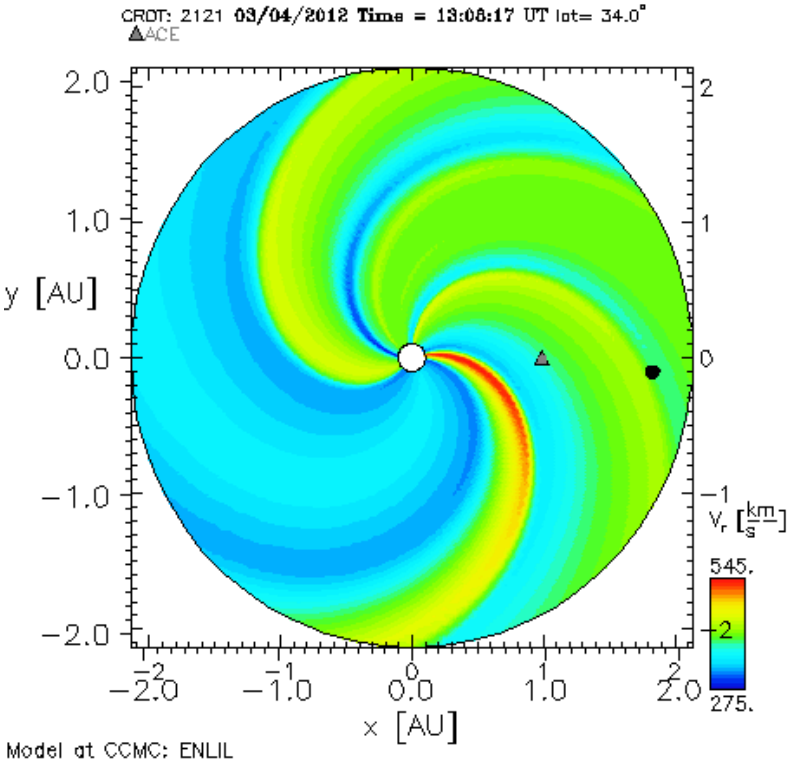

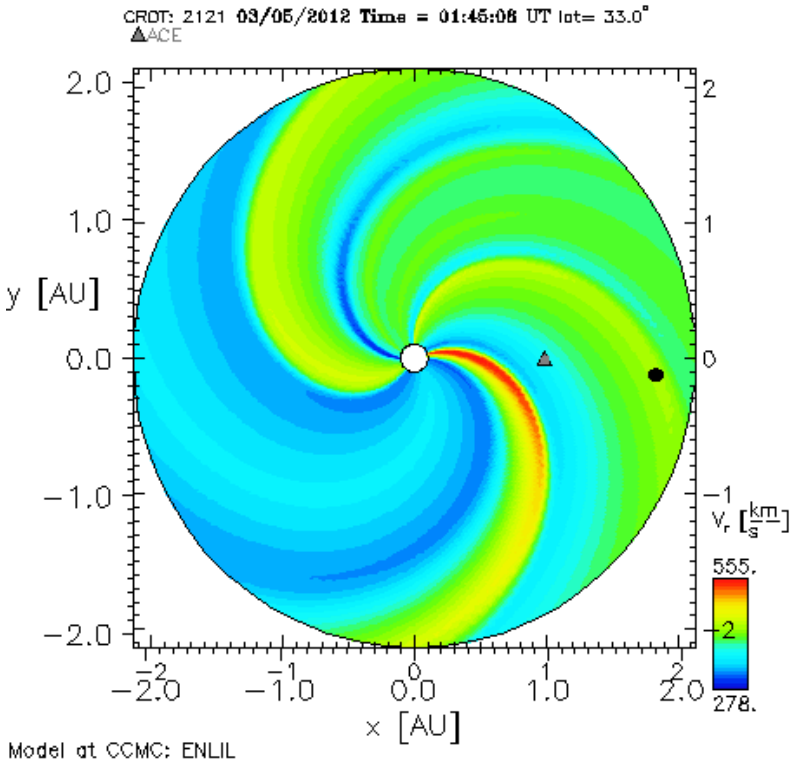

Figure 5.117: Comet encounters a small peak in velocity in the ambient solar wind speed of ~400 km s^{-1}.

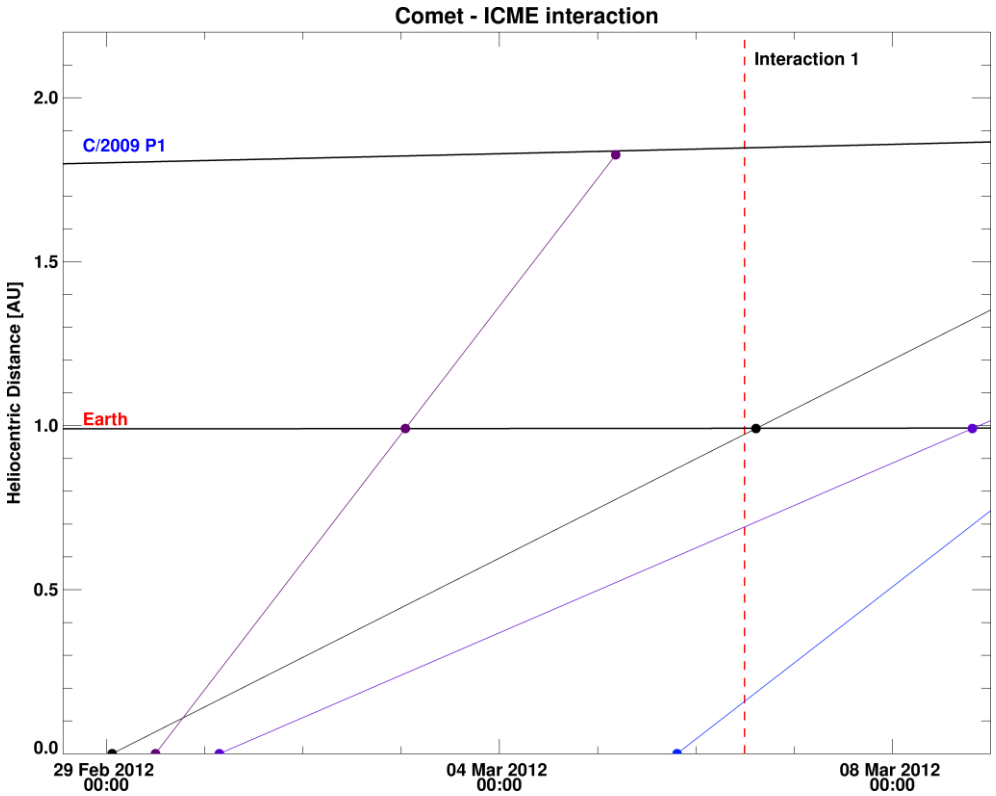

Figure 5.118: ICME SATs at the comet inducing a non-radial flow of the ion tail on 06/03/2012.

R. Ligustri managed to capture one of the most dynamic ion tails studied in this project. The image acquired in the morning of the 17th March 2012 shows a "3 tailed" comet. The bottommost tail is clearly a tail ray. The main tail straddles the Sun-comet prolonged vector with the bifurcating tail, splitting at 5 x 10^6 km downstream of the nucleus, bestriding it. The tail lagging the comet motion contains a large kink [Figure 5.119]. The large range of solar wind speeds is due to part of the tail lying on the radial vector. There are no CIRs or HCS predicted from the two ENLIL models used for comparison. Comparison with the Mercator map for CR 2121 [Figure 5.116] does not shed any light on the cause either.

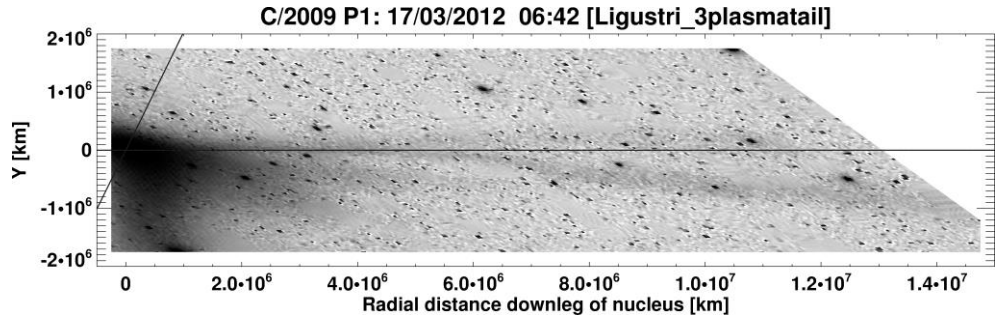

Figure 5.119: Bifurcating ion tail with the main ion tail showing a smooth bend in the middle. This is clear evidence for a transient solar wind phenomena. Image was obtained by Ligustri on 17/03/2012 at 06:42 UT.

After assessing Figure 5.120, an interaction with a fast halo CME, observed at 18:00 UT on 13/03/2012 with a linear plane-of-sky speed of 1296 km s^{-1}, is proposed. The solar axial tilt's position angle is -23° and the comet at a position angle of 197°. The ICME would have been decelerated by the surrounding slow solar wind in the interplanetary medium.

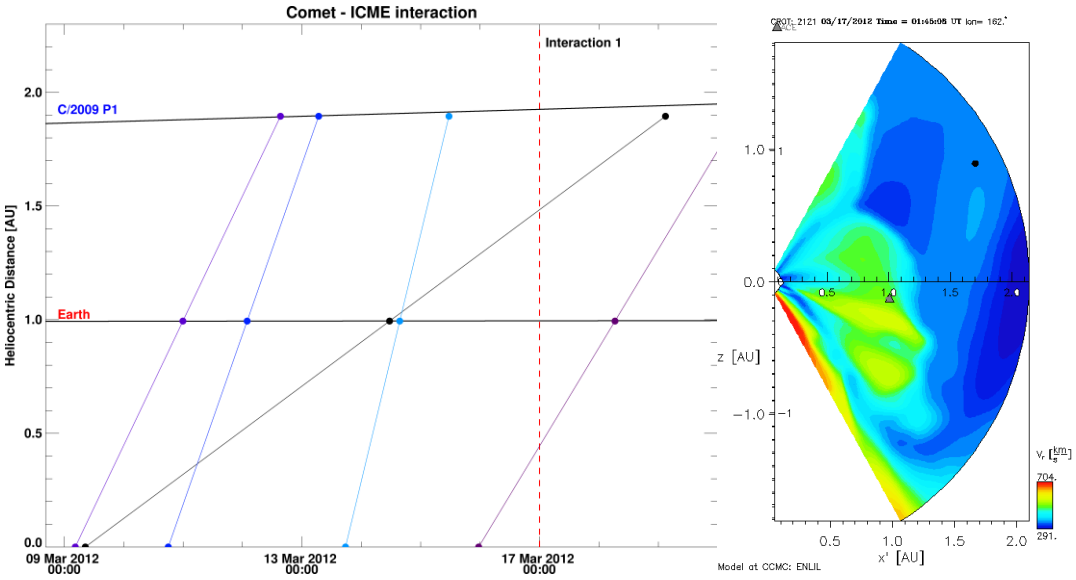

Figure 5.120: Expected arrival times for 3 halo CMEs (first three) at the comet, causing the appearance of 3 ion tails. The right hand side image shows the comet's location enveloped by the slow solar wind in heliographic coordinates.

CCMC ENLIL MHD velocities on 25th and 30th predict 350 km s^{-1} and 450 km s^{-1} for these respective periods. Modelled values for CR 2121, and comet C/2009 P1 (Garradd) in general, are in good agreement with estimates from remote observations of the ion tail.

5.4. Comet Pan-STARRS (C/2012 K1)

C/2012 K1 was a dynamically new comet to the inner solar system. The comet was on a retrograde orbit, inclined 142.4º to the ecliptic with its ascending node equal to 317.7º. This new comet was a source of pristine volatiles and dust grains, virtually unaltered by solar radiation due to its remote origins in the Oort cloud. Its apparent m_v rose steadily up to a peak of +6.9 in mid-October (+8.1 reported by JPL). C/2012 K1 had a closest approach of 1.05 AU to the Sun, and 0.95 AU to the Earth in October 2014, when it was at its brightest. Inclination (*i*) = 142.4º; ascending node = 317.7º, eccentricity (e) = 1.00; Perihelion date (T) = 27/08/2014, 15:50 UT

Data coverage

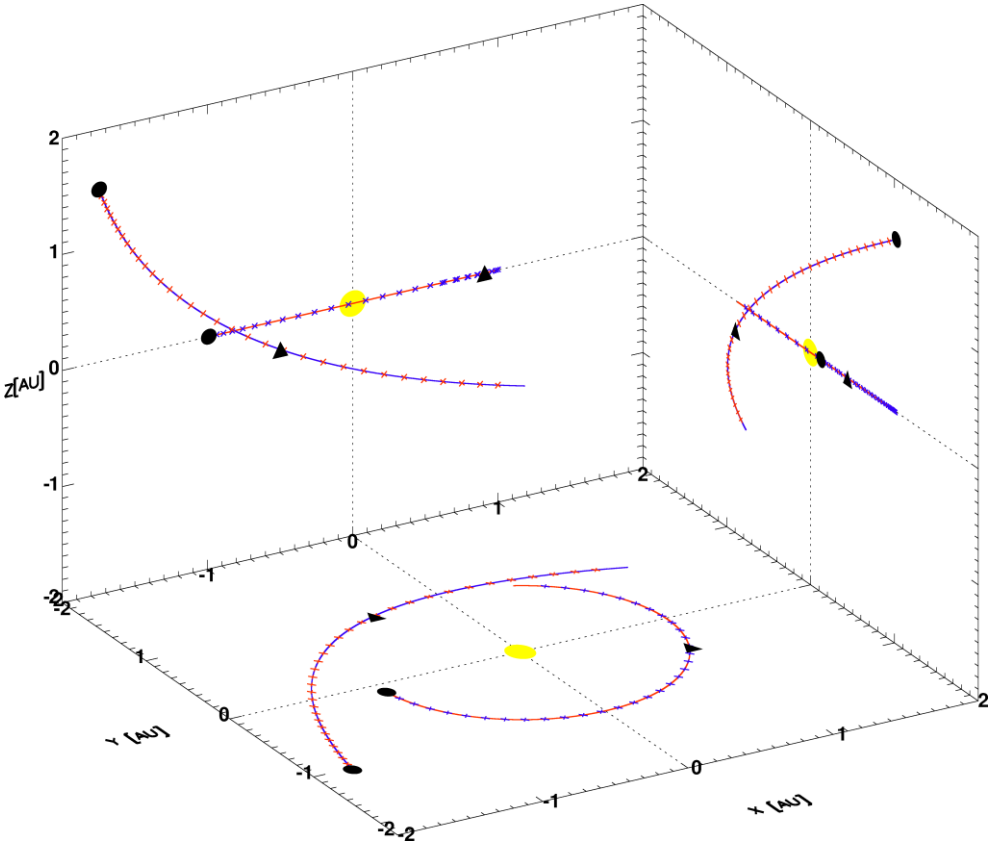

Figure 5.121: Heliocentric ecliptic coordinates of comet C/2012 K1 (Pan-STARRS). Black circles represent the start of the orbits and black triangles show the positions of the comet and the Earth at the comet's perihelion.

Observations were well interspersed across the comet's orbit during the first phase of the analysis [Figure 5.121], with most of the observations clustered post-perihelion [Figure 5.122]. I was unable to extract solar wind velocity estimates from the images available pre-perihelion and hence they are not included in Figure 5.122. The ion tail lay over the Sun-comet radial vector in these images, due to a low orbit plane angle at low solar elongation angles.

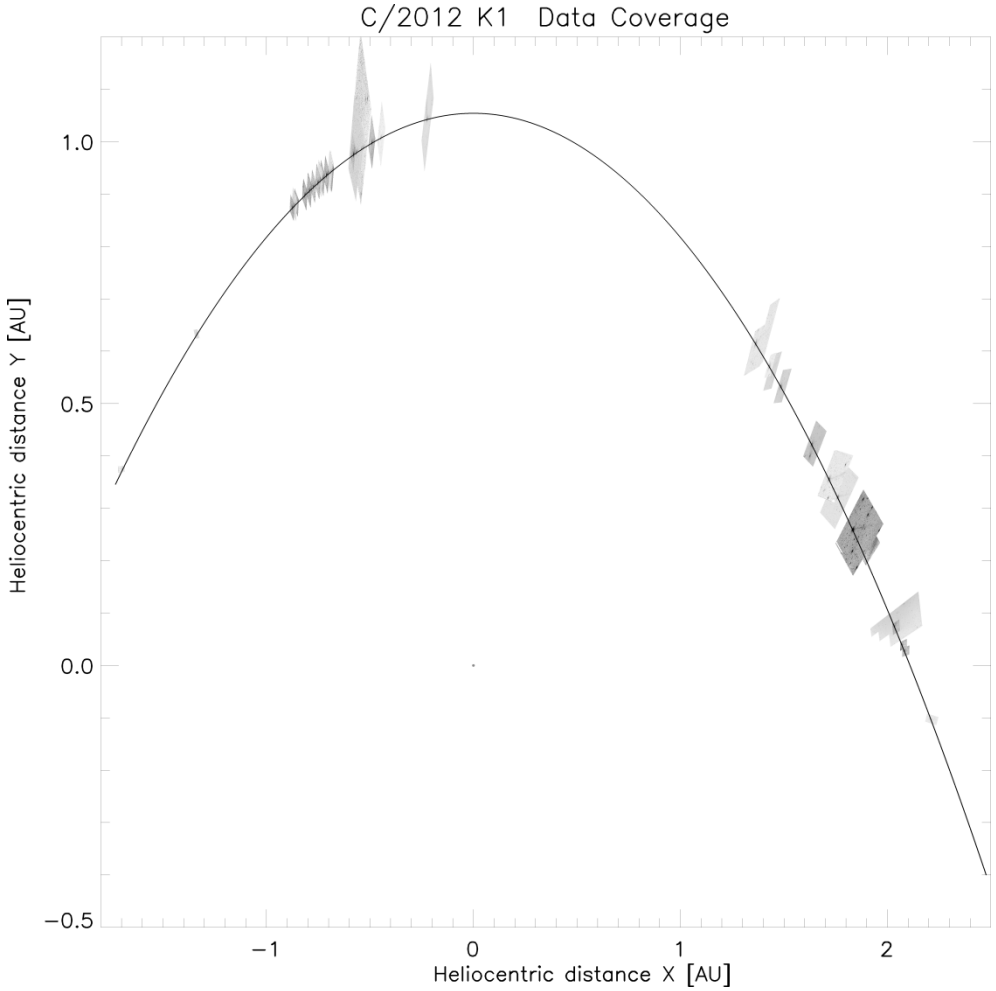

Figure 5.122: Data coverage for comet C/2012 K1 (Pan-STARRS). The images and the comet's orbit have been mapped so that the y-axis is defined as the direction to perihelion. Earliest image is to the right of the data coverage plot, increasing chronologically towards the left.

Image statistics

A total of 53 amateur photographs were processed for this comet. Only 46 made it through the Astrometry plate solving algorithm. After implementing our rejection criteria, 21 images were filtered out. A significant fraction of the rejected images showed the ion tail sitting along the prolonged Sun-comet vector. 71 solar wind estimates were ultimately extracted, of which one was determined to be unreliable, 17 were sampled when the tail showed large orientation changes and 12 had early sections of the ion tail lying on the radial vector. There were no tail rays or features to track in the final set of images.

5.4.1. Radial Solar Wind Speeds

The orbit plane angle of C/2012 K1 remained fairly low for the entirety of the studied images. The best observing geometry occurred in late October, when the orbit plane angle topped off at ~40º. I expect the solar wind velocity to have a large scatter of solar wind velocities due to the poor observing geometry.

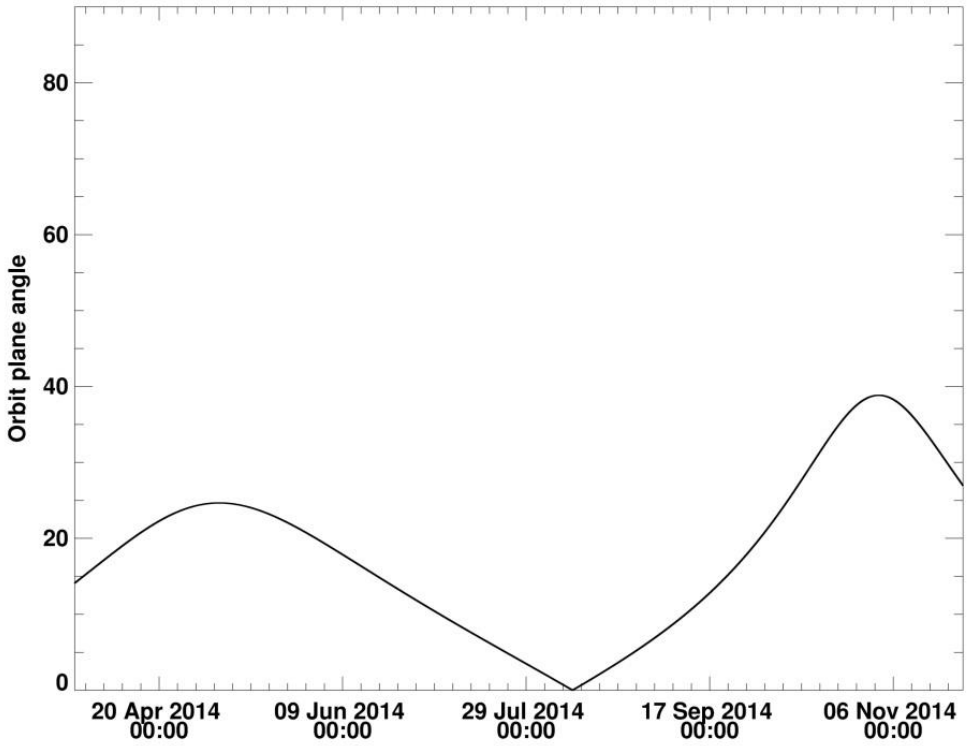

Figure 5.123: The orbit plane angle of C/2012 K1 (Pan-STARRS) is within ± 10º between 05/07/2015 and 09/09/2014. We expect observations of the ion tail to largely represent the non-radial solar plasma outflow during this period.

As per the previously set standard for data plots, green data points are mostly related to images where it was not possible to resolve the faint ion tail against the sky background once mapped onto the comet's orbital plane or if a significant section of tail laid on the radial vector. For this comet geometry, the technique produced slightly higher solar wind velocities but was still within expected ranges of the solar wind. It is unclear whether this ion tail orientation is a result of the observing geometry or solar wind influenced. The image quality for C/2012 K1 was slightly lower than the other studied comets. Once mapped onto the image plane, the ion tail appeared blurrier and was thus harder to accurately measure.

CR 2150

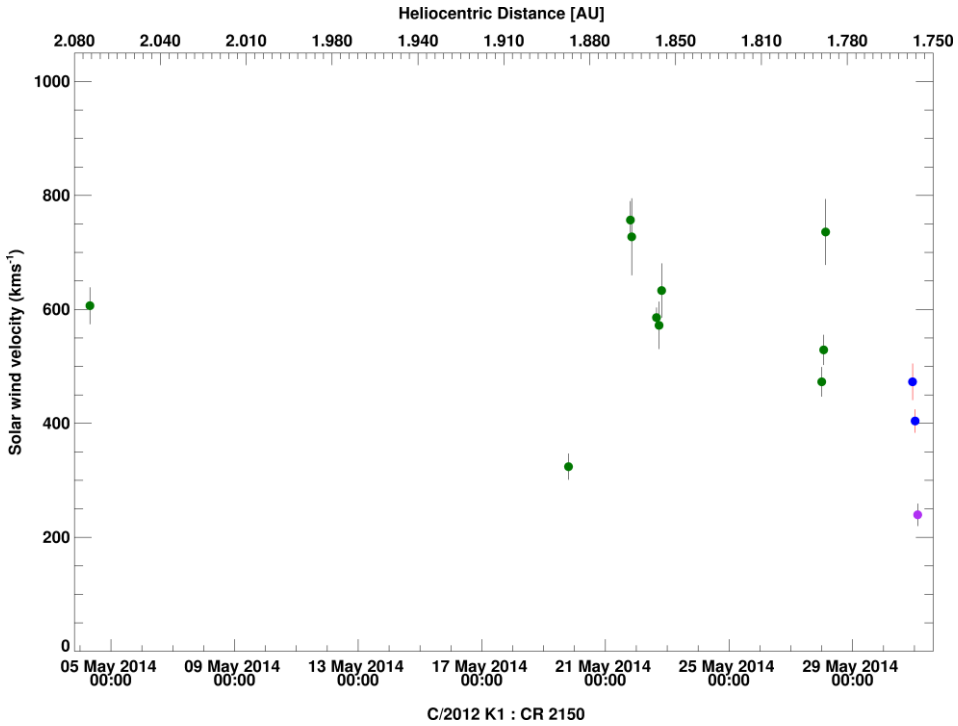

Figure 5.124: Solar wind velocities derived from C/2012 K1 during CR 2150.

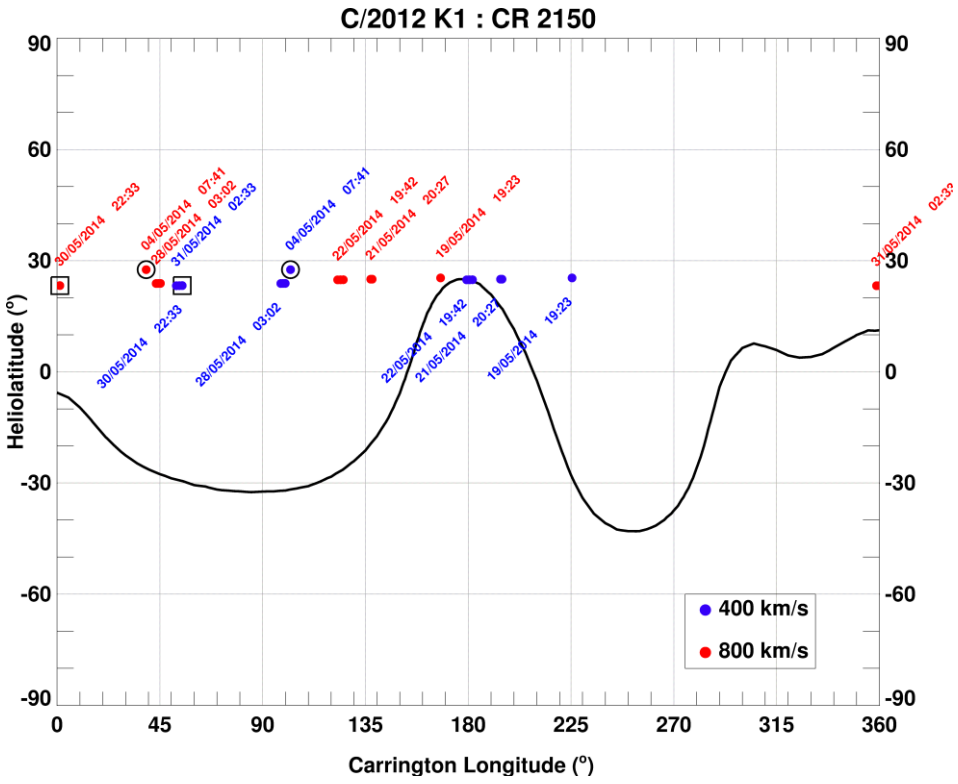

Figure 5.125: Mercator map for CR 2150. A DE is expected between the 21st and 22nd May 2014 if the comet interacts with slow solar wind streams either side of the neutral line on the solar wind source surface.

The comet is expected to mostly interact with fast solar wind speeds in the second half of CR 2150, with an HCS crossing on the 22nd May 2014. The comet should experience the slow solar wind on either side of this crossing. There were no HCS-related disconnection events in the data. Thus one could conclude from Figure 5.124 and Figure 5.125, that the comet does not encounter the propagated neutral sheet into the inner heliosphere.

The first ENLIL visualisation on 04/05/2014 starts a few hours after the first data point reported here, and predicted a slow solar wind region of 250 - 300 km s^{-1}. The ion tail is faint and lies on the Sun-comet extended radial vector. Thus these data should be considered uncertain. The extremely faint ion tail on 19/05/2014 lay on the radial vector. Though it matches well with the ENLIL expectations of ~ 400-450 km s^{-1}, it should be discounted as an irregular data point so as to be consistent with previous analysis. Images on the 21st and 22nd May 2014 are both affected by a similar tail orientation, whereby 20% of the visible ion tail lay on the radial vector. There were no enhancements in |B| or |N|, nor polarity reversals. The longitudinal velocity component was near 0 and the latitudinal component ~ 5 km s^{-1}. The orbit plane angle is between 10 and 20 degrees and the geometrical orientation of the ion tail and extended radial vector with respect to Earth is such that the radial velocities will be overestimated [Figure 5.126]. The cutplane below shows a projected position of the Earth's heliographic coordinates at 1.85 AU. From the Earth's vantage point at 1 AU, the projection of the ion tail at low orbit plane angles will be further warped towards the Sun-comet radial vector, giving the illusion of higher radial solar wind velocities. A curved ion tail accentuated by a mild latitudinal velocity component will be but a minor contribution towards this overestimation, though it would enhance the illusion of the tail semi-lying on the radial vector.

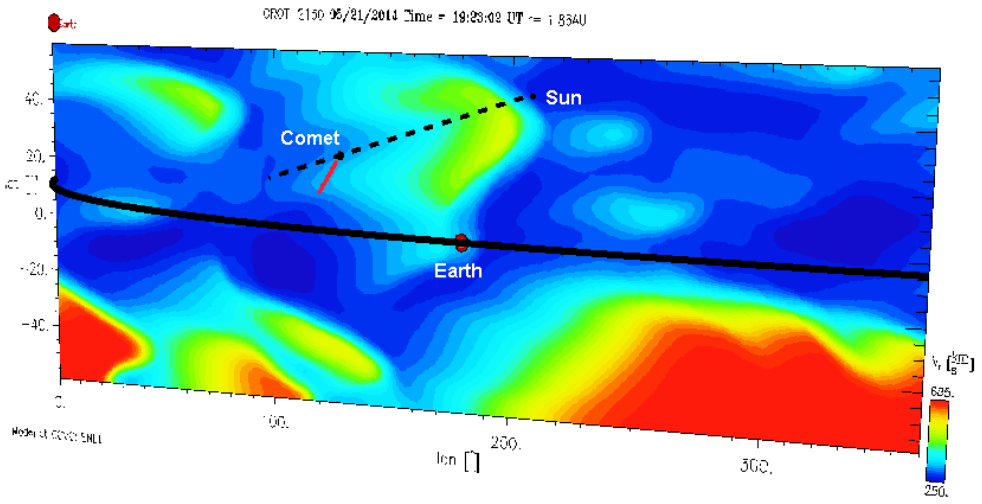

Figure 5.126: Warped cutplane of CR 2150 to show the extended Sun-comet radial vector, the ion tail's rough orientation along the comet's orbital plane and the Earth's "orbit". This cutplane is at 1.85 AU.

A similar scenario on 28/05/2014 has a higher latitudinal velocity component of ~15-20 km s^{-1} resulted in ~ 300 km s^{-1} higher than expected radial velocities. On 31/05/2014, the large aberration angle and curved tail near the nucleus is indicative of a transient phenomenon. The MHD model radial solar wind velocity is ~ 275 km s^{-1} and a fairly good match for the estimated values. Both the longitudinal and latitudinal components are near-zero, further consolidating the argument that non-radial components play a major role in the over- and under-estimation of the radial solar wind velocities at low orbit plane angles. There is, however a small kink in the ion tail, yet no predicted enhancements in |B|, |N|, polarity of the HMF streams or the non-radial components of the solar wind velocity. The relatively slow ICME that erupted on 21/05/2014 at 02:12 UT travelling at 431 km s^{-1} could have decelerated as it flowed through a slow solar wind speed of ~ 250 km s^{-1} and interacted with the comet on 31/05/2014 though this cannot be confirmed without a complete analysis of the external and internal forces acting upon the ICME. The ICME's CPA was 101° with an angular width of 80°.

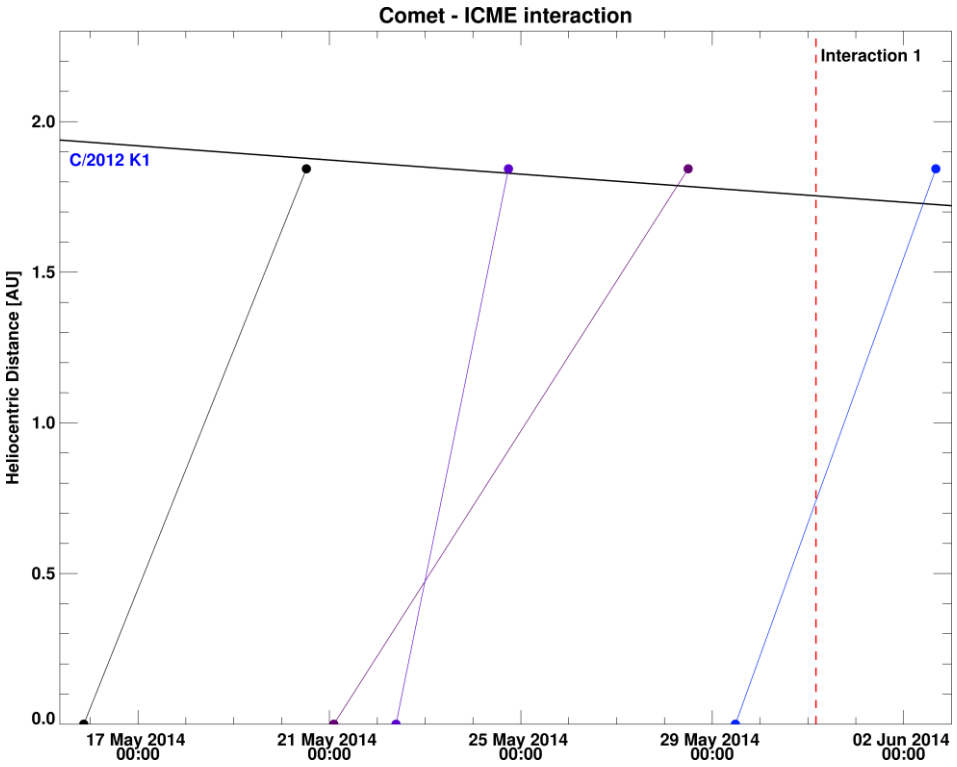

Figure 5.127: ICME SATs at C/2012 K1. The comet is a position angle of 119º and the position angle of the solar rotation axis at -17º.

CR 2154 – 2155

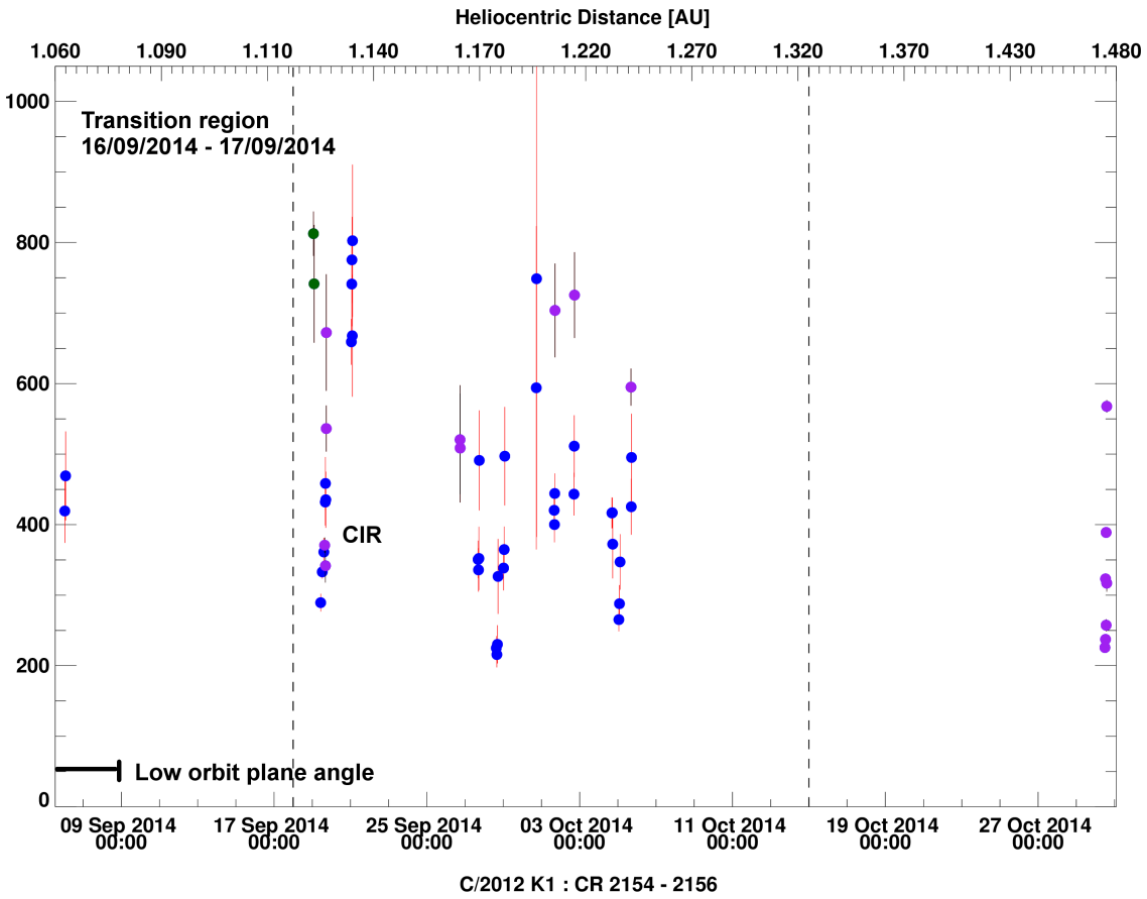

Figure 5.128: Solar wind velocities measured at the comet from CR 2154 to 2156. Note that each timestep represents a 2 day period.

CR 2154

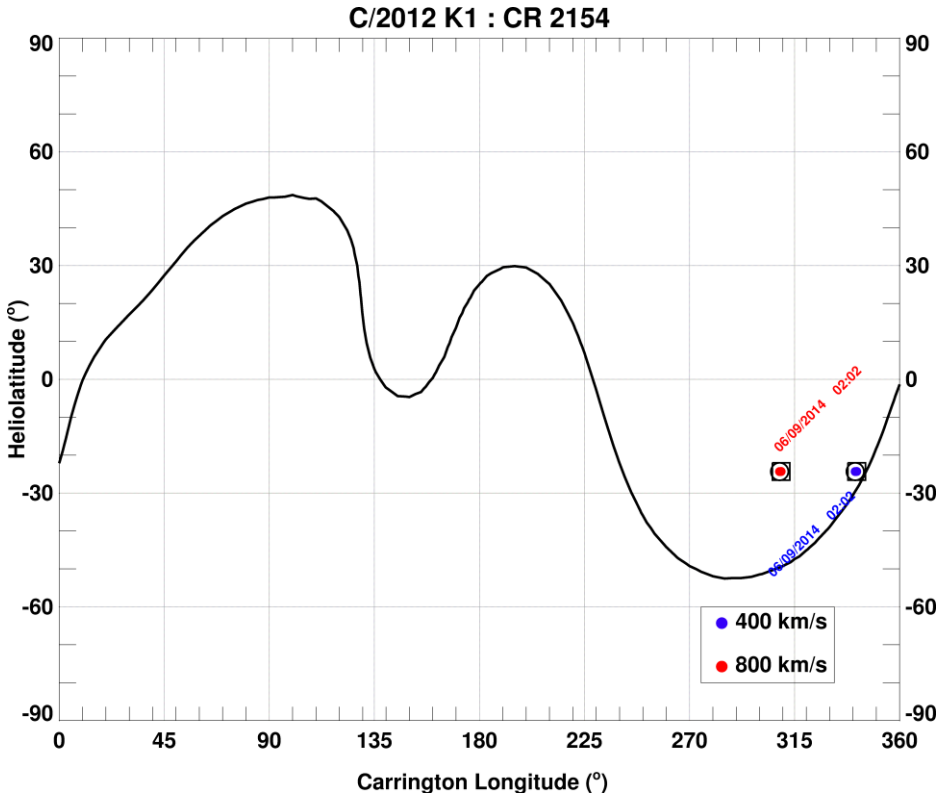

Figure 5.129: Mercator map for CR 2154 predicting slow solar wind speeds at the comet.

By September, the orbit plane angle is around 10° and increasing gradually. I derive a low radial solar wind velocity for this period and a non-radial solar wind velocity of 41.0 km s^{-1} down the tail. The ENLIL run used for comparison was from a high-resolution simulation using a WSA model with GONG data and its outer boundary set at Saturn. Predicted radial solar wind velocities from the MHD simulation are ~400 km s^{-1} matching my output velocities and the Mercator map predictions [Figure 5.129] well.

CR 2155

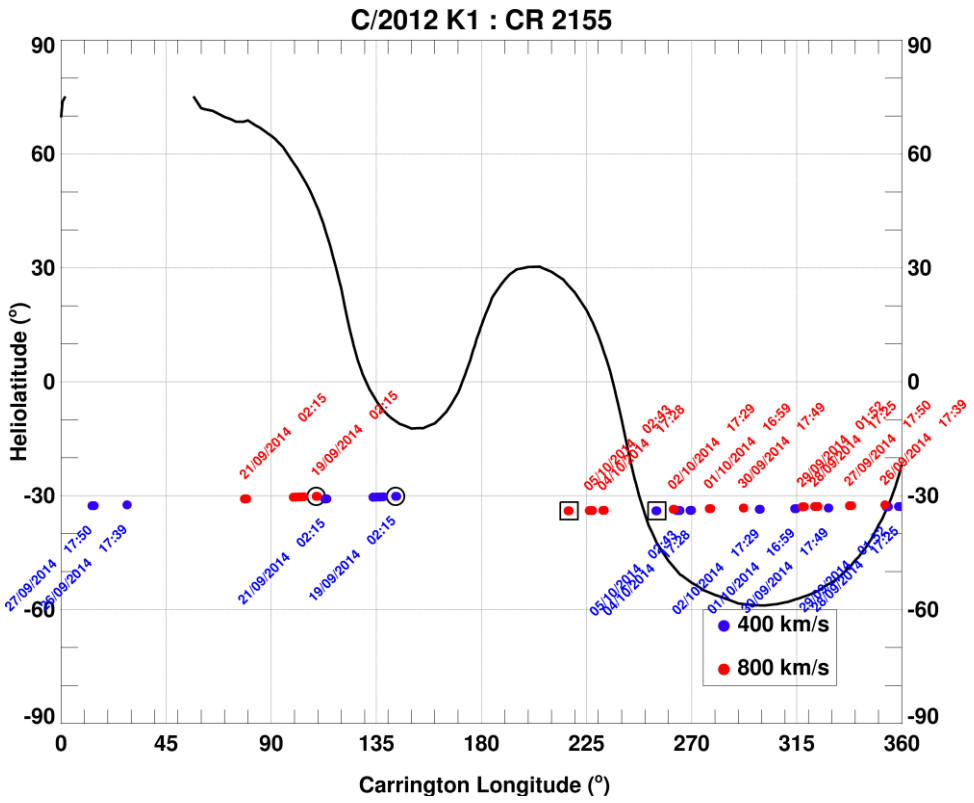

Figure 5.130: Mercator map for CR 2155.

No solar wind velocity estimates were taken from images on the 16th and 17th September 2014. The ion tail has a wavelike form on the 16th, which is followed by a large kink on the 17th. The MHD model predicts a transition region but no tell-tale signs of a CIR were evident. The kink is seen travelling along the Sun-comet radial vector in the mapped image. As the angle between the Earth and the comet's orbital plane increased, the dust and ion tails are observed at almost opposite ends of the nucleus, as viewed from Earth. This is ideal for observations as it reduces contamination from the dust-scattered light.

The large range of velocities derived on the 19th is due to a CIR predicted at the comet's location [Figure 5.131], where the comet encountered shocked solar wind with large predicted non-radial components. The ion tail momentarily overtook the comet's motion on 20/09/2014. The two high velocities were taken when the ion tail was lying on the radial vector and should be considered unreliable. Measurements taken in the evening of the 19th and up to the 21st coincides well with the expected increase from slow to fast solar wind velocities at the comet.

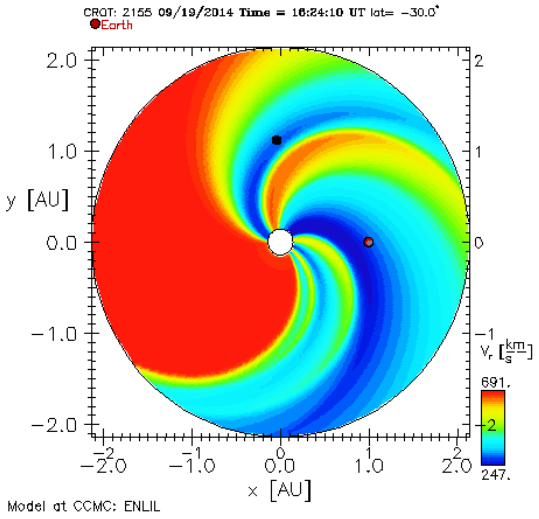
CRQT: 2155 09/19/2014 Time = 16:24:10 UT lat= -30.0°
Earth
y [AU]
x [AU]
V_r [km/s]
691.
247.
Model at CCMC: ENLIL

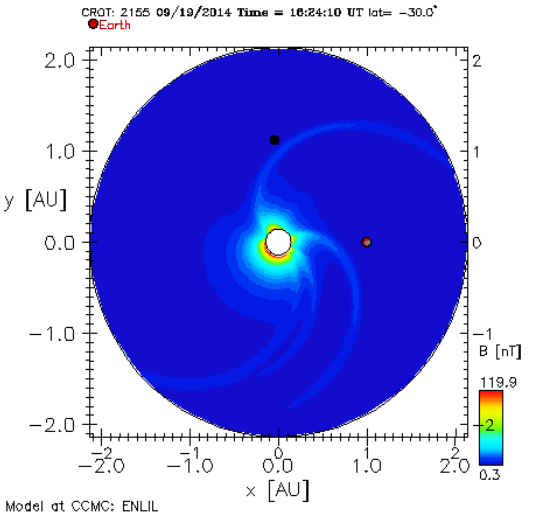
CRQT: 2155 09/19/2014 Time = 16:24:10 UT lat= -30.0°
Earth
y [AU]
x [AU]
B [nT]
119.9
0.3
Model at CCMC: ENLIL

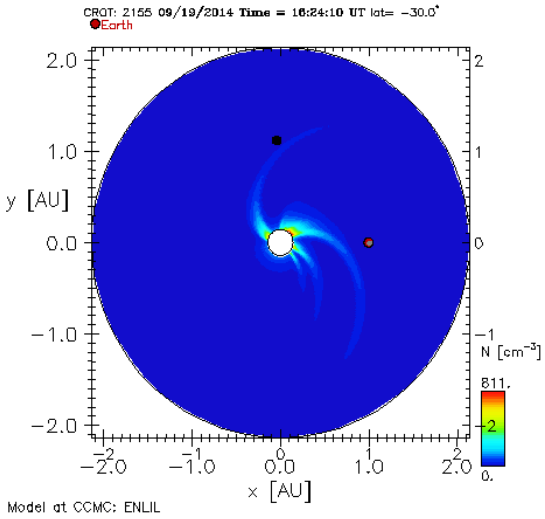
CRQT: 2155 09/19/2014 Time = 16:24:10 UT lat= -30.0°
Earth
y [AU]
x [AU]
N [cm^{-3}]
811.
0.
Model at CCMC: ENLIL

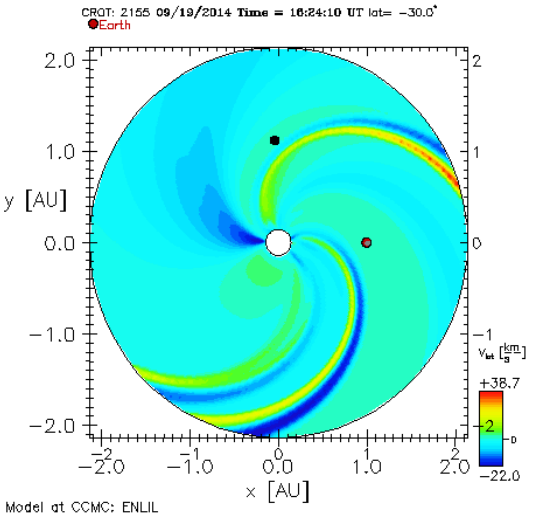
CRQT: 2155 09/19/2014 Time = 16:24:10 UT lat= -30.0°
Earth
y [AU]
x [AU]
V_{tot} [km/s]
+38.7
-22.0
Model at CCMC: ENLIL

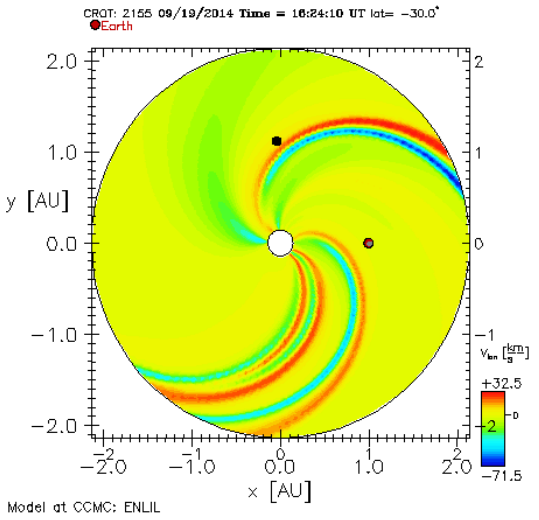
CRQT: 2155 09/19/2014 Time = 16:24:10 UT lat= -30.0°
Earth
y [AU]
x [AU]
V_{tan} [km/s]
+32.5
-71.5
Model at CCMC: ENLIL

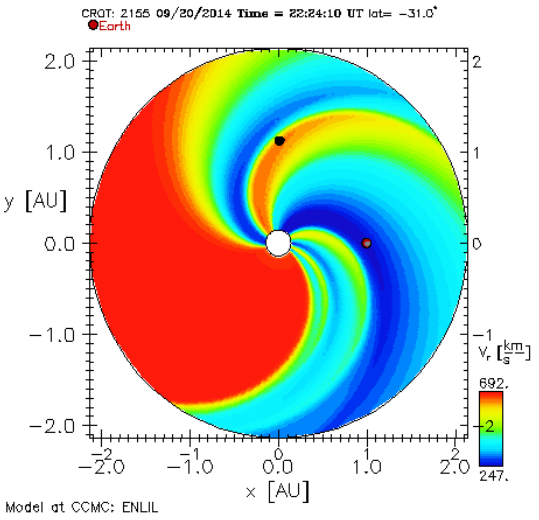
CRQT: 2155 09/20/2014 Time = 22:24:10 UT lat= -31.0°
Earth
y [AU]
x [AU]
V_r [km/s]
692.
247.
Model at CCMC: ENLIL

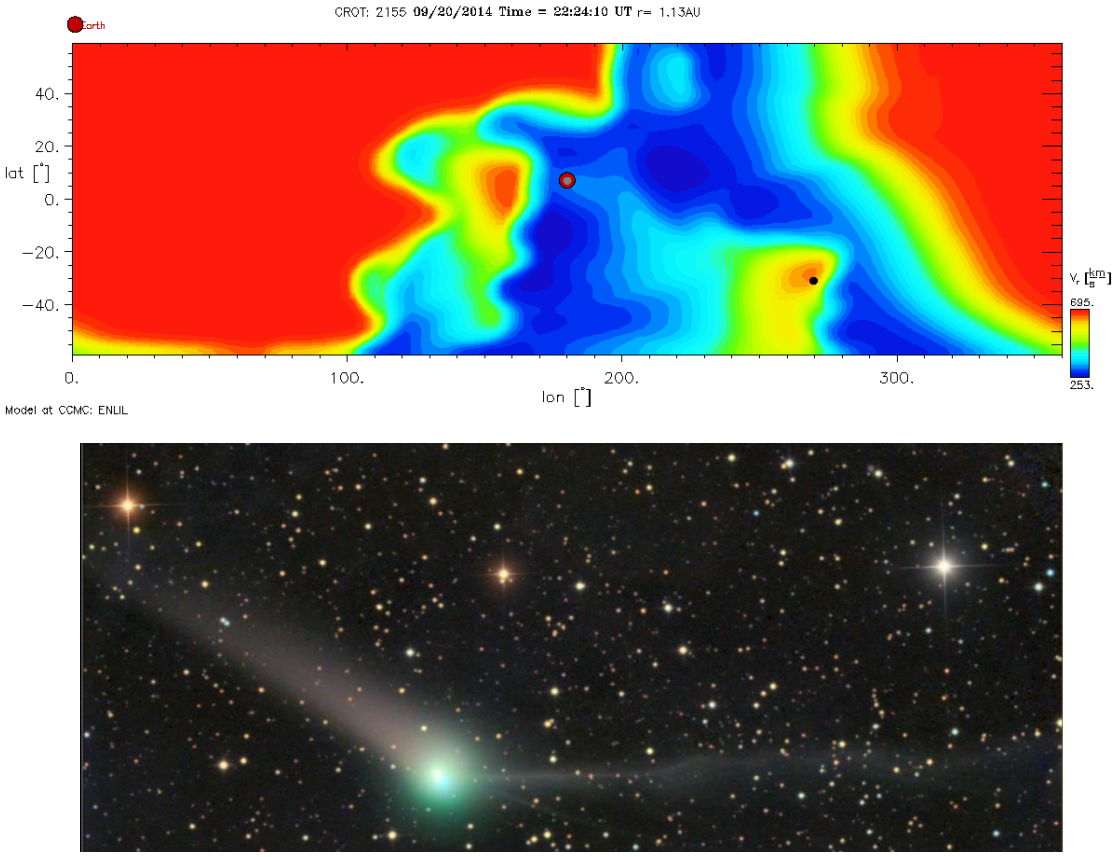

Figure 5.131: ENLIL MHD models predicting a CIR and an increase from slow to fast solar winds with large non-radial velocities. From top left, image is from 19/09/2014 16:24 UT showing the radial velocity, |B|, |N|, the latitudinal and longitudinal solar wind velocities and on far right, the radial velocity as the comet crossed the CIR and experienced ~700 km s^{-1} radial wind speeds on 20/09/2014 at 22:24 UT. Bottom MHD plot is taken from the same time period as previous image. The image was obtained by Peach on 19/09/2014 at 18:45 UT.

A large kinked ion tail bestrode the Sun-comet vector on the 26th September 2014, producing incorrectly large solar wind velocities. I decided to include the data as evidence for a turbulent ion tail rather than marking it in green [Figure 5.128]. The MHD models predict a second CIR though this does not occur until the 28th September. The comet should be encountering the slow solar wind streams, shown interacting with the Earth in Figure 5.131.

The comet encountered increasing velocities from 250 km s^{-1} to ~ 500 km s^{-1} from the 27th to 29th September 2014 at 04:00 UT. However, the longer trend of my velocities is one of slowly decreasing then increasing solar wind speeds in a short time period. The comet is expected to encounter a solar wind stream with a strong longitudinal velocity component between 28/09/2013 16:24 UT and 29/09/2014 04:24 UT. This is seen as a large change in the

dynamical aberration of the ion tail, producing the illusion of slower radial velocities. Combined with the low orbit plane angle, this explains the data scatter up to the 29th September, shown in Figure 5.128. This tangential discontinuity in the solar wind is trailed by an extended period of non-radial velocities. The first two plots in the second row of Figure 5.131 show the three tangential discontinuities predicted in the MHD model. The comet is expected to traverse this region and the ensuing transition region on the 1st October, with predicted velocities of 450 km s^{-1}, leading into high solar wind velocities of ~700 km s^{-1}. The predicted high-speed solar winds show no variation in the predicted model for an extensive period. The increase in velocities is replicated in the data scatter from the 29th September onwards.

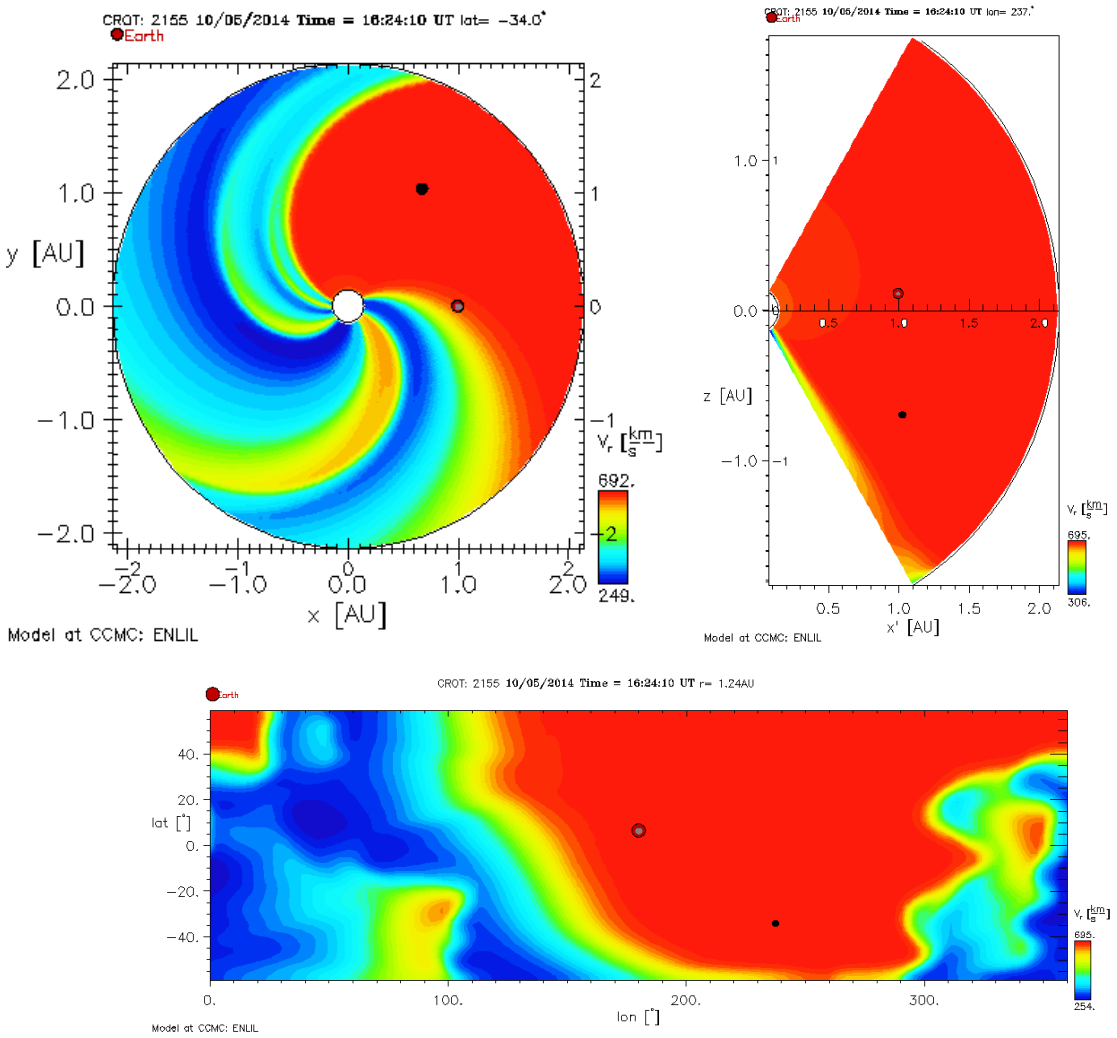

Figure 5.132: MHD simulations show the comet will have encountered fast, unipolar solar wind stream for an extended period of days towards the end of CR 2155.

This does not correspond to the observed changes in the comet's ion tail [Figure 5.133]. The tail is viewed as an extremely thin ion tail on the 1st October and a large kink on the 2nd, a likely result of the third CIR encounter. The comet will have experienced a period with small non-radiality to the plasma outflow, but it is not significant enough to account for the large velocity range. The extreme angular changes in the ion tail orientation on September 5, 2014 are very strong evidence for a disturbed solar wind medium.

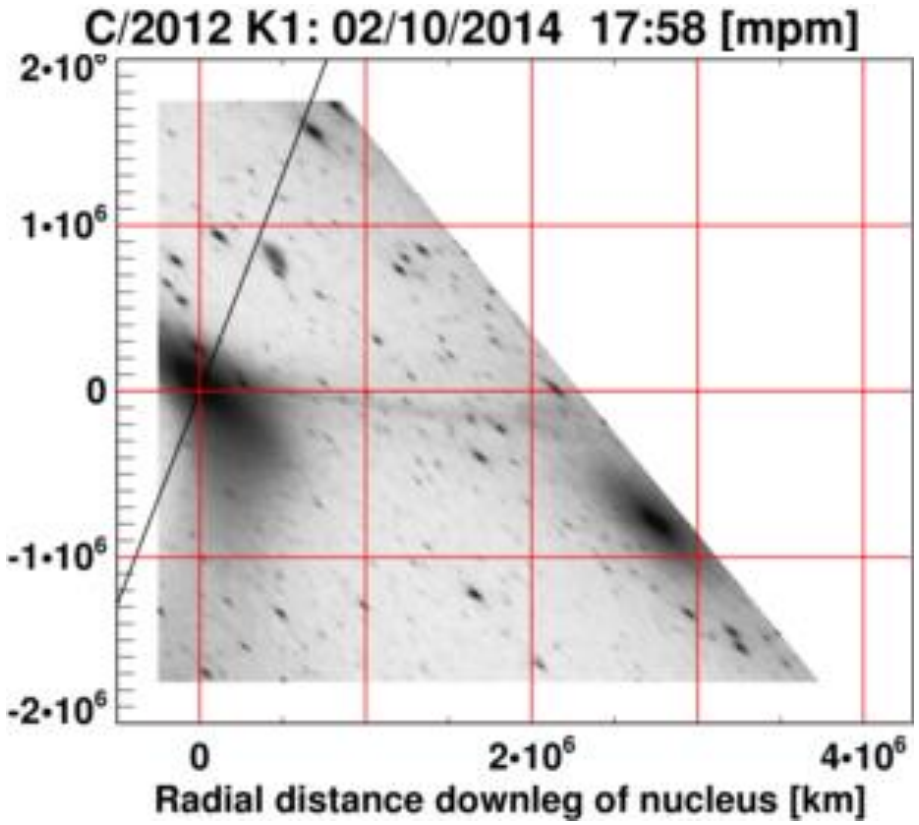

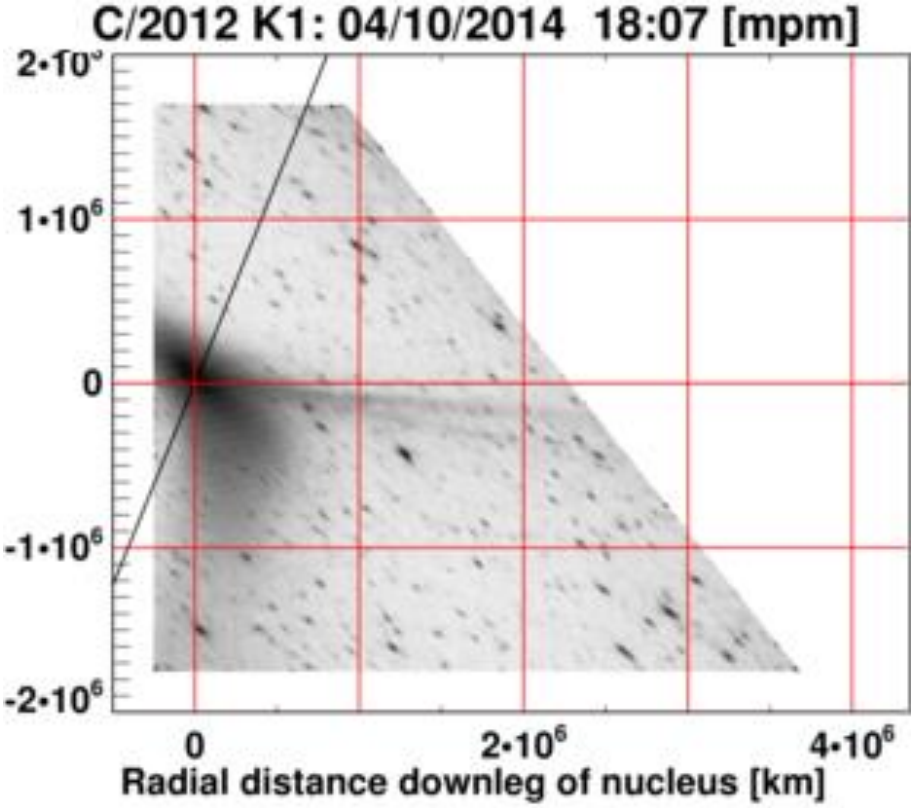
C/2012 K1: 04/10/2014 18:07 [mpm]
2•10⁶
1•10⁶
0
-1•10⁶
-2•10⁶
0
2•10⁶
4•10⁶
Radial distance downleg of nucleus [km]

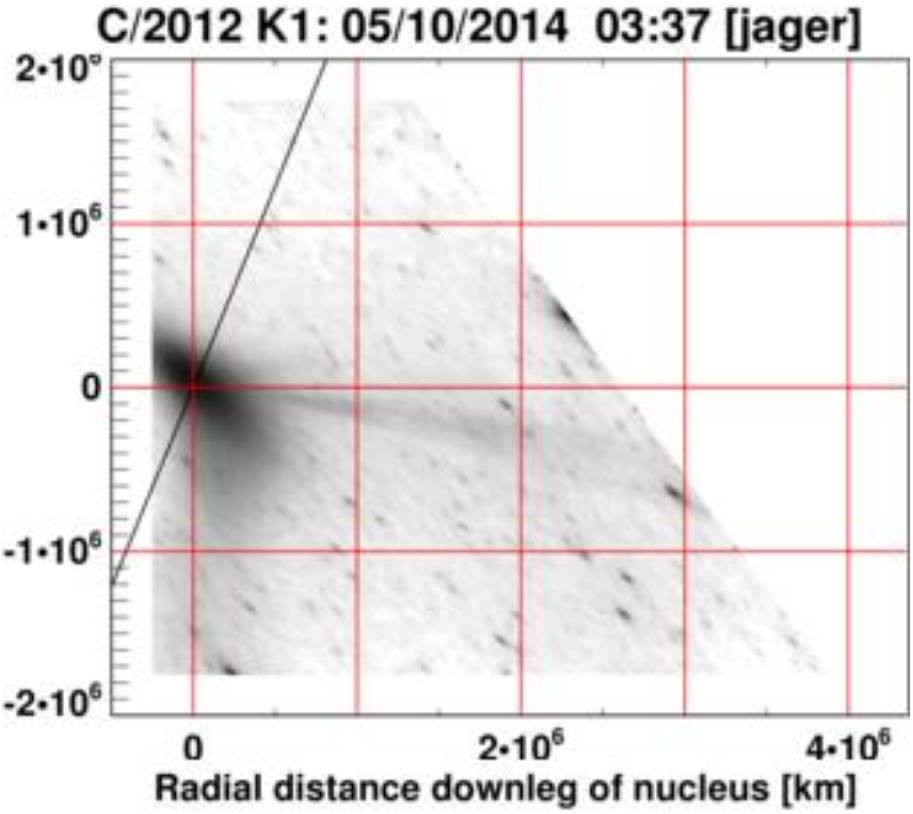
C/2012 K1: 05/10/2014 03:37 [jager]
2•10⁶
1•10⁶
0
-1•10⁶
-2•10⁶
0
2•10⁶
4•10⁶
Radial distance downleg of nucleus [km]

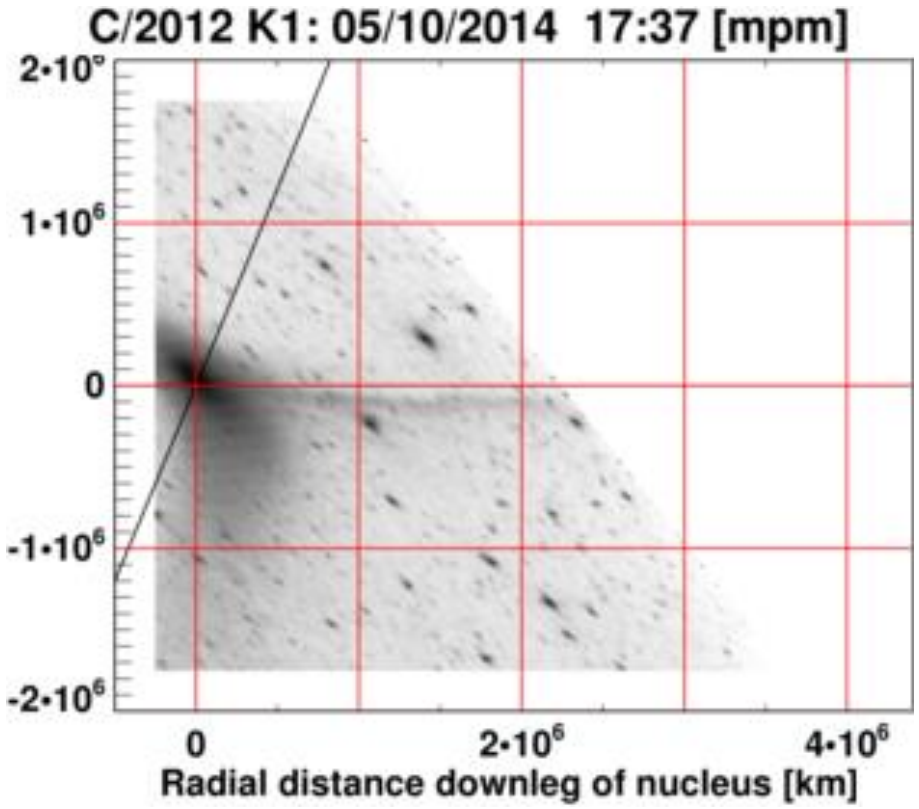

Figure 5.133: Evidence for a disturbed solar wind medium from the unusual ion tail orientations. Observers are Mobberley (mpm) and Jäger.

CR 2156

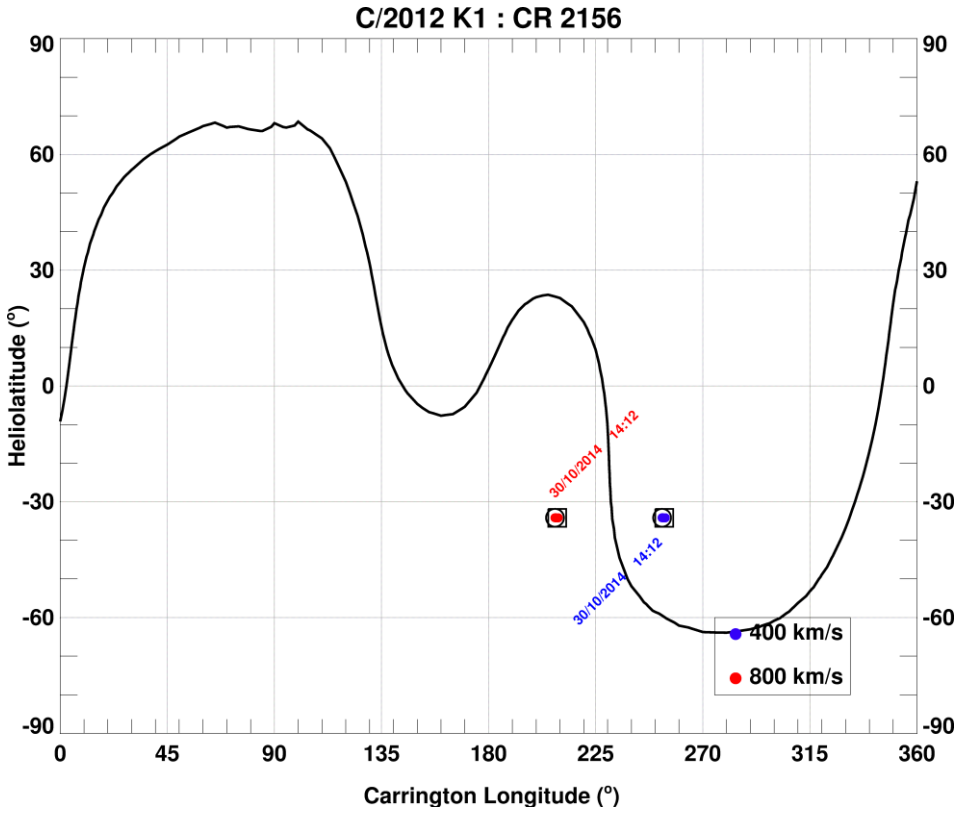

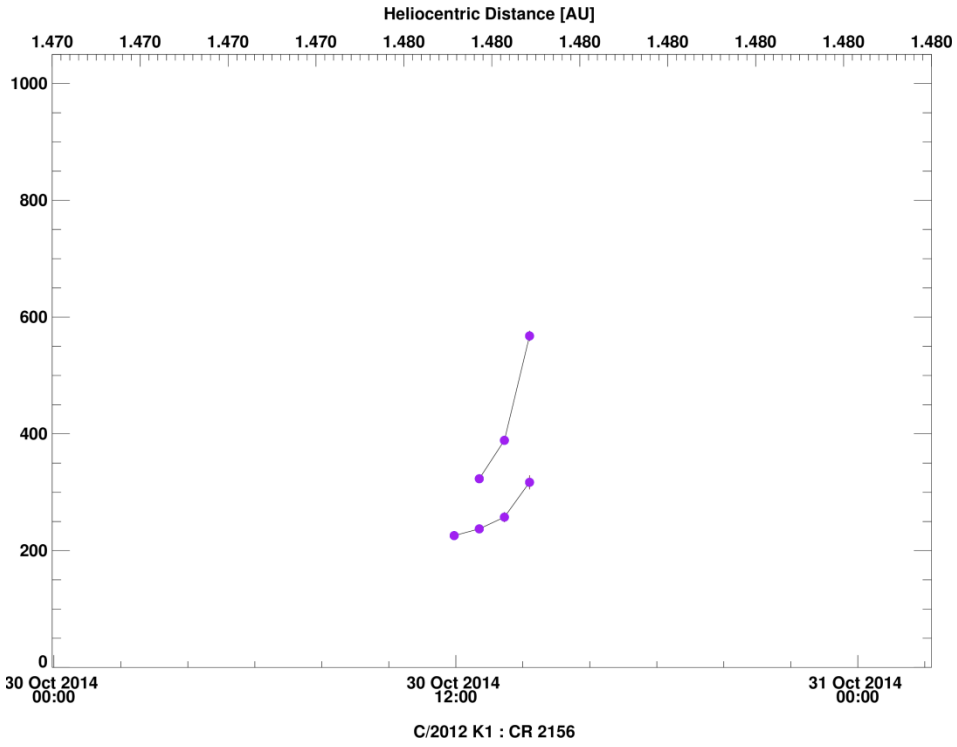

Figure 5.134: *Top:* **Mercator map showing that the comet would be experiencing solar wind streams from two regions of opposite magnetic polarity if it encountered a CIR.** *Bottom:* **Solar wind radial speeds.**

Figure 5.135 is a perfect example of a bifurcated tail, extending up to 2.5 x 10^6 km from the nucleus, by D. Peach. Velocity estimates were taken from both tail components, yielding results circa 250-350 km s^{-1} [Figure 5.134], aside from their first estimates. The three highest velocities were extracted from the tail with the smaller aberration angle. A possible explanation for the bifurcating tail could be that they are a pair of symmetrical tail rays, merging into an ion tail, post-DE. MHD predictions for the radial velocity are in the region of 280-300 km s^{-1}. There is no polarity reversal expected at the comet, so it is unlikely for the DE to have been related to the HCS crossing. There are no predicted CIRs at the comet with the solar wind outflow mostly radial with a small latitudinal velocity component. It is unlikely that the comet will have interacted with the fast ICME on 29/10/2014 as the ICME will have undergone deceleration by 1.5 AU due to the ambient slow solar wind.

Figure 5.135: A bifurcated tail captured by Peach on 30/10/2014 at 15:03 UT.

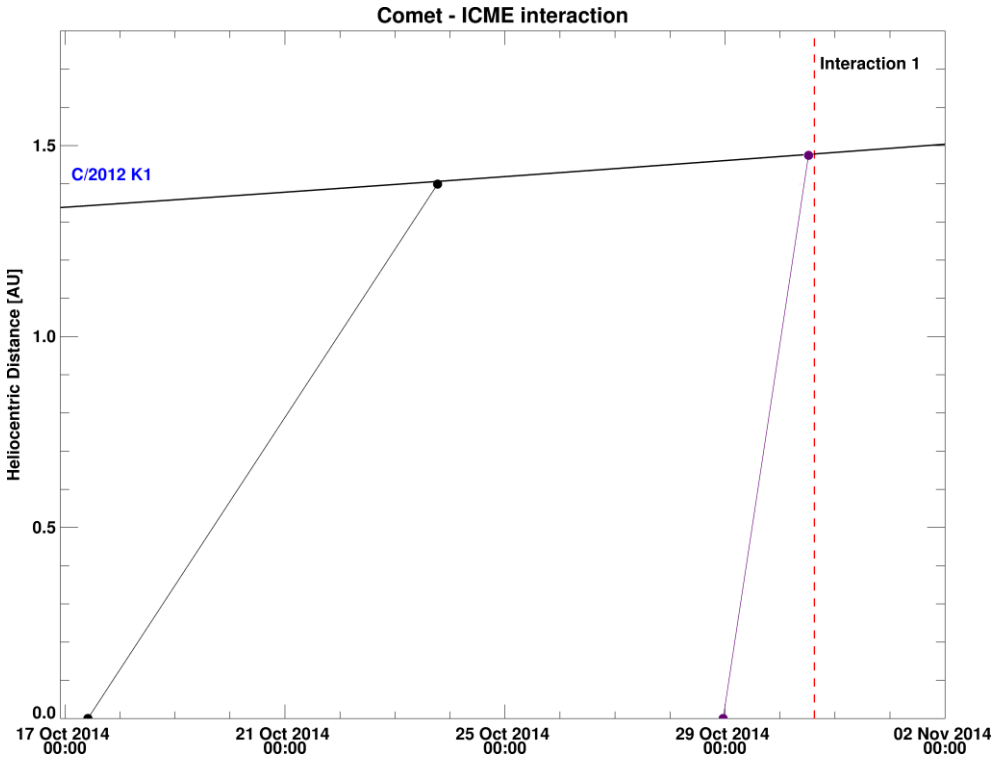

Figure 5.136: ICME SATs at C/2012 K1.

Solar wind velocities during the densest data period, during CR 2155, are complicated by turbulent, transient solar wind structures and a low orbit plane angle. It is clear that the observations of the ion tail still provided a fairly good match overall to the ENLIL predictions for both the radial and non-radial solar wind flow at the comet.

5.5. Comet Lovejoy (C/2013 R1)

Comet Lovejoy was the fourth comet discovered by Terry Lovejoy on September 7, 2013 and the first of three Lovejoy comets presented here. Only observations of C/2013 R1 that were conducted for a period of 2 weeks either side of its perihelion [Figure 5.138], were gathered and presented here. The comet's brightness peaked at m_v about +4.5 around perihelion (T = 22nd December 2013), where its solar elongation was 51^o. Its visual magnitude remained between +4 and +6 during most of the observations, according to Yoshida Seiichi's lightcurve (aerith.net) based on amateur observations. JPL Horizons puts the comet's total apparent magnitude range closer to 10 - 11. The progression of the comet's orbit can be seen in Figure 5.137 with relation to the Earth and the Sun in heliocentric Aries ecliptic coordinates. The set of amateur images were mapped onto the comet's orbital plane with the y-axis defined as the direction to the comet's perihelion [Figure 5.138]. The comet's orbital plane was inclined by 64.0^o to the ecliptic with the longitude of its ascending node being 70.7^o. C/2013 R1 allowed us to probe the inner solar system to intermediate heliographic latitudes from 34.0^o to 54.0^o. The amateur images amassed for this time period were supplemented by my own observations undertaken at the Isaac Newton Telescope in January 2014, presenting a unique opportunity to validate the quality of amateur images versus high quality observations from an established scientific observing facility (Isaac Newton Telescope (INT), La Palma, Canary Islands). The comet was at high heliographic latitudes during this time (~60^o).

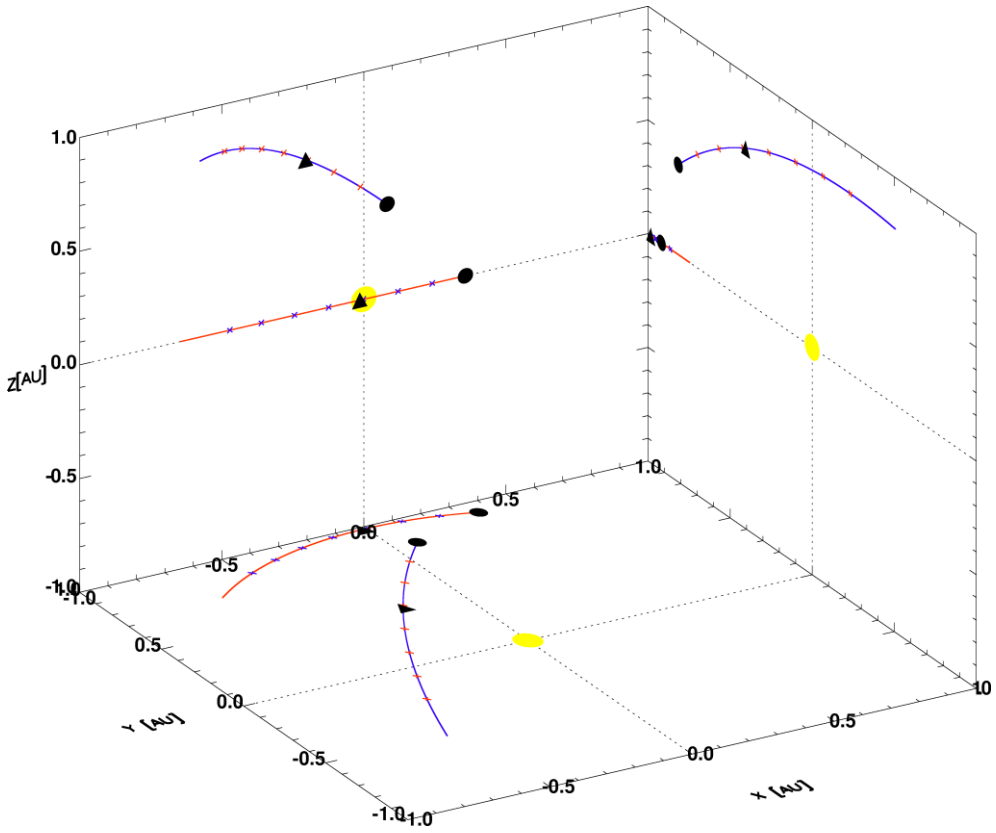

Figure 5.137: Heliocentric Aries ecliptic coordinates of C/2013 R1 (Lovejoy). The first point of each orbit (circle) and the perihelion date are shown.

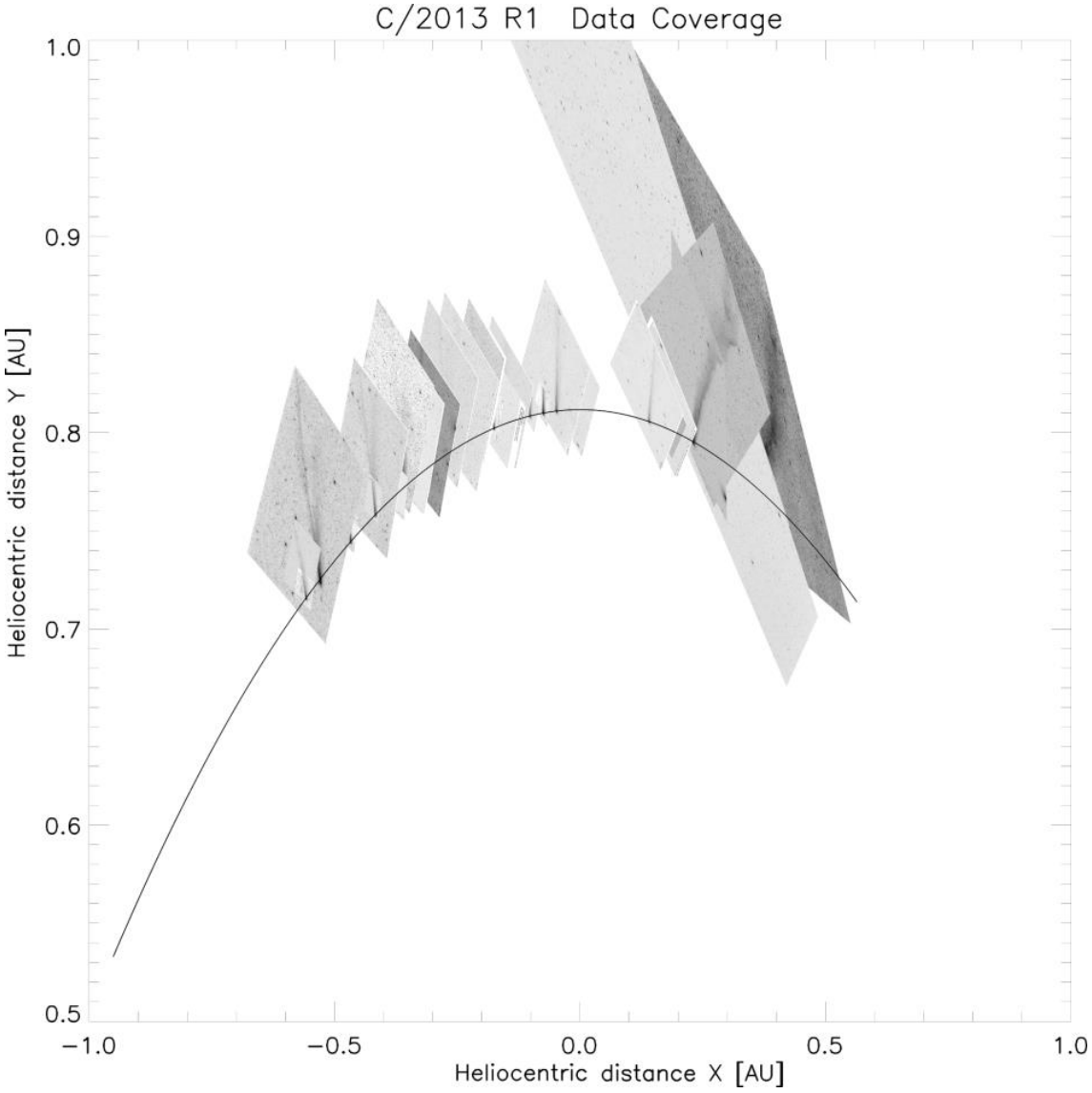

Figure 5.138: Data coverage for C/2013 R1 (Lovejoy). Only the amateur images have been mapped. Y-axis is defined as the direction to perihelion. Earliest image is to the right, increasing chronologically towards the left. Note that the X and Y axes are at different scales.

5.5.1. Isaac Newton Telescope Observations

I was the primary investigator of two consecutive observing proposals at the 2.5m INT telescope from the UK and Spanish Time Allocation Committee (TAC) to observe comet C/2012 S2 (ISON) in January 2014. C/2012 S1 fragmented approximately a month earlier, making C/2013 R1 my primary target. I, along with K. Birkett, observed comet C/2013 R1 from January 2, 2014 to January 7, 2014. The second proposal was for spectroscopic observations to determine abundances in the cometary coma and the ion tail, as well as velocity dispersions in the ion tail

along our line-of-sight. Due to heavy snowfall, observations had to be cut short. The comet was at a heliocentric distance of ~0.85 AU and 1.15 AU from Earth during the INT observations.

C/2013 R1 rose shortly before morning twilight. By the time it had cleared the INT's lowest observing limit (20^{o} elevation), we were constrained to a short observing window of 40 minutes to one hour, within which to acquire the images and sky flats (during twilight) for the whole observing night. As dark sky time dwindled, the sky background rose steadily until it became one of the major sources of noise. For the last few images taken during the night, the signal-to-noise ratio (SNR) was so low that it is difficult to make out the ion tail. By subtracting the sky contribution from the r filter images, we were able to extract a difference image with multiple tail rays and an ion tail fanning out, even in the twilight images. When feasible, the images were stitched together to create a larger mosaicked image of the comet's nucleus and its ion tail.

Figure 5.139 shows a view of C/2013 R1 mapped in equatorial coordinates, using an Astrometry.net processed image and Aladin Sky Atlas. Due to the limited FOV of the WFC (34' x 34'), this was a useful visualisation tool to optimise the orientation of the Isaac Newton telescope to capture the entire ion tail of comet Lovejoy over several exposures. CCD4 is defined as the nominal telescope detector. The input coordinates, in this instance the comet's nucleus, will thus default to the centre of chip 4. To map the entire ion tail requires new telescope pointings to be calculated. It bears noting that in the time taken to expose, readout the first image and slew the telescope to its new pointing, enough time has passed that there will be a small angular and positional error between the sections of the ion tail observed. If the total time taken between the two consecutive images is 2-3 minutes apart, this is enough time for the tail dynamics to have also evolved slightly, such that a mosaic of the two images will not be entirely accurate.

Furthermore, subsequent observing sessions did not always have the comet's nucleus consistently imaged on the same CCD pixels. This was a bigger issue during the first observing night as we were trying to ascertain acquisition and the adequate exposure time of the target. The mean exposure time is 60s. A list of the observations undertaken is given in Appendix C 'Image Sources'.

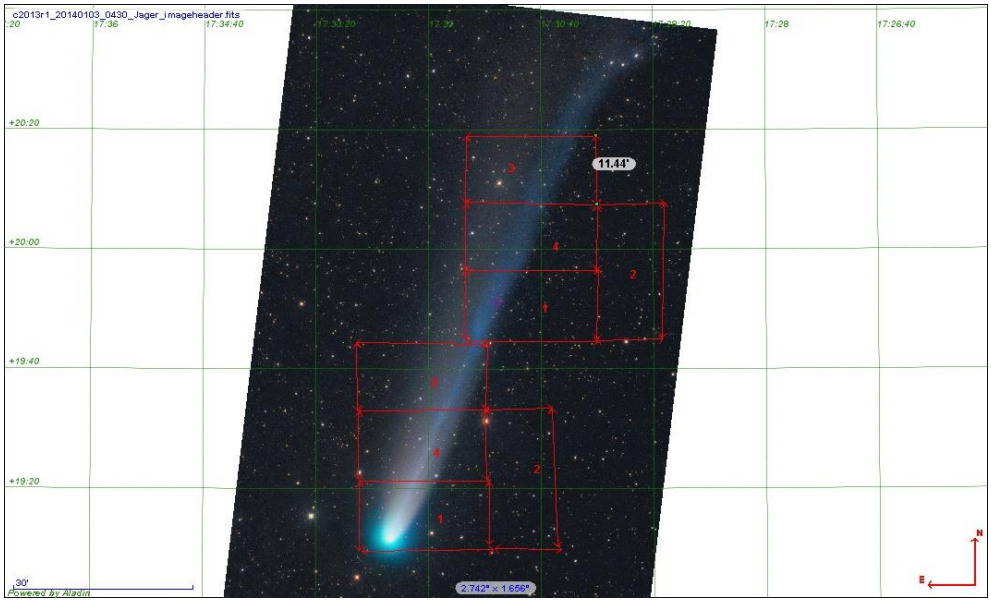

Figure 5.139: Astrometry.net processed image of comet C/2013 R1 (Lovejoy) by Jäger, with a ~2 degree ion tail mapped onto Aladdin's skymap.

The THELI software was initially used for the coaddition process. I had chosen THELI as the data reduction and coaddition package mainly for its optical distortion correction feature and use of the target's differential motion in its coaddition pipeline. This procedure was only successful for the first observing session, with incorrect astrometric solutions computed for the other observing nights. For example, two images taken minutes apart showed a difference of as much as 1.5 arcmins in declination. The incorrect solutions were due to the sky catalogue used and the low number of stars detected per CCD image, even with varying detection thresholds used. The end result was that the end stacked images were incorrectly coadded. For consistency, THELI was only used up to the bias and flat frame calibrations. An additional issue I encountered with THELI was the automatic brightness rescaling of each CCD from 0 to 65535 ADU (Analogue/Digital Unit) to an unknown, non-standard scale for all CCDs. An IDL version of the IRAF zscale procedure was implemented with my software to circumvent manually rescaling each CCD image. The zscaling feature operates by ranking each pixel in brightness and fitting a linear function to the brightness slope past the mid-point of this function. The difference images were contrast enhanced through GIMP and FITS liberator to extract as much information as available on the ion tail. However, this required significant human interaction with no appreciable net gain over using the zscaling feature.

The following specialised post-processing pipeline was incorporated within my IDL software. The THELI reduced observations were downsampled and processed through astrometry.net. The SIP polynomial distortion within Astrometry.net may be an adequate replacement for the THELI distortion correction map, though this was not tested. The coadded images were constructed from B and r images close to each other in time, so as to minimise motion blur in the dynamic ion tail. Due to short exposure times and restricted number of images in a group, the end result will be insensitive to large motion blurs. When coadding in IDL, each pixel was allocated the same weighting. For a more accurate photometric treatment, a pixel weight should be computed from the master flat. Since no photometry was required, the pixel weighting didn't seem to be a necessary component for my research. The coadded CCD images were projected using equatorial coordinates (astrometry.net solved) before performing the dust continuum subtraction (Wilson et al. 1998) in IDL [Figure 5.140]. To account for the different pixel locations of the nucleus, each coadded image in a set of difference images was warped using the astrometric parameters of a reference image. Out of the three interpolation routines available (nearest neighbours, bilinear and cubic), the cubic interpolation was chosen as the best estimator of the true pixel brightness (Popowicz et al. 2013) when applying the warping procedure. Regions of the warped images that did not match the reference image were discarded. The warping procedure was considered but not included in the coaddition pipeline due to its minimal net benefit. Dust continuum images were linearly scaled empirically to avoid washing out faint features in the ion tail.

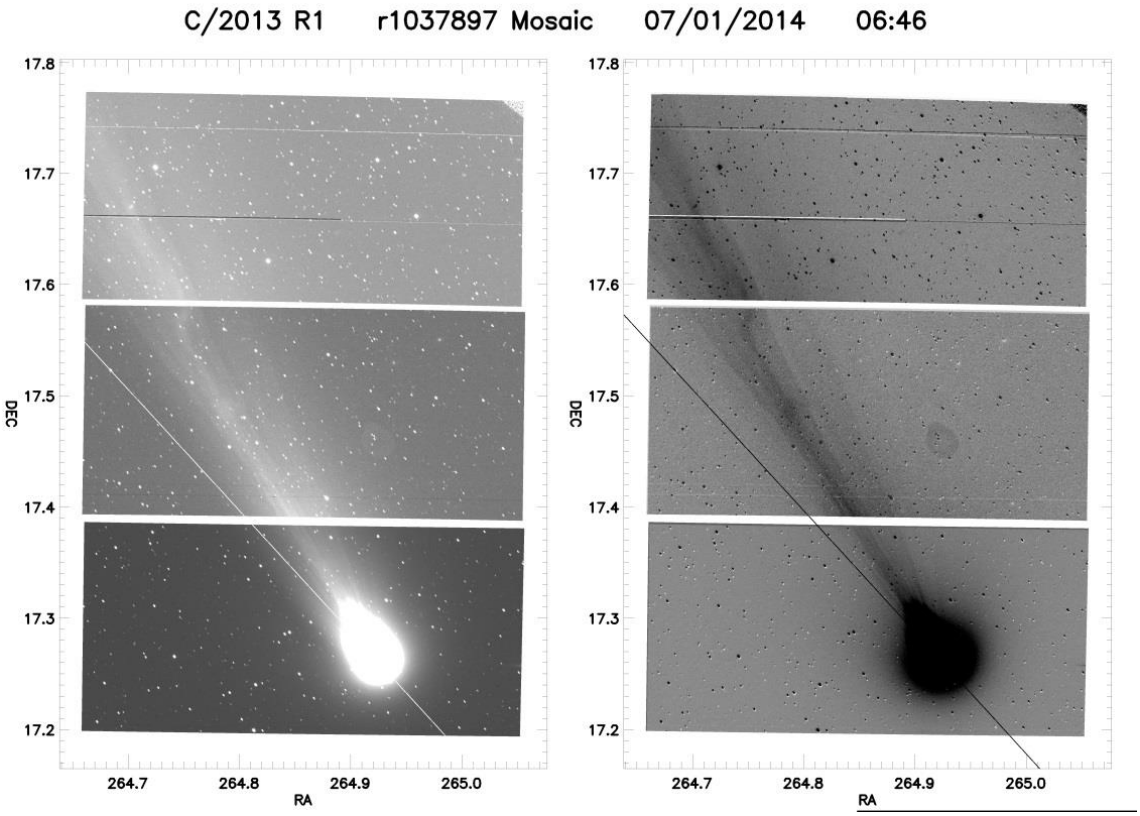

Figure 5.140: A coadded Harris B filter image of C/2013 R1 (left) and a dust-subtracted difference image (right) from a pair of coadded Harris B and Sloan r images. Observations were undertaken by K. Birkett and Y. Ramanjooloo on 07/01/2014.

The difference images were chosen for all analysis techniques as they depicted the fine structures more clearly than the calibrated or stacked images. There exist a few non-post processed images that could be analysed, however the time interval between the difference images and the non-post processed images are too small to provide added value to our radial velocity estimates or the feature tracking aspects.

A coadded and dust-subtracted composite image of the nucleus and one of the ion tail, were projected with different observing times onto the comet's orbital plane to create a mosaic stitching image, with the ion extending greater than 1 degree. Different observing times were used to account for the angular and radial motion of the ion tail with respect to the nucleus between exposures. Assuming a solar wind outflow of 400 km s^{-1}, the plasma bundles in the ion tail would have covered 3.6 x 10^5 km radially.

The timing error for each image is assumed to be half of a minute. The images were scaled according to their exposure time prior to coaddition. For the stacked images, the middle image is taken as the observing time so as to retain the correct astrometric parameters associated with that observing time. For the difference images, the WCS coordinates from each stacked B filter image is used and the relevant r images were distorted till they matched the astrometric coordinates of the stacked B image. The distorted r images were then subtracted from the B image to remove the dust contribution. It was recently found that the timing uncertainty was hardwired in the software and was thus incorrectly propagated for the coadded and difference images. The timing and solar wind velocity uncertainties for the INT images were slightly underestimated.

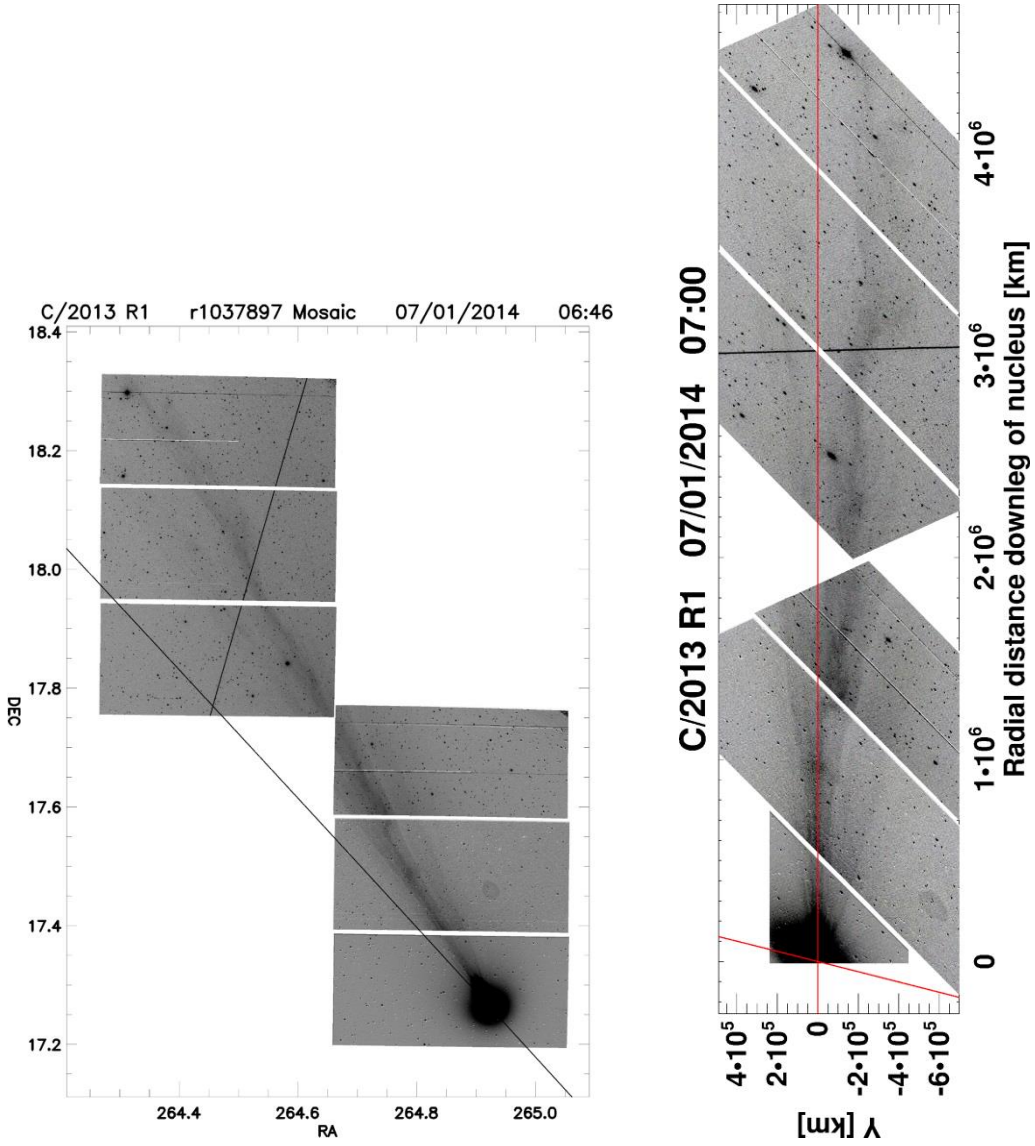

Figure 5.141: Stacked, dust subtracted mosaic image of C/2013 R1 in equatorial coordinates (left) and mapped onto the comet's orbital plane (right) depicting a turbulent ion tail with condensation knots and multiple orientation changes.

5.5.2. Radial Solar Wind Speeds

Amateur Image statistics

123 images with a detectable ion tail were processed through Astrometry.net. 44 of these did not yield a satisfactory astrometric solution. Of the remainder, only 50 were successfully processed through my software. I was only able to further analyse 36 images and extracted a

total of 109 solar wind velocity estimates. 7 were ultimately rejected and 43 showed a sinuous and turbulent ion tail.

INT Image statistics

76 images were observed with the Harris B broadband filter and 19 with a Sloan r broadband filter. Each image consists of 4 CCD frames, which had to be plate solved separately to account for the inter-chip gap. 13 B band and 1 r band images were rejected due to the B images being taken during twilight and the r image was taken whilst the telescope was moving. The images were post-processed through a coaddition, dust subtraction and contrast enhancement pipeline. The result was a set of 11 images showing intricate details of the fine structure within the ion tail and close to the nucleus. A total of 28 radial velocity estimates were extracted. 19 of these displayed signs of turbulence.

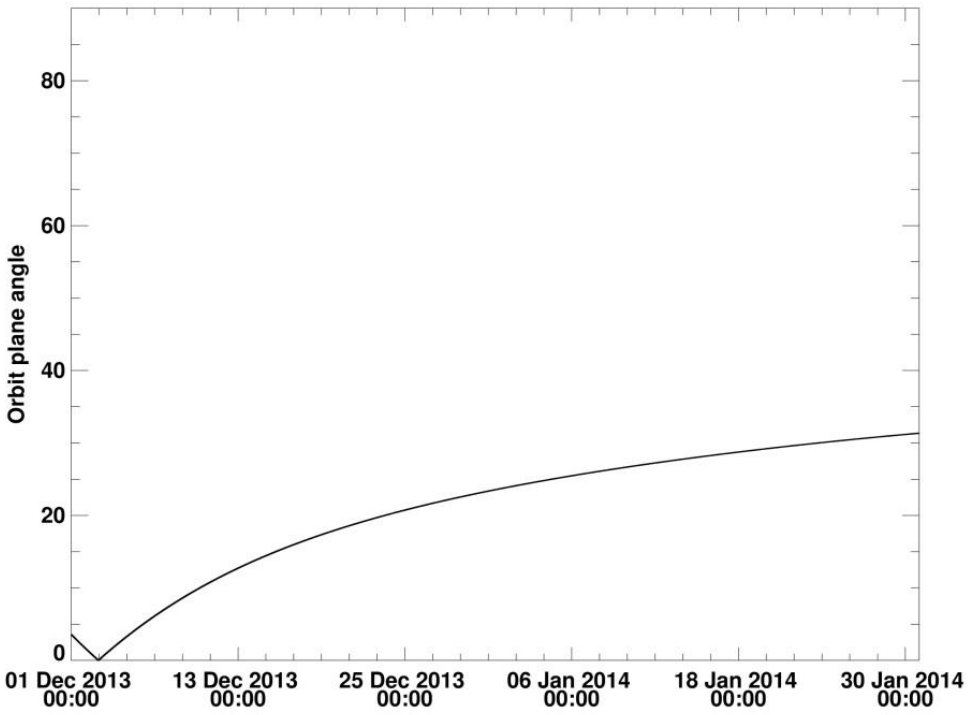

Figure 5.142: Orbit plane angle for C/2013 R1 showing a low orbit plane angle throughout the series of observation presented in this chapter. Orbit plane angle is less than 10º for the period from 01/12/2013 to 10/12/2013.

Both the amateur and INT observations are given in Figure 5.149. Estimates from the amateur observations are in blue and from the INT data in black. Estimates from turbulent ion tail images are represented as purple dots for Earth and orange for INT. The range of velocities derived from amateur images is nearly equivalent to the INT images for the period where they both overlap. This fortuitous overlap of observations demonstrates how far consumer technology has come and its benefits to interplanetary heliospheric research.

I previously used the manually compiled CDAW CME catalogue to determine potential ICME interactions at the comet. The thoroughness of the CME catalogue was my prime reason for using it. The latest update of the catalogue only contained CMEs up to March 2014. For comets C/2012 K1 and C/2014 Q2, I make use of the Computer Aided CME Tracking software (CACTus), an automatic recognition tool to determine CME eruptions from merged images of the LASCO C2 and C3 coronagraphs devised by Robbrecht & Berghmans (2004). The method of detection requires the CME to be a new, discrete, bright, white-light feature and to be radially propagating outward in the coronagraphs' FOV. Robbrecht et al. (2008) presented a comparative study with the CDAW CME catalogue, producing similar results, with a small number of CACTus-only events identified. These tended to be narrow transients from previous CME activity or slow solar wind intensity variations. I briefly compared results from the small chronological overlap between the CDAW and CACTus catalogues and observations of C/2013 R1. The ICMEs identified as potential interactors differed slightly in speed, CPA and angular width. The difference was significant enough that certain ICMEs identified in CDAW were missing from the CACTus catalogues and vice versa. Moreover, the CACTus catalogue has not been validated post-compilation and thus required a measure of human interaction in my study to ascertain that false positives were excluded. The LASCO images were compared against the list of potential impactors and non-ICMEs rejected. Without a method to reconcile the two disparate methods of detection, they are both assumed to be equally valid. The linear speed assumed for the CACTus catalogue is the median speed calculated over the width of the ICME.

CR 2144

From the Mercator map [Figure 5.143], there is a reasonable expectation for an observed heliospheric current sheet crossing in mid-December, sometime between the 12th and 13th December. The observer's projected position onto comet C/2013 R1's orbital plane remains low for the first two weeks of December 2013, only rising to about 20 degrees by late December. The orbit plane angle gradually improves, though it remains fairly low, peaking at around 30 degrees at the end of the observing period in January 2014. The early set of images, taken in CR 2144, will yield apparent velocities uncharacteristic of the solar wind due to the low orbit plane angle. The orbit plane angle is below 10° for the first half of CR 2144 and between 10° and 17° for the second half from December 13, 2013 to December 17, 2013. I further expect the comet to be immersed in a fast solar wind region from the 26th December to 9th January. Thereafter, the comet should be experiencing slower slow wind speeds as it approaches the neutral line.

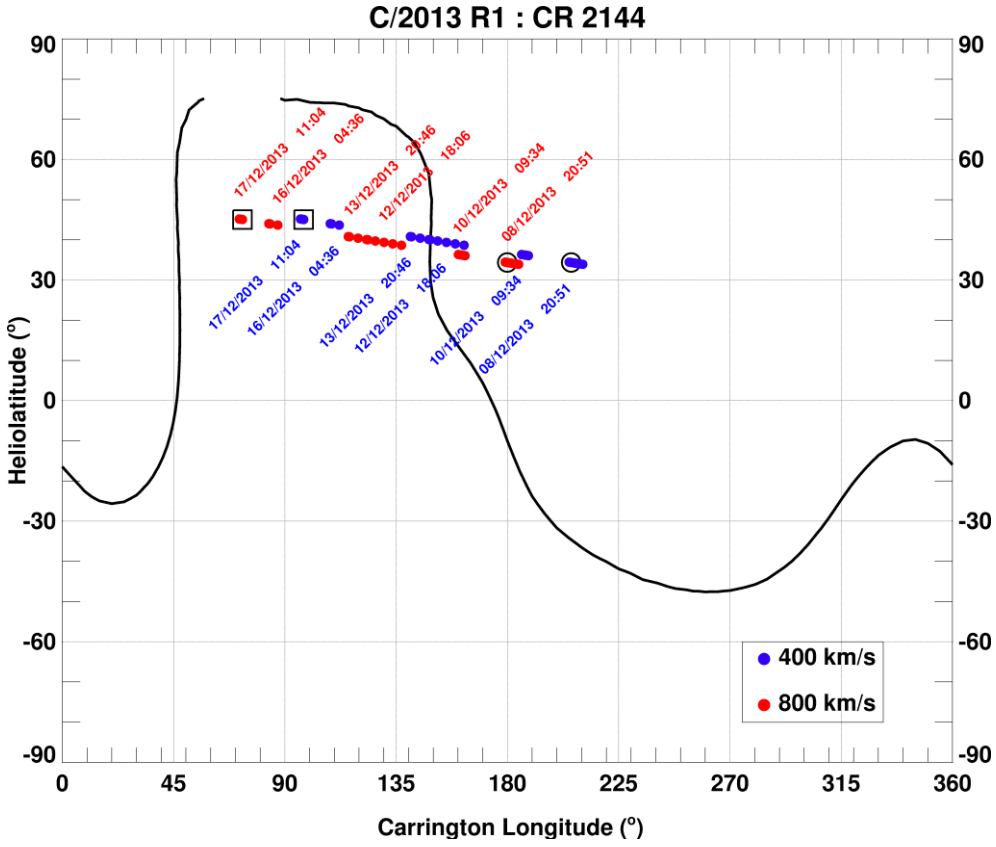

Figure 5.143: Mercator map for CR 2144 showing expected sources on the solar wind source surface of the solar plasma flux tubes interacting with the comet, assuming a fixed velocity for the bimodal solar wind outflow.

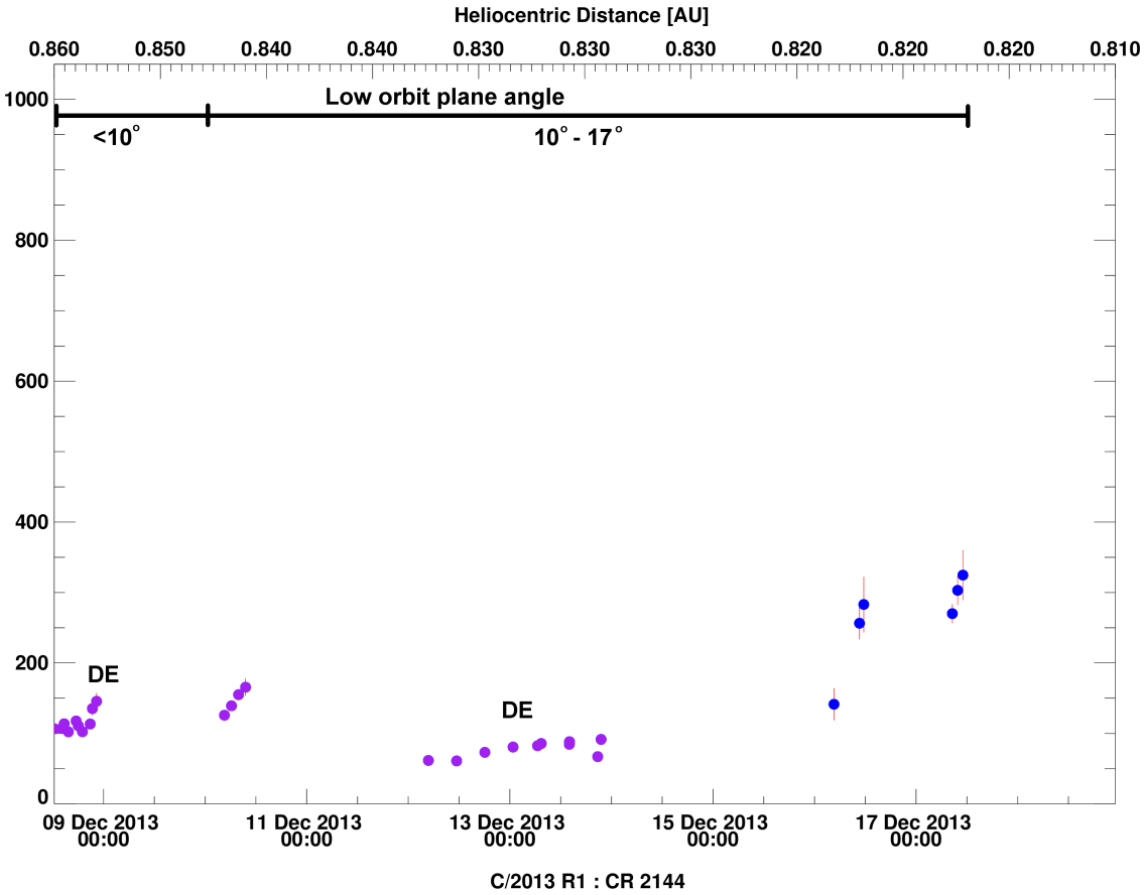

Figure 5.144: Solar wind velocities from amateur observations of C/2013 R1 during CR 2144.

The period spanning from 09/12/2013 to 17/12/2013 were observed at low orbit plane angles, producing radial solar wind velocity estimates in the range of 50-200 km s^{-1}. The dust tail and ion tail completely overlapped for most of this period, thus solar wind velocity measurements in Figure 5.144 are ineffective indicators of the radial solar wind velocity.

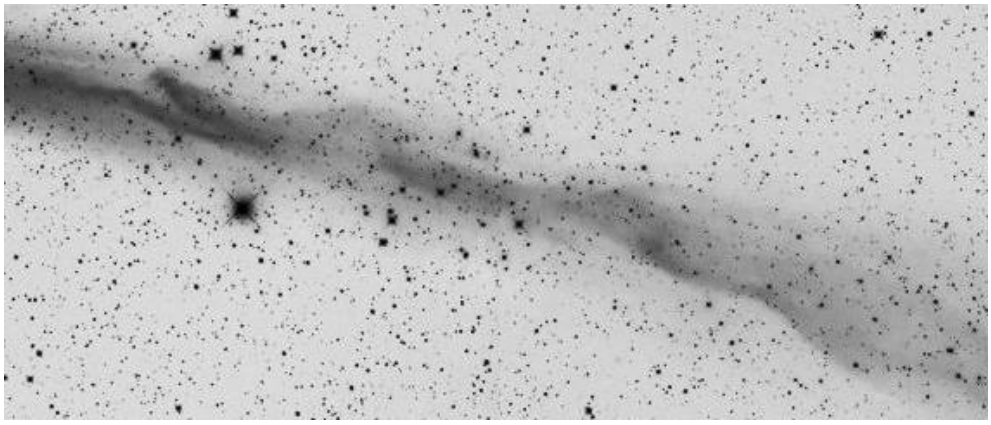

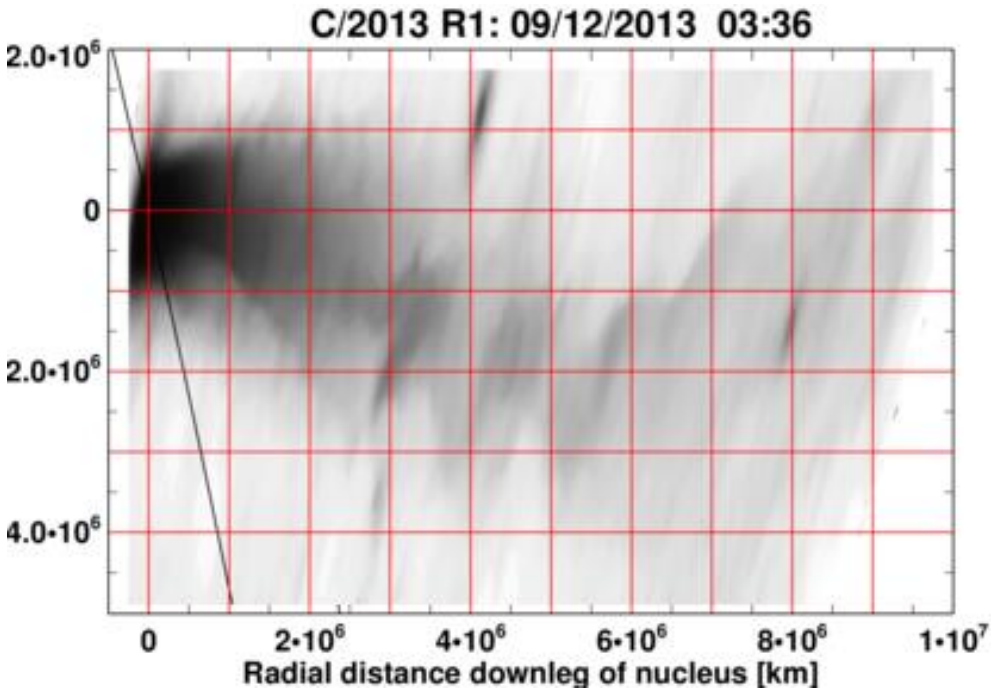

Figure 5.145: C/2013 R1 captured by Mrozek and Skorupa on 09/12/2013 03:36 UT, showing a tail disconnection and turbulent ion tail. The image has been mapped onto the comet's orbital plane in a cometocentric reference frame. Sunward direction is to the left.

Figure 5.145 is one of the best examples of the highly dynamic variations of an ion tail, with multiple kinks and a disconnection event. The ion tail changed orientation multiple times and curved back towards the radial vector generally indicating an acceleration of the lagging end of ion tail. However, the orbit plane angle remained just below 10^{o} during this time, thus obfuscating the determination of a realistic radial velocity. The structures visible before the near-90 degree bend in the ion tail direction, seemed to be entrained almost radially when compared with an image by the same observer half an hour later. ENLIL predicts low solar wind velocities ~ 250 km s^{-1} at the comet with a small latitudinal component [Figure 5.146]. The non-radial component included a reversal of the velocity vector acting upon the comet, thus explaining the arced tail in Figure 5.145.

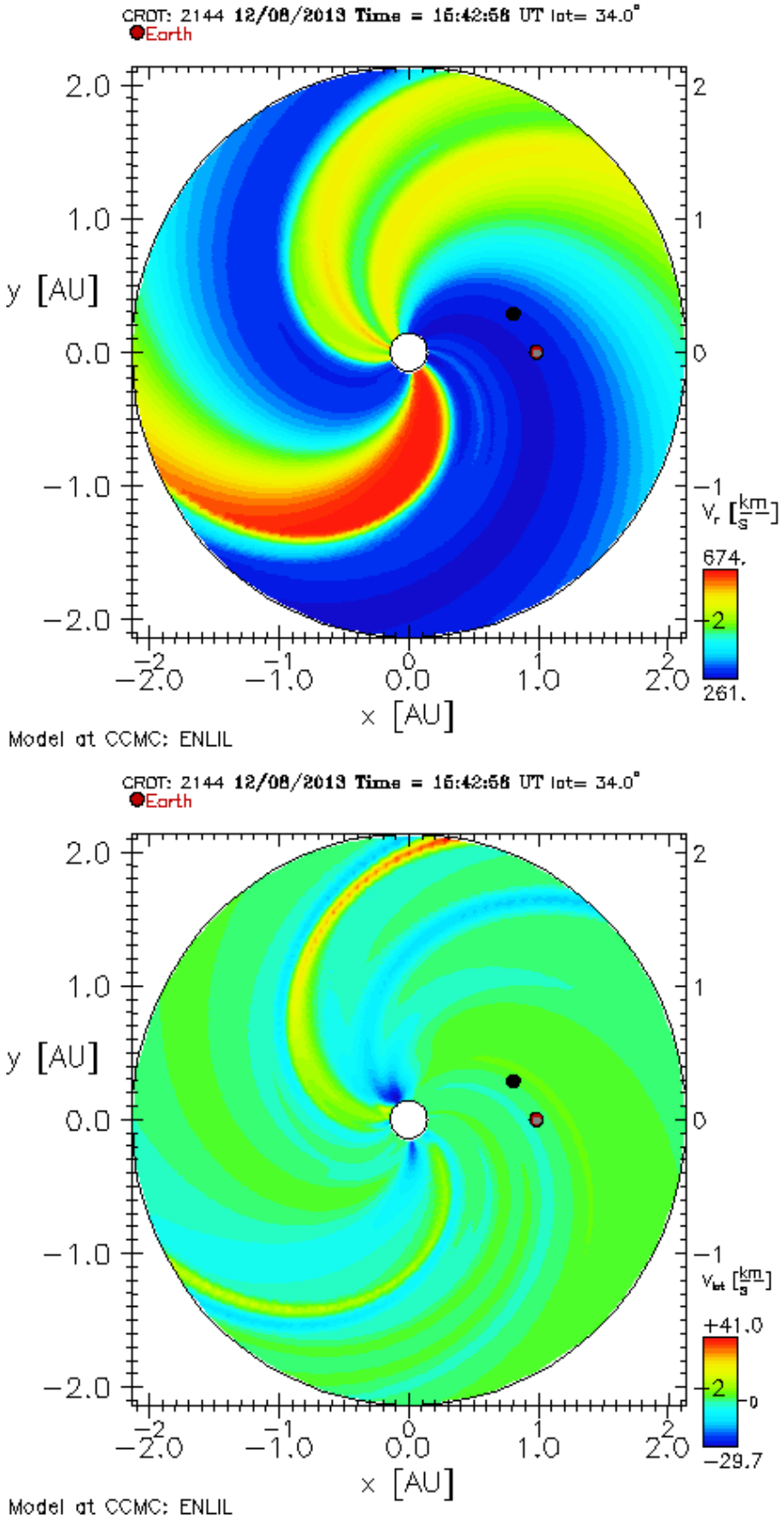

Figure 5.146: ENLIL MHD simulation for 08/12/2013 at 15:42 UT. The comet is predicted to encounter a non-radial component in the solar wind.

No velocities were extracted from the 12th to 13th December 2013 as the tail lead the comet's motion. The first image, by Rhemann on 12/12/2013, showed wave-like ripples down the tail and an asymmetrical number of tail rays. Another image, taken a day later by Rhemann, showed an equally dynamic tail, with a large condensation knot in the middle with a sharp angular change. This is reminiscent of disconnection events observed in previous comets. The tail was leading the comet motion in both cases. ENLIL predicts the comet will encounter solar wind flow of opposite magnetic polarity ahead of a CIR after 14/12/2013 06:00 UT and before 16/12/2013 00:00 UT.

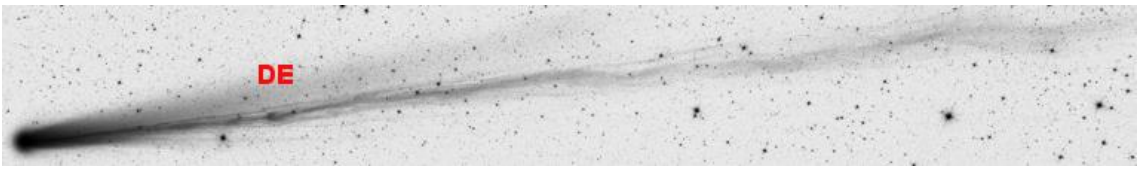

Figure 5.147: DE and a sinuous ion tail observed by Rhemann on 13/12/2013 03:41 UT. DE is located close to the nucleus, at approximately one-fifth the ion tail length.

Jäger and Rhemann images on 14/12/2013 exhibited a very extensive ion tail with a large aberration angle, extending into a wide, faintly connected set of ion cloud bundles. The plasma bundles, constituting the ion tail are expected to have departed from the approximate location of the comet's ionised coma starting from 12/12/2013 at ~04:00 UT. There is a large kink evident at the point where the ion tail width dramatically increases, suggesting a less than 180° HMF orientation has occurred upstream of the comet. We are likely viewing the ion tail edge-on in the thin section prior to rotation of the ion tail. Large non-radial components are predicted at the time of observation, though this cannot explain the existing ion tail configuration, considering that a low predicted radial solar wind speed of ~250 km s^{-1} would be insufficient to propagate throughout a 1.2 x 10^7 km tail in time.

According to ENLIL, the comet encountered a CIR on the 16th December 2013. The trend is present in my velocities, though velocities on the 16th and 17th are underestimated by ~ 200 km s^{-1} with respect to ENLIL. The discrepancy throughout this CR is clearly the result of projection effects, such that the ion tail curvature away from the radial direction, arising from the observer's

location with respect to the comet's location. This larger perceived aberration would produce much lower apparent solar wind velocities with this technique.

A collection of ICMEs, travelling in the general direction of the comet, and their SATs for the periods mentioned previously are shown in Figure 5.148, and the interactions they may have been the cause of are listed inTable 5-3. The comet's mean position angle was 343° and the position angle of the solar rotation axis was 13°.

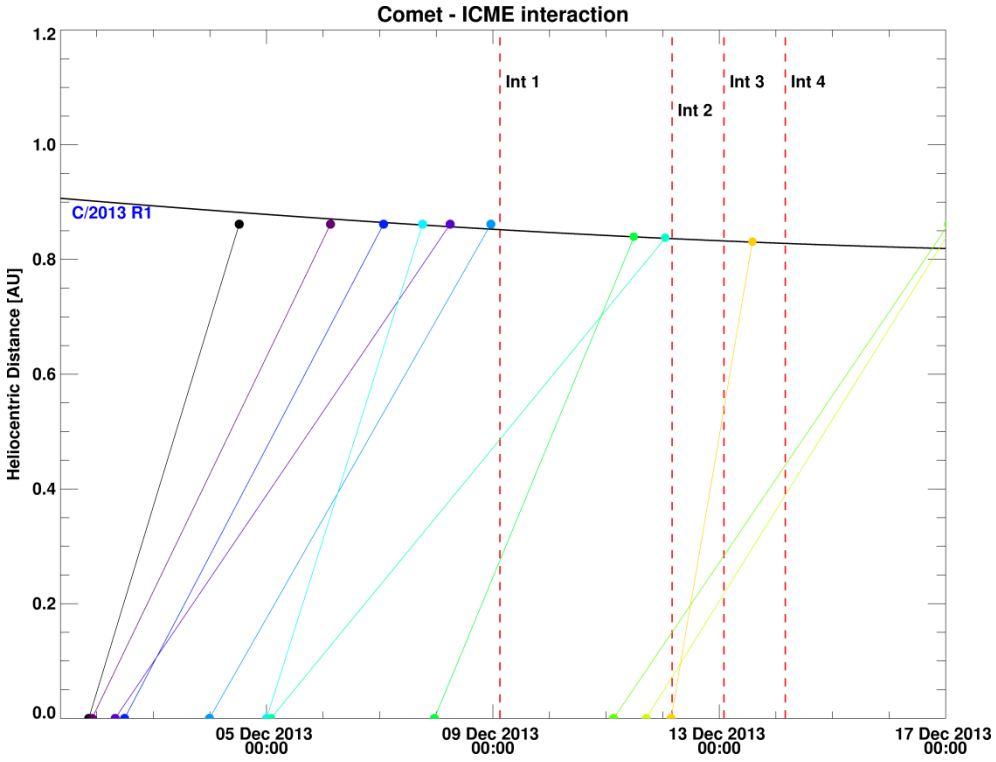

Figure 5.148: Potential ICME interaction candidates with C/2013 R1 with their SATs at the comet. Interactions marked above are the approximate times at which the images were taken and not the beginning of the interaction with disturbed solar wind medium.

Table 5-3: List of identified possible ICME interactions at comet.

Date	Time	Linear Speed (km s^{-1})	CPA (°)	Angular width (°)	Interaction
02/12/2013	07:48	252	352	56	1
02/12/2013	11:48	326	353	83	1
03/12/2013	23:48	300	331	16	1
05/12/2013	00:00	541	293	91	1
05/12/2013	01:48	208	315	82	2 or 3

07/12/2013	23:12	412	295	116	2 or 3
12/12/2013	03:36	1002	214	276	4

CR 2145

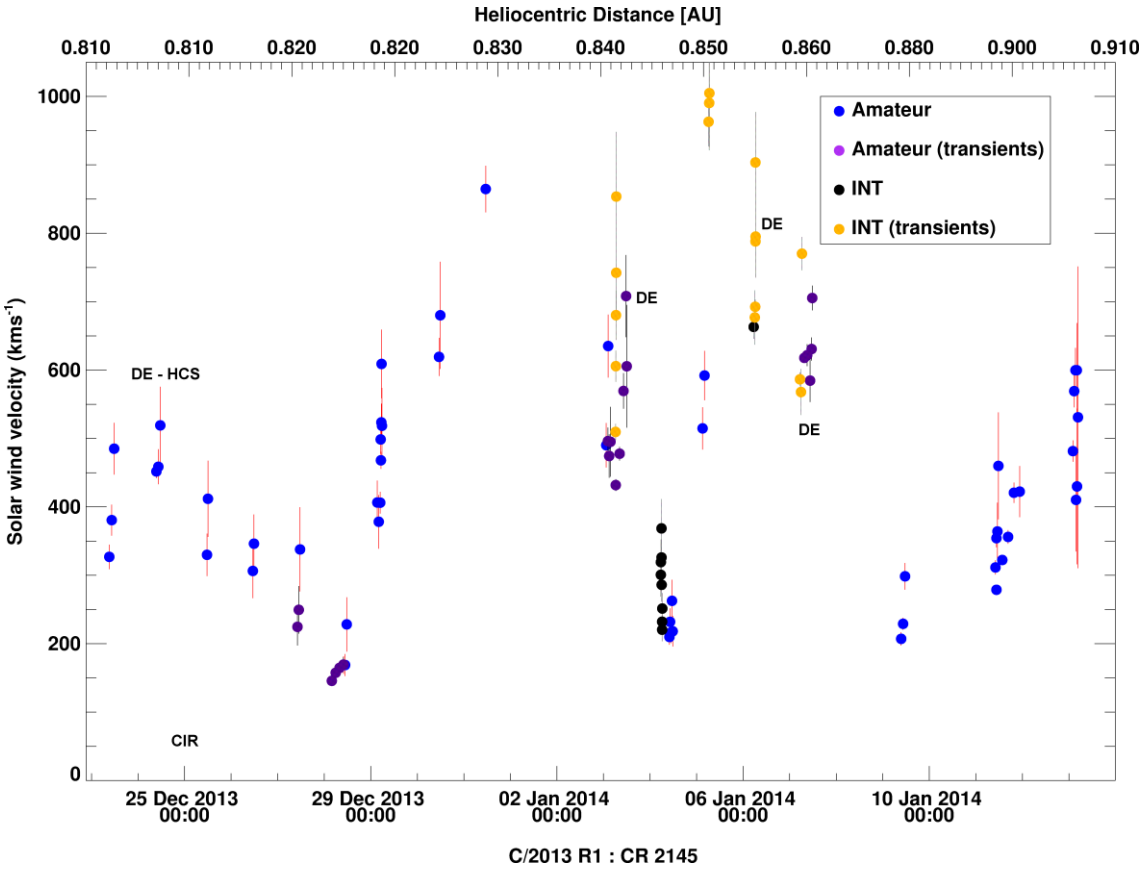

Figure 5.149: Solar wind velocities for CR 2145 derived from amateur (blue) and INT (black) observations. Transient physical structures in the ion tail such as kinks, density enhancements or DEs are marked in purple and orange for amateur and INT observations respectively.

Based on Figure 5.149 and Figure 5.150, it appears that the comet encountered slowly decreasing solar wind velocities. This is supported by ENLIL up to 25/12/2013, though predicted velocities at the comet are ~100 km s^{-1} lower. The comet is expected to encounter flows of opposite magnetic polarity on the 24th and a CIR with large non-radial flow components on the 25th. A high contrast enhanced image on the 24th December confirms the HCS crossing within this timeframe.

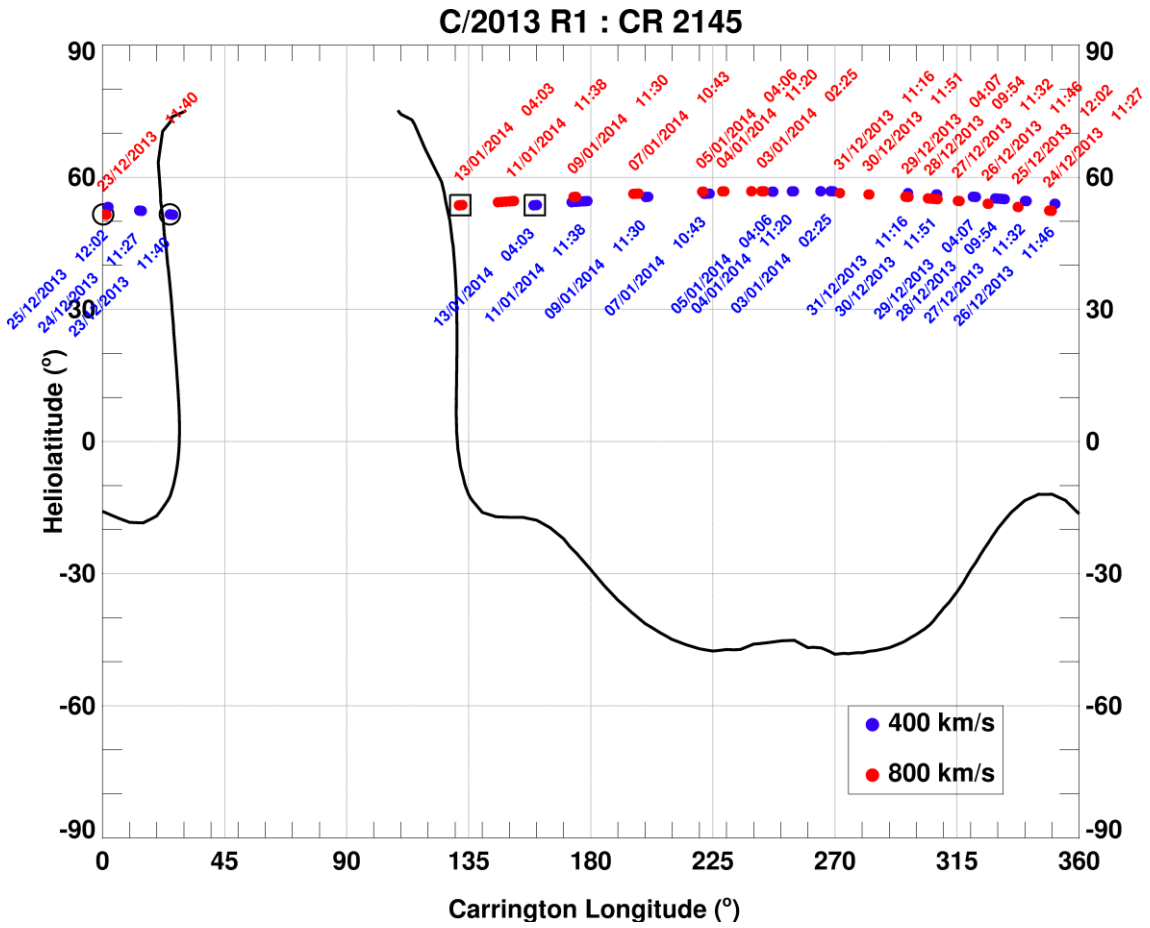

Figure 5.150: Mercator map for CR 2145. Only sources interacting with the comet in the amateur images have been mapped back to the solar wind source surface. Sources for the INT observations will fall between the 2nd and 7th January.

Direct observational evidence of kinks and a DE disputes the smooth, fast solar wind outflow predicted at the comet between 26/12 and 28/12. Therefore, the comet must have either encountered a slow moving disturbed solar wind, conveniently explaining the decreasing solar wind velocity, or the high latitudinal MHD solution is incorrect for this run. The sharp increase in velocity on 29/12/2013 likely marks the end of the disturbed solar wind outflow with velocities at the end matching expected fast solar wind velocities. The ENLIL fast solar wind region does not show any velocity gradients.

Observations by Rhemann and Jäger, on January 3, 2014, caught the onset of an ICME-related turbulent event, with what seems like small-scale ion tail variations. These propagate and produce a disconnection event as seen 8 hours later in image by D. Peach. The long, sinuous, disconnected tail was measured travelling radially at ~ 450 km s^{-1}. These observations

coincided with the start of my observing run at the Isaac Newton telescope where we observed a much closer region of the ion tail. The dichotomy between results taken at the same time on the 3rd January is due to solar wind measurements extracted from the disconnected ion tail over 1 x 10^7 km versus measurements taken from a newly formed ion tail over 1 x 10^6 km. The comet experienced a decrease in solar wind velocity corresponding to a rarefaction region lagging a CIR in the ENLIL model. The velocity samples from both INT and the amateur images are lower than predicted values by ~200 km s^{-1} again. The MHD predicted longitudinal velocity component at the comet is ~20-30 km s^{-1}.

Velocities from amateur images, shown in blue, sampled at the exact time of the ENLIL snapshots match well on the 5th. Samples from the INT images (orange dots), spanning only one-fifth of the distance covered in the amateur images, indicate a much higher velocity. The ion tail is almost parallel to the radial vector with subtle variations in the width and orientation downstream of the nucleus [Figure 5.151]. This could indicate a large scale transient in the solar wind since the extremely high velocities exceeding 1000 km s^{-1}, do not subside on the 6th January. This is likely a non-radial flow of the solar wind rather than a fast radial outflow.

Images on the 6th show a DE related knot moving at ~40 km s^{-1} and accelerating to ~150 km s^{-1}. Using the radial vector technique, the condensation knot is measured to be propagating radially at ~700 km s^{-1}. There are no CIRs or DEs expected that match our observations, thus this event must be ICME related. The inferred velocity range during this period is not dissimilar to that observed with the ACE extrapolated solar wind velocities for comet C/2004 Q2, when the comet experienced multiple solar wind streams near-simultaneously.

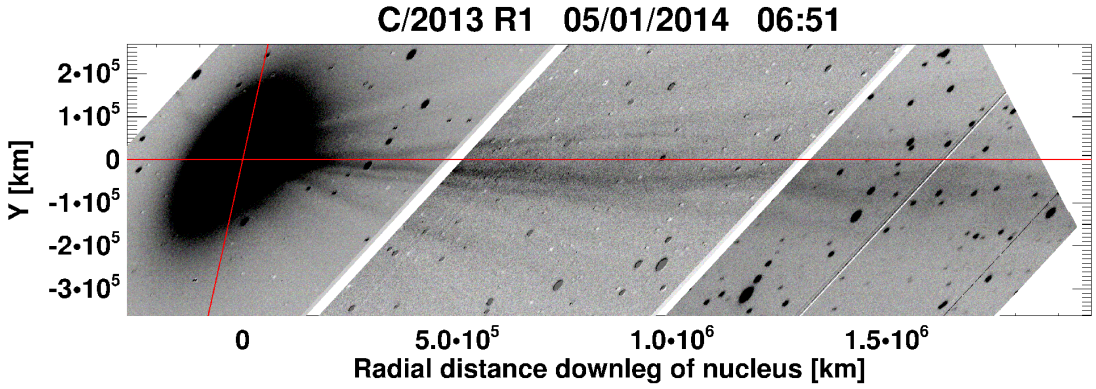

Figure 5.151: INT WFC observation of C/2013 R1 on 05/01/2014.

Turbulence in the ion tail continued in images from 07/01/2014. The INT images show multiple tail orientations and a large trackable kink evolving into a DE in an image taken 0.25 days later [Figure 5.152]. The comet is not expected to have encountered a polarity reversal in the solar wind flow.

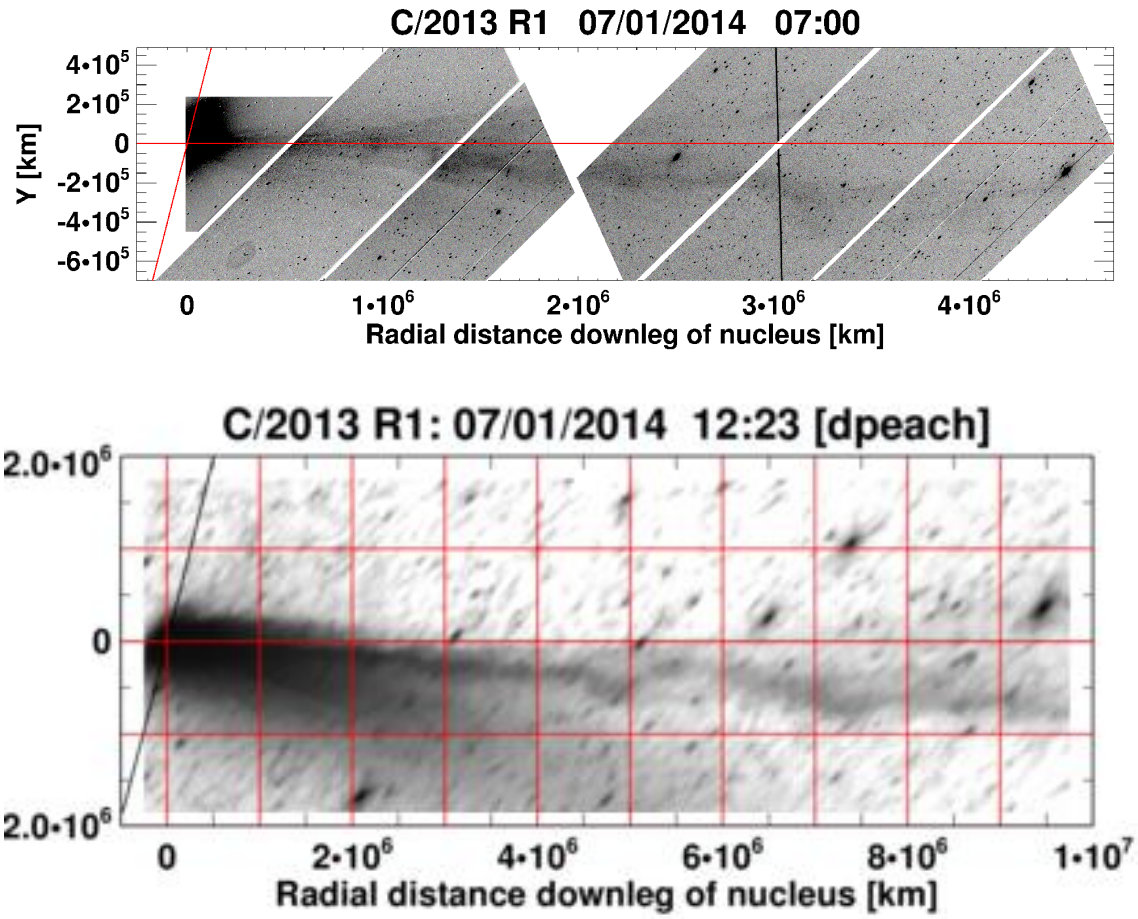

Figure 5.152: Top: Mosaic of stacked, difference image with 5 x Harris B (1 x 10s and 4 x 90s exposures) and 4 x sloan r images (90s), showing DE at ~1.3x10^6 km and kink at ~3x10^6 km. Bottom: Amateur image captured by Peach showing the same DE and kink 5.5 hours later, at ~4.7x10^6 km and ~7.2x10^6 km respectively.

A velocity check against the ENLIL model shows good agreement for values from 09/01/2014. For 10/01/2014, my velocities range between 250 and 450 km s^{-1} versus the predicted 250 km s^{-1}. There's a slight turbulence and a kink in the ion tail accounting for the range in the velocities reported. There is a small non-radial component to the solar wind on the 13th January

2014 but this does not account for the large discrepancy in the radial velocity of 150-200 km s^{-1} between observed and the predicted lower values.

A list of ICME interaction candidates is drawn up in Table 5-4 and their expected arrival times at the comet's location is given in Figure 5.153. Assuming that the fast ICMEs will slow down upon interaction with the solar wind and conversely for slow ICMEs, the unexplained ionic turbulences described for CR 2145 could be explained by interactions with ICMEs.

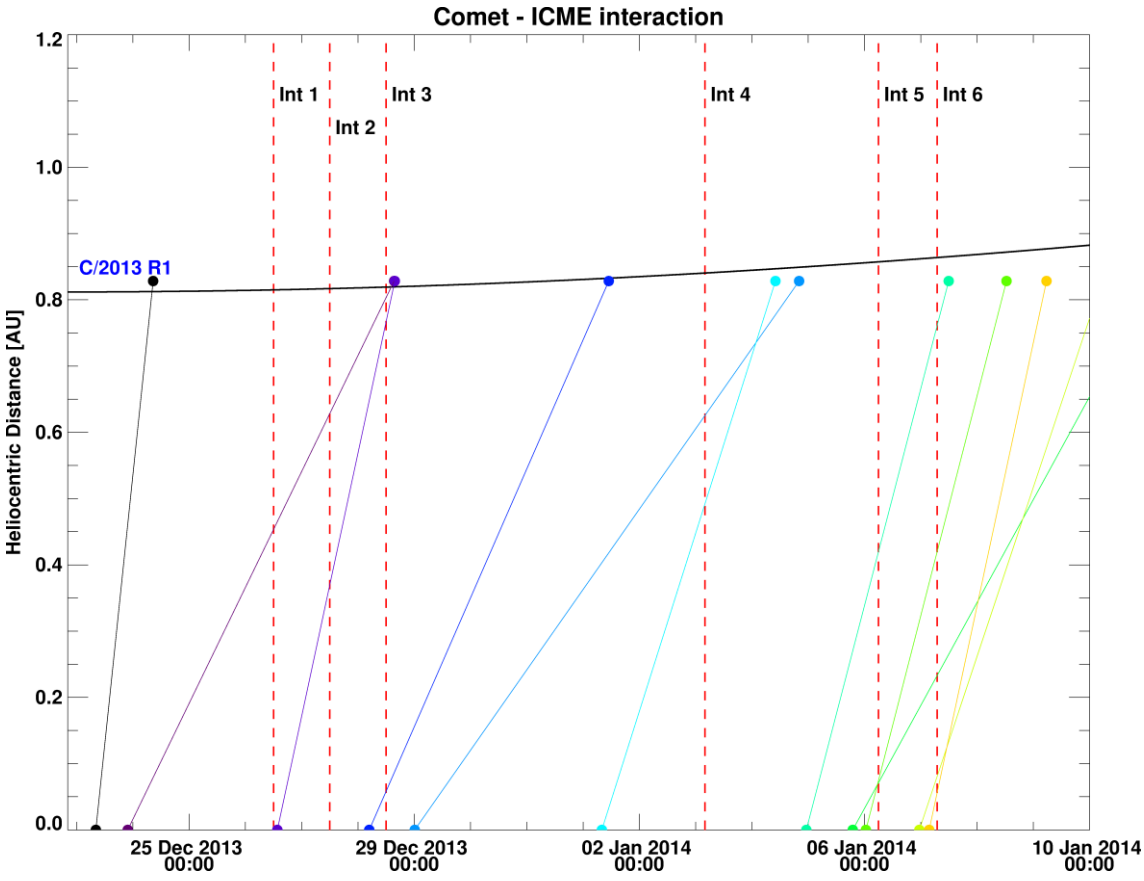

Figure 5.153: ICME interaction candidates that may have triggered the unexplained disturbances observed in the comet's ion tail.

Table 5-4: Likely ICME interactions and their parameters

Date	Time	Linear speed (km s^{-1})	CPA (º)	Angular width (º)	Interaction
23/12/2013	08:12	1409	308	94	1, 2 and 3 - maybe
23/12/2013	21:48	303	312	55	2 and 3 if sped up by fast solar wind
28/12/2013	04:48	337	355	57	4
29/12/2013	00:12	210	305	85	5, 6
01/01/2014	08:00	465	291	185	5, 6

Conclusion

A recurring theme across the radial velocity technique has been that measurements taken close to the nucleus are generally higher than those further down the tail. This is contrary to what we should expect according to theory. There is a distinct curvature to the ion tail present in most mapped images, with the degree of curvature lessening with decreasing distance to the nucleus. This unique morphology when mapped is the primary reason for the range of measured velocities. It bears noting that the INT observations were all taken within 1.5 x 10^6 km of the nucleus, with moving features identified and tracked as close as 5 x 10^5 km. During my analysis of the amateur images, the dust tail and ion tail are observed to overlap although this was mostly not a hindrance during data extraction. All the velocities derived for this comet were taken when the orbit plane angle was around 20^o. Contrary to previous comets, the ENLIL MHD visualisations offered little insight into the chaotic episodic flows observed at the comet. These sudden deviations from the fast solar wind speed can only be explained by ICME interactions since no HCS crossing or slow winds were expected.

Surprisingly, the velocities from amateur images (blue dots) are markedly better correlated with each other in comparison to previous comets, despite the low orbit plane angle. We can also see excellent agreement with the solar wind velocities derived from a professional grade observatory from both regular solar wind flow and transient features in the ion tail. This suggests that amateur observations afflicted by inclement weather and subjected to likely worse seeing conditions are as trustworthy.

5.5.3. Alternative Methods to derive Solar Wind Velocities

5.5.3.1. Low Orbit Plane Angle

A number of observations for CR 2145 were taken at low orbit plane angle, allowing for an estimate of the non-radial velocity components to be derived, as shown in Figure 5.154. Most images during this period will overlap with the extended Sun-comet radial vector. Only four

images showed a deviation off the comet's orbital plane, yielding comparable results to that derived from previous comets.

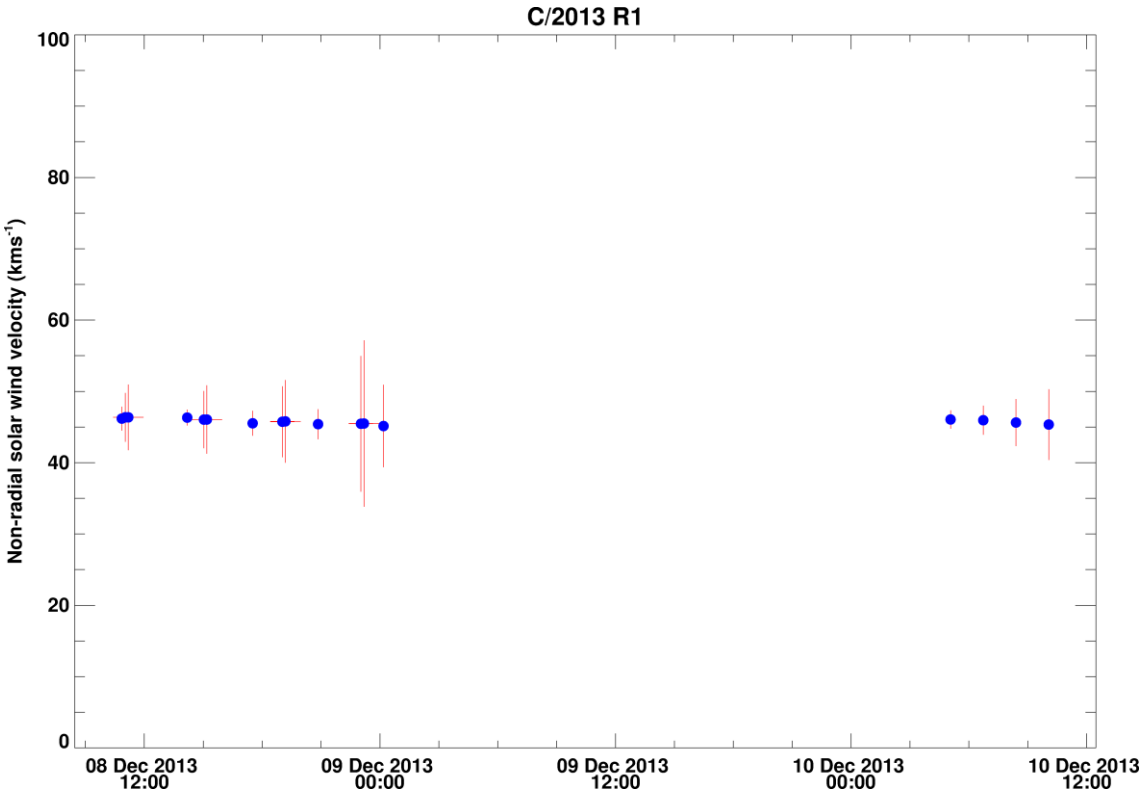

Figure 5.154: Non-radial velocity components of C/2013 R1's ion tail. These scenarios arise when the observer's latitudinal angular separation from the comet is small.

5.5.3.2. Vector Maps

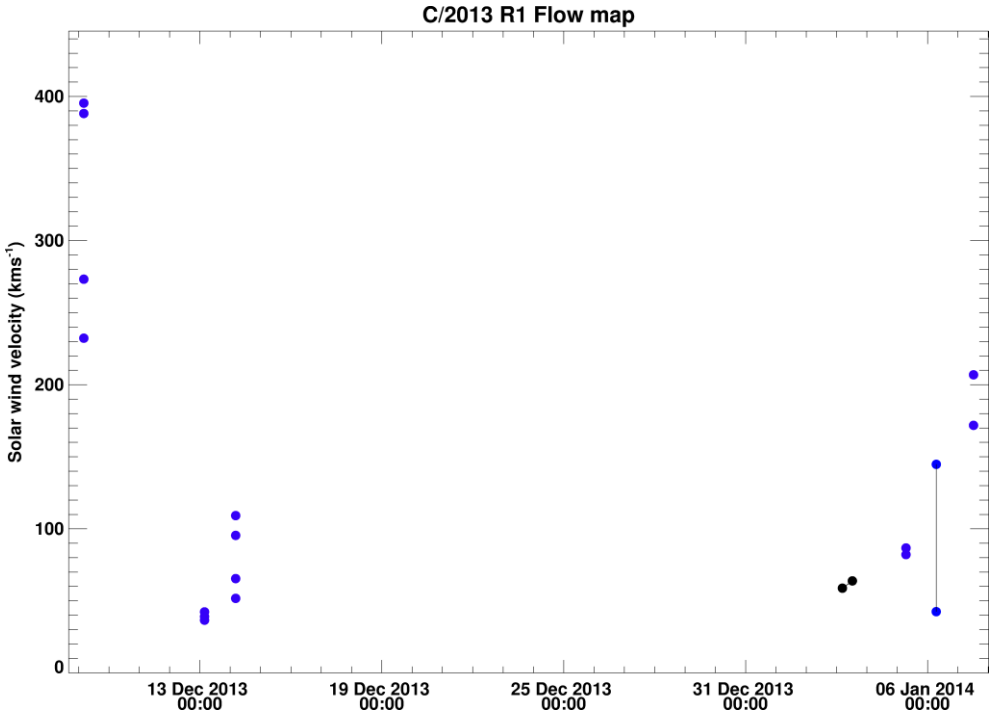

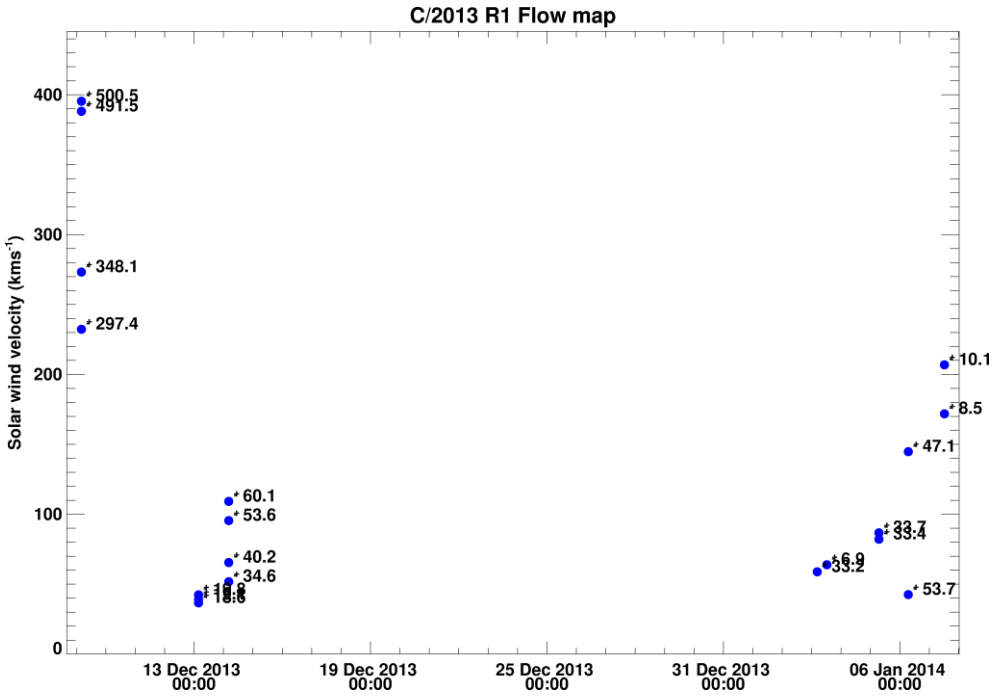

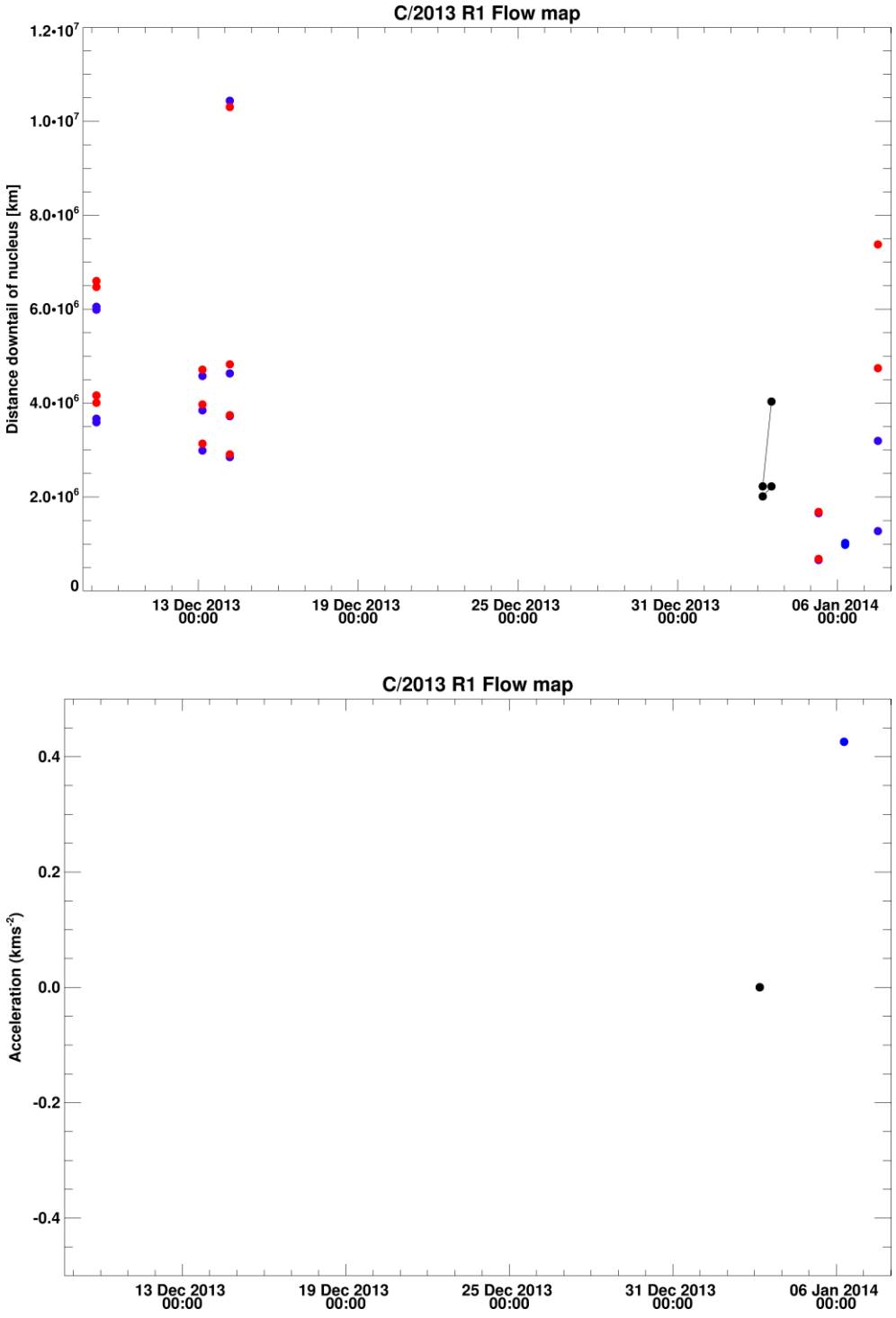

Figure 5.155: Velocity, errors, distances travelled and acceleration of identified features in the comet C/2013 R1's ion tail. Only two features were trackable in multiple, consecutive images. These are marked in a differently colour and connected together.

On 09/12/2013, two images taken at low orbit plane angle, showed a DE and turbulent ion tail, arising from non-radial flow at the comet. The features were observed to move near-radially at

the slow solar wind velocity. The velocity profile is increasing down the tail. Four measurements were taken in two pairs, the first corresponding to the disconnected tail and the second of the large kink in the ion tail. A pair of kinks was tracked, far from the nucleus, on 14/12/2013. The features were observed to be moving very slowly. Measurements will be subject to human error due to the large feature sizes involved. A kink was observed to evolve into a slow moving disconnected tail, with near 0 km s^{-2} acceleration, on 03/01/2014. Bulk, radial measurements, over this period, produced a range of velocities from 500 to 650 km s^{-1}. Observations at the INT allowed tracking of a DE knot as close as ~ 5 x 10^5 km near the nucleus. The knot is observed to accelerate from 40 km s^{-1} to 140 km s^{-1} in a matter of minutes. The initial velocity is similar to the velocities of 20 and 25 km s^{-1} along the tail and 3.8 and 2.2 km s^{-1} across the tail, reported by Yagi et al. (2015).

Since the current images used have been coadded and difference-imaged, the high temporal observing resolution is therefore lost. The individual images for 06/01/2014 were revisited and difference images created for most of the B filter images. Without the combined equivalent increase in exposure time by stacking images, the dust-subtraction routine added little benefit to the delineation of the knot edges for the twilight images. This resulted in an image cadence of 2 minutes, observed over a period of 21 minutes. Since the dust intensity contribution is scaled before subtraction, normalising the exposure times for each image was redundant and thus not executed.

Tracking an expanding amorphous blob is somewhat tricky, thus an approximate centre of the knot was chosen as the outstanding feature to track in order to limit erroneous measurements. This was found to be heuristically better than tracking the feature's edges, which become fuzzy as the image contrast is altered. The downside is that measurements are subjective and slight variations in the feature centre can translate to significant changes in the velocity. The feature was observed at ~ 1 x 10^6 km away from the nucleus.

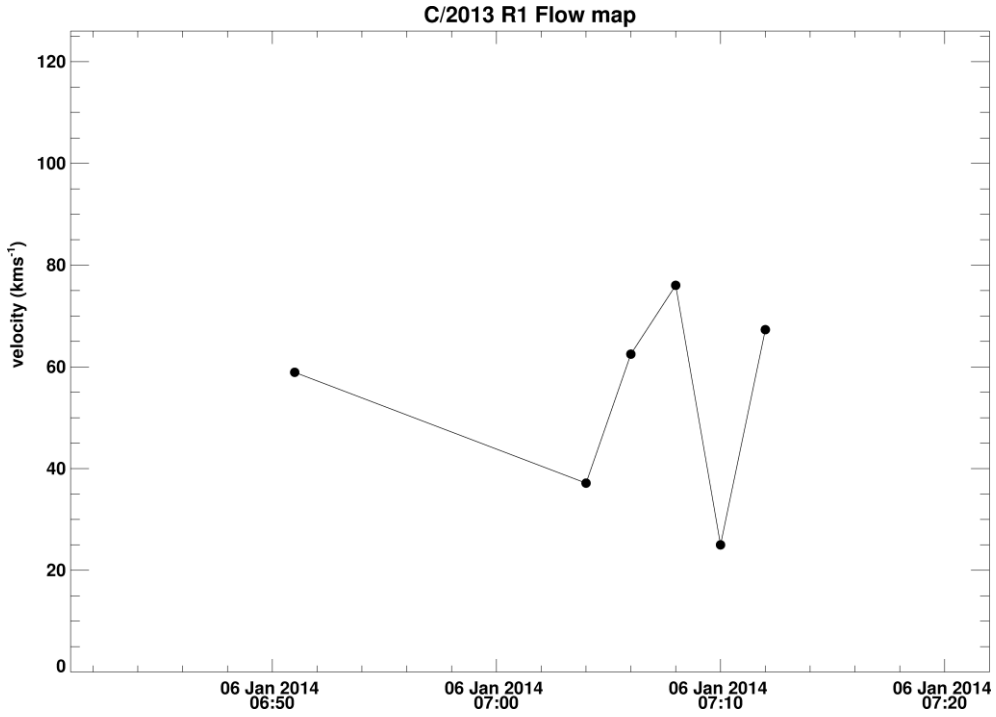
C/2013 R1 Flow map
velocity (kms-1)
120
100
80
60
40
20
0
06 Jan 2014
06:50
06 Jan 2014
07:00
06 Jan 2014
07:10
06 Jan 2014
07:20

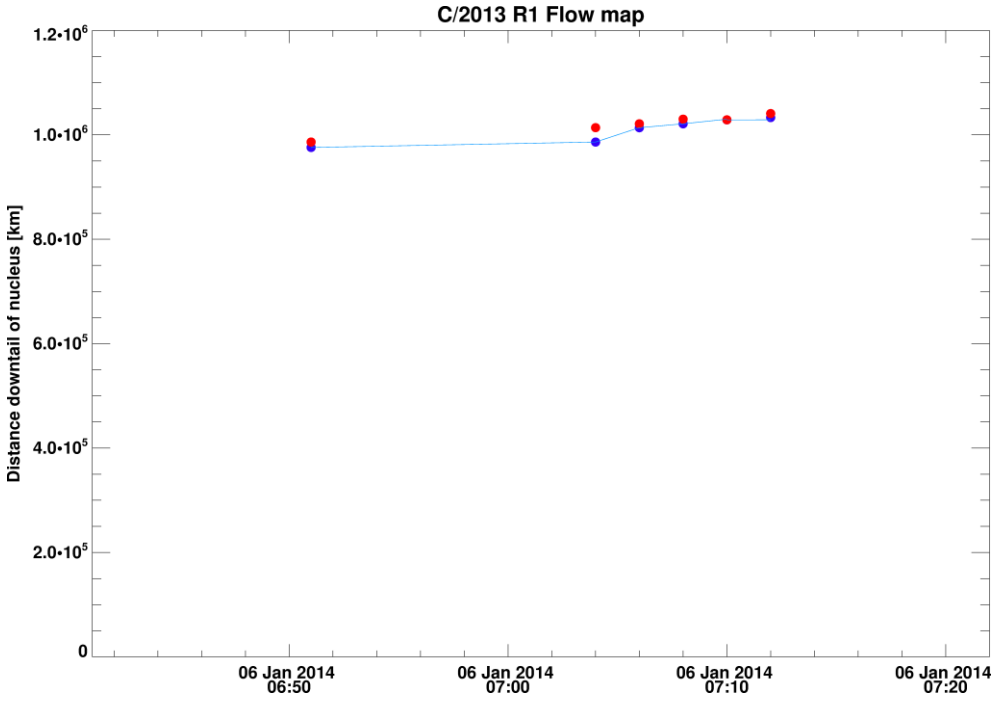
C/2013 R1 Flow map
Distance downtail of nucleus [km]
1.2•10^6
1.0•10^6
8.0•10^5
6.0•10^5
4.0•10^5
2.0•10^5
0
06 Jan 2014
06:50
06 Jan 2014
07:00
06 Jan 2014
07:10
06 Jan 2014
07:20

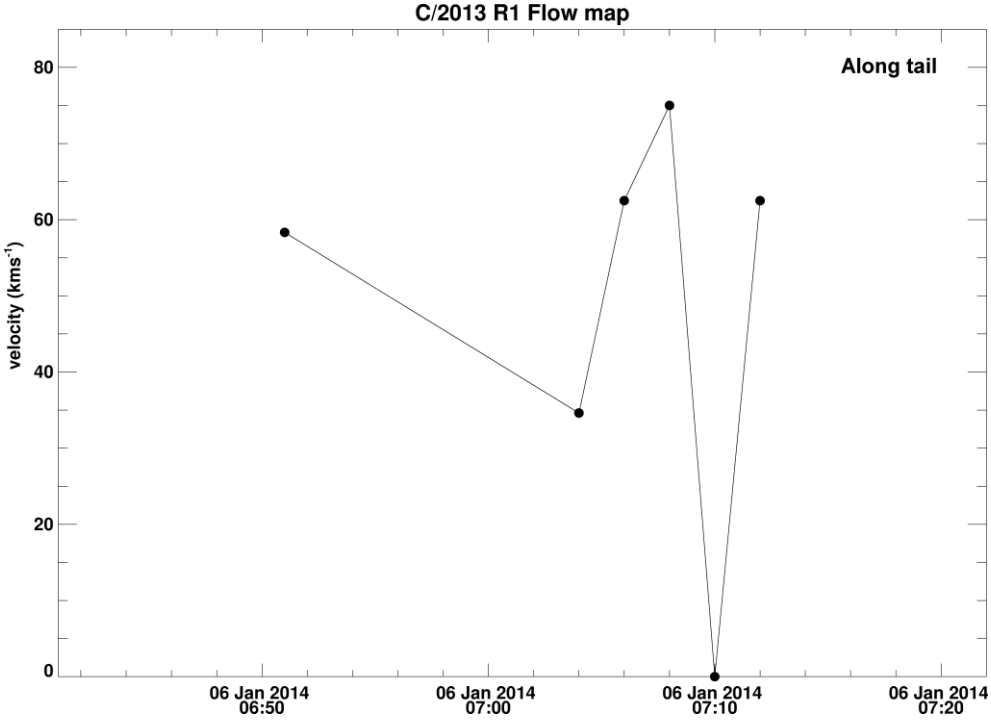
C/2013 R1 Flow map
Along tail
velocity (kms-1)
80
60
40
20
0
06 Jan 2014
06:50
06 Jan 2014
07:00
06 Jan 2014
07:10
06 Jan 2014
07:20

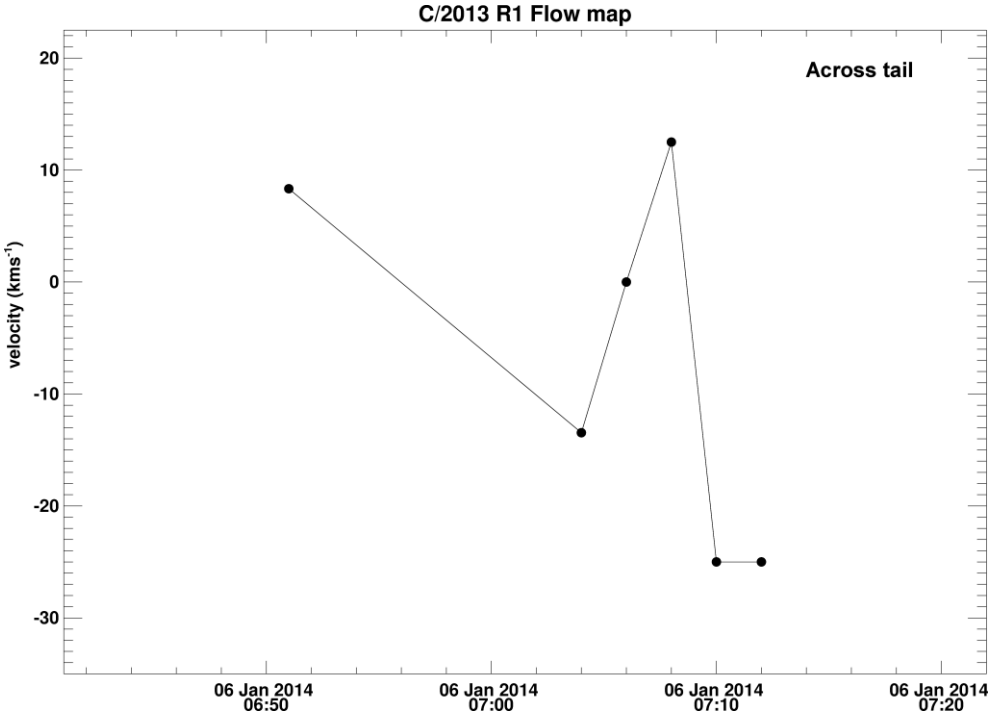
C/2013 R1 Flow map
Across tail
velocity (kms-1)
20
10
0
-10
-20
-30
06 Jan 2014
06:50
06 Jan 2014
07:00
06 Jan 2014
07:10
06 Jan 2014
07:20

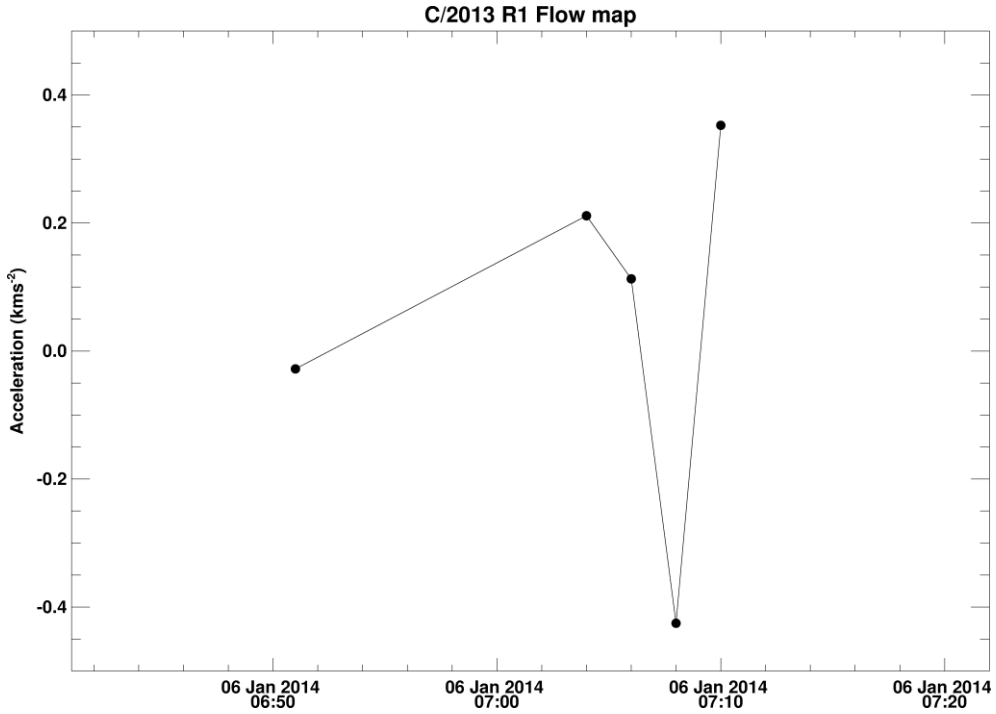

Figure 5.156: Solar wind velocity of plasma bundle, distance at which they were measured (red is from second image), the feature velocity along and across the tail and the acceleration of the feature based on plot 1.

Based on the overlap between positions 1 and 2 (second plot of Figure 5.156), we could surmise that the penultimate estimate was incorrectly measured. Excluding that, we see a mostly linear acceleration of the plasma bundle down the tail. The trending velocity along the tail is ~ 60 km s^{-1} ± 60 km s^{-1} and 10 km s^{-1} ± 54 km s^{-1}.

5.5.3.3. Folding Ion Tail Rays

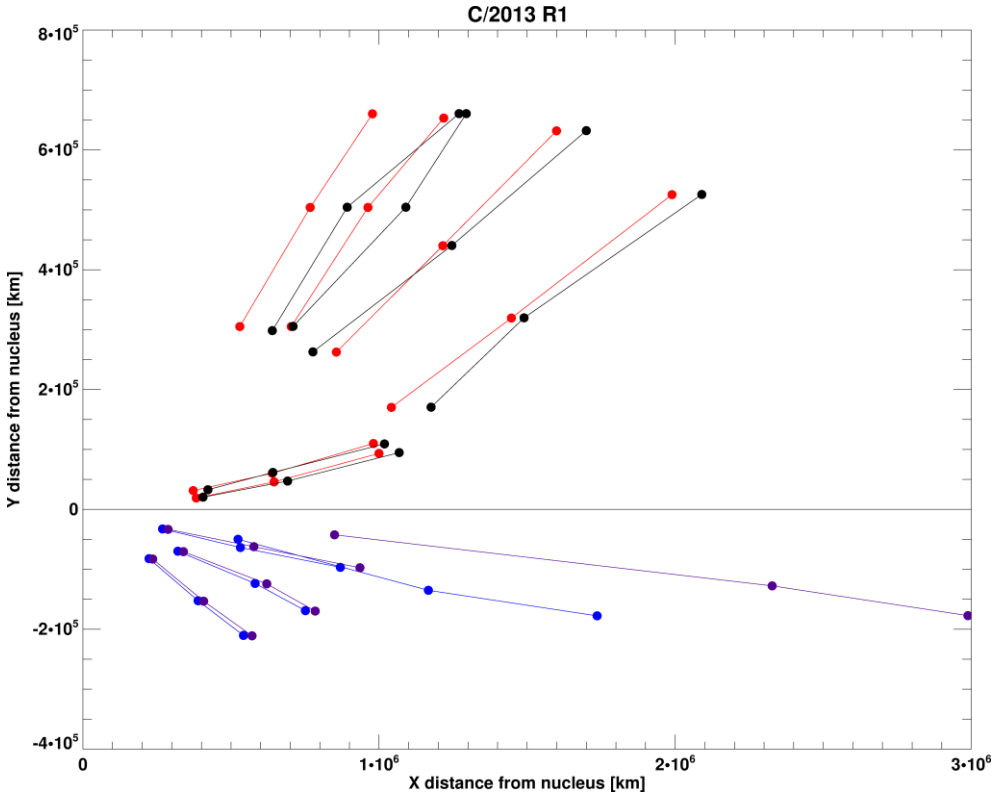

Figure 5.157: Measured samples of folding tail rays for comet C/2013 R1. Measurements are taken from consecutive images. Red and blue dots are taken from the first image. Blue and purple dots are the new positions of the ion tail rays taken along the extended radial vector from the Sun.

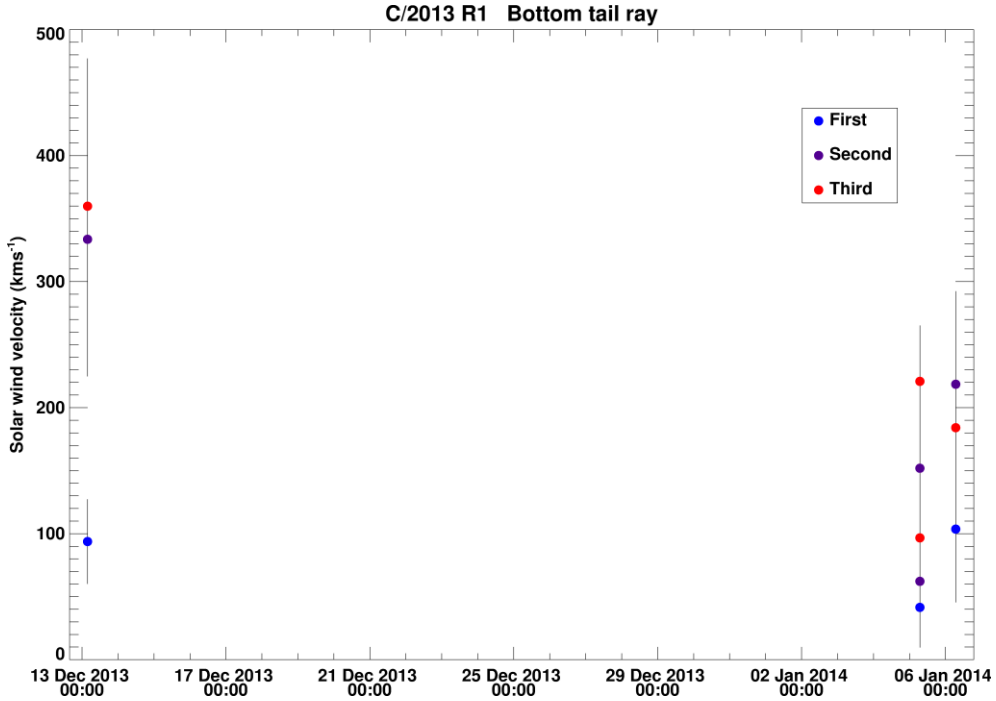

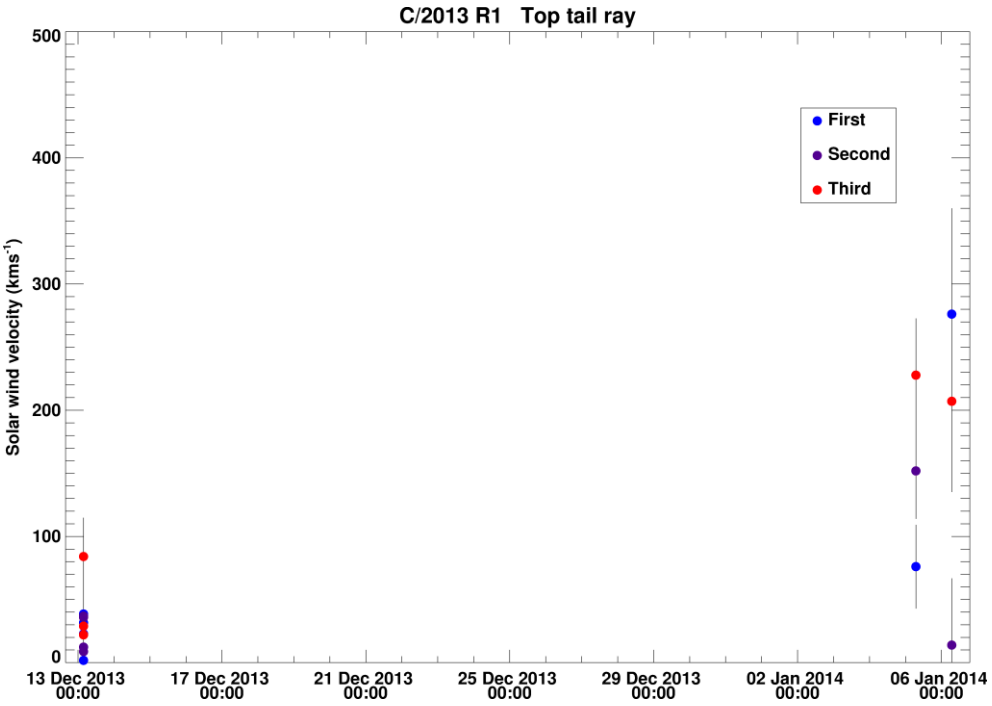

Figure 5.158: Solar wind velocities as a function of time taken for the folding tail rays. We expect measurements taken further down the folding ion tail ray to increase in velocity. The first sample (blue) is taken as close to the nucleus as possible.

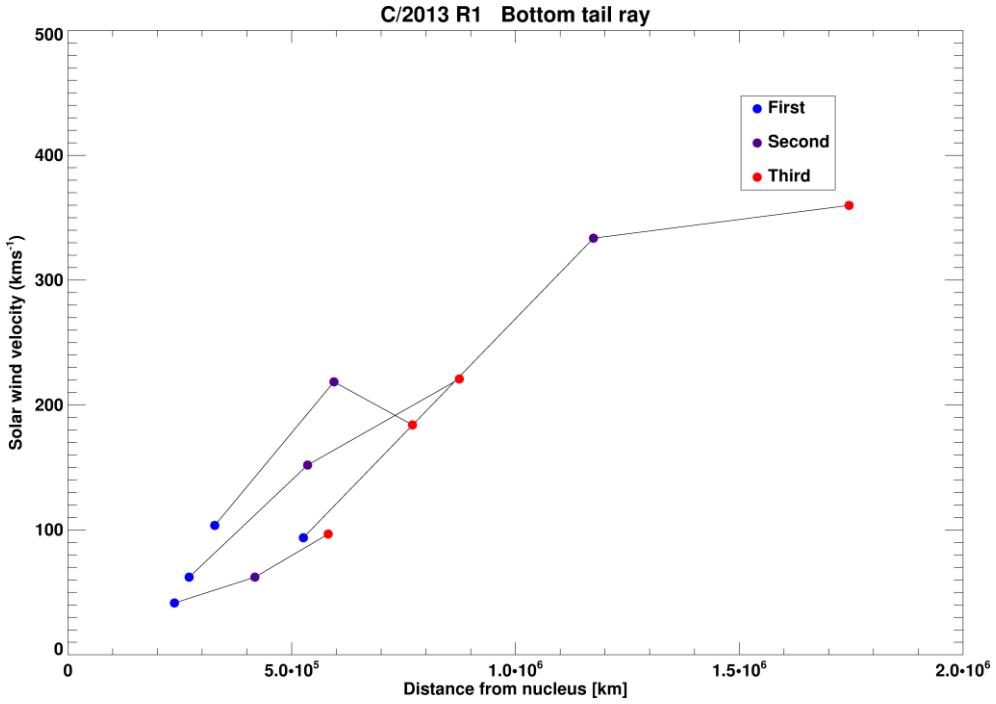

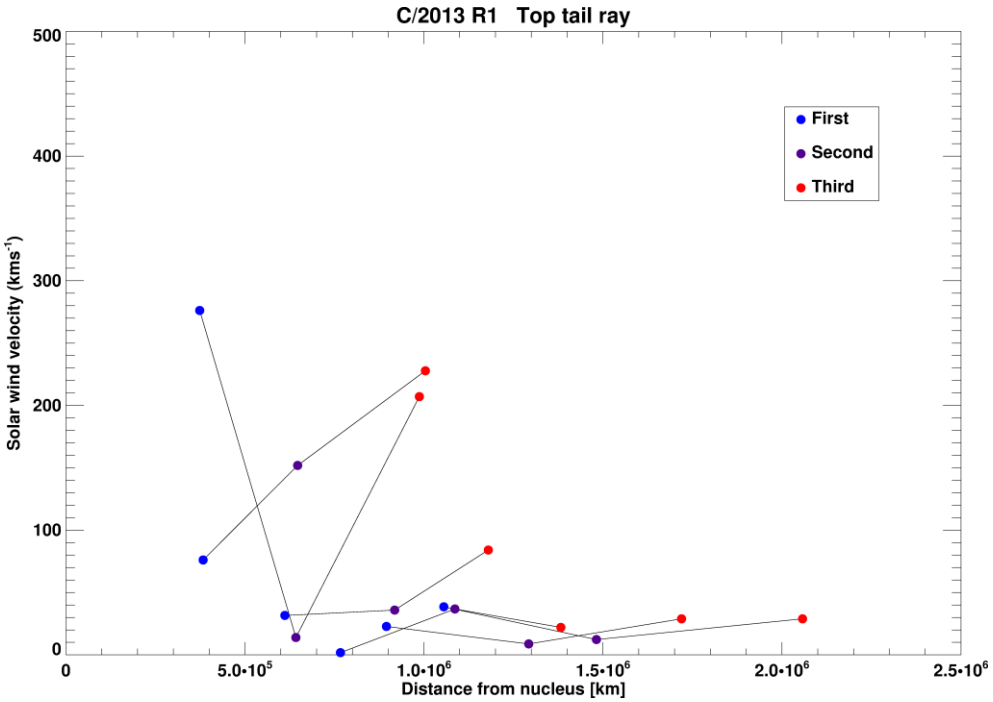

Figure 5.159: Solar wind velocity as a function of radial distance from nucleus. As expected, we mostly see an increase in velocity away from the nucleus.

There exist a few outliers shown in the velocity plots above, where the far end of the tail ray appeared to decrease in velocity. These are generally obtained from curved tail rays indicating a disturbed solar wind flow interfering with the expected evolution of tail rays. We also expect an increase in velocity with increasing nuclear distance. This is evident in the amateur images from 13/12/2013. The comet exhibited multiple top tail rays close to each other making it difficult to delineate the tail rays positions along the extended radial vector. The bottom tail ray was extensive (~ 3 x 10^6 km) and folded quickly about the main tail axis, producing velocities close to the slow solar wind velocity. From the third January onwards, these measurements were observed from my close-up INT images. The IDL contrast tool is not as efficient at stretching the image contrast as professional software. It was thus difficult to deduce the correct locations of the ion tail ray against the background and thus the results shown here should be considered with caution.

5.6. Comet Lovejoy (C/2014 Q2)

C/2014 Q2 is a new long period comet, originating from the Oort cloud and was observed during its first apparition. Its orbit is sharply inclined to the ecliptic [Figure 5.161] and it reached perihelion in late January 2015 at a heliocentric distance of 1.29 AU. Its closest approach to Earth occurred on 07/01/2015 at a geocentric distance of 0.47 AU, where it peaked in brightness at an apparent m_v of +4.32 (from JPL Horizons). The orbital elements (J2000) are Inclination (*i*) = 80.3^o; ascending node = 95.0^o, eccentricity (e) = 1.00; Perihelion date (T) = 30/01/2015, 01:42 UT

C/2014 Q2 easily counts itself as one of the most active comets so far this century. Its tail has been aesthetically resplendent and has been very closely monitored by the Professional – Amateur (PACA) collaborative group for disconnection events. As seen in the 11 -mage mosaic showcasing images observed by G. Rhemann [Figure 5.160], the ion tail spotlighted the highly variable solar wind phenomena influencing its general morphology and orientation, such as large orientation changes, kinks, condensation knots, disconnection events, tail rays and bifurcating tails. Recent narrow-field observations of the comet's coma have shown an abundance of well-defined tail rays. The comet would have been a fascinating target for study, however the timing of the comet's excursion into the inner solar system was inconvenient for the inclusion of all the observations in this body of work. As such, there is a limited presentation of the image catalogues currently available.

The collection of comet C/2014 Q2 Lovejoy images in Figure 5.160 includes 11 images observed on 20th, 21st, 22nd, 23rd, 27th and 28th in December 2014, on 17th, 18th and 21st in January 2015 and on 7th and 13th February 2015 respectively by G. Rhemann. Of these images, only the first two images were included in this analysis.

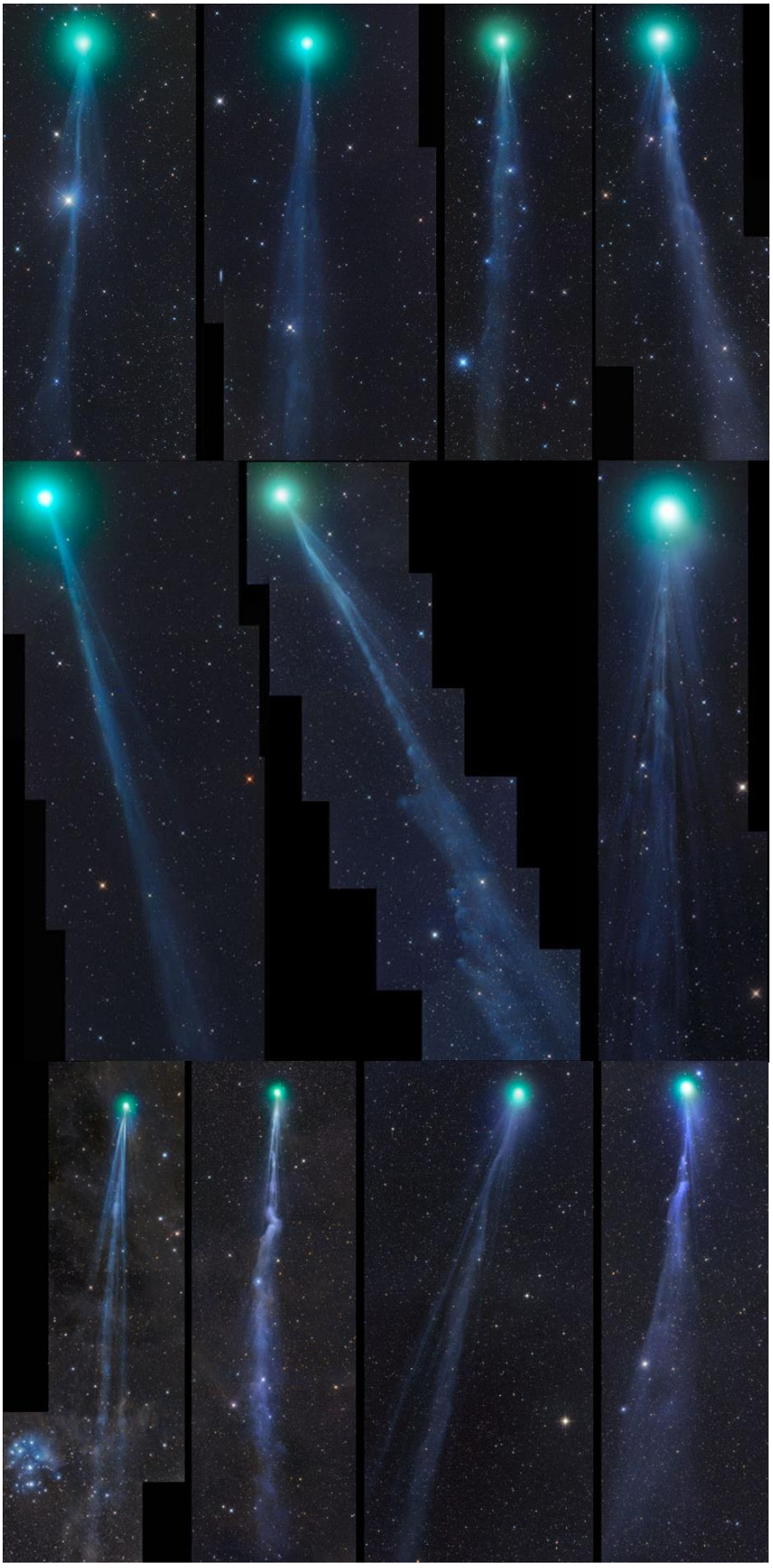

Figure 5.160: Mosaic of comet C/2014 Q2 by G. Rhemann.

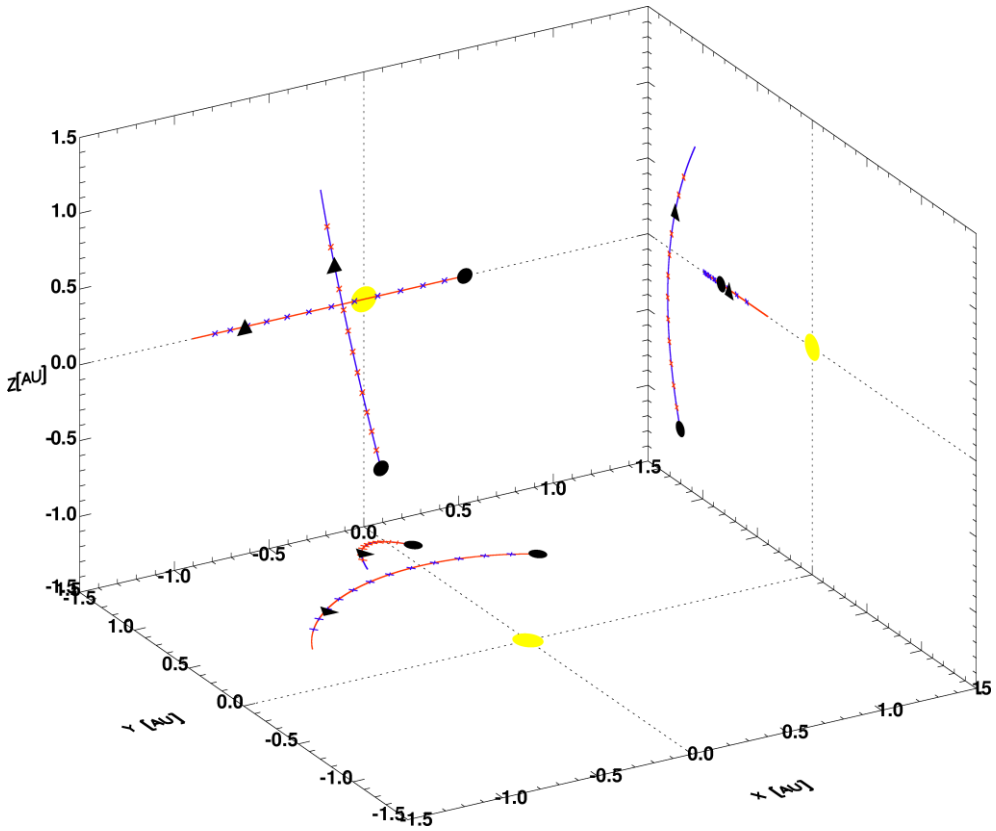

Figure 5.161: Heliocentric ecliptic coordinates of comet C/2014 Q2 (Lovejoy) and Earth from 20/11/2014 to 25/02/2015. I analysed observations of the comet obtained between 26/11/2014 and 21/01/2015. Black circles represent the start of the orbits.

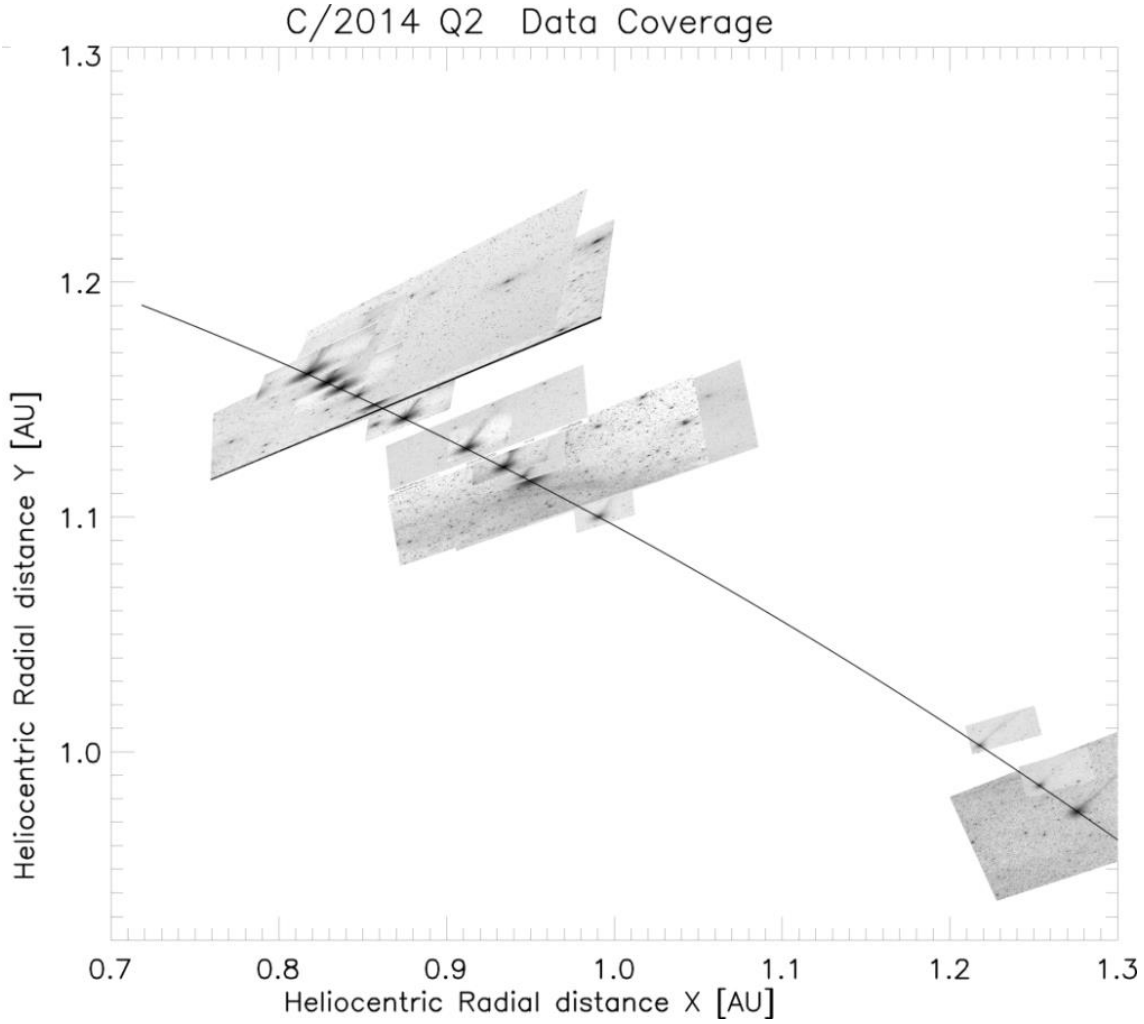

Figure 5.162: Data coverage for comet C/2014 Q2 (Lovejoy). The images and the comet's orbit have been mapped so that the y-axis is defined as the direction to perihelion. Earliest image is to the right of the data coverage plot, increasing chronologically towards the left. Note that the x and y axes are at different scales.

Image Statistics

At the time of writing, the comet was receding from the Sun and slowly dimming. A total of 63 intermittent images were processed [Figure 5.162]. 52 images were successfully processed through the Astrometry.net stage. 76 solar wind velocity samples were extracted from 27 images displaying a bright enough ion tail for analysis.

5.6.1. Radial Solar Wind Speeds

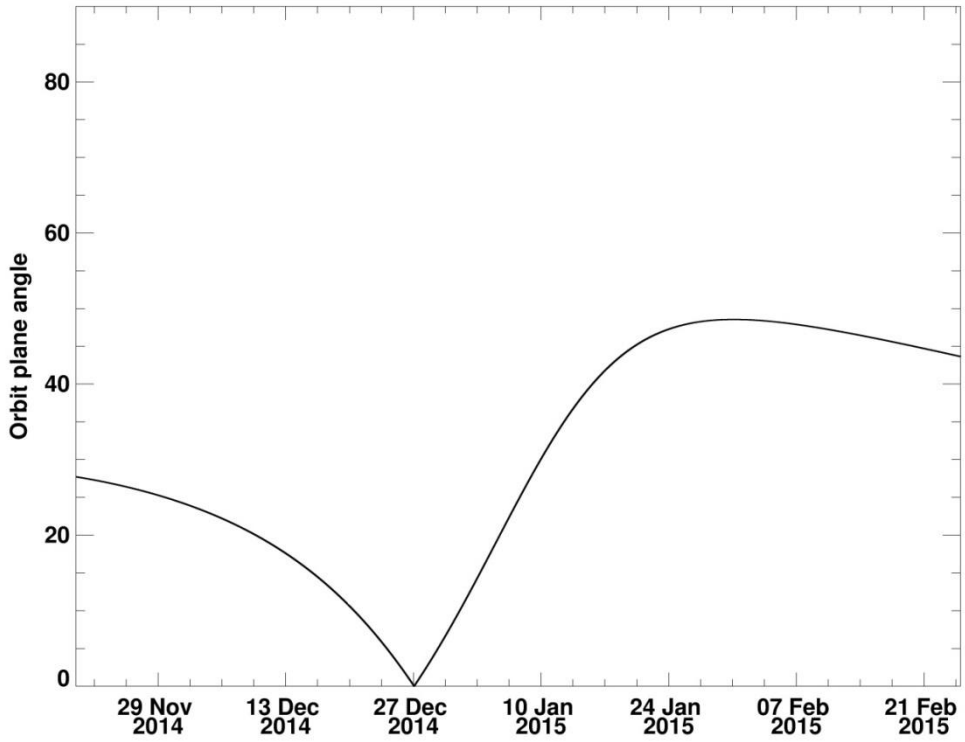

Figure 5.163: The orbit plane angle for C/2014 Q2 is below 10° for a short period between 20 Dec 2014 13:00 UT to 01/01/2015 00:00 UT before rapidly improving to a moderately good observing geometry.

The orbit plane angle is low and rapidly decreasing for observations during CR 2157 and 2158, so we expect to see a large data spread and a mismatch of velocities with the ENLIL model. The orbit plane angle rises quickly after 27/12/2014, so we would expect the data scatter to be high during the rapid increase and then to stabilise rapidly afterwards. The large data scatter cannot be confirmed due to a lack of solar wind velocity estimates in this period. Velocities derived on 21/01/2015, during peak orbit plane angle, are well correlated with each other.

Some data points are highlighted in green to mark periods of faint ion tail and/or part of the ion tail lying on extended Sun-comet radial vector. Comet C/2014 Q2 mostly experienced slow solar wind streams with the exception of a few peaks around 700 km s^{-1}, matching predictions from the Mercator maps.

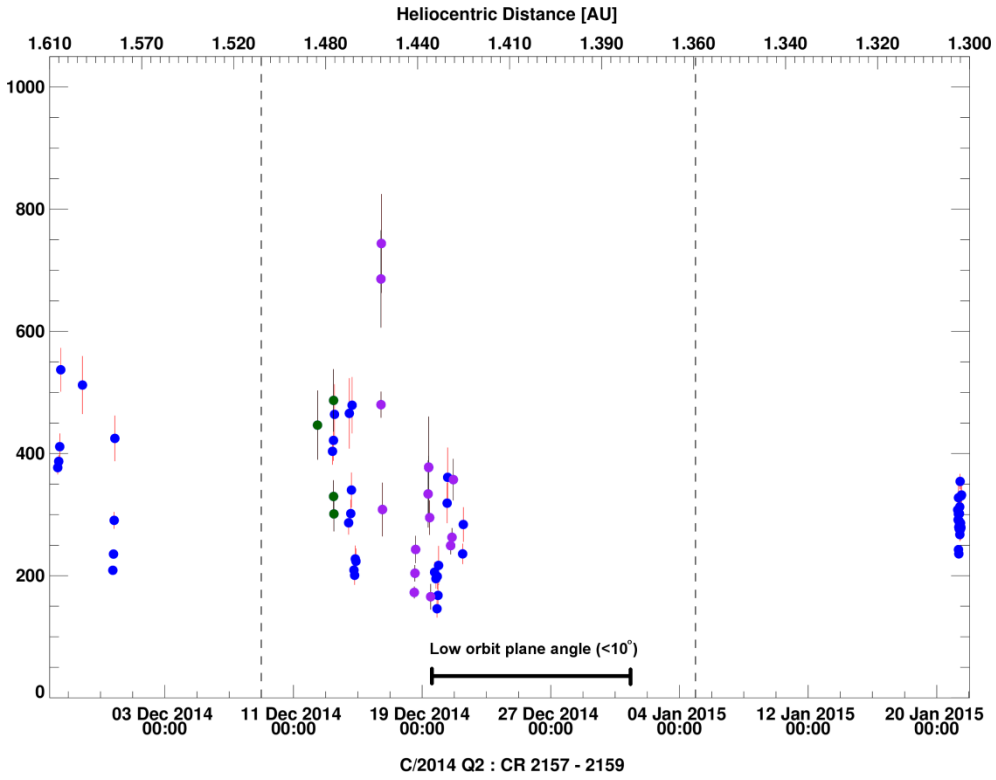

Figure 5.164: Solar wind velocity estimates from CRs 2157 to 2159. The blue dots are taken from images when ion tail showed little to no disturbance. Purple dots mark transient structures in the ion tail. Judging from these data points, the comet encountered mostly the slow solar wind regime.

CR 2157

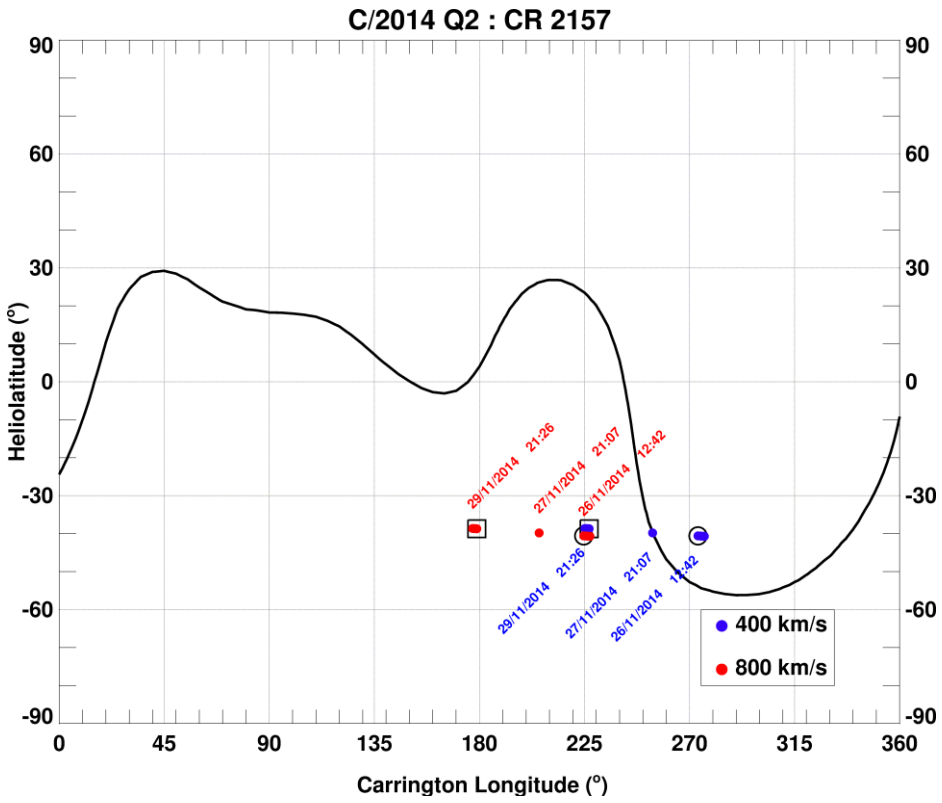

Figure 5.165: Mercator map for CR 2157. The comet is likely to encounter mostly slow solar wind velocities with the possibility of a HCS crossing on 27/11/2014 and a CIR on 29/11/2014.

The source of the magnetograms was switched to the National Science Observatory (NSO) for this CR due to poor modelled results from the previously used source (Kitt Peak). By means of the CCMC visuals, the comet is predicted to experience gradually decreasing solar wind velocities from 400 to 250 km s^{-1}. These match exceedingly well with extracted velocities [Figure 5.164], if the first estimate is not included. This feature of the technique, whereby estimates close to the comet head are constantly overestimated, has been pointed out on several occasions. There was no polarity reversal at the comet on 27/11/2014 and no DEs were observed during that period. It is unlikely that the comet crossed the HCS at 1.6 AU.

CR 2158

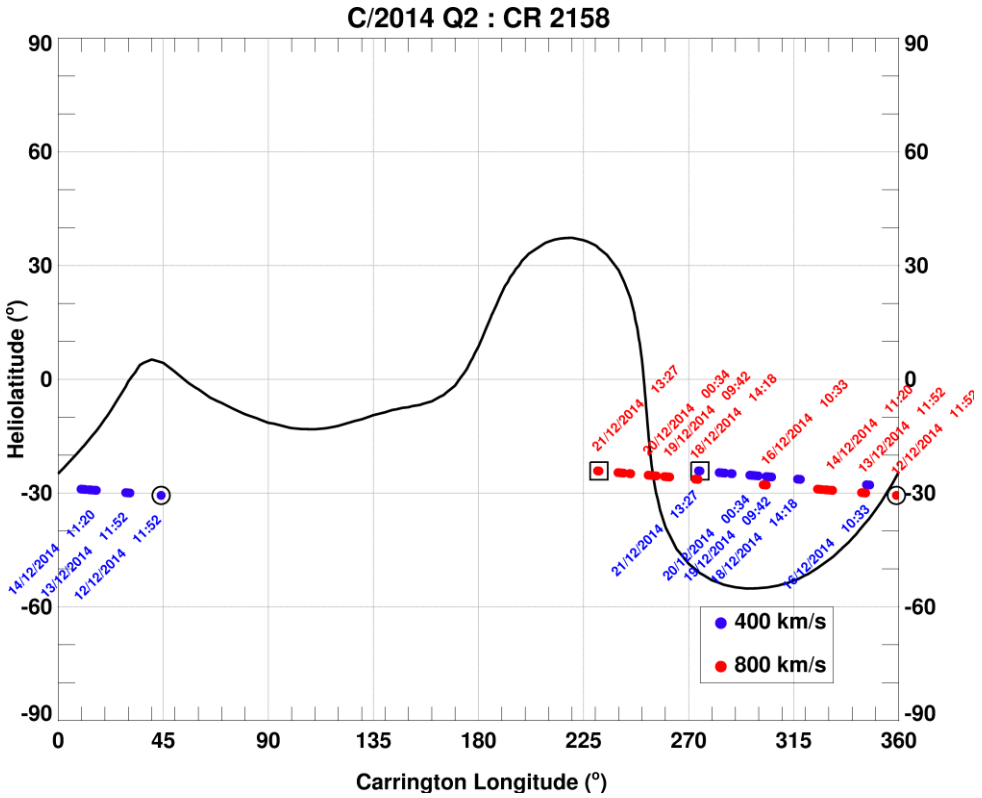

Figure 5.166: Mercator map for CR 2158. The comet should encounter slow solar wind speeds with a small chance of traversing fast solar wind streams on 16/12/2014.

ENLIL MHD solutions for this CR were also propagated using NSO source magnetograms. The orbit plane angle dropped below 20^{o} on the 13th December and continued to decrease until Earth crossed the comet's orbital plane on 27th December. It slowly increased and exceeded 20^{o} after 8th January, spending roughly three weeks at relatively low orbit plane angles.

Beginning from 12/12/2014 12:00 UT, the comet should have encountered a rarefaction region lagging a CIR and thus interacted with decreasing solar wind velocities from ~ 600 km s^{-1} down to ~450 km s^{-1} by 14/12/2014 12:00 UT. The solar wind is also expected to have a small latitudinal component of 5 - 10 km s^{-1}. Velocities measured from the images range between 300 – 500 km s^{-1}. The general trend is one of decreasing solar wind velocities. An image by Peach on 14/12/2014 depicted a wide, undulating ion tail (~5 x 10^{5} km). The visible pair of almost symmetrical ion tail rays also exhibited this meandering attribute. This structure corroborated by later images is a sign of variable solar wind velocity and suggests that the rarefaction region is not a smooth transition from fast to slow solar wind velocities.

On 15/12/2014, the ion tail widened rapidly with multiple tail rays. The wave-like nature of the ion tail is further exaggerated in this image. No measurements could be sampled as the tail sat along the projected Sun-comet vector, the outcome of a low orbit plane angle. This peculiar tail behaviour persisted until observations on 18/12/2014. Data points in purple on 16/12/2014 should be considered unreliable due to their orientation with respect to the radial vector. It is possible that the ion tail's position angle was influenced by an ICME interaction. This would require the fast ICME on 10/12/2014 in Figure 5.170 and Table 5-5 to have encountered slow solar wind streams and decelerated enough to interact with the comet between 15/12/2014 and 16/12/2014.

A bifurcating ion tail was observed on 18/12/2014 producing similar slow solar wind velocities followed by a unique ion tail configuration on 19th December 2014 [Figure 5.167], accompanied by a small peak in solar wind velocity. The first feature is predicted by the ENLIL model. The velocity bump is associated with a small enhancement in |B|, |N| and a discontinuity in both the longitudinal and latitudinal component of the solar wind velocity [Figure 5.168]. The slightly larger than expected inferred radial velocities is thus due to a non-radial flow.

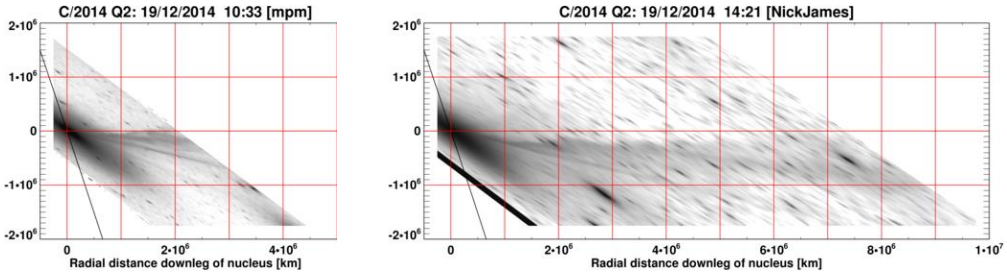

Figure 5.167: Mapped images from Mobberley (MPM) on 19/12/ 2014 at 10:33 UT and N. James at 14:21 UT. The image on the right suggests a large non-radial deflection of the ion tail. A radial interpretation of the tail morphology would represent the traversal from a fast to a slow solar wind stream.

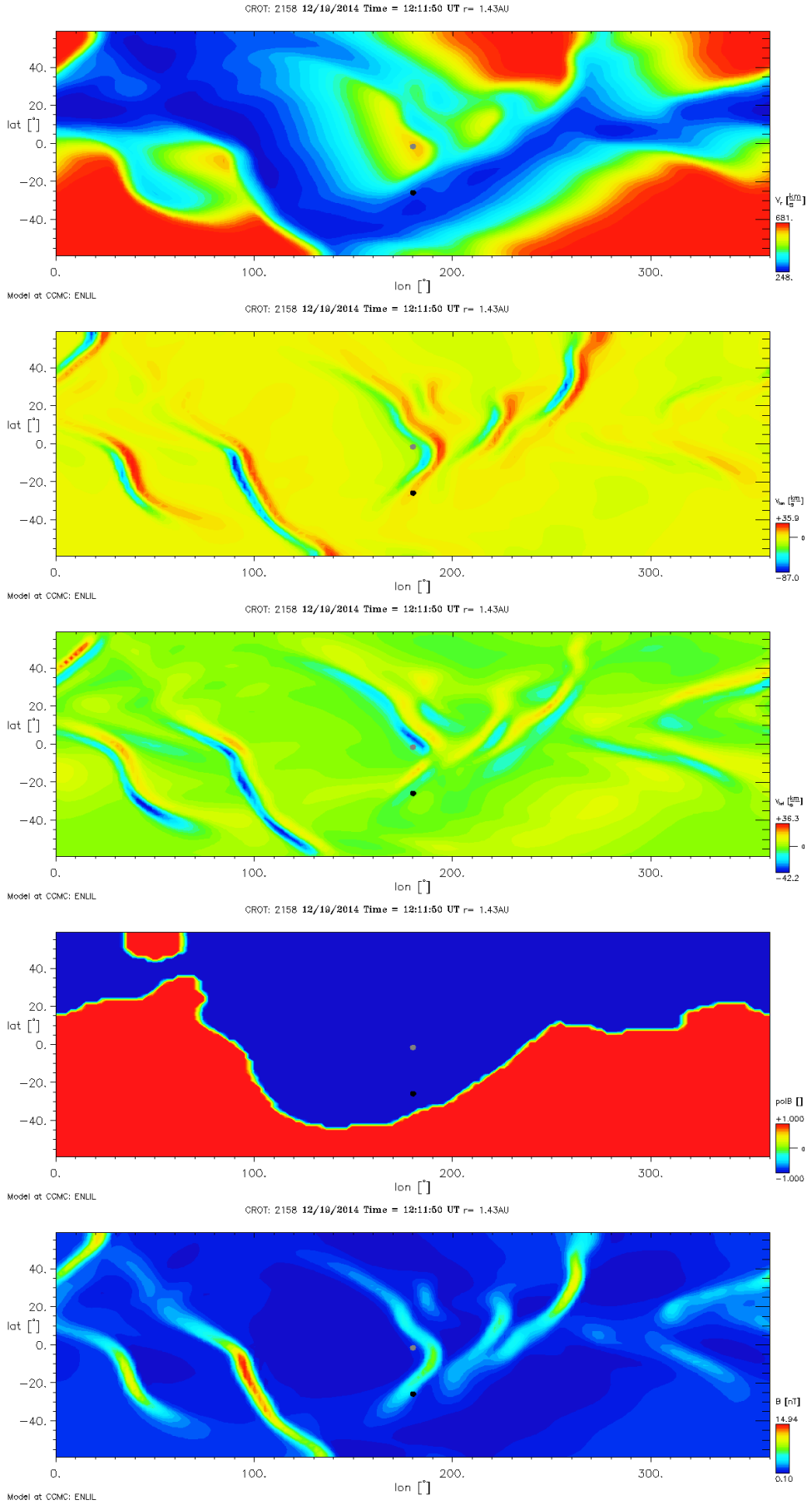
CROT: 2158 12/10/2014 Time = 12:11:50 UT r= 1.43AU
lat [°]
lon [°]
Model at CCMC: ENLIL
CROT: 2158 12/10/2014 Time = 12:11:50 UT r= 1.43AU
lat [°]
lon [°]
Model at CCMC: ENLIL
CROT: 2158 12/10/2014 Time = 12:11:50 UT r= 1.43AU
lat [°]
lon [°]
Model at CCMC: ENLIL
CROT: 2158 12/10/2014 Time = 12:11:50 UT r= 1.43AU
lat [°]
lon [°]
Model at CCMC: ENLIL
CROT: 2158 12/10/2014 Time = 12:11:50 UT r= 1.43AU
lat [°]
lon [°]
Model at CCMC: ENLIL

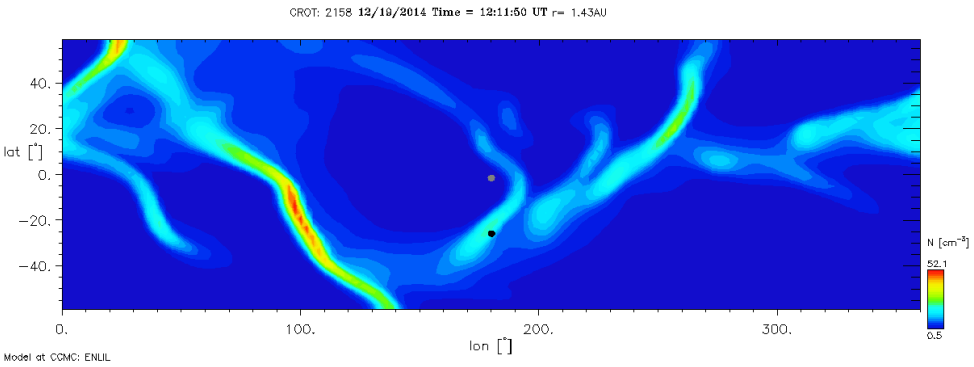

Figure 5.168: Plane cuts taken on 19/12/2014 at 12:11 UT at a heliocentric distance of 1.43 AU. The comet is at longitude 181º and latitude -26º in heliographic coordinates. Top three panels: MHD simulations of the radial velocity, longitudinal and latitudinal components. Bottom three panels show the modelled B, N and polarity values in the inner heliosphere.

The low solar wind velocities and the small increase in velocity on 20/12/2014 agree well with the ENLIL model. The non-radial velocity components are predicted to be near zero, hence the better than usual measurement of the radial solar wind velocity at low orbit plane angles. The orbit plane angle was ~ 8.5º between 20/12/2014 and 21/12/2014. Despite the low orbit plane angles, the mapping technique did not break down during this period and there is a good agreement of the solar wind velocity with predicted values. I had concluded previously for other comets, including a near-Sun comet, comet C/2011 W3 (Lovejoy), presented in chapter 6, that the projection of images produced extremely long pixel vectors at extremely low orbit plane angles, such that it was impossible to resolve the comet in the zoomed projected images. This is an unavoidable artefact of extrapolating along the observer's line of sight. It may be that the reason why the projection mapping worked in this instance is due to the small geocentric distance of ~ 0.5 AU, compared to the much larger distances from the observer for the images that failed.

It is unlikely that the non-radial motion of the solar wind on 20/12/2014 would have persisted long enough to cause the widening sinuous tail seen in Figure 5.169. I propose with caution that the relatively fast ICME eruption on 10/12/2014, in Figure 5.170 and Table 5-5, may have encountered slow solar wind velocity, thus reaching the comet by 'interaction 2'.

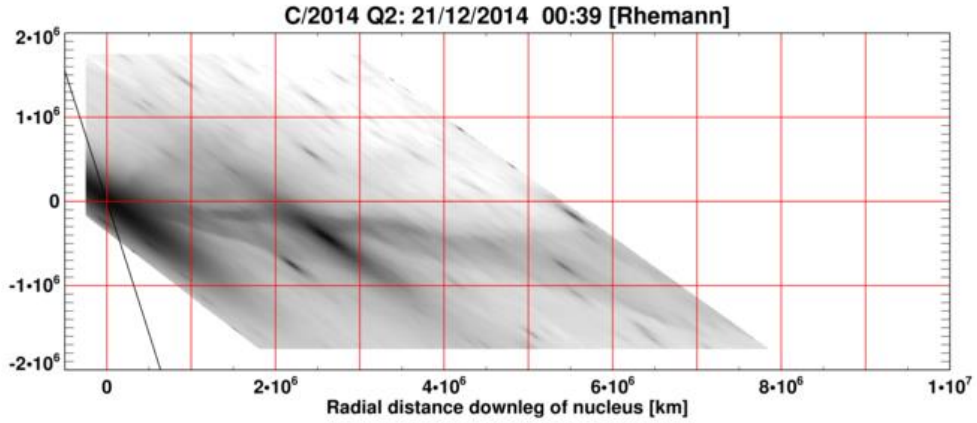

Figure 5.169: Image of C/2014 Q2 by Rhemann on 21/12/2014 at 00:39 UT showing a seemingly turbulent ion tail.

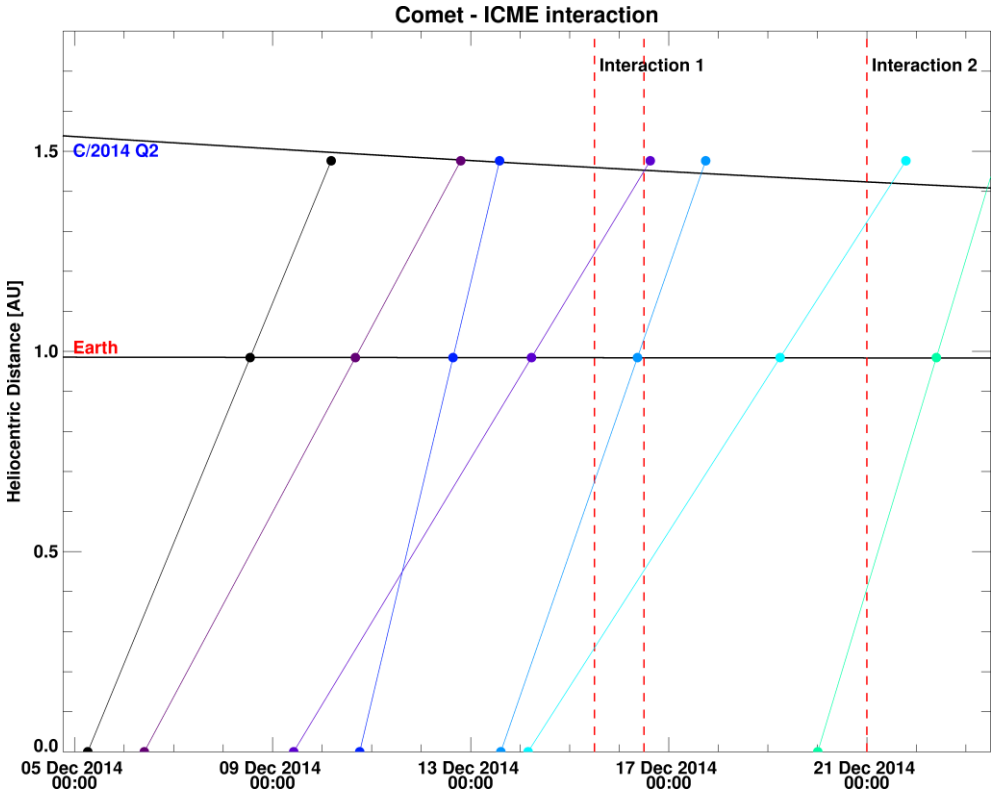

Figure 5.170: Potential ICME interactions at C/2014 Q2 and their arrival times at Earth and the comet. Interaction 1 marks a period of a day where the ion tail laid along the Sun-comet vector.

Table 5-5: Observation times and CME parameters from the autonomous CME detection software CACTus.

Date	Time	Linear speed (km s^{-1})	CPA (°)	Angular width (°)	Interaction
06/12/2014	09:48	400	287	96	1

10/12/2014	18:12	905	288	122	1
13/12/2014	14:36	618	333	80	2

5.6.2. Alternative Methods to derive Solar Wind Velocities

5.6.2.1. Low Orbit Plane Angle

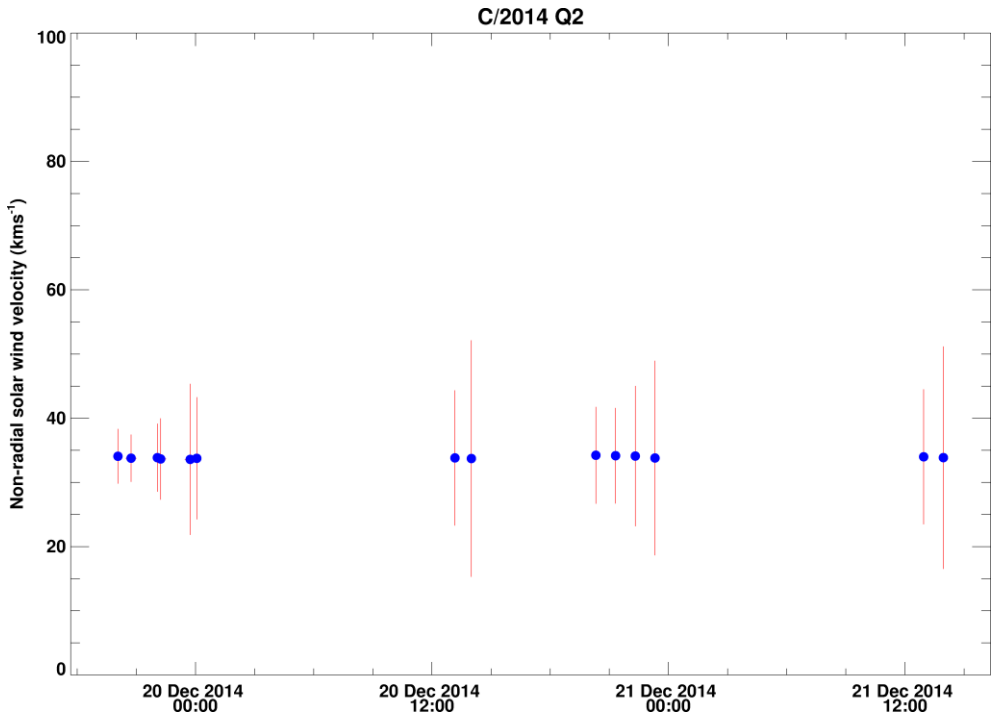

Figure 5.171: Non-radial solar wind velocity measured during low orbit plane angle periods.

The non-radial velocities measured at the comet are comparable to previous comets. The ENLIL simulations predict similarly strong longitudinal components at the comet between 19/12/2014 and 21/12/2014. Note that the comet's orbit is highly inclined to the ecliptic (i = 80.3^{o}). The Sun-comet-Earth geometry is such that the longitudinal component will be more noticeable from our vantage point.

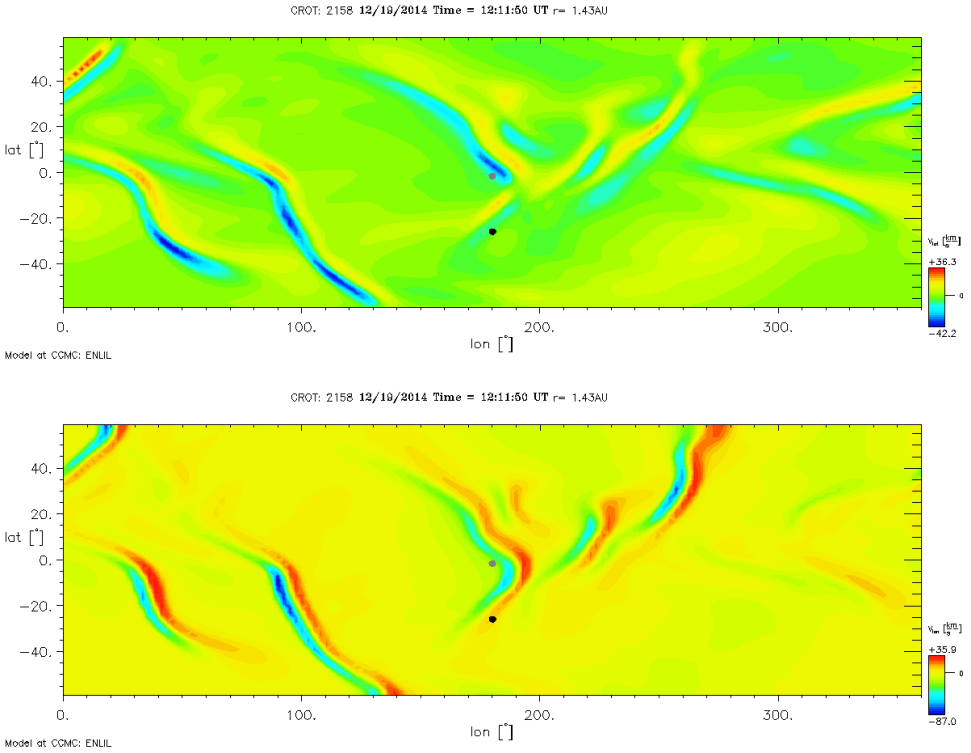

Figure 5.172: ENLIL modelled latitudinal and longitudinal solar wind velocity at the comet.

5.6.2.2. Folding Ion Ray Velocities

All three sets of tail ray measurements (15/12/2014, 19/12/2014 and 20/12/2014) were taken at low orbit plane angle, under seemingly turbulent conditions. They were bright and distinct in all images analysed [Figure 5.173]. Images on 19/12/2014 likely underwent a transient phenomenon between measurements. The first measurement of the tail ray in the second image coincided with the ion tail. The radial velocity decreased down the tail and there is a small change in tail ray morphology, with the tail ray appearing to move towards the Sun. This is most likely due to a widening of the ion tail ray and its non-radial motion.

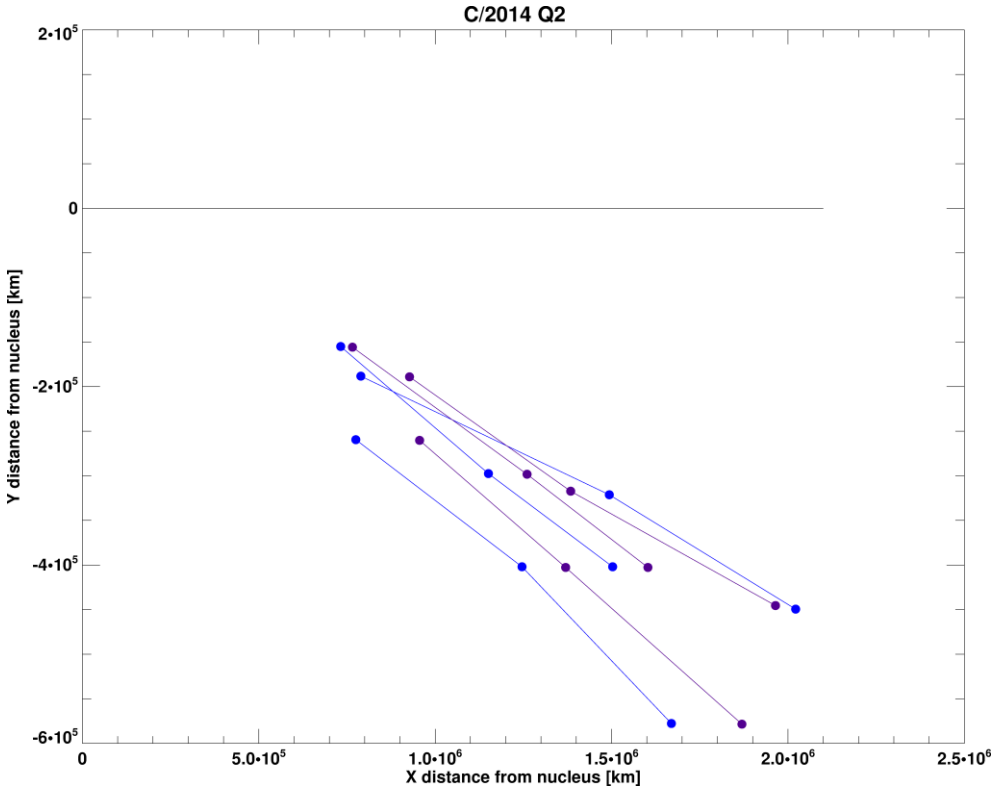

Figure 5.173: Three different sets of measurements of the bottom half of a tail ray pair. The top tail ray was not measured as it was not distinct or bright enough in the consecutive set of images.

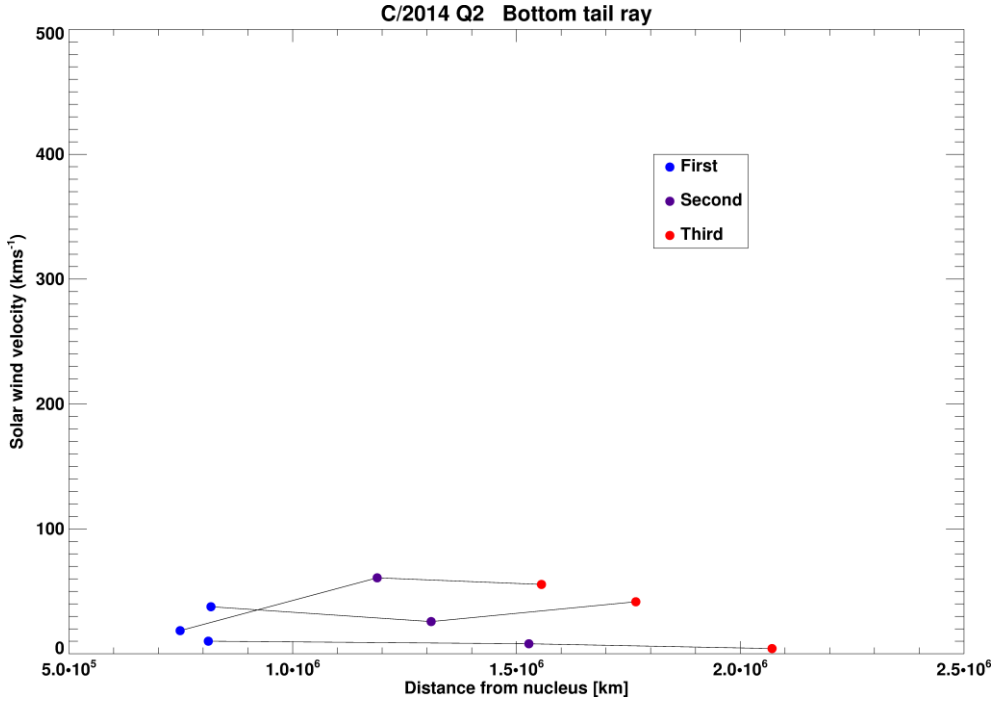

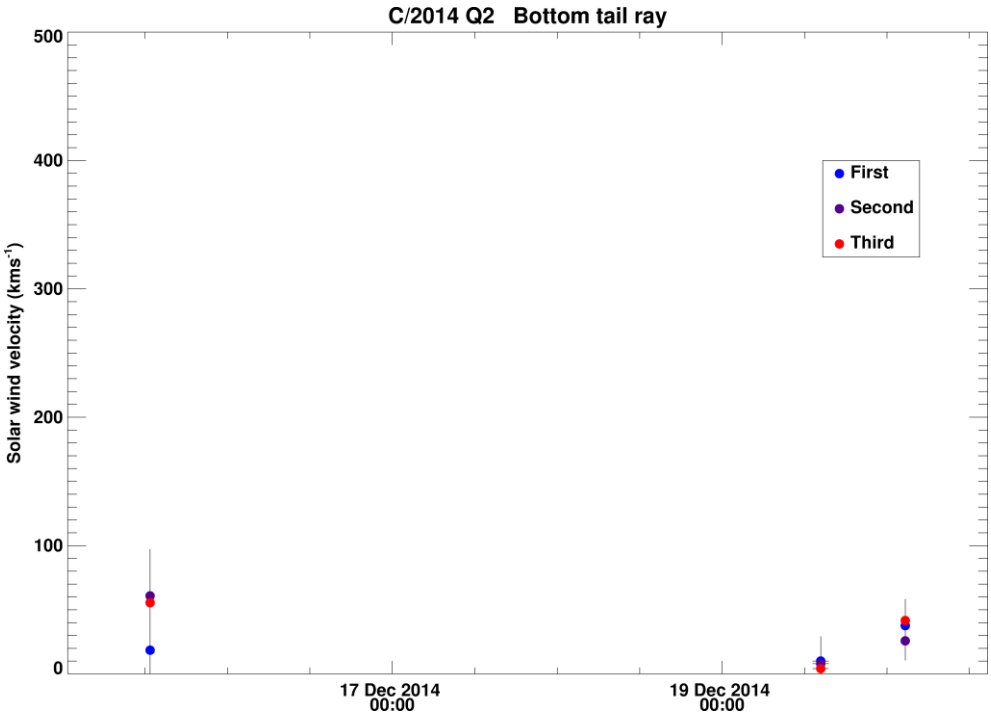

Figure 5.174: Tail ray velocity variation with time and distance. The first measurement was taken closest to the nucleus and the third at the furthest visible end of the tail ray.

5.6.2.3. Case Study: Van Yi animation (CR 2159)

On the 21st January 2015, amateur astrophotographer Van Yi recorded an image sequence, in China, encompassing clearly defined tail rays, a large kink and a large condensation cloud moving downtail of the nucleus. The latter could have been the result of an ICME or a change in the HMF orientation. It is not clear whether a disconnection event occurred. Through private communication with this observer, I managed to obtain high quality, high resolution images of the full star field of this exciting animation with the exact time information. Each of the images processed here is the result of stacking 10 frames of 30 s exposure each. The images were taken with an autoguider. The midpoint of each stacked image was calculated and the error is taken as half of the time interval between the first and last frame. The solar wind analysis, tail rays and vector maps were run for 6 images out of the 28 image sequence at intervals of ~ 30 minutes. Images were observed at 11:21, 11:56, 12:31, 13:02, 13:30, 14:01 (UT) on the 21st January 2015 [Figure 5.175]. For the radial solar wind measurements, the same time step was taken for all six images. The third sample cut crosses the thin ion tail and the wide ion cloud at

the edge of the image, suggesting a faster moving cloud if it was a radially outward flow. The orbit plane angle is around its highest during this observation, peaking at ~ 50°.

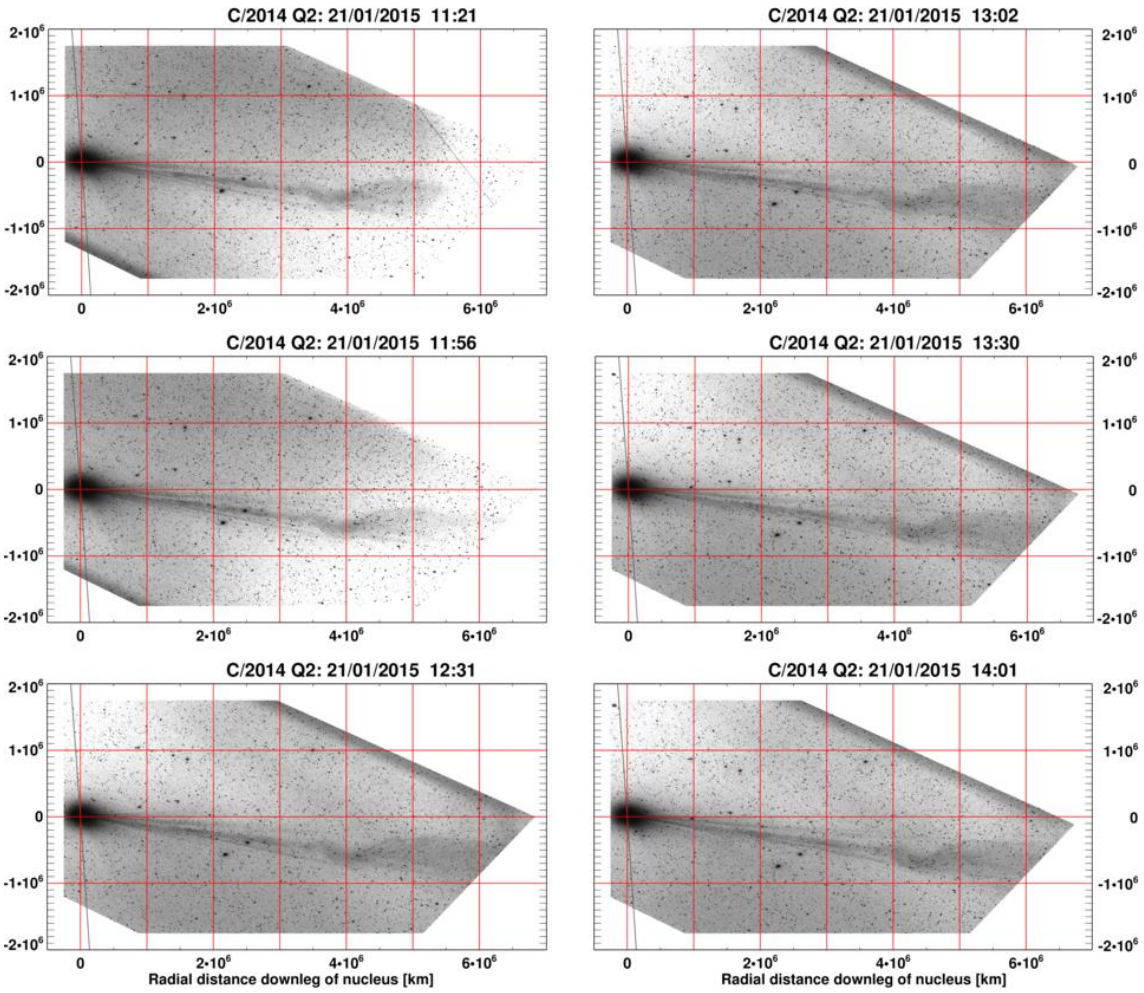

Figure 5.175: Extract of 23 image sequence showing the radial evolution of a double kink and an ion cloud.

The MHD modelled values predict a slow radial solar wind velocity of ~250 km s^{-1}, in close agreement with the velocities derived from the ion tail [Figure 5.176]. The solar wind streams also exhibit a small enhancement in non-radial velocities, |B| and |N| and a polarity reversal at the comet. This could explain the slightly higher radial velocity reported in Figure 5.176. The ENLIL cutplanes were produced using a recent high resolution (1280 x 30 x 180) run of CR 2159. The inner boundary conditions were propagated from the Mt Wilson Observatory magnetograms with the MAS model and the outer boundary of the ENLIL model was set at Saturn (~ 10 AU). The simulation grid is created with 256 radial grid points for a run with its outer boundary limited at 2 AU. The number of radial grid points is increased for simulations at a

greater outer boundary, so that the modelled output for the inner heliospheric region between 0.1 and 2 AU retains 256 grid points. Therefore, the solution quality of cutplanes within the inner heliosphere should be unaffected. The latitudinal grid is restricted to ± 30^{o} so as to maintain the angular resolution (private communication with P. J. MacNeice, CCMC contact for ENLIL model). Comparing my velocities to the ENLIL model is thus acceptable due to the high resolution simulation used and the comet being at a heliographic latitude of 1.5^{o}.

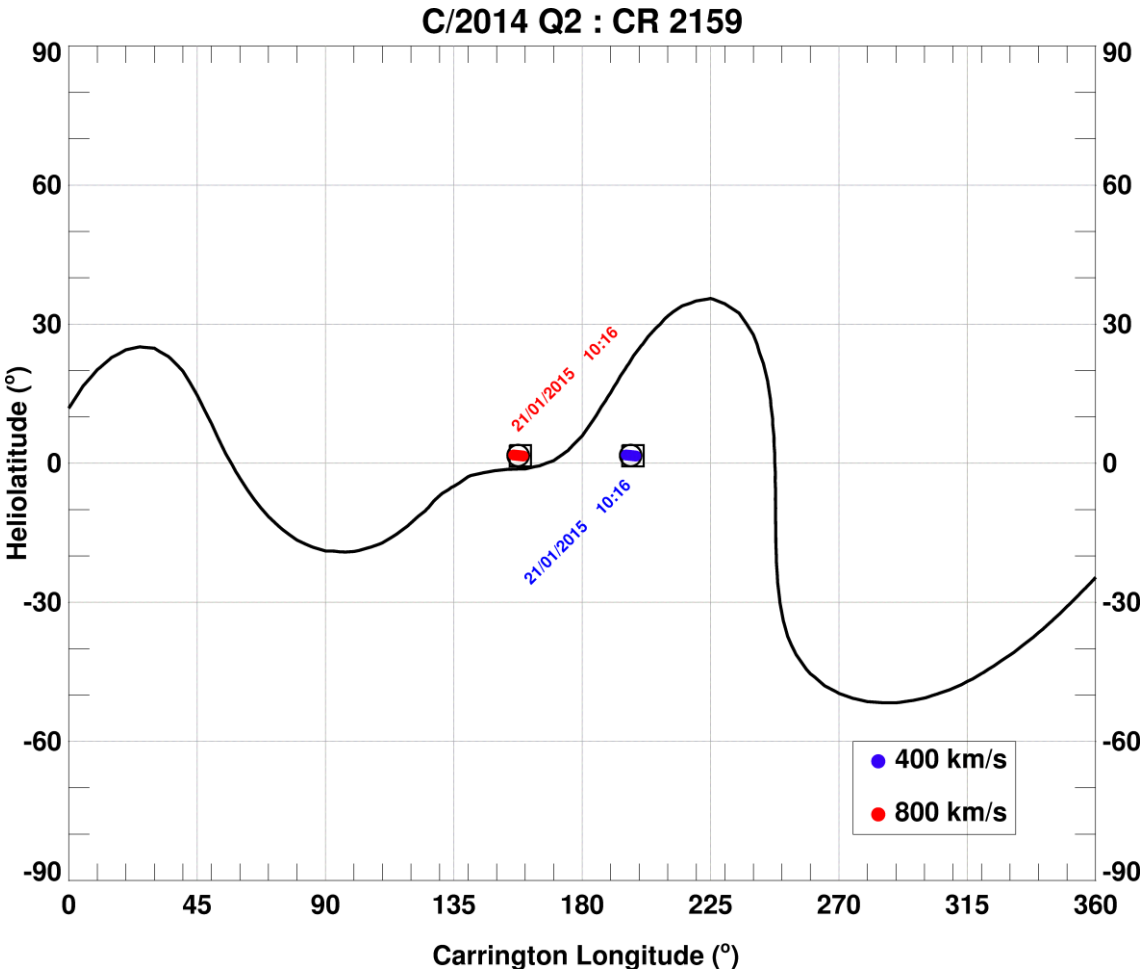

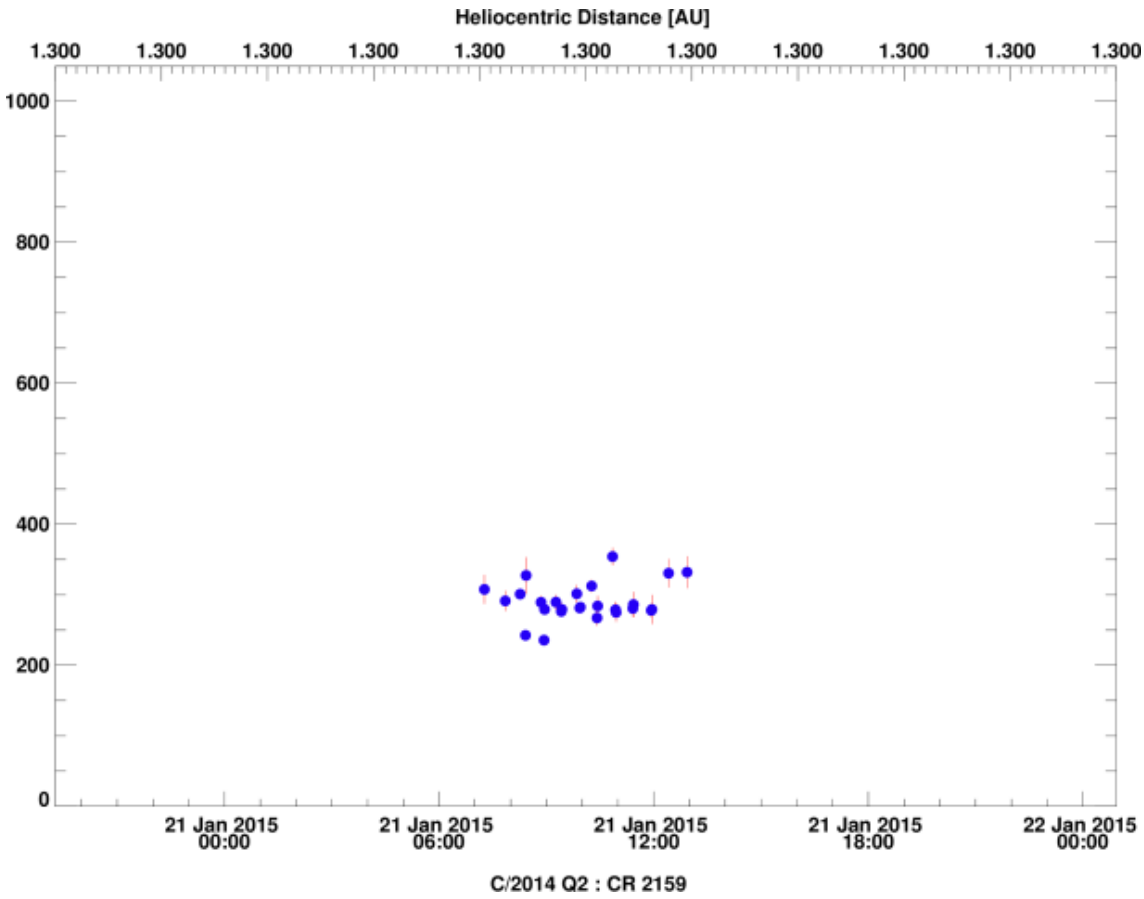

Figure 5.176: The comet experienced slow solar wind speeds matching expectations from the Mercator map.

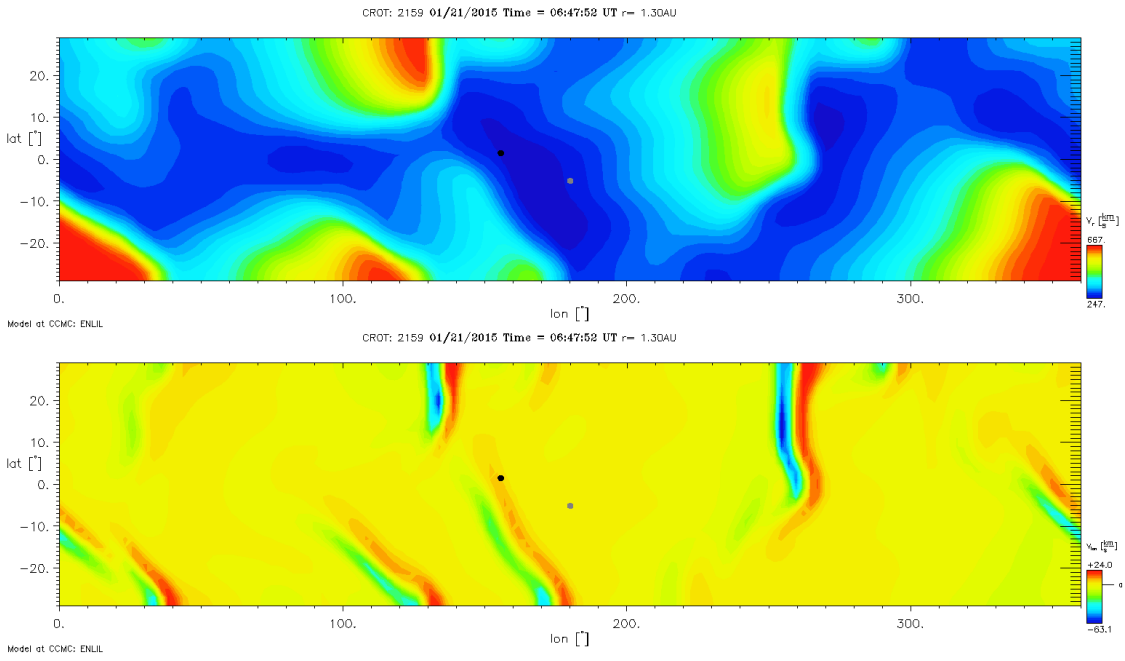

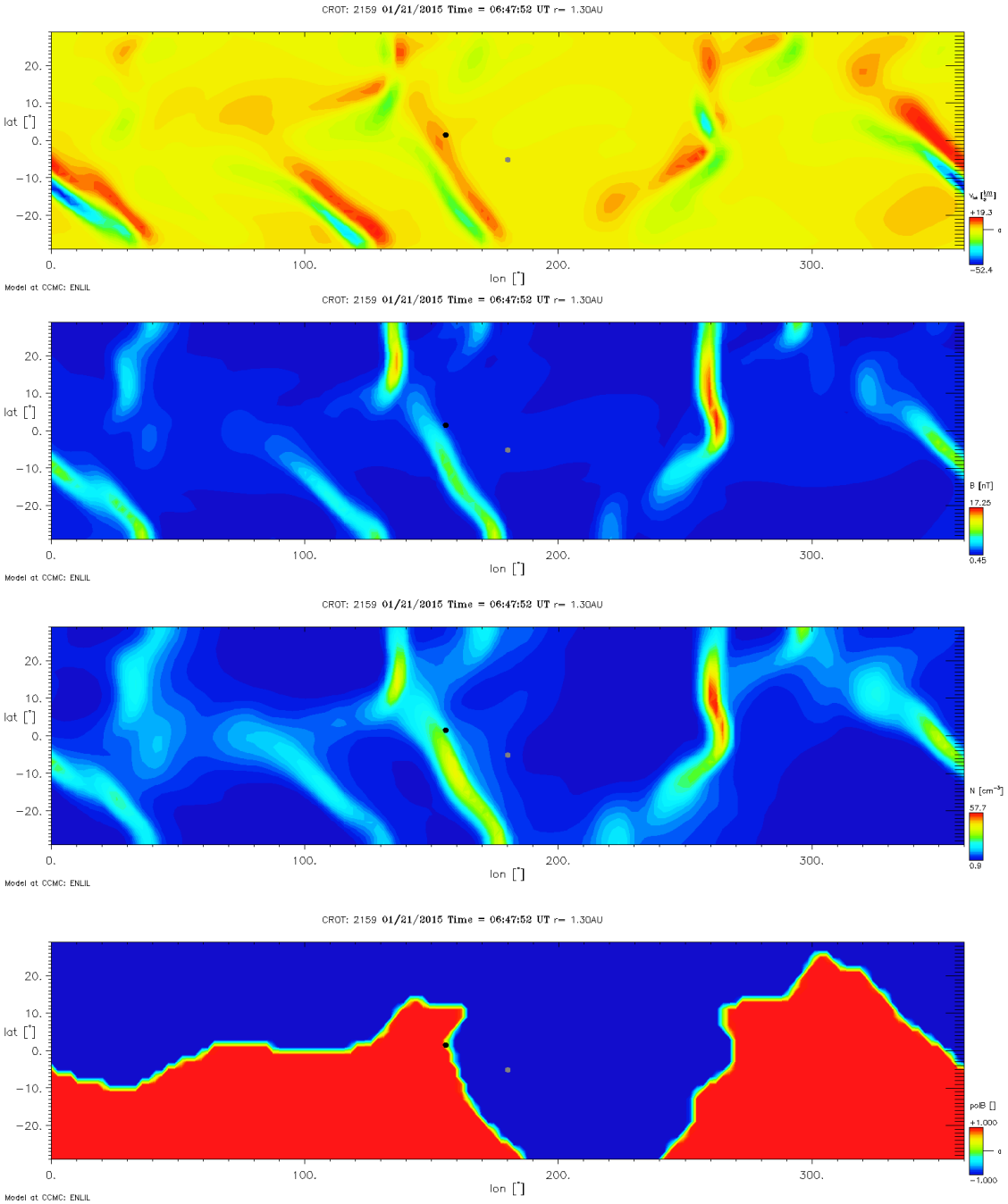

Figure 5.177: Predicted enhancement in V_{lon}, V_{lat}, |B|, |N| and a polarity reversal at the comet (longitude = 156°; latitude = 1.5°; heliographic coordinates are shifted so Earth is always at 180° longitude).

Vector maps

The errors for the image sequence in Figure 5.175 were underestimated as they do not account for the human error in measuring the exact position of the feature edges in all images. Small variations in measuring the bundle centre will significantly affect the sub-hundred km s^{-1} velocity

computed, thus accounting for the small fluctuations in the feature distance from nucleus, velocity and acceleration [Figure 5.178]. Though the net bulk radial velocity of the features is in explicit agreement with the MHD modelled velocities, assuming they are accurate, they contradict the inward flow of the plasma bundles within the ion tail. The structural integrity of the ion tail is maintained in a turbulent-like configuration moving at half the speed of the radial outflow. The features showed no accelerating trend if the fluctuation is about zero.

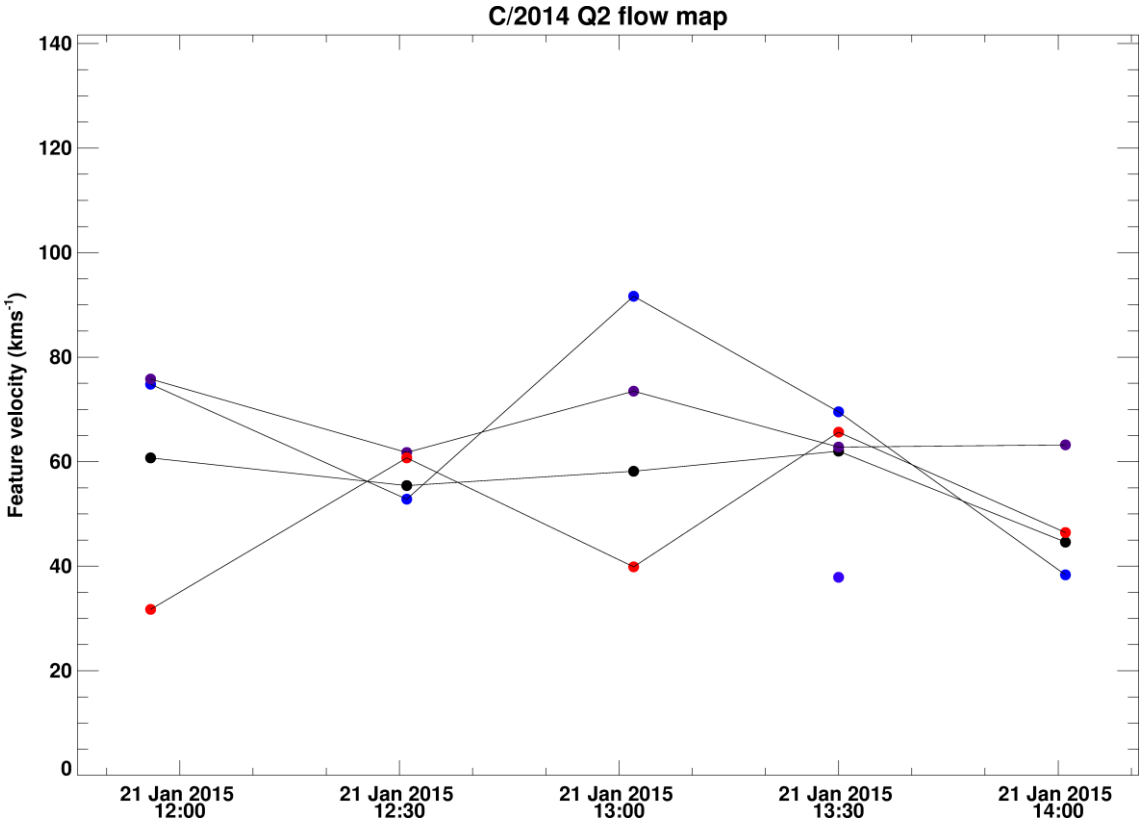

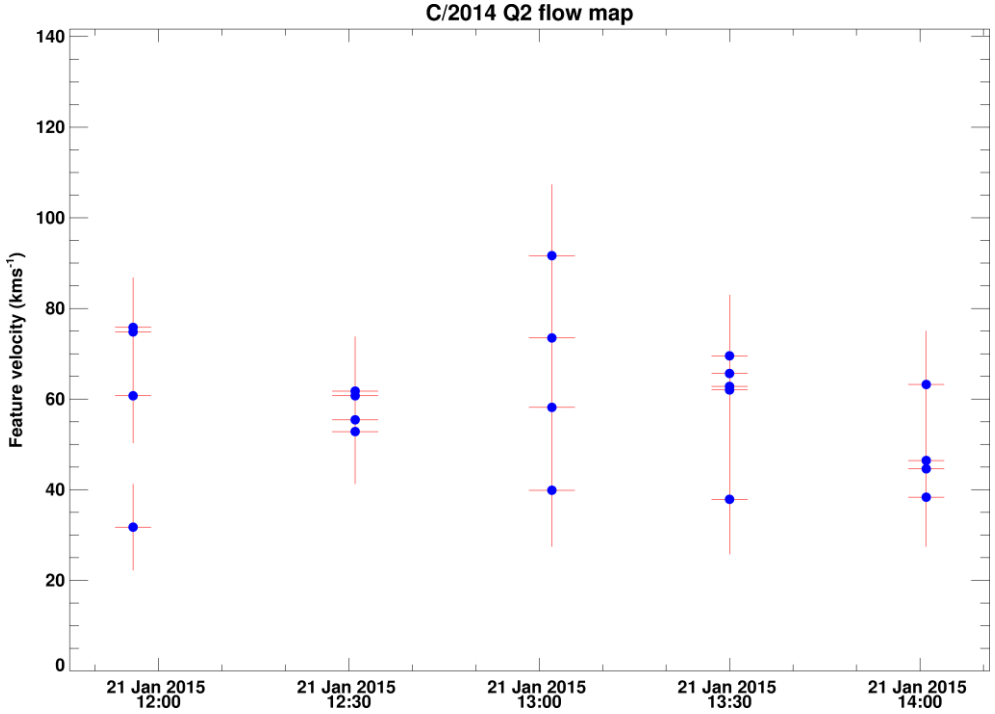
C/2014 Q2 flow map
Feature velocity (kms-1)
140
120
100
80
60
40
20
0
21 Jan 2015 12:00
21 Jan 2015 12:30
21 Jan 2015 13:00
21 Jan 2015 13:30
21 Jan 2015 14:00

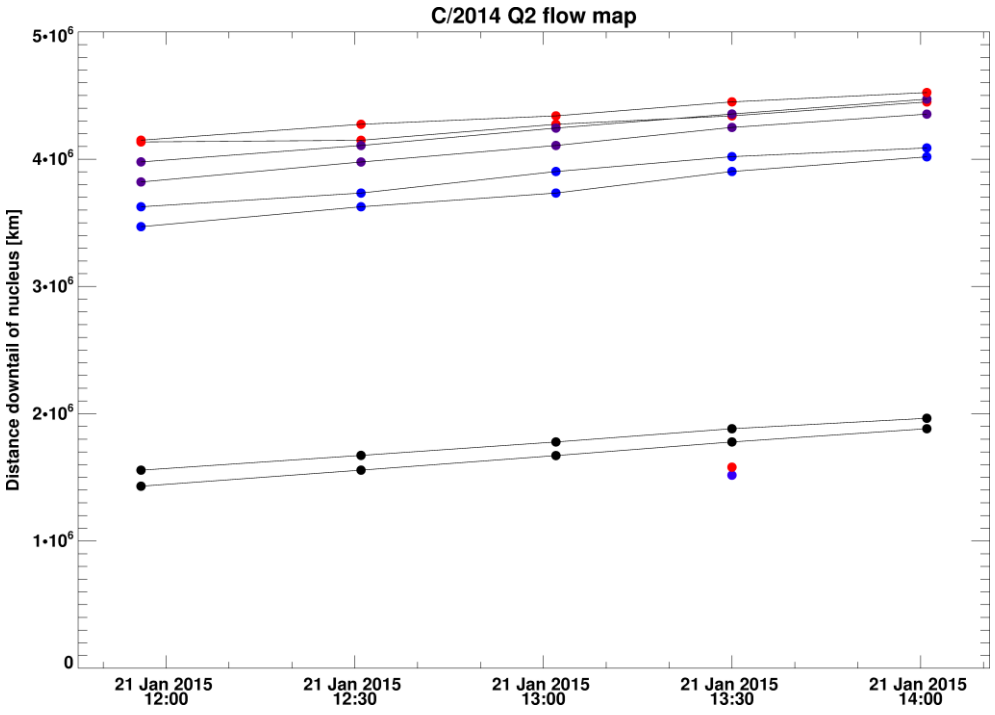
C/2014 Q2 flow map
Distance downtail of nucleus [km]
5•10^6
4•10^6
3•10^6
2•10^6
1•10^6
0
21 Jan 2015 12:00
21 Jan 2015 12:30
21 Jan 2015 13:00
21 Jan 2015 13:30
21 Jan 2015 14:00

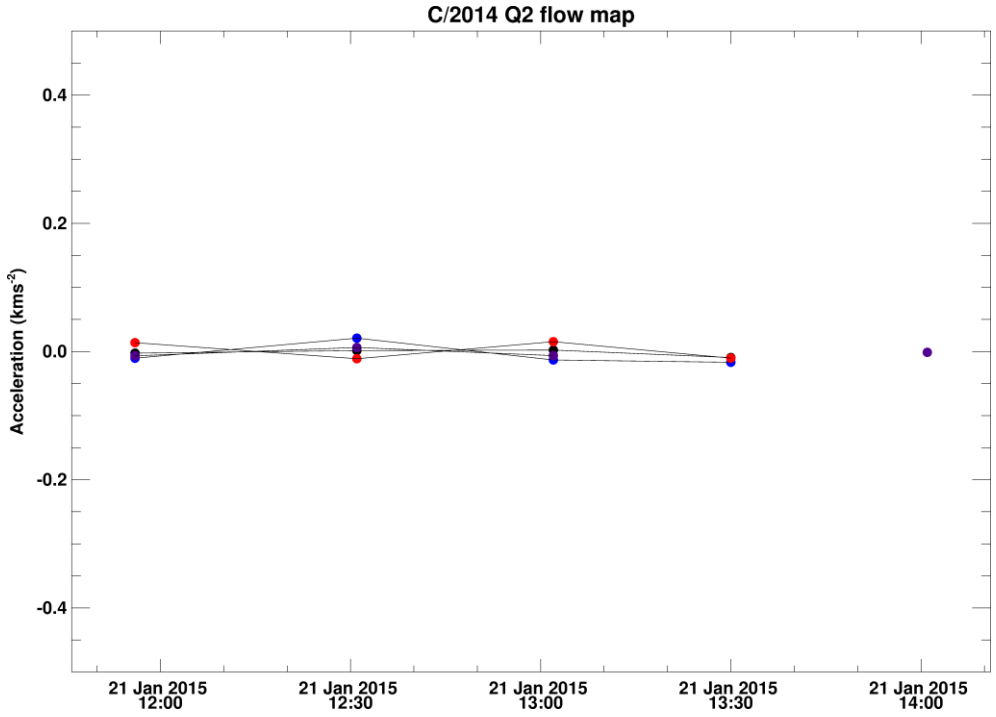

Figure 5.178: The feature velocities as tracked in a selection of images by Van Yi, observed on 21/01/2015. Top plots show relatively small variations in the solar wind velocity, fluctuating about a median of ~60 km s^{-1}. Bottom plots show distance travelled by identified features through multiple images and their acceleration or lack thereof.

Folding Ion Ray Velocities

As seen in Figure 5.179, the rates of increasing distance of measured samples along the radial vectors from the Sun are relatively low for the newly formed end of the top tail rays, i.e. the section closest to the nucleus. The blue and red samples were taken from the first image in a pair of consecutive images and the purple and black pair is their new radial locations in the subsequent image.

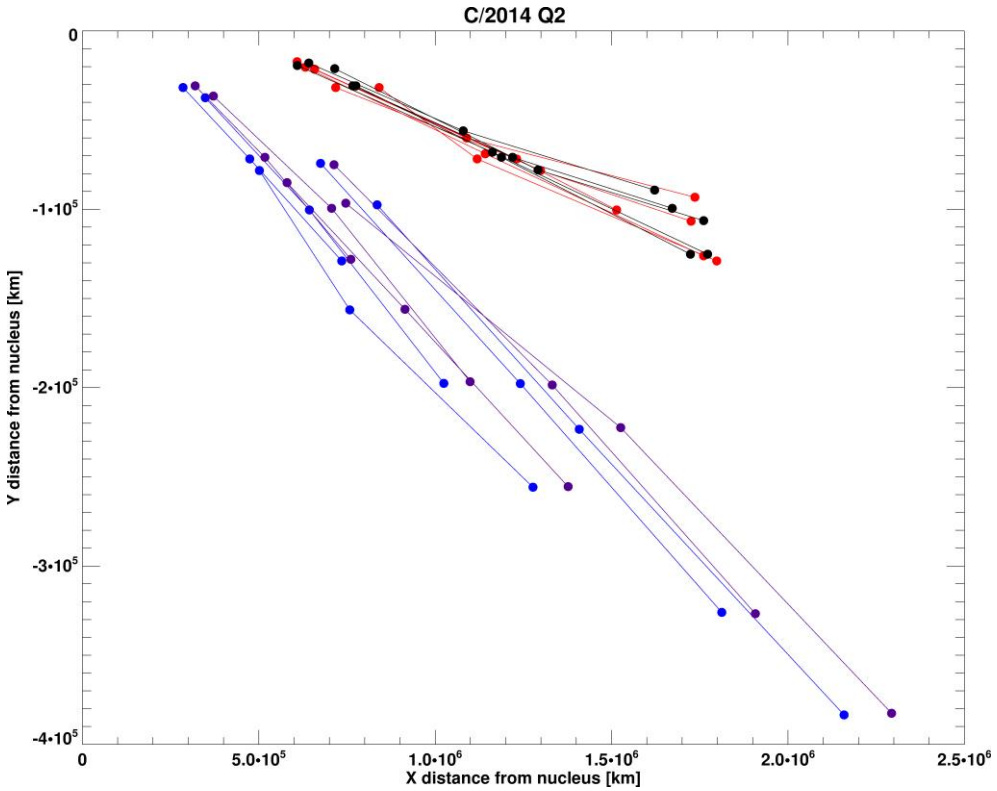

Figure 5.179: Tail ray positions sampled for the Van Yi sequence. Both tail rays lie below the extended radial vector, characteristic of a high orbit plane angle and a large aberration angle.

By looking closely at the furthest-right purple set of tail ray samples in Figure 5.179, it is clear that the first sample near the nucleus was chosen inaccurately since its corresponding blue pair lies after it, suggesting an opposing motion to the rest of the tail rays. This pair of triplet tail ray velocities corresponds to the first and second trio of data points in the top plot in Figure 5.180. Though they conform to expectations of velocity increase from first to third sample, the first blue solar wind velocity is clearly incorrect. Furthermore, the short distances travelled by tail rays in consecutive images are small enough to lead to erroneous velocities. The third plot of Figure 5.180 is baffling without comparison to the distance versus solar wind plot on its right. It is evident that the top tail rays all undergo a slight concave transformation as they lengthen and curve outwards. This is evidenced by a decrease in tail ray velocities in the middle of the ion tail ray, although this could possibly be due to an incorrect measurement of the tail ray location.

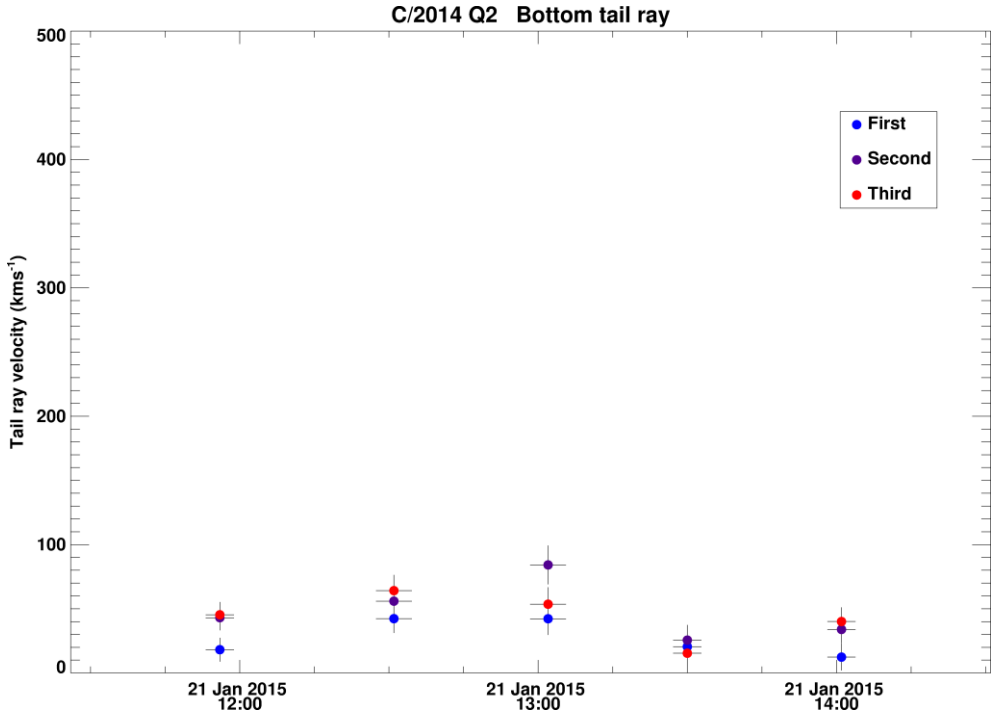
C/2014 Q2 Bottom tail ray
Tail ray velocity (kms-1)
500
400
300
200
100
0
First
Second
Third
21 Jan 2015
12:00
21 Jan 2015
13:00
21 Jan 2015
14:00

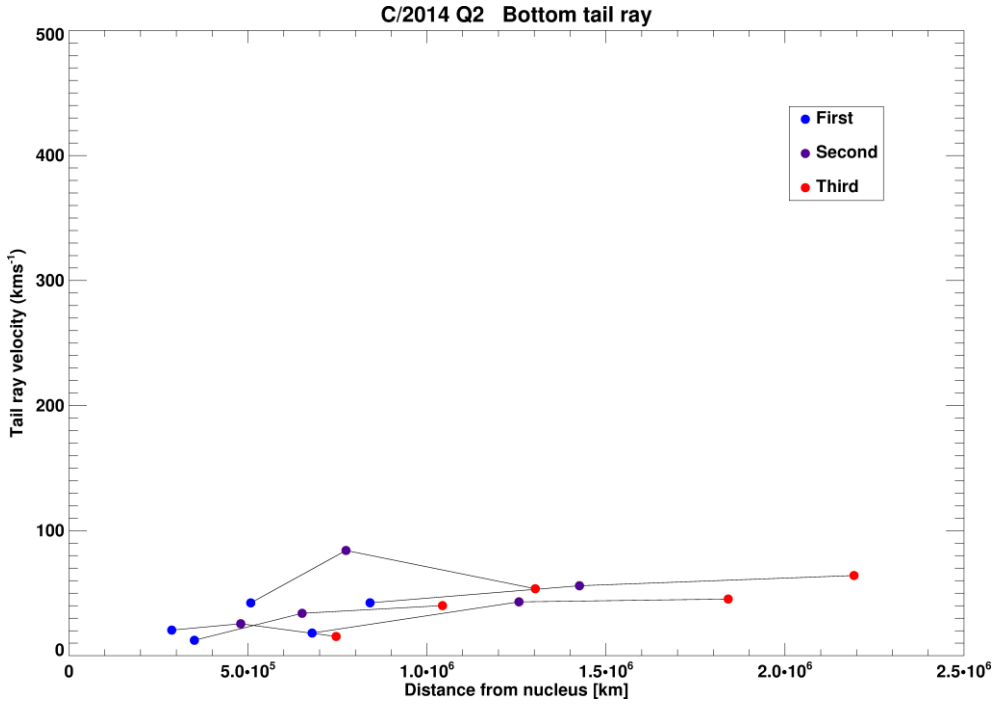
C/2014 Q2 Bottom tail ray
Tail ray velocity (kms-1)
500
400
300
200
100
0
First
Second
Third
0
5.0•10^5
1.0•10^6
1.5•10^6
2.0•10^6
2.5•10^6
Distance from nucleus [km]

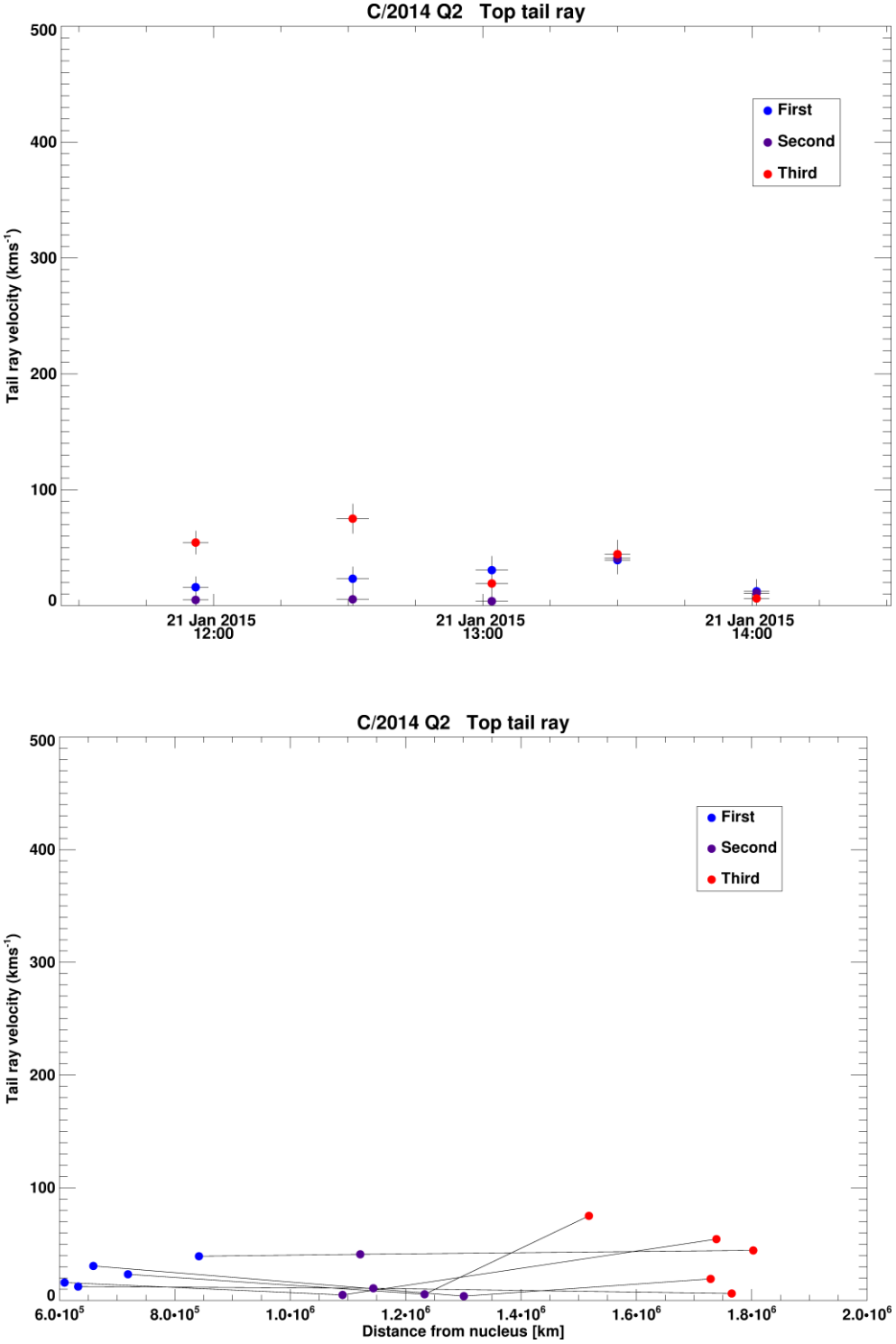

Figure 5.180: Tail ray velocities for the bottom and top tail rays with respect to their image times and distance from nucleus.

5.7. Conclusion

Turbulent events in the comet images are reflections of the solar wind variation upstream of the comet. As the incidence of turbulent events recorded in the ion tail decreases, I observed an increased correlation between my measured local radial solar wind velocities and the modelled values from M. Owens' and CCMC's ENLIL predictions. With each subsequent comet presented in chapter 5, it is clear that the solar wind velocities show good agreement with the quiet solar wind. The correlation between my measured velocities with the modelled values was good once rejection criteria were applied correctly to the extensive archive of amateur images, which had been impacted by the local weather, atmosphere, inconsistent instruments, image formats and processing techniques used by the observers for aesthetics. During turbulent solar wind periods, I have shown that it is often possible to identify the solar wind transient source influencing these large scale variations in the ion tail.

With the vector maps technique, I have attempted to measure non-radial solar wind speeds in the comet's orbital plane to complement the radial solar wind speeds measured during these turbulent tail events. It bears repeating that the large errors are due to the projection and mapping of each image and will thus appear overwhelmingly large. The actual error in the vector maps and tail rays should be much lower if we excluded the errors due to the pixel projections from the observer's line-of-sight and mapping the images onto the comet's orbital plane. As stated previously, the list of potential ICME interactors is useful for comparison, however without a more advanced method of calculating the ICME's path and speed variation prior to the cometary interaction, the list should be considered with caution. Further work on this topic will focus on better estimating the shock arrival times at the comet. In instances where the orbit plane angle is low, we have been able to resolve some images and obtain non-radial solar wind velocities, registered as motions out of the comet's orbital plane. This can be measured from the displacement along the y-axis in the mapped projected images. This was particularly useful to quantify non-radial solar wind velocities, which had been previously thought impossible to obtain with this technique. Furthermore, it was encouraging that the non-radial wind speeds were comparable to those measured at ACE over a 3-year period.

From the comparison of the amateur images with professional-grade images, we observe a very high correlation between the solar wind velocities measured from amateur and professional images for both the quiet and turbulent solar wind. This indicates that images observed by amateur astronomers are equivalent to professional images in terms of their scientific contribution to this project. In chapter 6, I will use images of bright comets observed from space-based observatories as a further validation of this technique. The lack of atmosphere and weather effects should lead to more accurate solar wind velocities, which should have a better correlation with each other. Furthermore, the spacecraft data will be consistent in terms of the instrument used, the field of view, image format and data reduction procedures, which will contribute to less noise in the measured solar wind velocities.

Two peculiar features are notable throughout all observations. The first was the curving of the ion tail away from the extended radial vector and towards the dust tail, which will be addressed briefly in chapter 6. This feature will required further investigation before the cause of it can be identified. The second feature is a near-consistent over- and under-estimation of the measured solar wind velocities with respect to the ENLIL predicted velocities. I conclude that this is due to the predicted geometrical perspective issues between the observer, the ion tail and the projected image of the ion tail onto the comet's orbital plane.

6. Near-Sun comets

Since 2011, two particularly bright sungrazing comets, C/2011 W3 (hereafter Lovejoy) and C/2012 S1 (hereafter ISON) reached perihelion and in so doing experienced extreme solar wind conditions and insolation of their nucleus, by approaching to within 8.3 x 10^5 km (1.19 $R_\odot$) and 1.9 x 10^6 km (2.79 $R_\odot$) of the solar centre, respectively. At such small heliocentric distances, a comet's velocity is comparable to that of the solar wind (Giordano et al. 2015) and may even exceed it . They both displayed a prominent ion tail, which is rare amongst observed sungrazers. These comets provide unprecedented access to study the solar wind in the heretofore unprobed innermost region of the corona. My third target of interest was a near-Sun comet, C/2011 L4 (hereafter Pan-STARRS), which reached perihelion within the orbit of Mercury, at 0.302 AU. C/2011 L4 was unique in its own respect, with observations undertaken by the solar observatories revealing an extensive, striated dust tail, a variable ion tail, quite possibly a double ion tail, and a neutral iron (Fe) tail. In comparison, the closest spacecraft in-situ sampling of the solar wind by the Helios probes reached 0.29 AU, just slightly closer to the Sun than C/2011 L4.

I will present the solar wind velocities derived from multiple observing locations of comets Lovejoy (14th – 19th December 2011), comet Pan-STARRS (11th – 16th March 2013) and comet ISON (12th – 29th November 2013). Observations were gathered from the SECCHI heliospheric imagers aboard STEREO A and B, the LASCO coronagraphs aboard SOHO, including coordinated ground-based amateur and professional observations. Overlapping observations from the spacecraft and ground-based efforts provided the perfect opportunity to use these comets as a diagnostic tool to understand solar wind variability close to the Sun.

Sungrazing comets

Sungrazing comets, though small in mass and size ranging from meters to tens of meters in radius (Biesecker et al. 2002; Knight et al. 2010), factor amongst the most populous subgroup of comets. The surface of this reservoir of comets has yet to be scratched. The comets share their orbital parameters and have thus been theorised to be remnants of multiple fragmentations of a giant progenitor comet (for more details, see Kreutz subgroup below). A paradigm put forth by Bailey (1992) is that long-period comets with initial high inclinations ($i \approx 90^o \pm 15^o$) and

perihelion distances (q) lesser than 2 AU, under the action of slow-acting secular perturbations, could have had their orbits precessed over large periods of time, on the order of Myr, to the natural evolutionary dead-end of a sungrazer state. Most SOHO-discovered sungrazers have only been observed pre-perihelion, suggesting total destruction of these relatively minuscule cometary nuclei within the solar corona due to extreme incident thermal and gravitational stresses.

Roche limit

Based on discussions of an international ISSI review team of near-sun and sungrazing comet experts (Jones et al., in preparation), it is proposed to clearly define these new subsets of comets. I thus adopt their definition of a sungrazer as having its perihelion within the solar Roche limit (3.45 $R_\odot$). The fluid solar Roche limit (d) is defined as the point where tidal forces acting upon the comet becomes significant to cause a disruption, often fatal at this distance, of the nucleus. $R_\odot$ is the solar radius, $\rho_\odot$ and ρ_{comet} are the solar and cometary-nucleus densities. A mean comet nucleus density of 500 kg m^{-3} is assumed (Gundlach et al. 2012; Davidsson et al. 2007; Thomas 2009).

$$d = 2.44\ R_\odot \sqrt[3]{\frac{\rho_\odot}{\rho_{comet}}}$$

Since most discoveries of this “new” group of comets were identified through the daily LASCO operations, an outer limit for the sungrazers of ~ 30 $R_\odot$ (~ 0.140 AU), i.e. the approximate FOV of the C3 coronagraph, was proposed. My study also includes comet C/2011 L4 (Pan-STARRS), a comet with a much further perihelion distance of 0.302 AU, dubbed a near-Sun comet as it has its orbit within that of Mercury’s at ~ 0.307 AU.

Sungrazing families routinely discovered/observed by SOHO:

Kreutz subgroup:

The sungrazing comets are commonly considered as four distinct sub-categories described by similar orbital parameters. The most populous amongst these is the Kreutz sungrazers, having delivered one of the most luminous comets of this decade, comet C/2011 W3 (Lovejoy), the only Kreutz comet to have survived its perihelion of late. The most unique feature of this comet family is its members' close solar approaches, to within 1 to 2 $R_\odot$ (696,000 km) of the solar surface (Biesecker et al. 2002). They exist on stable, short-period orbits on the order of centuries, ~500 to 1000 years (Knight et al. 2010; Schrijver et al. 2012), with small perihelion distance, q ~ 1 to 2 $R_\odot$ and high inclinations, $i \approx 143^o.2 \pm 3^o.9$ (Knight et al. 2010). It has been hypothesised that the entire Kreutz distribution can be traced back through multiple fragmentation events to a singular large progenitor comet within the last 2500 years (Sekanina & Chodas 2007). The dynamically linked system of daughter fragments will have further undergone a cascade of fragmentation events at varying heliocentric distances, up to and including its aphelion at 150 – 200 AU from the Sun (Sekanina & Chodas 2012). The separation velocities at each fragmentation thus gave rise to the range of orbital parameters observed. For example, a $1 ms^{-1}$ separation velocity at perihelion can cause an orbital period lag of 80 years (Sekanina & Chodas 2012), matching well with the temporal distribution of bright sungrazer clusters (Marsden 1967; Sekanina & Chodas 2007) and thus fragments are likely to be clustered together. The time interval between the observed Kreutz clusters is currently ~135 years and thus would require more than one apparition in the inner solar system to produce the spread of sungrazers. A possible interpretation is that my first target C/2011 W3 may herald the return of a bright Kreutz sungrazing cluster in the upcoming years. However, the large number of solar revolutions since the first parent comet may have caused the initially separate clusters to become temporally mixed after multiple revolutions and subsequent fragmentations. Knight et al. (2010) report a true increase in the cometesimal distribution along the orbit from 83.5 ± 8.4 cometesimals from 1997–2002 to 124.6 ± 6.6 cometesimals from 2003–2008.

Biesecker et al. (2002) analysed 141 Kreutz comets, discovered by the SOHO satellite from 1996 to 1998, and described their photometric lightcurves as two standard candles, universal curves 1 and 2 peaking at two characteristic distances of 12.3 $R_\odot$ and 11.2 $R_\odot$. (Kimura 2002), through numerical models, concluded that this coincided well with increased sublimation of dust grains with decreasing heliocentric distance, primarily that of amorphous olivines at 12.3 $R_\odot$,

crystalline olivines at 11.2 $R_\odot$ and the peak or plateauing seen at 7 $R_\odot$ could be due to sublimation of pyroxene volatiles. An alternative theory is that the brightness enhancement at 7 $R_\odot$ could be attributed to nuclear fragmentation (Biesecker et al. 2002). The majority of the 141 Kreutz sungrazers were discovered by automatic detection algorithms applied to the LASCO coronagraphs and an avid, group of internet forum members involved in active visual searches. The increase in discovery rate is largely due to the high temporal cadence, superior photometric quality and increase in FOV of the LASCO coronagraphs over ground-based and other space-borne observatories (Biesecker et al. 2002). To this day, the majority of sungrazers have been discovered by an enthusiastic team of amateur astronomers, further highlighting the benefits of easy data access and civilian science in the internet age. Currently, SOHO comet searchers can flag potential detections on the LASCO ‘‘sungrazer’’ web-site (http://sungrazer.nrl.navy.mil). These were subsequently verified by the LASCO team: D. Biesecker until 2001, D. Hammer from 2001 to 2003 and K. Battams thereafter (Lamy et al. 2013). A quantitative photometric analysis and determination of the orbital properties of a larger sample (924 Kreutz comets observed by SOHO from 1996 to 2005) was undertaken by M. Knight (2010), which disputes the bimodal attribute of the sungrazers' lightcurve, stating that the brightness peak distribution of the sungrazing comets pre-perihelion better fits a continuum between 10.5 $R_\odot$ and 14 $R_\odot$ centered around 12 $R_\odot$. This behaviour should hold true for all sungrazers though the previously quoted studies were performed for Kreutz sungrazers.

Knight et al. (2010) further report on the size distribution of typical sungrazers, finding that their radius estimates of 2 to 50 metres, based on the sungrazer's lightcurves, to be consistent with the upper limit of 63 m set by the lack of survivability of the Kreutz comets post-perihelion (Iseli 2002) and the estimates of the initial diameter range of 17 m to 200 m from an erosion model of 27 sungrazer light curves (Sekanina 2003). Knight et al. (2010) expect an upper limit of ~500 m, indicating that there is a likely disconnect between their calculated size distribution and the larger sungrazer members that have been observed from Earth, existing between 500 m to ~1000 m in radius. Integrating over this reported radius range of 5 to 500 m, Knight et al. (2010) estimate the total mass of these smaller set of cometesimals to be ~4 x 10^{14} g for a bulk density of 0.35 gcm^{-3}, the equivalent of the smallest mass in the larger sized ground-observed Kreutz

sungrazers. This means that the larger sized Kreutz comets, commonly observed as daytime comets, thus contain the majority of the original progenitor's mass. The Kreutz sungrazing comets can be further classified into subgroups according to their orbital elements, though this is not relevant to this discussion.

Marsden, Kracht and Meyer subgroups

The other subsets of the sungrazing family consist of the Meyer, Marsden and Kracht groups (Lamy et al. 2013) and are often referred to as "sunskirters", to differentiate their larger perihelion distances from the sungrazing comets. The Meyer group, second largest after Kreutz comets, have perihelia distances of 6.5 – 8.5 $R_\odot$, whilst those of Marsden are slightly larger at 9-11 $R_\odot$ and Kracht's are spread out over 6-12 $R_\odot$, with the bulk of comet clustered around 9-11 $R_\odot$ (Figs 4 and 5 of Lamy et al. 2013). The orbital period (P) is 5-6 years for both Marsden and Kracht but that of Meyer remains unknown. The sunskirting comets have been all observed post-perihelion, and are thus assumed to be resistant to total tidal fragmentation of the nucleus and are expected to orbit the Sun again, though an orbital period could only be determined for the Kracht and Marsden comets (5-6 years based on Table 4.1 of Knight (2008)).

Sungrazers' interactions with the solar corona

Remote observations of the sungrazers have been hindered by a superimposed ion and dust tail. Spaceborne observations of sungrazer C/2011 W3 (Lovejoy)'s distinct ion tail from multiple vantage points, SOHO/LASCO C2 and C3 and STEREO HI-1A and HI-1B are a historic first. As with bright regular comets, the morphology, orientation and turbulence in the ion tail provides unique insight into the radial and non-radial components of the solar wind, the HCS location and transition boundaries between solar wind streams close to the Sun.

Sungrazers are unique in that they not only provide an insight into the slower mass-loaded solar wind structure in the inner heliosphere but also that of the inner corona, where it is currently unfeasible to obtain in-situ measurements. Giordano et al. (2015) reported a blueshifting and

redshifting of the HI Lyα tail, attributing the redshift along one edge of the comet's tail to cometary H pickup ions – the first observation of its kind with the SOHO Ultraviolet Coronagraph Spectrometer (UVCS). In July 2011, the Atmospheric Imaging Assembly (AIA) onboard the Solar Dynamics Observatory (SDO) saw the first detailed close up destruction of fast-moving (~ 600 km s^{-1}) sungrazing comet C/2011 N3 (SOHO) as it came to within 0.146 $R_{\odot}$ of the solar surface (Schrijver et al. 2012). The entire series of observations took place in the extreme ultraviolet (EUV) bandpass. From the tail's deceleration, the small nucleus, ~10 – 50 m across, was estimated to have shed ~ 6 x 10^8 to 6 x 10^{10} g of cometary material in the closed-field inner corona, rather than to the solar wind. The decelerating ionised material formed arched striations along the magnetic field lines as comet's trajectory crossed its paths. Schrijver et al. (2012) attributed these EUV enhanced emissions to direct collisional excitation and charge exchange between the highly ionised hot corona and the ionisation and excitation of the sublimated heavy ion rich cometary volatiles (e.g. Fe ions), as they attempted to reach an equilibrium with the surrounding coronal plasma. From EUV enhancements of C/2011 W3 by AIA, Raymond et al. (2014) proposed that the magnetically influenced dust striations were due to high densities in the open and closed coronal magnetic flux tubes. Here, the ionised cometary plasma become confined to the flux tubes along the comet's trajectory and thus physically trace the fine field line structures. The cometary ions become unable to traverse from one flux tube to another, whilst the cometary neutrals that have yet to be ionised travel through the lower density plasma between flux tubes. By examining the total ionisation rate of photodissociated H and O, they deduce a density contrast of at least a factor of 6 between neighbouring flux tubes over a few thousand km in an open field region at ~1.3 $R_{\odot}$ above the solar surface.

Rasca et al. (2014) looked at 3-D MHD equations and a wave kinetic equation coupled model of mass-loading of the solar wind in the inner corona by a comet in anticipation of future in situ coronal missions, e.g. Solar Probe Plus. They predicted a drop in radial velocity, increase of plasma density and a magnetic cavity encased by magnetic field strength peaks, due to magnetic draping of field lines, for a probe located downstream of the nucleus. Radial velocity dips become sharper with decreasing distance to the nucleus source as per theoretical expectations.

6.1. Extension of software

The SOLARSOFT package (http://sohowww.nascom.nasa.gov/solarsoft/), recommended for the data reduction and analysis of the suite of solar instruments available, was integrated to work seamlessly with my software, with both level 1 and level 2 (L1 and L2) data from the STEREO Heliospheric Imagers and level 0.5 and level 1 (L0.5 and L1) data from the SOHO LASCO coronagraphs. The complete set of calibrations and corrections can be performed via Solarsoft. SOHO L0.5 data was utilised whenever L1 was unavailable. L1 data incorporates corrections to photometric calibrations, vignetting, geometric distortion effects and suppressing stray light (Morrill et al. 2006). Ultimately, I obtained access to high-quality difference images of comets C/2012 S1 (ISON) and C/2011 L4 (Pan-STARRS) through our Naval Research Laboratory (NRL) collaborator, K. Battams. These highlighted fainter substructures in the ion tail than my current methodology, making the method described below mostly redundant.

Progress was initially impeded on this project due to a lack of documentation regarding the latest Solarsoft software developments and the availability of data on spacecraft attitude. The L1 astrometric data contained corrected sun centre and spacecraft roll information (Battams & Rich, private communication). Without the necessary spacecraft ephemeris kernels, processing the L0.5 data would yield an incorrect mapping of the comet onto its orbit. The L0.5 to L1 cleaning can be performed within my software; this includes the F coronal background subtraction. Early and unsuccessful attempts at developing alternative techniques to integrate the solar data without the ephemeris files were discarded, in favour of an astrometric calibration via Astrometry.net. The resultant image quality is unsurprisingly poorer than the results when using formal procedures. An appropriate optical distortion correction also needed to be applied to each set of coronagraph images to account for the asymmetric curvatures. When performing this type of analysis, Level 2 (L2) STEREO data should ideally be used, for this includes the F corona subtraction. L0 data are the raw, uncalibrated data and L1, which can also be used in my software, contain flat-fielding, alignment and shutterless corrections to the L0 data. The F corona contribution will need to be subtracted for the L1 data, prior to processing in the main level code.

The coronagraphs observe the K-corona (Thomson scattered photospheric light from coronal electrons), the E corona due to spectral emission from coronal ion species and the F corona, light scattered by an interplanetary dust cloud envelope around the Sun (Kimura & Mann 1998; Morrill et al. 2006). Only the F corona was subtracted as the K and E corona's contribution were found to be minimal in ion tail images. Using 11 days' worth of uncalibrated minimum images, an empirical background model was devised for the background light removal. To compute the background image for a specific date, a daily median image, of the lowest 25% of pixels, is generated for 11 days stretching either side of the desired date. A disadvantage of this technique is that structures that persist for longer than 27 days can cause artefacts (Morrill et al. 2006).

The HI-1 frames are usually 30 minutes worth of exposures, stacked with 40 minute cadences. The error on the observing time is thus taken to be ±15 mins. The timing uncertainties on the C2 and C3 images are 10 and 15 minutes respectively. Due to a software bug, these were not factored into the projection mapping error propagation, thus slightly underestimating the LASCO-derived solar wind velocity uncertainties. These only impact my results for the C/2011 W3 (Lovejoy) solar wind velocities. The 'blooming' saturation effect did not pose a problem for this study.

6.2. Lovejoy (C/2011 W3)

Comet Lovejoy (C/2011 W3), a very bright Kreutz sungrazer which plunged into the solar corona and largely survived its perihelion at 1.19 $R_{\odot}$ (Sekanina & Chodas 2012), on 16th December at 00:17 UT (JPL Horizons). A near-exception amongst sungrazers, it displayed a prominent ion tail both pre-perihelion and post-perihelion. C/2011 W3 was discovered three weeks before its perihelion, providing sufficient advance warning to launch a coordinated international collaboration of both professional and amateur astronomers. Comet Lovejoy was observed with numerous instruments aboard ESA/NASA SOHO, ESA Proba-2, NASA STEREO and SDO, and JAXA Hinode satellites and ground-based telescopes across a large range of wavelengths, over a period of several days either side of its perihelion. In that time, C/2011 W3 left its mark in the inner solar corona and was observed to emit in both EUV

and X-rays by SDO's AIA and the X-Ray Telescope (XRT) aboard Hinode (McCauley et al. 2013). Post-perihelion observations indicate that the cometary nucleus survived ~1.6 days after perihelion before disintegrating (Sekanina & Chodas 2012; Raymond et al. 2014), though a nuclear condensation-less dust tail could be observed over a period of 3 months (Sekanina & Chodas 2012; Knight et al. 2012 reported Spitzer observations in early February 2012). McCauley et al. (2013) advanced a minimum diameter of 400 m for the comet nucleus ~ 25 minutes after perihelion, based on their estimated total mass loss of 10^{13} g. Assuming a bulk density, they estimated that the nucleus would have been merely 254 m in diameter during its egress from the AIA FOV.

If the comet had a low tensile and cohesive strength, i.e. conforming to the canonical loosely bound rubble pile model, then the comet would have disintegrated at perihelion (McCauley et al. 2013). However, computations by Gundlach et al. (2012) introduced the idea that a sungrazer of low tensile strength could survive this period if enough icy material is outgassed. Using this, they derived a maximum radius of 11 km for C/2011 W3 to be able to survive the solar Roche limit whilst noting that a minimum radius of 200m is required for C/2011 W3 to survive its perihelion simply by providing enough material for the solar erosion. This conflicts with Sekanina & Chodas (2012)'s estimate of 75m to 100m radius for C/2011 W3, though the authors reckoned that the delayed destruction of C/2011 W3 is enough evidence that the rubble pile model is not a good fit for what was likely a more cohesive nucleus with larger than expected tensile strength. They further inferred that the comet expired by multiple internal fragmentations due to crystallisation of amorphous ice pockets at ~130 K rather than gradual erosion.

My analysis focuses solely on images from the LASCO C3 coronagraph and the SECCHI HI-1A imager during 2011 December 14 – 19. My results indicate that comet Lovejoy was immersed in a non-radial solar wind flow, and that its ion tail, rather than being linear for a fixed solar wind speed, was continuously curved towards the comet's dust tail. The comet's orbital elements were the following: Inclination (i) = 134^{o}.4; ascending node = 326^{o}.4, Perihelion date (T) = 16/12/2011, 00:17 UT (JPL Horizons), Period 698 ± 2 years (J2000.0) (Sekanina & Chodas 2012)

Data coverage

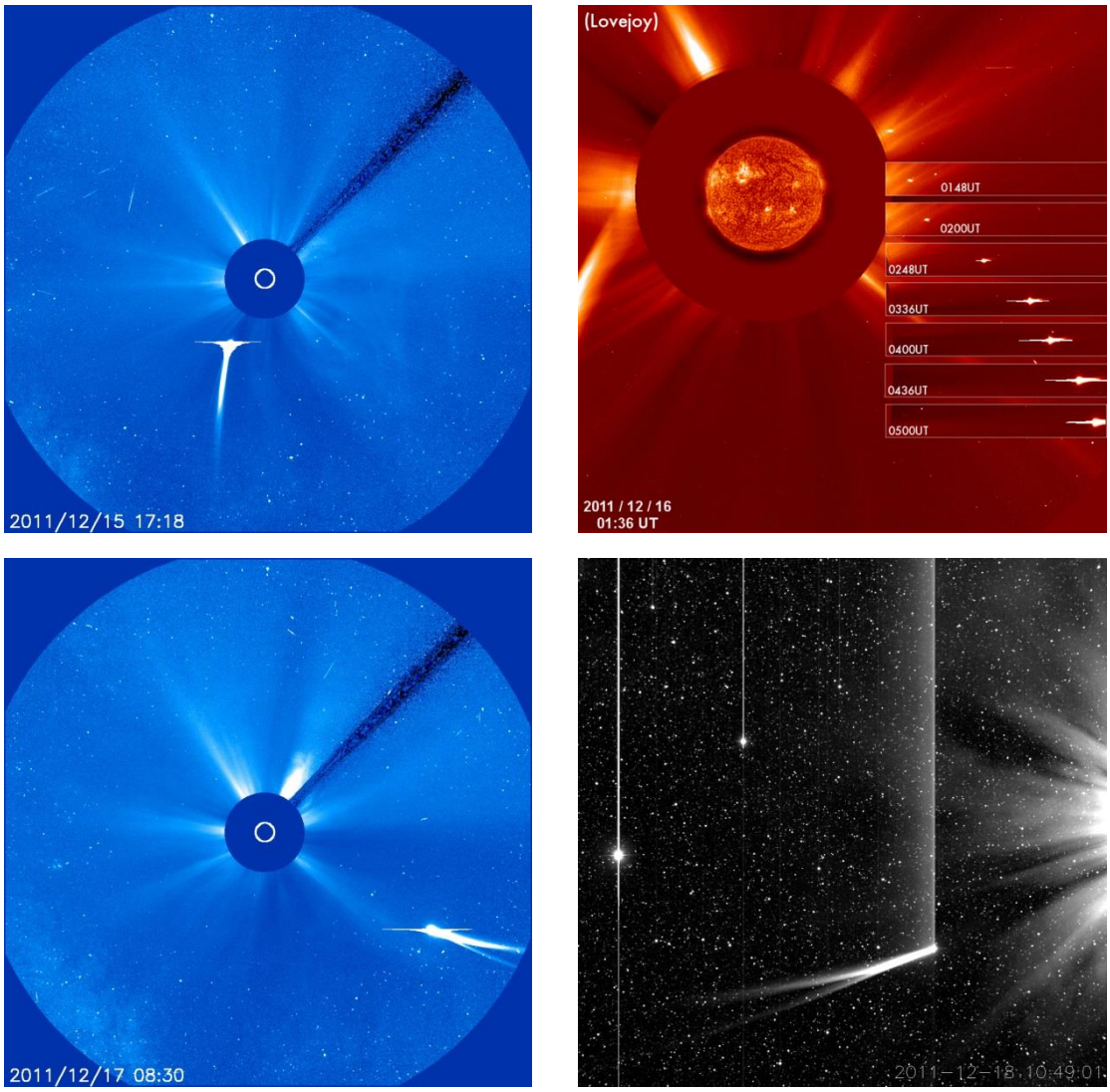

Figure 6.1: Images of comet Lovejoy from C3, C2, C3 and STEREO A, pre-perihelion and post-perihelion. Image courtesy of SOHO and STEREO team. The coma and dust tail can be seen growing shortly after perihelion in a composite of SOHO C2 images (panel 2).

Observations with the C3 coronagraph and STEREO HI 1A yielded an extensive data set of the evolution of comet Lovejoy's ion tail [Figure 6.1 and Table 6-1]. During this period, C/2011 W3 moved from 11.59 $R_\odot$ down to 1.19 $R_\odot$ at perihelion and back outwards to 54.49 $R_\odot$ [Figure 6.2]. There is no photographic evidence of the period when comet Lovejoy was within 2.5 $R_\odot$, the theoretical boundary within which the comet would have experienced purely non-radial magnetic field lines. The comet's ion tail remained distinctively smooth and featureless, as

viewed from the SOHO C2 and C3 coronagraphs and the STEREO A and STEREO B space observatories during its solar approach and egress from the inner solar system. Only images from the LASCO C3 instrument showed a clear ion tail both pre-perihelion and post-perihelion. There is an 8 hour data gap for the comet's ion tail around the comet's perihelion, as the comet occulted the Sun. Post-perihelion images from STEREO A showed a distinct ion tail curving slightly towards the dust tail.

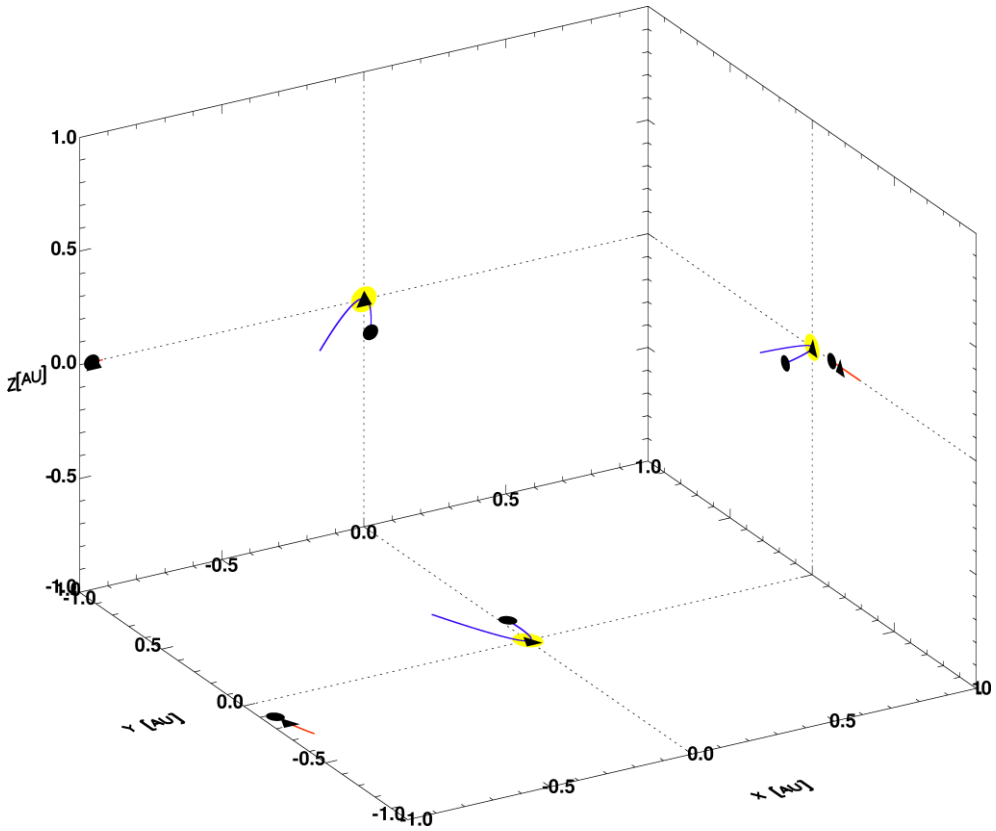

Figure 6.2: Heliocentric ecliptic coordinates of the highly inclined orbit of C/2011 W3 (Lovejoy). Black circles represent the start of the orbits and the black triangles show the comet and STEREO A's positions at the time of the comet's perihelion.

Table 6-1: Data coverage of comet C/2011 W3 from SOHO LASCO C3 and STEREO HI1 A.

Spacecraft	Instrument	Field of View	Data range (Dec 2011) UT
SOHO	C3	16°	15.64 – 17.72
STEREO A	HI 1	20°	16.59 – 19.62

Image statistics

STEREO A

I extracted 491 ion tail positions from 104 images, which were successfully processed through the software with only 6 that produced no solar wind data. After careful analysis, all solar wind velocity estimates were considered reliable with all images being of high quality. Aside from a pronounced curving tail, the ion tail remained featureless. The unexpected survival of the comet post-perihelion meant that the instrument team could not compensate the exposure time to prevent brightness of the coma and accompanying dust tail from overwhelming the ion tail close to the nucleus.

SOHO:

Though C2 coronagraph images exist, only the C3 standard filter images were analysed. The non-standard filters dataset has been reduced, though this was not available when this study was undertaken. The ion tail was thin and faint compared to the dust tail pre-perihelion, this may have a role in the relatively large data scatter seen as the tail edges become poorly defined with decreasing brightness of the ion tail. 348 solar wind estimates were extracted out of 77 images from the original 114 selected C3 standard filter images. Only one estimate was deemed unreliable and 9 are highlighted in green due to the following reasons: (i) its projected solar proximity to the ion tail, (ii) faintness of the ion tail shortly after perihelion once it had formed again, (iii) scattered light contamination from the bright dust tail.

STEREO B and ground-based

110 images from STEREO HI-1B, taken between 16.59 and 19.62 December 2011, were unsuccessfully processed due to the low orbit plane angle, with no resolvable nuclear condensation or ion tail in the extremely elongated pixel vectors.

Despite its extreme southerly declination, C/2011 W3 was observed by amateur astronomers in the southern hemisphere. The ion and dust tails extended to great lengths, up to 30^{o} in the plane of sky, though the two overlapped. I could not derive any solar wind velocities from these images.

Observing Geometry

Figure 6.3 is a recreation of the STEREO Science Centre plots of the locations of STEREO A, STEREO B and Earth on day of the comet's perihelion. The SOHO spacecraft is at L1, sunward of the Earth along the Sun-Earth vector. On the right hand side, I mapped images from STEREO A and SOHO onto the comet's orbital plane with the comet's perihelion defined as the Y-axis. The two topmost images are taken with the LASCO C3 coronagraph aboard SOHO (in blue), and the bottom two from STEREO A's HI heliospheric white-light image (in black). Comet Lovejoy's ion tail is seen to be curving slightly towards the dust tail in the STEREO A images.

Figure 6.4 shows the orbit plane angle for comet Lovejoy from the solar observatories presented here. Adopting a heuristic orbit plane angle greater than 30^{o} to represent good observing geometries for this technique, we can expect high quality data from both STEREO A and SOHO, whilst the technique becomes unusable for STEREO B observations.

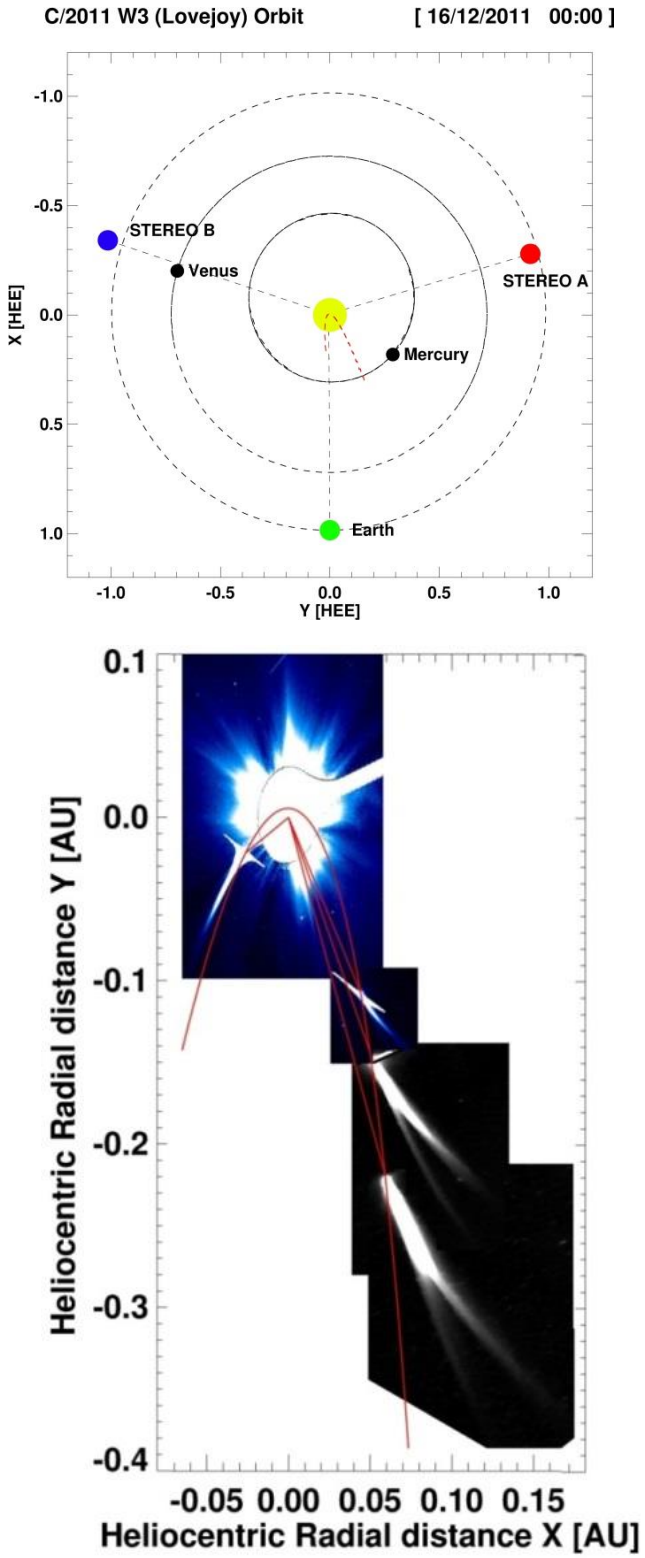

Figure 6.3: *Top*: **Positions of the 3 vantage points from which comet Lovejoy was observed as it plunged into the solar atmosphere (1.19 $R_\odot$) and survived high coronal temperatures (~10^6 K). Locations of Earth and spacecraft are shown for midnight on perihelion day.** *Bottom*: **Wxample images, two from SOHO LASCO C3 coronagraph in blue and two from STEREO HI-1A in black are mapped onto the comet's orbital plane. Comet's orbit is south of ecliptic, except for a few hours around perihelion. The direction of perihelion is along the Y-axis.**

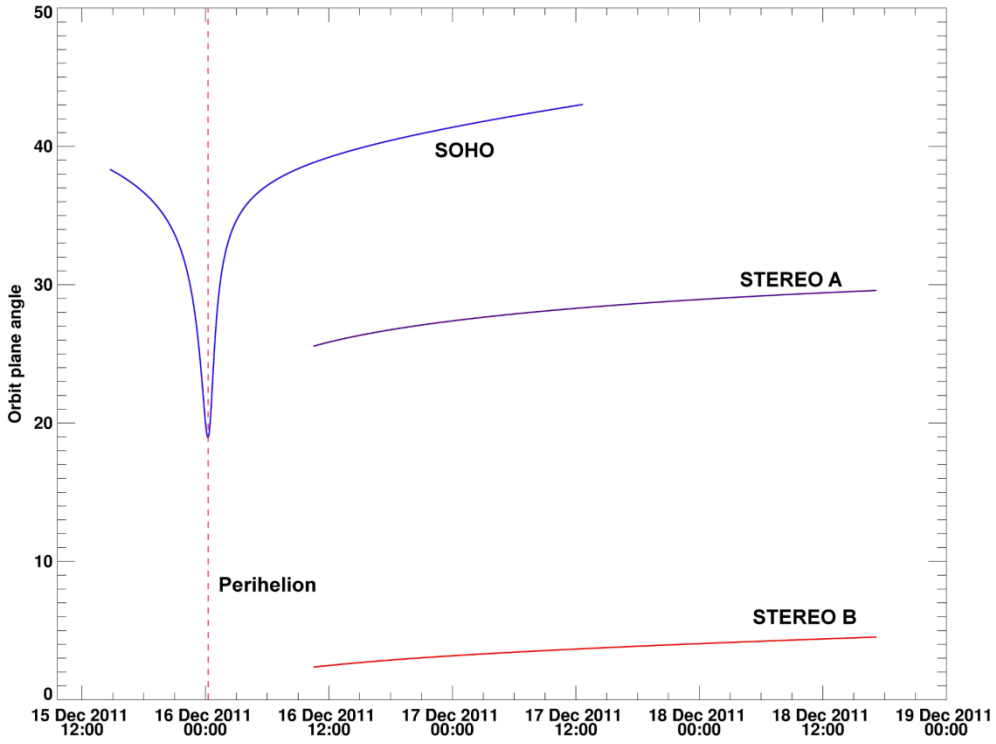

Figure 6.4: Orbit plane angle from STEREO A (purple), STEREO B (red) and SOHO (blue). The comet's perihelion is marked (dashed red line) on the plot.

The low orbit plane angles of STEREO B indicate that the observing location was close to the comet's orbital plane and the cometary ion tail was viewed edge on. Projections of STEREO B images could not be used to identify the non-radial displacements of the tail plasma. There were no strong links identified between the rate of change of the orbit plane angle and the velocity scatter [Figure 6.6] but results from the previous amateur observations seemed to hint that a more gradual change would have yielded less of a scatter.

Mercator map

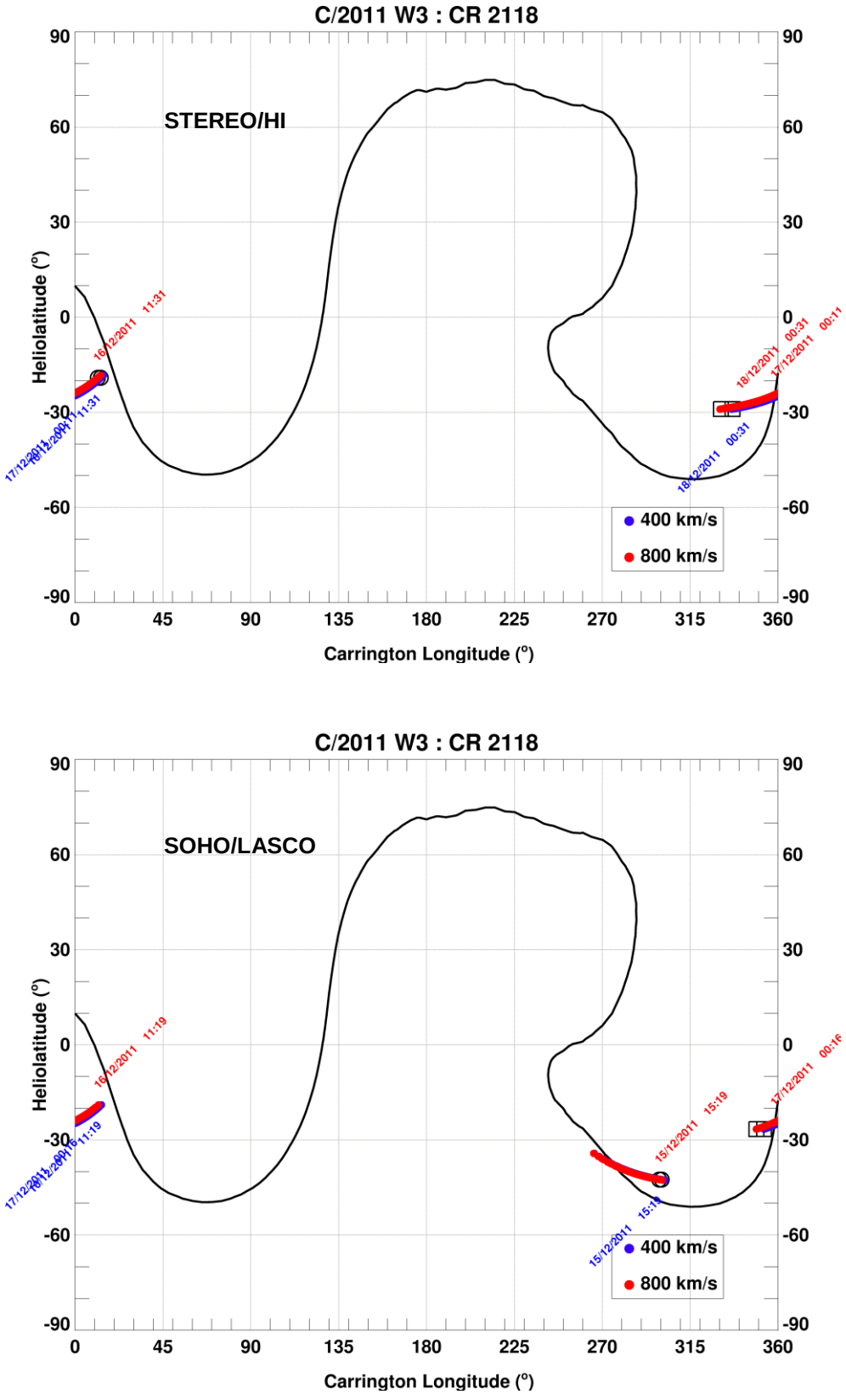

Figure 6.5: Mercator map of solar wind source surface for Carrington rotation 2118. Image credit for Mercator map: Wilcox Solar Observatory. Sampled positions for the STEREO A observations are on the top and the SOHO observations on the bottom.

Figure 6.5 shows the Mercator map of the solar wind source surface for Carrington rotation 2118 (CR 2118). The black line is the estimated position of the neutral line separating the inward and outward-directed heliospheric magnetic fields at the solar wind source surface (2.5 $R_{\odot}$). The solar wind plasma interacting with comet Lovejoy at the comet's orbit has been mapped back to SW source surface using a fixed solar wind velocity of 400 km s^{-1} (blue) and 800 km s^{-1} (red). The comet's close proximity to the Sun indicates that the longitude of the source position was not a strong function of solar wind speed. From the Mercator map of the sub-comet track, in the STEREO A data, we expect comet Lovejoy to broadly experience increasing solar wind speeds as time progresses if the neutral line is an indicator of the slow solar wind envelope. This is the inverse of what is recorded.

6.2.1. Radial solar wind speeds

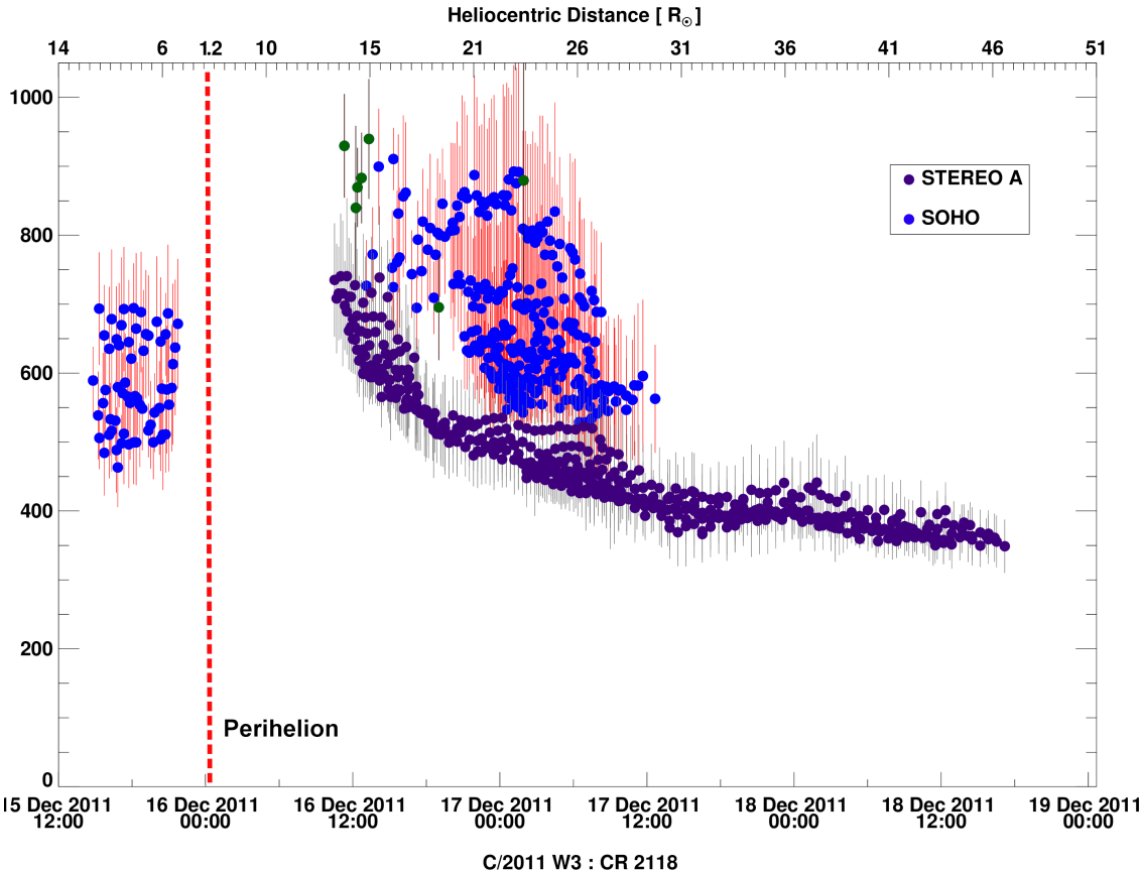

Figure 6.6: Solar wind velocities extracted from comet Lovejoy images. The blue dots represent solar wind velocities from the LASCO C3 (standard filter) images. The purple dots are solar wind velocities from STEREO A images. X and Y error bars are shown in red for STEREO A and grey for SOHO. Multiple velocities are extracted from each image,

whenever possible. The x-axis represents the time at which the plasma bundle left the comet's orbit. Samples of the ion tail where part of it laid on the extended radial vector are highlighted in green. This only affected the SOHO observations.

The solar wind velocity measurements from images taken during the period of 15th December 15:18 UT to 19th December 14:49 UT are shown in Figure 6.6. The last data point for STEREO A was sampled nearly 20 hours before the observation time for the last STEREO A image. The measurement uncertainty for the tail centre, as before, is estimated to be ± one-sixth of the distance from edge to edge of the ion tail, along extended radial vector. The timing and solar wind velocity uncertainties for SOHO have been slightly underestimated due to the timing uncertainty software bug reported previously.

The comet reached its perihelion behind the solar disk with respect to Earth's location, obscuring it from the SOHO coronagraphs. The data gap between the SOHO solar wind velocity data corresponds to a few hours either side of the perihelion. In spite of its good observing geometry, the scatter for the SOHO-derived solar wind velocities is large, spanning a range of ~250 km s^{-1} pre-perihelion and ~300 km s^{-1} post-perihelion. A clear trend can be observed, upon comparison with solar wind velocities from the STEREO A data, albeit slightly higher. The solar wind is thought to be mostly non-radial inside the solar wind source surface (~ 2.5 $R_\odot$ from solar centre). Comet Lovejoy is within this limit between 15 December 23:15 UT and 16 December 01:33 UT. All solar wind velocity estimates were evaluated outside of this boundary. The large scatter is predominantly caused by a curving ion tail corresponding to a velocity difference of ~200 km s^{-1} from end to end of the ion tail. As the tail brightened and lengthened, this effect is reflected in the large scatter produced between the two datasets. The ion tail can be seen to straighten out as it moved out of the C3 FOV around 07:00 UT on 17th December 2011. The comparatively higher noise in the SOHO velocity estimates could also be related to the faintness of the ion tail, which makes determination of the tail edges a difficult task at times.

6.2.2. Discussion

The Mercator map for Carrington rotation 2118 [Figure 6.5] needs to be considered in conjunction with the orbit plane angle plot for comet Lovejoy [Figure 6.4] to correctly interpret

the solar wind velocities results in Figure 6.6. Velocity comparisons to the orbit plane angle suggest that the observing geometries were good enough to produce valid estimates of the solar wind. Therefore, the discrepancy between the two solar wind velocity distributions cannot be attributed solely to geometrical effects, arising from the orientation between the comet and the imaging instruments. Based on the Mercator map, we would rightly expect the comet to register slow solar wind velocities and a likely DE as it crossed the HCS. The ion tail was continuously monitored from both spacecraft, showing no DE. Thus both the SOHO and STEREO A derived velocities and observational confirmation of no DE contradict the theory based on the Mercator map.

ENLIL visualisations

A pre-existing high-resolution stationary solar wind simulation was used for CR 2118 with its inner boundary condition set by MAS, and the input magnetogram sourced from NSO. The ENLIL model is limited to ~ 30 $R_\odot$ at the inner boundary, which restricts comparisons to the period from ~00:00 UT to ~18:00 UT on 18 December 2011, where the comet was between r_H ~0.168 AU (~36 $R_\odot$) and ~0.209 AU (~ 45 $R_\odot$), heliographic longitudes 214^o and 212^o and latitudes -28^o and -29^o.

There is very little simulated non-radiality to the solar wind sampled from December 18 at midnight onwards, with the modelled radial solar wind velocity of ~250 km s^{-1} very close to my measurements of ~400 km s^{-1} down to ~350 km s^{-1}. There is a slight longitudinal component, which would create a perspective of slower velocities down the tail and increased curvature of the ion tail towards dust tail. We can see evidence of the tail straightening out as the comet leaves the SOHO and STEREO A FOVs [RHS of Figure 6.3].

As the comet's longitude decreased, its southern latitude increased. The Mercator map [Figure 6.5] provides an approximate range of heliographic latitudes sampled when the comet was within 30 $R_\odot$ of the Sun. As can be seen, the comet is at ~20^o latitude south on December 16 and increasing. From Figure 6.3 and the longitudinal and latitudinal cutplanes of the radial solar wind velocity [Figure 6.7], it is safe to infer that the comet would have initially encountered a fast

solar wind stream ~ 600 km s^{-1}, had a brief foray into the smooth fast solar wind region around its perihelion, followed by decreasing solar wind speeds upon its egress. This behaviour matches our velocity profile exactly.

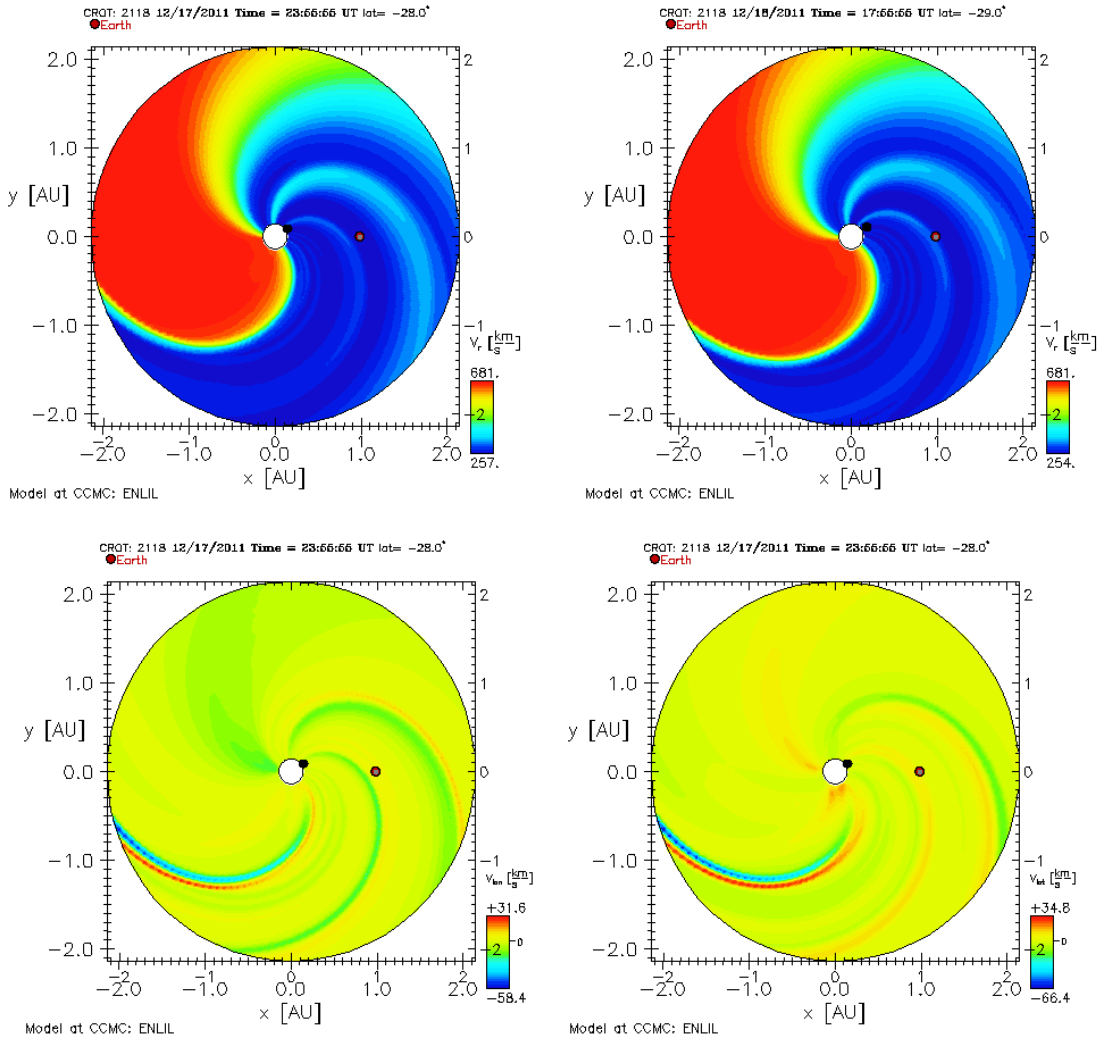

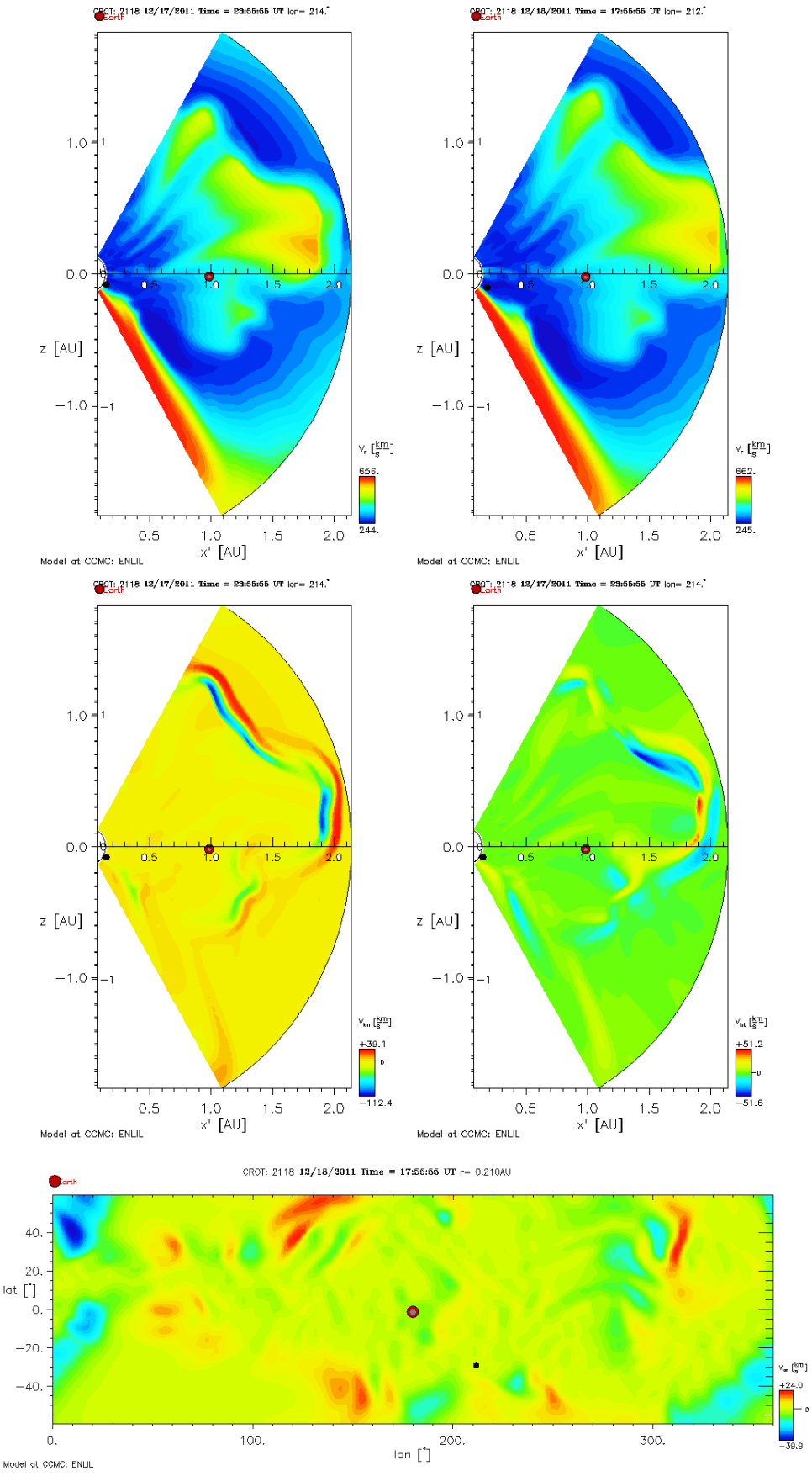

Figure 6.7: Longitude and latitude cutplanes of ENLIL MHD model. The first two images for each set are the radial solar wind velocities on 17/12/2011 23:55 UT and 18/12/2011

17:55 UT. The second half of each set are the longitudinal and latitudinal components of the solar wind velocity. The last cutplane is taken at a heliocentric distance of 0.21 AU, showing more clearly the low non-radial velocity component of the solar wind.

The Mercator map Figure 6.5 indicated a high probability of a HCS crossing in the evening of 15/12/2011. This is further reinforced by the ENLIL model, indicating a likelihood of a polarity reversal at the comet, though no such observations were noted with neither the SOHO nor the STEREO spacecraft. Therefore, it is possible that the comet's trajectory narrowly grazed this sector boundary, without encountering it.

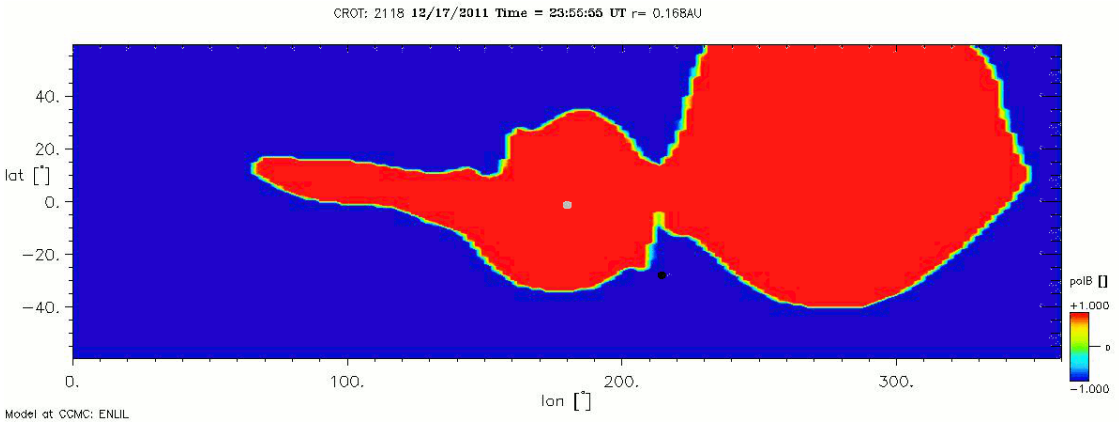

Figure 6.8: MHD model predicting a polarity reversal in solar wind outflow near the comet's location.

I outline and discuss the validity of three scenarios as potential explanations for my results from Figure 6.6.

Are we looking at the sodium tail in the LASCO C3 images?

Comets such as Lovejoy are known to be strong sources of sodium, and it is possible that they could have clear sodium tails (Knight et al. 2010), as observed at Hale-Bopp. The SOHO images were compared with a non-standard orange filter from SOHO. The presence of a tail at the same location in both the blue and orange filters implies that this is not a sodium tail. Analysis of the tail's position showed it not to be consistent with a neutral sodium tail; we therefore believe that the observed tail is an ion tail.

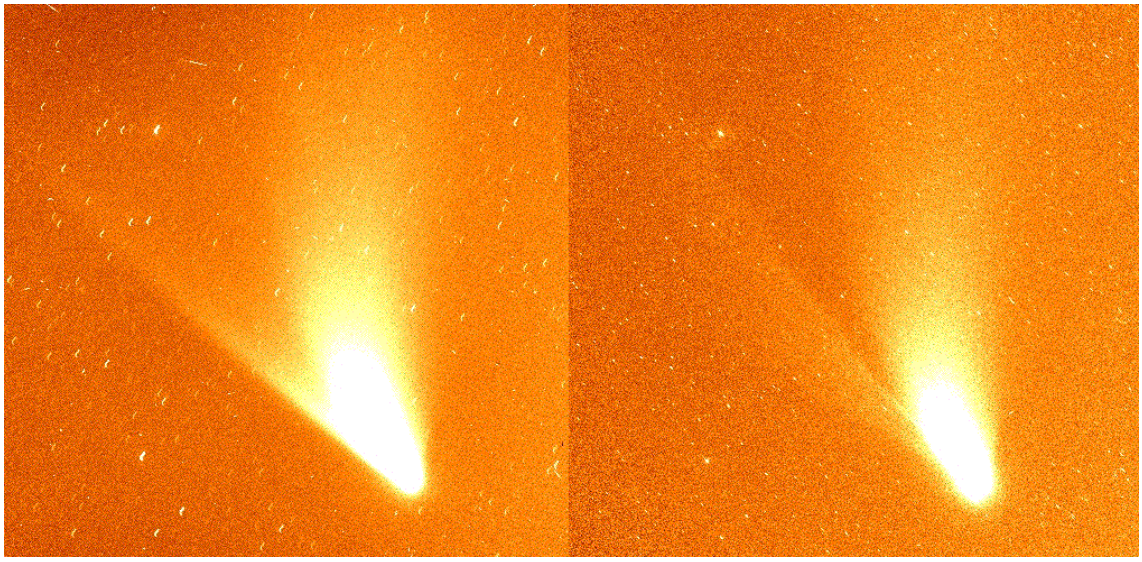

Figure 6.9: Ion tail (left) versus sodium tail (right) placements for C/1995 O1.

Are we looking at a non-radial ion tail or a curved ion tail towards the dust tail?

There is a clear discrepancy between the solar wind velocity measurements for comet Lovejoy from SOHO and STEREO A. We would expect an almost perfect match during the overlapping period of the two observatories for a purely radial solar wind.

Evidence for a non-radial ion tail

Non-radial components of the solar wind would cause the ion tail to also flow out of its orbital plane. This observational effect means that the two spacecraft, SOHO and STEREO A, would view two different projected angles of the ion tail, thus producing two different sets of solar wind velocity values derived with the same technique, which is what we see from our results. It would be useful to conduct a separate project analysing the three dimensional solar wind flow at the comet from the stereoscopic views from SOHO and STEREO A. To the author's knowledge, such a study has yet to be accomplished for any comet. This technique would only be successful for a small window of comet and existing spacecraft locations as both a large radial distance between the target and observers and a small angular separation between the observing satellites are required. Thompson (2009) analysed the three-dimensional position of sungrazing comet C/2007 L3 (SOHO)'s dust tail when STEREO A and B were 12^{o} apart.

Evidence for a curved ion tail

As previously remarked with other comets in Chapter 5 (Snapshots of the inner heliosphere) and confirmed by analysis of C/2002 V1 undertaken by G. H. Jones, the ion tail of comet Lovejoy seemed to consistently curve towards the dust tail. This was more noticeable in the C2 and C3 images [Figure 6.10] than in the SECCHI images. Velocity measurements for a consistently curved tail will get progressively smaller as samples are obtained further down the tail. It appears that this may be a consistent feature of comets near the Sun when there is a large ion source in the dust tail in addition to the nucleus-centered coma.

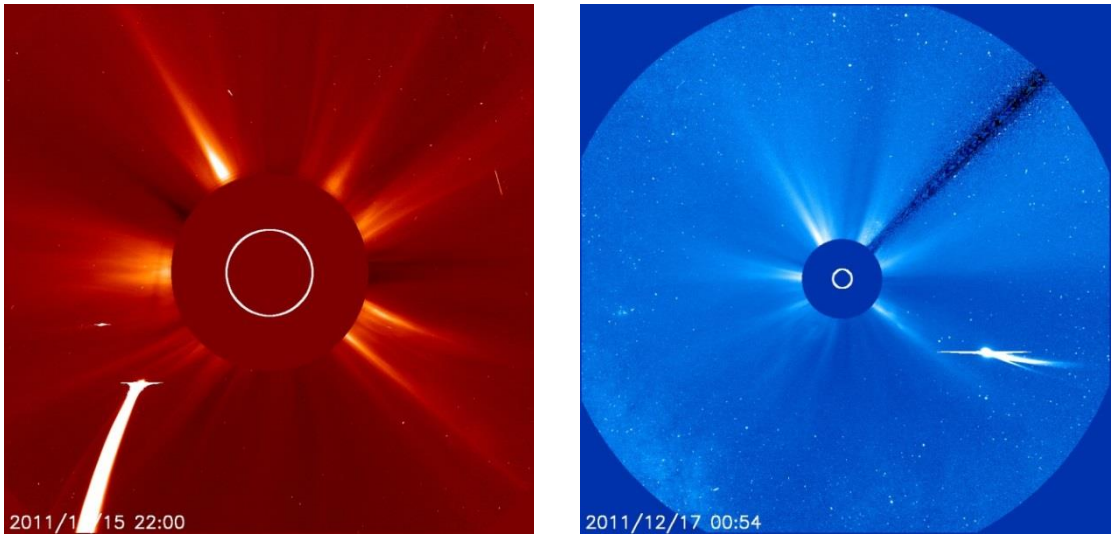

Figure 6.10: Pre-perihelion (C2) and post-perihelion (C3) observations of C/2011 W3 (Lovejoy). Bearing in mind, that C2 FOV is much smaller than C3's, the ion tail is distinctly curved in both images.

6.2.3. Tail ray

The tail ray velocities presented below are from an Astrometry.net processed difference image of C/2011 W3 (Lovejoy). The quality is thus lower than what is expected from STEREO A data and the tail ray itself was often hard to discern against the sky background and the near-saturated image of the dust tail close to the nucleus.

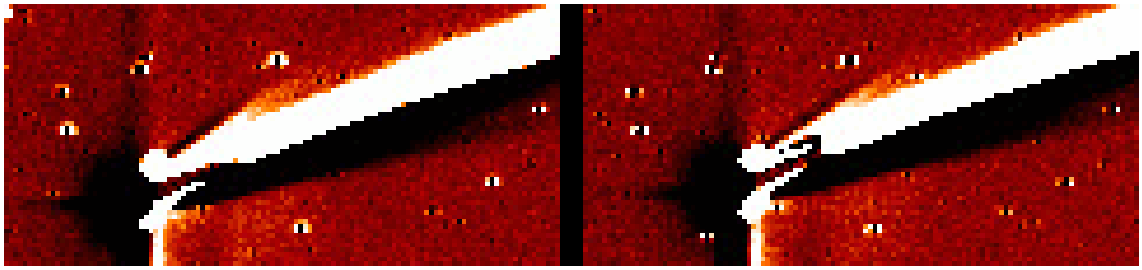

Figure 6.11: Tail ray evolution between two difference images of STEREO A. The tail ray can be seen on the topside of the nucleus in this image.

I measured the tail ray section just after the darkened edge of the tail ray, so as to retain a trackable structure [Figure 6.11]. This was the only method to assure some consistency in measurements. The difference images were split into three different tail ray sequences, with each set having a different tail ray progressing distinctly from each other. The image times were all determined with my software and thus contained all the limitations and uncertainties discussed in Chapter 5. The results of this section should thus be considered lightly. Tail ray set 1 was very problematic to measure, whilst sets 2 and 3 proved easier, except for the last tail ray measurement for set 2.

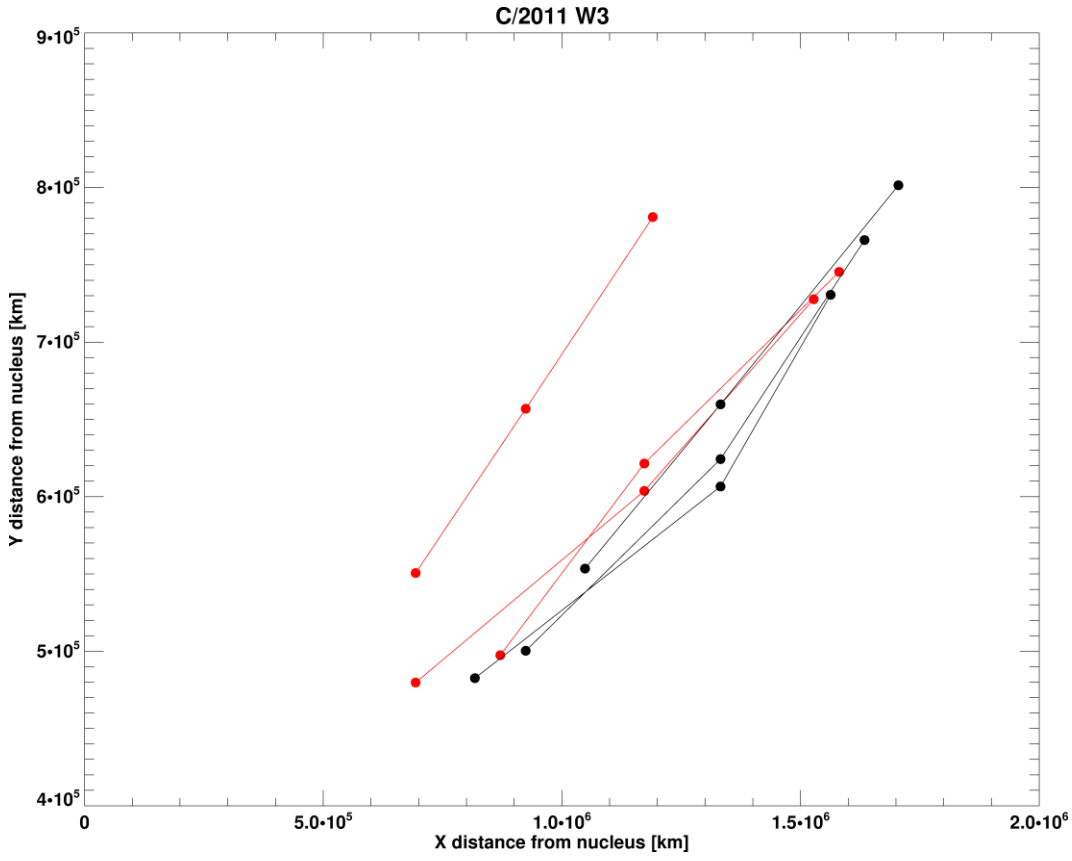

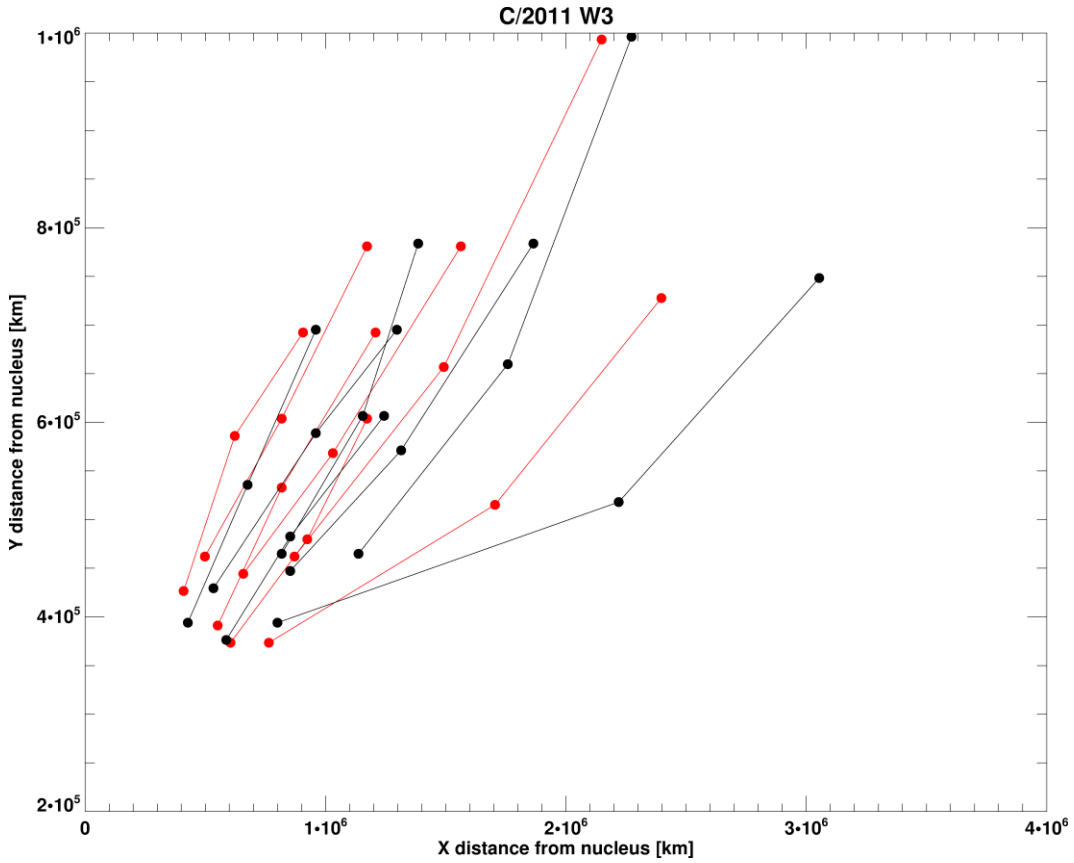
C/2011 W3
1•10^6
8•10^5
6•10^5
4•10^5
2•10^5
Y distance from nucleus [km]
0
1•10^6
2•10^6
3•10^6
4•10^6
X distance from nucleus [km]

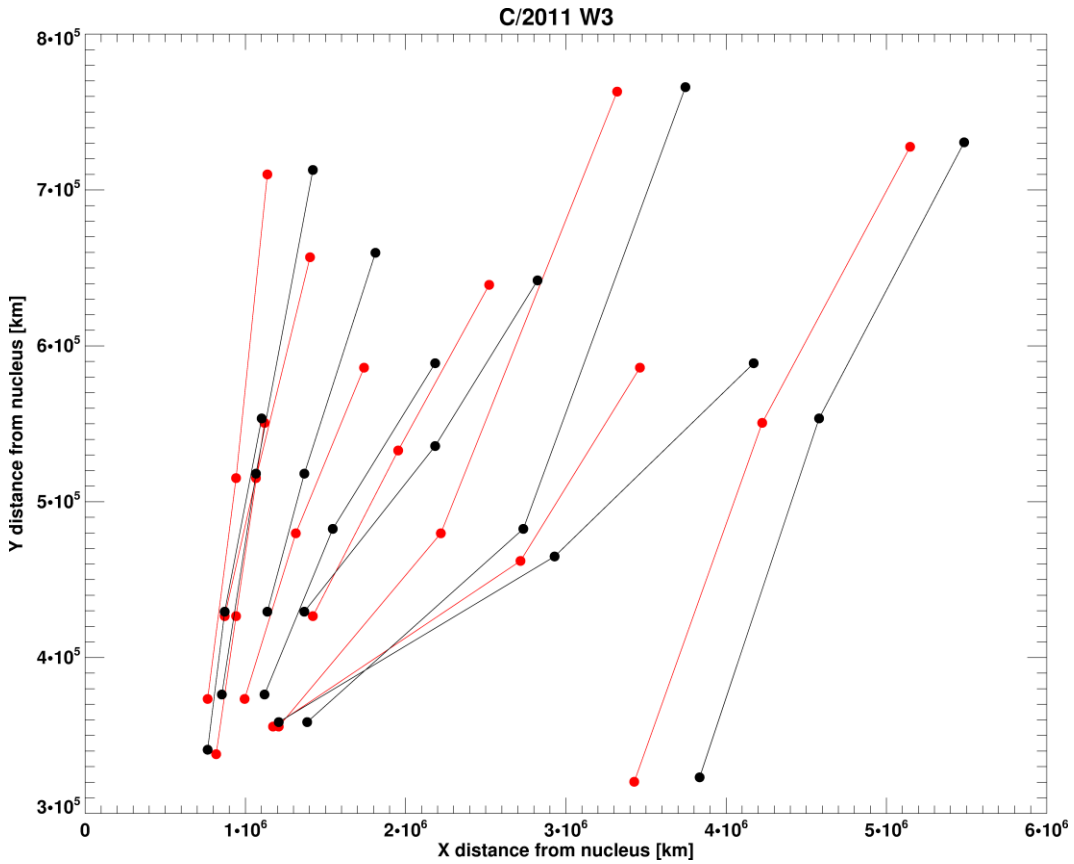
C/2011 W3
8•10^5
7•10^5
6•10^5
5•10^5
4•10^5
3•10^5
Y distance from nucleus [km]
0
1•10^6
2•10^6
3•10^6
4•10^6
5•10^6
6•10^6
X distance from nucleus [km]

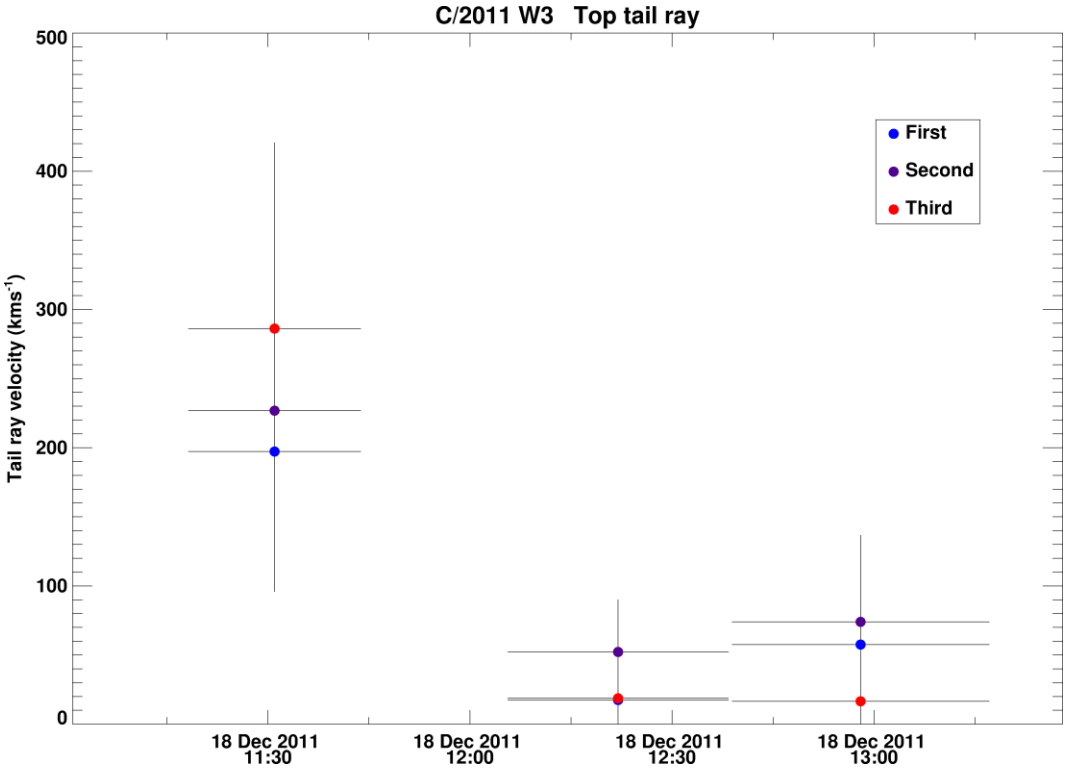
C/2011 W3 Top tail ray
Tail ray velocity (kms^{-1})
500
400
300
200
100
0
First
Second
Third
18 Dec 2011
11:30
18 Dec 2011
12:00
18 Dec 2011
12:30
18 Dec 2011
13:00

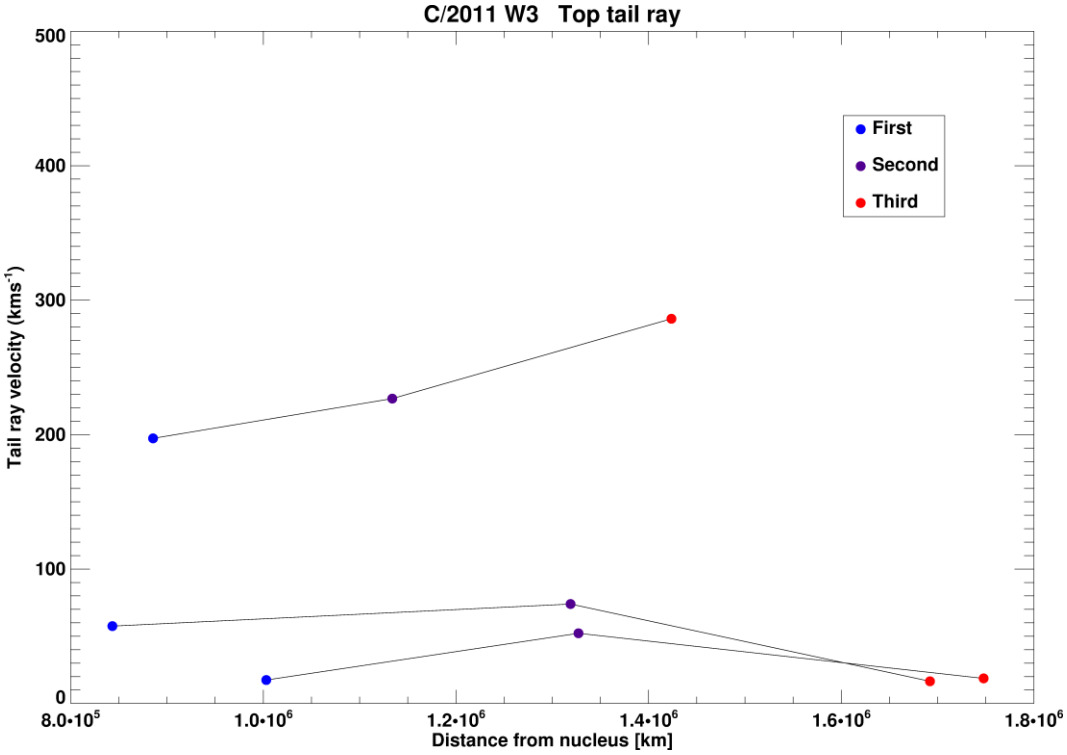
C/2011 W3 Top tail ray
Tail ray velocity (kms^{-1})
500
400
300
200
100
0
First
Second
Third
8.0•10^5
1.0•10^6
1.2•10^6
1.4•10^6
1.6•10^6
1.8•10^6
Distance from nucleus [km]

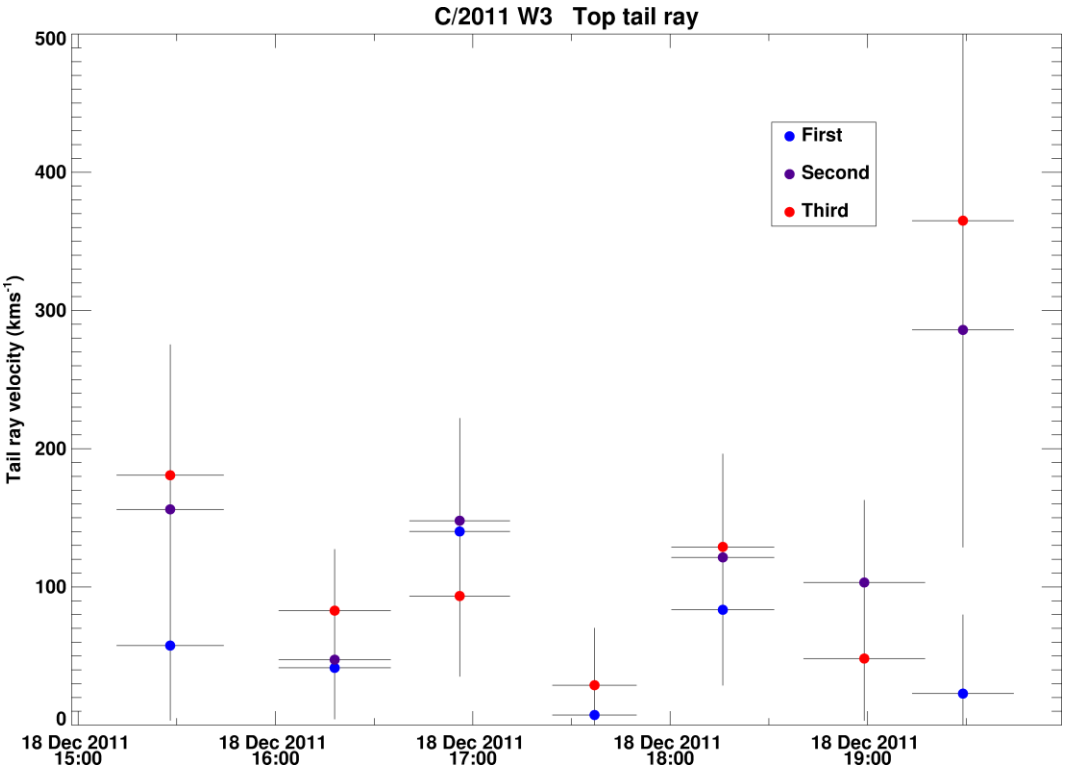
C/2011 W3 Top tail ray
Tail ray velocity (kms-1)
500
400
300
200
100
0
First
Second
Third
18 Dec 2011
15:00
18 Dec 2011
16:00
18 Dec 2011
17:00
18 Dec 2011
18:00
18 Dec 2011
19:00

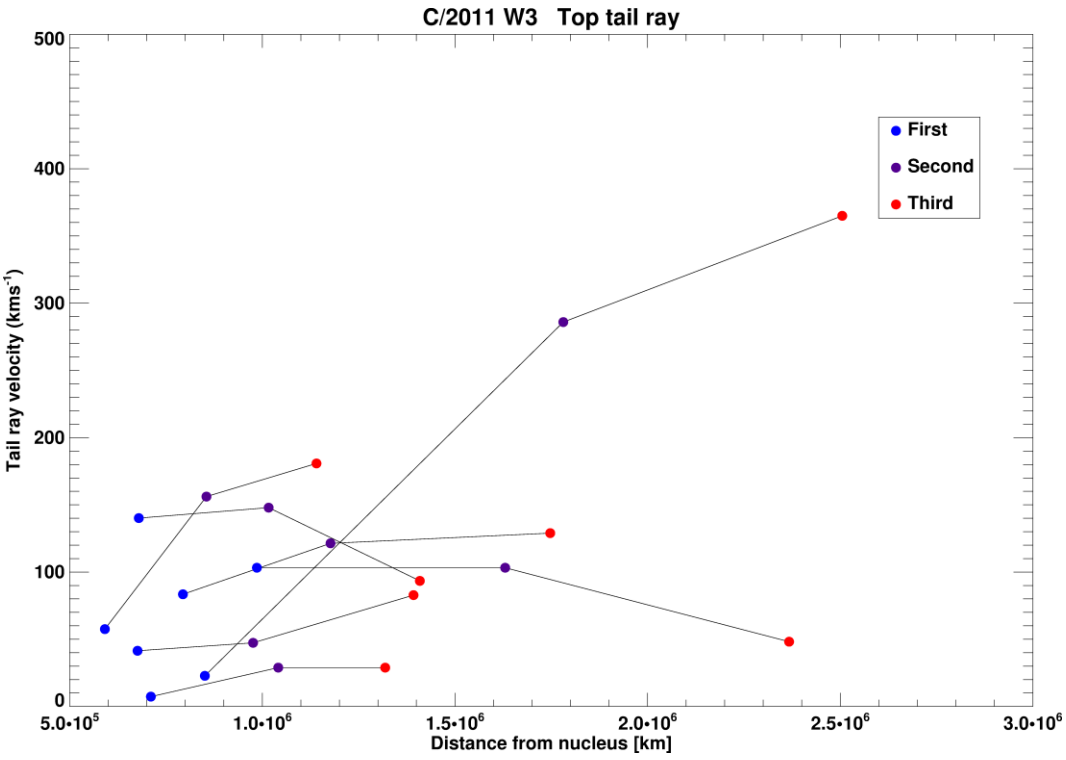
C/2011 W3 Top tail ray
Tail ray velocity (kms-1)
500
400
300
200
100
0
First
Second
Third
5.0•10^5
1.0•10^6
1.5•10^6
2.0•10^6
2.5•10^6
3.0•10^6
Distance from nucleus [km]

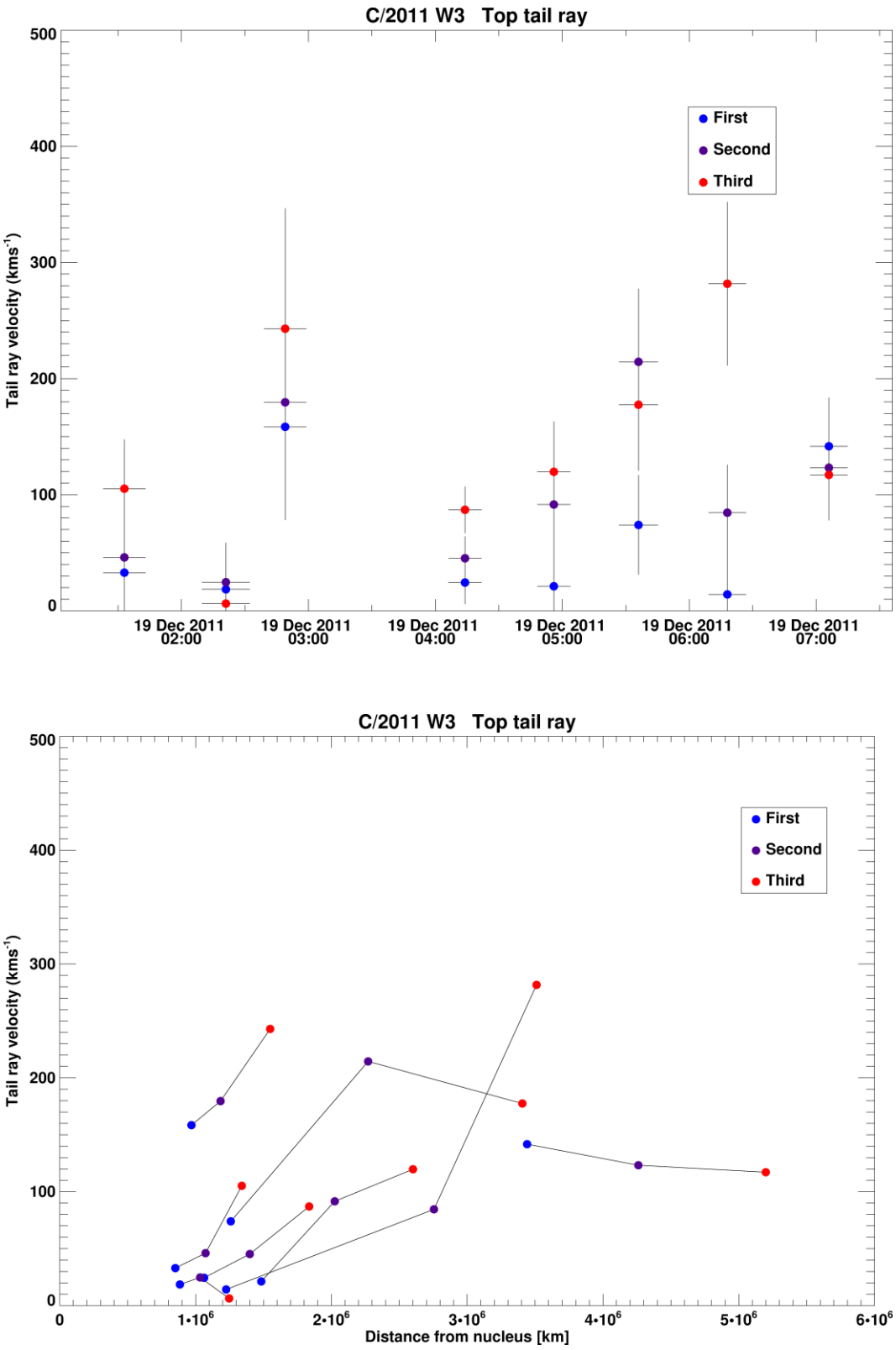

Figure 6.12: Measured positions of sets 1-3 are shown in the top 3 panels. The tail ray velocity variations with respect to each image and distance from the nucleus for each set in ascending order.

Aside from set 3, which was the most straightforward to measure, the tail ray velocities did not seem to conform to expectations of increasing velocities down the tail ray and away from the nucleus. Overall, it is clear that the tail rays are getting accelerated to slow solar wind velocities.

6.2.4. Conclusion

Comet Lovejoy exhibited characteristics of both a non-radial tail and a ion tail curving towards the dust tail. If the high velocities in the LASCO C3 data are temporarily excluded, the general trend of the LASCO C3 solar wind velocity data points is similar to the STEREO A data plot. This further strengthens the case for a strongly non-radial solar wind flow. I conclude from this study that the observations are complicated by a combination of a non-radial solar wind flow and a ion tail whose curvature is influenced by ions emanating from the dust tail.

6.3. ISON (C/2012 S1)

Comet C/2012 S1 (ISON), a dynamically new Oort cloud comet, was discovered on 21 September 2012 by Nevski and Novichonok with the International Scientific and Optical Network (ISON) telescopes. The comet displayed a highly dynamical and bright tail before perihelion. The brightness predictions fell below that of the initially predicted lightcurve. Had it survived perihelion, comet ISON would have likely exhibited a similar brightness profile increase post-perihelion as comet C/2011 W3. This was unfortunate for my two observing proposals (P13 and C166) at the Isaac Newton Telescope to follow its evolution post-perihelion.

There had been incisive discussions within the community as to whether comet C/2012 S1 would survive its perihelion with its nucleus intact. The now defunct comet fragmented shortly before its predicted perihelion at 2.79 $R_{\odot}$ on 2013 November 28 18:41 UT (Sekanina 2013). Knight & Battams (2014) report that the central condensation disappeared around November 28 12:00 UT with the leading edge, where the nucleus should have been, becoming progressively more elongated towards perihelion, suggesting disruption of the nucleus into multiple fragments. No central condensation was observed post-perihelion, though a long, narrow trail traced the

comet's orbit, before broadening and subsequently fading. Knight & Battams (2014) provide a full list of observations by different instruments, aboard SOHO and the twin STEREO spacecraft, and compare the photometric and morphological evolution of C/2012 S1 to that of small Kreutz comets of several tens of metres in radius. Thus they infer that the comet was likely tens of meters in diameter pre-perihelion after undergoing significant mass-loss from a > 50m radius object, in the days and weeks preceding its perihelion.

The early discovery of C/2012 S1, a few months after C/2011 W3, allowed both the professional and the amateur observing communities to coordinate their spaceborne (namely STEREO, SOHO and SDO) and ground-based observations. SDO was off-pointed four times to target C/2012 S1, though AIA did not observe the comet in the EUV spectrum. Druckmüller et al. (2014) attributed this null result to too weak an EUV signal since the EUV emission intensity, being proportional to the product of the ion and electron density along SDO's line of sight, would decrease sharply with increasing heliocentric distance. The authors argue that the sharp dust trail observed post-perihelion is evidence that large fragments had survived perihelion passage. SWAN observations of comet C/2012 S1 (ISON) up through its outburst late in 2013 November, computed its water production rates of 2×10^{30} s^{-1} (Combi, Fougere, et al. 2014). The J2000.0 orbital elements of the comet are: Inclination (i) = $62^{o}.4$; ascending node = $295^{o}.7$, Perihelion date (T) = 28/11/2013, 18:41 UT (JPL Horizons)

Orbit geometry

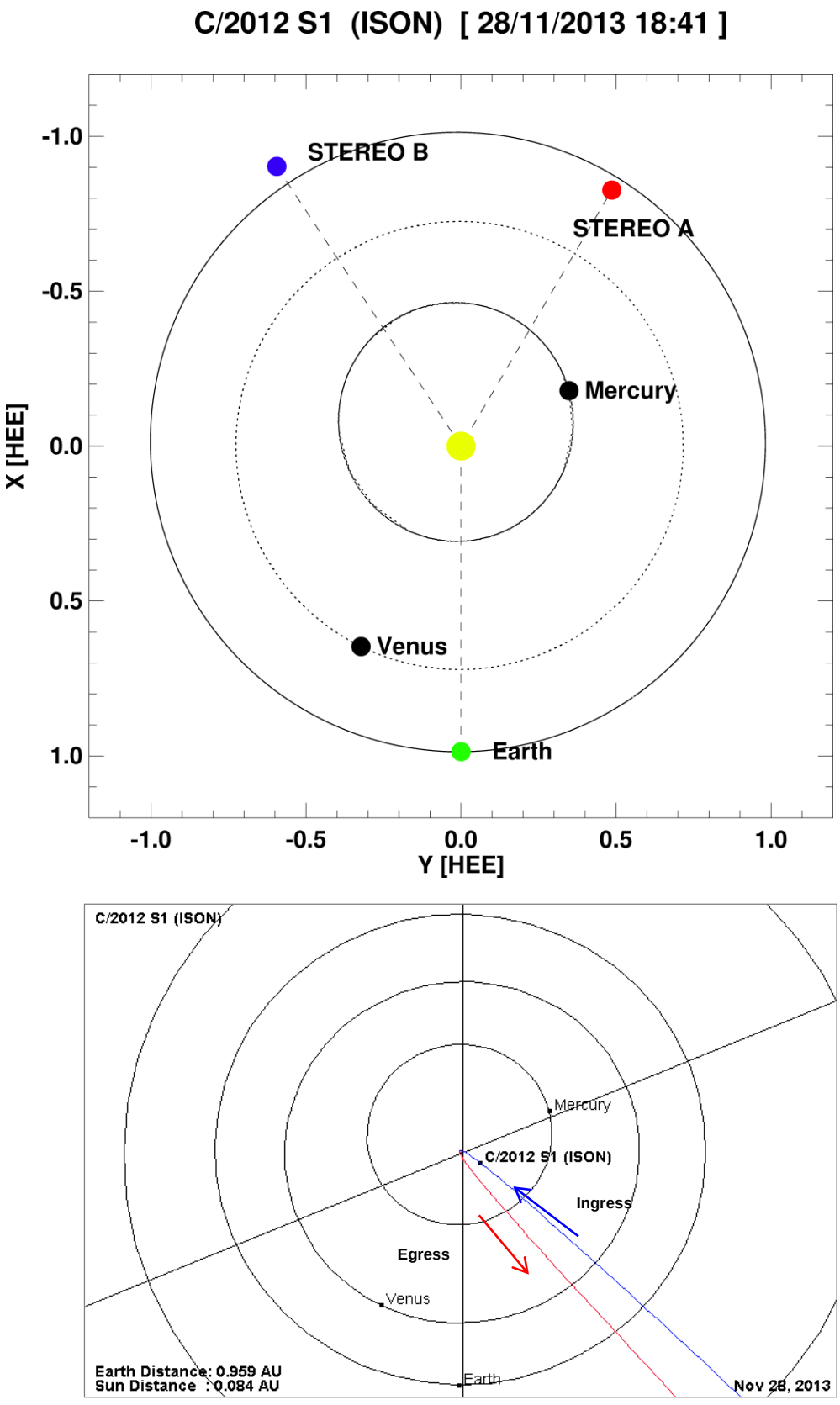

Figure 6.13: *Top:* **X-Y plane view of the orbit geometry of the multiple vantage points from which C/2012 S1 (ISON) was observed at the comet's perihelion.** *Bottom:* **Edited image from the JPL small-body database showing the comet's orbit on the day of its perihelion.**

Figure 6.13 demonstrates a view from the north of C/2012 S1's orbit in relation to the Earth and the STEREO satellites at the comet's perihelion. SOHO orbits just sunward of the Earth at L1. The comet's orbit was produced using the JPL small-body database (http://ssd.jpl.nasa.gov/sbdb.cgi?help=1). The orbit went from south to north of the ecliptic post-perihelion.

Orbit plane angle

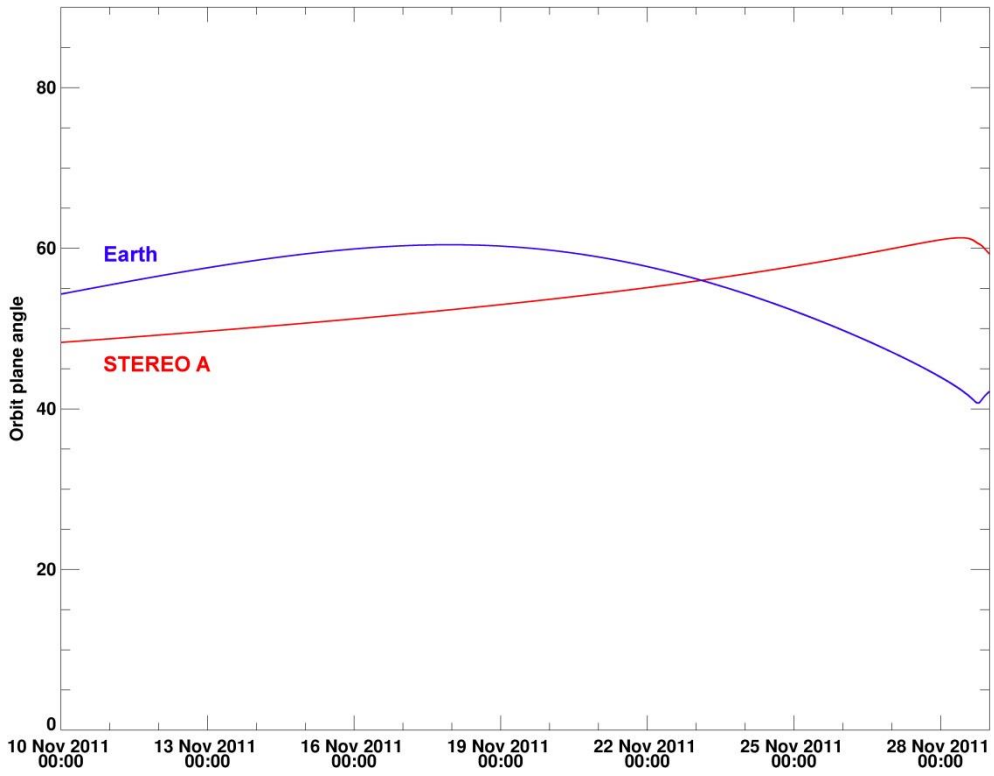

Figure 6.14: Orbit plane angle of C/2012 S1 from both observing locations used in this study.

The observing geometry from both STEREO A and the Earth were the most favourable out of all the comets studied for this thesis, mainly due to the moderately high orbit plane angle and its steady rate of change [Figure 6.14]. Aside from a small perspective over/under estimation of the radial solar wind velocities, no complications from the orbit plane angle is expected in this study.

6.3.1. Radial solar wind speeds

Encke

Comet 2P/Encke was simultaneously observed in the STEREO HI-1A images during observations of C/2012 S1. The observing geometry between STEREO A and 2P/Encke was less than ideal with a low orbit plane angle of ~10-20^{o} [Figure 6.15]. The comet reached perihelion on 2013 November 21 16:53 UT at 0.336 AU from the Sun. Its trajectory brought it closer to STEREO A, from 0.80 to 0.55 AU for the time period shown in Figure 6.15. Combined with low apparent solar elongations from 20^{o} to 8^{o}, the poor observing geometry meant that no usable projected images were produced and thus no solar wind velocity estimates could be derived for comet 2P/Encke.

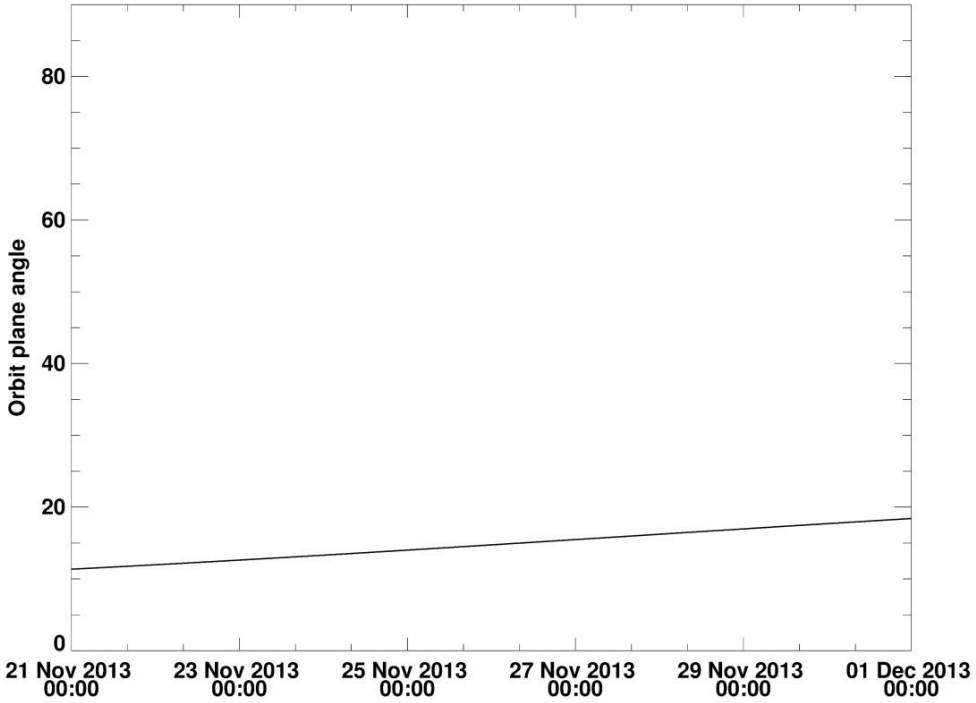

Figure 6.15: Orbit plane angle of comet 2P/Encke from STEREO A

6.3.1.1. STEREO A

Results from C/2012 S1 were derived from the L2 dataset, prior to receiving the difference images. As such, the edges of the ion tail are more difficult to interpret and contribute to the noise in the measurements. Of 141 images analysed, 119 displayed an ion tail with only 64

used to extract 221 solar wind velocities. An image-by-image analysis was not carried out as the tail was atypical for most of the period of interest. The vector maps and tail ray analysis were conducted with the difference images, which showed far greater detail of the fine tail structures.

Once mapped, the comet's projected orbit is close to the radial vector in both the STEREO A data [Figure 6.16] and the ground-based observations. When the ion tail is near anti-parallel to the comet's projected orbit from the line of sight [Figure 6.16], it is difficult to accurately resolve the radial speed of the solar wind. With the tail orientation being this close to the comet's orbit, the plasma bundles may not have fully accelerated to the solar wind speed. The tail shows dynamic activity with the ion tail straddling the radial vector for long periods of time. No radial solar wind estimates were taken until 23rd November 2013. By that time, the comet had undergone a disconnection event and a brand new ion tail had formed whose projection overlaid the comet's orbit as viewed from the spacecraft's position, whilst the old ion tail was still propagating radially outwards along the radial vector. Larger FOV images revealed that a large kink formed later on November 23 and travelled downtail of the main ion tail at an angle [Figure 6.16].

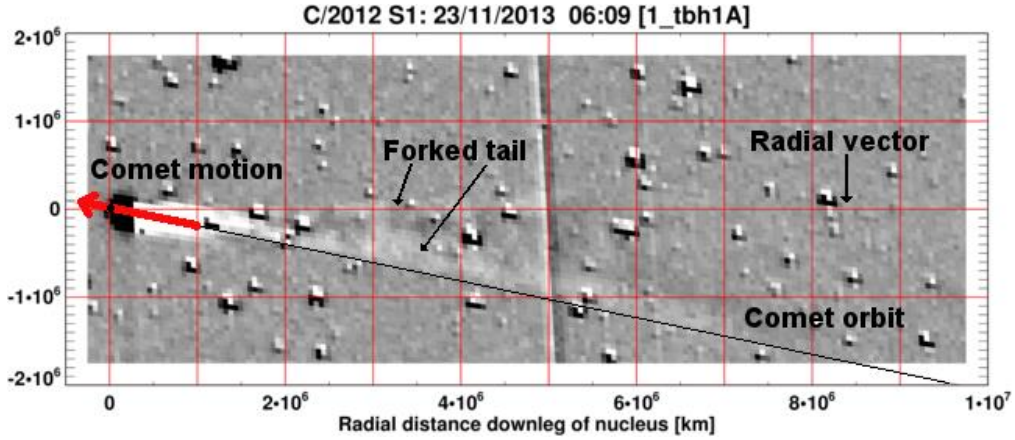

Figure 6.16: STEREO HI 1A image of comet C/2012 S1 showing a forked ion tail. The new tail is partially lying on the extended radial vector and the older tail is close to the comet's projected orbit.

Starting on November 24 00:00 UT, a clear tail disturbance appeared that lasted 12 hours, whereby condensation knots propagated anti-sunward and parallel to the projected orbit vector. A final tail disconnection is observed at 3 x 10^6 km downstream of the nucleus on November 24

at 07:29 UT, likely the last residues of plasma clouds spewing outwards from the comet's ionosphere. The final disconnection likely occurred between November 24 2013 03:29 UT and 04:49 UT. The plasma bundles dissipated from the HI-1A FOV by the 25th November, leaving just the nucleus and the dust tail. No new ion tail was seen thereafter as seen from STEREO A. The dust tail lengthened and split into two tails on close approach to the Sun with the newly formed, thin dust tail being composed of heavier dust grains. Comet 2P/Encke occupied the same FOV and experienced a disconnection event as comet C/2012 S1 exits HI 1A. On November 27 at 04:09 UT, the comet interacted with an ICME. A shock front was observed in the apparent dust tail's orientation [Figure 6.17]. Given the extreme faintness of ICME signature, it is challenging to determine whether this is truly a shock-dust tail interaction or whether the combined brightness of a distant background ICME and the dust tail combined to give the impression of a shock.

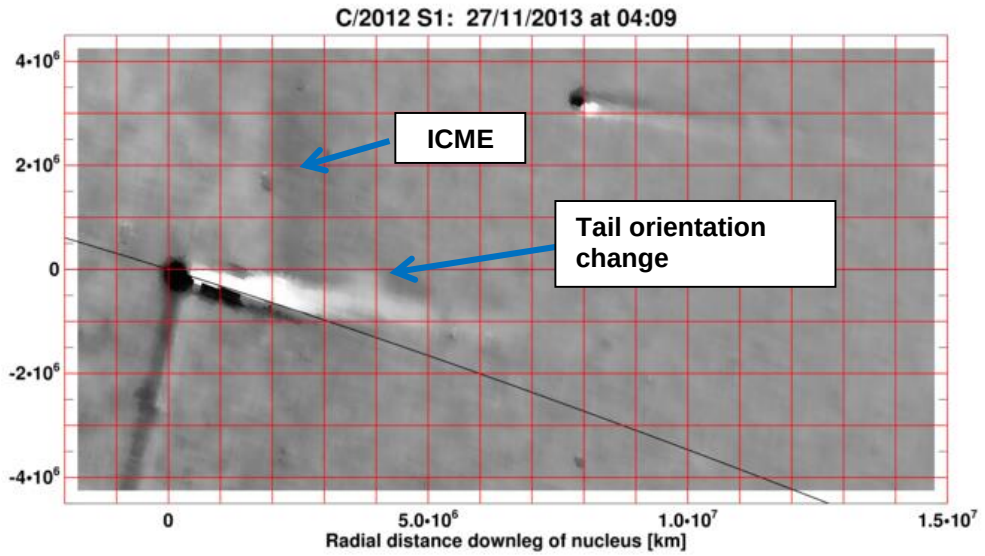

Figure 6.17: Comet ISON observed from STEREO HI 1A taken ~1.5 days before perihelion.

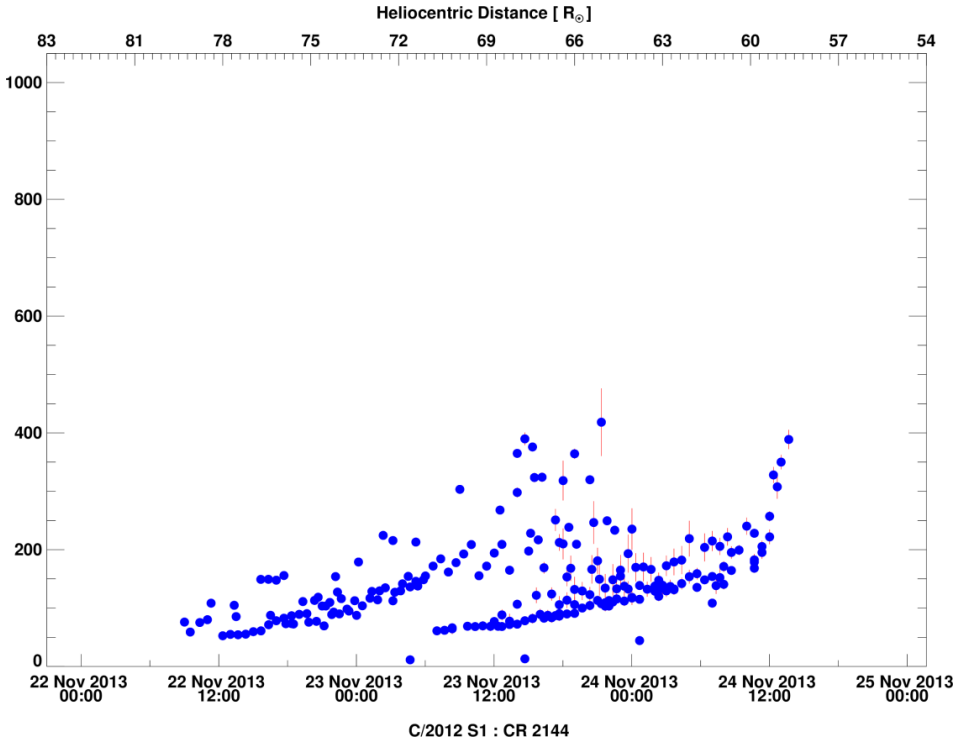

Figure 6.18: Solar wind velocities from C/2012 S1 derived from STEREO HI-1A observations.

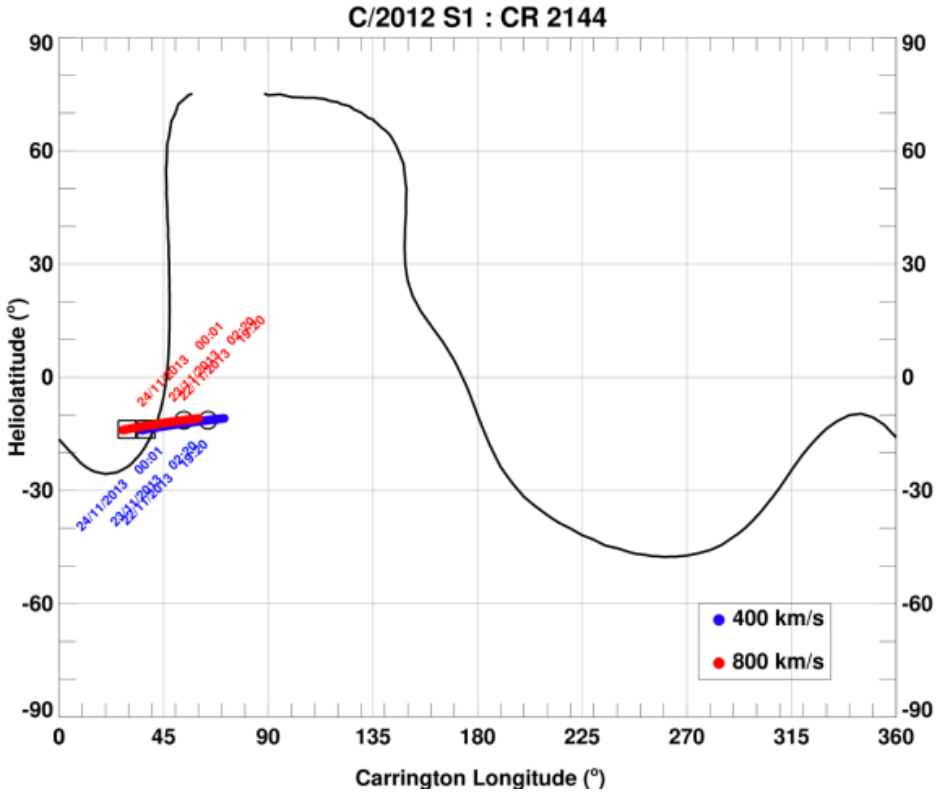

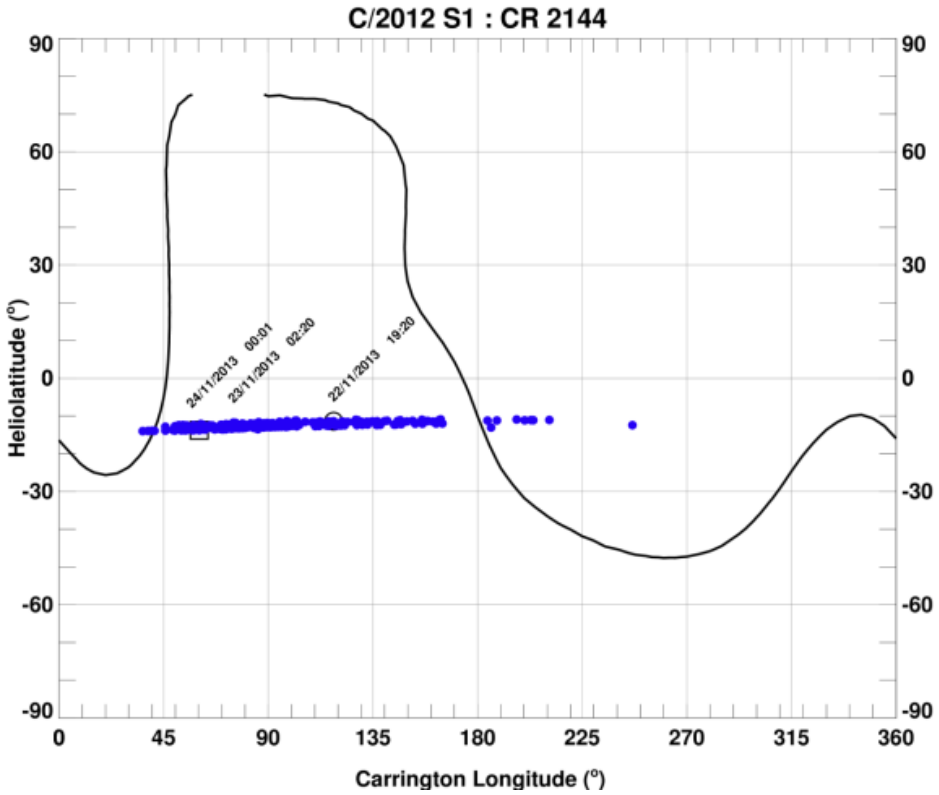

Figure 6.19: Mercator map for CR 2144 with the plasma bundles mapped back to the solar wind source surface, using a fixed solar wind velocity (top) and the measured solar wind velocities (bottom).

The comet might be expected to sample slow solar wind velocities based on the upper plot in Figure 6.19. On the right, I also include a plot of the plasma bundles sources mapped back to the solar wind source surface using the values measured in this study. The solar wind streams originating from a large range of heliolongitudes could have produced the observed turbulent appearance. The low velocities were corroborated by our NRL collaborator (priv. comm.) by using plane of sky measurements of the individual plasma bundles' rate of motion.

The data in Figure 6.18 correspond to the period when the comet was between ~79 $R_\odot$ (~0.366 AU) and ~59 $R_\odot$ (~0.271 AU) as it approached the Sun. The comet was between heliographic longitudes 238° and 237° and latitudes -11° and -14°. My solar wind velocities are between 50 – 200 km s^{-1}, fairly close to the 250 – 300 km s^{-1} wind predicted by the ENLIL MHD model from CCMC. The predicted non-radial longitudinal and latitudinal components of the solar wind are ~5-10 km s^{-1}. From the observer's perspective, this can contribute to existing geometrical effects. For example, the non-radial components may cause the ion tail to appear closer or

further away from the extended radial vector depending on the observer's position with respect to the comet's orbit. For this particular set of observations of C/2012 S1, this would cause the ion tail to appear as a slower moving ion tail from STEREO A's vantage point and a slightly faster moving tail from Earth's, though the perspective complications would be lesser from Earth. Despite predictions of low solar wind velocities and an understanding of an appreciable underestimation, there are no indications as to why my measured solar wind velocities are so low.

6.3.1.2. STEREO A - Vector map

A flow vector map analysis from the difference images were undertaken from 21 November 2013 06:49 UT to 25 November 2013 04:49 UT. As seen in Figure 6.20, both techniques produced similar solar wind velocities when mapped onto the comet's orbital plane.

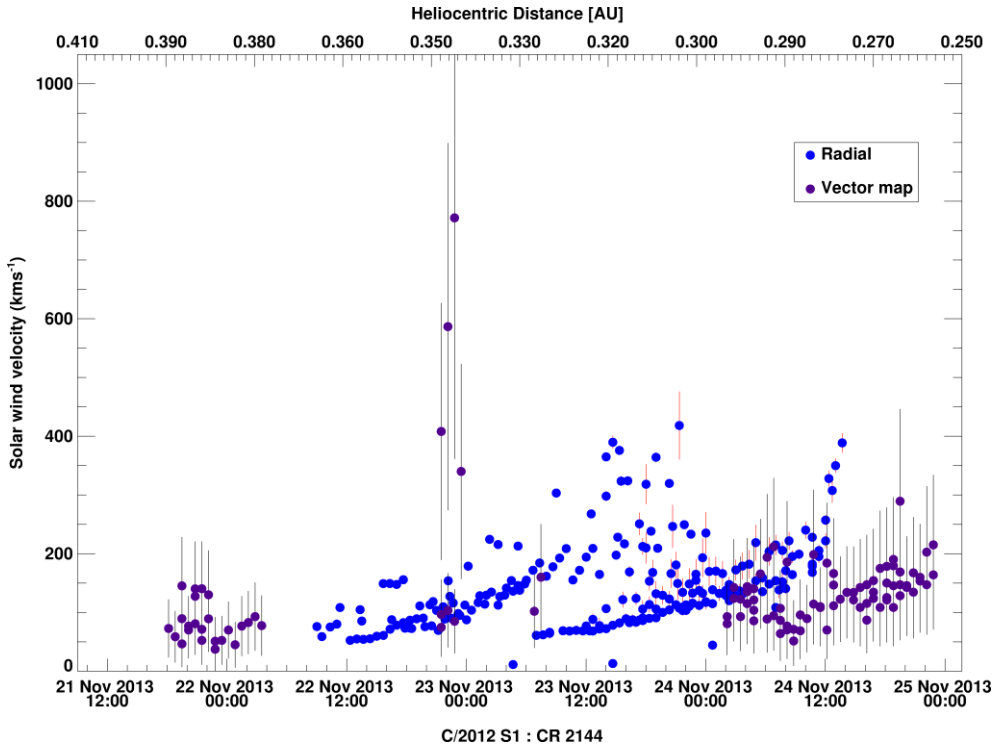

Figure 6.20: Solar wind velocities as deduced from C/2012 S1 (ISON) from both techniques yielded similar estimates.

The images were categorised in four groups according to separate sets of features and their evolution tracked over short temporal scales [Figure 6.21]. The second image group produced the deviating set of fast velocities on 23/12/2013 00:00 UT, which displayed an abrupt kink forming and travelling rapidly downtail. This does seem to be a cometary tail feature, producing a tail DE, though it is difficult to resolve these small scale features clearly. The last measurement of the four fast velocities is of the tail DE. Feature set 4 is of the final tail disconnection. The plasma bundles disappeared and reappeared as distinct features as they evolved, making it sometimes difficult to track these features against the sky background. From 24/11/2013 19:29 UT, the plasma bundles are fuzzy and therefore, estimates should be considered to have a larger uncertainty than reported here.

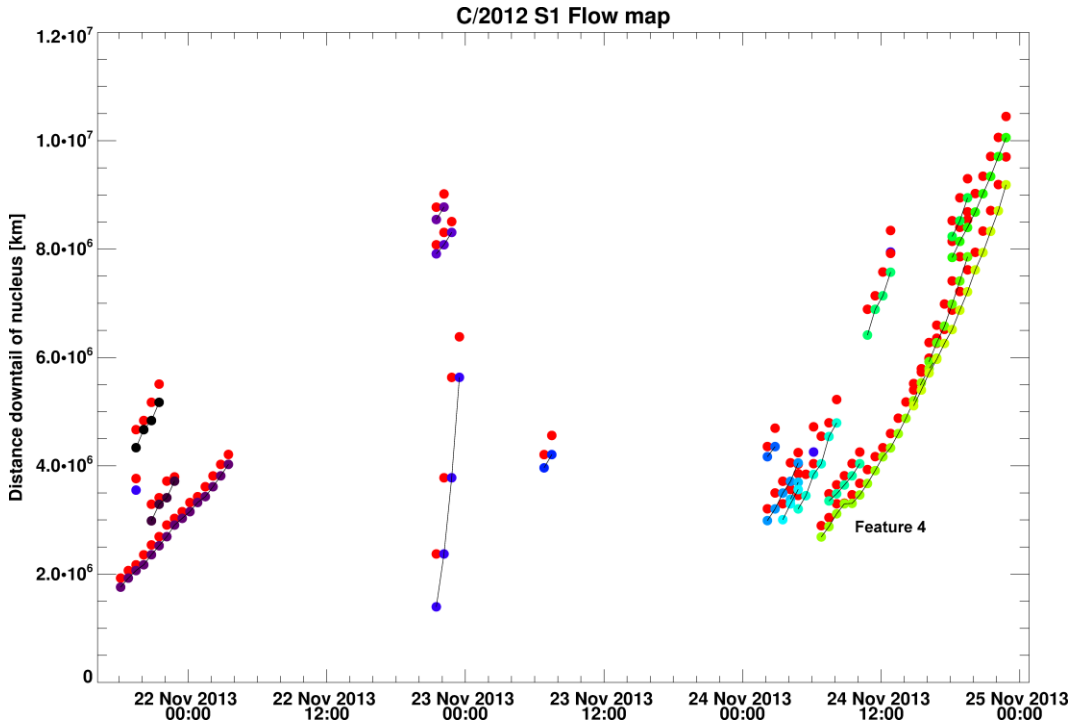

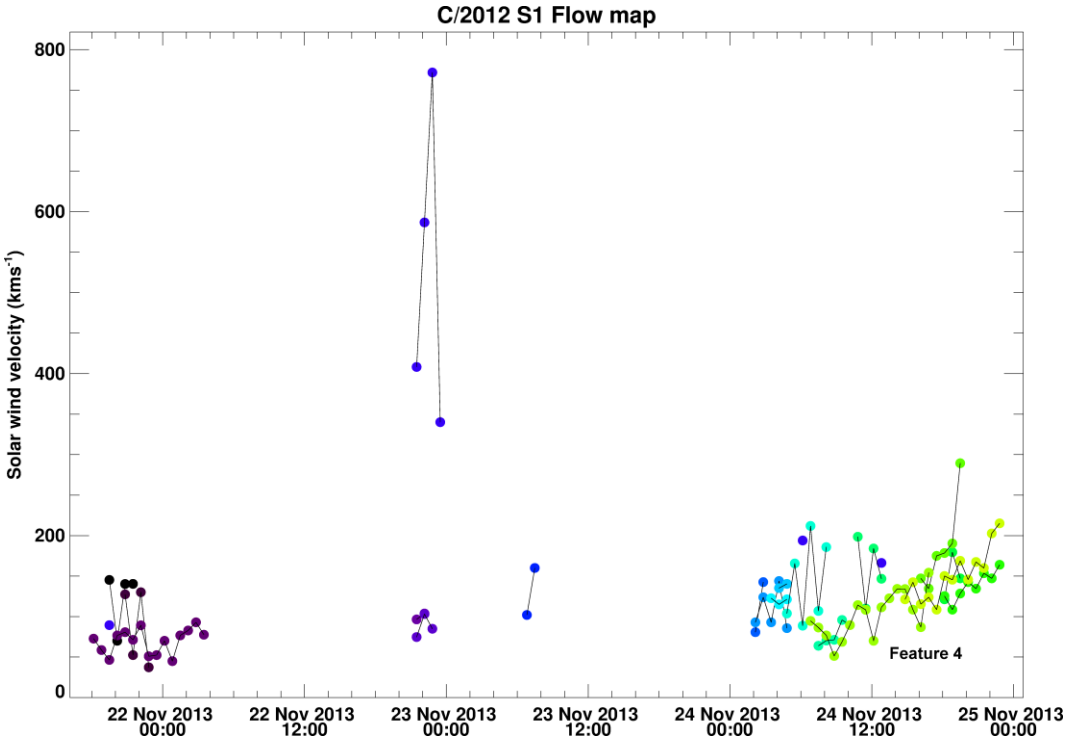
C/2012 S1 Flow map
Solar wind velocity (kms-1)
800
600
400
200
0
Feature 4
22 Nov 2013 00:00
22 Nov 2013 12:00
23 Nov 2013 00:00
23 Nov 2013 12:00
24 Nov 2013 00:00
24 Nov 2013 12:00
25 Nov 2013 00:00

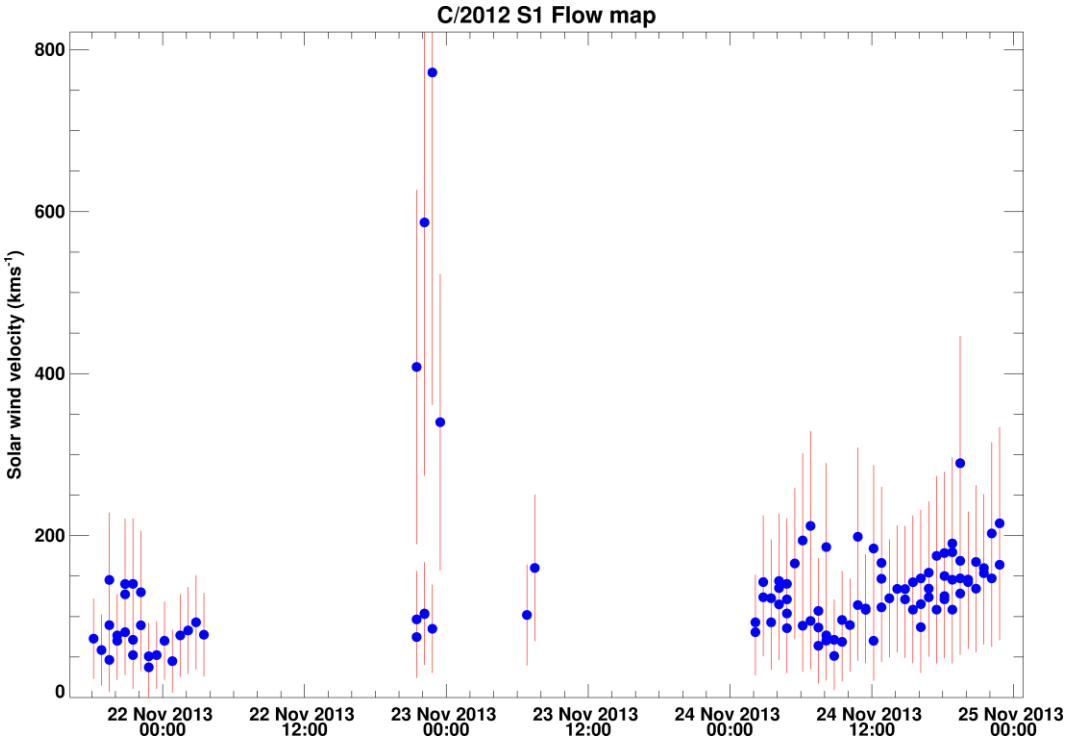
C/2012 S1 Flow map
Solar wind velocity (kms-1)
800
600
400
200
0
22 Nov 2013 00:00
22 Nov 2013 12:00
23 Nov 2013 00:00
23 Nov 2013 12:00
24 Nov 2013 00:00
24 Nov 2013 12:00
25 Nov 2013 00:00

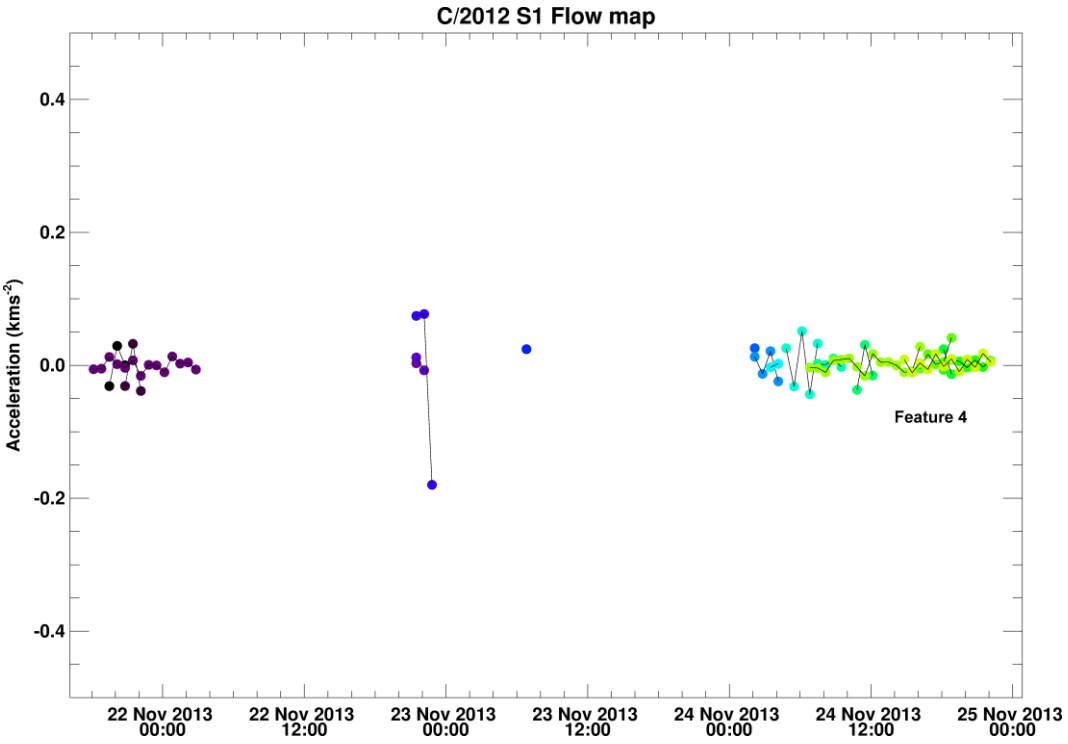

Figure 6.21: Solar wind velocities deduced from the motions of individual plasma bundles in consecutive STEREO A images of the ion tail. Plot 1 shows the distances at which each plasma bundle was measured. Features that could be recognised in subsequent images are linked and coloured differently. Plots 2 and 3 show the solar wind velocities for each feature set and the errors. Plot 4 shows the acceleration of each plasma bundle.

6.3.1.3. Ground-based observations

Image statistics

Of 71 initial test images, only 3 images were successfully processed with a total of 10 solar wind velocities extracted from them. Of the rest, two were not plate-solved correctly and it was not possible to extract solar wind velocities from 51 images that had been successfully processed through my software. For most images, the angle between the extended radial vector and the comet's orbital plane remained narrow for most of the observing period. The majority of the images showed the highly dynamical and fine structured ion tail of comet ISON fanning widely with its edges either lying on the radial vector or leading the comet motion.

Data coverage

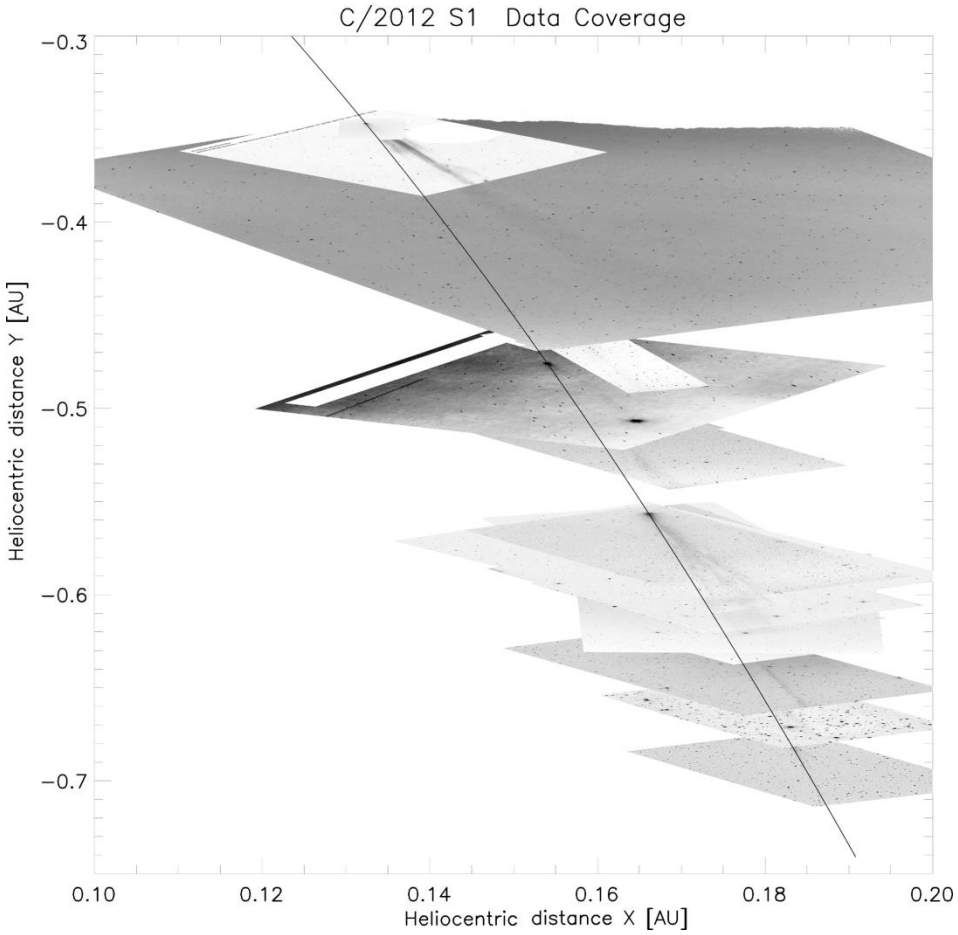

Figure 6.22: Date coverage of C/2012 S1 pre-perihelion. The images were collected by a dedicated network of amateur astronomers worldwide.

Figure 6.22 only shows the data coverage of the images that were successfully processed within my software from 12/11/2013 to 22/11/2013.

Results

The few radial velocities obtained were similar to the low velocities from the STEREO A data. Seven of the estimates ranged from 50-100 km s^{-1} with the remaining 3 centred at about 200 km s^{-1}. Both the slow and fast solar wind sources, using a fixed 400 km s^{-1} and 800 km s^{-1} speed) would have originated from neighbouring regions on the solar wind source surface [Figure 6.23] as the comet sampled the inner heliosphere 0.40 - 0.45 AU from the solar centre.

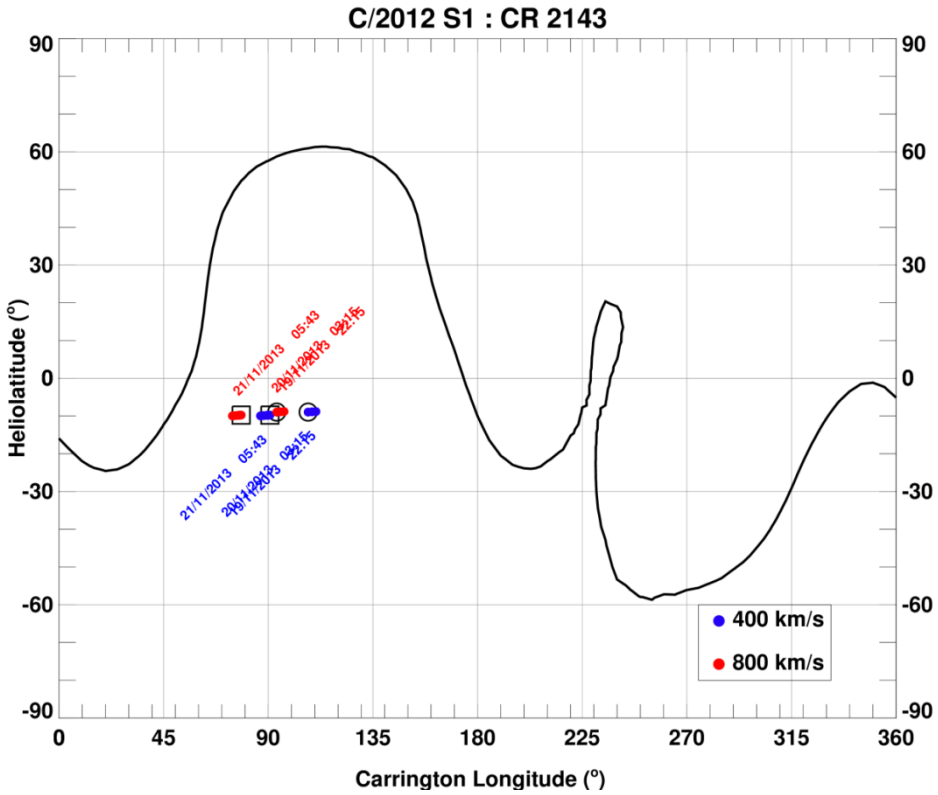

Figure 6.23: Mercator map for C/2012 S1 for CR 2143

These low values are not unprecedented. Sizonenko (2007) reported two similar velocity estimates to those presented here for comet C/2004 Q2, which they attributed to a large change in the tail orientation of the comet, the likely cause of which was a transition region.

6.3.1.4. Ground-based Vector maps:

Four images out of a ten-frame sequence on 16/11/2013 by W. Skorupa were analysed. The image series showed faint trackable structures moving radially over a period of 45 minutes. The edges of the structures were difficult to determine, though they implied low velocities, similar to the results of the radial technique.

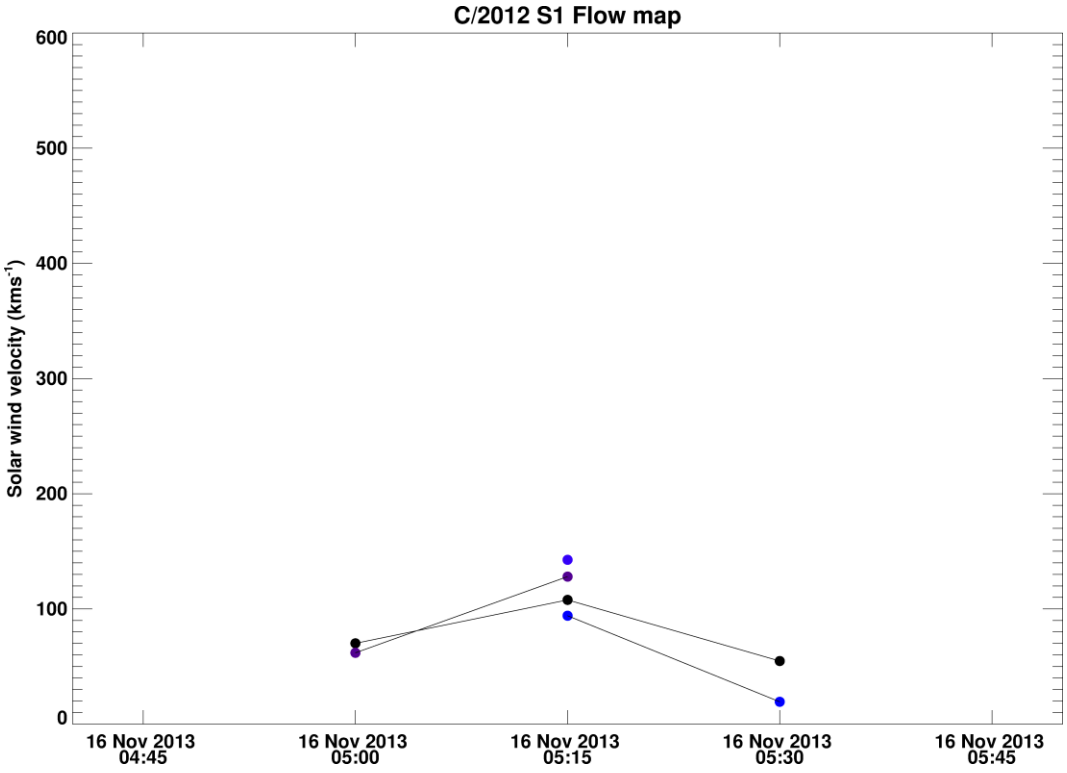
C/2012 S1 Flow map
Solar wind velocity (kms^{-1})
600
500
400
300
200
100
0
16 Nov 2013
04:45
16 Nov 2013
05:00
16 Nov 2013
05:15
16 Nov 2013
05:30
16 Nov 2013
05:45

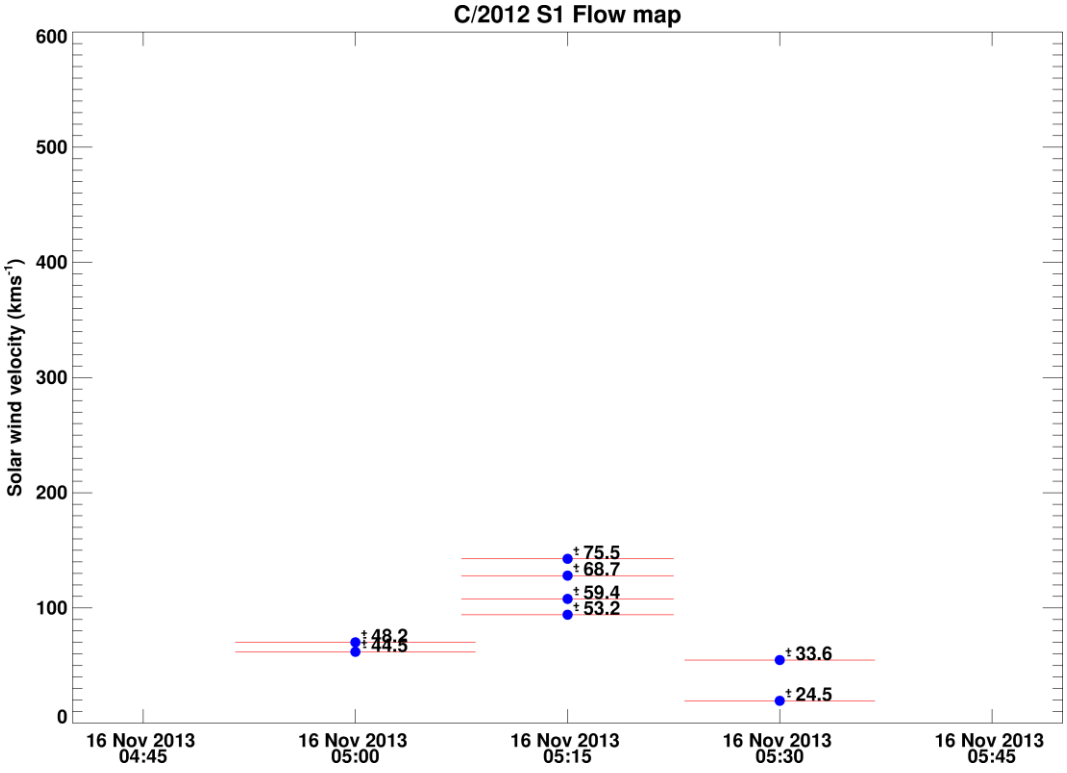
C/2012 S1 Flow map
Solar wind velocity (kms^{-1})
600
500
400
300
200
100
0
± 75.5
± 68.7
± 59.4
± 53.2
± 48.2
± 44.5
± 33.6
± 24.5
16 Nov 2013
04:45
16 Nov 2013
05:00
16 Nov 2013
05:15
16 Nov 2013
05:30
16 Nov 2013
05:45

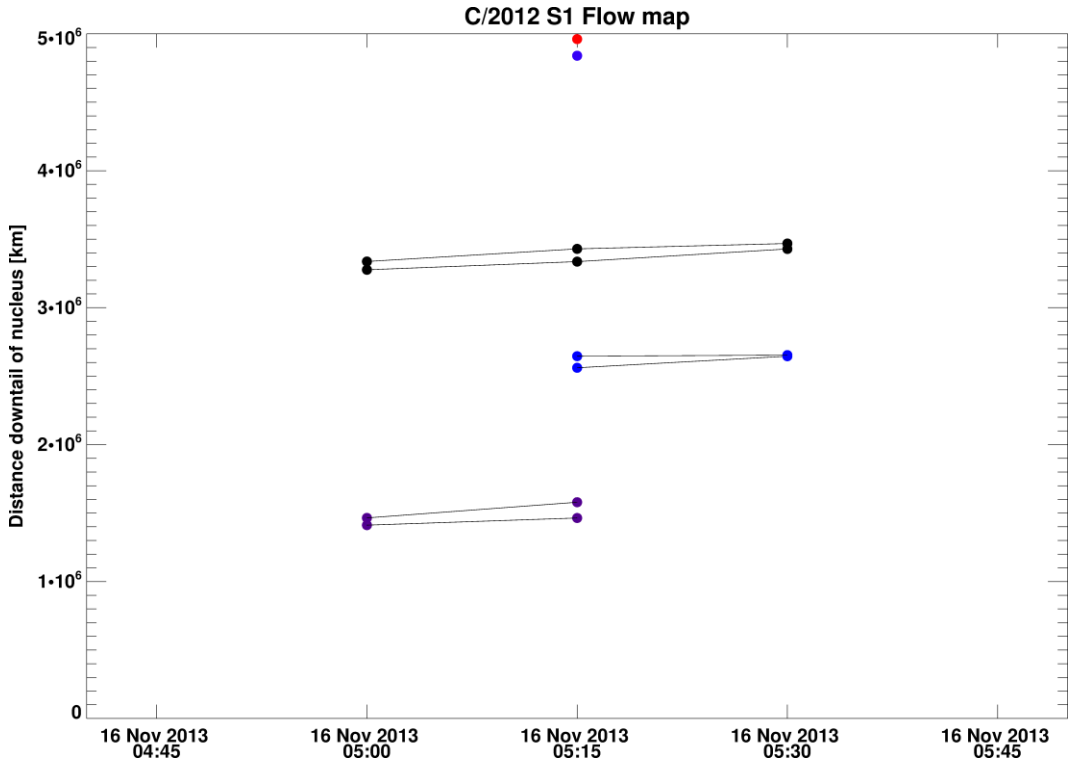

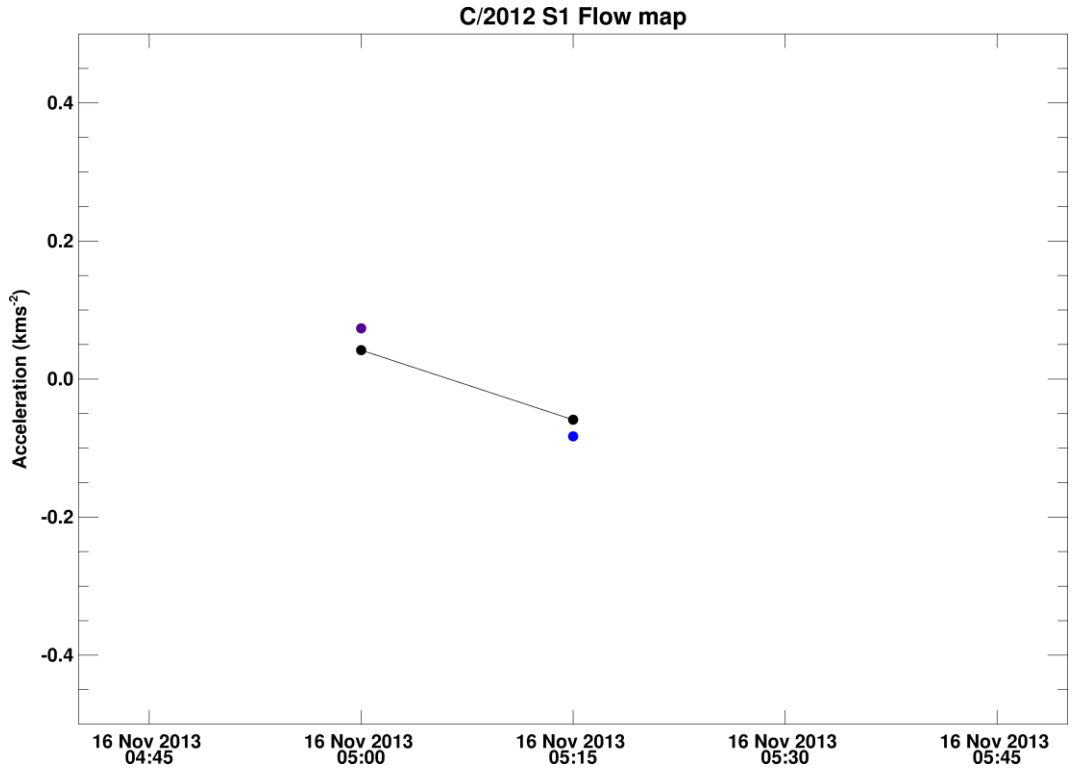

Figure 6.24: Solar wind velocities determined from an animation sequence by W. Skorupa.

6.3.1.5. Ground-based Tail ray

Images of C/2012 S1 from Earth commonly displayed wing-like structures enveloping the ion tail. Figure 6.25 is a reproduction of the different tail rays sampled for four separate sets of tail rays over a period of ~3 days.

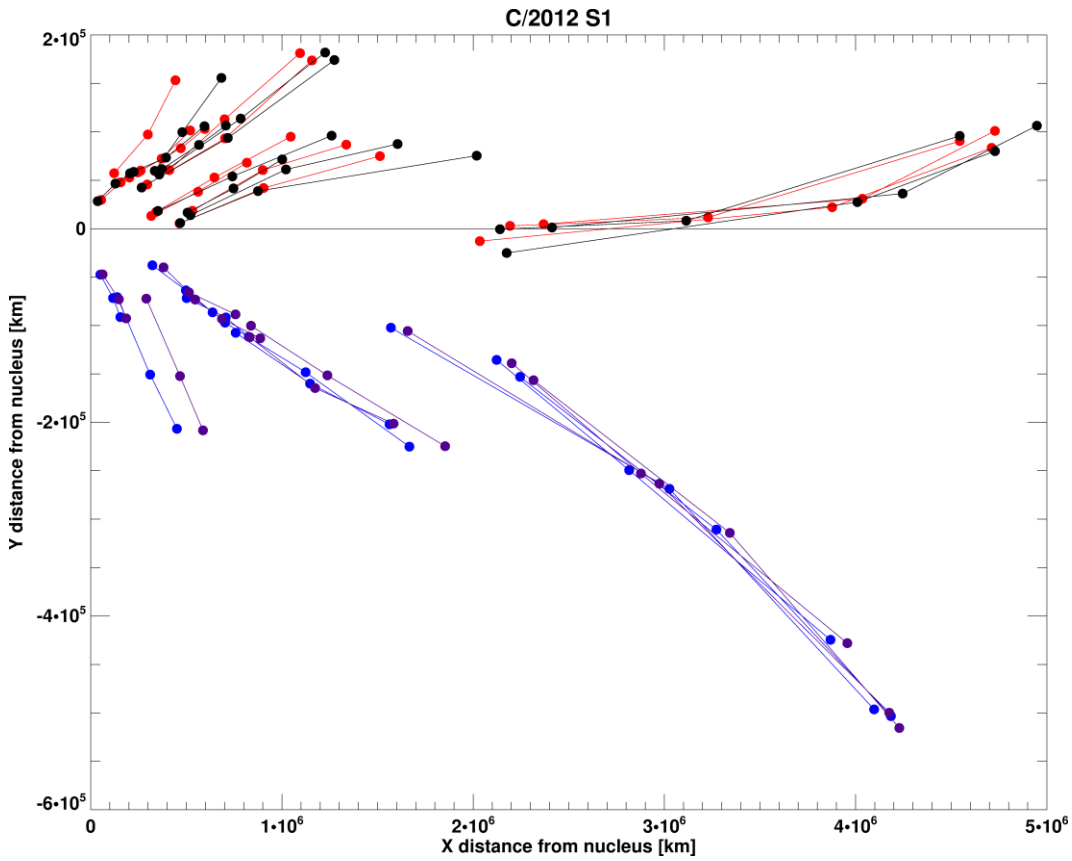

Figure 6.25: Sampled tail rays for C/2012 S1 from 4 separate sets of tail ray sequences, covering a span of ~3 days. Each image was mapped onto the comet's orbital plane.

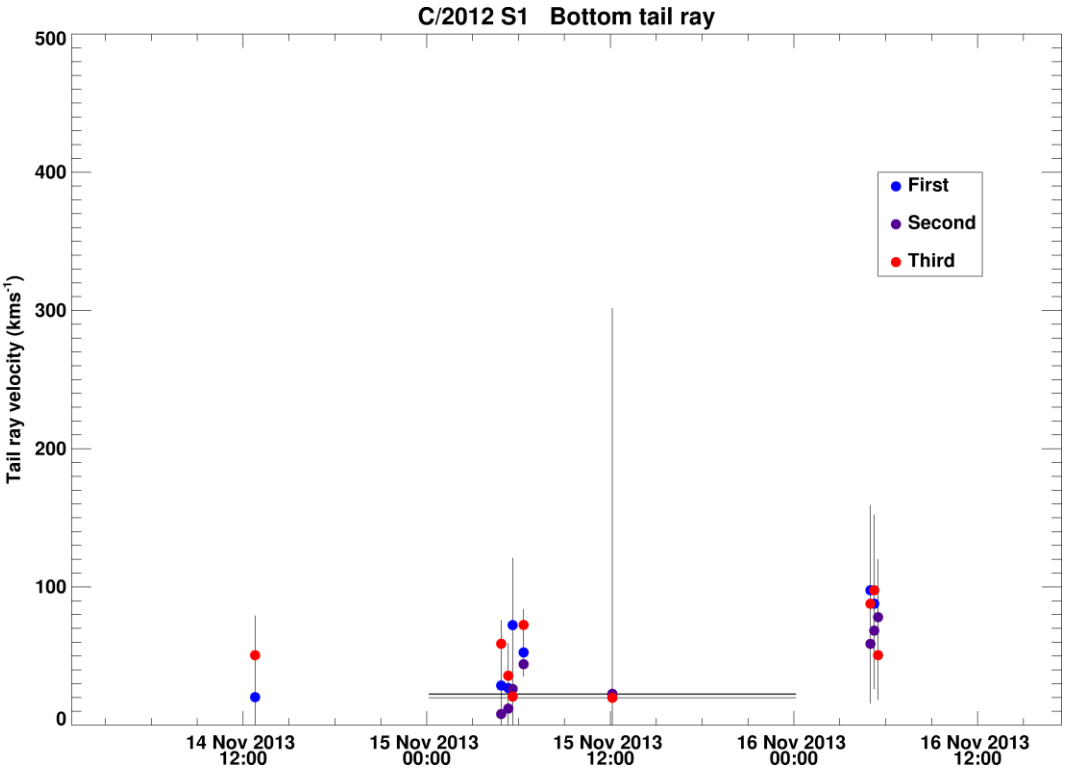
C/2012 S1 Bottom tail ray
Tail ray velocity (kms^{-1})
500
400
300
200
100
0
First
Second
Third
14 Nov 2013 12:00
15 Nov 2013 00:00
15 Nov 2013 12:00
16 Nov 2013 00:00
16 Nov 2013 12:00

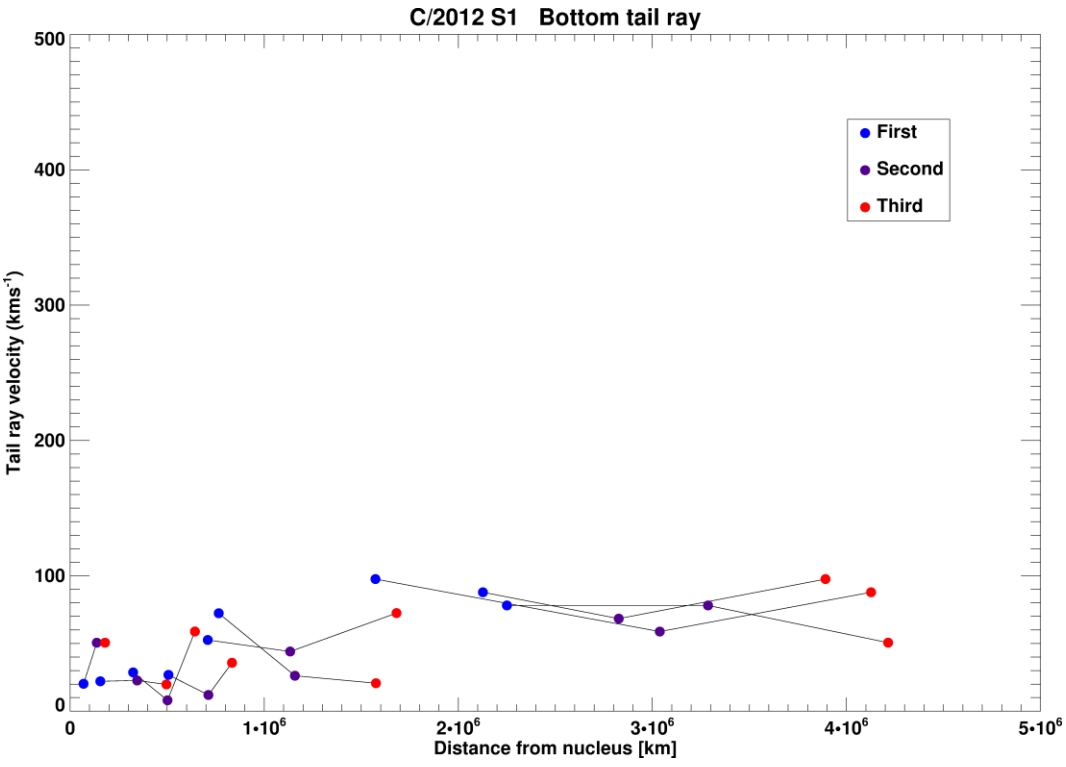
C/2012 S1 Bottom tail ray
Tail ray velocity (kms^{-1})
500
400
300
200
100
0
First
Second
Third
0
1•10^6
2•10^6
3•10^6
4•10^6
5•10^6
Distance from nucleus [km]

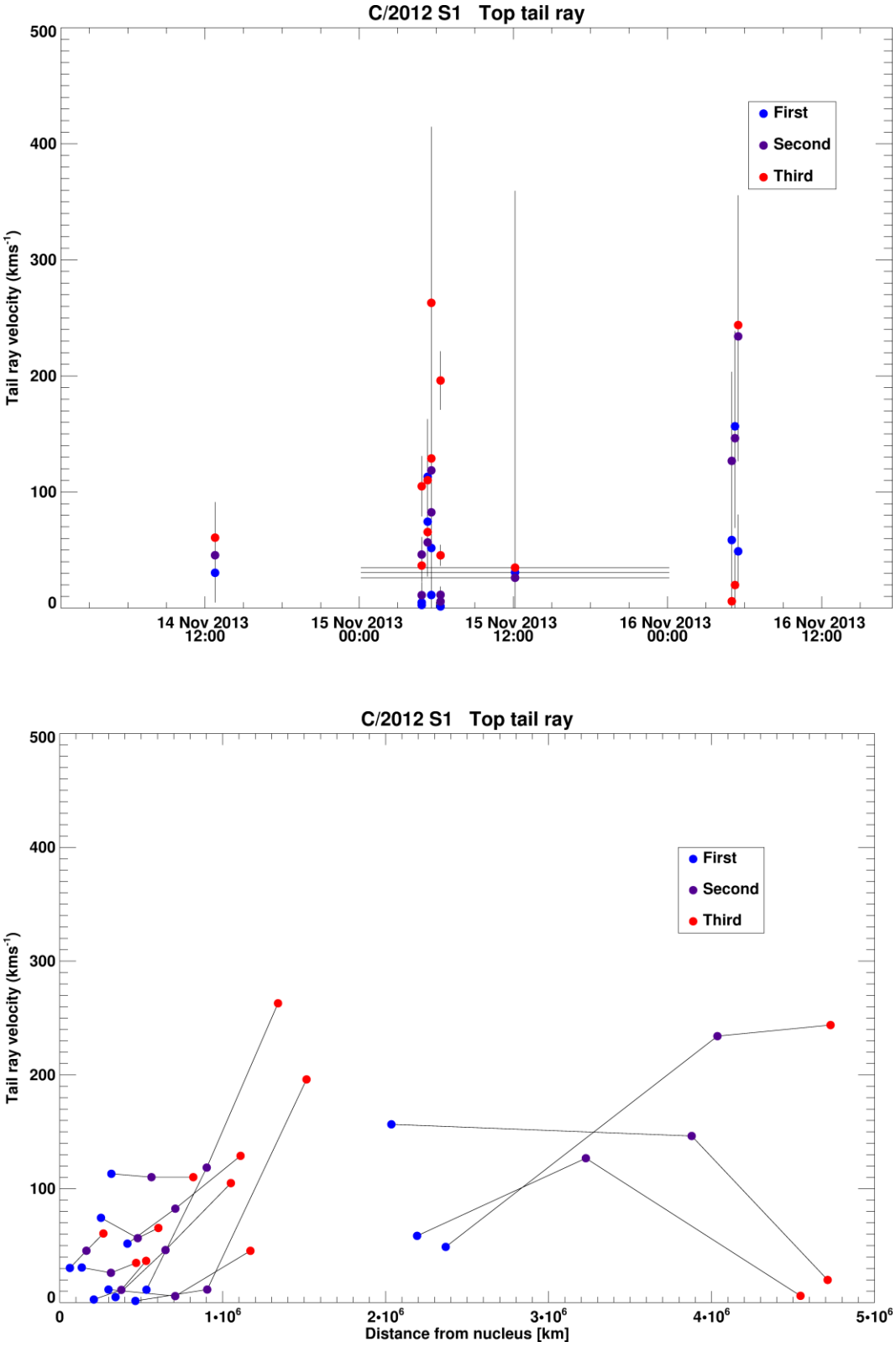

Figure 6.26: Tail ray velocities as observed from Earth.

The four sets of images were combined in Figure 6.26. The first set of tail rays were tricky to measure. More symmetrical pairs were visible but not measured due to their proximity to the main tail axis, with their orientation near-parallel to the radial vector. Set 2 were perfect examples of clearly defined, well separated top tail rays, i.e. tail rays on the northern side of the main ion tail. The bottom tail rays proved harder to measure: their full extent could not be sampled. Both halves exhibited wave-like structures. The top tail rays were observed to accelerate to slow solar wind speeds, whilst velocities from the bottom tail rays were harder to interpret. The longest tail ray pairs (set 4) were taken from an animation by W. Skorupa. The tail rays extended up to 8 x 10^6 km. The decreasing brightness of the tail rays would have made further estimates unreliable. The measurements were taken from the wing-like tail rays, with the tail rays mostly producing slow solar wind velocities. As previously, these measurements should be taken lightly as small errors in sampling the tail ray centre can lead to large variations in the tail ray velocities determined. Overall, the top tail rays, mostly show an accelerating trend, whilst the bottom tail ray showed a flat velocity profile along the tail ray.

6.3.1.6. GTC observations

A set of 19 uncalibrated images observed with 2-second exposures in the U, G and R bands from the Gran Telescopio Canarias (GTC) show evolution of the near-nuclear tail rays. The GTC images comprise the output of two CCDs, peppered with a small number of stars due to their small combined FOV. When compared with a sky catalogue, the astrometric parameters within the FITS WCS matrix showed that the images were off by ~6 seconds in right ascension and ~ 70-75 arcseconds in declination [Figure 6.27]. This causes a significant shift of the comet's nucleus off the predicted orbit. Whilst they do coincide, this would yield erroneous values of the tail ray folding rate, since the projection mapping will not be calculated correctly. The images were also processed through IDL and plotted in equatorial coordinates [Figure 6.28], thus confirming that the image's astrometry is incorrect. To circumvent the issue, the images were processed through Astrometry.net, though the lack of stars on both chips made identification of the correct coordinates unfeasible. The incorrect FITS astrometric parameters for these images are still under investigation.

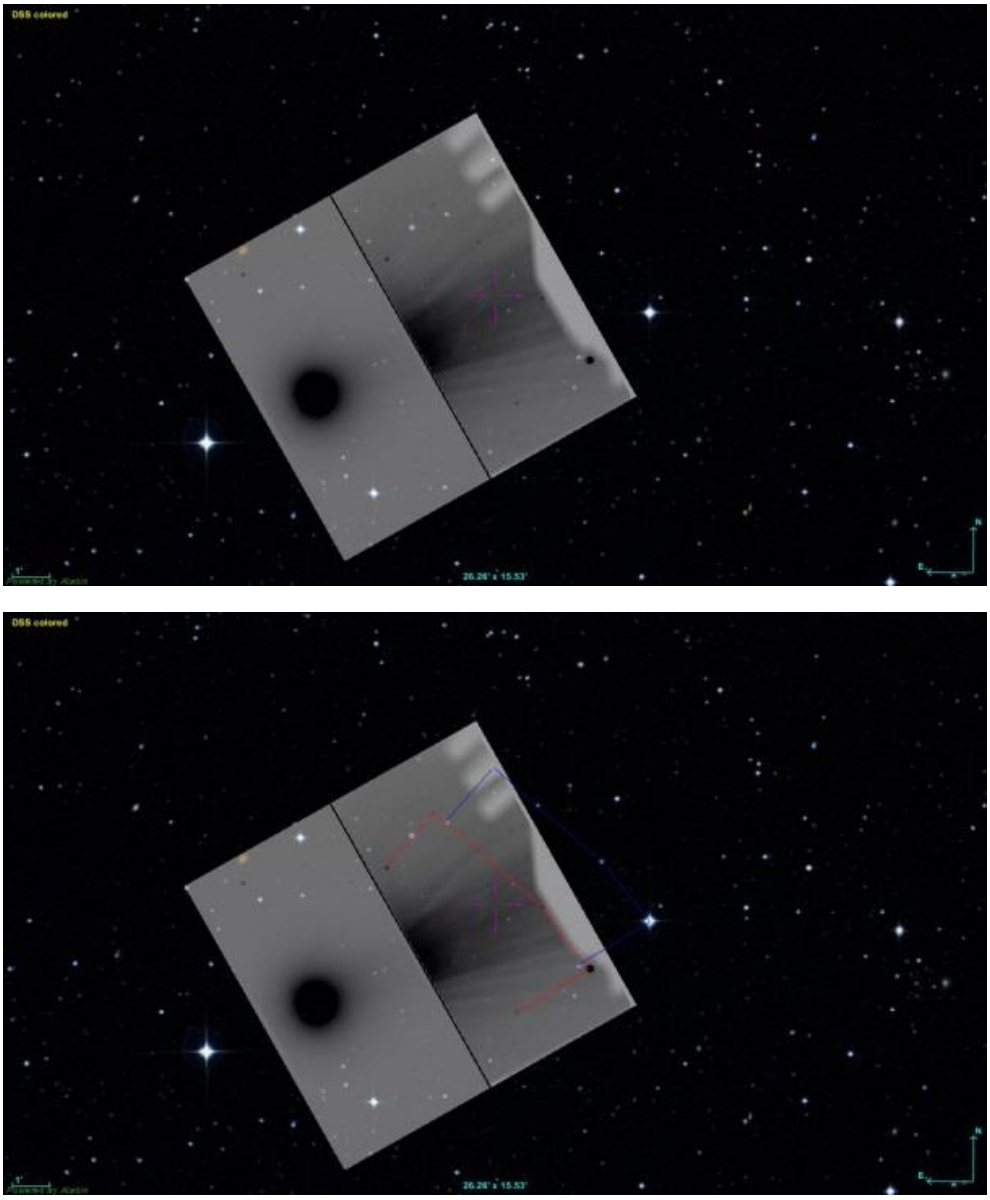

Figure 6.27: GTC image of comet ISON overlaid over the DSS catalogue in Aladin. If astrometric solutions were correct, the stellar positions should have aligned. On the bottom, I include a manual grouping of bright stars, easily identified in both the sky catalogue and the GTC image. It is clear from the similar constellation shape, that the offset is due to incorrect WCS information.

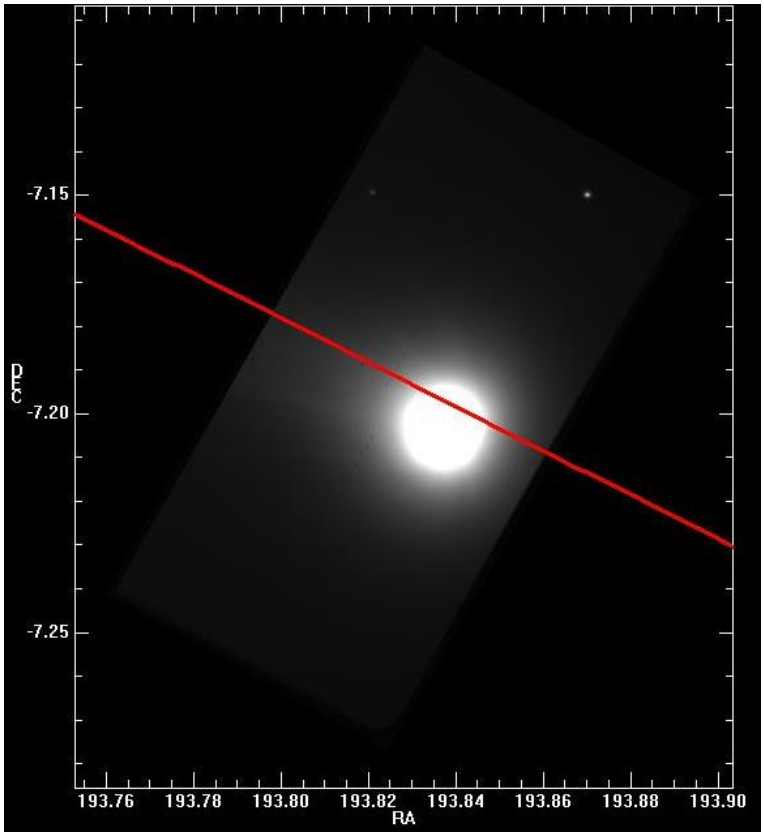

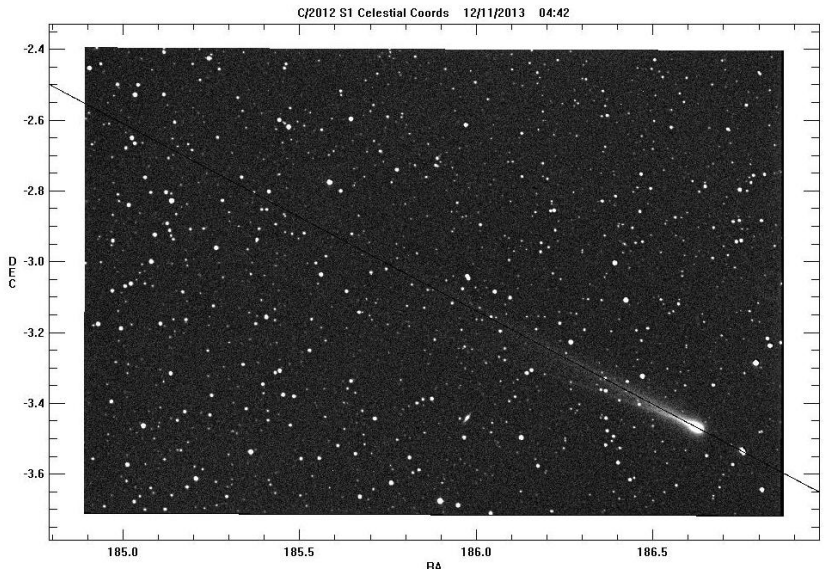

Figure 6.28: As further evidence, the image on the left is CCD2 of the previous GTC image showing the nucleus of comet ISON mapped onto its equatorial coordinates using the provided WCS information. The comet's orbit is in red. On the right, an amateur image of comet ISON by Angel and Hartinen is shown in the same reference frame and the comet's orbit in black. As can be seen here, the orbit passes through the comet nucleus neatly and must thus be due to the encoded WCS matrix.

6.4. Pan-STARRS (C/2011 L4)

Discovered on 2011 June 6 (Wainscoat et al. 2011), the first apparition of Oort cloud comet C/2011 L4 (Combi, Bertaux, et al. 2014) was well observed both from Earth and STEREO B. C/2011 L4 was not as well studied as the two previously described sungrazing comets, though SOHO/SWAN UV observations of the comet's Hydrogen Lyα coma revealed an asymmetry in its water production behaviour pre- and post- perihelion (Combi, Bertaux, et al. 2014), which matched up well with its lightcurve trend (See aerith.net for C/2011 L4). Its most striking feature was the extensive striated dust tail as view from STEREO B and from Earth for a shorter period. As Earth transited the comet's orbital plane, we were presented with an edge-on view of the comet's dust tail, producing the rare optical phenomenon of an anti-tail, i.e. a sunward spike of the dust tail, with the main dust tail 180^{o} away, pointing in the anti-sunward direction [Figure 6.29]. Ivanova et al. (2014) remarked that the dust production activity was already quite high whilst the comet was at ~ 4 AU. The J2000.0 orbital elements were Inclination (i) = 84^{o}.2; ascending node = 65^{o}.7, Perihelion date (T) = 10/03/2013, 04:05 UT (JPL Horizons)

6.4.1. Ground based observations

Of 41 fully processed images post-perihelion [Figure 6.30], only 3 samples could be extracted from 1 image. Most images did not have an observable ion tail. The ion tail, when observed, was extensive, straight and very close to the radial vector and lacked any features usually associated with a turbulent solar wind flow. High velocities between 1100 and 1400 km s^{-1} were measured along the tail. No distinct cause of the extreme velocities could be identified. The main goals for amateur astrophotographers were likely the aesthetics of the dust tail and anti-tail and determining the comet's photometry and Afρ (Afrho) measurements. Images for comet Pan-STARRS (C/2011 L4) were seldom exposed long enough to image the ion tail. This is likely due to the comet's extensive and bright dust tail, which overlapped with the ion tail's orientation. The other images were unusable as the Earth traversed the comet's orbit in late May 2013 and the technique failed during this period. Afρ (A'Hearn et al. 1984) is a measure of the product of the albedo, optical density of the dusty coma, i.e. the total cross section of grains filling the

FOV, and the radius of the coma (in km). It can be used as a proxy for the dust production rate – the larger the Afρ value, the dustier the comet (http://cara.uai.it/measuring-comets).

Figure 6.29: Image of extensive dust tail with a small anti-tail as viewed from Earth. Observer: Mobberley on 21/03/2013 at 09:19 UT.

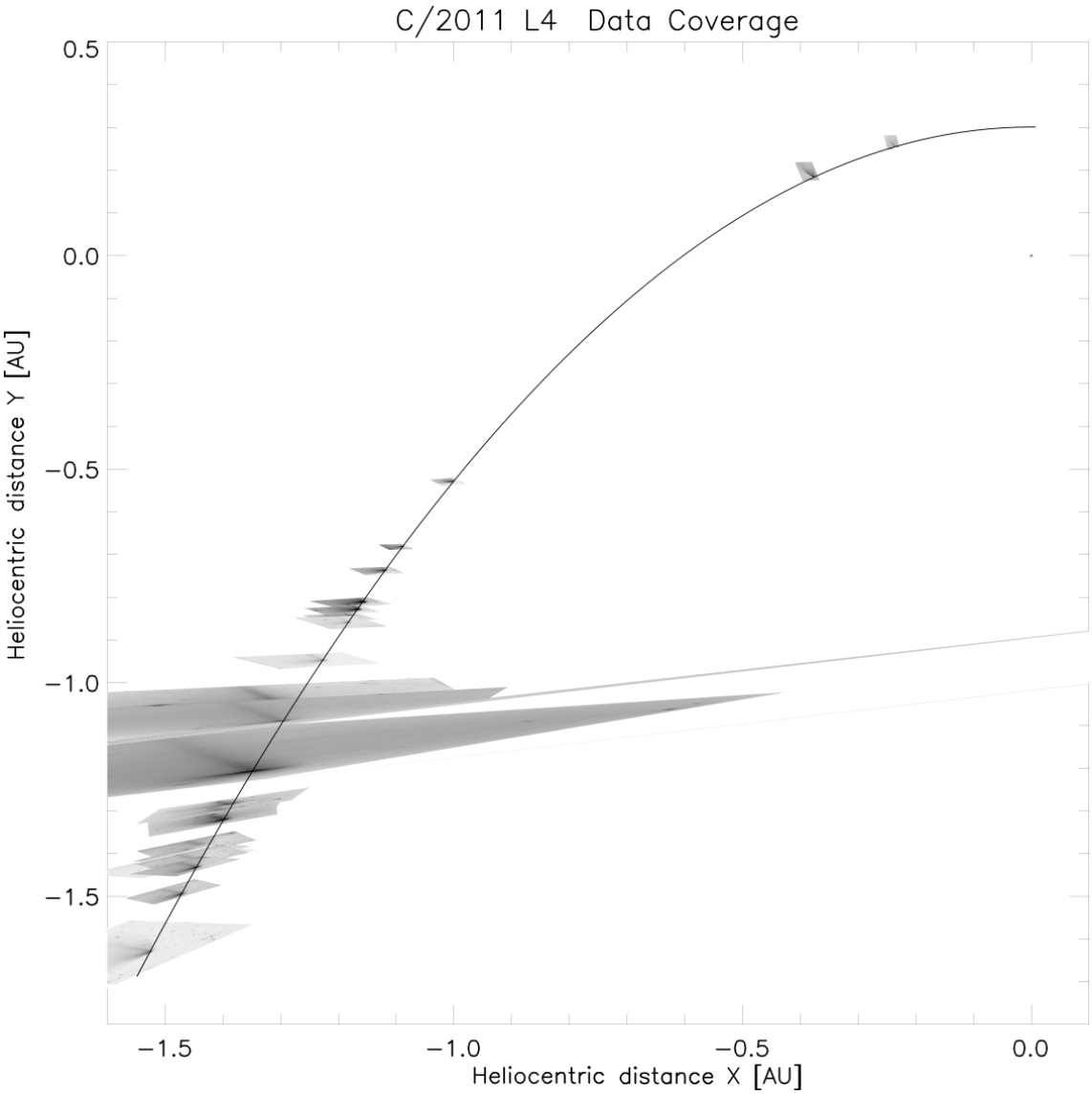

Figure 6.30: Post-perihelion data coverage of C/2011 L4 from Earth.

6.4.2. STEREO B

197 difference images were fully processed. 742 solar wind velocity estimates were extracted from 190 images. The 7 images that were rejected were due to the ion tail's proximity to the dust tail or image defects, which would have made my analysis unreliable. There were no data points deemed to be unreliable. There were a number of turbulent periods; hence these images were not identified individually. C/2011 L4 showed no folding ion tail rays.

This comet was an ideal target for the velocity vector map. The ion tail was very dynamic, leading just ahead of a wide and very bright, well-structured dust tail and lagging behind what may be a neutral iron (Fe) tail (Fulle et al. 2007). The difference images revealed an aberrant, sinuous tail over a large extent of the observations with multiple trackable plasma blobs and disconnection events as the comet left the STEREO HI-1B FOV. The results oscillated about conventional slow solar wind velocities. The variations seen in the later measurements corresponded to large orientation changes and increase in turbulent dynamicity in the ion tail. On March 13, 2013, the comet appeared to have two ion tails, one stemming from the expected location, the other jutting out from one of the top dust striae. This is likely a matter of perspective with a turbulent ion tail masked by the saturated, curved dust tail.

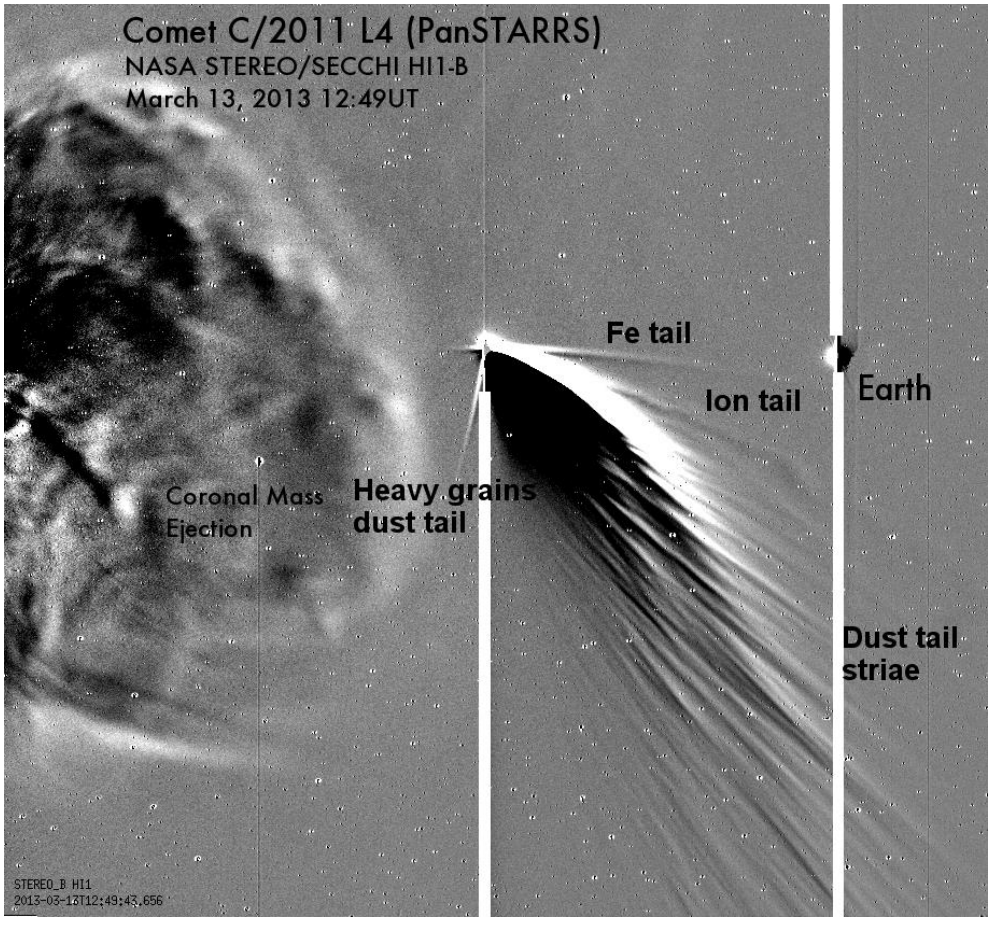

Figure 6.31: STEREO B FOV of a CME and the multiple tails of C/2011 L4 on 13/03/2013 12:49 UT. Note that it is not necessary that the CME will have interacted with the comet. The CCD blooming has been masked by the white columns.

Orbit geometry

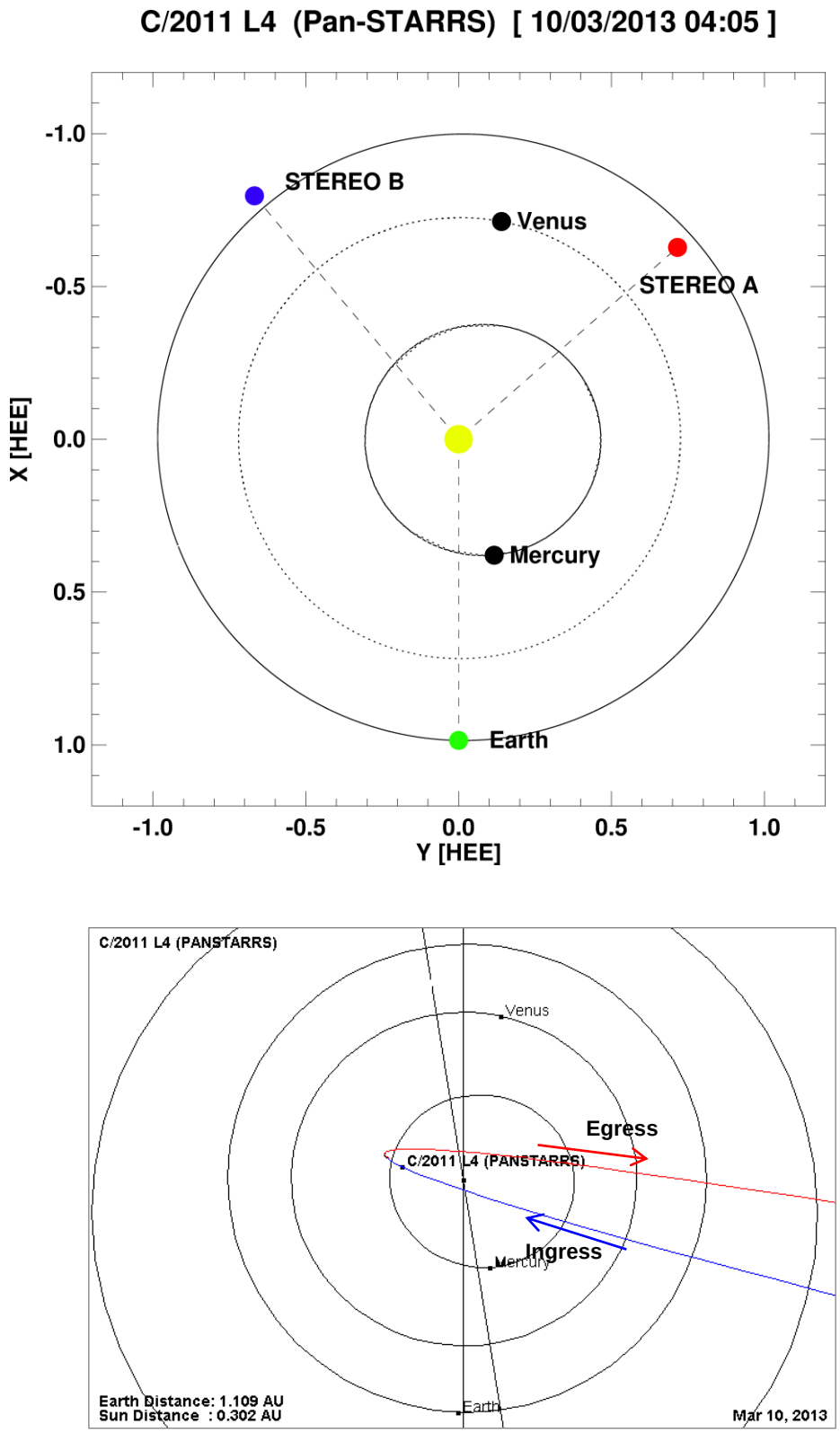

Figure 6.32: *Top*: **Orbit geometry of the multiple vantage points from which C/2011 L4 (Pan-STARRS) was observed at the comet's perihelion.** *Bottom*: **Edited image from the JPL small-body database showing the comet's orbit on the day of its perihelion.**

My period of analysis started shortly after perihelion, and extended from March 10.673 UT to 16.478 UT, when the comet was moving from southward (blue) to northward of the ecliptic plane (red) [RHS of Figure 6.32]. Although this geometry was disadvantageous for ground-based ion tail observations, STEREO B was well positioned on the far side of the Sun. Figure 6.31 shows that the orbit plane angle for STEREO B remains stable and large enough to produce reliable solar wind estimates; that of Earth clearly shows the deteriorating observing geometry, albeit over a longer period of time.

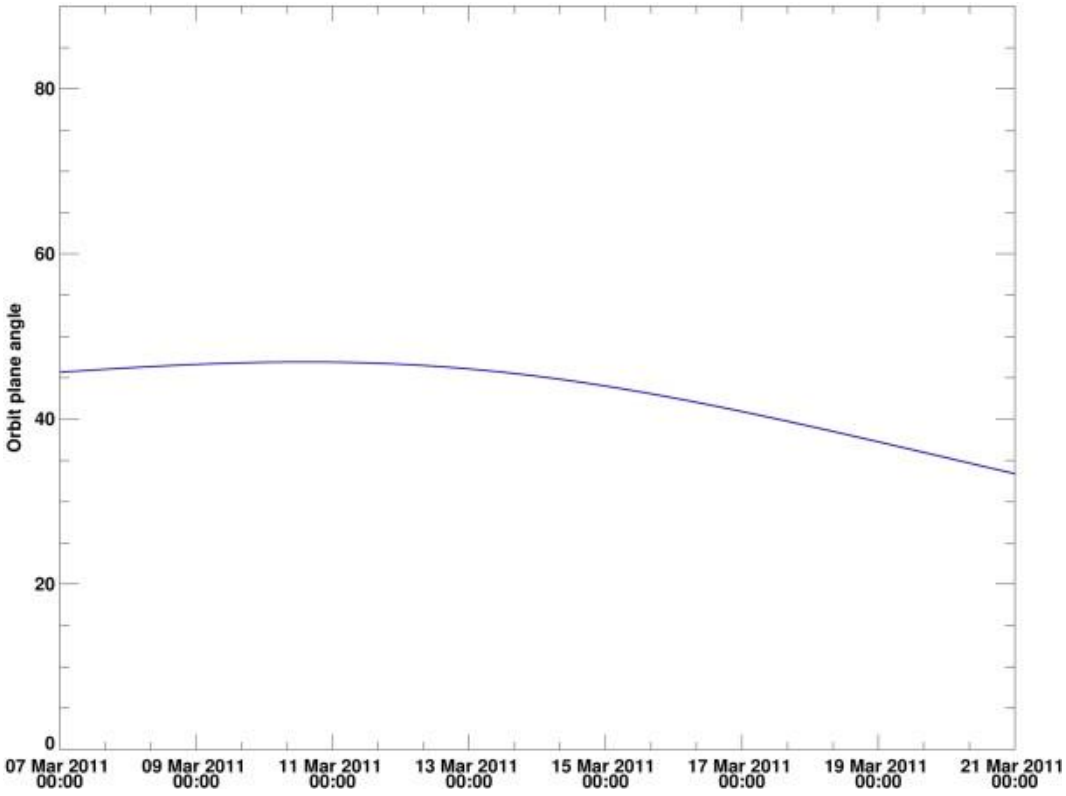

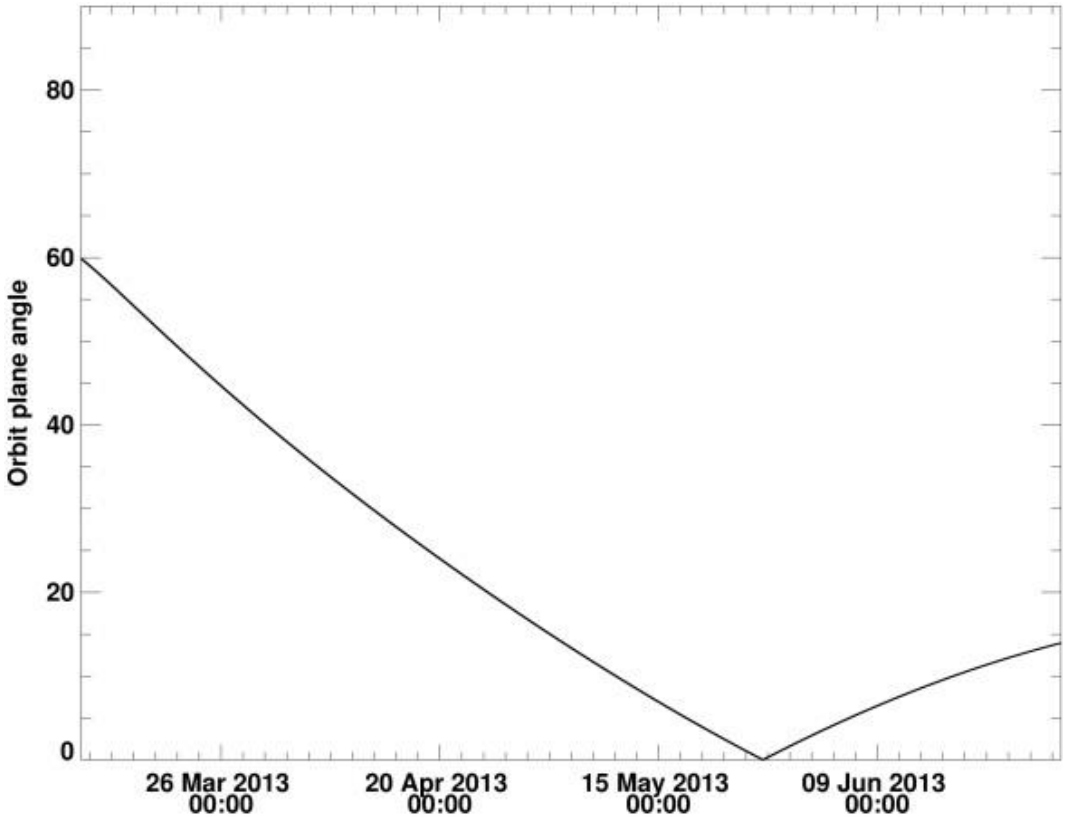

Figure 6.33: Orbit plane angle of comet C/2011 L4 from STEREO B and Earth.

6.4.3. Radial solar wind speeds

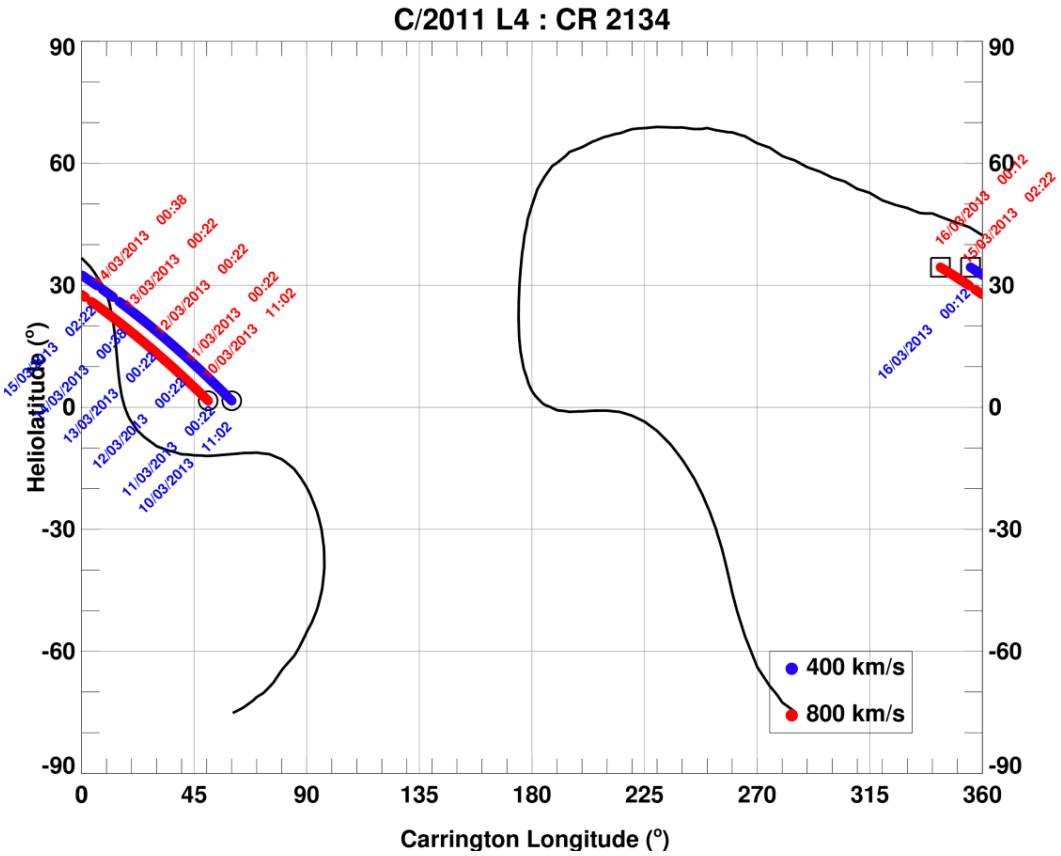

Figure 6.34: Mercator map for CR 2134. The comet should experience slow solar wind speeds as it samples solar wind plasma sources ever closer to the neutral line.

Assuming a bimodal distribution of radial solar wind speeds of 400 km s^{-1} and 800 km s^{-1} [Figure 6.34], we can estimate the approximate origins of the solar wind plasma flux tubes on the solar wind source surface. The predicted sources on the Mercator map corroborate the solar wind velocity estimates we derive from comet C/2011 L4 as we expect to mostly encounter a turbulent, equatorial flow of the slow solar wind. According to the Mercator map, the comet will encounter the HCS between the 14th and 15th March. A dedicated solar observatory allowed the continuous, regular monitoring of the HCS crossing and the resultant DE. The tail may have detached at midnight on the 15th March 2013, followed by an outflow of multiple distinct condensation knots over several hours. There is a large tail orientation change between 12:09 and 16:09 UT. The data gap around 15/03/2013 00:00 UT corresponds to image defects due to incorrect processing for the difference images in the period shortly following the predicted HCS

crossing. The ion tail was analysed, though no data was saved during this period to prevent unreliable estimates of the solar wind velocity. The measured values hovered at ~ 300 km s^{-1}, in line with the other measured velocities.

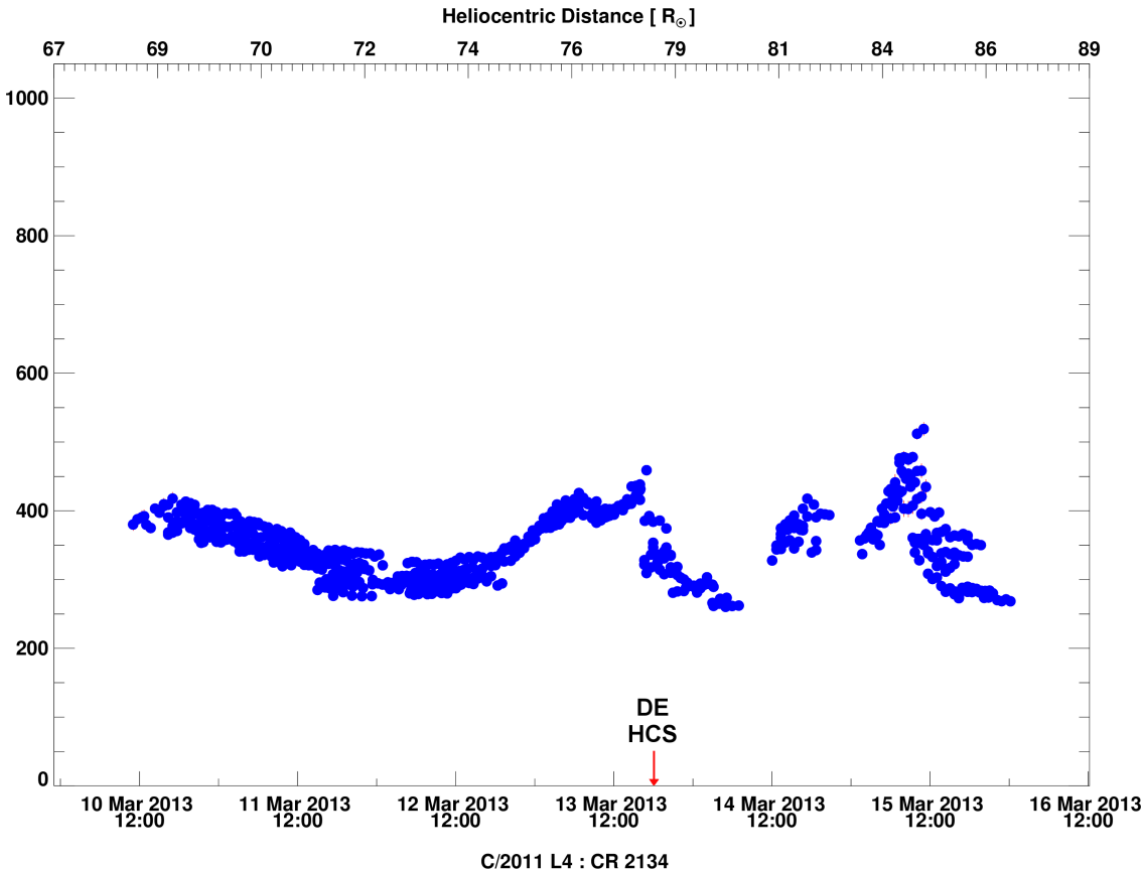

Figure 6.35: Post-perihelion solar wind velocities for C/2011 L4, based on observations with STEREO HI-1B.

Table 6-2: Observed time for CME eruptions, speed, central position angle (CPA) and angular width from the CDAW CME catalogue. The comet is between position angles 95º to 55º and the solar axial tilt is -23º.

Date	Time (UT)	Linear speed (km s^{-1})	CPA (º)	Angular width (º)
11/03/2013	13:48	241	93	116
12/03/2013	10:36	1024	74	196
12/03/2013	23:48	481	1	112
13/03/2013	00:24	523	124	127

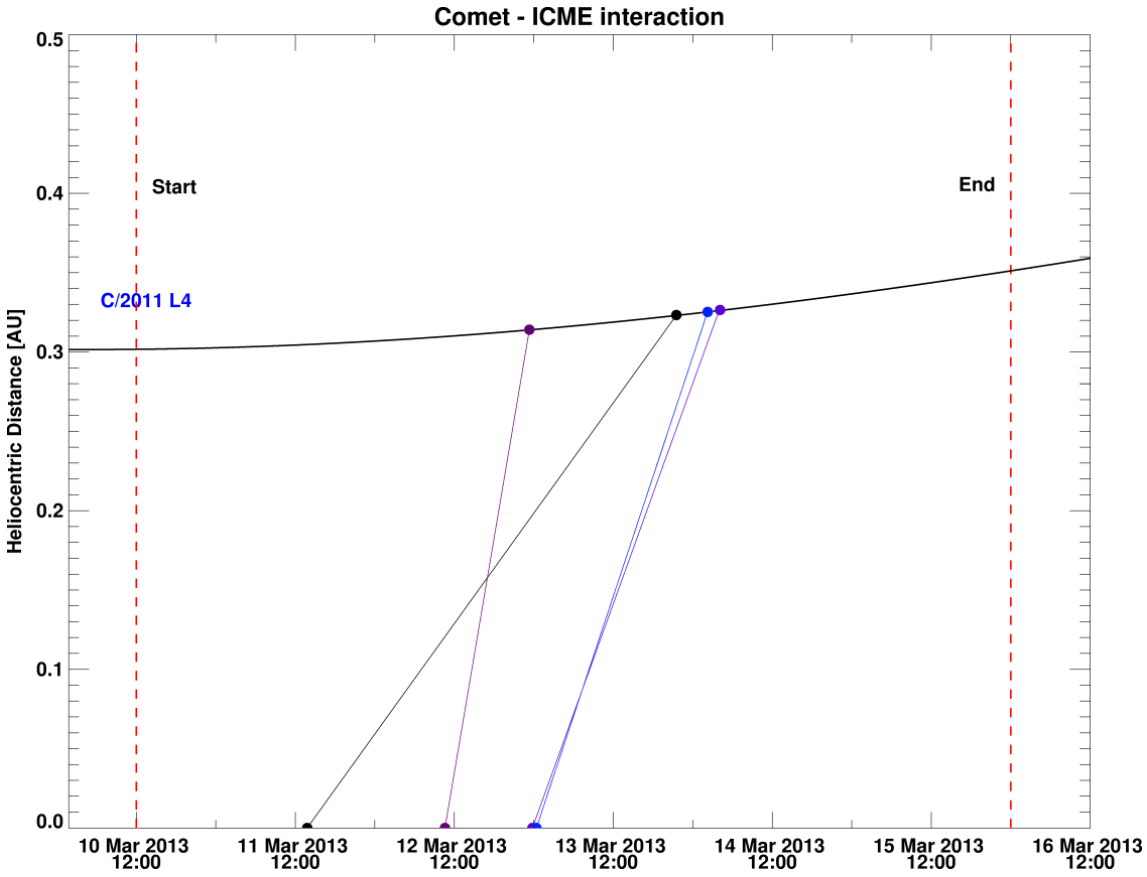

Figure 6.36: Shock Arrival Times (SATs) at C/2011 L4's orbit during my analysis.

The comet's outbound trajectory sampled the solar wind between r_H ~68 $R_\odot$ (~0.316 AU) and ~87 $R_\odot$ (~0.405 AU). The velocities match well with the ENLIL predictions. The MHD model predicts a velocity drop from ~400 km s^{-1} to 250 km s^{-1}, a steady slow solar wind of ~250 km s^{-1} up to 14/03/2013, when it would encounter a moderately fast solar wind flux tube. This would correspond to a speed hump of 450 – 550 km s^{-1} starting 14/03/2013 ~12:00 UT and lasting for two days. The velocity peak would occur at approximately 15/03/2013 21:00 UT, where I register a decreasing solar wind flow. The start of the enhanced solar wind velocity region matches well with my data, though the ensuing period indicates that the comet would have traversed the fast solar wind region by 15/03/2013 18:00 UT. It should be noted that this region comes with a notably large longitudinal and latitudinal non-radial velocity components (~20 km s^{-1} for both). The expected velocity peak also agrees well with my results. The deviation from the MHD model occurs during the previously described continuous condensation knots at the predicted HCS crossing. It is far more likely that this turbulent period is associated

with an ICME-on-ICME interaction from the last two CMEs reported in Table 6-2 and Figure 6.36. The two ICMEs would have encountered and slowed down to the ambient slow solar wind speed of ~250 km s^{-1}. The possible merging of the two ICMEs would have resulted in a complex ICME-solar wind outflow at the comet, which may have compressed the fast solar wind flux tube ahead.

The density enhancements on 12/03/2013 at 22:09 UT at ~1 x 10^7 km from comet head coincides well with the expected arrival of the fast ICME, observed at 12/03/2013 10:36 UT), at the comet. A double dynamically responsive tail with fairly similar initial propagation direction, was observed emerging in close proximity from the extensive dust tail. The two tails appear to cross over at ~ 1.3 - 1.4 x 10^7 km, followed by a DE. The morphology of the bottom tail is that of a dust stria, which may have undergone a clumping of dust grains. It is unclear whether the second density enhancement is dust or ionic in nature.

With regards to the HCS crossing, the ENLIL MHD predicts two polarity reversals at the comet on 12/03/2013 ~ 09:00 UT and 13/03/2013 ~15:40 UT. There are no tail DE identified due to large data gaps and image processing defects during the first period. The second polarity reversal is expected around 18:00 UT on the 13th, matching well with the observed formation of a DE at 18:49 UT in the STEREO A images. The disconnected tail also coincided with the edge of the merged ICME around the same time. The second highest maxima in the velocity distribution on 13/03/2013 ~18:00 UT are velocities from the disconnected tail.

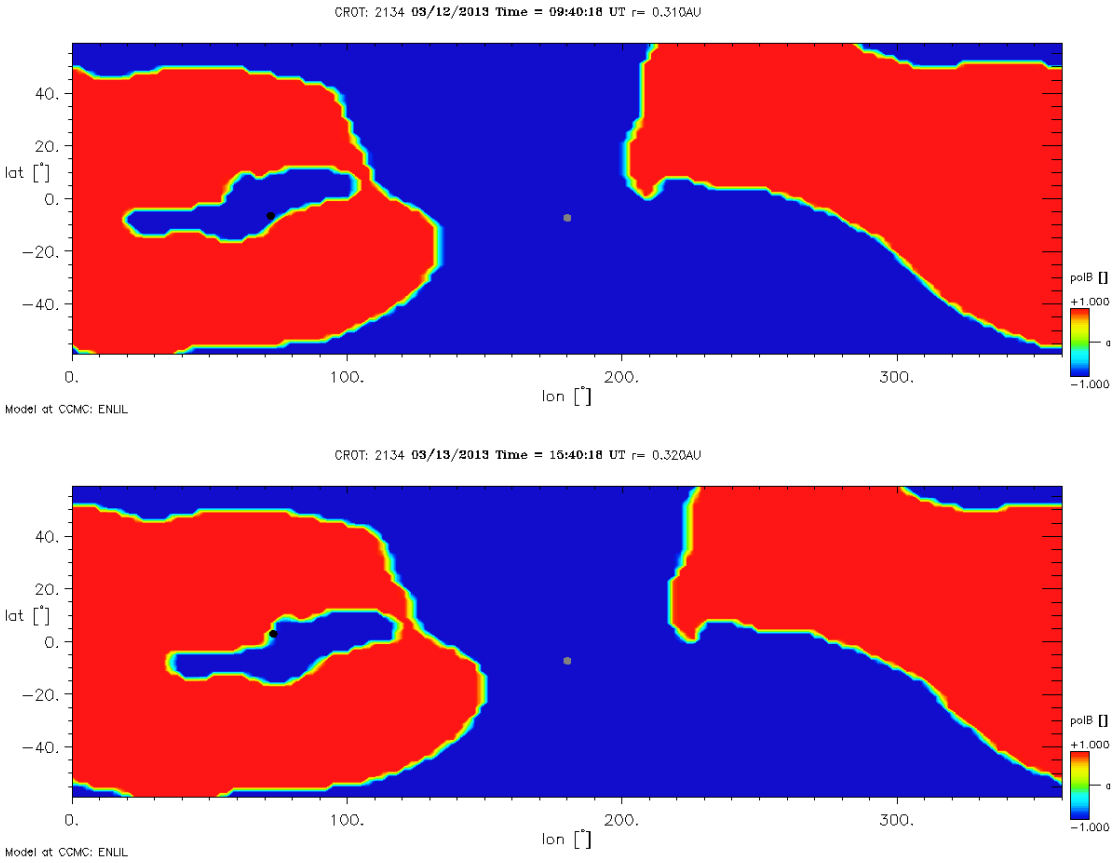

Figure 6.37: ENLIL MHD model predicting two DEs connected to sector boundary crossings

It remains unclear as to why the ion tail undergoes a large orientation change at 15/02/2013 13:29 UT at a cometocentric distance of ~ 6 x 10^6 km. This would have been initiated slightly earlier at the comet's head. A very faint solar wind plasma cloud can be seen in the larger STEREO HI-1B FOV arriving at the comet at 06:09 UT, whilst the comet was already undergoing turbulent ion tail flow. It is evident that the comet traversed a disturbed medium, which likely corresponds to the merged ICMEs. The link between the two is tenuous, though it is the only obvious solar wind phenomenon that could account for the atypical ion tail behaviour.

During this period, the comet was at:

Heliocentric distance: ~0.302AU and ~0.349AU

Heliographic longitude: 70º and 74º

Heliographic latitude: -22º and 18º

Overall, C/2011 L4 was an interesting study of the turbulent equatorial region of the solar wind as solar cycle 24 tended towards its maximum.

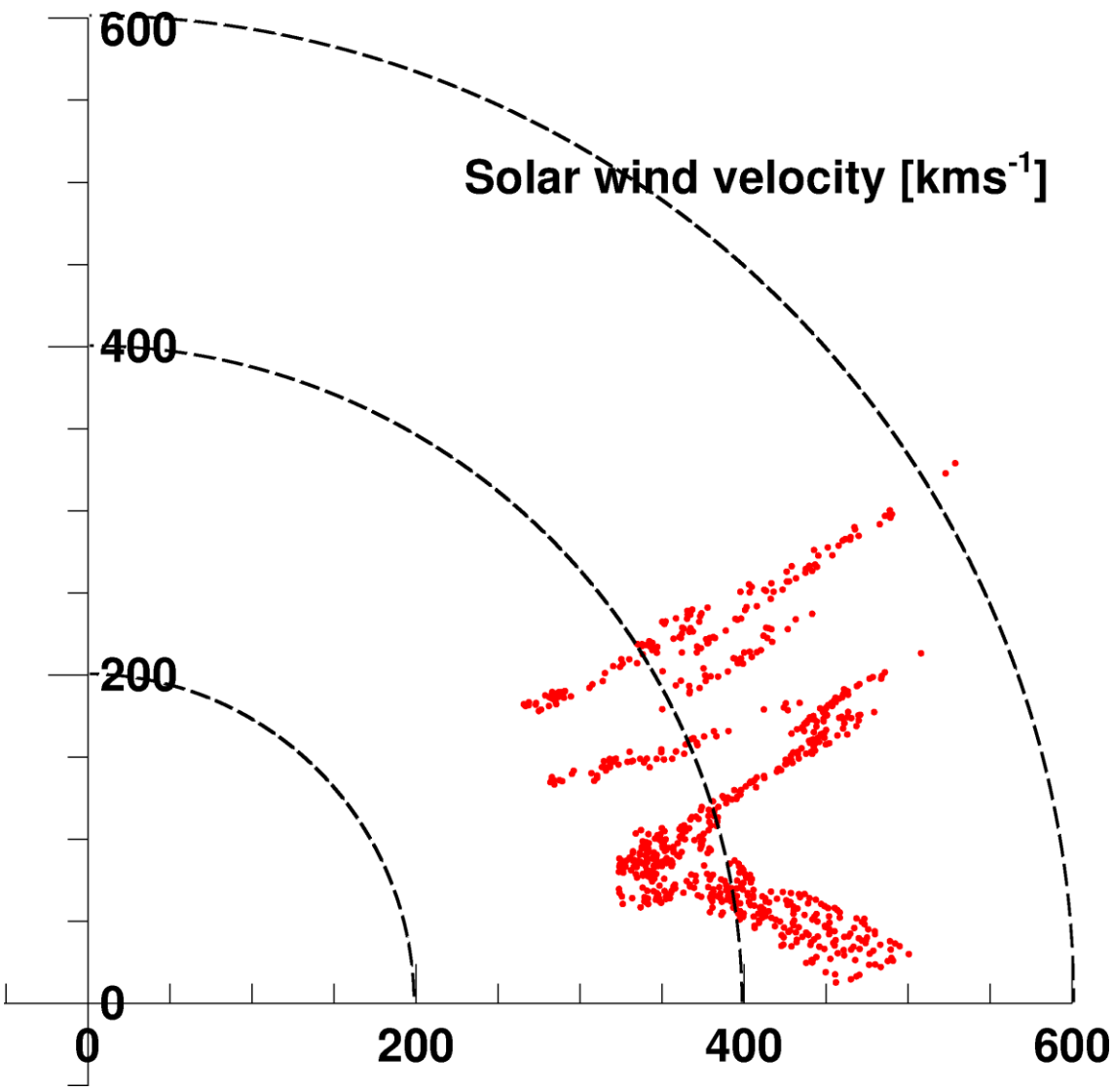

Figure 6.38: Solar wind velocities from C/2011 L4 versus its heliographic latitudes. The circles represent isovelocity contours for a fixed radial solar wind velocity at increments of 200 km s^{-1} from 0º to +90º.

6.4.4. Vector maps

The prominent features in the disturbed ion tail maintained their radial motion. Most features were hence tracked with a time interval of 1h 20 min between images, instead of the available cadence, since no spurious off-radial motions are expected. At certain points, for example on

13/03/2013 from 00:29 UT to 03:29 UT, it would appear that the comet had two ion tails [feature set 2 in Figure 6.39]. Both were measured in the vector maps, although only the top tail, the real ion tail, was included in the radial velocity investigation. It is difficult to make sense of these velocities, though they mostly show solar wind velocities centred about 300 km s^{-1}. Feature set 3 followed the acceleration of a kink and a potential disconnected ion tail as it accelerated to ambient solar wind velocity. The root cause of this disconnection was not identified. Set 4 corresponds to the HCS tail disconnection. The tail slowed down initially to create a kinked tail. Once disconnected, the tail was rapidly accelerated up to 240 km s^{-1}, close to the MHD predicted solar wind velocity. The acceleration appears to decrease, though it is impossible to state whether the disconnected tail velocity profile would have flattened. A radial velocity interpretation of this image produced a radial solar wind velocity of ~400 km s^{-1}, further reinforcing that DEs in the ion tail will produce slightly erroneous solar wind velocities. This is because the disconnected tail will appear to momentarily not respond to the radial flow of the solar wind. Velocity group 5 was taken during poorly processed difference image, which had been linked to a period of ICME-ICME interaction with the ion tail. The differing trend between different sections of the ion tail is further evidence of a complex non-radial flow at the comet. The small velocity variations could be due to human measuring error. This dataset fills in the velocity data gap in Figure 6.35, though there is a clear mismatch between the two techniques.

The last 5 features can be separated into two groups. The first (feature set 6) was measured from the second half of the poorly processed difference images and tracked the formation of a newly formed turbulent ion tail. This new tail segment is the large orientation change, also linked to an interaction with the ICME-ICME disturbed medium. The final feature set correlates well with the radial velocity technique, supporting my hypothesis that the comet will have traversed the coronal hole faster than predicted by the ENLIL model.

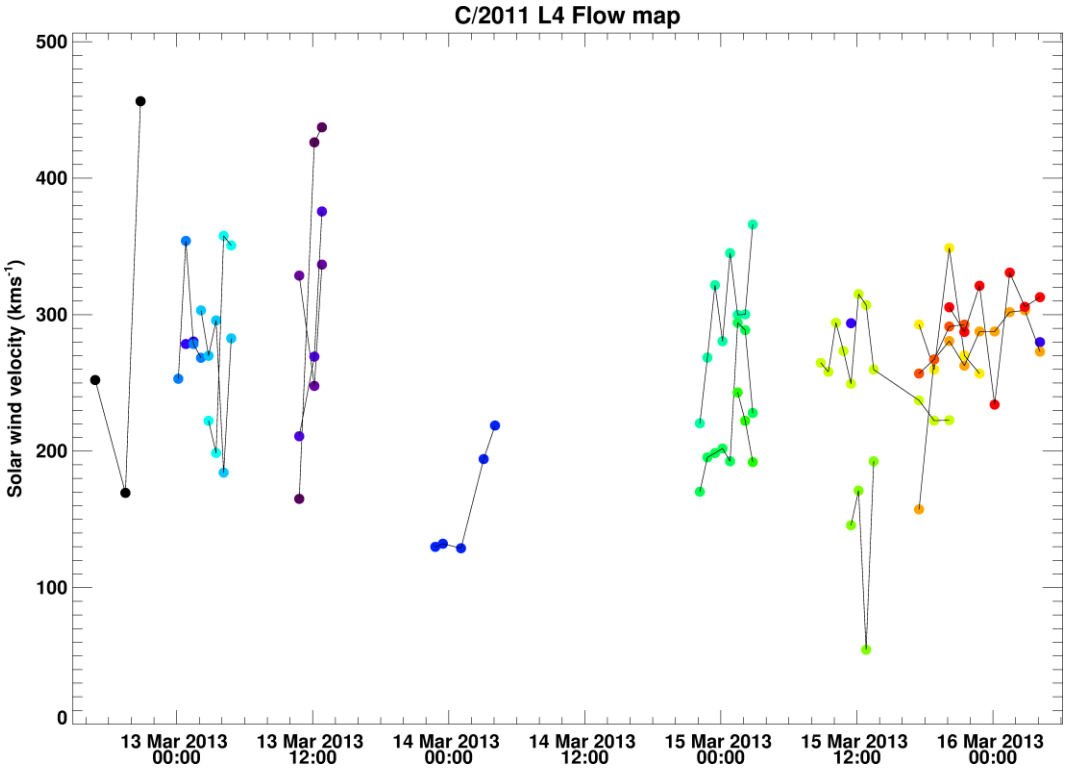
C/2011 L4 Flow map
Solar wind velocity (kms^{-1})
500
400
300
200
100
0
13 Mar 2013 00:00
13 Mar 2013 12:00
14 Mar 2013 00:00
14 Mar 2013 12:00
15 Mar 2013 00:00
15 Mar 2013 12:00
16 Mar 2013 00:00

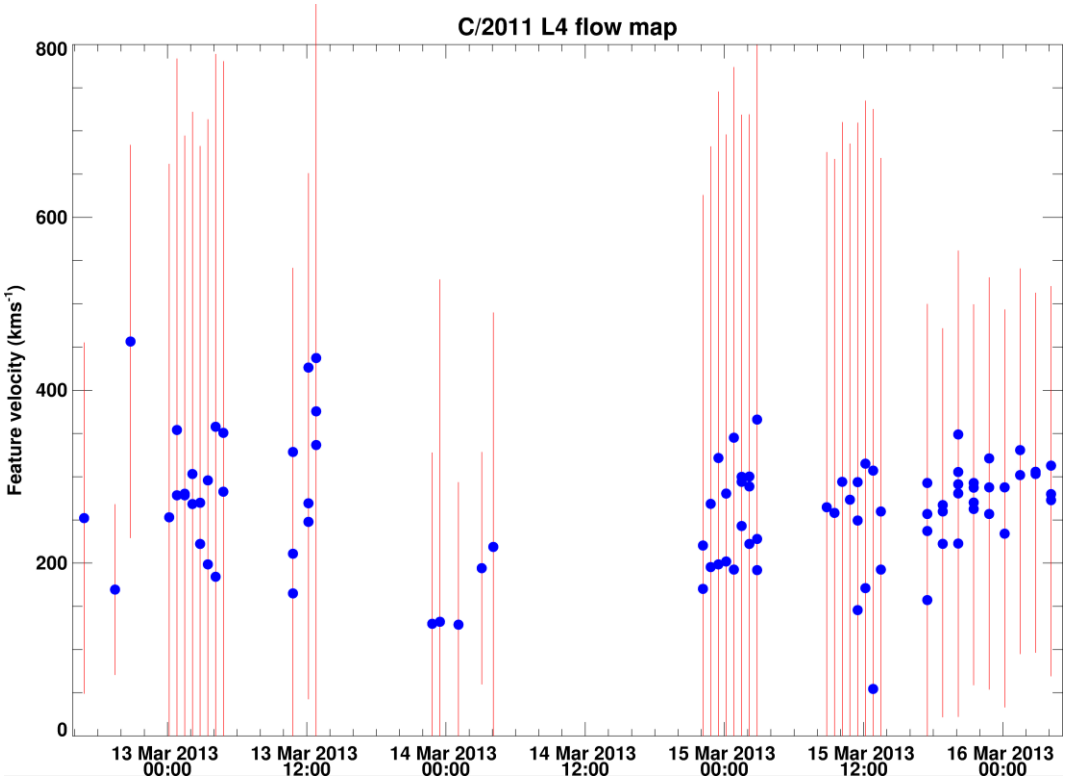
C/2011 L4 flow map
Feature velocity (kms^{-1})
800
600
400
200
0
13 Mar 2013 00:00
13 Mar 2013 12:00
14 Mar 2013 00:00
14 Mar 2013 12:00
15 Mar 2013 00:00
15 Mar 2013 12:00
16 Mar 2013 00:00

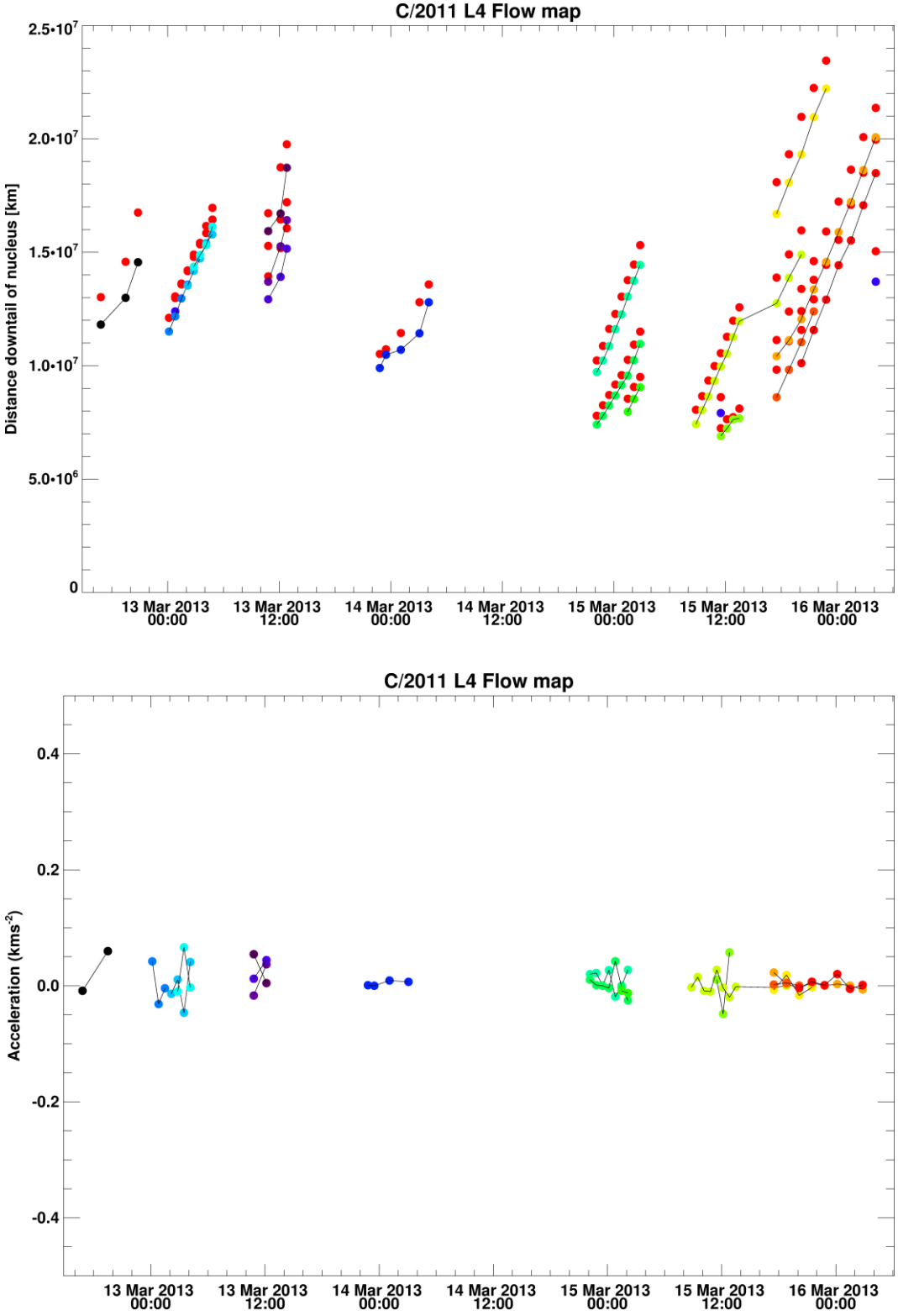

Figure 6.39: The top two panels are the solar wind velocities derived from consecutive images. The bottom panels show the sampled cometocentric distances down the tail and the acceleration of the plasma bundles.

The close correlation between the solar wind velocities derived from the vector maps and the near-zero acceleration from Figure 6.39 suggests that the turbulent equatorial solar wind encountered by comet C/2011 L4 was mostly radial during this period.

6.5. Conclusion

Similarly to the amateur images, images from the spacecraft data show a curved ion tail. This feature was more prominent in the more extensive ion tails seen in the STEREO HI1 A and B datasets for the sungrazing and near-Sun comets than the smaller FOVs of the amateur observers. It is as yet unknown without further investigation whether this is due to an artefact of this technique or whether dusty-plasma effects will contribute towards an apparent curving of the ion tail.

The measured solar wind velocities for all three comets presented here are closer to expected solar wind velocities are correlate well with the predicted ENLIL solar wind velocities. This confirms my initial hypothesis presented in the summary of chapter 5, which is that the data scatter of the measured solar wind velocities will be much less due to the high-quality of consistent observing and data reduction procedures as well as the lack of an atmosphere and thus weather effects influencing the image quality. In addition, my image archive consisted of a large number of images taken at a fixed cadence over a period of several days from multiple spacecraft, allowing the near-continuous monitoring of the comet's orbit near the Sun. My analysis of the spacecraft data yielded a far greater number of data points for the solar wind velocity than the amateur observations, as the ion tail extended over greater distances. The sungrazing comets probed regions of the solar wind which had been heretofore difficult to sample. In particular, comet C/2011 W3 experienced the solar wind within 50 solar radii, much closer than any spacecraft in-situ measurements of the solar wind. The sungrazing and near-Sun comets are thus the best case studies for the technique presented in this thesis. Chapter 6 confirms that this technique clearly works though it is subject to the observing geometry.

7. Discussion and Conclusion

There are few published large scale studies of the ion tail of comets as proxies for studies of the mass-loaded solar wind. Brandt & Heise (1970) undertook a statistical analysis of comet ion tail orientations, which were suggestive of mean radial velocities of 450 ± 11 km s^{-1} with a tangential component of 8.4 ± 1.3 km s^{-1}. They further proposed a revision of their previously quoted lower bound of the radial solar wind velocity from 150 to 225 km s^{-1}, which is in accordance with some of the velocities recorded in this thesis.

Spacecraft sampling remains the best and most accurate method of providing detailed in-situ information on the solar wind, but the number of points of measurement is extremely small, and the sampled space is small both temporally and spatially. So are the remote sensing techniques expounded in chapter 4 viable alternative solutions for solar wind velocities and structure inference or are space probes the only reliable method? The close agreement between my results and the ENLIL MHD model demonstrate that even though these methods and my software are not the definitive method to measure the solar wind speed, they retain the potential to devolve the dynamical aberration into a series of velocities as long as we adhere to a strict set of imaging standards and conformity.

A more in-depth study assessing the data quality of spaceborne observations against ground-based amateur images would be useful to further validate this technique in the future, if there is a sufficiently large dataset with a significant temporal overlap between the two vantage points. In reality, this is difficult to achieve as the solar-observing spacecraft will image the comet as it approaches its perihelion, whilst the low solar elongation would render ground-based observations challenging due to the luminosity contrast.

Tracking the radial evolution of folding tail rays using the mapped images is a theoretically sound concept. Accurately pinpointing the radial locations of the tail rays requires a smaller scale contrast between the tail rays and the image FOV than is available with amateur images. A series of images taken with an hourly cadence and small FOV is highly recommended for this technique. The GTC images of C/2012 S1 (ISON) would have been an apt opportunity to validate my recommendation.

7.1. Orbit Plane Angle

It is notable that there is a systematic overestimation or underestimation of the solar wind velocity. This is likely due to the orbit plane angle and the observing geometry as discussed in chapter 4. The orbit plane angle can pose a great hindrance to the value of this technique. At low angles, the projection mapping breaks down as the pixel vectors are stretched to near-infinity when the orbit plane angle approaches zero.

In the JPL Horizons data, positive values of the orbit plane angle indicate that the observer is above the comet's orbital plane along the positive z-axis in the inertial reference frame. My orbit plane angle plots only show the absolute value, as it is assumed that the observer's location above or below the comet's orbital plane is irrelevant. In an idealised scenario for a straight ion tail with no complications, the geometry reduces to the three-dimensional position of the observer with respect to the comet and the extended Sun-comet radial vector. Assuming the anti-sunward solar wind flow at the comet is purely radial, the ion tail will be constrained to the plane of the comet's orbit. When the observer is ahead of the comet, with the Sun-comet line between the observer and the ion tail, the projected uncertainty will always be underestimated, regardless of the observer's z-position with respect to the comet's orbital plane. Vice versa, when the observer is lagging the comet's motion such that the ion tail flows between the observer and the Sun-comet vector, the projected ion tail will appear to have a smaller aberration angle. In a realistic situation, factoring in a curving ion tail from radial speed variations and non-radial plasma flows, the orbit plane angle becomes an important criterion in the distorted projection.

Unless this angle is near 90 degrees, there will always be an element of over- or under-estimation. A simple comparison between the over/under estimation of comet Machholz versus its exact orbit plane angle showed that there was no clear evidence that being on one side of the comet's orbital plane would cause an over estimation and vice versa if the observer was on the other side. However, for non-radial tails, it is evident that the three-dimensional location of the observer with relation to the comet's tail will be a contributing factor towards the disparity between the measured and observed values. My investigation was impacted by a low orbit plane angle of ~ 20^{o} for the entire observing period for 4 out of my 6 amateur-observed

comets. The near-Sun comets had a slightly higher orbit plane angle of ~ 40^{o} when observed from STEREO and SOHO spacecraft. C/2012 S1 (ISON) had the best observing geometry of all the comets, however the analysis techniques' usefulness was impeded due to the small angular separation between the prolonged radial vector and the comet's orbit. To truly test this technique, spacecraft observations with high temporal resolution of a comet's ion tail with a near-90^{o} orbit plane angle would help to remove the geometrical perspective redundancies.

Can the perspective problem be resolved into an expression that can be used to correct future estimates? One possibility for instances where the solar wind velocity estimates match the MHD solar wind velocity profile, is that this discrepancy could be used to derive a relationship between the two. However, since the technique yields wildly varying estimates from amateur images, due largely to identified transient events, the current datasets for comets C/2004 Q2 and C/2001 Q4 cannot be used in this manner.

An alternative would be to use the high-quality data from the SOHO/LASCO C2 and C3 coronagraphs and the STEREO/ECCHI HI 1 heliospheric imagers to pin down an expression describing the inaccuracies in estimating the solar wind due to the geometry. This is only possible with our Comet Lovejoy (C/2011 W3) dataset which contains overlapping data from STEREO A and SOHO. This would be a feasible technique if the two trends match identically, however the large spread in the LASCO data would make this challenging and unreliable. Modelled solar wind velocities for sungrazers are challenging to predict close to the Sun due to the increase in the non-radial components of the solar wind flow. Therefore, this remains a valid method, only if we manage to obtain overlapping datasets for near-Sun comets in the future, and if we can pin down the non-radial component of the ion tail. This relies on the assumption that my solar wind velocity technique works accurately and reliably enough for space observatories.

Even if the underlying relationship is derived, it is possible that the resulting correction expression may be wholly dependent on having overlapping data, i.e., the expression relating the orbit plane angle and the solar wind cannot be applied to another comet, unless it has been observed from a different viewing point or there is a matching modelled solar wind profile.

Sizonenko (2007) pointed out similar discrepancies between their solar wind velocities derived from comet observations and those measured by space-based instruments. They linked these to the low accuracy of cometary observations and to differing solar wind conditions experienced by Earth and the comet, although they had no clear cause. The M. Owens model has been extrapolated to the comet's environment. My results' discrepancies with the Owens ENLIL model coupled with the CCMC ENLIL model predictions strongly suggests the comet encountered a disturbed solar wind flow, likely a HCS embedded within a CIR.

It is unclear how much of an effect the observing geometry would contribute towards this discrepancy. Sizonenko (2007) reported that there may be an unaccounted force which could have affected their observed velocities. In my analysis, I noticed that the ion tail almost consistently curved towards the dust tail for a majority of the projected images.

The tail curvature appeared to vary between comets but a measure of curvature was not recorded. No investigations were made to link this to the solar wind speed, the comet's heliocentric, geocentric distance, orbit plane angle or its dust production rate.

7.2. Amateur vs Professional Observations

Ground-based observations of the comets revealed a much larger data scatter than the smooth slopes derived from spacecraft images of the near-Sun comets. What are the factors that influence the varying image quality of ground-based observations to produce such a large scatter?

For one, data aboard spacecraft are consistently recorded with the same equipment and manner with little external macroscopic influence on the way the data is processed and saved. Equally, sources of noise for the spacecraft instruments, commissioned by professional scientists, will be better constrained and more consistently removed from the data. Amateur observers are uncoordinated in this respect. They are limited by the consumer technology available and their individual budgets. This leads to a wide array of telescopes, CCDs and field of views being used to monitor the target, often without the use of any filters. There is no method of ensuring the equipment is set up correctly and that the observing strategy and data

reduction is performed consistently. Though most amateur images of comets are likely to be calibrated, they will not be subjected to the same scientific rigour as observatory processing pipelines or spacecraft observations and may not have obtained all the necessary calibration frames. Furthermore, there tends to be an observational bias in the ion tail images gathered by amateur observers. Most of these images were acquired by volunteer astrophotographers and thus will publish their most aestheticically-pleasing and dynamic ion tail images. There is a higher likelihood that more astrophotographers will be observing during periods of high ion tail turbulence as reports of these events are communicated through various mailing groups. The timescales for the observations also differ. Spacecraft observations have delivered a high cadence of observations from the same instrument over a short period of time. Amateur astronomers tend to observe in short bursts over long periods of time.

Optical observations are prone to optical distortions largely due to the curvature of telescope lenses and mirrors. Astrometry.net calculates a SIP distortion polynomial of order 2, which is applied when mapping the photographs into their equatorial coordinates. Considering the maximum field of view of the astronomical images are only a few degrees apart, with the comet often covering a subsection of that, the optical distortion would not cause a large discrepancy in the orbital plane mapping. It is thus deemed unnecessary to derive and apply a specific distortion correction map for each amateur image.

Changing weather patterns and local turbulence in the atmosphere will also play a role in the image quality. Seeing is an astronomical phenomenon controlled by turbulent mixing of air layers in the atmosphere resulting in a blurring of faint features in the ion tail. This, however, will not be a problem when determining the star positions in the image. With amateur images, it is rarely possible, if at all, to differentiate between images taken under good observing conditions and those taken during poor weather conditions. Inclement weather can often stymie consecutive observations leading to large data gaps in our resulting plots.

Knowing the accuracy of the image time is paramount to the success of my software. The unknown timing information plays a larger role than had been initially anticipated in determining accurate solar wind velocity estimates. Despite my built-in “failsafe” ‘imagetimeheaders’ module, the range of possible times for optocentres covering a large pixel area can lead to the image

being mapped incorrectly. In such instances, it may seem that the ion tail is closer to the radial vector, which will lead to faster solar wind speed estimates. The opposite scenario can also occur where the ion tail is further from the radial vector, which will yield slower solar wind speed estimates. Analysis of the amateur images presented in this thesis is plagued by this unknown quantity.

Although we have the means to determine the approximate times, the images will often have been dramatically altered to enhance the aesthetics of the image to the detriment of information near the nucleus and coma. Such a bright optocentre as discussed throughout the thesis poses large problems, mainly in determining the correct observing time. An example would be an animation sequence taken for comet Machholz whereby the large optocentre results in image number 7 having a later time than image number 8. The image time is primarily used to define the nucleus position on orbit and the observer's position. An incorrect time here can result in a significant offset of the projected image in relation to the extended radial vector. In the larger view of determining the bulk solar wind velocity, it will be a significant contributor to the over- and underestimation of the solar wind velocity, thus contributing to the large data scatter seen in our results. For feature tracking and tail rays, the velocity calculations are inversely proportional to the time between observations. Using these features as proxies for the solar wind will therefore end in these solar wind velocities being the most impacted by the incorrect times, however minute those may be. The only true solution to remedy this would be to use the raw FITS file to determine the image times or to have the correct timing metadata recorded by the amateur astronomers in the first place. Whilst the community is getting better at reporting this information, our professional-amateur collaboration would benefit immensely by organising mass requests of images and being specific about the information required. In future, it would be useful to undertake a study where the image times are accurately known. This would prove a better test of professional vs amateur image data. I predict with more accurately known times, as with spacecraft data, the solar wind velocities computed for comet C/2004 Q2 and C/2001 Q4 would more closely resemble the modelled solar wind velocities. A scatter would still exist largely due to the systematic curving of the ion tail when mapped onto comet's orbital plane. Furthermore, the technique requires all the images to be consistently astrometrically plate solved, i.e. as an extreme example, two images taken simultaneously by two different observers

at antipodes should be solved such that each pixel will have a very similar right ascension and declination. In reality, Astrometry.net solutions will not be as consistent and small variations in the image coordinates can result in a slight mapping offset. This is not an issue for the radial solar wind velocity measurements. However, the sensitivity of the feature-tracking software to tiny rotations of the mapped image, can negatively impact the velocity determination.

This ideal level of data format, calibration consistency and accurate reporting of the observation times may only be achievable by a professional-grade observatory or a spacecraft, although the need for the scheduling for professional observations to be carried out in advance can be a major drawback when it comes to observations of newly discovered comets.

7.3. Turbulent Events/Non-Radial Flows

Transient interplanetary events were partially responsible for deviations from the modelled solar wind velocities. Large radial velocities exceeding 1000 km s^{-1}, peaking at ~1650 km s^{-1}, were recorded. Solar wind velocities during undisturbed solar wind flow and under good observing geometry closely matched the expected range of solar wind velocities.

Velocity vector maps of turbulent ionic features in consecutive images suggested that it was possible to at least constrain the velocity and expansion of the interaction region between ICMEs and the comet's ion tail. By comparing our image catalogue, my velocity estimates, ACE data for near-Earth comets, modelled solar wind values and the SOHO LASCO CME catalogue, we can identify turbulent events and even narrow down the list of these transient events. Thus, amateur images serve as a useful source for tracking and identifying transient structures in the solar wind. However, my radial velocity estimates using this technique are not always reliable. For these events, it would be best to use my vector map techniques. Some disturbances in the ion tail can often look like ICME-related turbulent events, appearing as a kink or a 'double ion' tail, in certain instances. These could be due to the perspective viewing of a fast ionic tail bundle catching up with an earlier, slower moving condensation cloud.

At low orbit plane angles, when the ion tail deviated from the comet's orbital plane, non-radial velocity components could be derived. On average, they were ~40 km s^{-1} and are comparable to the observed ~30 km s^{-1} by ACE over nearly 3 years and from the ENLIL MHD model. Tracking the motion of kinks or DEs during low orbit plane angle would yield a better measure of the non-radial velocity component. This was only possible for a pair of images for comet C/2001 Q4 (NEAT) in our vast dataset. Two opposite ends of a DE were tracked and a surprisingly large non-radial velocity component of ~190 km s^{-1} was measured.

7.4. Curving Ion Tail

The salient topic of this thesis is the radial velocity profile of the ion tail. For almost all comets observed, the ion tail seems to curve slightly towards the dust tail. The curving ion tail yielded apparently slower radial velocities with increasing distance from the nucleus. The degree of curvature increased with slower local solar wind velocities. This was particularly noticeable in the C/2011 W3 (Lovejoy) images from STEREO A, where the effect could have been due to a large dust production rate post-perihelion.

There were multiple images, for all analysed comets, where the initial 1 x 10^6 km - 1.5 x 10^6 km of the ion tail lay directly on the sun-comet line. This implied infinite radial solar wind velocities for that segment, where the theory expects the solar wind flow to be accelerating up to the ambient solar wind velocity. Estimates taken near the nucleus were not considered to be a good representative of the solar wind velocity. This subset of the data was not rejected entirely as there are no valid arguments for doing so. This was particularly problematic for images with small fields of view as regions being sampled were less than 1 x 10^6 km from the nucleus for the first estimate. These tended to have larger velocities and will match up with some of the higher than expected solar wind velocities seen in the data. There is no distinction in the velocity plots between images where a larger extent of the ion tail was measured versus a smaller sampling distance from the nucleus.

Is the curving ion tail a natural consequence inherent in using this technique or is it a true representation of the ion tail once projected onto its comet's orbital plane? Could this curvature

of the ion tail be due to the dust tail being an additional source of ions to the plasma tail? Further study will be required to confirm the true nature of the ion tail projection and whether determining the correct orientation of the ion tail requires more than the composite vector of the local solar wind velocity and the perpendicular component of the comet's orbital velocity.

7.5. Conclusion

The techniques I have developed rely heavily on comets with a large amount of sublimating volatiles and lying close enough to the Sun to form a bright, observable ion tail. Nonetheless, the frequency of bright comets is significant enough to create a catalogue of solar wind velocities in the inner heliosphere. The comets were observed over 28 distinct Carrington rotations overall. This includes an overlap of two CR by comets C/2004 Q2 and C/2011 W3 for CR 2118 and comets C/2012 S1 and C/2013 R1 for CR 2144.

Comets	Carrington Rotation
C/2001 Q4 (NEAT)	CR 2015-2017
C/2004 Q2 (Machholz)	CR 2023-2028
C/2009 P1 (Garradd)	CR 2115-2121
C/2011 W3 (Lovejoy)	CR 2118-2118
C/2011 L4 (Pan-STARRS)	CR 2134-2134
C/2012 S1 (ISON)	CR 2143-2144
C/2013 R1 (Lovejoy)	CR 2144-2145
C/2012 K1 (Pan-STARRS)	CR 2150-2150 CR 2154-2156
C/2014 Q2 (Lovejoy)	CR 2157-2159

Table 7-1: Comets analysed for the past decade providing a snapshot of the solar wind over 28 Carrington Rotations

Uncertainties in the solar wind velocities may arise from a number of identified and quantified error sources, chief amongst which are non-radial components of the solar wind velocity.

Mapping the images onto the comet's orbital plane provides a good estimate of radial solar wind speed but the inherent uncertainties always need to be borne in mind. To summarise our caveats:

1. The core technique of this thesis is mainly a determination the radial solar wind speed.
2. Ground-based observations are at the mercy of the elements and there isn't much the amateur astrophotographers can do to minimise this effect on data quality.
3. It is unclear which amateur images have been calibrated and treated with due scientific rigour. This will only get better by improving collaborations between professional and amateur observers, in the same vein as the CIOC and PACA campaigns.
4. Our technique seems to be impeded by a recurring curving ion tail. It remains to be determined whether this is a characteristic of all comets or whether the technique will incorrectly underestimate solar wind velocities far from the nucleus and overestimate values close to the comet head.

The initial hypothesis was to validate the use of amateur images of comets to perform high quality heliospheric research to:

- ❖ estimate local radial solar wind velocities at the comet
- ❖ provide multi-point, multi-latitudinal measurements of the solar wind over a large range and time
- ❖ infer general solar wind variations with solar cycle.
- ❖ remotely determine HCS crossings.
- ❖ extract multipoint measurements of CMEs

The big picture view was to build a comprehensive picture of the large scale and small scale variations throughout the inner heliosphere over past solar cycles.

It could be argued that the local solar wind velocity estimates derived with this technique tend to match modelled values from the model of the inner heliosphere [M. Owens and others] during quiescent solar wind conditions and high orbit plane angles. Multiple transient interplanetary events can be inferred from images of the plasma tail, as well as the large scatter of the solar wind velocity plots. These events were not always registered by ACE, which is to be expected as ACE and the comet would be experiencing different solar wind flows for most of the comets' orbits. The period during which the ACE data was extrapolated for comet C/2004 Q2 (Machholz) showed good correlation between the two data sets. The large error bars for the solar wind velocity estimates arise either due to poor image quality, the plasma tail sampling technique or wide and diffuse plasma tails.

The technique described in this report shows that the inexpensive and wide availability of images by amateur astronomers can provide a rough indication of the bulk plasma flow velocity, though at times this is marred by the numerous heliospheric phenomena causing turbulence in the cometary ion tail. In stark contrast, the spacecraft data yielded a mostly smooth variation for the solar wind velocities. A high orbit plane angle of near 90^{o} is considered to be the optimal observing scenario to produce high-quality, reliable estimates of the solar wind velocity.

The results of my multi-latitudinal catalogue of the global structure of the solar wind were mostly limited to the equatorial plane, which showed large spikes in radial solar wind speeds. They do not always match the extrapolated near-Earth data or ENLIL MHD model perfectly. However, the close correlation during quiescent solar wind periods and the identified transient solar wind phenomena for most of the non-corresponding periods clearly show that the technique holds potential to diminish our knowledge gap of the solar wind variation in the inner heliosphere, as a complementary dataset to MHD models. The results of this PhD do not entirely support our original hypothesis that amateur images of comets can be used as a reliable source for remote investigation of the solar wind. The observing geometry is an unexpectedly large factor in controlling the quality of the results. When applied to professional spaceborne observations, the technique yields comparable estimates of the solar wind velocity. In conclusion, solar wind velocity estimates derived for amateur images are useful hints as to the solar wind behaviour as long as they are strictly considered under the caveats discussed previously.

7.5.1. Future Research

The technology demonstrated herein can thus still be a valuable contribution towards compiling solar wind velocities from amateur and professional imaging of comets and providing critical insight into the compositional structural evolution of the solar wind. With continued efforts towards ameliorating the image quality and transfer of information, amateur astrophotographers retain their value as a unique data resource of comet-solar wind interactions. If we can impress the importance of maintaining consistency and performing CCD calibrations, the software developed in this thesis could be invaluable to the scientific community. An added bonus would be to have a select group of skilled amateur astrophotographers dispersed globally and equipped with a red and blue broadband filter at a minimum and ideally also with narrowband filters.

As it stands, this “open source” software is close to distribution though somewhat limited by the user requiring an IDL licence. In the future, a translation into a free programming language, for example Python, would be essential so as to better integrate this software into an easy-to-use web platform. The workflow has been streamlined into a series of clicks and minimal user interaction. The restricting factor is our inability to automatically extract the ion tail crossing points with the extended radial vector. With improved data quality and CCD calibrations, a high-pass filter and convolution package may actually be successful in emphasizing the ionic features for automatic extraction of the radial tail crossings. The benefit of this software may only come in a few years as better and more affordable consumer technology comes to the market. Furthermore, as a prime example of professional-amateur outreach, this project could be used to inspire future astrophotographers with the ultimate goal of increasing our knowledge of the inner heliosphere.

An interesting side topic would be to characterise the solar wind-geometrical dependency with a three dimensional triangulation of the plasma tail. This is achievable by comparing simultaneous observations of the ion tail from different vantage points. A similar study was done by Thompson (2009). They could only apply their technique to the dust tail as there were no stereoscopic observation of the ion tail until C/2011 W3 (Lovejoy) was observed. The technique

cannot be translated to the ion tail due to the complexity of the ion tail's non-radial motion and the observer's geometrical perspective.

A secondary avenue worth investigating would be to identify the causal factor for the arcing nature of the ion tail. Simply determining whether the decreasing velocity trend downtail is a physical manifestation of the interaction between the mass-loaded solar wind and the charged dust tail, or whether it is an artefact of this technique, would be very informative.

"Writing your thesis is like banging your head against a wall, it feels good when it stops."

– Prof. Carey Lisse.

Data Acknowledgements

Amateur astronomers

This excellent and very proactive community of amateur astronomers have helped make this project very interesting. Their willingness to contribute their data freely towards science has been near unanimous and I would like to thank them for making this research possible.

SOHO/LASCO

The SOHO/LASCO data used here are produced by a consortium of the Naval Research Laboratory (USA), Max-Planck-Institut fuer Aeronomie, now known as Max-Planck-Institut for Sonnensystemforschung (MPS), (Germany), Laboratoire d'Astronomie, now known as Laboratoire d'Astrophysique Marseille (LAM), (France), and the University of Birmingham (UK). SOHO is a project of international cooperation between ESA and NASA.

ACE/SWEPAM data

ACE/SWEPAM data was obtained from NASA's National Space Science Data Center and Space Physics Data Facility.

LASCO CME catalogue

This CME catalogue is generated and maintained at the CDAW Data Center by NASA and The Catholic University of America in cooperation with the Naval Research Laboratory.

CACTus CME catalogue

This thesis uses data from the CACTus CME catalogue, generated and maintained by the SIDC at the Royal Observatory of Belgium.

STEREO

Thanks to the SOHO/LASCO and UK SECCHI science team at RAL for the data, advice and timely assistance and to R. Howard (NRL), PI of both the LASCO and SECCHI instruments.

Wilcox Solar observatory

Wilcox Solar Observatory data used in this study was obtained via the web site http://wso.stanford.edu courtesy of J.T. Hoeksema; The Wilcox Solar Observatory is currently supported by NASA

INT data – proposal and D nights

A critical aspect of this project would have been unfeasible without the training and data acquired during both INT discretionary times and my own proposal.

GTC data

Thanks to the Gran Telescopio Canarias for providing images of comet C/2012 S1 (ISON).

Specialised software useful for this project: IDL, THELI, GIMP, DeepSkyStacker, FITS Liberator, GraphDark, ALADIN

I made use of multiple freely available astronomical and Photo manipulation software. These were tremendously useful at understanding the data and how to best manipulate it.

ENLIL data

Simulation results have been provided by the Community Coordinated Modeling Center at Goddard Space Flight Center through their public Runs on Request system (http://ccmc.gsfc.nasa.gov). The CCMC is a multi-agency partnership between NASA, AFMC, AFOSR, AFRL, AFWA, NOAA, NSF and ONR. The ENLIL Model was developed by Odstrcil, D. at University of Colorado at Boulder.

Special Thanks

I am particularly grateful to STFC, RAS, IOP and the Daiwa Anglo-Japanese Foundation for funding during my studentship.

Acknowledgements

I'd first like to thank Geraint H. Jones, my supervisor over the last few years, not only for the support, dedication and expertise he has put towards making this project a success, but also for his friendship and advice. Thanks for pushing me beyond my comfort zone. I cannot imagine the PhD would have been this memorable otherwise. I cannot forget my second supervisor Andrew Coates for providing constant support and encouragement. Your prompt and supportive feedback has helped me achieve my goals during the PhD.

Though they need no acknowledgement, I feel it is important that I thank my parents, family and close friends for all their support before, during and hopefully after the PhD is done and dusted. Special thanks are extended to my sister, Deekshita for her tremendous help and support throughout the PhD. There are too many friends to name, so thank you to my anonymous friends who helped me out even by lending an ear when times were tough. I especially appreciate those who accommodated me in London whenever I needed it. To the friends in the students flat who kept me sane when unusual things mysteriously happened during our first year, you are awesome.

The people you encounter in life will shape your experiences and memories. Prime amongst these exemplary souls are my ‘210’ and ‘108’ officemates, without whom, my life would be dull and PG-rated. Special thanks to Gethyn Lewis, Chris Arridge and Sheila Kanani for guiding me during the early stages of a PhD and their advice regarding “professional” scientific behaviour during conferences. My gratitude to the Nandos challenge crew for pushing me beyond the limits of gluttony and to Matt Taylor for teaching me about fashion sense in science.

On a professional note, I’d like to extend my thanks to Lin Gilbert, Gethyn and Chris and the STEREO software team for help on the trickier aspects of the software development. Thanks to the Isaac Newton Group of telescopes for offering me a studentship support astronomer role at the Isaac Newton Telescope. ‘La isla bonita’ was an incredible though brief abeyance from the PhD offering unique experiences such as working in a world renowned observatory, hikes

through gorgeous landscapes and the friendship of excellent international support astronomers and local Palmeros. Our time on the island together was far too short.

Finally, I would like to say thanks to the great scientists, future scientists and random fellow travellers that made my conferences memorable and helped to provide a breath of inspiration after each event.

To everyone who helped make the last few years a memorable and very enjoyable chapter of my life, thank you.

Final thanks to the incredible support I received on social media:

"Once you have a PhD, every meeting you go to becomes a doctor's appointment." – unknown

Appendix A. Data Timeline

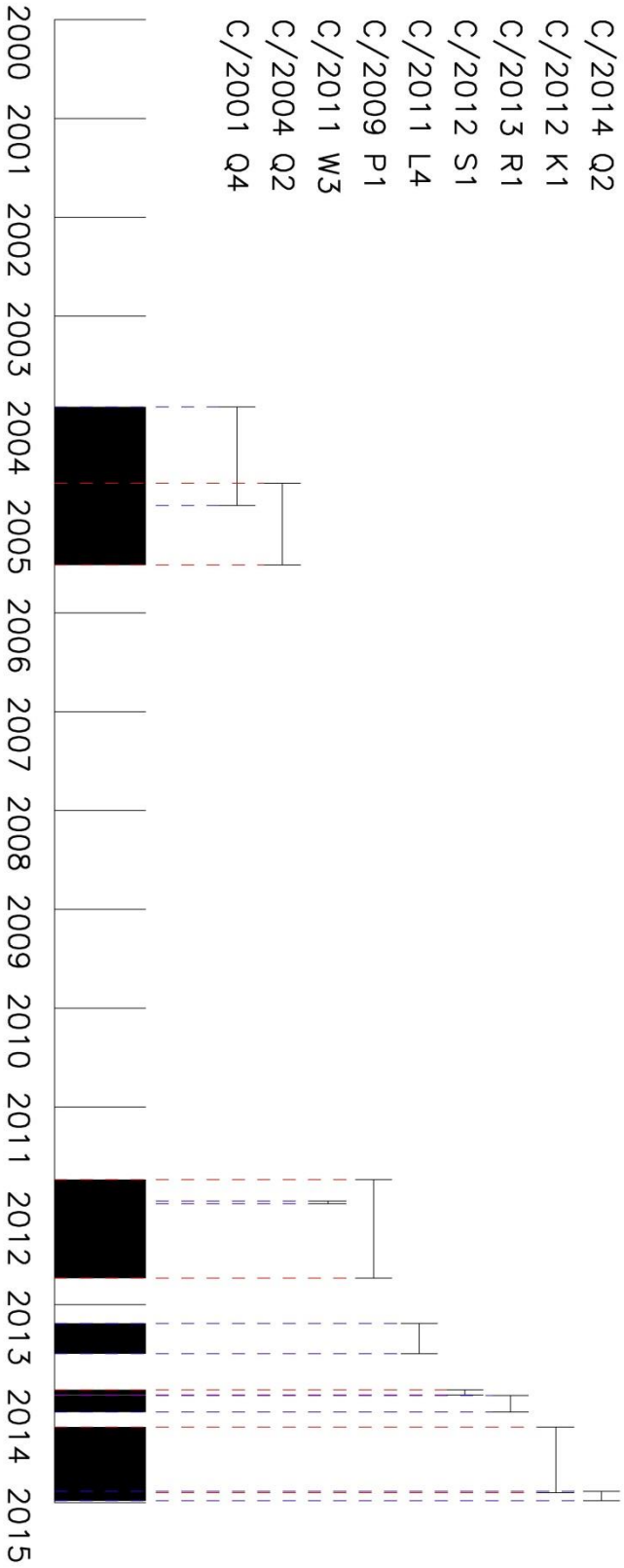

Appendix B. THELI

THELI is an automated data reduction pipeline for calibration, sky background and optical distortion correction of astronomical images. It was used to reduce images of C/2013 R1 (Lovejoy) acquired with the Isaac Newton Telescope's Wide Field Camera. The Graphical User Interface (GUI) software is designed to function in multiple linear stages with each step focussing on a particular aspect of the data reduction through to an image stacking routine. The data calibration phase incorporates a non-linearity correction for the WFC detector. Though deviations in CCD linearity are minimal, this feature has been activated when reducing this set of images.

Global weights are created for each pixel, such that each image will have an individual weight map, created from the normalised flat field, for the coaddition process. A binned preview (bin 1x1) is created to produce a calibrated multi-chip mosaic of each image.

The preferred star catalogue for astrometric solutions of the image is UCAC4 for the most accurate astrometry, however the star field is less dense. Alternatively, SDSS-DR9 can be used or USNO-B1. The latter has a denser star field at the detriment of astrometric accuracy. If these fail, then other star catalogues are used to find an appropriate match. THELI uses SExtractor for to detect stars within each image and either SCAMP or Astrometry.net to compute its astrometry, although distortion corrections for the latter is currently deactivated. The 'Mosaic_type' setting is set to same CR value for each image. The RA and DEC are extracted from the INT headers with a search radius of 25 arcmins is chosen, within which reference sources are retrieved. The limiting magnitude is set to 22 for the INT. No sky subtraction is applied to the image due to our extended targets of interest. A distortion polynomial order of 3 is chosen. This indicates a quadratic variation of the pixel scale as a function of position. The distortion correction should be symmetrical as seen in Figure 3.11. The image is resampled with the LANCZOS3 kernel and a TAN sky projection is selected. Finally, the images can also be calibrated for absolute flux, though this is not processed here, and coadded by using the known proper motion vector of the comet to increase the image SNR. The coadded images will be normalised to an effective exposure time of 1 second at this stage. THELI was chosen as the

data reduction software, mainly because of its advanced optical distortion correction functionality for the INT telescope. The inability to constantly produce symmetrical concentric distortion correction maps for each image, meant that the mid-stage binned previews (1 x 1 binning) were processed through FITS liberator and Astrometry.net. The coaddition phase was skipped as a correct distortion map could not be calculated using the UCAC4 catalogue.

Appendix C. Image Sources

All Observations

The observers listed below are all those whose images were collected via Google or their personal websites and forums. The images were successfully processed through Astrometry.net. They were not all successfully converted into data points for the thesis.

Due to the large number of observers, there is a possibility that a name may have been misspelt or initials omitted. I wish to extend my sincere apologies in the event that this occurs.

Comets	Date coverage	Observers
Garradd (C/2009 P1)	30/09/2011 to 18/04/2012	Brimacombe, J.; Buczynski, D.; Chambo, J.; Guido, E.; Hernandez (Francisco) Ligustri, R.; Howes, N.; Jäger, M.; Maruska, T.; Mikuz, H.; Mobberley, M.; Mrozek, N.; Observatori la Cambra Relf, G.; Rhemann, G.; Sharp, I.; Sherrod, C.; Skorupa, W.; Sostero, G.; Van Duin, A.
ISON (C/2012 S1)	12/11/2013 to 22/11/2013	Angel, T.; Brimacombe, J.; Cabrera, Q.; Conu, A.; Coulehan; Gater, W. (INT Vixen 20cm); Hankey,M.; Gonzalez, J.; Harlingten, C.; Harradine, T.; Hemmerich, F.; Hita Observatorio, Italy; Holloway, M.; Jäger, M.; Ligustri, R.; Lodriguss, J.; Chumack, J.; Mobberley, M.; Nassr, J.; Nevski, V.; Ortiz, M.; Peach, D.; Ramanjooloo, Y. (INT Vixen 20cm); Rhemann, G.; Sandbank, B.; Skorupa, W.; Wong, C. STEREO HI 1 A
Lovejoy (C/2011 W3)	15/12/2011 to 19/12/2011	SOHO LASCO, STEREO HI 1 A, STEREO HI 1B
Lovejoy (C/2014 Q2)	26/11/2014 to 21/01/2015	Chambo, J.; Hernandez, F.; James (Nick); Ligustri, R.; Mobberley M.; Paul (Nirmal); Peach, D.; Rhemann, G.; Tough, A.; Valvasori, A.; Van Yi
Lovejoy (C/2013 R1)	01/12/2013 to 13/01/2014	Birkett, K. (INT 2.5m); Bouchama, V.; Brahic, J.; Bryssinck, E.; Buczynski, D.; Chambo, J.; Emmanouilidi, C.; Gonzalez Hernandez, F. (Juanjo); Holloway, M.; Jäger, M.; Labordena (Carlos); Ligustri, R.; Martinez (Fernando); Mikuz, H.; Mobberley, M.; Mrozek, N.; Peach, D.; Ramanjooloo, Y. (INT 2.5m); Rhemann, G.; Skorupa, W.; Soulier, J.; Tosi, S.
Machholz (C/2004 Q2)	04/10/2004 to 03/07/2005	Akashi, T.; Akutsu, T.; Arai, M.; Aruga, Y.; Bares, A.; Beck, S.; Bender, D.; Benintende, G.; Buil, C.; Candy, P.; Chiavenna, P.; Colzani, E.; Cosmacini, M.; Eliasek, J.; Fujii, A.; Fujio, K.; Fukuda, C.; Garofalo Garzia, S.; Giuliani, Drummond, J.; Hackmann, J.; Hamada; Hanatsuka; Harada;

		Hari; Hashimoto, M.; Hayakawa; Hayashi, K.; Hirata; Holloway, M.; Hung; Hyakkai; Imaizumi; Ishikawa; Ishikura; Ito, T.; Jäger, M.; Kai; Kamibayashi; Kan; Kawashima, N.; Kenmochi; Kentou; Kimura, H.; Kobayashi, H.; Koga; Koprolin, W.; Koyama; Kubo; Kuboniwa, A.; Kubotera, K.; Kugel, F.; Kurita, N.; Kushida, Y.; Kuwabara; La Volpe, M.; Ligustri, R.; Machholz, D.; Martin, B.; Maruoka; Mashitani; Masi, G.; Mikuz, H.; Mobberly, M.; Mori; Morimoto; Morita; Murashima; Myslivec, M.; Mzorek N.; Nagao; Nakagawa; Nakajima; Nakamura, A.; Nakashima; Nishiyama; Noda; Nojima; Oono; Oonuki; Oosugi; Ozawa; Russiani; Saeki; Saitou; Sakaki; Salvato; Ootsuki, I.; Pardo, E.; Perissinotto, E.; Rhemann, G.; Satou; Schedler, J.; Schiaparelli; Segawa; Shen, Z.; Shimomura, N.; Shinohara, I.; Skorupa, W.; Sostero, G.; Sotokawa; Suzuki, M.; Taguchi, G.; Tajiri; Takagi, T.; Takahashi, K.; Takao, K.; Takimoto, I.; Takizawa, M.; Tamura, M.; Tanaka; Terashima, Y.; Tomisawa, Tsukamoto, H.; Tronchin; Umehara, H.; Usui, F.; Uto, F.; Utsumi, T.; Verschatse, D.; Wienerroither, P.; Yajima, H.; Yamada, K.; Yamamoto, Y.; Yamashita, T.; Yamauchi, M.; Yamazaki, A.; Yanagihara, H.; Yokota; Yokoyama, T.; Yoshida, S.; Yoshimi
NEAT (C/2001 Q4)	08/02/2004 to 18/10/2004	Bares, A.; Buczynski, D.; Buzzi, L.; Darias, C.; Drummond, J.; Gavin (Maurice); Holloway, M.; Ito, T.; James (Nick); Jäger, M.; Kerschhuber G.; Kurita (Naoyuki); Labrador, J.; Lovejoy, T.; Masi, G.; Mikuz, H.; Mobberley, M.; Montanucci, F.; Rhemann, G.; Schedler, J.; Shears, J.; Sostero, G.; Strange, D.; Tabur, V.; Tan, L.; Verschatse, D.; Ward, B.; Yen, B.
Pan-STARRS (C/2011 L4)	15/03/2013 to 26/06/2013	Chambo, J.; Mikuz, H.; Mobberley, M.; Peach, D.; Rhemann, G. STEREO HI 1 B
Pan-STARRS (C/2012 K1)	02/04/2014 to 22/11/2014	Buczynski, D.; Jäger, M.; Kardasis, M.; Ligustri, R.; Mobberley, M.; Paul (Nirmal); Peach, D.; Rhemann, G.; Skorupa, W.

Table 8-1: List of all observers for each comet and time span of data coverage

INT observing log (C/2013 R1 only)

Date (2014)	Mid-Time (UT)	Exp Time (s)	Filter	Rh (AU)	Δ (AU)	Phase (º)	Orbit plane (º)
Jan 03	06:50	60	B	0.8410	1.1218	333.5	-24.6
	06:52	60	B	0.8410	1.1219	333.5	-24.6
	06:53	60	B	0.8410	1.1219	333.5	-24.6
	06:55	60	B	0.8410	1.1219	333.5	-24.6
	06:57	60	B	0.8410	1.1219	333.5	-24.6
	06:59	60	r	0.8410	1.1219	333.5	-24.6
	07:01	60	r	0.8410	1.1220	333.5	-24.6
	07:03	60	r	0.8410	1.1220	333.5	-24.6
	07:04	30	r	0.8410	1.1220	333.5	-24.6

Jan 04	06:45	10	B	0.8461	1.1388	332.5	-24.9
	06:47	1	B	0.8461	1.1388	332.5	-24.9
	06:50	1	B	0.8461	1.1388	332.5	-24.9
	06:51	10	B	0.8461	1.1389	332.5	-24.9
	06:52	5	B	0.8461	1.1389	332.5	-24.9
	06:53	10	B	0.8461	1.1389	332.5	-24.9
	06:54	10	B	0.8461	1.1389	332.5	-24.9
	06:55	10	B	0.8461	1.1389	332.5	-24.9
	06:55	10	B	0.8461	1.1389	332.5	-24.9
	06:56	10	B	0.8462	1.1389	332.5	-24.9
	06:57	10	B	0.8462	1.1389	332.5	-24.9
	06:57	10	B	0.8462	1.1389	332.5	-24.9
	06:58	10	B	0.8462	1.1389	332.5	-24.9
	06:59	10	B	0.8462	1.1390	332.5	-24.9
	06:59	10	B	0.8462	1.1390	332.5	-24.9
	07:00	10	r	0.8462	1.1390	332.5	-24.9
	07:01	10	r	0.8462	1.1390	332.5	-24.9
	07:01	10	r	0.8462	1.1390	332.5	-24.9
	07:02	10	r	0.8462	1.1390	332.5	-24.9
	07:03	10	r	0.8462	1.1390	332.5	-24.9
	07:04	10	B	0.8462	1.1390	332.5	-24.9
	07:04	10	B	0.8462	1.1390	332.5	-24.9
	07:05	10	B	0.8462	1.1390	332.5	-24.9
	07:05	10	B	0.8462	1.1390	332.5	-24.9
	07:06	10	B	0.8462	1.1390	332.5	-24.9
	07:07	10	B	0.8462	1.1390	332.5	-24.9
	07:07	10	B	0.8462	1.1390	332.5	-24.9
	07:08	10	B	0.8462	1.1391	332.5	-24.9
	07:09	10	B	0.8462	1.1391	332.5	-24.9
	07:09	10	B	0.8462	1.1391	332.5	-24.9
	07:10	10	B	0.8462	1.1391	332.5	-24.9
	07:11	10	B	0.8462	1.1391	332.5	-24.9
	07:11	10	B	0.8462	1.1391	332.5	-24.9
	07:12	10	B	0.8462	1.1391	332.5	-24.9
	07:13	10	B	0.8462	1.1391	332.5	-24.9
	07:13	10	B	0.8462	1.1391	332.5	-24.9
	07:14	10	B	0.8462	1.1391	332.5	-24.9
	07:15	10	B	0.8462	1.1391	332.5	-24.9
	07:15	10	B	0.8462	1.1391	332.5	-24.9
	07:16	10	B	0.8462	1.1392	332.5	-24.9
Jan 05	06:46	10	B	0.8516	1.1555	331.5	-25.2
	06:48	10	B	0.8516	1.1555	331.5	-25.2
	06:49	60	B	0.8516	1.1556	331.5	-25.2
	06:51	60	B	0.8516	1.1556	331.5	-25.2
	06:53	60	B	0.8517	1.1556	331.5	-25.2

	06:54	60	B	0.8517	1.1556	331.5	-25.2
	06:56	60	B	0.8517	1.1556	331.5	-25.2
	06:57	60	B	0.8517	1.1556	331.5	-25.2
	06:59	60	r	0.8517	1.1557	331.5	-25.2
	07:00	60	r	0.8517	1.1557	331.5	-25.2
	07:02	60	r	0.8517	1.1557	331.5	-25.2
	07:03	60	B	0.8517	1.1557	331.5	-25.2
	07:05	10	B	0.8517	1.1557	331.5	-25.2
	07:06	10	B	0.8517	1.1557	331.5	-25.2
	07:08	60	B	0.8517	1.1558	331.5	-25.2
	07:10	60	B	0.8517	1.1558	331.5	-25.2
	07:11	60	B	0.8517	1.1558	331.5	-25.2
	07:13	60	B	0.8517	1.1558	331.5	-25.2
	07:15	60	B	0.8517	1.1559	331.5	-25.2
	07:17	120	B	0.8517	1.1559	331.5	-25.2
Jan 06	06:43	10	B	0.8575	1.1719	330.5	-25.6
	06:44	60	B	0.8575	1.1719	330.5	-25.6
	06:46	60	r	0.8575	1.1719	330.5	-25.6
	06:48	90	B	0.8575	1.1720	330.5	-25.6
	06:51	60	B	0.8575	1.1720	330.5	-25.6
	06:54	90	B	0.8575	1.1720	330.5	-25.6
	06:55	60	B	0.8575	1.1720	330.5	-25.6
	06:57	60	r	0.8575	1.1721	330.5	-25.6
	06:59	90	B	0.8576	1.1721	330.5	-25.6
	07:02	89	r	0.8576	1.1721	330.5	-25.6
	07:04	90	B	0.8576	1.1721	330.5	-25.6
	07:06	90	B	0.8576	1.1722	330.5	-25.6
	07:08	90	B	0.8576	1.1722	330.5	-25.6
	07:10	90	B	0.8576	1.1722	330.5	-25.6
	07:12	60	B	0.8576	1.1722	330.5	-25.6
Jan 07	06:44	10	B	0.8637	1.1880	329.4	-25.9
	06:46	90	B	0.8637	1.1880	329.4	-25.9
	06:48	90	B	0.8637	1.1881	329.4	-25.9
	06:50	90	r	0.8638	1.1881	329.4	-25.9
	06:52	90	r	0.8638	1.1881	329.4	-25.9
	06:54	90	B	0.8638	1.1881	329.4	-25.9
	06:58	90	B	0.8638	1.1882	329.4	-25.9
	07:00	90	B	0.8638	1.1882	329.4	-25.9
	07:02	90	r	0.8638	1.1882	329.4	-25.9
	07:04	90	r	0.8638	1.1882	329.4	-25.9
	07:07	120	B	0.8638	1.1883	329.4	-25.9

Table 8-2: INT observing log for comet C/2013 R1 (Lovejoy). Observers were Ramanjooloo, Y. (PI) and Birkett, K. Images were calibrated, stacked and a difference image was obtained from the stacked images.

References

A'Hearn, M.F. et al., 1984. Comet Bowell 1980b. *Astronomical journal*, 89, pp.579–591.

Altschuler, M.D. & Newkirk, G., 1969. Magnetic fields and the structure of the solar corona - I: Methods of calculating coronal fields. *Solar Physics*, 9(1), pp.131–149.

Altwegg, K. et al., 1999. Cometary materials: Progress toward understanding the composition in the outer solar nebula. *Space Science Reviews*, 90(1-2), pp.373–389.

Altwegg, K. et al., 2015. 67P/Churyumov-Gerasimenko, a Jupiter family comet with a high D/H ratio. *Science*, 347(6220).

Auster, H.U. et al., 2015. The nonmagnetic nucleus of comet 67P/Churyumov-Gerasimenko. *Science Express*, (April).

Bailey, M., 1992. Origin of sungrazers-A frequent cometary end-state. *Astronomy and Astrophysics*, 257(1), pp.315–322.

Belton, M.J.S. & Brandt, J.C., 1966. Interplanetary Gas. XII. a Catalogue of Comet-Tail Orientations. *The Astrophysical Journal Supplement Series*, 13, p.125.

Benn, C.R. & Ellison, S.L., 1998. La Palma Night-Sky Brightness. *La Palma technical note 115*. Available at: http://www.ing.iac.es/Astronomy/observing/conditions/skybr/skybr.html.

Bertucci, C. et al., 2011. The Induced Magnetospheres of Mars, Venus, and Titan. *Space Science Reviews*, 162(1-4), pp.113–171.

Biermann, L., 1957. Solar corpuscular radiation and the interplanetary gas. *The Observatory*, 77, pp.109–110.

Biesecker, D. a. et al., 2002. Sungrazing Comets Discovered with the SOHO/LASCO Coronagraphs 1996–1998. *Icarus*, 157(2), pp.323–348.

Blanco, J.J. et al., 2013. Energetic-particle-flux decreases related to magnetic cloud passages as observed by the Helios 1 and 2 spacecraft. *Astronomy & Astrophysics*, 556(A146).

Bockelée-Morvan, D. et al., 2004. The composition of cometary volatiles. In M. C. Festou, H. U. Keller, & H. A. Weaver, eds. *Comets II*. Tucson, AZ: Univ. Arizona Press, pp. 391–423.

Bouratzis, C. et al., 2010. CME on CME Interaction on January 17, 2005. , (2004), p.2.

Brandt, J.C., 1967. Interplanetary Gas. XIII. Gross Plasma Velocities from the Orientations of Ionic Comet Tails. *The Astrophysical Journal*, 147, p.201.

Brandt, J.C., 1968. The Physics of Comet Tails. *Annual Review of Astronomy and Astrophysics*, 6(1), pp.267–286.

Brandt, J.C. & Heise, J., 1970. Interplanetary Gas. XV. Nonradial Plasma Motions from the Orientations of Ionic Comet Tails. *The Astrophysical Journal*, 159, p.1057.

Brandt, J.C., Roosen, R.G. & Harrington, R.S., 1972. Interplanetary gas. XVII. an astrometric determination of solar wind velocities from orientations of ionic comet tails. *The Astrophysical Journal*, 177, p.277.

Brandt, J.C., Harrington, S.R. & Roosen, R.G., 1973. Interplanetary Gas. XIX. Observational Evidence for a Meridional Solar-Wind Flow Diverging from the Plane of the Solar Equator. *The Astrophysical Journal*, 184, p.27.

Brandt, J.C. et al., 1997. Comet de Vico (122P) and latitude variations of plasma phenomena. *Planetary and Space Science*, 45(7), pp.813–819.

Brandt, J.C., 1999. Disconnection Events (DEs) in Halley's Comet 1985–1986: The Correlation with Crossings of the Heliospheric Current Sheet (HCS). *Icarus*, 137(1), pp.69–83.

Brandt, J.C. & Snow, M., 2000. Heliospheric Latitude Variations of Properties of Cometary Plasma Tails: A Test of the Ulysses Comet Watch Paradigm. *Icarus*, 148(1), pp.52–64.

Brandt, J.C. & Chapman, R.D., 2004. *Introduction to comets* 2nd ed., Cambridge Univ. Press.

Brown, M.E. et al., 1998. Sodium Velocities and Sources in Hale–Bopp. *Icarus*, 134(2), pp.228–234.

Brueckner, G.E. et al., 1995. The Large Angle Spectroscopic Coronagraph (LASCO). *Solar Physics*, 162(1-2), pp.357–402.

Buffington, a. et al., 2008. Analysis of Plasma Tail Motions for Comets C/2001 Q4 (NEAT) and C/2002 T7 (LINEAR) Using Observations from SMEI. *The Astrophysical Journal*, 677(1), pp.798–807.

Chiu, M. & Von-Mehlem, U., 1998. ACE spacecraft. *Space Science Reviews*, 86(1/4), pp.257–284.

Clover, J.M. et al., 2010. Solar Wind Speed Inferred from Cometary Plasma Tails using Observations from STEREO HI-1. *The Astrophysical Journal*, 713, pp.394–397.

Coates, a. J., 1997. Ionospheres and magnetospheres of comets. *Advances in Space Research*, 20(2), pp.255–266.

Coates, a. J., 2004. Ion pickup at comets. *Advances in Space Research*, 33(11), pp.1977–1988.

Coates, a. J. & Jones, G.H., 2009. Plasma environment of Jupiter family comets. *Planetary and Space Science*, 57(10), pp.1175–1191.

Cochran, A.L. & Cochran, W.D., 2002. A High Spectral Resolution Atlas of Comet 122P/de Vico. *Icarus*, 157(2), pp.297–308.

Combi, M.R. & Disanti, M. a, 1997. The Spatial Distribution of Gaseous Atomic Sodium in the Comae of Comets : Evidence for Direct Nucleus and Extended Plasma Sources. *Icarus*, 130, pp.336–354.

Combi, M.R., Harris, W.M. & Smyth, W.H., 2004. Gas dynamics and kinetics in the cometary coma: theory and observations. In M. C. Festou, H. U. Keller, & H. A. Weaver, eds. *Comets II*. Tucson, AZ: Univ. Arizona Press, pp. 523–552.

Combi, M.R., Fougere, N., et al., 2014. Unusual Water Production Activity of Comet C/2012 S1 (ISON): Outbursts and Continuous Fragmentation. *The Astrophysical Journal Letters*, 788(1), p.L7.

Combi, M.R., Bertaux, J.-L., et al., 2014. Water Production in Comets C/2011 L4 (PanSTARRS) AND C/2012 F6 (LEMMON) from Observations with SOHO /SWAN. *The Astronomical Journal*, 147(6), p.126.

Cravens, T.E. et al., 1987. Electron impact ionization in the vicinity of comets. *Journal of Geophysical Research*, 92(A7), p.7341.

Cravens, T.E., 1987. Theory and observations of cometary ionospheres. *Advances in Space Research*, 7(12), pp.147–158.

Cravens, T.E., 1991a. Plasma processes in the inner coma. *In: Comets in the post-Halley era. Vol. 2 (A93-13551 02-90)*, 2, pp.1211–1255.

Cravens, T.E., 1991b. *Collisional Processes in Cometary Plasmas* H. Reme, ed., American Geophysical Union.

Cravens, T.E., 2002. X-ray emission from comets. *Science (New York, N.Y.)*, 296(5570), pp.1042–5.

Cravens, T.E., 2004. *Physics of Solar System Plasmas*,

Cravens, T.E. & Gombosi, T.I., 2004. Cometary magnetospheres: a tutorial. *Advances in Space Research*, 33(11), pp.1968–1976.

Cremonese, G. et al., 1997. Neutral sodium from comet Hale-Bopp: a third type of tail. *The Astrophysical Journal*, 490(2), pp.L199–L202.

St. Cyr, O.C. et al., 2000. Properties of coronal mass ejections: SOHO LASCO observations from January 1996 to June 1998. *Journal of Geophysical Research*, 105(A8), pp.18169–18185.

Davidsson, B.J.R., Gutiérrez, P.J. & Rickman, H., 2007. Nucleus properties of Comet 9P/Tempel 1 estimated from non-gravitational force modeling. *Icarus*, 191(2 SUPPL.), pp.547–561.

DeForest, C.E., Howard, T. a. & Tappin, S.J., 2011. Observations of Detailed Structure in the Solar Wind at 1AU with STEREO /HI-2. *The Astrophysical Journal*, 738(1), p.103.

Degroote, P., Bodewits, D. & Reyniers, M., 2008. Folding ion rays in comet C/2004 Q2 (Machholz) and the connection with the solar wind. *Astronomy & Astrophysics*, 477, pp.L41 – L44.

Delsemme, a. H., 1988. The Chemistry of Comets. *Philosophical Transactions of the Royal Society A: Mathematical, Physical and Engineering Sciences*, 325(1587), pp.509–523.

Delva, M. et al., 1991. Comet Halley remote plasma tail observations and in situ solar wind properties: VEGA- IMF/plasma observations and ground-based optical observations from 1 December 1985 to 1 May 1986. *Planetary and Space Science*, 39(5), pp.697–708.

Domingo, V., Fleck, B. & Poland, A.I., 1995. The SOHO mission: An overview. *Solar Physics*, 162(1-2), pp.1–37.

Druckmüller, M. et al., 2014. Imaging Comet ISON C/2012 S1 in the Inner Corona at Perihelion. *The Astrophysical Journal*, 784(2), p.L22.

Erben, T. et al., 2005. GaBoDS: The Garching-Bonn Deep Survey. *Astronomische Nachrichten*, 326(6), pp.432–464.

Eyles, C.J. et al., 2008. The Heliospheric Imagers Onboard the STEREO Mission. *Solar Physics*, 254(2), pp.387–445.

Feldman, P.D., Cochran, A.L. & Combi, M.R., 2004. Spectroscopic investigations of fragment species in the coma. In M. C. Festou, H. U. Keller, & H. A. Weaver, eds. *Comets II*. Tucson, AZ: Univ. Arizona Press, pp. 425–447.

Fernandez, J.A. & Jockers, K., 1983. Nature and origin of comets. *Reports on Progress in Physics*, 46(6), pp.665–772.

Forsyth, R.J. et al., 1997. Ulysses observations of the northward extension of the heliospheric current sheet. *Geophysical Research Letters*, 24(23), pp.3101–3104.

Forsyth, R.J. & Marsch, E., 1999. Solar origin and interplanetary evolution of stream interfaces. *Space Sci. Rev.*, 89, pp.7–20.

Fränz, M. & Harper, D., 2002. Heliospheric coordinate systems. *Planetary and Space Science*, 50(2), pp.217–233.

Fulle, M., 2004. Motion of cometary dust. In M. C. Festou, H. U. Keller, & H. A. Weaver, eds. *Comets II*. Tucson, AZ: Univ. Arizona Press, pp. 565–575.

Fulle, M. et al., 2007. Discovery of the Atomic Iron Tail of Comet M c Naught Using the Heliospheric Imager on STEREO. *The Astrophysical Journal*, 661(1), pp.L93–L96.

Gicquel, A. et al., 2014. The evolution of volatile production in C/2009 P1 (Garradd) during its 2011-2012 apparition. *Asteroids, Comets, Meteors 2014 Conference proceedings*, 30 June - (Edited by K. Muinonen et al.).

Giordano, S. et al., 2015. PROBING THE SOLAR WIND ACCELERATION REGION WITH THE SUN-GRAZING COMET C/2002 S2. *The Astrophysical Journal*, 798(1), p.47.

Giorgini, J.D. et al., 1996. JPL's On-Line Solar System Data Service. *American Astronomical Society*, 28.

Gopalswamy, N., 2005. Coronal mass ejections and other extreme characteristics of the 2003 October–November solar eruptions. *Journal of Geophysical Research*, 110(A9), p.A09S15.

Gopalswamy, N. et al., 2009. The SOHO/LASCO CME catalog. In *Earth, Moon and Planets*. pp. 295–313.

Gosling, J.T. et al., 1993. Solar wind corotating stream interaction regions out of the ecliptic plane: Ulysses. *Geophysical Research Letters*, 20(24), pp.2789–2792.

Gosling, J.T. & Pizzo, V.J., 1999. Formation and Evolution of Corotating Interaction Regions and their Three Dimensional Structure. *Space Science Reviews*, 89(1/2), pp.21–52.

Gundlach, B., Blum, J. & Keller, H.U., 2012. A note on the survival of the sungrazing comet C/2011 W3 (Lovejoy) within the Roche limit. *arXiv*, 3, pp.1–5.

Hapgood, M.A., 1992. Space physics coordinate transformations: A user guide. *Planetary and Space Science*, 40(5), pp.711–717.

Harris, W.M., 1997. Evidence for Interacting Gas Flows and an Extended Volatile Source Distribution in the Coma of Comet C/1996 B2 (Hyakutake). *Science*, 277(5326), pp.676–681.

Hildreth, E.C., 1985. Edge Detection. , 207, pp.187–217.

Hoeksema, J.T., 1991. Large-scale solar and heliospheric magnetic fields. *Advances in Space Research*, 11(1), pp.15–24.

Hoffmeister, C., 1943. Physikalische Untersuchungen an Kometen. I. Die Beziehungen des primären Schweifstrahls zum Radiusvektor. *Zeitschrift für Astrophysik*, 22, p.265.

Hogg, D.W., Lang, D. & Bailer-Jones, C.A.L., 2008. Astronomical imaging: The theory of everything. In *AIP Conference Proceedings*. AIP, pp. 331–338.

Howard, R.A. et al., 2008. Sun Earth Connection Coronal and Heliospheric Investigation (SECCHI). *Space Science Reviews*, 136(1-4), pp.67–115.

Hsieh, H.H. & Jewitt, D., 2006. A population of comets in the main asteroid belt. *Science (New York, N.Y.)*, 312(5773), pp.561–3.

Hundhausen, A.J., 1972. *Coronal Expansion and Solar Wind*, Berlin, Heidelberg: Springer Berlin Heidelberg.

Ip, W.-H., 1980. On the dynamical response of a cometary ion tail to a solar-wind event. *The Astrophysical Journal*, 238, p.388.

Ip, W.-H., 2004. Global solar wind interaction and ionospheric dynamics. In M. C. Festou, H. U. Keller, & H. A. Weaver, eds. *Comets II*. Tucson, AZ: Univ. Arizona Press, pp. 605–629.

Iseli, M., 2002. Sungrazing Comets: Properties of Nuclei and in Situ Detectability of Cometary Ions at 1 AU. *Icarus*, 155(2), pp.350–364.

Ivanova, O., Borysenko, S. & Golovin, A., 2014. Photometry of Comet C/2011 L4 (PANSTARRS) at 4.4–4.2AU heliocentric distances. *Icarus*, 227, pp.202–205.

Jia, Y.D. et al., 2009. Study of the April 20, 2007 CME-Comet Interaction Event with an MHD Model. *The Astrophysical Journal*, 696(1), p.13.

Jockers, K., 1981. Plasma dynamics in the tail of Comet Kohoutek 1973 XII. *Icarus*, 47(3), pp.397–411.

Jones, G., Balogh, A. & Horbury, T., 2000. Identification of comet Hyakutake's extremely long ion tail from magnetic field signatures. *Nature*, 404(April), pp.7–9.

Jones, G.H. et al., 2002. The draping of heliospheric magnetic fields upstream of coronal mass ejecta. *Geophysical Research Letters*, 29(11).

Jones, G.H., Balogh, A. & Smith, E.J., 2003. Solar magnetic field reversal as seen at Ulysses. *Geophysical Research Letters*, 30(19), p.8028.

Jones, G.H. & Brandt, J.C., 2004. The interaction of comet 153P/Ikeya-Zhang with interplanetary coronal mass ejections: Identification of fast ICME signatures. *Geophysical Research Letters*, 31(20), p.L20805.

Kaiser, M.L., 2005. The STEREO mission: An overview. In *Advances in Space Research*. pp. 1483–1488.

Keller, H.U. et al., 2004. In situ observations of cometary nuclei. In M. C. Festou, H. U. Keller, & H. A. Weaver, eds. *Comets II*. Tucson, AZ: Univ. Arizona Press, pp. 211–222.

Kimura, H. & Mann, I., 1998. Brightness of the solar F -corona. *Earth, Planets and Space*, 50(1996), pp.493–499.

Kimura, H., 2002. Dust Grains in the Comae and Tails of Sungrazing Comets: Modeling of Their Mineralogical and Morphological Properties. *Icarus*, 159(2), pp.529–541.

Kivelson, M.G. & Russell, C.T., 1995. *Introduction to Space Physics*,

Knight, M.M. & Hearn, A.M.F.A., 2008. Studies of SOHO Comets. *PhD Thesis*, p.202 pages.

Knight, M.M. et al., 2010. Photometric study of the Kreutz Comets Observed by SOHO from 1996 to 2005. *The Astronomical Journal*, 139(3), pp.926–949.

Knight, M.M. et al., 2012. A Multiwavelength Investigation of the Remains of Sungrazing Comet Lovejoy (C/2011 W3). *Asteroids*.

Knight, M.M. & Battams, K., 2014. Preliminary Analysis of SOHO/STEREO Observations of Sungrazing Comet ISON (C/2012 S1) Around Perihelion. *The Astrophysical Journal*, 782(2), p.L37.

Konopleva, V.P. & Rozenbush, V.K., 1974. Perspective projection of cometary images on to the orbital plane. *Astrometriia i Astrofizika*, 22, pp.61–69.

Kuchar, T. a. et al., 2008. Observations of a comet tail disruption induced by the passage of a CME. *Journal of Geophysical Research: Space Physics*, 113, pp.1–11.

Lamy, P.L. et al., 2004. The sizes, shapes, albedos, and colors of cometary nuclei. In M. C. Festou, H. U. Keller, & H. A. Weaver, eds. *Comets II*. Tucson, AZ: Univ. Arizona Press, pp. 223–264.

Lamy, P. et al., 2013. Sunskirting comets discovered with the LASCO coronagraphs over the decade 1996–2008. *Icarus*, 226(2), pp.1350–1398.

Lang, D. et al., 2010. Astrometry.net: Blind Astrometric Calibration of Arbitrary Astronomical Images. *The Astronomical Journal*, 139(5), pp.1782–1800.

Lang, D. & Hogg, D.W., 2012. Searching for Comets on the World Wide Web: The Orbit of 17P/Holmes from the Behaviour of Photographers. *The Astronomical Journal*, 144(2), p.46.

Linker, J.A. et al., 1999. Magnetohydrodynamic modeling of the solar corona during Whole Sun Month. *Journal of Geophysical Research*, 104(A5), p.9809.

Lisse, C.M. et al., 2001. Charge exchange-induced X-ray emission from comet C/1999 S4 (LINEAR). *Science (New York, N.Y.)*, 292(5520), pp.1343–8.

Llebaria, A., Lamy, P.L. & Bout, M. V., 2004. Lessons Learnt from the SOHO LASCO-C2 Coronagraph. In S. Fineschi & M. A. Gummin, eds. *Optical Science and Technology, SPIE's 48th Annual Meeting*. International Society for Optics and Photonics, pp. 26–37.

Luhmann, J.G., Ledvina, S. a. & Russell, C.T., 2004. Induced magnetospheres. *Advances in Space Research*, 33(11), pp.1905–1912.

Marsch, E., 2006. Solar wind responses to the solar activity cycle. *Advances in Space Research*, 38(5), pp.921–930.

Marsden, B.G., 1967. The sungrazing comet group. *The Astronomical Journal*, 72, p.1170.

Marsden, B.G., 2009. Orbital properties of Jupiter-family comets. *Planetary and Space Science*, 57(10), pp.1098–1105.

McCauley, P.I. et al., 2013. Extreme-Ultraviolet and X-Ray Observations of Comet Lovejoy (C/2011 W3) in the Lower Corona. *The Astrophysical Journal*, 768(2), p.161.

McComas, D.J. et al., 1998. Solar Wind Electron Proton Alpha Monitor (SWEPAM) for the Advanced Composition Explorer. *Space Science Reviews*, (1), pp.563–612.

McComas, D.J., 2002. Solar wind from high-latitude coronal holes at solar maximum. *Geophysical Research Letters*, 29(9), p.1314.

McComas, D.J. et al., 2008. Weaker solar wind from the polar coronal holes and the whole Sun. *Geophysical Research Letters*, 35(18), pp.1–5.

Meech, K.J., Jewitt, D. & Ricker, G.R., 1986. Early photometry of comet p/Halley - Development of the coma. *Icarus*, 66(3), pp.561–574.

Meech, K.J., Hainaut, O.R. & Marsden, B.G., 2004. Comet nucleus size distributions from HST and Keck telescopes. *Icarus*, 170(2), pp.463–491.

Merkin, V.G. et al., 2011. Disruption of a heliospheric current sheet fold. *Geophysical Research Letters*, 38(14), p.n/a–n/a.

Mikic, Z. et al., 1999. Magnetohydrodynamic modeling of the solar corona. *Physics of Plasmas*, 6(2217).

Minami, S. & White, R.S., 1986. An acceleration mechanism for cometary plasma tails. *Geophysical Research Letters*, 13(8), pp.849–852.

Moore, E., 1991. Cometary ray closing rates-Comet Kobayashi-Berger-Milon. *Astronomy and Astrophysics*, 247(1), pp.247–251.

Morrill, J.S. et al., 2006. Calibration of the Soho/Lasco C3 White Light Coronagraph. *Solar Physics*, 233(2), pp.331–372.

Ness, N.F. & Donn, B.D., 1966. Concerning a new theory of type I comet tails. *Mem. Soc. R. Liege*, 5(12), pp.141–144.

Neubauer, F.M., 1990. Magnetic field regions formed by the interaction of the solar wind plasma with comet Halley. In E. Horwood, ed. *Comet Halley. Investigations, results, interpretations*. pp. 79–96.

Neugebauer, M. et al., 2000. The relation of temporal variations of soft X-ray emission from comet Hyakutake to variations of ion fluxes in the solar wind. *Journal of Geophysical Research*, 105, p.20949.

Niedner, M.B.J. & Brandt, J., 1978. Interplanetary gas. XXII-Plasma tail disconnection events in comets-Evidence for magnetic field line reconnection at interplanetary sector boundaries. *The Astrophysical Journal*, 223, pp.655–670.

Nilsson, H. et al., 2015. Birth of a comet magnetosphere: A spring of water ions. *Science (New York, N.Y.)*, 347(6220).

Odstrcil, D., 2003. Modeling 3-D solar wind structure. *Advances in Space Research*, 32(4), pp.497–506.

Owens, M.J. & Cargill, P., 2004. Non-radial solar wind flows induced by the motion of interplanetary coronal mass ejections. *Annales Geophysicae*, 22, pp.4397–4406.

Owens, M.J. & Forsyth, R.J., 2013. The Heliospheric Magnetic Field. *Living Reviews in Solar Physics*, 10.

Popowicz, a, Kurek, a. R. & Filus, Z., 2013. Bad Pixel Modified Interpolation for Astronomical Images. *Publications of the Astronomical Society of the Pacific*, 125(September), pp.1119–1125.

Rasca, A.P., Oran, R. & Horányi, M., 2014. Mass loading of the solar wind by a sungrazing comet. *Geophysical Research Letters*, 41(15), pp.5376–5381.

Rauer, H. & Jockers, K., 1990. Focal Reducer Observations of Comets Liller 1988a and P/Tempel 2 1987g. *Asteroids, comets, meteors III, Proceedings of a meeting (AMC 89)*, p.417.

Rauer, H. & Jockers, K., 1993. Doppler Measurements of the H2O+ Ion Velocity in the Plasma Tail of Comet Levy 1990c. *Icarus*, 102(1), pp.117–133.

Raymond, J.C. et al., 2014. The Solar Corona as Probed by Comet Lovejoy (C/2011 W3). *The Astrophysical Journal*, 788(2), p.152.

Reme, H., 1991. Cometary plasma observations between the shock and the contact surface. In A. Johnstone, ed. *Geophysical Monograph Series*. American Geophysical Union, Washington, D. C., pp. 87–105.

Reyniers, M. et al., 2009. The rotation and coma profiles of comet C/2004 Q2 (Machholz). *Astronomy & Astrophysics*, 494(1), pp.379–389.

Richardson, J.D. et al., 1996. Non-Radial Flows in the Solar Wind. In D. Winterhalter, ed. *AIP Conference Proceedings*. p. 479.

Rickman, H., 1989. The nucleus of comet Halley: Surface structure, mean density, gas and dust production. *Advances in Space Research*, 9(3), pp.59–71.

Rickman, H. & Huebner, W.F., 1990. Comet formation and evolution. In W. F. Huebner, ed. *Physics and chemistry of comets*. Springer-Verlag, Berlin & Heidelberg, pp. 245–302.

Robbrecht, E. & Berghmans, D., 2004. Automated recognition of coronal mass ejections (CMEs) in near-real-time data. *Astronomy and Astrophysics*, 425(3), pp.1097–1106.

Robbrecht, E., Berghmans, D. & Van der Linden, R. a. M., 2008. Automated LASCO CME catalog for solar cycle 23: are CMEs scale invariant? , (1997), p.13.

Roberts, L.G., 1965. Machine Perception of Three-Dimensional Solids. In J. T. Tippett et al., ed. *Optical and Electro-Optical Information Processing*. MIT Press, Cambridge, Mass., pp. 159–197.

Rouillard, a. P. et al., 2008. First imaging of corotating interaction regions using the STEREO spacecraft. *Geophysical Research Letters*, 35(10), p.L10110.

Russell, C.T. et al., 1986. Near-tail reconnection as the cause of cometary tail disconnections. *Journal of Geophysical Research*, 91(A2), pp.1417–1423.

Schatten, K.H., Wilcox, J.M. & Ness, N.F., 1969. A model of interplanetary and coronal magnetic fields. *Solar Physics*, 6(3), pp.442–455.

Scherb, F. et al., 1990. Fabry-Perot observations of Comet Halley H2O+. *Icarus*, 86(1), pp.172–188.

Schirmer, M., 2013. THELI: Convenient Reduction of Optical, Near-Infrared, and Mid-Infrared Imaging Data. *The Astrophysical Journal Supplement Series*, 209(2), p.21.

Schlosser, W., 1966. Photographic structures within comet Morehouse 1908 III. *Mem. Soc. R. Liege*, 5(12), pp.335–342.

Schmidt, H.U. & Wegmann, R., 1982. Plasma Flow and Magnetic Fields in Comets. In *Comets. Edited by L.L. Wilkening. Space Science Series. Tucson*. p. 538.

Schrijver, C.J. et al., 2012. Destruction of Sun-grazing comet C/2011 N3 (SOHO) within the low solar corona. *Science (New York, N.Y.)*, 335(6066), pp.324–8.

Schwenn, R., 2001. Solar Wind : Global Properties. *Encyclopedia of Astronomy and Astrophysics*, (785998), pp.1–9.

Sekanina, Z., 2003. Erosion Model for the Sungrazing Comets Observed with the Solar and Heliospheric Observatory. *The Astrophysical Journal*, 597(2), pp.1237–1265.

Sekanina, Z. & Chodas, P.W., 2007. Fragmentation Hierarchy of Bright Sungrazing Comets and the Birth and Orbital Evolution of the Kreutz System. II. The Case for Cascading Fragmentation. *The Astrophysical Journal*, 663(1), pp.657–676.

Sekanina, Z. & Chodas, P.W., 2012. Comet C/2011 W3 (Lovejoy): Orbit Determination, Outbursts, Disintegration of Nucleus, Dust-Tail Morphology, and Relationship to New Cluster of Bright Sungrazers. *The Astrophysical Journal*, 757(2), p.127.

Sekanina, Z., 2013. Brightness and Orbital Motion Peculiarities of Comet C/2012 S1 (ISON): Comparison with Two Very Different Comets. , 1, p.5.

Shen, F. et al., 2012. Acceleration and deceleration of coronal mass ejections during propagation and interaction. *Journal of Geophysical Research: Space Physics*, 117(November), pp.1–12.

Sierks, H. et al., 2015. On the nucleus structure and activity of comet 67P/Churyumov-Gerasimenko. *Science*.

Siscoe, G.L. et al., 1986. Statics and dynamics of Giacobini-Zinner magnetic tail. *Geophysical Research Letters*, 13(3), pp.287–290.

Sizonenko, Y. V., 2007. Comets C/2001 Q4 and C/2004 Q2: Structure of plasma tails. *Kinematics and Physics of Celestial Bodies*, 23(5), pp.207–213.

Skoug, R.M., 2004. Extremely high speed solar wind: 29–30 October 2003. *Journal of Geophysical Research*, 109(A9), p.A09102.

Snow, M. et al., 2004. Comet Hyakutake (C/1996 B2): Spectacular disconnection event and the latitudinal structure of the solar wind. *Planetary and Space Science*, 52(4), pp.313–323.

Sobel, I. & Feldman, G., 1968. A 3x3 Isotropic Gradient Operator for Image Processing. *Stanford Artificial Intelligence Project (SAIL)*.

Taylor, M.G.G.T. et al., 2015. Rosetta begins its Comet Tale. *Science*, 347(6220).

Thomas, N., 2009. The nuclei of Jupiter family comets: A critical review of our present knowledge. *Planetary and Space Science*, 57(10), pp.1106–1117.

Thompson, W.T., 2009. 3D triangulation of a Sun-grazing comet. *Icarus*, 200(2), pp.351–357.

Tsurutani, B.T. et al., 2006. The extreme Halloween 2003 solar flares (and Bastille Day, 2000 Flare), ICMEs, and resultant extreme ionospheric effects: A review. *Advances in Space Research*, 37(8), pp.1583–1588.

Voelzke, M.R., 2005. Disconnection events processes in cometary tails. In *Earth, Moon and Planets*. pp. 399–409.

Vourlidas, A. et al., 2002. Mass and energy properties of LASCO CMEs. *Solar Variability: From Core to Outer Frontiers*, 506, pp.91–94.

Vourlidas, A. et al., 2007. First Direct Observation of the Interaction between a Comet and a Coronal Mass Ejection Leading to a Complete Plasma Tail Disconnection. *The Astrophysical Journal*, 668(1), pp.L79–L82.

Wainscoat, R. et al., 2011. Comet C/2011 L4 (Panstarrs). *IAU Circ.*

Watanabe, J.I., 1991. Measurement of the solar wind velocity with cometary tail rays. *Solar Physics*, 132(2), pp.395–407.

Wegmann, R., 2000. The effect of some solar wind disturbances on the plasma tail of a comet: models and observations. *Astronomy & Astrophysics*, 358, pp.759–775.

Weidenschilling, S., 1997. The Origin of Comets in the Solar Nebula: A Unified Model. *Icarus*, 127(2), pp.290–306.

Weidenschilling, S.J., 2004. From icy grains to comets. In M. C. Festou, H. U. Keller, & H. A. Weaver, eds. *Comets II*. Tucson, AZ: Univ. Arizona Press, pp. 97–104.

Weissman, P.R., Asphaug, E. & Lowry, S.C., 2004. Structure and density of cometary nuclei. In M. C. Festou, H. U. Keller, & H. A. Weaver, eds. *Comets II*. Tucson, AZ: Univ. Arizona Press, pp. 337–357.

Wilson, J.K., Baumgardner, J. & Mendillo, M., 1998. Three tails of comet Hale-Bopp. *Geophysical Research Letters*, 25(3), pp.225–228.

Wolff, R.S. et al., 1985. Cometary rays - Magnetically channeled outflow. *Geophysical Research Letters*, 12, pp.749–752.

Wurm, K. & Mammano, A., 1972. Contributions to the kinematics of type I tails of comets. *Astrophysics and Space Science*, 18(2), pp.273–286.

Yagi, M. et al., 2015. Initial Speed of Knots in the Plasma Tail of C/2013 R1 (Lovejoy). *The Astronomical Journal*, 149(3), p.97.

Yashiro, S. et al., 2004. A catalog of white light coronal mass ejections observed by the SOHO spacecraft. *Journal of Geophysical Research: Space Physics*, 109(A7), pp.1–11.

Yoshida, S., Aerith.net. Available at: http://www.aerith.net/index.html.